

Science

Science
Advances

Science
Immunology

Science
Robotics

Science
Signaling

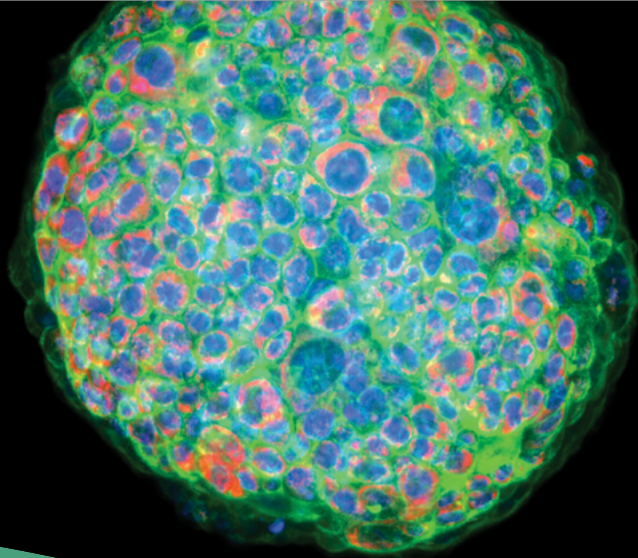
Science
Translational
Medicine

[SPECIAL
EDITION]

NEUROSCIENCE

 AAAS

aaas.org/science-journals



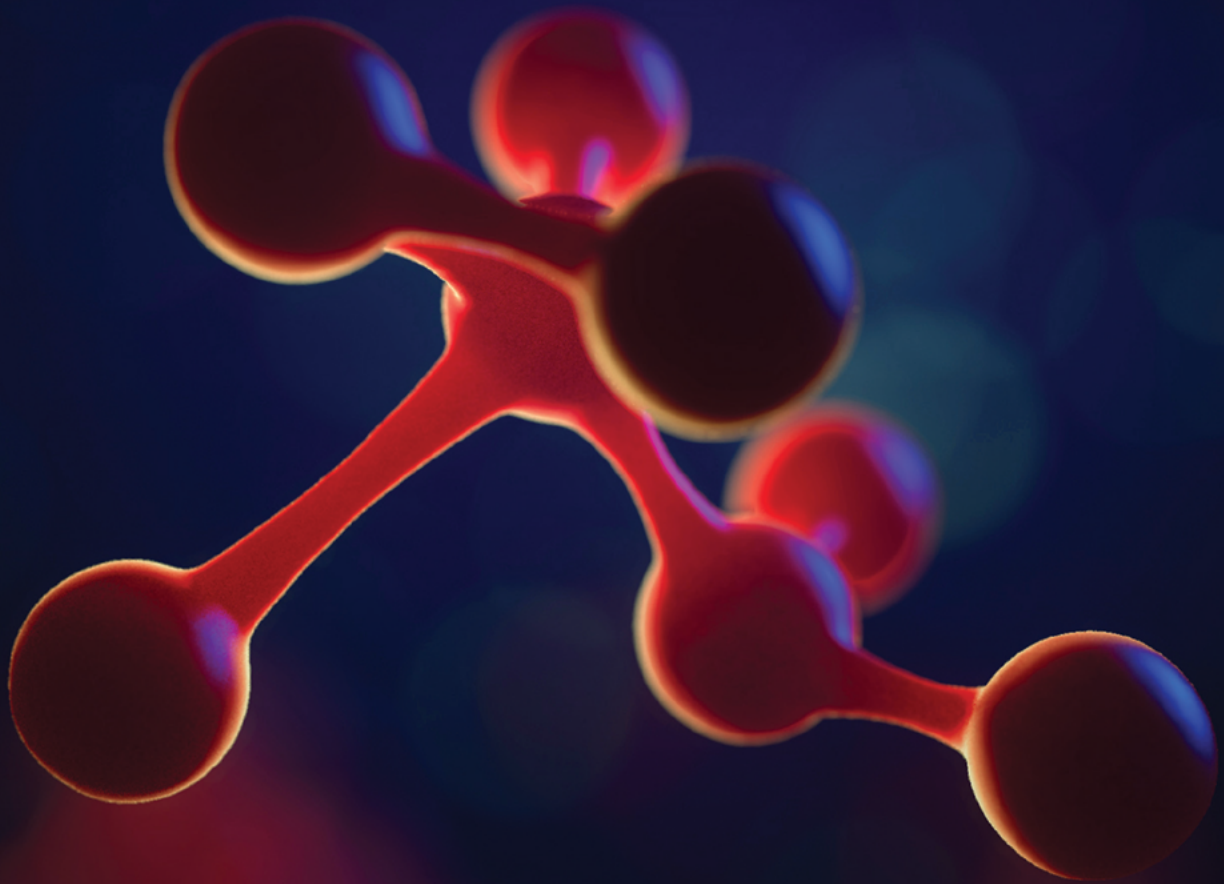
CAPTURE the micro moments that matter

NEW Water Immersion Objectives

Gain the sensitivity to capture more phenotypic data at greater depths. Our high-content imagers and team are here to help your lab simplify imaging and analysis of complex, 3D assay workflows and fast-track discoveries.

Learn more at
moleculardevices.com/water





Publish your research in the *Science* family of journals

The *Science* family of journals (*Science*, *Science Advances*, *Science Immunology*, *Science Robotics*, *Science Signaling*, and *Science Translational Medicine*) are among the most highly-regarded journals in the world for quality and selectivity. Our peer-reviewed journals are committed to publishing cutting-edge research, incisive scientific commentary, and insights on what's important to the scientific world at the highest standards.

Submit your research today!

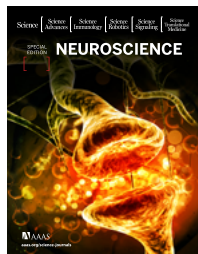
Learn more at [ScienceMag.org/journals](https://www.sciencemag.org/journals)

Science
JOURNALS AAAS

SPECIAL EDITION: Neuroscience

Select research published in *Science*, *Science Advances*, *Science Immunology*, *Science Signaling*, *Science Robotics*, and *Science Translational Medicine*

All *Science* family journals are Green Open Access with the exception of *Science Advances* which is Gold Open Access.



This booklet features research articles from all six journals of the *Science* family. These articles cover a range of topics, including perception, behavior, neuroinflammation, neuroimaging, neurodevelopment, neuroprosthetics, and neurodegenerative diseases.

Image: istock/Mohammed Haneefa Nizamudeen



Editor-in-Chief

H. Holden Thorp, Ph.D.
Science family of journals
AAAS, Washington, DC

Science | AAAS

Science is a leading outlet for scientific news, commentary, and cutting-edge research. The journal publishes original peer-reviewed research across the sciences, with articles that consistently rank among the most cited in the world.

Editors

Lisa D. Chong, Ph.D.
Valda J. Vinson, Ph.D.
Jake S. Yeston, Ph.D.

Neuroscience Editors

Pamela J. Hines, Ph.D.
Stella Hurtley, Ph.D.
Peter Stern, Ph.D.

Science Advances | AAAS OPEN ACCESS

Science Advances is the digital, open access expansion of *Science* magazine. The journal publishes significant, innovative original research that advances the frontiers of science across a broad range of disciplines, from bioscience and medicine to neuroscience, physics, ecology, and material sciences.

Editor

Ali Shilatifard, Ph.D.

Managing Editor

Laura Remis

Deputy Editors

Mark Aldenderfer, Ph.D.
Lynden Archer, Ph.D.
Janelle Ayres, Ph.D.
Julia Chan, Ph.D.
Navdeep Chandel, Ph.D.
Jane Chang, Ph.D.
Aaron Clauset, Ph.D.
Juan de Pablo, Ph.D.
Dale Dorset, Ph.D.
Omolola Eniola-Adefeso, Ph.D.
John Fyfe, Ph.D.
Karen Gleason, Ph.D.
Douglas Green, Ph.D.
Elizabeth Haswell, Ph.D.
Kip Hodges, Ph.D.
Jeremy Jackson, Ph.D.
Mietek Jaroniec, Ph.D.

Ricky Johnstone, Ph.D.
Alexandra Joyner, Ph.D.
Jonathan Katz, Ph.D.
Kevin LaBar, Ph.D.
Michael Levine, Ph.D.
David Lou, Ph.D.
Laura Na Liu, Ph.D.
George Malliaras, Ph.D.
Shahid Naeem, Ph.D.
Geeta Narlikar, Ph.D.
Nicholas Peppas, Sc.D.
John Rogers, Ph.D.
D. James Surmeier, Ph.D.
Leslie Vosshall, Ph.D.
Philip Yeagle, Ph.D.
Warren Warren, Ph.D.

Science Immunology | AAAS

Science Immunology publishes original, peer-reviewed, science-based research articles that report critical advances in all areas of immunological research, including important new tools and techniques.

Editor

Ifor Williams, M.D., Ph.D.

Editorial Team

Claire Olingy, Ph.D.

Science Robotics | AAAS

Science Robotics publishes peer-reviewed, original research articles that advance the field of robotics and provides commentary on the latest developments in robotics and related technologies.

Chief Scientific Advisor

and Founding Editor
Guang-Zhong Yang, Ph.D.
Shanghai Jiao Tong University

Editor

Michael M. Lee, DPhil

Editorial Team

Trista Wagoner
Brianna Costache

Editorial Board

Howie Choset, Ph.D.
Steve Collins, Ph.D.
Peer Fischer, Ph.D.
Dario Floreano, Ph.D.
Ken Goldberg, Ph.D.
Neil Jacobstein
Danica Kragic, Ph.D.
Cecilia Laschi, Ph.D.
Hod Lipson, Ph.D.
Brad Nelson, Ph.D.
Robert Wood, Ph.D.
Yulia Sandamirskaya, Ph.D.

Science Signaling | AAAS

Science Signaling publishes peer-reviewed, original research investigating cell signaling that underlies physiology and disease, on the molecular, cellular, intercellular and organismal levels.

Chief Scientific Advisor

and Academic Editor
Michael B. Yaffe, M.D., Ph.D.
Massachusetts Institute of Technology

Editor

John F. Foley, Ph.D.

Deputy Editor

Wei Wong, Ph.D.

Editorial Team

Leslie K. Ferrarelli, Ph.D.
Annalisa M. VanHook, Ph.D.

Science Translational Medicine | AAAS

Science Translational Medicine is an interdisciplinary journal that publishes translational research with impact for human health that fills the knowledge gaps between preclinical studies and clinical applications.

Chief Scientific Advisors

Elazer R. Edelman, M.D., Ph.D.
Massachusetts Institute of Technology
Garret FitzGerald, M.D.
University of Pennsylvania

Editor

Orla M. Smith, Ph.D.

Editorial Team

Catherine A. Charneski, Ph.D.
Caitlin A. Czajka, Ph.D.
Courtney Malo, Ph.D.
Mattia Maroso, Ph.D.
Melissa Norton, M.D.

Learn more and submit your research today: [aas.org/science-journals](https://www.aas.org/science-journals)

COUNTER INTELLIGENCE

The Scepter™ 3.0 Automated Handheld Cell Counter

Upgrade your tissue culture room by getting accurate cell counts quickly, and recording results digitally. Our Scepter™ 3.0 handheld cell counter combines smart capabilities with the Coulter impedance principal to hand you precise, consistent counts in seconds.



Accuracy you can count on, smarter than ever.

To learn more, visit SigmaAldrich.com/Scepter



© 2019 Merck KGaA, Darmstadt, Germany and/or its affiliates. All Rights Reserved. MilliporeSigma and the vibrant M are trademarks of Merck KGaA, Darmstadt, Germany or its affiliates. All other trademarks are the property of their respective owners. Detailed information on trademarks is available via publicly accessible resources. 2019-21675

The life science business of Merck KGaA, Darmstadt, Germany operates as MilliporeSigma in the U.S. and Canada.

Millipore®

Preparation, Separation, Filtration & Monitoring Products

IN THIS BOOKLET

Science

- 7** **REPORT**
Microglia mediate forgetting via complement-dependent synaptic elimination
Chao Wang *et al.* (Yan Gu)
- 13** **RESEARCH ARTICLE**
Huntington's disease alters human neurodevelopment
Monia Barnat *et al.* (Alexandra Durr and Sandrine Humbert)

Science Advances

- 20** **RESEARCH ARTICLE**
Non-neuronal expression of SARS-CoV-2 entry genes in the olfactory system suggests mechanisms underlying COVID-19-associated anosmia
David H. Brann *et al.* (Sandeep Robert Datta)
- 39** **RESEARCH ARTICLE**
Temporal circuit of macroscale dynamic brain activity supports human consciousness
Zirui Huang *et al.* (Anthony G. Hudetz)

Science Immunology

- 54** **RESEARCH ARTICLE**
T cell engagement of cross-presenting microglia protects the brain from a nasal virus infection
E. Ashley Moseman *et al.* (Dorian B. McGavern)
- 67** **RESEARCH ARTICLE**
Human antibodies neutralize enterovirus D68 and protect against infection and paralytic disease
Matthew R. Vogt *et al.* (James E. Crowe Jr.)

Science Robotics

- 80** **RESEARCH ARTICLE**
Beyond imitation: Zero-shot task transfer on robots by learning concepts as cognitive programs
Miguel Lázaro-Gredilla *et al.* (Dileep George)
- 95** **FOCUS**
Toward high-performance, memory-efficient, and fast reinforcement learning—Lessons from decision neuroscience
Jee Hang Lee *et al.* (Sang Wan Lee)

Science Signaling

- 98** **RESEARCH ARTICLE**
 μ -Opioid receptor-induced synaptic plasticity in dopamine neurons mediates the rewarding properties of anabolic androgenic steroids
Leonardo Bontempi and Antonello Bonci
- 109** **RESEARCH RESOURCE**
A dynamic mouse peptidome landscape reveals probiotic modulation of the gut-brain axis
Pei Zhang *et al.* (Chenxi Jia)

Science Translational Medicine

- 123** **RESEARCH ARTICLE**
Prospective longitudinal atrophy in Alzheimer's disease correlates with the intensity and topography of baseline tau-PET
Renaud La Joie *et al.* (Gil D. Rabinovici)
- 135** **RESEARCH ARTICLE**
Gene therapy delivering a paraoxonase 1 variant offers long-term prophylactic protection against nerve agents in mice
Venkaiah Betapudi *et al.* (Nageswararao Chilukuri)



Publisher/Science family of journals: **Bill Moran**
AD/Business Development: **Justin Sawyers**
Marketing Manager: **Shawana Arnold**
Layout/Design: **Kim Huynh**

Sponsorship Opportunities:

Tracy Holmes, *Science*
tholmes@science-int.co.uk | (44) 1223 326525 ext 5525
1200 New York Ave NW, Washington DC 20005

Learn more and submit your research today: aaas.org/science-journals

NEUROSCIENCE

Copyright © 2020. The Authors, some rights reserved *

Microglia mediate forgetting via complement-dependent synaptic elimination

Chao Wang^{1,2*}, Huimin Yue^{1,2*}, Zhechun Hu^{1,2}, Yuwen Shen^{1,2}, Jiao Ma³, Jie Li^{1,2}, Xiao-Dong Wang^{4,5}, Liang Wang⁶, Binggui Sun⁷, Peng Shi⁸, Lang Wang^{3,†}, Yan Gu^{1,2,9,†}

Synapses between engram cells are believed to be substrates for memory storage, and the weakening or loss of these synapses leads to the forgetting of related memories. We found engulfment of synaptic components by microglia in the hippocampi of healthy adult mice. Depletion of microglia or inhibition of microglial phagocytosis prevented forgetting and the dissociation of engram cells. By introducing CD55 to inhibit complement pathways, specifically in engram cells, we further demonstrated that microglia regulated forgetting in a complement- and activity-dependent manner. Additionally, microglia were involved in both neurogenesis-related and neurogenesis-unrelated memory degradation. Together, our findings revealed complement-dependent synapse elimination by microglia as a mechanism underlying the forgetting of remote memories.

Memory is coded and allocated to engrams within related brain regions (1, 2). Reactivation of engram cells is essential for memory recall, whereas failure in reactivation of engram cells leads to the forgetting of related memories (3). Synaptic connections between engram cells are believed to be substrates for memory storage (4, 5). Circuit rewiring and synaptic reorganization may lead to loss or weakening of synaptic connections between engram cells, resulting in the forgetting of previously existing memories. For example, massive synaptic reorganization takes place in the dentate gyrus (DG) as continuously generated newborn neurons integrate into the hippocampal neural circuit, which leads to the forgetting of hippocampus-dependent memories (6–8). Even in mature neurons, experience- and learning-dependent, dynamic remodeling of synapses occurs con-

stantly throughout life (9–13), providing a potential mechanism for the erasure of stored memories in the synaptic connections of these cells. Microglia are not only important for pruning excessive synapses during postnatal brain development but are also involved in the dynamics of synapses in the adult brain (14–17). Because they survey the brain and play crucial roles in monitoring synapses and determining the wiring of the brain (15, 18, 19), microglia may affect the stability of synaptic connections within the neural circuits where memories are allocated.

First, we used contextual fear conditioning (CFC) to assess the memory retention in C57BL/6 mice. We measured the freezing behavior of the animals during a test performed 5 or 35 days after three training sessions, each training session consisting of three weak foot shocks (Fig. 1A). We observed a significant decrease in the freezing of animals at 35 days compared with 5 days after training (Fig. 1B). We then carried out CFC training using CD11b-DTR mice, in which diphtheria toxin receptor (DTR) is specifically expressed in CD11b-expressing myeloid cells, including microglia in the brain (20). By intracerebroventricularly administering diphtheria toxin (DT) daily after training, we depleted microglia in these CD11b-DTR mice until the test (fig. S1). Thirty-five days later, CD11b-DTR mice treated with DT showed significantly higher freezing levels than those in the saline group (fig. S1). To avoid the effect of daily injection on animal behaviors, we depleted microglia in C57BL/6 mice with PLX3397 (PLX), a CSF1R/c-kit antagonist (21), via mouse diet after CFC training (Fig. 1C). Thirty-five days later, PLX treatment significantly increased freezing of the animals (Fig. 1D), with microglia depleted in the brain (Fig. 1, E and F), consistent with the results obtained from CD11b-DTR mice.

To exclude the possibility that depleting microglia may affect formation or retrieval

of memories, we tested the freezing of mice a short time (5 days) after training (fig. S2A). We found that PLX treatment did not alter the freezing of animals (fig. S2B). Furthermore, we started administration of PLX to deplete microglia before the training and tested 24 hours later (fig. S2C). No significant difference was observed between control and PLX-treated animals (fig. S2D). Further behavioral tests showed that PLX treatment for 35 days did not significantly change the behavior of animals in an elevated plus maze or an open field (fig. S3).

Memory retrieval requires reactivation of engram cells (3), whereas dissociation of engram cells—i.e., engram cells being unable to reactivate at the same time—leads to forgetting. To test whether the microglia-mediated forgetting of already-formed memory correlates with dissociation of engram cells, we used a FosTRAP strategy for tagging activated neurons during CFC training (22). We trained c-Fos-Cre^{EKT2}::Ai14 mice for contextual fear memory and administered tamoxifen (TAM) before the last training session to induce permanent expression of dTomato in activated engram neurons. Immunofluorescent staining for c-Fos was performed after the test, and the reactivation rate of engram cells was assessed by analyzing c-Fos⁺dTomato⁺ colocalization in the DG (Fig. 1, G and H). Under physiological conditions, the reactivation rate of engram cells 35 days after training significantly decreased compared with that measured at 5 days, which correlates with the forgetting of related memory (Fig. 1I). Thirty-five days but not 5 days after training, PLX treatment significantly increased the reactivation rate of the engram cells (Fig. 1I), without altering the number of dTomato⁺ engram cells in the DG (fig. S4). The freezing of animals during the test positively correlates with the reactivation rate of engram cells (Fig. 1J).

During postnatal development, microglia are involved in synaptic reorganization and circuitry refinement by synaptic pruning (15). We imaged microglia in the DG of adult CX3CR1^{GFP/+} mice, in which microglia were labeled with green fluorescent protein (GFP). When costained with synaptophysin or PSD95, markers for pre- or postsynaptic components, we found synaptophysin⁺ and PSD95⁺ puncta were present in GFP⁺ microglia, colocalizing with lysosome marker Lamp1 (Fig. 2, A and B, and movies S1 and S2).

To test whether synaptic elimination by microglial phagocytosis may mediate forgetting, we systemically administered minocycline (Mino)—which has been shown to inhibit microglial engulfment of synapses in vitro and in vivo (15, 23)—after CFC training until the test (fig. S5A). Thirty-five days later, Mino-treated animals showed significantly longer freezing time (fig. S5B). Immunostaining showed that microglia in Mino-treated CX3CR1^{GFP/+} animals

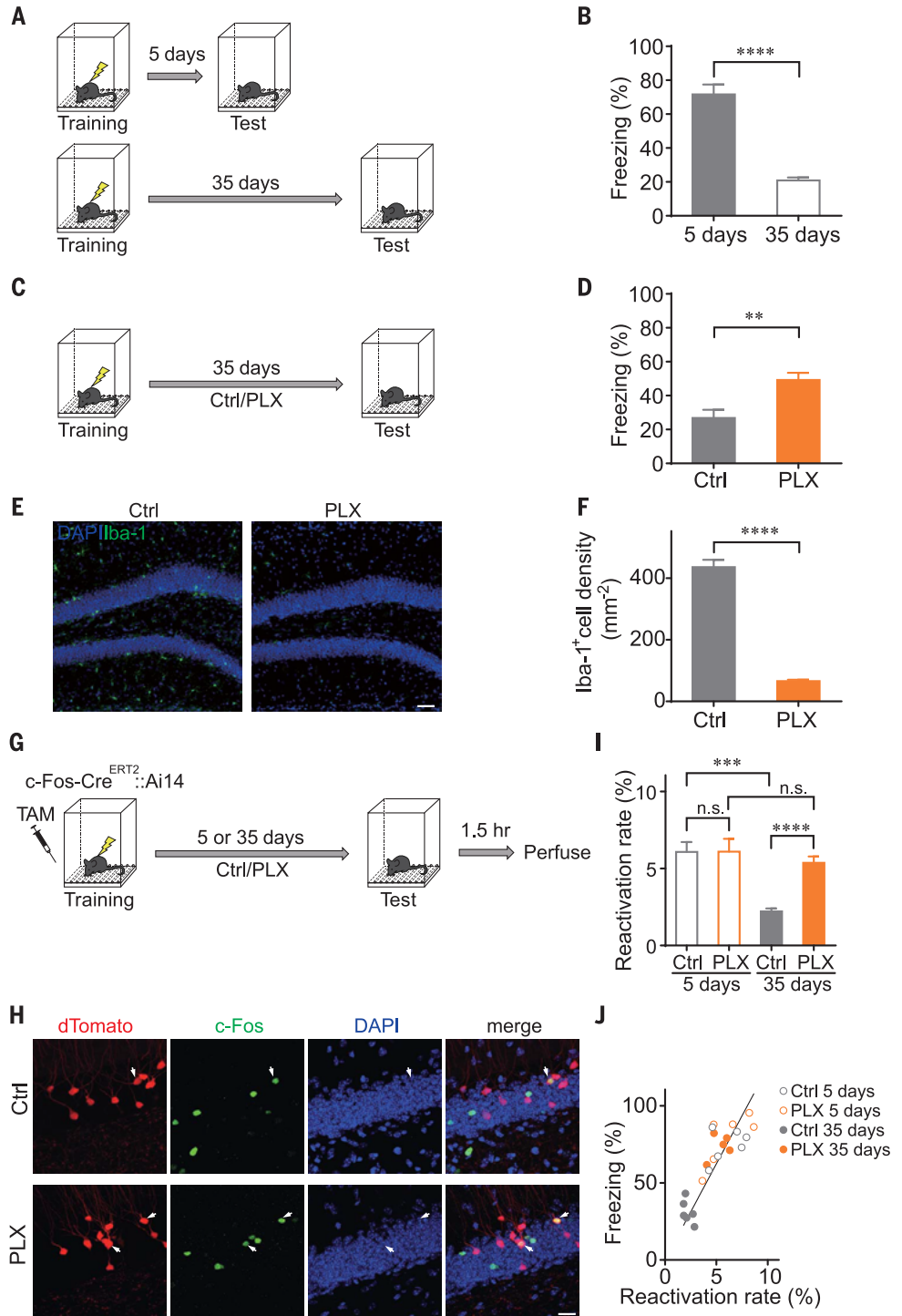
¹Institute of Neuroscience and Department of Neurology of the Second Affiliated Hospital, NHC and CAMS Key Laboratory of Medical Neurobiology, Zhejiang University School of Medicine, Hangzhou 310058, China. ²Center for Stem Cell and Regenerative Medicine, Zhejiang University School of Medicine, Hangzhou 310058, China. ³Department of Neurology of the First Affiliated Hospital, Interdisciplinary Institute of Neuroscience and Technology, Zhejiang University School of Medicine, Hangzhou 310029, China. ⁴Department of Neurobiology, Institute of Neuroscience, NHC and CAMS Key Laboratory of Medical Neurobiology, Zhejiang University School of Medicine, Hangzhou 310058, China. ⁵Department of Psychiatry, Sir Run Run Shaw Hospital, Zhejiang University School of Medicine, Hangzhou 310016, China. ⁶Institute of Neuroscience and Department of Neurology of the Second Affiliated Hospital, Mental Health Center, NHC and CAMS Key Laboratory of Medical Neurobiology, Zhejiang University School of Medicine, Hangzhou 310058, China. ⁷Center for Neuroscience and Department of Neurology of the First Affiliated Hospital, NHC and CAMS Key Laboratory of Medical Neurobiology, Zhejiang University School of Medicine, Hangzhou 310058, China. ⁸Department of Cardiology of the Second Affiliated Hospital, Zhejiang University School of Medicine, Hangzhou 310058, China. ⁹Zhejiang Provincial Key Laboratory of Tissue Engineering and Regenerative Medicine, Hangzhou 310058, China.

*These authors contributed equally to this work.

†Corresponding author. Email: wanglang@zju.edu.cn (L.W.); guyan2015@zju.edu.cn (Y.G.)

Fig. 1. Depletion of microglia prevents memory forgetting and engram dissociation.

(A) Adult mice received CFC training and were tested 5 or 35 days later. **(B)** Animals showed significantly reduced freezing 35 days after training compared with 5 days after training. $n = 9$ mice per group; $t = 8.316$, $df = 16$; $****P < 0.0001$. Error bars indicate standard error of the mean (SEM). **(C)** After CFC training, mice received normal food [control (Ctrl)] or food containing PLX before the test 35 days after training. **(D)** PLX treatment decreased forgetting. Ctrl $n = 19$ mice, PLX $n = 17$ mice; $t = 3.443$, $df = 34$, $**P = 0.0015$. **(E)** Confocal images showing decreased number of microglia (Iba1⁺) in the DG of PLX-treated animals. Scale bar, 50 μm ; DAPI, 4',6-diamidino-2-phenylindole. **(F)** PLX significantly decreased the density of microglia in the DG. Ctrl $n = 4$ mice, PLX $n = 7$ mice; $t = 20.39$, $df = 9$, $****P < 0.0001$. **(G)** c-Fos-Cre^{ERT2}::Ai14 mice were treated with TAM before the last training and then received Ctrl or PLX food until the test 5 or 35 days after training. **(H)** Confocal images showing the reactivation of engram cells in the DG of c-Fos-Cre^{ERT2}::Ai14 mice. White arrows indicate reactivated engram cells (c-Fos⁺dTomato⁺) during test. Scale bar, 20 μm . **(I)** Reactivation rate of engram cells (c-Fos⁺dTomato⁺/dTomato⁺) decreased from 5 days to 35 days after training (Ctrl 5 days, $n = 6$ mice, versus Ctrl 35 days, $n = 6$ mice, $t = 5.750$, $df = 10$, $***P = 0.0002$), whereas PLX3397 treatment prevented the decrease of reactivation rate over time (PLX 5 days, $n = 6$ mice, versus PLX 35 days, $n = 5$ mice, $t = 0.7272$, $df = 9$, $P = 0.4856$). PLX3397 treatment increased the reactivation rate of engram cells 35 days after training (Ctrl 35 days versus PLX 35 days, $t = 7.340$, $df = 9$, $****P < 0.0001$), but not 5 days (Ctrl 5 days versus PLX 5 days, $t = 0.01618$, $df = 10$, $P = 0.9874$). n.s., not significant. **(J)** The reactivation rate of DG engram cells is positively correlated with freezing of animals. Ctrl 5 days, gray open circles, $n = 6$ mice; PLX 5 days, orange open circles, $n = 6$ mice; Ctrl 35 days, gray solid circles, $n = 6$ mice; PLX 35 days, orange solid circles, $n = 5$ mice. Solid line indicates linear fitting of all points; $R^2 = 0.5998$, where R^2 is the coefficient of determination.



contained smaller synaptophysin⁺ puncta (fig. S5, C and D) or PSD95⁺ puncta (fig. S5, E and F).

Complement cascades are important for tagging synapses to be eliminated by microglia during brain development. C1q, the initiating protein of the classical complement cascade, localizes to synapses during developmental circuit refinement (24). C1q-tagging of the synapses leads to deposition of C3, which activates C3 receptors on microglia and triggers

synaptic elimination by microglial phagocytosis (15, 24). We found that C1q was present within microglia, colocalizing with PSD95 and CD68, a microglial lysosomal marker (Fig. 2C and movie S3). Furthermore, using brain sections from c-Fos-Cre^{ERT2}::Ai14 mice, in which engram cells were labeled with dTomato, we found colocalization of C1q with $\sim 1.193 \pm 0.335\%$ of the dendritic spines of engram cells (Fig. 2, D and E, and movie S4) as well as colocalization

of dTomato, PSD95, and CD68 within microglia (Fig. 2F and movie. S5). Correspondingly, engram cells showed higher spine density in PLX-treated animals (fig. S6).

To test whether complement pathways are responsible for microglia-mediated engram dissociation and forgetting, we constructed a Cre-dependent adeno-associated virus (AAV) vector expressing CD55 (also known as decay-accelerating factor, or DAF), which is a

Fig. 2. Microglia mediate forgetting through complement system. (A and B) Superresolution microscopy images and three-dimensional (3D) reconstructions showing the presence of synaptophysin (Syn) or PSD95 in microglia (GFP⁺), colocalizing with Lamp1, in the DG of CX3CR1^{GFP/+} mice. Scale bars, 5 μm; white arrows indicate Syn⁺Lamp1⁺ (A) or PSD95⁺Lamp1⁺ (B) puncta within microglia. (C) Images and 3D reconstruction showing the presence of C1q and PSD95 in microglia, colocalizing with CD68. Scale bars, 5 μm; white arrows indicate PSD95⁺CD68⁺C1q⁺ puncta within microglia. (D) Images and 3D reconstruction showing colocalization of C1q with a dendritic spine of an engram cell (dTomato⁺) in the DG. Scale bars, 1 μm; white arrows indicate colocalization of C1q with a dendritic spine of an engram cell. (E) Percentage of engram cell dendritic spines showing colocalization with C1q. *n* = 3 mice, *N* = 76 dendritic segments. (F) Images and 3D reconstruction showing the presence of engram cell components (dTomato⁺) in the microglia (Iba-1⁺), colocalizing with PSD95 and CD68. Scale bars, 5 μm; white arrows indicate dTomato⁺CD68⁺PSD95⁺ puncta within microglia. (G) Diagram of AAV vectors. (H) Experimental scheme for expressing CD55 in engram cells in the DG of c-Fos-Cre^{ERT2} mice. (I) CD55 animals showed higher freezing level. mCherry *n* = 21 mice, CD55 *n* = 17 mice; *t* = 5.033, *df* = 36, *****P* < 0.0001. (J) Images showing engram cells labeled by mCherry or CD55 AAV vectors (red) in the DG and neurons activated during the test expressed by c-Fos (green). White arrows indicate reactivated engram cells (mCherry⁺c-Fos⁺). Insets show the colocalization of mCherry and c-Fos. Scale bar, 20 μm. (K) Reactivation rate of engram cells (c-Fos⁺mCherry⁺/mCherry⁺) showed an increase in CD55 animals. *n* = 8 mice, CD55 *n* = 9 mice; *t* = 5.916, *df* = 15, *****P* < 0.0001. (L) Images showing engram cell components (mCherry⁺) colocalizing with CD68 in microglia (Iba-1⁺) in mCherry mice, but not in CD55 animals. White arrows indicate mCherry⁺CD68⁺ puncta in microglia. Scale bars, 5 μm; white arrows indicate mCherry⁺CD68⁺ (mCherry) puncta or mCherry⁻CD68⁺ (CD55) puncta in microglia. (M) Percentage of microglia containing mCherry⁺ puncta decreased in CD55 mice. mCherry *n* = 3 mice, *N* = 36 cells; CD55 *n* = 4 mice, *N* = 34 cells; *t* = 24.16, *df* = 5, *****P* < 0.0001. (N) CD55 expression in engram cells decreased the volume of mCherry⁺ puncta in microglia containing mCherry⁺ signals. mCherry *n* = 3 mice, *N* = 34 cells; CD55 *n* = 4 mice, *N* = 9 cells; *t* = 3.755, *df* = 41, ****P* = 0.0005.

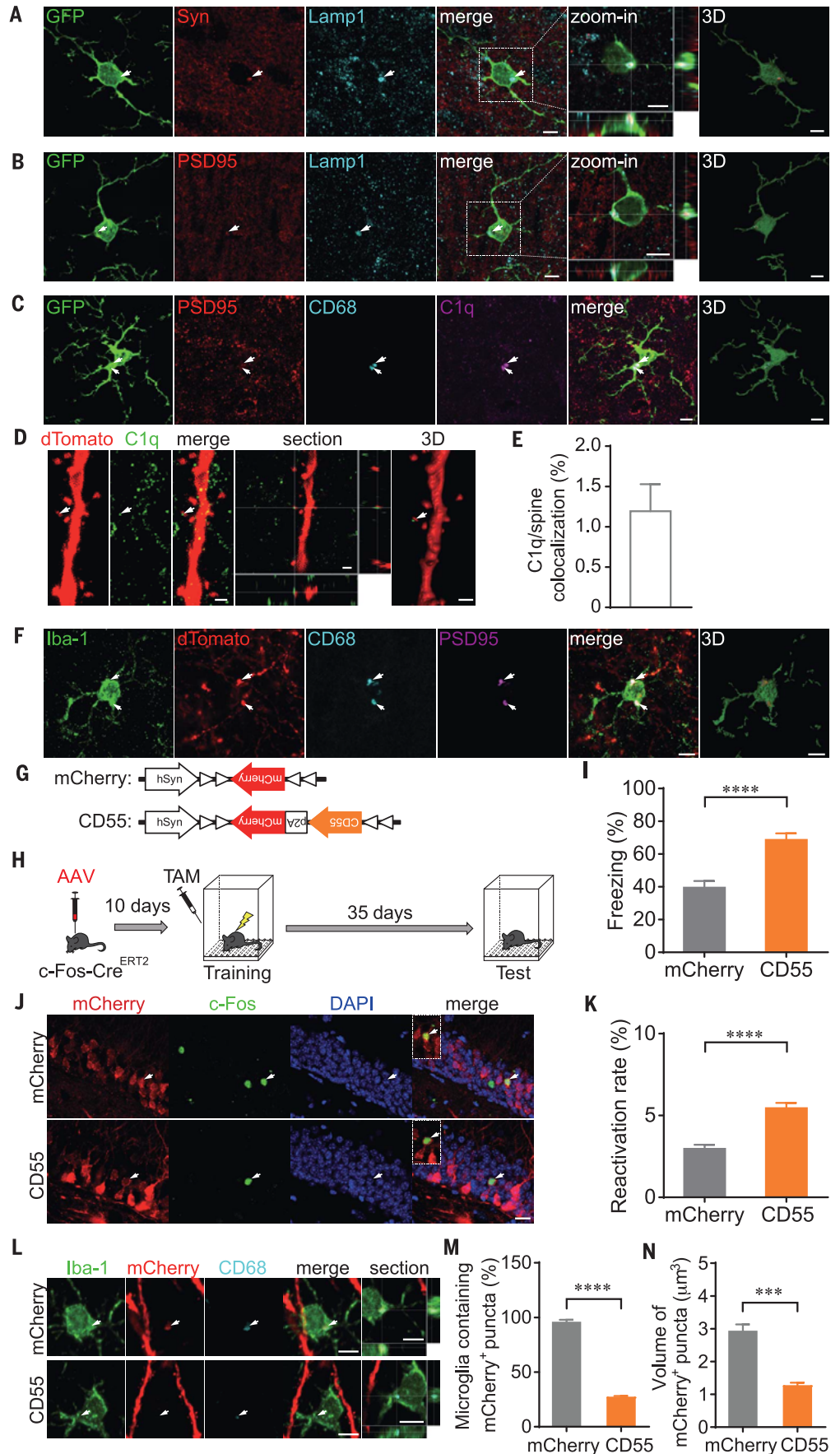
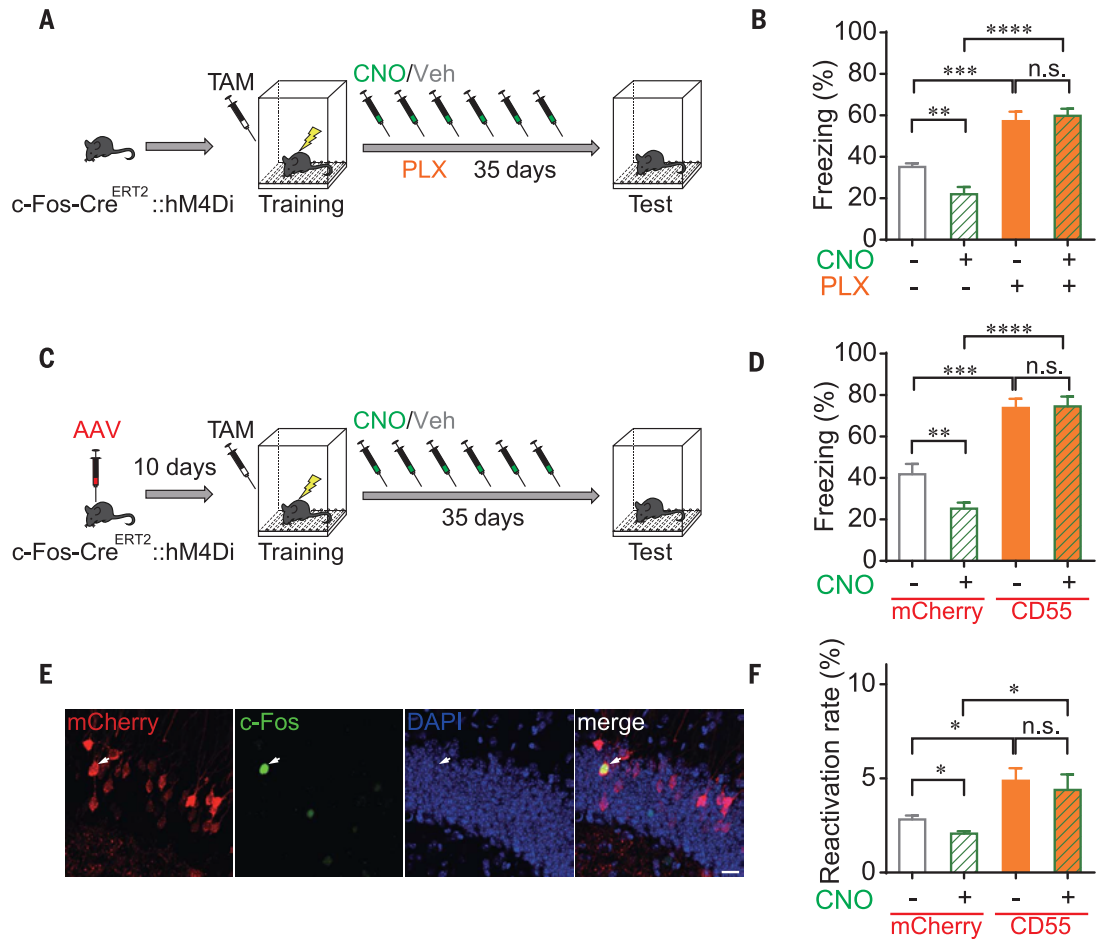


Fig. 3. Microglia mediate forgetting and dissociation of engram cells in an activity-dependent manner. (A) TAM was administered to c-Fos-Cre^{ERT2}::hM4Di mice before the last training. After training, animals were given food containing PLX and received daily injection of CNO or vehicle (Veh). (B) Freezing of animals during the test 35 days after training. CNO-PLX⁻ *n* = 10 mice, CNO⁺PLX⁻ *n* = 8 mice, CNO⁻PLX⁺ *n* = 7 mice, CNO⁺PLX⁺ *n* = 10 mice; CNO⁻PLX⁻ versus CNO⁺PLX⁻ *t* = 3.571, *df* = 16, ***P* = 0.0026; CNO⁻PLX⁻ versus CNO⁻PLX⁺ *t* = 5.068, *df* = 15, ****P* = 0.0001; CNO⁺PLX⁻ versus CNO⁺PLX⁺ *t* = 7.649, *df* = 16, *****P* < 0.0001; CNO⁻PLX⁺ versus CNO⁺PLX⁺ *t* = 0.4716, *df* = 15, *P* = 0.6440. (C) 10 days before CFC training, AAV vectors (mCherry: AAV-hSyn-DIO-mCherry; CD55: AAV-hSyn-DIO-CD55-p2A-mCherry) were injected into the DG of c-Fos-Cre^{ERT2}::hM4Di mice, and TAM was administered to the animals before the last training. After training, animals received injection of CNO or Veh every other day. (D) Freezing of animals during the test 35 days later. CNO⁻mCherry *n* = 9 mice, CNO⁺mCherry *n* = 12 mice, CNO⁻CD55 *n* = 10 mice, CNO⁺CD55 *n* = 12 mice; CNO⁻mCherry versus CNO⁺mCherry *t* = 3.035, *df* = 19, ***P* = 0.0068; CNO⁻mCherry versus CNO⁻CD55 *t* = 4.843, *df* = 17, ****P* = 0.0002; CNO⁺mCherry versus CNO⁺CD55 *t* = 8.823, *df* = 22, *****P* < 0.0001; CNO⁻CD55 versus CNO⁺CD55 *t* = 0.1057, *df* = 20, *P* = 0.9169. (E) Confocal images showing reactivated (c-Fos⁺) engram cells (mCherry⁺) in the DG during test. White arrows indicate an mCherry⁺c-Fos⁺ cell. Scale bar, 20 μm; white arrows



indicate a reactivated engram cell in the DG (mCherry⁺c-Fos⁺). (F) CNO treatment decreased the reactivation rate of engram cells, (CNO⁻mCherry *n* = 4 mice, CNO⁺mCherry *n* = 4 mice, CNO⁻CD55 *n* = 4 mice, CNO⁺CD55 *n* = 5 mice; CNO⁻mCherry versus CNO⁺mCherry *t* = 2.937, *df* = 6, **P* = 0.0260), whereas expression of CD55 in engram cells prevented the decrease of reactivation rate (CNO⁻mCherry versus CNO⁺CD55 *t* = 2.895, *df* = 6, **P* = 0.0275; CNO⁺mCherry versus CNO⁺CD55 *t* = 2.435, *df* = 7, **P* = 0.0451; CNO⁻CD55 versus CNO⁺CD55 *t* = 0.4375, *df* = 7, *P* = 0.6749).

known inhibitor of both classical and alternative complement pathways (25). We injected AAV-hSyn-DIO-CD55-p2A-mCherry (CD55) or AAV-hSyn-DIO-mCherry (mCherry) viruses into the DG of c-Fos-Cre^{ERT2} mice 10 days before CFC training, and TAM was administered before the last training to induce the expression of CD55 or mCherry only in DG engram neurons (Fig. 2, G and H, and fig. S7). Thirty-five days after training, mice in the CD55 group showed higher freezing (Fig. 2I) and a higher reactivation rate of engram cells (Fig. 2, J and K). Post hoc staining showed significantly fewer microglia containing mCherry⁺ puncta (Fig. 2, L and M) and smaller mCherry⁺ puncta within Iba-1⁺ microglia in the CD55 group of animals (Fig. 2N).

Connectivity between engram cells is essential for memories (26), whereas microglia-dependent synaptic elimination preferentially targets weak or less-active synapses (15). We next examined whether microglia-mediated forgetting depends

on the activity of engram neurons. We trained c-Fos-Cre^{ERT2}::hM4Di mice for contextual fear memory and administered TAM to induce the expression of inhibitory DREADD (designer receptors exclusively activated by designer drugs) receptor hM4Di in tagged engram cells. DREADD ligand clozapine-*N*-oxide (CNO) was administered every other day after CFC training to repetitively suppress the activity of tagged engram cells (Fig. 3A). Thirty-five days later, the animals treated with CNO alone exhibited significantly decreased freezing (Fig. 3B), whereas administration of PLX after training prevented the facilitated forgetting in CNO-treated animals (Fig. 3B).

To confirm this result, we injected AAV-hSyn-DIO-CD55-mCherry or AAV-hSyn-DIO-mCherry into the DG of c-Fos-Cre^{ERT2}::hM4Di mice and trained them for conditioned contextual fear memory. TAM was administered to express both hM4Di and CD55/mCherry in

the engram cells (Fig. 3C). The animals treated with CNO alone showed reduced freezing (Fig. 3D) and decreased reactivation rate of labeled engram cells (Fig. 3, E and F). Expression of CD55 prevented the accelerated forgetting (Fig. 3D) and the decreased reactivation rate of engram cells induced by CNO-mediated DREADD inhibition of these cells (Fig. 3F).

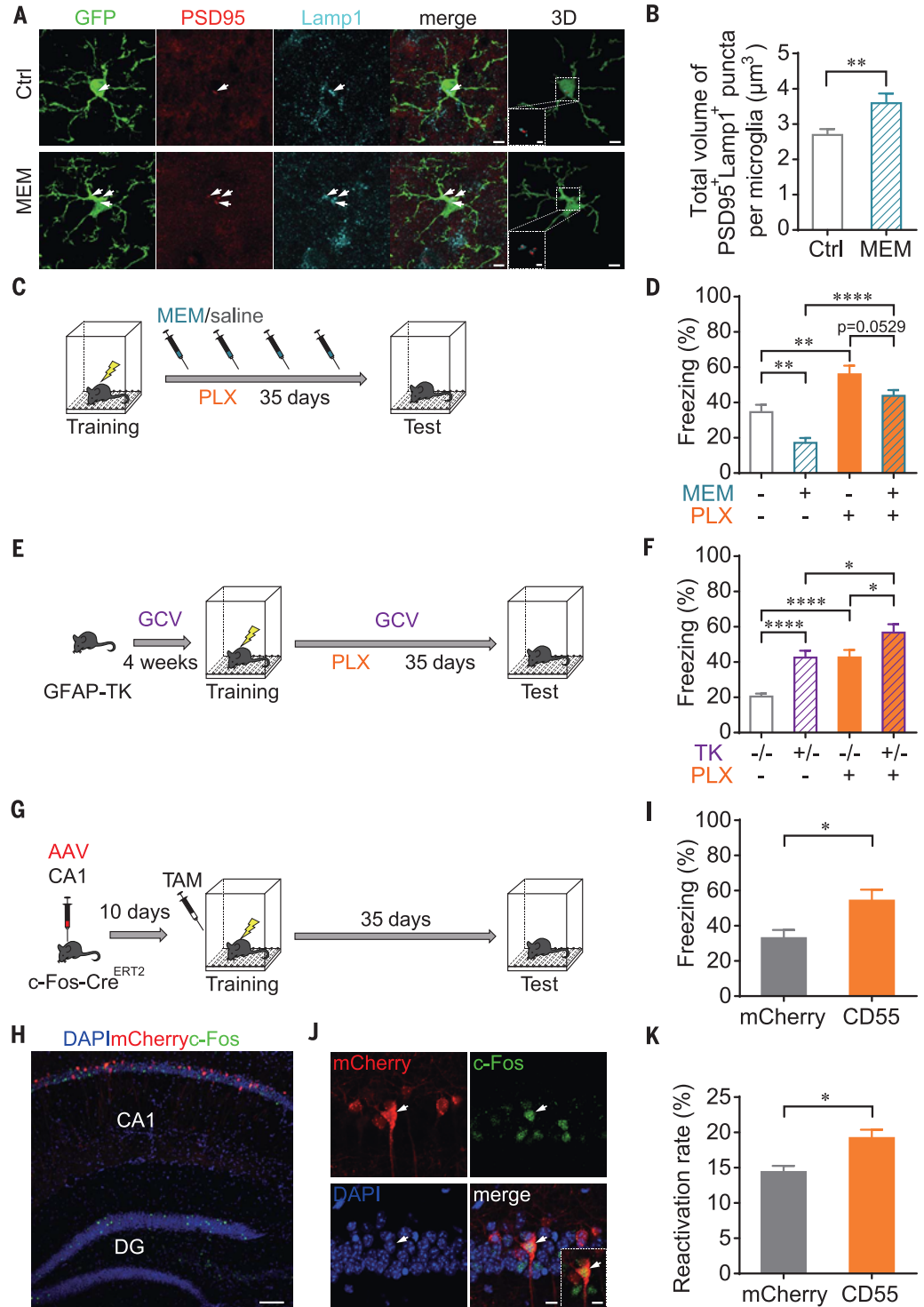
In the hippocampal DG, newborn neurons are continuously generated and integrate into the hippocampal neural circuits. This leads to drastic synaptic reorganization and circuit rewiring (7, 27, 28) and the forgetting of hippocampus-dependent memories, especially during infancy when massive neurogenesis is occurring within the DG (6). To investigate the relationship between microglia-mediated memory loss and neurogenesis-mediated forgetting, we enhanced neurogenesis in the DG of CX3CR1^{GFP/+} mice by treating them with memantine (MEM), a pro-neurogenic drug

Fig. 4. Microglia contribute to both neurogenesis-mediated and non-neurogenesis-mediated forgetting.

(A) Superresolution images and 3D reconstruction showing the PSD95⁺Lamp1⁺ puncta in microglia in Ctrl and MEM-treated CX3CR1^{GFP/+} mice. Scale bars, 5 μ m; white arrows indicate PSD95⁺Lamp1⁺ puncta in microglia. Insets are enlarged 3D reconstructions of PSD95⁺Lamp1⁺ puncta in microglia. Scale bars, 2 μ m. (B) MEM-treatment increased the volume of PSD95⁺Lamp1⁺ puncta in each microglia. Ctrl $n = 3$ mice, $N = 29$ cells; MEM $n = 3$ mice, $N = 30$ cells; $t = 2.774$, $df = 57$, $**P = 0.0075$. (C) PLX and MEM treatment administered to mice.

(D) Freezing of animals during the test 35 days after training. MEM⁻PLX⁻ $n = 10$ mice, versus MEM⁺PLX⁻ $n = 10$ mice, $t = 3.511$, $df = 18$, $**P = 0.0025$; MEM⁻PLX⁻ versus MEM⁺PLX⁺ $n = 10$ mice, $t = 3.341$, $df = 18$, $**P = 0.0036$; MEM⁻PLX⁺ versus MEM⁺PLX⁺ $n = 10$ mice, $t = 6.277$, $df = 18$, $****P < 0.0001$; MEM⁻PLX⁺ versus MEM⁺PLX⁻ $t = 2.072$, $df = 18$, $P = 0.0529$. (E) GCV and PLX treatment administered to GFAP-TK^{+/-} or GFAP-TK^{-/-} mice. (F) Freezing during the test 35 days after training. TK^{-/-}PLX⁻ $n = 14$ mice versus TK^{+/-}PLX⁻ $n = 14$ mice, $t = 5.181$, $df = 26$, $****P < 0.0001$; TK^{-/-}PLX⁻ versus TK^{+/-}PLX⁺ $n = 14$ mice, $t = 4.895$, $df = 26$, $****P < 0.0001$; TK^{+/-}PLX⁻ versus TK^{+/-}PLX⁺ $n = 13$ mice, $t = 2.333$, $df = 25$, $*P = 0.0280$; TK^{-/-}PLX⁺ versus TK^{+/-}PLX⁺ $t = 2.2426$, $df = 25$, $*P = 0.0341$. (G) c-Fos-Cre^{ERT2} mice received AAV injection into CA1 and recovered for 10 days before CFC training. TAM was administered before the last training, and freezing was tested 35 days later. (H) Confocal image showing engram cells (mCherry⁺) in CA1 but not in the DG. Scale bar, 100 μ m. (I) CD55 animals showed higher freezing level. mCherry $n = 11$ mice, CD55 $n = 11$ mice; $t = 2.728$, $df = 20$, $*P = 0.0130$.

(J) Confocal images showing the reactivation of engram cells in CA1. White arrows indicate a reactivated engram cell (mCherry⁺c-Fos⁺) in CA1. Inset shows the colocalization of mCherry and c-Fos; Scale bars, 20 μ m. (K) Reactivation rate of engram cells in CA1 was increased in CD55 animals. mCherry $n = 5$ mice, CD55 $n = 5$ mice; $t = 3.268$, $df = 8$, $*P = 0.0114$.



(6), for 4 weeks. MEM-treatment significantly increased the number of DCX⁺ cells in the DG, indicating enhanced neurogenesis (fig. S8). We found significantly larger volumes of PSD95⁺Lamp1⁺ puncta within microglia in MEM-treated animals (Fig. 4, A and B). Additionally, MEM treatment facilitated forgetting after CFC training (Fig. 4, C and D), whereas

administering PLX blocked MEM-facilitated forgetting (Fig. 4D) without altering the enhanced neurogenesis by MEM (fig. S8).

To further investigate whether microglia also contribute to neurogenesis-unrelated forgetting, we used a GFAP-TK transgenic mouse line, which expresses herpes simplex virus thymidine kinase (TK) under the control of

the glial fibrillary acidic protein (GFAP) promoter. Administration of the antiviral drug ganciclovir (GCV) ablates only mitotic GFAP⁺ cells that express TK, thus depleting neurogenesis (29). To completely deplete integration of new neurons, we started treating TK^{+/-} mice and their wild-type littermates (TK^{-/-}) with GCV 4 weeks before CFC training and

continued until the test (Fig. 4E and fig. S9). PLX was administered after training to deplete microglia. GCV treatment in TK^{+/-} mice prevented forgetting, whereas TK^{+/-} mice treated with both PLX and GCV showed significantly higher levels of memory retention than TK^{+/-} mice treated with GCV only (Fig. 4F).

To confirm that microglia-mediated forgetting contributes to neurogenesis-unrelated forgetting, we injected AAV-DIO-CD55-mCherry or AAV-DIO-mCherry into c-Fos-Cre^{ERT2} mice to label engram cells in hippocampal CA1 (Fig. 4, G and H), which is not a neurogenic region. We found that expression of CD55 in CA1 engram cells also prevented forgetting (Fig. 4I) and dissociation of engram cells (Fig. 4, J and K).

Synaptic connections in the brain are highly dynamic and variable in strength and connectivity (14). Our study shows that microglia eliminate synaptic components in the adult hippocampus, whereas depleting microglia or inhibiting phagocytosis of microglia prevents forgetting. This suggests that synapse elimination by microglia leads to dissociation of engrams and the forgetting of previously learned contextual fear memory. In the developing brain, microglial engulfment of synapses depends on the classical complement cascade (15). Disruption of the microglia-specific phagocytic pathway by knocking out complement components, such as C1q, C3, or CR3, results in sustained deficits in synaptic connectivity (15, 24). C1q levels in the brain increase during aging, whereas C1q-deficient mice exhibit enhanced synaptic plasticity and less cognitive and memory decline when aged (30). Notably, our study showed that the C1q-dependent complement pathway is actively involved in synapse elimination by microglia in the healthy adult hippocampus. CD55 is a known inhibitor of complement pathways in the immune system and is expressed in neurons in response to chronic inflammation (31). We overexpressed CD55 to inhibit the complement pathways, specifically in engram cells, without affecting microglia or other neurons in the circuits, and we found that forgetting was prevented. This indicates that the elimination of synaptic structures by microglia in the DG of the healthy adult brain occurs in a complement-dependent manner. Moreover, inhibiting the activity of engram cells facilitates the forgetting of related memory, which could be blocked by depleting microglia or inhibiting complement pathways in

engram cells. This indicates that synapse elimination by microglia is also activity-dependent, following similar rules in the developing brain (15), thus resulting in the erasure of less-active memories. Besides eliminating synapses, microglia have also been reported to be able to trigger long-term synaptic depression via AMPA receptor internalization, through activation of CR3 (32), which may also contribute to forgetting.

New neurons are continuously generated in the DG, providing a substrate for massive synaptic reorganization and circuit rewiring in this region. Newborn dentate granule neurons integrate into hippocampal neural circuits by competitively replacing existing synaptic connections formed by mature granule neurons (7, 27), thus leading to the forgetting of hippocampal-dependent contextual fear memory (6). Our study shows that MEM-induced enhanced neurogenesis leads to increased synaptic engulfment by microglia, whereas depletion of microglia blocks facilitated memory forgetting induced by enhanced neurogenesis, suggesting that microglia contribute to neurogenesis-induced synaptic reorganization. Besides the rewiring of neural circuits caused by the continuous integration of newborn neurons, mature neurons are also able to reorganize their connectivity. We found that depletion of microglia in the DG without neurogenesis or inhibition of complement pathways in CA1 engram cells prevents forgetting. This indicates that microglia-mediated synaptic reorganization is also happening in mature hippocampal neurons, thus leading to weakening or loss of connections between engram cells and the forgetting of encoded memories. This also suggests that, in species lacking adult neurogenesis, or in non-neurogenic brain regions such as the cortex, microglia could be one major force contributing to synapse loss and forgetting.

REFERENCES AND NOTES

1. J. H. Han et al., *Science* **316**, 457–460 (2007).
2. S. A. Josselyn, S. Köhler, P. W. Frankland, *Nat. Rev. Neurosci.* **16**, 521–534 (2015).
3. S. Tonegawa, M. Pignatelli, D. S. Roy, T. J. Ryan, *Curr. Opin. Neurobiol.* **35**, 101–109 (2015).
4. S. B. Hofer, T. D. Mrcic-Flogel, T. Bonhoeffer, M. Hübener, *Nature* **457**, 313–317 (2009).
5. G. Yang, F. Pan, W. B. Gan, *Nature* **462**, 920–924 (2009).
6. K. G. Akers et al., *Science* **344**, 598–602 (2014).
7. N. Toni, A. F. Schinder, *Cold Spring Harb. Perspect. Biol.* **8**, a018903 (2015).
8. P. W. Frankland, S. Köhler, S. A. Josselyn, *Trends Neurosci.* **36**, 497–503 (2013).

9. M. Fu, Y. Zuo, *Trends Neurosci.* **34**, 177–187 (2011).
10. D. Tropea, A. K. Majewska, R. Garcia, M. Sur, *J. Neurosci.* **30**, 11086–11095 (2010).
11. J. T. Trachtenberg et al., *Nature* **420**, 788–794 (2002).
12. J. E. Coleman et al., *J. Neurosci.* **30**, 9670–9682 (2010).
13. A. Attardo, J. E. Fitzgerald, M. J. Schnitzer, *Nature* **523**, 592–596 (2015).
14. Y. Wu, L. Dissing-Olesen, B. A. MacVicar, B. Stevens, *Trends Immunol.* **36**, 605–613 (2015).
15. D. P. Schafer et al., *Neuron* **74**, 691–705 (2012).
16. R. C. Paolicelli et al., *Science* **333**, 1456–1458 (2011).
17. M. E. Tremblay, R. L. Lowery, A. K. Majewska, *PLOS Biol.* **8**, e1000527 (2010).
18. C. Madry et al., *Neuron* **97**, 299–312.e6 (2018).
19. H. Wake, A. J. Moorhouse, S. Jinno, S. Kohsaka, J. Nabekura, *J. Neurosci.* **29**, 3974–3980 (2009).
20. M. Prinz, J. Priller, S. S. Sisodia, R. M. Ransohoff, *Nat. Neurosci.* **14**, 1227–1235 (2011).
21. R. A. Rice et al., *J. Neurosci.* **35**, 9977–9989 (2015).
22. C. J. Guenther, K. Miyamichi, H. H. Yang, H. C. Heller, L. Luo, *Neuron* **78**, 773–784 (2013).
23. C. M. Selgren et al., *Nat. Neurosci.* **22**, 374–385 (2019).
24. B. Stevens et al., *Cell* **131**, 1164–1178 (2007).
25. A. Nicholson-Weller, C. E. Wang, *J. Lab. Clin. Med.* **123**, 485–491 (1994).
26. M. M. Poo et al., *BMC Biol.* **14**, 40 (2016).
27. N. Toni et al., *Nat. Neurosci.* **10**, 727–734 (2007).
28. N. Toni et al., *Nat. Neurosci.* **11**, 901–907 (2008).
29. J. S. Snyder, A. Soumier, M. Brewer, J. Pickel, H. A. Cameron, *Nature* **476**, 458–461 (2011).
30. A. H. Stephan et al., *J. Neurosci.* **33**, 13460–13474 (2013).
31. J. van Beek et al., *J. Immunol.* **174**, 2353–2365 (2005).
32. J. Zhang et al., *Neuron* **82**, 195–207 (2014).

ACKNOWLEDGMENTS

We thank all the members of the Y.G. and La.W. laboratories for the discussion and constructive suggestions for this project. We thank P. Frankland for his critical comments. We are grateful to the Core Facilities of Zhejiang University School of Medicine for technical assistance. **Funding:** This work was supported by grants from the National Key R&D Program of China (2017YFA0104200), the Zhejiang Provincial Natural Science Foundation of China (LR17C090001) to Y.G., the National Natural Science Foundation of China (31700888) to La.W., and the Natural Science Foundation of Zhejiang Province (LZ19C090001) to B.S. **Author contributions:** C.W., H.Y., La.W., and Y.G. designed all of the experiments; C.W. performed all behavior tests, imaging, and most of the analysis; H.Y. performed vector constructions, viral injections, and some imaging; Z.H. and Y.S. performed some image analysis; J.M. and J.L. helped in genotyping some animals; X.-D.W. provided c-Fos-Cre^{ERT2} and m4MDi mice; Li.W. provided Ai14 mice; B.S. provided GFAP-TK mice; P.S. provided CX3CR1^{GFPT+} and CD11b-DTR mice; C.W., H.Y., La.W., and Y.G. discussed the results and wrote the manuscript; and all authors discussed the manuscript. **Competing interests:** The authors declare no competing interests. **Data and materials availability:** All data needed to understand and assess the conclusions of this study are included in the text, figures, and the supplementary materials.

SUPPLEMENTARY MATERIALS

science.sciencemag.org/content/367/6478/688/suppl/DC1
Materials and Methods
Figs. S1 to S9
References (33, 34)
Movies S1 to S5

[View/request a protocol for this paper from Bio-protocol.](#)

27 August 2019; accepted 6 January 2020
10.1126/science.aaz2288

Copyright © 2020. The Authors, some rights reserved; exclusive licensee American Association for the Advancement of Science. No claim to original U.S. Government Works.

NEURODEVELOPMENT

Huntington's disease alters human neurodevelopment

Monia Barnat¹, Mariacristina Capizzi^{1*}, Esther Aparicio^{1*}, Susana Boluda², Doris Wennagel¹, Radhia Kacher¹, Rayane Kassem¹, Sophie Lenoir¹, Fabienne Agasse¹, Barbara Y. Braz¹, Jeh-Ping Liu³, Julien Ighil⁴, Aude Tessier⁵, Scott O. Zeitlin³, Charles Duyckaerts², Marc Dommergues⁴, Alexandra Durr^{6†}, Sandrine Humbert^{1†}

Although Huntington's disease is a late-manifesting neurodegenerative disorder, both mouse studies and neuroimaging studies of presymptomatic mutation carriers suggest that Huntington's disease might affect neurodevelopment. To determine whether this is actually the case, we examined tissue from human fetuses (13 weeks gestation) that carried the Huntington's disease mutation. These tissues showed clear abnormalities in the developing cortex, including mislocalization of mutant huntingtin and junctional complex proteins, defects in neuroprogenitor cell polarity and differentiation, abnormal ciliogenesis, and changes in mitosis and cell cycle progression. We observed the same phenomena in Huntington's disease mouse embryos, where we linked these abnormalities to defects in interkinetic nuclear migration of progenitor cells. Huntington's disease thus has a neurodevelopmental component and is not solely a degenerative disease.

Huntington's disease (HD) is a neurodegenerative disease that is part of the larger family of "proteopathies," which includes the polyglutamine diseases, amyotrophic lateral sclerosis, and Alzheimer's and Parkinson's diseases. These diverse disorders share a delayed onset in mid-adulthood or later despite the expression, at least in hereditary cases, of the disease-driving protein from the first days of life. This raises the question of whether early events might set the stage for later disease. For example, huntingtin (HTT), the protein mutated in HD, is essential for development, at least in mice (1–3). The mutant HTT (mHTT) impairs neural progenitor cell division and neuronal migration and maturation (4–6), giving HD mice a thinner cortex (7). The fact that expression of either mHTT or hypomorphic HTT solely during early life is sufficient to produce HD features in adult mice strongly suggests that there is a developmental component to the disease (8, 9).

In support of this notion, human neuroimaging studies have revealed smaller intracranial volume in HD mutation carriers as young as 7 years of age (10, 11). Loss of cortical volume takes place long before any symptoms appear, and defects in the corticostriatal net-

work lead to striatal dysfunction and degeneration (12–15). Studies in neurons derived from HD human induced pluripotent stem cells (iPSCs) have identified changes in gene expression that support an altered developmental program (16, 17), and mHTT alters neuronal identity in cortical populations of HD brain organoids (18). But does mHTT affect early human development? And if so, how early? To answer these questions, we recruited HD mutation carriers who sought prenatal testing in order to determine whether the fetus carried an HD-causing mutation.

Mutant huntingtin mislocalizes in human and mouse embryos

We were able to procure rare intact cortical tissues from four HD mutation carrier fetuses and four healthy controls at gestation week 13 (GW13) (table S1). At this developmental stage, the cortical neurons that project to the striatum and later deteriorate in HD are arising from the division of progenitor cells at the ventricular zone. These apical progenitors extend processes toward both the apical and basal surfaces of the neuroepithelial wall, and their nuclei move back and forth between surfaces in concert with cell cycle progression in a process known as interkinetic nuclear migration. This process, common to all developing pseudostratified neuroepithelia (19, 20), maintains the balance between progenitor renewal and differentiation by controlling when apical progenitor nuclei are exposed to proliferative versus neurogenic signals, and in what proportions.

To examine the expression pattern of HTT at the ventricular zone of the GW13 cortex, we used an antibody that recognizes both HTT and mHTT (4C8; Fig. 1, A and B, and fig. S1A). In wild-type tissues, HTT staining demarcated

the apical surface of the ventricular zone and spread diffusely throughout the basal region. In cortical tissue of HD mutation carriers, however, HTT staining concentrated at the apical endfeet (the apical surface of the processes).

Given the preciousness of the human tissue, we turned to mice to further investigate these observations, using embryonic day 13.5 (E13.5) mouse embryos, which correspond to GW13 in human neurodevelopment. We studied an HD knock-in mouse model in which the first exon of the *HTT* gene is replaced by human exon 1 carrying 111 CAG repeats (Hdh^{Q111/Q111}) (21). Immunostaining coronal sections revealed a pattern of HTT expression that paralleled our observations in human fetuses (fig. S1B). To determine the distribution of mHTT specifically, we used another HD knock-in mouse model in which Flag tags are inserted in the N terminus of wild-type HTT (Hdh^{F7Q/+}) or mutant HTT carrying 140 CAG repeats (Hdh^{F140Q/+}) (22) (fig. S1C). The Flag labeling showed that mHTT localized to the apical surface and was decreased in the basal region.

Mutant huntingtin impairs endosome secretion and recycling

Apical progenitors maintain their polarity through endocytosis and the trafficking of proteins from the trans-Golgi network to the plasma membrane at the apical endfeet (19). In HD, both endocytosis and Golgi-membrane trafficking are dysregulated (23). Because one of HTT's main functions is to transport vesicles, we used markers of the endosomal pathway to map the subcellular localization of HTT in HD and to gauge whether transport is affected this early in HD.

We stained for calnexin (a marker of the endoplasmic reticulum), GRASP65 (Golgi assembly stacking protein of 65 kDa to mark the cis-Golgi network), TGN38 (trans-Golgi network integral membrane protein 38), EEA1 (early endosome antigen 1), and transferrin receptor (recycling endosomes). In control samples, HTT colocalized partially with these markers (figs. S2 and S3). In both human and mouse HD samples, however, HTT strongly colocalized with TGN38, EEA1, and transferrin receptor, and to a lesser extent with calnexin and GRASP65. These results suggest that mHTT hinders endosomal trafficking in apical progenitors, even at this very early stage of development.

Mutant huntingtin disrupts neuroepithelial junctional complexes

Apical endfeet contain junctional complexes (19, 24) composed of tight-junction and adherens-junction proteins, including ZO1, PAR3, NCAD, and β -catenin (25), that link neighboring progenitors to each other, thereby sealing the neuroepithelium. Because HTT regulates the trafficking of these proteins,

¹Univ. Grenoble Alpes, INSERM, U1216, Grenoble Institut Neurosciences, Grenoble, France. ²Department of Neuropathology Raymond Escourolle, AP-HP, Pitié-Salpêtrière University Hospital, Paris, France. ³Department of Neuroscience, University of Virginia School of Medicine, Charlottesville, VA 22908, USA. ⁴AP-HP, Sorbonne University, Service de Gynécologie Obstétrique, Pitié-Salpêtrière Hospital, Paris, France. ⁵AP-HP, Unité d'Embryofœtopathologie, Necker Hospital, Paris, France. ⁶Sorbonne University, Paris Brain Institute, APHP, INSERM U1127, CNRS UMR7225, Pitié-Salpêtrière Hospital, Paris, France

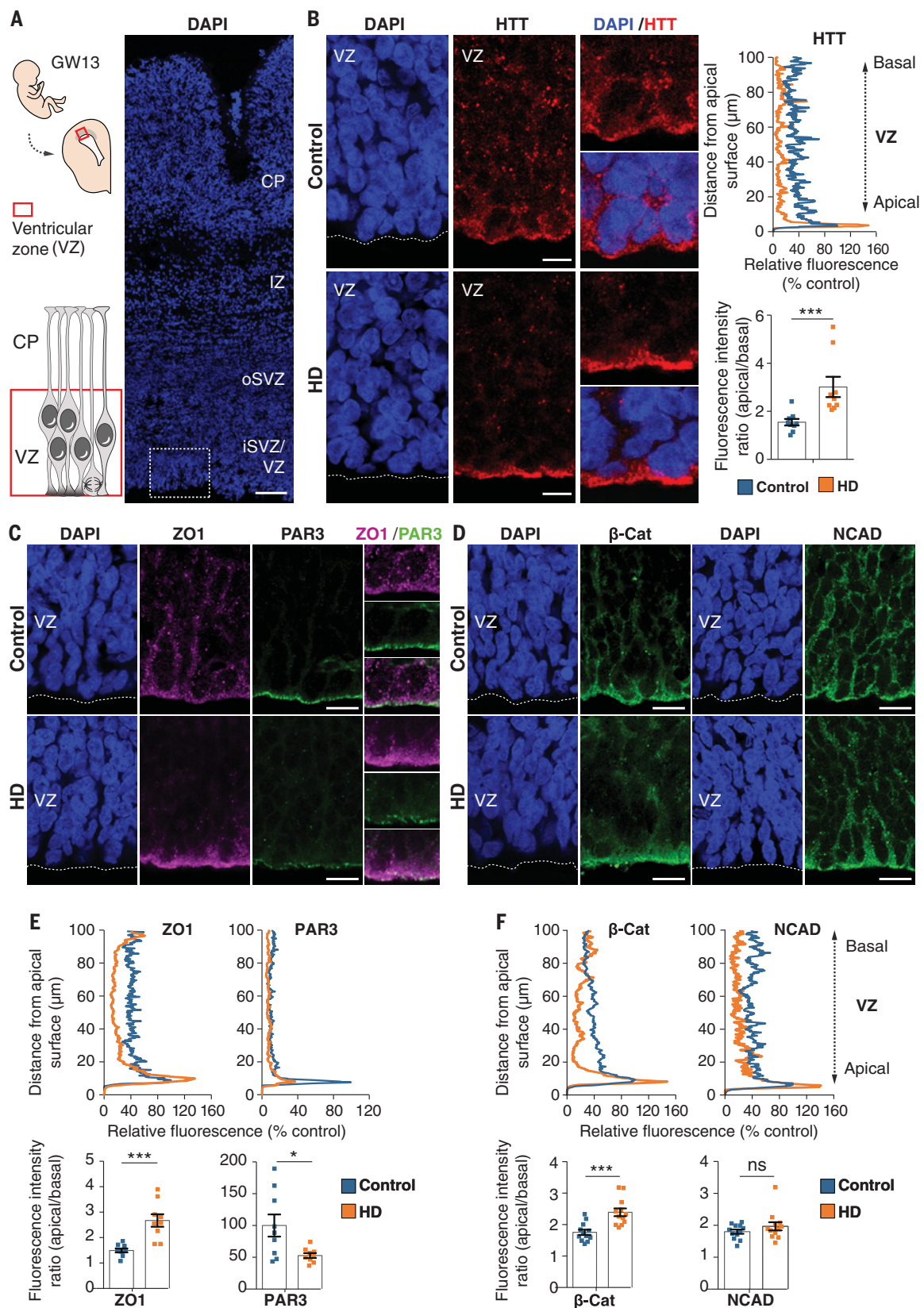
*These authors contributed equally to this work.

†Corresponding author. Email: alexandra.durr@upmc.fr (A.D.); sandrine.humbert@inserm.fr (S.H.)

Fig. 1. Huntingtin and junctional complex proteins mislocalize in the ventricular zone of human fetuses carrying HD-causing mutations. (A) Left: Diagram showing the position of the fetal ventricular zone relative to the cortical plate (CP). Right: Coronal brain sections of GW13 control human cortex were counterstained with 4',6-diamidino-2-phenylindole (DAPI). The dotted square shows the region imaged in (B). Scale bar, 100 μ m.

(B) Left: Coronal GW13 brain sections from control fetus and fetus carrying HD-causing mutation were immunostained for HTT. Scale bars, 10 μ m. Right: Representative line-scan analysis (relative fluorescence intensity) of HTT immunostaining and quantification of apical/basal human HTT fluorescence intensity in the ventricular zone. For each condition, $n = 3$ fetuses from different mothers; $***P = 0.0044$ (unpaired t test).

(C and D) Coronal GW13 fetal brain sections were immunostained for ZO1 and PAR3 (C) and β -catenin and NCAD (D). Scale bars, 15 μ m. (E and F) Representative line-scan analysis (relative fluorescence intensity) of indicated immunostainings (top) and quantification of indicated fluorescence intensities in the ventricular zone (bottom graphs). For each condition, $n = 3$ fetuses from different mothers. ZO1: $***P = 0.0003$ (unpaired t test); PAR3: $*P = 0.0177$ (unpaired t test); β -cat: $***P = 0.0003$ (unpaired t test); NCAD: $P = 0.4682$ (Mann-Whitney U test), ns (not significant). Results are means \pm SEM. VZ, ventricular zone; iSVZ, inner subventricular zone; oSVZ, outer subventricular zone; IZ, intermediate zone; CP, cortical plate. Nuclei were counterstained with DAPI.



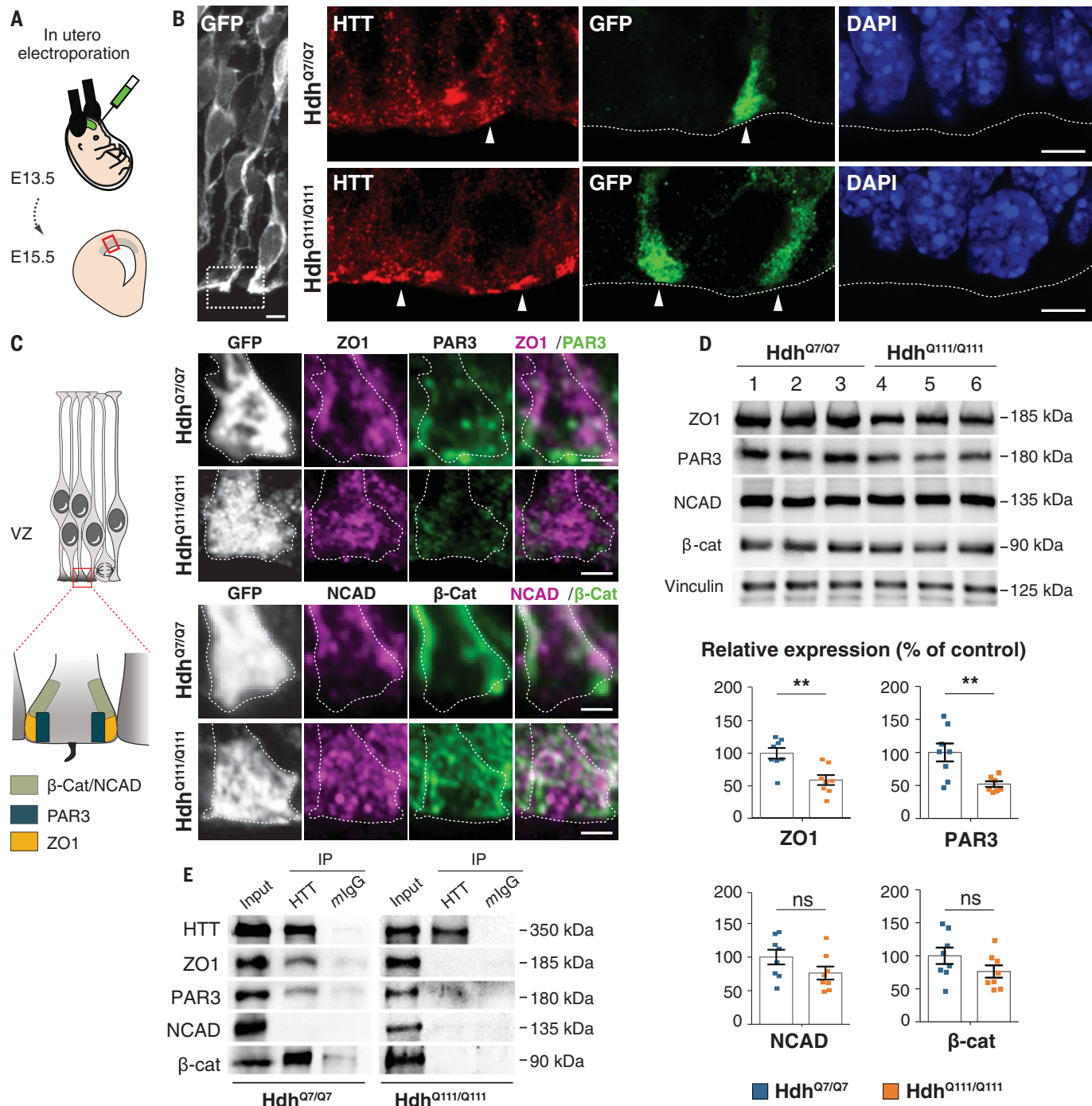


Fig. 2. Junctional protein complexes are disrupted in the apical endfeet of HD mouse embryos. (A) Schematic of the in utero electroporation experiment. (B and C) Mouse embryos were electroporated at E13.5 with a pCAG-GFP construct to delineate the apical endfoot in E15.5 cortices. (B) Hdh^{Q7/Q7} and Hdh^{Q111/Q111} cortical sections were immunostained for GFP (left) and for HTT and GFP (right). White arrowheads point to apical endfeet. Nuclei were counterstained with DAPI. (C) Left: Diagram indicating the position of junctional complexes at the apical endfeet. Right: Cortical sections were immunostained for GFP, ZO1, and PAR3 (upper panel) and GFP, NCAD, and β-Cat (lower panel). Scale bars, 5 μm (B), 2 μm (C). (D) ZO1, PAR3, NCAD, β-catenin, and vinculin immunoblotting analyses of lysates from E15.5 Hdh^{Q7/Q7} and Hdh^{Q111/Q111} cortices. Bar graphs correspond to the quantitative evaluation of the indicated proteins. For each condition, n = at least 7 embryos from different mothers. ZO1: **P = 0.0026; PAR3: **P = 0.0075; NCAD: P = 0.1255; β-cat: P = 0.1476 (unpaired t tests). Results are means ± SEM. (E) HTT-associated complexes were immunoprecipitated with the 4C8 antibody from E15.5 Hdh^{Q7/Q7} and Hdh^{Q111/Q111} cortical extracts. Mouse IgG (mlgG) was used as a negative control.

NCAD, and β-Cat (lower panel). Scale bars, 5 μm (B), 2 μm (C). (D) ZO1, PAR3, NCAD, β-catenin, and vinculin immunoblotting analyses of lysates from E15.5 Hdh^{Q7/Q7} and Hdh^{Q111/Q111} cortices. Bar graphs correspond to the quantitative evaluation of the indicated proteins. For each condition, n = at least 7 embryos from different mothers. ZO1: **P = 0.0026; PAR3: **P = 0.0075; NCAD: P = 0.1255; β-cat: P = 0.1476 (unpaired t tests). Results are means ± SEM. (E) HTT-associated complexes were immunoprecipitated with the 4C8 antibody from E15.5 Hdh^{Q7/Q7} and Hdh^{Q111/Q111} cortical extracts. Mouse IgG (mlgG) was used as a negative control.

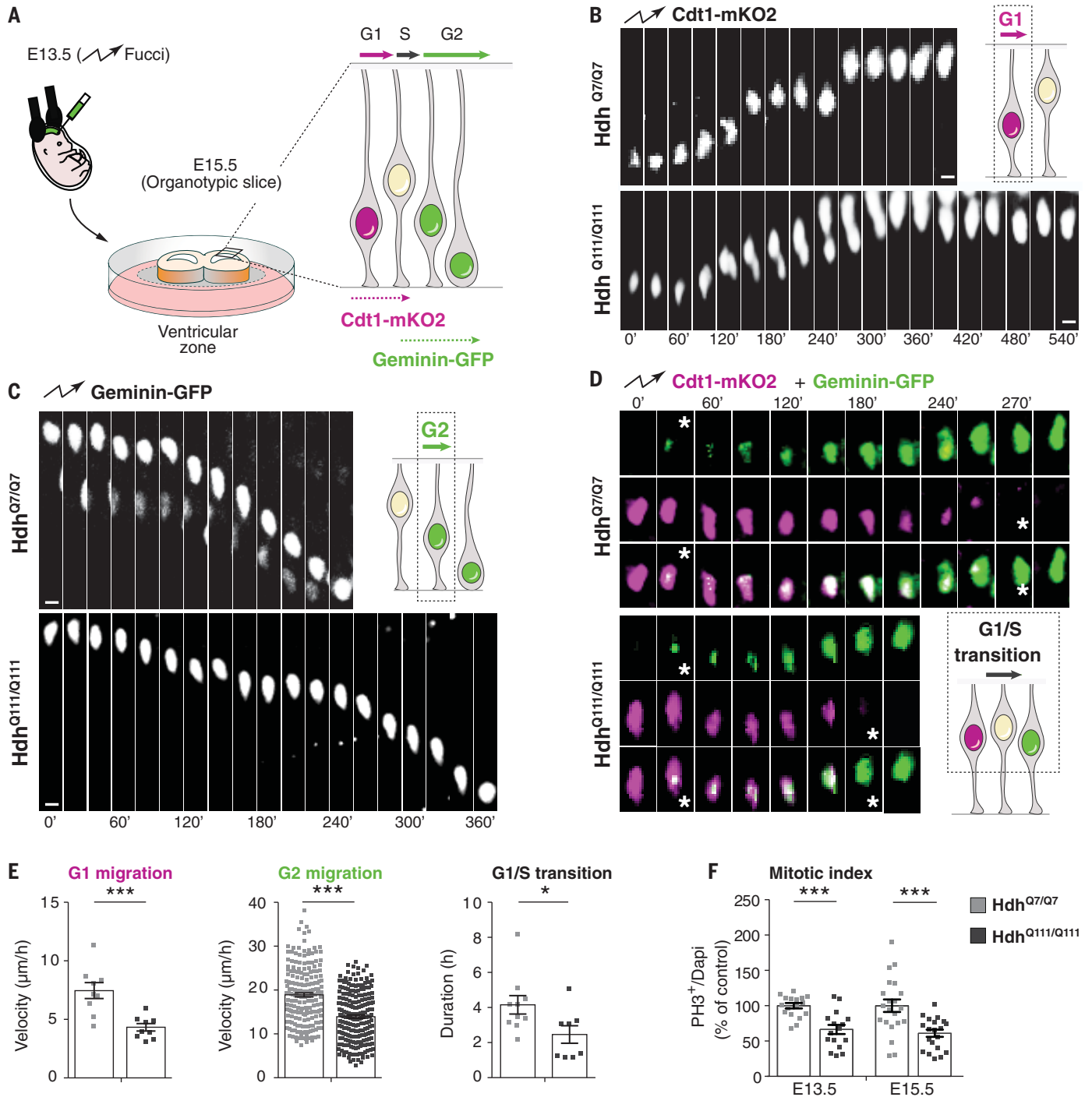


Fig. 3. Interkinetic nuclear migration and mitosis of cortical apical progenitors are impaired in HD mouse embryos. (A) Schematic of the experiment for analysis of interkinetic nuclear migration. E13.5 Hdh^{Q7/Q7} and Hdh^{Q111/Q111} embryos were electroporated with Cdt1-mKO2 and geminin-GFP constructs. After 48 hours, the movement of the GFP- and mKO2-labeled nuclei was followed by spinning disc microscopy, taking one image every 10 or 15 min for 10 hours. (B to D) Representative images showing the movement of nuclei in G₁, G₂, and G₁/S transition phases as indicated. (D) Stars indicate the beginning and ending of the G₁/S transition. Scale bars, 5 μm. (E) Quantitative differences in the velocity of G₁-phase nuclei [for each condition, $n = 9$ cells from three

embryos from different mothers; $***P = 0.0008$ (unpaired t test)], velocity of G₂-phase nuclei [for each condition, $n =$ at least 202 cells from four embryos from different mothers; $***P < 0.0001$ (Mann-Whitney U test)], and length of G₁/S transition [for each condition, $n =$ at least 8 cells from three embryos from different mothers; $*P = 0.0356$ (unpaired t test)]. (F) Bar graphs show the percentage of phospho-histone 3 (PH3) cells (mitotic index) of dividing progenitors [E13.5: for each condition, $n =$ at least 2151 cells from four embryos from different mothers, $***P < 0.0001$ (unpaired t test); E15.5: for each condition, $n =$ at least 1801 cells from three embryos from different mothers, $***P = 0.0005$ (unpaired t test)]. Results are means \pm SEM.

which are dysregulated in HD (6, 26–30), we hypothesized that mHTT hinders the correct positioning of these junctions, which would diminish the integrity of the neuroepithelium. As predicted, HTT partially codistributed with

ZO1, PAR3, β -catenin, and NCAD at the apical endfeet of human GW13 control and mouse E13.5 neuroepithelium (figs. S4 and S5A). The levels of ZO1, NCAD, and β -catenin were high at the apical surface of the human and

mouse control ventricular zone and even higher in HD tissues, with a concomitant reduction in these proteins in the basal region (Fig. 1, C to F, and fig. S5, B to E). PAR3 was also misregulated in HD but in a different pattern

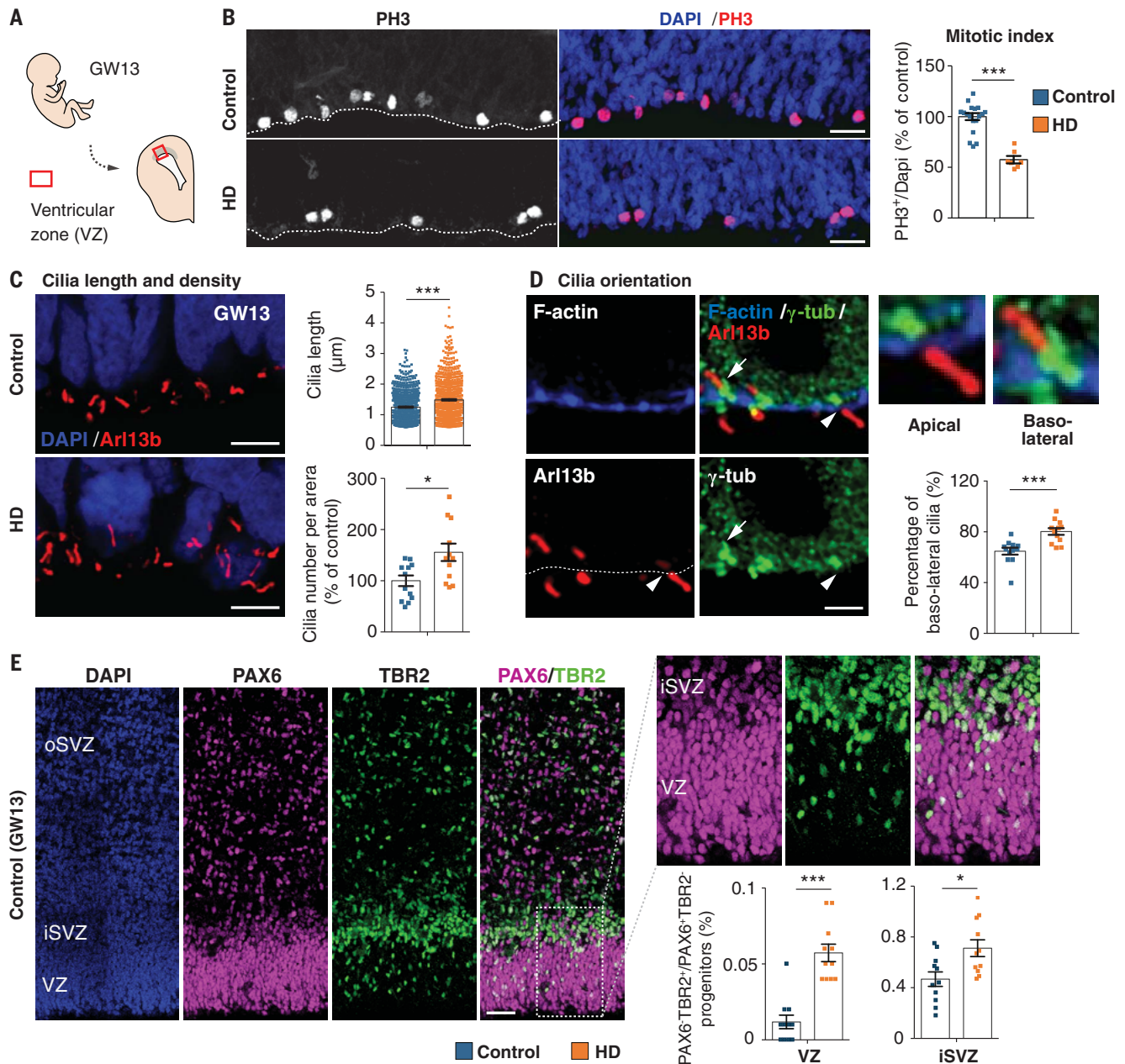


Fig. 4. Mutant huntingtin shifts neurogenesis toward neuronal lineage.

(A) Diagram showing the position of the fetal ventricular zone. (B) Cortical sections of GW13 fetuses were immunostained with antibody against phospho-histone 3 (PH3) and the mitotic index was quantified. For each condition, $n =$ at least 1146 cells from three fetuses from different mothers; $***P < 0.0001$ (Mann-Whitney U test). Scale bars, 25 μm . (C) Coronal GW13 brain sections from control fetus and fetus carrying HD-causing mutation (HD) were immunostained for the cilia marker Arl13b. Scale bars, 5 μm . Bar graphs show cilia length [for each condition, $n =$ at least 770 cilia from four fetuses from different mothers; $***P < 0.0001$ (Mann-Whitney U test)] and cilia density [for each condition, $n = 4$ fetuses from different mothers; $*P = 0.0104$ (unpaired t test)] at the apical surface. (D) Coronal brain sections of GW13

human cortex were immunostained for F-actin, γ -tubulin (γ -tub), and Arl13b. Scale bars, 2 μm . White arrowheads and white arrows show apical and basolateral cilia, respectively. Bar graph shows the percentage of basolateral cilia at the apical surface. For each condition, $n =$ at least 260 cilia from four fetuses from different mothers; $***P = 0.0003$ (Mann-Whitney U test). (E) Typical PAX6 and TBR2 staining of a GW13 human fetal sample analyzed. Scale bars, 50 μm . Bar graphs show the percentage of PAX6 $^+$ /TBR2 $^+$ progenitors [for each condition, three fetuses from different mothers were analyzed; VZ, $n =$ at least 2447 cells, $***P < 0.0001$ (Mann-Whitney U test); iSVZ, $n =$ at least 1580 cells, $*P = 0.011$ (unpaired t test)]. Results are means \pm SEM. Nuclei were counterstained with DAPI.

from these other proteins: Its expression levels were down-regulated, so its demarcation of the apical surface in control samples was diminished, rather than intensified, in HD.

To better understand how junctional complexes in individual apical endfeet are affected in HD, we electroporated E13.5 control and HD mouse embryos in utero with a pCAG-GFP (green fluorescent protein) construct and performed immunohistochemistry on E15.5 coronal sections (Fig. 2, A and B). At this stage in mice and at the corresponding stage GW16 in humans (table S1), the mislocalization of HTT and junction proteins in HD apical progenitors persisted (figs. S6 and S7). Indeed, GFP-expressing knock-in HD progenitors, but not controls, showed a bright line of HTT along the apical surface (Fig. 2B). In control embryos, ZO1, NCAD, and β -catenin immunostaining marked the sides of the apical endfeet; PAR3 staining was more apical (Fig. 2C). In Hdh^{Q111/Q111} embryos, ZO1, NCAD, and β -catenin spread throughout the apical endfeet and PAR3 staining was diminished. These observations were corroborated by immunoblotting protein extracts from Hdh^{Q7/Q7} and Hdh^{Q111/Q111} E15.5 cortices (Fig. 2D). The levels of NCAD and β -catenin were similar in control and HD conditions, but ZO1 and PAR3 protein levels were lower in the mutant mice. Coimmunoprecipitation showed that HTT associates with ZO1, PAR3, and β -catenin, but these interactions were disrupted in HD (Fig. 2E and fig. S8).

Mutant HTT alters progression through the cell cycle

The integrity of the apical junctional complexes is essential for progression through interkinetic nuclear migration, when the nuclei of progenitor cells born at the apical surface move toward the basal side during the G₁ phase of the cell cycle, enter and complete the S phase, then return to the apical surface, where they undergo division (19, 20, 31, 32). Given that the junctional complexes do not form properly with mHTT, we examined cell cycle progression in the apical progenitors.

To measure apical (G₁ phase) and basal (G₂ phase) movements in vivo, we used the fluorescent ubiquitination-based cell cycle indicator (FUCCI), which tracks the expression of markers of the different phases of the cell cycle (33). We electroporated wild-type E13.5 embryos with plasmids encoding CDT1 (chromatin licensing and DNA replication factor 1)-mKO2 and geminin-GFP, then carried out time-lapse imaging on acute cortical slices 2 days after in utero electroporation (Fig. 3A) so that we could distinguish cycling progenitors in G₁ from neurons exiting the cell cycle and migrating away from the ventricular zone (fig. S9A and movie S1). As expected, CDT1 levels peaked during G₁ and fell upon entry into S phase, whereas geminin levels were high during S phase and

G₂ (fig. S9B and movie S2). The velocities of nuclear movement in G₁ and G₂ in control cells were as previously reported (34) (Fig. 3, B, C, and E, and movies S3 to S6), but in Hdh^{Q111/Q111} embryos, migrating nuclei moved more slowly in both G₁ and G₂, causing these phases to lengthen while the G₁/S phase transition was shortened (Fig. 3, D and E, and movies S7 and S8). We next immunostained cortical sections of Hdh^{Q111/Q111} embryos and GW13 HD carrier fetuses with antibody against phospho-histone 3 (PH3), a marker of mitosis, and evaluated the mitotic index (Fig. 3F and Fig. 4, A and B). HD mice and human mutation carriers had roughly half the mitotic index of controls. In HD, therefore, the pool of proliferating cells is diminished.

Mutant HTT biases neurogenesis toward the neuronal lineage

The cell cycle correlates with the assembly (during G₀) and disassembly (at the onset of M phase) of the primary cilium at the apical progenitor endfeet (29, 32). Immunostaining with the cilia marker Arl13b, a member of the adenosine diphosphate ribosylation factor-like family, revealed that both the length and density of the cilia were greater at the apical area of the developing cortex in HD human and mouse samples than in controls (Fig. 4C and fig. S10A), which confirms that the cells were not progressing through the cell cycle properly (20). Because a longer G₁ phase and a shorter G₁/S transition characterize progenitors committed toward the neuronal lineage (32, 35), we asked whether mHTT favors the production of apical over basal progenitors.

We evaluated cilia orientation by labeling brain sections with F-actin (to delineate the apical surface) and Arl13b and γ -tubulin (to label the basal body) (Fig. 4D and fig. S10B). The proportion of basolateral cilia, which signal the generation of basal progenitors (36), was greater in HD human and mouse samples than in controls. To discriminate between apical progenitors and basal progenitors, which are more engaged in the neuronal lineage (37), we labeled for the transcription factors PAX6 and TBR2, respectively. HD human and mouse samples showed a greater proportion of basal progenitors at the ventricular zone, subventricular zone, and inner subventricular zone than did controls (Fig. 4E and fig. S10C).

Discussion

Our data show that mHTT mislocalizes at junctional complexes, disrupts the polarity of human and mouse neuroepithelium, and interferes with the cell cycle of apical progenitors, leading to fewer proliferating cells and more neural progenitors prematurely entering lineage specification. This is consistent with previous evidence that HTT regulates

cellular adhesion, polarity, and epithelial organization (27). In the presence of mHTT, the epithelial-mesenchymal transition is accelerated (28). It is possible that mHTT contributes to cellular disorganization through other means as well, such as by interfering with the orientation of the mitotic spindle (7). Given that HTT also establishes apical polarity in the mammary epithelium, where it forms a complex with PAR3, aPKC, and RAB11A and ensures the apical translocation of PAR3-aPKC through RAB11A (29), we speculate that HTT may act to maintain epithelial cell polarity throughout the body.

A recent neuroimaging study found that the posterior Sylvian fissure, normally asymmetrical between the right and left hemispheres, lacks asymmetry in the HD population studied (38). Because the Sylvian fissure appears early in utero, the authors concluded that this abnormal symmetry arises during fetal development. Our results show that mHTT does alter very early stages of brain development in human HD, even though the samples we analyzed were from mutation carriers with small pathological expansions (39, 40, and 42 repeats) that would typically cause later manifestations of HD. The defects we observed likely render the corticostriatal circuitry more vulnerable to the later dysfunctions characteristic of HD (23), as proposed for another polyglutamine disease, spinocerebellar ataxia type 1 (39). The path to degeneration is complex, however, and weaves together both pathogenic and compensatory mechanisms. For example, a recent study found that HD mutation carriers as young as 6 years of age show compensatory hyperconnectivity between the striatum and cerebellum; this initially enlarges the striatum but the metabolic load soon overwhelms it, the connections are rapidly lost, and the striatum atrophies well before the onset of motor symptoms (40).

It is now beyond doubt that neurodegenerative diseases can have a developmental component. For HD, this discovery opens the door for future studies to identify molecular treatments. For example, the HD iPSC Consortium characterized isoxazole-9 after finding that it reverts abnormal neuronal differentiation in HD-derived pluripotent stem cells (17). It may be that treatment should be given very early in life; it remains to be seen whether reducing mHTT levels in adulthood, even in the prodromal stage, would be sufficient to forestall symptom progression, because the brain circuitry is already altered.

REFERENCES AND NOTES

1. M. P. Duyao *et al.*, *Science* **269**, 407–410 (1995).
2. S. Zeitlin, J. P. Liu, D. L. Chapman, V. E. Papaioannou, A. Elstratidis, *Nat. Genet.* **11**, 155–163 (1995).
3. A. Reiner, I. Dragatsis, S. Zeitlin, D. Goldowitz, *Mol. Neurobiol.* **28**, 259–276 (2003).
4. J. D. Godin *et al.*, *Neuron* **67**, 392–406 (2010).

5. S. U. McKinstry *et al.*, *J. Neurosci.* **34**, 9455–9472 (2014).
6. M. Barnat, J. Le Friec, C. Benstaali, S. Humbert, *Neuron* **93**, 99–114 (2017).
7. M. Molina-Calavita *et al.*, *J. Neurosci.* **34**, 10034–10040 (2014).
8. E. E. Arteaga-Bracho *et al.*, *Neurobiol. Dis.* **96**, 144–155 (2016).
9. A. E. Molero *et al.*, *Proc. Natl. Acad. Sci. U.S.A.* **113**, 5736–5741 (2016).
10. J. K. Lee *et al.*, *Neurology* **79**, 668–674 (2012).
11. P. C. Nopoulos *et al.*, *Brain* **134**, 137–142 (2011).
12. S. J. Tabrizi *et al.*, *Lancet Neurol.* **10**, 31–42 (2011).
13. C. C. Tang *et al.*, *J. Clin. Invest.* **123**, 4076–4088 (2013).
14. A. Virlogeux *et al.*, *Cell Rep.* **22**, 110–122 (2018).
15. X. Zhao *et al.*, *Proc. Natl. Acad. Sci. U.S.A.* **113**, E5655–E5664 (2016).
16. K. L. Ring *et al.*, *Stem Cell Rep.* **5**, 1023–1038 (2015).
17. HD iPSC Consortium, *Nat. Neurosci.* **20**, 648–660 (2017).
18. P. Conforti *et al.*, *Proc. Natl. Acad. Sci. U.S.A.* **115**, E762–E771 (2018).
19. Y. Arai, E. Taverna, *Front. Cell. Neurosci.* **11**, 384 (2017).
20. T. Miyata, M. Okamoto, T. Shinoda, A. Kawaguchi, *Front. Cell. Neurosci.* **8**, 473 (2015).
21. V. C. Wheeler *et al.*, *Hum. Mol. Genet.* **11**, 633–640 (2002).
22. S. Zheng, N. Ghitani, J. S. Blackburn, J. P. Liu, S. O. Zeitlin, *Mol. Brain* **5**, 28 (2012).
23. F. Saudou, S. Humbert, *Neuron* **89**, 910–926 (2016).
24. F. S. Chou, R. Li, P. S. Wang, *Cell. Mol. Life Sci.* **75**, 1027–1041 (2018).
25. R. S. Bultje *et al.*, *Neuron* **63**, 189–202 (2009).
26. J. D. Godin, G. Poizat, M. A. Hickey, F. Maschat, S. Humbert, *EMBO J.* **29**, 2433–2445 (2010).
27. V. Lo Sardo *et al.*, *Nat. Neurosci.* **15**, 713–721 (2012).
28. C. Moreira Sousa *et al.*, *EMBO Mol. Med.* **5**, 309–325 (2013).
29. S. Elias, J. R. McGuire, H. Yu, S. Humbert, *PLOS Biol.* **13**, e1002142 (2015).
30. M. S. Thion *et al.*, *J. Natl. Cancer Inst.* **107**, djv208 (2015).
31. E. Taverna, M. Götz, W. B. Huttner, *Annu. Rev. Cell Dev. Biol.* **30**, 465–502 (2014).
32. C. Norden, *J. Cell Sci.* **130**, 1859–1863 (2017).
33. A. Sakaue-Sawano *et al.*, *Cell* **132**, 487–498 (2008).
34. Y. Kosodo *et al.*, *EMBO J.* **30**, 1690–1704 (2011).
35. Y. Arai *et al.*, *Nat. Commun.* **2**, 154–165 (2011).
36. M. Wilsch-Bräuninger, J. Peters, J. T. Paridaen, W. B. Huttner, *Development* **139**, 95–105 (2012).
37. M. N. Manuel, D. Mi, J. O. Mason, D. J. Price, *Front. Cell. Neurosci.* **9**, 70 (2015).
38. J. F. Mangin *et al.*, *Neuroimage Clin.* **26**, 102211 (2020).
39. C. R. Edamakanti, J. Do, A. Didonna, M. Martina, P. Opal, *J. Clin. Invest.* **128**, 2252–2265 (2018).
40. A. V. Tereshchenko *et al.*, *Neurology* **94**, e1908–e1915 (2020).

ACKNOWLEDGMENTS

We are grateful to the patients and their families. We thank L. Benammar and M. Biet for their logistical help; midwife O. Philippon for her support; C. Benstaali and E. Martin for help with experiments; staff of the animal facility and of the Photonic Imaging Center (part of the ISdV core facility and certified by the IBISA label) of GIN for technical help; F. Saudou, members of the Humbert laboratory, and V. L. Brandt for helpful discussions; and the Association Huntington France (AHF) for continuous support. **Funding:** Supported by grants from Agence Nationale pour la

Recherche (ANR-15-IDEX-02 NeuroCoG, S.H.; Network of centers of excellence in neurodegeneration COEN, A.D. and S.H.); Fondation pour la Recherche Médicale (DEQ 20170336752, S.H.); Fondation pour la Recherche sur le Cerveau (S.H.); and the AGEMED program from INSERM (S.H.). M.B. and S.H. are INSERM investigators. E.A. was supported by a CIFRE (2012-0401) doctoral fellowship. M.C. is supported by a La ligue contre le cancer post-doctoral fellowship. J.-P.L. and S.O.Z. are supported by NIH NS077926. **Author contributions:** M.B., A.D., and S.H. designed the study; M.B. and S.H. wrote the manuscript, which was commented on by all authors; M.B. performed most of the experiments; M.C. performed biochemical experiments and immunohistochemistry; E.A. performed interkinetic nuclear migration experiments; D.W., R.Kac., R.Kas., and F.A. performed immunohistochemistry; S.L. and B.Y.B. provided mouse embryonic brains; J.L., A.T., A.D., and M.D. collected human data; S.B. and C.D. performed fetopathological examinations; and J.-P.L. and S.O.Z. provided embryonic brains from Flag-tagged Hdh mice. **Competing interests:** None declared. **Data and materials availability:** All data are available in the manuscript or the supplementary materials.

SUPPLEMENTARY MATERIALS

science.sciencemag.org/content/369/6505/787/suppl/DC1

Materials and Methods

Figs. S1 to S10

Table S1

Movies S1 to S8

15 March 2019; resubmitted 27 April 2020

Accepted 29 June 2020

Published online 16 July 2020

10.1126/science.aax3338

CORONAVIRUS

Non-neuronal expression of SARS-CoV-2 entry genes in the olfactory system suggests mechanisms underlying COVID-19–associated anosmia

David H. Brann^{1*}, Tatsuya Tsukahara^{1*}, Caleb Weinreb^{1*}, Marcela Lipovsek², Koen Van den Berge^{3,4}, Boying Gong⁵, Rebecca Chance⁶, Iain C. Macaulay⁷, Hsin-Jung Chou⁶, Russell B. Fletcher^{6†}, Diya Das^{6,8‡}, Kelly Street^{9,10}, Hector Roux de Bezieux^{5,11}, Yoon Gi Choi¹², Davide Risso¹³, Sandrine Dudoit^{3,5}, Elizabeth Purdom³, Jonathan Mill¹⁴, Ralph Abi Hachem¹⁵, Hiroaki Matsunami¹⁶, Darren W. Logan¹⁷, Bradley J. Goldstein¹⁵, Matthew S. Grubb², John Ngai^{6,12,18§}, Sandeep Robert Datta^{1||}

Altered olfactory function is a common symptom of COVID-19 (coronavirus disease 2019), but its etiology is unknown. A key question is whether SARS-CoV-2 (severe acute respiratory syndrome coronavirus 2; CoV-2)—the causal agent in COVID-19—affects olfaction directly, by infecting olfactory sensory neurons or their targets in the olfactory bulb, or indirectly, by perturbing support cells. Bulk and single-cell RNA sequencing revealed that support and stem cells in the human and mouse olfactory epithelium and vascular pericytes in the mouse olfactory bulb express angiotensin-converting enzyme 2 (ACE2), which is essential for CoV-2 cell entry. In contrast, ACE2 was not detected in either olfactory sensory neurons or olfactory bulb neurons. Immunostaining confirmed these results and revealed pervasive expression of ACE2 protein in dorsally located olfactory epithelial sustentacular cells and mouse olfactory bulb pericytes. These findings suggest that CoV-2 infection of non-neuronal cell types leads to olfactory dysfunction in patients with COVID-19.

INTRODUCTION

SARS-CoV-2 (severe acute respiratory syndrome coronavirus 2; CoV-2) is a pandemic coronavirus that causes the COVID-19 (coronavirus disease 2019) syndrome, which can include upper respiratory infection (URI) symptoms, severe respiratory distress, acute cardiac injury, and death (1–4). CoV-2 is closely related to other coronaviruses, including the causal agents in pandemic SARS and MERS (Middle East respiratory syndrome) (SARS-CoV and

MERS-CoV, respectively) and endemic viruses typically associated with mild URI syndromes (HCoV-OC43, HCoV-HKU1, HCoV-229E, and HCoV-NL63) (5–7). Clinical reports suggest that infection with CoV-2 is associated with high rates of disturbances in smell and taste perception, including anosmia (8–13). While many viruses (including coronaviruses) induce transient changes in odor perception due to inflammatory responses, in at least some cases, COVID-19–related anosmia has been reported to occur in the absence of significant nasal inflammation or coryzal symptoms (11, 14–16). Furthermore, recovery from COVID-19–related anosmia often occurs over weeks (11, 17, 18), while recovery from typical postviral anosmia—which is often caused by direct damage to olfactory sensory neurons (OSNs)—frequently takes months (19–21). These observations suggest that CoV-2 might target odor processing through mechanisms distinct from those used by other viruses, although the specific means through which CoV-2 alters odor perception remains unknown.

CoV-2—like SARS-CoV—infects cells through interactions between its spike (S) protein and the angiotensin-converting enzyme 2 (ACE2) protein on target cells. This interaction requires cleavage of the S protein, likely by the cell surface protease TMPRSS2 (transmembrane serine protease 2), although other proteases [such as cathepsin B and L (CTSB/CTSL)] may also be involved (4–6, 22–25). Other coronaviruses use different cell surface receptors and proteases to facilitate cellular entry, including DPP4, FURIN, and HSPA5 for MERS-CoV; ANPEP for HCoV-229E; TMPRSS11D for SARS-CoV (in addition to ACE2 and TMPRSS2); and ST6GAL1 and ST3GAL4 for HCoV-OC43 and HCoV-HKU1 (6, 26–28).

We hypothesized that identifying the specific cell types susceptible to direct CoV-2 infection (due to, e.g., ACE2 and TMPRSS2 expression) would provide insight into possible mechanisms through which COVID-19 alters smell perception. The nasal epithelium is divided into a respiratory epithelium (RE) and olfactory epithelium

¹Harvard Medical School Department of Neurobiology, Boston, MA 02115, USA. ²Centre for Developmental Neurobiology, Institute of Psychiatry, Psychology and Neuroscience (IoPPN), King's College London, London SE1 1UL, UK. ³Department of Statistics, University of California, Berkeley, Berkeley, CA 94720, USA. ⁴Department of Applied Mathematics, Computer Science and Statistics, Ghent University, Ghent, Belgium. ⁵Division of Biostatistics, School of Public Health, University of California, Berkeley, Berkeley, CA 94720, USA. ⁶Department of Molecular and Cell Biology, University of California, Berkeley, Berkeley, CA 94720, USA. ⁷Earlham Institute, Norwich Research Park, Norwich NR4 7UZ, UK. ⁸Berkeley Institute for Data Science, University of California, Berkeley, Berkeley, CA 94720, USA. ⁹Department of Data Sciences, Dana-Farber Cancer Institute, Boston, MA 02115, USA. ¹⁰Department of Biostatistics, Harvard T.H. Chan School of Public Health, Boston, MA 02115, USA. ¹¹Center for Computational Biology, University of California, Berkeley, Berkeley, CA 94720, USA. ¹²QB3 Functional Genomics Laboratory, University of California, Berkeley, Berkeley, CA 94720, USA. ¹³Department of Statistical Sciences, University of Padova, Padova, Italy. ¹⁴University of Exeter Medical School, College of Medicine and Health, University of Exeter, Exeter EX2 5DW, UK. ¹⁵Department of Head and Neck Surgery and Communication Sciences, Duke University School of Medicine, Durham, NC 27717, USA. ¹⁶Department of Molecular Genetics and Microbiology, Department of Neurobiology, Duke University School of Medicine, Duke Institute for Brain Sciences, Durham, NC 27710, USA. ¹⁷Waltham Petcare Science Institute, Leicestershire LE14 4RT, UK. ¹⁸Helen Wills Neuroscience Institute, University of California, Berkeley, Berkeley, CA 94720, USA.

*These authors contributed equally to this work.

†Present address: Surrozen Inc., South San Francisco, CA 94080, USA.

‡Present address: Genentech Inc., South San Francisco, CA 94080, USA.

§Present address: National Institute of Neurological Disorders and Stroke, National Institutes of Health, Bethesda, MD 20892, USA.

||Corresponding author. Email: srdatta@hms.harvard.edu

Copyright © 2020 The Authors, some rights reserved; exclusive licensee American Association for the Advancement of Science. No claim to original U.S. Government Works. Distributed under a Creative Commons Attribution License 4.0 (CC BY).

(OE), whose functions and cell types differ. The nasal RE is continuous with the epithelium that lines much of the respiratory tract and is thought to humidify air as it enters the nose; main cell types include basal cells, ciliated cells, secretory cells (including goblet cells), and brush/microvillar (MV) cells (Fig. 1) (29, 30). The OE, in contrast, is responsible for odor detection, as it houses mature OSNs (mOSNs) that interact with odors via receptors localized on their dendritic cilia. OSNs are supported by sustentacular (SUS) cells, which act to structurally support sensory neurons and phagocytose and/or detoxify potentially damaging agents, and maintain local salt and water balance (31–33); MV cells and mucus-secreting Bowman's gland (BG) cells also play important roles in maintaining OE homeostasis and function (Fig. 1) (29, 34). In addition, the OE contains globose basal cells (GBCs), which are primarily responsible for regenerating OSNs during normal epithelial turnover, and horizontal basal cells (HBCs), which are reserve stem cells activated upon tissue damage (35–37). Although studies defining the lineage relationships between GBCs, HBCs, and their progeny have necessarily been performed in rodents, basal progenitor populations with similar transcriptional profiles are present in adult human OE, suggesting closely related homeostatic and injury-response mechanisms (37, 38). Odor information is conveyed from the OE to the brain by OSN axons, which puncture the cribriform plate at the base of the skull and terminate in the olfactory bulb (OB). Within the OB, local circuits process olfactory information before sending it to higher brain centers (Fig. 1).

It has recently been demonstrated through single-cell RNA sequencing (RNA-seq) analysis (referred to herein as scSeq) that cells from the human upper airway—including nasal RE goblet and ciliated cells—express high levels of *ACE2* and *TMPRSS2*, suggesting that these RE cell types may serve as a viral reservoir during CoV-2 infection (39, 40). However, analyzed samples in these datasets did not include any OSNs or SUS cells, indicating that tissue

sampling in these experiments did not include the OE (41, 42). Here, we query both new and previously published bulk RNA-seq and scSeq datasets from the olfactory system for expression of *ACE2*, *TMPRSS2*, and other genes implicated in coronavirus entry. We find that non-neuronal cells in the OE and OB, including support, stem, and perivascular cells, express CoV-2 entry-associated transcripts and their associated proteins, suggesting that infection of these non-neuronal cell types contributes to anosmia in patients with COVID-19.

RESULTS

Expression of CoV-2 entry genes in human OE

To determine whether genes relevant to CoV-2 entry are expressed in OSNs or other cell types in the human OE, we queried previously published bulk RNA-seq data derived from the whole olfactory mucosa (WOM) of macaque, marmoset, and human (43) and found expression of almost all CoV-2 entry-related genes in all WOM samples (fig. S1A). To identify the specific cell types in human OE that express *ACE2*, we quantified gene expression in scSeq derived from four human nasal biopsy samples recently reported by Durante *et al.* (38). Neither *ACE2* nor *TMPRSS2* was detected in mOSNs, whereas these genes were detected in both SUS cells and HBCs (Fig. 2, A to D, and fig. S1, B to E). In contrast, genes relevant to cell entry of other CoVs were expressed in OSNs, as well as in other OE cell types. We confirmed the expression of *ACE2* protein via immunostaining of human OE biopsy tissue, which revealed expression in SUS and HBC cells, and an absence of *ACE2* protein in OSNs (Fig. 2E and fig. S2). Together, these results demonstrate that SUS and olfactory stem cells, but not OSNs, are potentially direct targets of CoV-2 in the human OE.

Given that the nasopharynx is a major site of infection for CoV-2 (10), we compared the frequency of *ACE2* and *TMPRSS2* expression among the cell types in the human RE and OE (38). SUS cells exhibited the highest frequency of *ACE2* expression in the OE (2.9% of cells), although this frequency was slightly lower than that observed in respiratory ciliated and secretory cells (3.6 and 3.9%, respectively). While all HBC subtypes expressed *ACE2*, the frequency of expression of *ACE2* was lower in olfactory HBCs (0.8% of cells) compared to respiratory HBCs (1.7% of cells) (Fig. 2D). In addition, all other RE subtypes showed higher frequencies of *ACE2* and *TMPRSS2* expression than was apparent in OE cells.

These results demonstrate the presence of key CoV-2 entry-related genes in specific cell types in the OE but at lower levels of expression than in RE isolated from the human nasal mucosa. We wondered whether these lower levels of expression might nonetheless be sufficient for infection by CoV-2. It was recently reported that the nasal RE has higher expression of CoV-2 entry genes than the RE that lines the trachea or lungs (44), and we therefore asked where the OE fell within this previously established spectrum of expression. To address this question, we developed a two-step alignment procedure in which we first sought to identify cell types that were common across the OE and RE and then leveraged gene expression patterns in these common cell types to normalize gene expression levels across all cell types in the OE and RE (Fig. 3 and fig. S3). This approach revealed correspondences between submucosal gland goblet cells in the RE and BG cells in the OE (96% mapping probability; see Materials and Methods) and between pulmonary ionocytes in the RE and a subset of MV cells in the OE (99% mapping

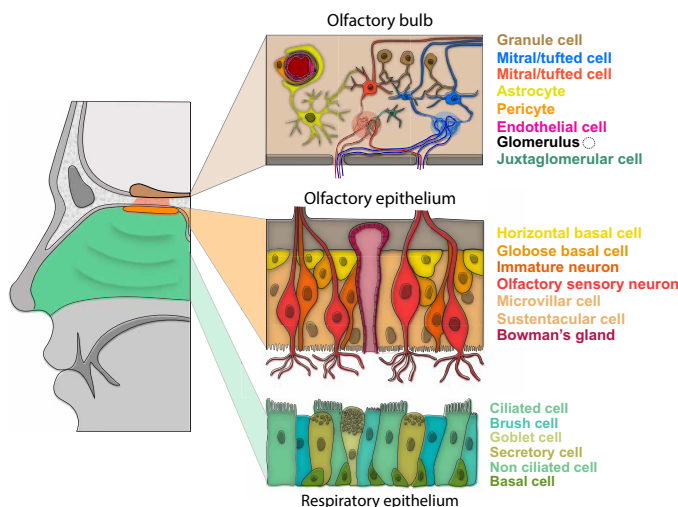


Fig. 1. Schematic of the nasal RE, OE, and the OB. Left: Sagittal view of the human nasal cavity, in which respiratory and olfactory epithelia are colored. Right: For each type of epithelium, a schematic of the anatomy and known major cell types are shown. In the OB in the brain (tan), the axons of OSNs coalesce into glomeruli, and mitral/tufted cells innervate these glomeruli and send olfactory projections to downstream olfactory areas. Glomeruli are also innervated by juxtglomerular cells, a subset of which are dopaminergic.

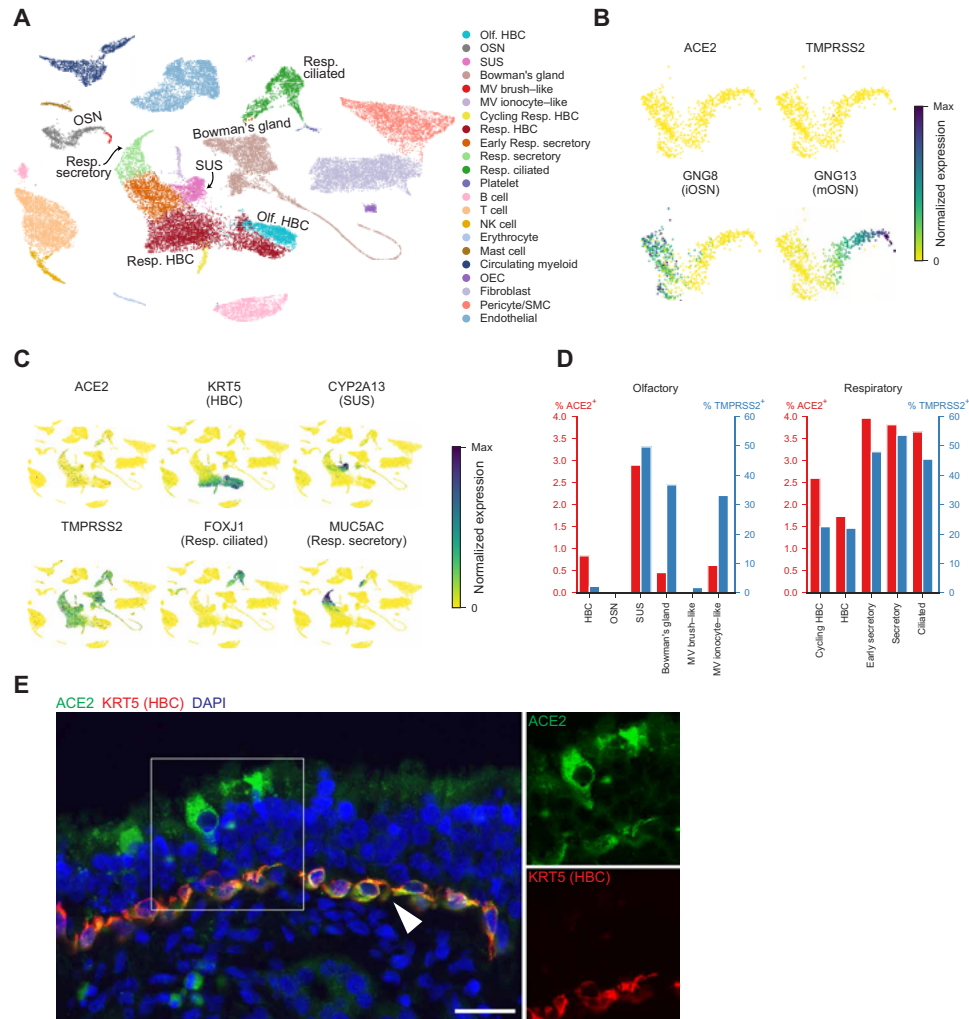


Fig. 2. Coronavirus cell entry–related genes are expressed in human RE and OE but are not detected in human OSNs. (A) UMAP representation of cell types in human nasal biopsy scSeq data from Durante *et al.* (38). Each dot represents an individual cell, colored by cell type. Resp., respiratory; OEC, olfactory ensheathing cell; SMC, smooth muscle cell; NK, natural killer. (B) UMAP representations of 865 detected immature (*GNG8*) and mature (*GNG13*) OSNs. Neither *ACE2* nor *TMPRSS2* is detected in either population of OSNs. The color represents the normalized expression level for each gene (number of UMIs for a given gene divided by the total number of UMIs for each cell). (C) UMAP representations of all cells, depicting the normalized expression of CoV-2–related genes *ACE2* and *TMPRSS2*, as well as several cell-type markers. *ACE2* and *TMPRSS2* are expressed in respiratory and olfactory cell types but not in OSNs. *ACE2* and *TMPRSS2* are detected in HBC (*KRT5*) and SUS (*CYP2A13*) cells, as well as other respiratory epithelial cell types, including respiratory ciliated (*FOXJ1*) cells. (D) Percentage of cells expressing *ACE2* and *TMPRSS2*. *ACE2* was not detected in any OSNs, but was observed in SUS cells and HBCs, among other olfactory and respiratory epithelial cell types. Olfactory and respiratory cell types are shown separately. *ACE2* and *TMPRSS2* were also significantly coexpressed (odds ratio, 7.088; $P = 3.74 \times 10^{-57}$, Fisher's exact test). (E) *ACE2* immunostaining of a human olfactory mucosal biopsy (taken from a 28-year-old female). *ACE2* protein (green) is detected in SUS cells and *KRT5*-positive HBCs (red; white arrowhead). Nuclei were stained with 4',6-diamidino-2-phenylindole (DAPI) (blue). Scale bar, 25 μ m. The *ACE2* and *KRT5* channels from the box on the left are shown individually on the right.

probability; see Materials and Methods and fig. S3); after alignment, human OE SUS cells were found to express *ACE2* and *TMPRSS2* at levels similar to those observed in the remainder of the non-nasal respiratory tract (Fig. 3C) (44). As CoV-2 can infect cells in the lower respiratory tract (40, 45), these results are consistent with the possibility that specific cell types in the human OE express *ACE2* at a level that is permissive for direct infection.

Expression of CoV-2 entry genes in mouse OE

To further explore the distribution of CoV-2 cell entry genes in the olfactory system, we turned to the mouse, which enables interrogative experiments not possible in humans. To evaluate whether mouse ex-

pression patterns correspond to those observed in the human OE, we examined published datasets in which RNA-seq was independently performed on mouse WOM and on purified populations of mOSNs (46–48). The CoV-2 receptor *Ace2* and the protease *Tmprss2* were expressed in WOM, as were the cathepsins *Ctsb* and *Ctsl* (Fig. 4A and fig. S4A) (46). However, expression of these genes (with the exception of *Ctsb*) was much lower, and *Ace2* expression was nearly absent in purified OSN samples (Fig. 4A and fig. S4A, see legend for counts). Genes used for cell entry by other CoVs (except *St3gal4*) were also expressed in WOM, and de-enriched in purified OSNs. The de-enrichment of *Ace2* and *Tmprss2* in OSNs relative to WOM was also observed in two other mouse RNA-seq datasets (fig. S4B) (47, 48).

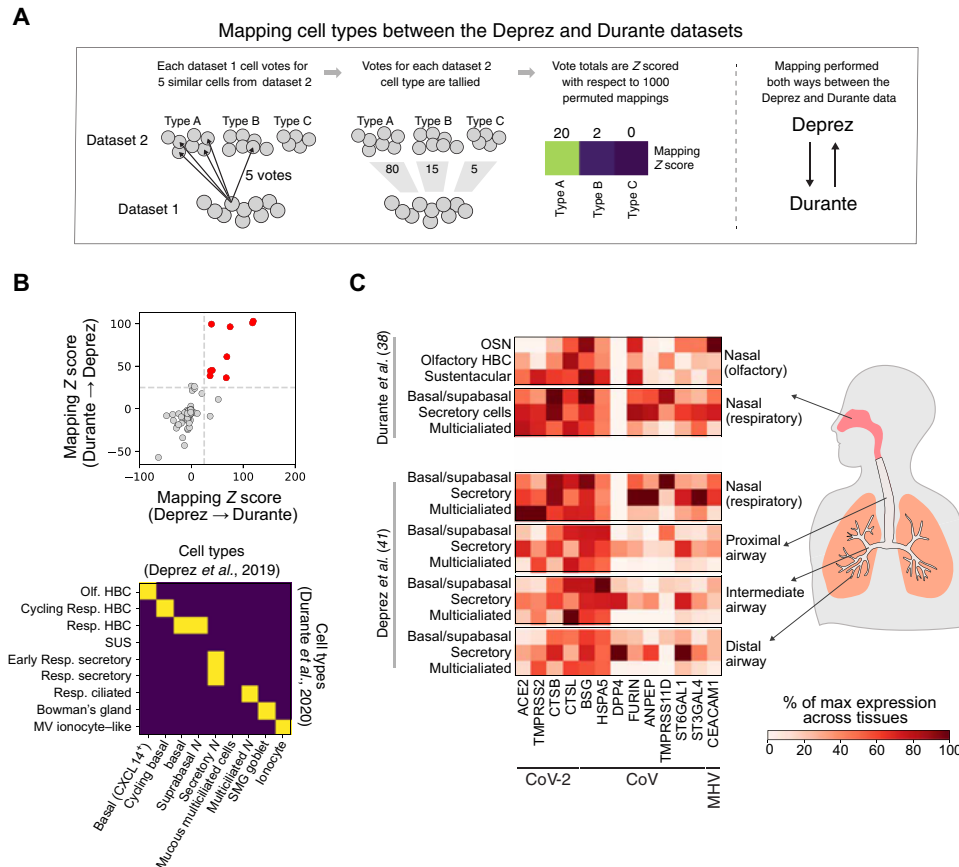


Fig. 3. Coronavirus cell entry-related genes are expressed at comparable levels across respiratory and olfactory epithelial datasets. (A) Schematic of the mapping strategy used to identify similar cell types across datasets, applied to a toy example. Each cell type from dataset 1 is mapped to cell types from dataset 2. From left to right: Each dataset 1 cell voted on its five most similar cells in dataset 2; the total number of votes cast for each dataset 2 cell type was quantified; and vote totals were Z-scored against 1000 shuffles where cell-type labels were permuted. (B) Mapping was performed bidirectionally between the Deprez *et al.* (41) and Durante *et al.* (38) datasets, and the mapping Z scores in each direction are compared. Top: The set of cell-type correspondences with high Z scores (>25) in both directions are colored red. Bottom: The set of cell-type correspondences with high bidirectional mappings shown in red in top panel are highlighted in yellow. (C) Gene expression across cell types and tissues in Durante *et al.* (top) and Deprez *et al.* (bottom). Each gene is normalized to its maximum value across all tissues. Gene expression from Durante *et al.* was normalized to that in Deprez *et al.* to enable comparisons (see Materials and Methods and fig. S3). The tissues correspond to the indicated positions along the airway from nasal to distal lung. *Ace2* expression in olfactory HBC and SUS cells is comparable to that observed in other cell types in the lower respiratory tract.

The presence of *Ace2* and *Tmprs2* transcripts in mouse WOM and their (near total) absence in purified OSNs suggest that the molecular components that enable CoV-2 entry into cells are expressed in non-neuronal cell types in the mouse nasal epithelium. To identify the specific cell types that express *Ace2* and *Tmprs2*, we performed scSeq (via Drop-seq; see Materials and Methods) on mouse WOM (Fig. 4B). These results were consistent with observations made in the human epithelium: *Ace2* and *Tmprs2* were expressed in a fraction of SUS and BG cells and a very small fraction of stem cells but not in OSNs (zero of 17,666 identified mOSNs; Fig. 4C and fig. S4, C and D). Of note, only dorsally located SUS cells, which express the markers *Sult1c1* and *Acsm4*, were positive for *Ace2* (Fig. 4D and fig. S4, D and E). Based upon this observation, we reanalyzed the human OE scSeq data, which revealed that all positive SUS cells expressed genetic markers associated with the dorsal epithelium (fig. S1D). An independent mouse scSeq dataset (obtained using the 10x Chromium platform; see Materials and Methods) confirmed that OSNs did not express *Ace2* (2 of 28,769 mOSNs were positive for *Ace2*),

while expression was observed in a fraction of BG cells and HBCs (fig. S5 and see Materials and Methods). Expression in SUS cells was not observed in this dataset, which included relatively few dorsal SUS cells (a possible consequence of the specific cell isolation procedure associated with the 10x Chromium platform; compare fig. S5C and Fig. 4D).

Staining of the mouse WOM with anti-ACE2 antibodies confirmed that ACE2 protein is expressed in SUS cells and is specifically localized to the SUS cell microvilli (Fig. 5). ACE2⁺ SUS cells were identified exclusively within the dorsal subregion of the OE; critically, within that region, many (and possibly all) SUS cells expressed ACE2 (Fig. 5, B to E). Staining was also observed in BG cells, but not in OSNs, and in subsets of RE cells (Fig. 5, F and G). Together, these data demonstrate that ACE2 is expressed by SUS cells that specifically reside in the dorsal epithelium in both mouse and human.

Expression of CoV-2 entry genes in injured mouse OE

Viral injury can lead to broad changes in OE physiology that are accompanied by recruitment of stem cell populations tasked

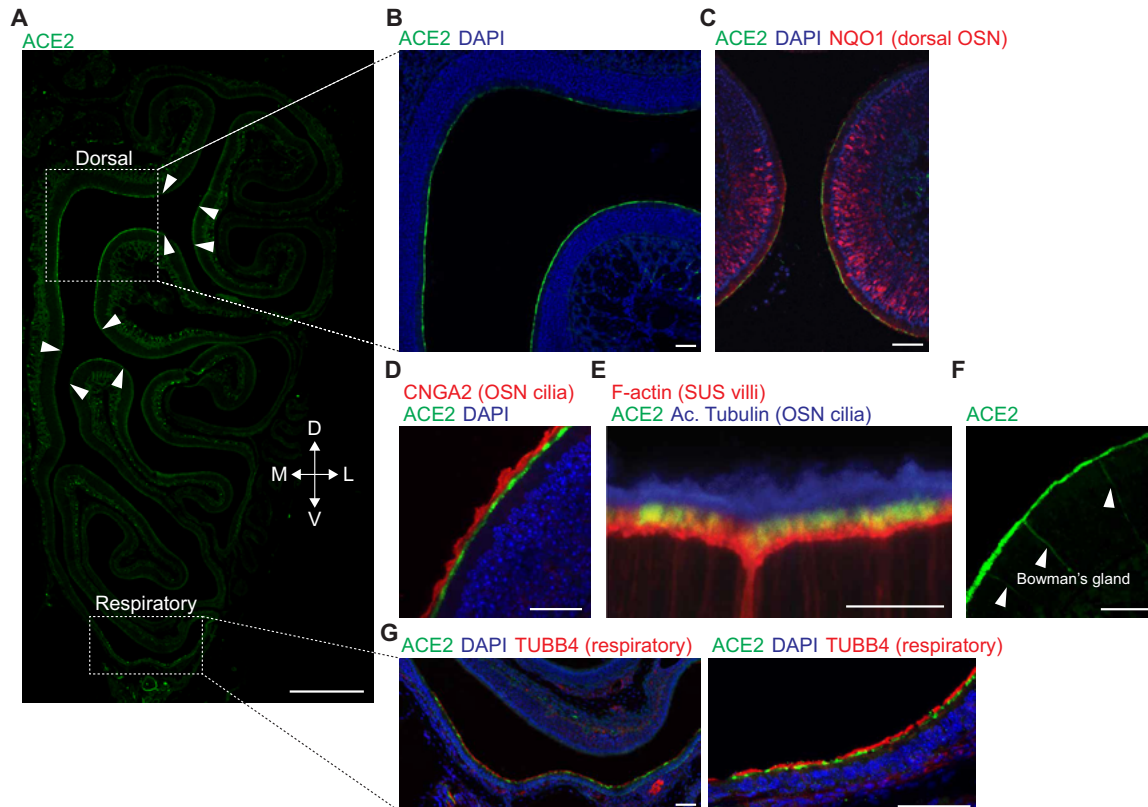


Fig. 5. ACE2 protein is detected in the mouse OE and RE. (A) ACE2 immunostaining of mouse main OE. As shown in this coronal section, ACE2 protein is detected in the dorsal zone and RE. The punctate Ace2 staining beneath the epithelial layer is likely associated with vasculature. Scale bar, 500 μ m. Arrowheads depict the edges of ACE2 expression, corresponding to the presumptive dorsal zone [confirmed in (C)]. Dashed boxes indicate the areas shown in (B) and (G) (left). D, dorsal; L, lateral; M, medial; V, ventral. (B) ACE2 protein is detected in the dorsal zone of the OE. Scale bar, 50 μ m. (C) Dorsal zone–specific expression of ACE2 in the OE was confirmed by costaining with NQO1, a protein expressed in dorsal zone OSNs. Scale bar, 50 μ m. (D) ACE2 signal in dorsal OE does not overlap with the cilia of OSNs, as visualized by CNGA2. Scale bar, 50 μ m. (E) High-magnification image of the apical end of the OE reveals that ACE2 signal is localized at the tip of villi of SUS cells, visualized by phalloidin (F-actin), but does not overlap with cilia of OSNs, as visualized by acetylated tubulin (Ac. Tubulin). Scale bar, 10 μ m. (F) BGs, which span from the lamina propria to the apical surface (arrowheads), were positive for ACE2 staining. Scale bar, 50 μ m. (G) ACE2 expression in the RE was confirmed by costaining with TUBB4. Scale bars, 50 μ m.

Immunostaining in the OB revealed that blood vessels expressed high levels of ACE2 protein, particularly in pericytes; nearly all pericytes exhibited some degree of staining with ACE2 antibodies. Consistent with the scSeq results, staining was not observed in any neuronal cell type (Fig. 7, F and G). These observations may also hold true for at least some other brain regions, as reanalysis of 10 deeply sequenced scSeq datasets from different regions of the nervous system demonstrated that *Ace2* and *Tmprss2* expression is almost completely absent from neurons, consistent with prior immunostaining results (fig. S10) (52, 53). Given the extensive similarities detailed above in expression patterns for ACE2 and TMPRSS2 in the mouse and human, these findings (from mouse experiments) suggest that OB neurons are likely not a primary site of infection, but that vascular pericytes may be sensitive to CoV-2.

DISCUSSION

Here, we show that subsets of OE SUS cells, HBCs, and BG cells in both mouse and human samples express the CoV-2 receptor ACE2 and the S protein protease TMPRSS2. Human OE SUS cells express these genes at levels comparable to those observed in lung cells. In contrast, we failed to detect ACE2 expression in human or mouse OSNs at either the transcript or protein levels. Similarly,

mouse vascular pericytes in the OB express ACE2, while we did not detect ACE2 in OB neurons. Thus, primary infection of non-neuronal cell types—rather than sensory or bulb neurons—may be responsible for anosmia and related disturbances in odor perception in patients with COVID-19.

The identification of non-neuronal cell types in the OE and OB susceptible to CoV-2 infection suggests four possible, non-mutually exclusive mechanisms for the acute loss of smell reported in patients with COVID-19. First, local infection of support and vascular cells in the nose and bulb could cause significant inflammatory responses (including cytokine release) whose downstream effects could block effective odor conduction or alter the function of OSNs or OB neurons (14, 54). Second, damage to support cells (which are responsible for local water and ion balance) could indirectly influence signaling from OSNs to the brain (55). Third, damage to SUS cells and BG cells in mouse models can lead to OSN death, which in turn could abrogate smell perception (56). Last, vascular damage could lead to hypoperfusion and inflammation leading to changes in OB function.

Although scSeq revealed *ACE2* transcripts in only a subset of OE cells, this low level of observed expression matches or exceeds that observed in respiratory cell types that are infected by CoV-2 in patients with COVID-19 (Fig. 3) (39). Critically, immunostaining in

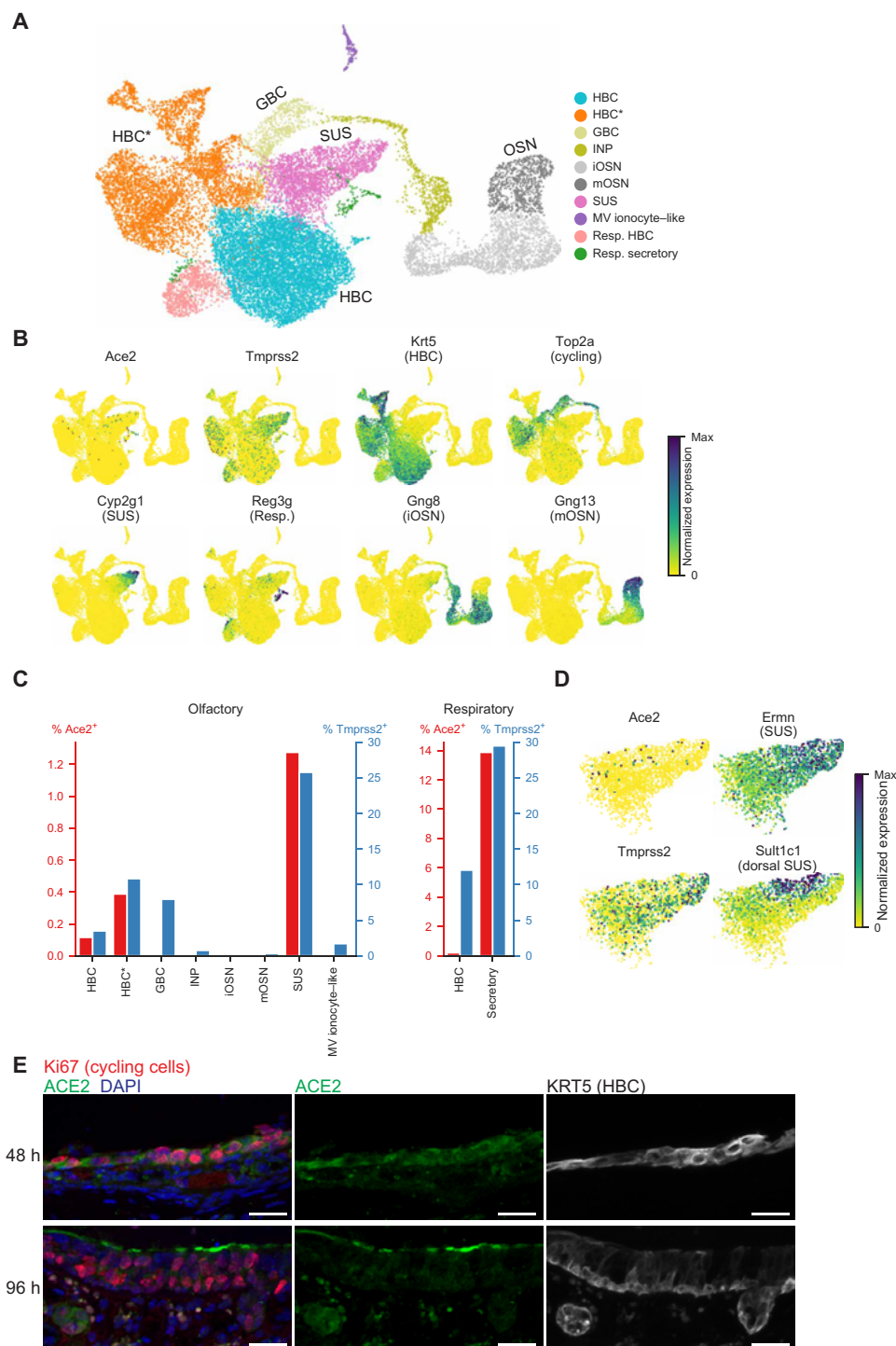


Fig. 6. ACE2 is expressed in the mouse nasal epithelium in an injury model. (A) UMAP representation of data from an scSeq HBC lineage dataset, which includes several time points after epithelial injury induced by methimazole. HBC*, activated or cycling HBCs. (B) UMAP representation of CoV-2–related genes *Ace2* and *Tmprss2*, as well as marker genes for the HBC-derived cell types. The color represents normalized expression (number of UMIs for a given gene divided by the total number of UMIs for each cell). (C) Percentage of cells expressing *Ace2* and *Tmprss2*. *Ace2* is detected in SUS cells, HBCs, activated/cycling HBCs, and respiratory cells. (D) UMAP representation of all SUS cells, indicating the normalized expression of CoV-2–related genes *Ace2* and *Tmprss2*, as well as SUS (*Ernm*) cell markers. *Ace2*⁺ SUS cells are largely a subset of dorsal SUS cells, as identified via the expression of *Sult1c1*. *Sult1c1*⁺ SUS cells have higher levels of *Ace2* ($P = 1.87 \times 10^{-3}$, Mann-Whitney test), and *Ace2*⁺ SUS cells have higher levels of *Sult1c1* ($P = 8.06 \times 10^{-7}$, Mann-Whitney test). (E) ACE2 immunostaining of mouse nasal epithelium after methimazole treatment, together with cycling cell marker Ki67 and HBC marker KRT5. Top: At 48 hours after treatment, ACE2 signal is detected in Ki67⁺/KRT5⁺-activated HBCs. Bottom: At 96 hours after treatment, ACE2 signal is observed at the apical surface of Ki67⁺ cells. Some ACE2⁺ cells express low levels of the HBC marker KRT5 and have immunostaining patterns similar to that of dorsal SUS cells, suggesting that they are SUS cells in the process of differentiating from their HBC precursors. Scale bars, 25 μ m.

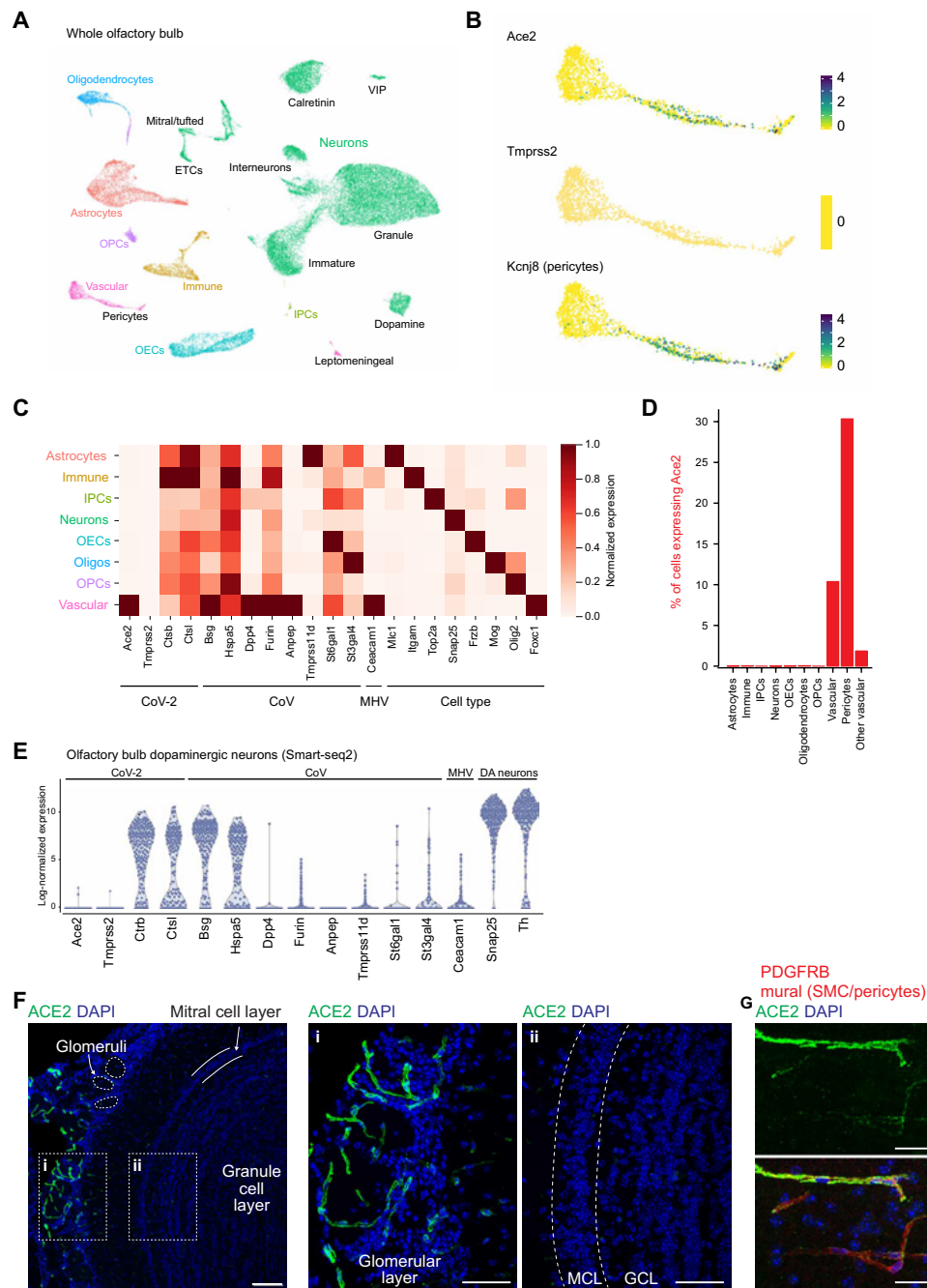


Fig. 7. Expression of coronavirus cell entry-related genes in mouse OB. (A) UMAP visualization of OB scSeq highlighting the main cell classes and subtypes from two integrated scSeq datasets (see Materials and Methods). VIP, vasoactive intestinal peptide-expressing neurons; ETCs, external tufted cells; OPCs, oligodendrocyte precursor cells; IPCs, intermediate precursor cells. Cluster information is summarized in figs. S7 and S8. (B) UMAP representation of the vascular cell cluster showing expression of CoV-2 entry-related genes (*Ace2* and *Tmprss2*) and *Kcnj8*, a pericyte marker. Color scale depicts log-normalized UMI counts. (C) Normalized gene expression of coronavirus cell entry-related genes and cell class markers in mouse OB. Color scale shows scaled mean expression level per cell type, normalized by their maximum expression across cell types. *Ace2* is specifically expressed in vascular cells. (D) Percentage of cells expressing *Ace2*. “Other vascular” denotes all vascular cells excluding pericytes. *Ace2* expression was only detected in vascular cell types. (E) Log₂-normalized expression [$\log_2(\text{TPM} + 1)$] of coronavirus entry genes and dopaminergic neuron markers in manually sorted and deeply sequenced single OB dopaminergic neurons. (F) ACE2 immunostaining of the mouse main OB. Left: Section of OB containing the glomerular layer (with example glomeruli circled), mitral cell layer (MCL), and granule cell layer (GCL). ACE2 protein is present in vascular mural cells but not in OB neurons or OSN axons. Boxes (i) and (ii) indicate the locations of enlarged images. Scale bar, 100 μm . (i) Middle: Enlarged image of glomerular layer. ACE2 protein staining was restricted to vascular cells. Scale bar, 50 μm . (ii) Right: Enlarged image of MCL (dashed line) and GCL showing the lack of ACE2. Scale bar, 50 μm . (G) An OB section showing ACE2 protein is detected in PDGFRB⁺ mural cells, including smooth muscle cells and pericytes. Top: ACE2 channel alone. Scale bars, 25 μm .

the mouse suggests that ACE2 protein is (nearly) ubiquitously expressed in SUS cells in the dorsal OE, despite sparse detection of *Ace2* transcripts using scSeq. Similarly, nearly all vascular pericytes also expressed ACE2 protein, although only a fraction of OB pericytes were positive for *Ace2* transcripts when assessed using scSeq. Although *Ace2* transcripts were more rarely detected than protein, there was a clear concordance at the cell-type level: Expression of *Ace2* mRNA in a particular cell type accurately predicted the presence of ACE2 protein, while *Ace2* transcript-negative cell types (including OSNs) did not express ACE2 protein. These observations are consistent with recent findings in the RE, suggesting that scSeq substantially underestimates the fraction of a given cell type that expresses the *Ace2* transcript, but that “new” *Ace2*-expressing cell types are not found with more sensitive forms of analysis (40). If our findings in the mouse OE translate to the human (a reasonable possibility given the precise match in olfactory cell types that express CoV-2 cell entry genes between the two species), then ACE2 protein is likely to be expressed in a significant subset of human SUS cells. Thus, there may be many olfactory support cells available for CoV-2 infection in the human epithelium, which in turn could nucleate a pathophysiological process that culminates in anosmia. However, it remains possible that damage to the OE could be caused by more limited cell infection. For example, infection of subsets of SUS cells by the coronavirus SDAV (sialodacryoadenitis virus) in rats ultimately leads to disruption of the global architecture of the OE, suggesting that focal coronavirus infection may be sufficient to cause diffuse epithelial damage (56).

We observe that activated HBCs, which are recruited after injury, express *Ace2* at higher levels than those apparent in resting stem cells. The natural history of CoV-2-induced anosmia is only now being defined; while recovery of smell on time scales of weeks in many patients has been reported, it remains unclear whether, in a subset of patients, smell disturbances will be long-lasting or permanent (8–12, 57). While on its own it is unlikely that infection of stem cells would cause acute smell deficits, the capacity of CoV-2 to infect stem cells may play an important role in those cases in which COVID-19-associated anosmia is persistent, a context in which infection of stem cells could inhibit OE regeneration and repair over time.

Two anosmic patients with COVID-19 have presented with functional magnetic resonance imaging-identified hyperintensity in both OBs that reverted to normal after resolution of the anosmia (58, 59), consistent with central involvement in at least some cases. Many viruses, including coronaviruses, have been shown to propagate from the nasal epithelium past the cribriform plate to infect the OB; this form of central infection has been suggested to mediate olfactory deficits, even in the absence of lasting OE damage (60–65). The rodent coronavirus MHV (mouse hepatitis virus) passes from the nose to the bulb, although rodent OSNs do not express *Ceacam1*, the main MHV receptor (figs. S4C, S5E, and S6A) (61, 66), suggesting that CoVs in the nasal mucosa can reach the brain through mechanisms independent of axonal transport by sensory nerves; OB dopaminergic juxtglomerular cells express *Ceacam1* (Fig. 7E), which likely supports the ability of MHV to target the bulb and change odor perception. Although SARS-CoV has been shown to infect the OB in a transgenic mouse model that ectopically expresses human ACE2 (65), it is unclear to what extent similar results will be observed for CoV-2 in this mouse and in recently developed mouse models expressing human ACE2 that better recapitulate native expression patterns (67–69). One speculative possibility is that local seeding of

the OE with CoV-2-infected cells can result in OSN-independent transfer of virions from the nose to the bulb, perhaps via the vascular supply shared between the OB and the OSN axons that comprise CN I. Although CN I was not directly queried in our datasets, it is reasonable to infer that vascular pericytes in CN I also express ACE2, which suggests a possible route of entry for CoV-2 from the nose into the brain. Given the absence of ACE2 in mouse OB neurons—and the near-ubiquity of ACE2 expression in OB pericytes—we speculate that any central olfactory dysfunction in COVID-19 is the secondary consequence of inflammation arising locally from pericytes, or in response to diffusible factors arising from more distant sources (51).

Multiple immunostaining studies reveal that ACE2 protein in the human brain is predominantly or exclusively expressed in vasculature (and specifically expressed within pericytes) (52, 53, 70), and many neurological symptoms associated with CoV-2 infection such as stroke or altered consciousness are consistent with an underlying vasculopathy (71–76). In addition, human cerebrospinal fluid (CSF) samples have failed thus far to reveal CoV-2 RNA (73, 77), and autopsies from human patients have found that the brain contains the lowest levels of CoV-2 across organs sampled (78). On the other hand, multiple other studies have suggested that ACE2 may be expressed in human neurons and glia (79–82). In addition, two recent studies in mouse models expressing human ACE2 have found CoV-2 in the brain after intranasal inoculation (67, 68), although neither specifically queried the OB; this work stands in contrast to results in a nonhuman primate model of COVID-19, in which nasal infection did not lead to the presence of identifiable CoV-2 antigens in the brain (83). Further work will be required to resolve these inconsistencies and to definitively characterize the distribution of ACE2 protein and ultimately CoV-2-infected cells in the human OB and brain.

We note several caveats that temper our conclusions. Although current data suggest that ACE2 is the most likely receptor for CoV-2 in vivo, it is possible (although it has not yet been demonstrated) that other molecules such as BSG (basigin) may enable CoV-2 entry independently of ACE2 (figs. S1E, S4C, S5E, and S6A) (84, 85). In addition, it has recently been reported that low-level expression of ACE2 can support CoV-2 cell entry (86); it is possible, therefore, that ACE2 expression beneath the level of detection in our assays may yet enable CoV-2 infection of apparently ACE2-negative cell types. We also propose that damage to the olfactory system is due to either primary infection or secondary inflammation; it is possible (although it has not yet been demonstrated) that cells infected with CoV-2 can form syncytia with cells that do not express ACE2. Such a mechanism could damage neurons adjacent to infected cells. Last, it has recently been reported that inflammation can induce expression of ACE2 in human cells (87, 88). It is therefore possible that our survey of ACE2 expression, and other recent reports demonstrating expression of ACE2 in OE support and stem cells but not neurons (81, 89, 90), might underrepresent the cell types that express ACE2 under conditions of CoV-2 infection.

Any reasonable pathophysiological mechanism for COVID-19-associated anosmia must account for the high penetrance of smell disorders relative to endemic viruses (12, 91, 92), the apparent suddenness of smell loss that can precede the development of other symptoms (11, 13), and the transient nature of dysfunction in many patients (11, 17, 18); definitive identification of the disease mechanisms underlying COVID-19-mediated anosmia will require additional research. Nonetheless, our identification of cells in the OE and OB

expressing molecules known to be involved in CoV-2 entry illuminates a path forward for future studies.

MATERIALS AND METHODS

Human nasal scSeq dataset

Human scSeq data from Durante *et al.* (38) were downloaded from the Gene Expression Omnibus (GEO) at accession GSE139522. 10× Genomics mtx files were filtered to remove any cells with fewer than 500 total counts. Additional preprocessing, including normalizing total counts to the median total counts for each cell and filtering for highly variable genes, was performed using the SPRING gene filtering function “filter_genes” with parameters (90, 3, 10). The resulting data were visualized in SPRING and partitioned using Louvain clustering on the SPRING *k*-nearest neighbor graph. Four clusters were removed for quality control, including two with low total counts (likely background) and two with high mitochondrial counts (likely stressed or dying cells). Putative doublets were also identified using Scrublet and removed (7% of cells). The remaining cells were projected to 40 dimensions using principal components analysis (PCA). PCA batch correction was performed using patient 4 as a reference, as previously described (93). The filtered data were then repartitioned using Louvain clustering on the SPRING graph, and each cluster was annotated using known marker genes, as described in (38). For example, immature OSNs (iOSNs) and mOSNs were identified via their expression of *GNG8* and *GNG13*, respectively. HBCs were identified via the expression of *KRT5* and *TP63*, and olfactory HBCs were distinguished from respiratory HBCs via the expression of *CXCL14* and *MEG3*. Identification of SUS cells (*CYP2A13* and *CYP2J2*), BG (*SOX9* and *GPX3*), and MV ionocyte-like cells (*ASCL3*, *CFTR*, and *FOXI1*) was also performed using known marker genes. For visualization, the top 40 principal components (PCs) were reduced to two dimensions using UMAP with parameters (*n_neighbors* = 15, *min_dist* = 0.4).

The filtered human scSeq dataset contained 33,358 cells. Each of the samples contained cells from both the OE and RE, although the frequency of OSNs and respiratory cells varied across patients, as previously described (38). A total of 295 cells expressed *ACE2*, and 4953 cells expressed *TMPRSS2*. Of the 865 identified OSNs, including both immature and mature cells, none of the cells express *ACE2*, and only 2 (0.23%) expressed *TMPRSS2*. In contrast, *ACE2* was reliably detected in at least 2%, and *TMPRSS2* was expressed in close to 50% of multiple respiratory epithelial subtypes. The expression of both known cell-type markers and known CoV-related genes was also examined across respiratory and olfactory epithelial cell types. For these gene sets, the mean expression in each cell type was calculated and normalized by the maximum across cell types.

Mapping scSeq datasets to each other

Data from Deprez *et al.* (41) were downloaded from the Human Cell Atlas website [www.genomique.eu/cellbrowser/HCA/; “Single-cell atlas of the airway epithelium (Grch38 human genome)"]. A subset of these data was combined with a subset of the Durante *et al.* data for mapping between cell types. For the Deprez *et al.* data, the subset consisted of samples from the nasal RE that belonged to a cell type with >20 cells, including basal, cycling basal, suprabasal, secretory, mucous multiciliated cells, multiciliated, SMG (submucosal gland) goblet, and ionocyte. We observed two distinct subpopulations of basal cells, with one of the two populations distinguished by expression

of *CXCL14*. The cells in this population were manually identified using SPRING and defined for downstream analysis as a separate cell-type annotation called “basal (*CXCL14*+).” For the Durante data, the subset consisted of cells from cell types that had some putative similarity to cells in the Deprez dataset, including olfactory HBC, cycling respiratory HBC, respiratory HBC, early respiratory secretory cells, respiratory secretory cells, SUS cells, BG, and olfactory MV cells.

To establish a cell-type mapping:

1) Data from Durante *et al.* (38) and Deprez *et al.* (41) were combined, and gene expression values were linearly scaled so that all cells across datasets had the same total counts. PCA was then performed using highly variable genes (*n* = 1477 genes) and PCA batch correction (93) with the Durante *et al.* data as a reference set.

2) Mapping was then performed bidirectionally between the two datasets. Each cell from “dataset 1” “voted” for the five most similar cells in “dataset 2,” using distance in PCA space as the measure of similarity. A table *T* counting votes across cell types was then computed, where for cell type *i* in dataset 1 and cell type *j* in dataset 2

$$T_{ij} = \{\text{number of votes cast from cells of type } i \text{ to cells of type } j\}$$

Thus, if dataset 1 has *N* cells, then *T* would count $5 \times N$ votes ($\sum T_{ij} = 5N$).

3) The table of votes *T* was *z*-scored against a null distribution, generated by repeating the procedure above 1000 times with shuffled cell-type labels.

The resulting *z* scores were similar between the two possible mapping directions (Durante → Deprez versus Deprez → Durante; *R* = 0.87 Pearson correlation of mapping *z* scores). The mapping *z* scores were also highly robust upon varying the number of votes cast per cell (*R* > 0.98 correlation of mapping *z* scores upon changing the vote numbers to 1 or 50 as opposed to 5). Only cell-type correspondences with a high *z* score in both mapping directions (*z* score > 25) were used for downstream analysis.

To establish a common scale of gene expression between datasets, we restricted our analyses to cell-type correspondences that were supported both by bioinformatic mapping and shared a nominal cell-type designation based on marker genes. These included basal/suprabasal cells = “respiratory HBCs” from Durante *et al.* and “basal” and “suprabasal” cells from Deprez *et al.*; secretory cells = “early respiratory secretory cells” and “respiratory secretory cells” from Durante *et al.* and “secretory” cells from Deprez *et al.*; and multiciliated cells = “respiratory ciliated cells” from Durante *et al.* and “multiciliated” cells from Deprez *et al.*

We next sought a transformation of the Durante *et al.* data so that it would agree with the Deprez *et al.* data within the corresponding cell types identified above. To account for differing normalization strategies applied to each dataset before download (log normalization and rescaling with cell-specific factors for Deprez *et al.* but not for Durante *et al.*), we used the following ansatz for the transformation, where the pseudo-count *p* is a global latent parameter and the rescaling factors *f_i* are fit to each gene separately. In the equation below, *T* denotes the transformation, and *e_{ij}* represents a gene expression value for cell *i* and gene *j* in the Durante data

$$T(e_{ij}) = (\log(e_{ij} + p) - \log(p))/f_j$$

The parameter *p* was fit by maximizing the correlation of average gene expression across all genes between each of the cell-type correspondences listed above. The rescaling factors *f_i* were then fitted separately for each gene by taking the quotient of average gene expression

between the Deprez *et al.* data and the log-transformed Durante *et al.* data, again across the cell-type correspondences listed above.

Mouse bulk RNA-seq datasets

Normalized gene expression tables were obtained from previous published datasets (Table 1) (43, 46–48). For the mouse datasets, the means of the replicates from WOM or OSN were used to calculate log₂ fold changes. For the mouse data from Saraiva *et al.* (43, 46) and the primate datasets, the normalized counts of the genes of interest from individual replicates were plotted.

Mouse WOM Drop-seq experiments

Tissue dissection and single-cell dissociation for nasal epithelium

A new dataset of WOM scSeq was generated from adult male mice (8 to 12 weeks old). All mouse husbandry and experiments were performed following institutional and federal guidelines and approved by Harvard Medical School's Institutional Animal Care and Use Committee (IACUC). Briefly, dissected main OE was cleaned up in 750 μ l of EBSS (Earle's balanced salt solution; Worthington), and epithelium tissues were isolated in 750 μ l of papain (20 U/ml in EBSS) and 50 μ l of deoxyribonuclease I (DNase I) (2000 U/ml). Tissue pieces were transferred to a 5-ml round-bottom tube (BD), and 1.75 ml of papain and 450 μ l of DNase I were added. After 1- to 1.5-hour incubation with rocking at 37°C, the suspension was triturated with a 5-ml pipette 15 times and passed through a 40- μ m cell strainer (BD), and the strainer was washed with 1 ml of Dulbecco's modified Eagle's medium (DMEM) + 10% fetal bovine serum (FBS) (Invitrogen). The cell suspension was centrifuged at 300g for 5 min. Cells were resuspended with 4 ml of DMEM + 10% FBS and centrifuged at 300g for 5 min. Cells were suspended with phosphate-buffered saline (PBS) + 0.01% bovine serum albumin (BSA), and concentration was measured by a hemocytometer.

Drop-seq experiments

Drop-seq experiments were performed as previously described (94). Microfluidics devices were obtained from FlowJEM, and barcode beads were obtained from ChemGenes. Eight 15-min Drop-seq runs were collected in total, which were obtained from five mice.

Sequencing of Drop-seq samples

Eight replicates of Drop-seq samples were sequenced across five runs on an Illumina NextSeq 500 platform. Paired-end reads from

the fastq files were trimmed, aligned, and tagged via the Drop-seq tools (v1.13) pipeline, using STAR (v2.5.4a) with genomic indices from Ensembl Release 93. The digital gene expression matrix was generated for 4000 cells for 0126_2; 5000 cells for 0105, 0126_1, 051916_DS11, 051916_DS12, and 051916_DS22; 5500 cells for 051916_DS21; and 9500 cells for 0106.

Preprocessing of Drop-seq samples

Processing of the WOM Drop-seq samples was performed in Seurat (v2.3.1). Cells with less than 500 UMIs or more than 15,000 unique molecular identifiers (UMIs), or higher than 5% mitochondrial genes, were removed. Potential doublets were removed using Scrublet. Cells were initially preprocessed using the Seurat pipeline. Variable genes "FindVariableGenes" ($y.cutoff = 0.6$) were scaled [regressing out effects due to number of UMIs (nUMI), the percentage of mitochondrial genes, and replicate ids], and the data were clustered using 50 PCs with the Louvain algorithm (resolution = 0.8). In a fraction of SUS cells, we observed coexpression of markers for SUS cells and other cell types (e.g., OSNs). Reclustering of SUS cells alone separated these presumed doublets from the rest of the SUS cells, and the presumed doublets were removed for the analyses described below.

Processing of Drop-seq samples

The filtered cells from the preprocessing steps were reanalyzed in Python using Scanpy and SPRING. In brief, the raw gene counts in each cell were total counts normalized, and variable genes were identified using the SPRING gene filtering function "filter_genes" with parameters (85, 3, 3); mitochondrial and olfactory receptor genes were excluded from the variable gene lists. The resulting 2083 variable genes were Z-scored, and the dimensionality of the data was reduced to 35 via PCA. The k -nearest neighbor graph ($n_neighbors = 15$) of these 35 PCs was clustered using the Leiden algorithm (resolution = 1.2) and was reduced to two dimensions for visualization via the UMAP method ($min_dist = 0.42$). Clusters were manually annotated on the basis of known marker genes, and those sharing markers (e.g. OSNs) were merged.

The mouse WOM Drop-seq dataset contained 29,585 cells that passed the above filtering. Each of the 16 clusters identified contained cells from all eight replicates in roughly equal proportions. Of the 17,666 mOSNs and the 4674 iOSNs, none of the cells express *Ace2*.

Table 1. Sample information for the bulk RNA-seq data analyzed in this study. Three different mouse bulk RNA-seq datasets were used, each with replicates from WOM or purified OSNs. An additional dataset contained bulk RNA-seq data from humans and nonhuman primates. n.s., not specified; OMP, olfactory marker protein; IRES, internal ribosomal entry site; GFP, green fluorescent protein; WT, wild type; NA, not applicable.

| | Source | Species | Reps | Samples per rep | Sex (M/F) | Age | Strain | Geno |
|---------------------------------|--------|----------|------|-----------------|-----------|-------------|--------------|------------------|
| Saraiva <i>et al.</i> (46) | WOM | Mouse | 3 | 1 | 2/1 | P21 | OMP-IRES-GFP | GFP/+ |
| | OSN | Mouse | 3 | 14–16 | Mixed | P25 | OMP-IRES-GFP | GFP/+ |
| Kanageswaran <i>et al.</i> (47) | WOM | Mouse | 4 | 3 | F | 4 weeks | C57BL/6J | WT |
| | OSN | Mouse | 2 | 6–8 | Mixed | Adult | OMP-IRES-GFP | GFP/+ or GFP/GFP |
| Colquitt <i>et al.</i> (48) | WOM | Mouse | 2 | n.s. | n.s. | 3 weeks | Dnmt3a | WT |
| | OSN | Mouse | 2 | n.s. | n.s. | 3 weeks | Dnmt3a | WT |
| Saraiva <i>et al.</i> (43) | WOM | Human | 3 | 1 | 3/0 | n.s. | NA | |
| | WOM | Macaque | 3 | 1 | n.s. | ~4.5 years | NA | |
| | WOM | Marmoset | 3 | 1 | n.s. | ~1–10 years | NA | |

In contrast, in the olfactory epithelial cells, *Ace2* expression was observed in the BG, olfactory HBCs, and dorsal SUS cells.

Immunohistochemistry and in situ hybridization of mouse and human tissue

Mouse OE tissue processing

Mice were euthanized with a lethal dose of xylazine, and nasal epithelium with attached OBs was dissected and fixed in 4% paraformaldehyde (Electron Microscope Sciences, 19202) in PBS overnight at 4°C or for 2 hours at room temperature. Tissues were washed three times in PBS (5 min each) and incubated in 0.45 M EDTA in PBS overnight at 4°C. The following day, tissues were rinsed by PBS, incubated in 30% sucrose in PBS for at least 30 min, transferred to Tissue Freezing Medium (VWR, 15146-025) for at least 45 min, frozen on crushed dry ice, and stored at -80°C until sectioning. Tissue sections (20 µm thick for the OB and 12 µm thick for nasal epithelium) were collected on Superfrost Plus glass slides (VWR, 48311703) and stored at -80°C until immunostaining. For methimazole-treated samples, adult C57BL/6J mice (6 to 12 weeks old; JAX stock no. 000664) were given intraperitoneal injections of 50 µg of methimazole per gram of body weight (Sigma-Aldrich, M8506) and euthanized at 24-, 48-, and 96-hour time points.

Immunostaining for mouse tissue

Sections were permeabilized with 0.1% Triton X-100 in PBS for 20 min and then rinsed three times in PBS. Sections were then incubated for 45 to 60 min in blocking solution that consisted of PBS containing 3% BSA (Jackson ImmunoResearch, 001-000-162) and 3% Donkey Serum (Jackson ImmunoResearch, 017-000-121) at room temperature, followed by overnight incubation at 4°C with primary antibodies diluted in the same blocking solution. Primary antibodies used are as follows: goat anti-ACE2 (Thermo Fisher Scientific, PA5-47488; 1:40), mouse anti-TUBB4 (Sigma-Aldrich, T7941; 1:4000), rabbit anti-KRT5 (Abcam, ab52635; 1:200), goat anti-NQO1 (Abcam, ab2346; 1:200), mouse antiacetylated tubulin (Abcam, ab24610; 1:500), rabbit anti-CNGA2 (Abcam, ab79261; 1:100), and rat anti-CD140b/PDGFRB (Thermo Fisher Scientific, 14-1402-82; 1:100).

On the following day, sections were rinsed once and washed three times for 5 to 10 min in PBS and then incubated for 45 min with secondary antibodies diluted in blocking solution at 1:300 ratios and/or Alexa Fluor 555-conjugated phalloidin (1:400). Secondary antibodies used were as follows: donkey anti-goat immunoglobulin G (IgG) Alexa Fluor 488 (Jackson ImmunoResearch, 705-546-147), donkey anti-goat IgG Alexa 555, (Invitrogen, A21432), donkey anti-rabbit IgG Alexa 555 (Invitrogen, A31572), donkey anti-rabbit IgG Alexa 647 (Jackson ImmunoResearch, 711-605-152), donkey anti-mouse IgG Alexa 555 (Invitrogen, A31570), donkey anti-mouse IgG Alexa 647 (Invitrogen, A31571), and donkey anti-rat IgG Alexa 488 (Invitrogen, A21208).

After secondary antibody incubation, sections were washed twice for 5 to 10 min in PBS, incubated with 300 nM 4',6-diamidino-2-phenylindole (DAPI) in PBS for 10 min, and then rinsed with PBS. Slides were mounted with glass coverslips using VECTASHIELD Mounting Medium (Vector Laboratories, H-1000) or ProLong Diamond Antifade Mountant (Invitrogen, P36961).

For costaining of ACE2 and NQO1, slides were first stained with ACE2 primary antibody and donkey anti-goat IgG Alexa 488 secondary. After three washes of secondary antibody, tissues were incubated with unconjugated donkey anti-goat IgG Fab fragments (Jackson ImmunoResearch, 705-007-003) at 30 µg/ml diluted in

blocking solution for 1 hour at room temperature. Tissues were washed twice with PBS, once in blocking solution, and incubated in blocking solution for 30 to 40 min at room temperature, followed by a second round of staining with the NQO1 primary antibody and donkey anti-goat IgG Alexa 555 secondary antibody.

Confocal images were acquired using a Leica SPE microscope (Harvard Medical School Neurobiology Imaging Facility) with 405-, 488-, 561-, and 635-nm laser lines. Multislice Z-stack images were acquired, and their maximal intensity projections are shown. For Fig. 5A, tiled images were acquired and stitched by the Leica LAS X software. Images were processed using Fiji ImageJ software (95), and noisy images were median-smoothed using the *Remove Outliers* function built into Fiji.

Fluorescence in situ hybridization for mouse tissue

Sult1c1 RNA was detected by fluorescent RNAscope assay (Advanced Cell Diagnostics, kit 320851) using probe 539921-C2, following the manufacturer's protocol (RNAscope Fluorescent Multiplex Kit User Manual, 320293-UM Date 03142017) for paraformaldehyde-fixed tissue. Before initiating the hybridization protocol, the tissue was pretreated with two successive incubations (first 30 min and then 15 min long) in RNAscope Protease III (Advanced Cell Diagnostics, 322337) at 40°C and then washed in distilled water. At the end of the protocol, the tissue was washed in PBS and subjected to the 2-day immunostaining protocol described above.

Immunostaining of human nasal tissue

Human olfactory mucosa biopsies were obtained via the Institutional Review Board-approved protocol at Duke University School of Medicine, from nasal septum or superior turbinate during endoscopic sinus surgery. Tissue was fixed with 4% paraformaldehyde and cryosectioned at 10 µm, and sections were processed for immunostaining, as previously described (38).

Sections from a 28-year-old female nasal septum biopsy were stained for ACE2 (Fig. 2E) using the same goat anti-ACE2 (Thermo Fisher Scientific, PA5-47488; 1:40) and the protocol described above for mouse tissue. The human sections were costained with rabbit anti-keratin 5 (Abcam, ab24647; AB_448212, 1:1000) and were detected with Alexa Fluor 488 donkey anti-goat (Jackson ImmunoResearch, 705-545-147) and Alexa Fluor 594 donkey anti-rabbit (Jackson ImmunoResearch, 711-585-152) secondary antibodies (1:300).

As further validation of ACE2 expression and to confirm the lack of ACE2 expression in human OSNs (fig. S2), sections were stained with a rabbit anti-ACE2 (Abcam, ab15348; RRID:AB_301861, used at 1:100) antibody immunogenized against human ACE2 and a mouse Tuj1 antibody against neuron-specific tubulin (BioLegend, 801201; RRID:AB_2313773). Anti-ACE2 was raised against a C-terminal synthetic peptide for human ACE2 and was validated by the manufacturer to not cross-react with ACE1 for immunohistochemical labeling of ACE2 in fruit bat nasal tissue and in human lower airway. Recombinant human ACE2 abolished labeling with this antibody in a previous study in human tissue, further demonstrating its specificity (53). The Tuj1 antibody was validated, as previously described (38). Biotinylated secondary antibodies (Vector Laboratories), avidin-biotinylated horseradish peroxidase kit (Vector Laboratories), and fluorescein tyramide signal amplification (PerkinElmer) were applied per the manufacturer's instructions. For dual staining, Tuj1 was visualized using Alexa Fluor 594 goat anti-mouse (Jackson ImmunoResearch, 115-585-146; RRID: AB_2338881).

Human sections were counterstained with DAPI, and coverslips were mounted using ProLong Gold (Invitrogen) for imaging, using

a Leica DMi8 microscope system. Images were processed using Fiji ImageJ software (National Institutes of Health). Scale bars were applied directly from the Leica acquisition software metadata in ImageJ tools. Unsharp mask was applied in ImageJ, and brightness/contrast was adjusted globally.

WOM and HBC lineage-tracing mouse 10× scSeq experiments

Mice

Two-month-old and 18-month-old wild-type C57BL/6J mice were obtained from the National Institute on Aging Aged Rodent Colony and used for the WOM experiments; each experimental condition consisted of one male and one female mouse to aid doublet detection. Mice containing the transgenic *Krt5-CreER(T2)* driver (96) and *Rosa26-yellow fluorescent protein (YFP)* reporter allele (97) were used for the HBC lineage-tracing dataset. All mice were assumed to be of normal immune status. Animals were maintained and treated according to federal guidelines under IACUC oversight at the University of California, Berkeley.

Single-cell RNA sequencing

The OE was surgically removed, and the dorsal, sensory portion was dissected and dissociated, as previously described (36). For WOM experiments, dissociated cells were subjected to fluorescence-activated cell sorting (FACS) using propidium iodide to identify and select against dead or dying cells; 100,000 cells per sample were collected in 10% FBS. For the HBC lineage-tracing experiments, *Krt5-CreER*; *Rosa26YFP/YFP* mice were injected once with tamoxifen (0.25 mg of tamoxifen per gram of body weight) at postnatal day 21 (P21) to P23 of age and euthanized at 24 hours, 48 hours, 96 hours, 7 days, and 14 days after injury, as previously described (36, 98). For each experimental time point, YFP⁺ cells were isolated by FACS based on YFP expression and negative for propidium iodide, a vital dye.

Cells isolated by FACS were subjected to scSeq. Three replicates (defined here as a FACS collection run) per age were analyzed for the WOM experiment; at least two biological replicates were collected for each experimental condition for the HBC lineage-tracing experiment. Single-cell complementary DNA (cDNA) libraries from the isolated cells were prepared using the Chromium Single Cell 3' System according to the manufacturer's instructions. The WOM preparation used v3 chemistry with the following modification: The cell suspension was directly added to the reverse transcription master mix, along with the appropriate volume of water to achieve the approximate cell capture target. The HBC lineage-tracing experiments were performed using v2 chemistry. The 0.04% (w/v) BSA washing step was omitted to minimize cell loss. Completed libraries were sequenced on Illumina HiSeq 4000 to produce paired-end 100-nucleotide reads.

Sequence data were processed with the 10× Genomics Cell Ranger pipeline (2.0.0 for v2 chemistry), resulting in the initial starting number before filtering of 60,408 WOM cells and 25,469 HBC lineage-traced cells. The *scone* R/Bioconductor package (99) was used to filter out lowly expressed genes (fewer than two UMIs in fewer than five cells) and low-quality libraries (using the *metric_sample_filter* function with arguments *hard_reads* = 2000, *zcut* = 4).

Preliminary filtering

Cells with coexpression of male (*Ddx3y*, *Eif2s3y*, *Kdm5d*, and *Uty*) and female marker genes (*Xist*) were removed as potential doublets from the WOM dataset. For both datasets, doublet cell detection was performed per sample using DoubletFinder (100) and Scrublet (101). Genes with at least three UMIs in at least five cells were used

for downstream clustering and cell-type identification. For the HBC lineage-tracing dataset, the Bioconductor package *scone* was used to pick the top normalization ("none,fq,ruv_k = 1,no_bio,batch"), corresponding to full quantile normalization, batch correction, and removing one factor of unwanted variation using the RUVSeq Bioconductor package (102). A range of cluster labels were created by clustering using the partitioning around medoids algorithm and hierarchical clustering in the *clusterExperiment* Bioconductor package (103), with parameters *k0s* = (10, 13, 16, 19, 22, 25) and *alpha* = (NA, 0.1, 0.2, 0.3). Clusters that did not show differential expression were merged (using the function *mergeClusters* with arguments *mergeMethod* = "adjP," *cutoff* = 0.01, and *DEMethod* = "limma" for the lineage-traced dataset). Initial clustering identified one macrophage (*Msr1⁺*) cluster consisting of 252 cells; upon its removal and restarting from the normalization step, a subsequent set of 15 clusters was obtained. These clusters were used to filter out 1515 cells for which no stable clustering could be found (i.e., "unassigned" cells) and four clusters respectively consisting of 31, 29 and 23 and 305 cells. Doublets were identified using DoubletFinder, and 271 putative doublets were removed. Inspection of the data in a three-dimensional UMAP embedding identified two groups of cells whose experimentally sampled time point did not match their position along the HBC differentiation trajectory, and these additional 219 cells were also removed from subsequent analyses.

Analysis of CoV-related genes in WOM and HBC lineage 10× datasets

Analysis of WOM scSeq data was performed in Python using the open-source Scanpy software starting from the raw UMI count matrix of the 40,179 cells passing the initial filtering and quality control criteria described above. UMIs were total count-normalized and scaled by 10,000 [TPT (tag per ten thousands)] and then log-normalized. For each gene, the residuals from linear regression models using the total number of UMIs per cell as predictors were then scaled via *Z* scoring. PCA was then performed on a set of highly variable genes (excluding olfactory receptor genes) calculated using the "highly_variable_genes" function with the following parameters: *min_mean* = 0.01, *max_mean* = 10, and *min_disp* = 0.5. A batch-corrected neighborhood graph was constructed by the "bbknn" function with 42 PCs with the following parameters: *local_connectivity* = 1.5 and embedding two dimensions using the UMAP function with default parameters (*min_dist* = 0.5). Cells were clustered using the neighborhood graph via the Leiden algorithm (resolution = 1.2). Identified clusters were manually merged and annotated on the basis of known marker gene expression. We removed 281 cells containing mixtures of marker genes with no clear gene expression signature. The identified cell types and the number of each of the remaining 39,898 cells detected were as follows: 28,769 mOSNs, 2607 iOSNs, 859 immediate neural precursors (INPs), 623 GBCs, HBCs (1083 olfactory and 626 respiratory), 480 SUS cells, 331 BG, MV cells (563 brush-like and 1530 ionocyte-like), 92 olfactory ensheathing cells (OECs), 76 respiratory secretory cells, 227 respiratory unspecified cells, 172 atypical OSNs, 1757 various immune cells, and 103 red blood cells. TPT gene expression levels were visualized in two-dimensional UMAP plots.

The filtered HBC lineage dataset containing 21,722 cells was analyzing in Python and processed for visualization using pipelines in SPRING and Scanpy (104, 105). In brief, total counts were normalized to the median total counts for each cell, and highly variable genes were selected using the SPRING gene filtering function ("filter_genes") using parameters (90, 3, 3). The dimensionality of the data

was reduced to 20 using PCA and visualized in two dimensions using the UMAP method with parameters ($n_neighbors = 20$, $min_dist = 0.5$). Clustering was performed using the Leiden algorithm ($resolution = 1.45$), and clusters were merged manually using known marker genes. The identified cell types and number of each type were 929 mOSNs, 2073 iOSNs, 786 INPs, 755 GBCs, HBCs (7782 olfactory, 5418 regenerating, and 964 respiratory), 2666 SUS cells, and 176 ionocyte-like MV cells.

Expression of candidate CoV-2-related genes was defined if at least one transcript (UMI) was detected in that cell, and the percentage of cells expressing candidate genes was calculated for each cell type. In the WOM dataset, *Ace2* was only detected in 2 of 28,769 mOSNs (0.007%), and in the HBC lineage dataset, *Ace2* was not detected in any OSNs. Furthermore, *Ace2* was not detected in immature sensory neurons (GBCs, INPs, or iOSNs) in either dataset.

Mouse HBC lineage Smart-seq2 dataset

scSeq data from HBC-derived cells from Fletcher *et al.* (36) and Gadye *et al.* (98), labeled via *Krt5-CreER* driver mice, were downloaded from GEO at accession GSE99251 using the file “GSE95601_oeHBCdiff_Cufflinks_eSet_counts_table.txt.gz”. Processing was performed as described above, including total count normalization and filtering for highly variable genes using the SPRING gene filtering function “filter_genes” with parameters (75, 20, 10). The resulting data were visualized in SPRING, and a subset of cells were removed for quality control, including a cluster of cells with low total counts and another with predominantly reads from ERCC (External RNA Controls Consortium) spike-in controls. Putative doublets were also identified using Scrublet and removed (6% of cells) (101). The resulting data were visualized in SPRING and partitioned using Louvain clustering on the SPRING k -nearest neighbor graph using the top 40 PCs. Cell-type annotation was performed manually using the same set of marker genes listed above. Three clusters were removed for quality control, including one with low total counts, one with predominantly reads from ERCC spike-in controls (likely background), and one with high mitochondrial counts (likely stressed cells). For visualization and clustering, the remaining cells were projected to 15 dimensions using PCA and visualized with UMAP with parameters ($n_neighbors = 15$, $min_dist = 0.4$, $alpha = 0.5$, $maxiter = 500$). Clustering was performed using the Leiden algorithm ($resolution = 0.4$), and cell types were manually annotated using known marker genes.

The filtered dataset of mouse HBC-derived cells contained 1450 cells. The percentage of cells expressing each marker gene was calculated as described above. Of the 51 OSNs identified, none of them expressed *Ace2*, and only 1 of 194 INPs and iOSNs expressed *Ace2*. In contrast, *Ace2* and *Tmprss2* were both detected in HBCs and SUS cells.

Juvenile and adult mouse whole OB scSeq dataset

Juvenile mouse data

scSeq data from whole mouse OB (50) were downloaded from mousebrain.org/loomfiles_level_L1.html in loom format (l1 olfactory.loom) and converted to a Seurat object. Samples were obtained from juvenile mice (age P26 to P29). This dataset comprises 20,514 cells that passed cell quality filters, excluding 122 cells identified as potential doublets.

Tissue dissection and single-cell dissociation

A new dataset of whole OB scSeq was generated from adult male mice (8 to 12 weeks old). All mouse husbandry and experiments were

performed following institutional and federal guidelines and approved by Harvard Medical School's IACUC. Briefly, dissected OBs (including the accessory OB and fractions of the anterior olfactory nucleus) were dissociated in 750 μ l of dissociation medium (DM; Hanks' balanced salt solution containing 10 mM Hepes, 1 mM $MgCl_2$, and 33 mM D-glucose) with papain (28 U/ml) and DNase I (386 U/ml; Worthington). Minced tissue pieces were transferred to a 5-ml round-bottom tube (BD). DM was added to a final volume of 3.3 ml, and the tissue was mechanically triturated five times with a P1000 pipette tip. After 1-hour incubation with rocking at 37°C, the suspension was triturated with a 10-ml pipette 10 times, and 2.3 ml was passed through 40- μ m cell strainer (BD). The suspension was then mechanically triturated with a P1000 pipette tip 10 times, and 800 μ l was filtered on the same strainer. The cell suspension was further triturated with a P200 pipette tip 10 times and filtered. One milliliter of Quench buffer (22 ml of DM, 2.5 ml of protease inhibitor prepared by resuspending one vial of protease inhibitor with 32 ml of DM, and 2000 U of DNase I) was added to the suspension and centrifuged at 300g for 5 min. Cells were resuspended with 3 ml of Quench buffer, overlaid gently on top of 5 ml of protease inhibitor, and then spun down at 70g for 10 min. The pellet was resuspended using DM supplemented with 0.04% BSA and spun down at 300g for 5 min. Cells were resuspended in 400 μ l of DM with 0.04% BSA.

OB Drop-seq experiments

Drop-seq experiments were performed as previously described (94). Microfluidics devices were obtained from FlowJEM, and barcode beads were obtained from ChemGenes. Two 15-min Drop-seq runs were collected from a single dissociation preparation obtained from two mice. Two such dissociations were performed, giving four total replicates.

Sequencing of Drop-seq samples

Four replicates of Drop-seq samples were pooled and sequenced across three runs on an Illumina NextSeq 500 platform. Paired-end reads from the fastq files were trimmed, aligned, and tagged via the Drop-seq tools (1-2.0) pipeline, using STAR (2.4.2a) with genomic indices from Ensembl Release 82. The digital gene expression matrix was generated for 8000 cells per replicate.

Preprocessing of Drop-seq samples

Cells with low numbers of genes (500), low numbers of UMIs (700), or high numbers of UMIs (>10,000) were removed (6% of cells). Potential doublets were identified via Scrublet and removed (3.5% of cells). Overall, this new dataset comprised 27,004 cells.

Integration of whole OB scSeq datasets

Raw UMI counts from juvenile and adult whole OB samples were integrated in Seurat (106). Integrating the datasets ensured that clusters with rare cell types could be identified and that corresponding cell types could be accurately matched. As described below (see fig. S7), although some cell types were observed with different frequencies, the integration procedure yielded stable clusters with cells from both datasets. Briefly, raw counts were log-normalized separately, and the 10,000 most variable genes were identified by variance stabilizing transformation for each dataset. The 4529 variable genes present in both datasets, and the first 30 PCs were used as features for identifying the integration anchors. The integrated expression matrix was scaled and dimensionality-reduced using PCA. On the basis of their percentage of explained variance, the first 28 PCs were chosen for UMAP visualization and clustering.

Graph-based clustering was performed using the Louvain algorithm following the standard Seurat workflow. Cluster stability was analyzed

with Clustree on a range of resolution values (0.4 to 1.4), with 0.6 yielding the most stable set of clusters (107). Overall, 26 clusters were identified, the smallest of which contained only 43 cells with gene expression patterns consistent with blood cells, which were excluded from further visualization plots. Clustering the two datasets separately yielded similar results. Moreover, the distribution of cells from each dataset across clusters was homogeneous (fig. S7), and the clusters corresponded to previous cell class and subtype annotations (50). As previously reported, a small cluster of excitatory neurons (cluster 13) contained neurons from the anterior olfactory nucleus. UMAP visualizations of expression level for cell class and cell-type markers, and for genes coding for coronavirus entry proteins, depict log-normalized UMI counts. The heatmap in Fig. 7C shows the mean expression level for each cell class, normalized to the maximum mean value. The percentage of cells per cell class expressing *Ace2* was defined as the percentage of cells with at least one UMI. In cells from both datasets, *Ace2* was enriched in pericytes but was not detected in neurons.

Smart-seq2 sequencing of manually sorted OB dopaminergic neurons

Tissue dissociation and manual cell sorting

Acute OB 300- μ m slices were obtained from *Dat-Cre/Flox-tdTomato* [B6.SJL-*Slc6a3*^{tm1.1(cre) Bkmm/J}], JAX stock 006660/B6.Cg-*Gt(ROSA)26Sor*^{tm9(CAG-tdTomato)Hze}, JAX stock 007909] P28 mice as previously described (108). As part of a wider study, at P27, these mice had undergone brief 24-hour unilateral naris occlusion via a plastic plug insert ($n = 5$ mice) or were subjected to a sham control manipulation ($n = 5$ mice); all observed effects here were independent of these treatment groups. Single-cell suspensions were generated using the Neural Tissue Dissociation Kit–Postnatal Neurons (Miltenyi Biotec, catalog no. 130-094-802), following the manufacturer's instructions for manual dissociation, using three fired-polished Pasteur pipettes of progressively smaller diameter. After enzymatic and mechanical dissociations, cells were filtered through a 30- μ m cell strainer, centrifuged for 10 min at 4°C, resuspended in 500 μ l of artificial cerebrospinal fluid (ACSF) (140 mM NaCl, 1.25 mM KCl, 1.25 mM NaH₂PO₄, 10 mM Hepes, 25 mM glucose, 3 mM MgCl₂, and 1 mM CaCl₂) with channel blockers [0.1 μ M tetrodotoxin (TTX), 20 μ M 6-cyano-7-nitroquinoxaline-2,3-dione (CNQX), and 50 μ M D-aminophosphovalerate (AP-V)], and kept on ice to minimize excitotoxicity and cell death.

For manual sorting of fluorescently labeled dopaminergic neurons, we adapted a previously described protocol (109). Fifty microliters of single-cell suspension was dispersed on 3.5-mm petri dishes (with a Sylgard-covered base) containing 2 ml of ACSF + channel blockers. Dishes were left undisturbed for 15 min to allow the cells to sink and settle. Throughout, dishes were kept on a metal plate on top of ice. tdTomato⁺ cells were identified by their red fluorescence under a stereoscope. Using a pulled glass capillary pipette attached to a mouthpiece, individual cells were aspirated and transferred to a clean, empty dish containing 2 ml of ACSF + channel blockers. The same cell was then transferred to a third clean plate, changing pipettes for every plate change. Last, each individual cell was transferred to a 0.2-ml polymerase chain reaction (PCR) tube containing 2 μ l of lysis buffer (RLT Plus, QIAGEN). The tube was immediately placed on a metal plate sitting on top of dry ice for flash-freezing. Collected cells were stored at –80°C until further processing. Positive (more than 10 cells) and negative (sample collection procedure without picking a cell) controls were collected for each sorting session. In

total, we collected samples from 10 mice, averaging 50 tdTomato⁺ cells collected per session. Overall, less than 2.5 hours elapsed between mouse sacrifice and collection of the last cell in any session.

Preparation and amplification of full-length cDNA and sequencing libraries

Samples were processed using a modified version of the Smart-seq2 protocol (110). Briefly, 1 μ l of a 1:2,000,000 dilution of ERCC spike-ins (Invitrogen, catalog no. 4456740) was added to each sample, and mRNA was captured using modified oligo (dT) biotinylated beads (Dynabeads, Invitrogen). PCR amplification was performed for 22 cycles. Amplified cDNA was cleaned with a 0.8:1 ratio of Ampure-XP beads (Beckman Coulter). cDNAs were quantified on Qubit using HS DNA reagents (Invitrogen), and selected samples were run on a Bioanalyzer HS DNA chip (Agilent) to evaluate size distribution.

To generate the sequencing libraries, individual cDNA samples were normalized to 0.2 ng/ μ l, and 1 μ l was used for one-quarter standard-sized Nextera XT (Illumina) tagmentation reactions, with 12 amplification cycles. Sample indexing was performed using index sets A and D (Illumina). At this point, individual samples were pooled according to their index set. Pooled libraries were cleaned using a 0.6:1 ratio of Ampure beads and quantified on Qubit using HS DNA reagents and with the KAPA Library Quantification Kits for Illumina (Roche). Samples were sequenced on two separate rapid runs on HiSeq 2500 (Illumina), generating 100–base pair paired-end reads. An additional five samples were sequenced on MiSeq (Illumina).

Full-length cDNA sequencing data processing and analysis

Paired-end read fastq files were demultiplexed, quality-controlled using FastQC (www.bioinformatics.babraham.ac.uk/projects/fastqc/), and trimmed using Trim Galore (www.bioinformatics.babraham.ac.uk/projects/trim_galore/). Reads were pseudo-aligned and quantified using kallisto (111) against a reference transcriptome from Ensembl Release 89 (Gencode Release M17 GRCm38.p6) with sequences corresponding to the ERCC spike-ins and the *Cre* recombinase and *tdT* (*tdTomato*) genes added to the index. Transcripts were collapsed into genes using the sumAcrossFeatures function in scater.

Cell-level quality control and cell filtering were performed in scater (112). Cells with <1000 genes, <100,000 reads, >75% reads mapping to ERCC spike-ins, >10% reads mapping to mitochondrial genes, or low library complexity were discarded (14% samples). The population of OB cells labeled in *Dat-Cre/Flox-tdTomato* mice is known to include a minor nondopaminergic calretinin⁺ subgroup (113), so calretinin-expressing cells were excluded from all analyses. The scTransform function in Seurat was used to remove technical batch effects.

Expression of CoV-relevant genes in scSeq datasets from various brain regions and sensory systems

An analysis of single-cell gene expression data from 10 studies was performed to investigate the expression of genes coding for coronavirus entry proteins in neurons from a range of brain regions and sensory systems. Processed gene expression data tables were obtained from scSeq studies that evaluated gene expression in retina (GSE81905) (114), inner ear sensory epithelium (GSE115934) (115, 116), spiral ganglion (GSE114997) (117), ventral midbrain (GSE76381) (118), hippocampus (GSE100449) (119), cortex (GSE107632) (120), hypothalamus (GSE74672) (121), visceral motor neurons (GSE78845) (122), dorsal root ganglia (GSE59739) (123), and spinal cord dorsal horn (GSE103840) (124). Smart-seq2 sequencing data from *Vsx2*–green fluorescent protein (GFP)⁺ cells were used from the retina

dataset. A subset of the expression matrix that corresponds to day 0 (i.e., control, undisturbed neurons) was used from the layer VI somatosensory cortex dataset. A subset of the data containing neurons from untreated (control) mice were used from the hypothalamic neuron dataset. From the ventral midbrain dopaminergic neuron dataset, a subset comprising *DAT-Cre/tdTomato*⁺ neurons from P28 mice was used. A subset comprising type I neurons from wild-type mice was used from the spiral ganglion dataset. The “unclassified” neurons were excluded from the visceral motor neuron dataset. A subset containing neurons that were collected at room temperature was used from the dorsal root ganglia dataset. Expression data from dorsal horn neurons obtained from C57/BL6 wild-type mice and *vGat-Cre-tdTomato* and *vGlut2-eGFP* mouse lines were used from the spinal cord dataset. Inspection of all datasets for batch effects was performed using the scater package (version 1.10.1) (112). Publicly available raw count expression matrices were used for the retina, hippocampus, hypothalamus, midbrain, visceral motor neurons, and spinal cord datasets, whereas the normalized expression data were used from the inner ear hair cell datasets. For datasets containing raw counts, normalization was performed for each dataset separately by computing pool-based size factors that are subsequently deconvolved to obtain cell-based size factors using the scran package (version 1.10.2) (125). Violin plots were generated in scater.

SUPPLEMENTARY MATERIALS

Supplementary material for this article is available at <http://advances.sciencemag.org/cgi/content/full/6/31/eabc5801/DC1>

[View/request a protocol for this paper from Bio-protocol.](#)

REFERENCES AND NOTES

1. W.-J. Guan, Z.-Y. Ni, Y. Hu, W.-H. Liang, C.-Q. Ou, J.-X. He, L. Liu, H. Shan, C.-L. Lei, D. S. C. Hui, B. Du, L.-J. Li, G. Zeng, K.-Y. Yuen, R.-C. Chen, C.-L. Tang, T. Wang, P.-Y. Chen, J. Xiang, S.-Y. Li, J.-L. Wang, Z.-J. Liang, Y.-X. Peng, L. Wei, Y. Liu, Y.-H. Hu, P. Peng, J.-M. Wang, J.-Y. Liu, Z. Chen, G. Li, Z.-J. Zheng, S.-Q. Qiu, J. Luo, C.-J. Ye, S.-Y. Zhu, N.-S. Zhong; China Medical Treatment Expert Group for Covid-19, Clinical characteristics of coronavirus disease 2019 in China. *N. Engl. J. Med.* **382**, 1708–1720 (2020).
2. H. A. Rothan, S. N. Byrareddy, The epidemiology and pathogenesis of coronavirus disease (COVID-19) outbreak. *J. Autoimmun.* **109**, 102433 (2020).
3. Z. Wu, J. M. McGoogan, Characteristics of and important lessons from the coronavirus disease 2019 (COVID-19) outbreak in China. *JAMA* **323**, 1239 (2020).
4. P. Zhou, X.-L. Yang, X.-G. Wang, B. Hu, L. Zhang, W. Zhang, H.-R. Si, Y. Zhu, B. Li, C.-L. Huang, H.-D. Chen, J. Chen, Y. Luo, H. Guo, R.-D. Jiang, M.-Q. Liu, Y. Chen, X.-R. Shen, X.-S. Zheng, K. Zhao, Q.-J. Chen, F. Deng, L.-L. Liu, B. Yan, F.-X. Zhan, Y.-Y. Wang, G.-F. Xiao, Z.-L. Shi, A pneumonia outbreak associated with a new coronavirus of probable bat origin. *Nature* **579**, 270–273 (2020).
5. M. Ceccarelli, M. Berretta, E. Venanzi Rullo, G. Nunnari, B. Copardo, Differences and similarities between Severe Acute Respiratory Syndrome (SARS)-CoronaVirus (CoV) and SARS-CoV-2. Would a rose by another name smell as sweet? *Eur. Rev. Med. Pharmacol. Sci.* **24**, 2781–2783 (2020).
6. A. Zumla, J. F. W. Chan, E. I. Azhar, D. S. C. Hui, K.-Y. Yuen, Coronaviruses—Drug discovery and therapeutic options. *Nat. Rev. Drug Discov.* **15**, 327–347 (2016).
7. V. M. Corman, D. Muth, D. Niemeyer, C. Drosten, Hosts and sources of endemic human coronaviruses. *Adv. Virus Res.* **100**, 163–188 (2018).
8. S. H. R. Bagheri, A. M. Asghari, M. Farhadi, A. R. Shamschiri, A. Kabir, S. K. Kamrava, M. Jallessi, A. Mohebbi, R. Alizadeh, A. A. Honarmand, Coincidence of COVID-19 epidemic and olfactory dysfunction outbreak. medRxiv 20041889 [Preprint]. 27 March 2020. <https://doi.org/10.1101/2020.03.23.20041889>.
9. A. Giacomelli, L. Pezzati, F. Conti, D. Bernacchia, M. Siano, L. Oreni, S. Rusconi, C. Gervasoni, A. L. Ridolfo, G. Rizzardini, S. Antinori, M. Galli, Self-reported olfactory and taste disorders in patients with severe acute respiratory coronavirus 2 infection: A cross-sectional study. *Clin. Infect. Dis.* **26**, ciaa330 (2020).
10. R. Wölfel, V. M. Corman, W. Guggemos, M. Seilmaier, S. Zange, M. A. Müller, D. Niemeyer, T. C. Jones, P. Vollmar, C. Rothe, M. Hoelscher, T. Bleicker, S. Brünink, J. Schneider, R. Ehmann, K. Zwirgmaier, C. Drosten, C. Wendtner, Virological assessment of hospitalized patients with COVID-2019. *Nature* **581**, 465–469 (2020).
11. J. R. Lechien, C. M. Chiesa-Estomba, D. R. de Siaty, M. Horoi, S. D. le Bon, A. Rodriguez, D. Dequanter, S. Blecic, F. el Afia, L. Distinguin, Y. Chekkoury-Idrissi, S. Hans, I. L. Delgado, C. Calvo-Henriquez, P. Lavigne, C. Falanga, M. R. Barillari, G. Cammaroto, M. Khalife, P. Leich, C. Souchay, C. Rossi, F. Journe, J. Hsieh, M. Edjlali, R. Carlier, L. Ris, A. Lovato, C. de Filippis, F. Coppee, N. Fakhry, T. Ayad, S. Saussez, Olfactory and gustatory dysfunctions as a clinical presentation of mild-to-moderate forms of the coronavirus disease (COVID-19): A multicenter European study. *Eur. Arch. Otorhinolaryngol.* **6**, 1–11 (2020).
12. C. Menni, A. M. Valdes, M. B. Freidin, C. H. Sudre, L. H. Nguyen, D. A. Drew, S. Ganesh, T. Varsavsky, M. J. Cardoso, J. S. El-Sayed Moustafa, A. Visconti, P. Hysi, R. C. E. Bowyer, M. Mangino, M. Falchi, J. Wolf, S. Ourselin, A. T. Chan, C. J. Steves, T. D. Spector, Real-time tracking of self-reported symptoms to predict potential COVID-19. *Nat. Med.* **10.1038/s41591-020-0916-2** (2020).
13. G. Spinato, C. Fabbri, J. Polese, D. Cazzador, D. Borsetto, C. Hopkins, P. Boscolo-Rizzo, Alterations in smell or taste in mildly symptomatic outpatients with SARS-CoV-2 infection. *JAMA* **323**, 2089 (2020).
14. M. Eliezer, C. Hautefort, A. L. Hamel, B. Verillaud, P. Herman, E. Houdart, C. Eloit, Sudden and complete olfactory loss function as a possible symptom of COVID-19. *JAMA Otolaryngol. Head Neck Surg.* **10.1001/jamaoto.2020.0832** (2020).
15. J. R. Lechien, C. M. Chiesa-Estomba, S. Place, Y. van Laethem, P. Cabaraux, Q. Mat, K. Huet, J. Plzak, M. Horoi, S. Hans, M. Rosaria Barillari, G. Cammaroto, N. Fakhry, D. Martiny, T. Ayad, L. Joffe, C. Hopkins, S. Saussez; COVID-19 Task Force of YO-IFOS, S. Blecic, D. R. de Siaty, P. Leich, C. Souchay, C. Rossi, F. Journe, J. Hsieh, L. Ris, F. el Afia, B. Harmegnies, L. Distinguin, Y. Chekkoury-Idrissi, M. Circiu, P. Lavigne, I. Lopez Delgado, C. Calvo-Henriquez, C. Falanga, F. Coppee, S. D. Bon, A. Rodriguez, D. Dequanter, J.-P. Cornelis, S. Vergez, L. Koenen, M. Giuditta, G. Molteni, M. Tucciarone, T. Radulesco, M. Khalife, A.-F. Fourneau, S. Cherifi, M. Manto, J. Michel, T. Radulesco, G. Molteni, M. Tucciarone, G. Mannelli, G. Cantarella, Clinical and epidemiological characteristics of 1420 European patients with mild-to-moderate coronavirus disease 2019. *J. Intern. Med.* **10.1111/joim.13089** (2020).
16. V. Parma, K. Ohla, M. G. Veldhuizen, M. Y. Niv, C. E. Kelly, A. J. Bakke, K. W. Cooper, C. Bouysset, N. Pirastu, M. Dibattista, R. Kaur, M. T. Liuzza, M. Y. Pepino, V. Schöpf, V. Pereda-Loth, S. B. Olsson, R. C. Gerkin, P. R. Dominguez, J. Albayay, M. C. Farruggia, S. Bhutani, A. W. Fjaeldstad, R. Kumar, A. Menini, M. Bensafi, M. Sandell, I. Konstantinidis, A. D. Pizio, F. Genovese, L. Öztürk, T. Thomas-Danguin, J. Frasnelli, S. Boesveldt, Ö. Saatci, L. R. Saraiva, C. Lin, J. Golebiowski, L.-D. Hwang, M. H. Ozdener, M. D. Guàrdia, C. Laudamiel, M. Ritchie, J. Havlíček, D. Pierron, E. Roura, M. Navarro, A. A. Nolden, J. Lim, K. L. Whitcroft, L. R. Colquitt, C. Ferdenzi, E. V. Brindha, A. Altundag, A. Macchi, A. Nunez-Parra, Z. M. Patel, S. Fiorucci, C. M. Philpott, B. C. Smith, J. N. Lundström, C. Mucignat, J. K. Parker, M. van den Brink, M. Schmuker, F. P. S. Fischmeister, T. Heinbockel, V. D. C. Shields, F. Faraji, E. E. Santamaría, W. E. A. Fredborg, G. Morini, J. K. Olofsson, M. Jallessi, N. Karni, A. D'Errico, R. Alizadeh, R. Pellegrino, P. Meyer, C. Huart, B. Chen, G. M. Soler, M. K. Alwashahi, O. Abdulrahman, A. Welge-Lüssen, P. Dalton, J. Freiherr, C. H. Yan, Jasper H. B. de Groot, V. V. Voznessenskaya, H. Klein, J. Chen, M. Okamoto, E. A. Sell, P. B. Singh, J. Walsh-Messinger, N. S. Archer, S. Koyama, V. Deary, S. Craig Roberts, H. Yanik, S. Albayrak, L. M. Nováková, I. Croijmans, P. P. Mazal, S. T. Moein, E. Margulis, C. Mignot, S. Mariño, D. Georgiev, P. K. Kaushik, B. Malnic, H. Wang, S. Seyed-Allaei, N. Yoluk, S. Razzaghi, J. M. Justice, D. Restrepo, J. W. Hsieh, D. R. Reed, T. Hummel, S. D. Munger, J. E. Hayes, More than smell. COVID-19 is associated with severe impairment of smell, taste, and chemesthesis. medRxiv 20090902 [Preprint]. 24 May 2020. <https://doi.org/10.1101/2020.05.04.20090902>.
17. Y. Lee, P. Min, S. Lee, S.-W. Kim, Prevalence and duration of acute loss of smell or taste in COVID-19 patients. *J. Korean Med. Sci.* **35**, e174 (2020).
18. C. H. Yan, F. Faraji, D. P. Prajapati, C. E. Boone, A. S. DeConde, Association of chemosensory dysfunction and Covid-19 in patients presenting with influenza-like symptoms. *Int. Forum Allergy Rhinol.* **10.1002/alr.22579** (2020).
19. A. Welge-Lussen, M. Wolfensberger, Olfactory disorders following upper respiratory tract infections. *Adv Otorhinolaryngol.* **63**, 125–132 (2006).
20. H. J. Duncan, A. M. Seiden, Long-term follow-up of olfactory loss secondary to head trauma and upper respiratory tract infection. *Arch. Otolaryngol Head Neck Surg.* **121**, 1183–1187 (1995).
21. A. Cavazzana, M. Larsson, M. Münch, A. Hähner, T. Hummel, Postinfectious olfactory loss: A retrospective study on 791 patients. *Laryngoscope* **128**, 10–15 (2018).
22. M. Hoffmann, H. Kleine-Weber, S. Schroeder, N. Krüger, T. Herrler, S. Erichsen, T. S. Schiergens, G. Herrler, N. H. Wu, A. Nitsche, M. A. Müller, C. Drosten, S. Pöhlmann, SARS-CoV-2 cell entry depends on ACE2 and TMPRSS2 and is blocked by a clinically proven protease inhibitor. *Cell* **181**, 271–280.e8 (2020).
23. W. Li, M. J. Moore, N. Vasilieva, J. Sui, S. K. Wong, M. A. Berne, M. Somasundaran, J. L. Sullivan, K. Luzuriaga, T. C. Greenough, H. Choe, M. Farzan, Angiotensin-converting enzyme 2 is a functional receptor for the SARS coronavirus. *Nature* **426**, 450–454 (2003).
24. W. Li, T. C. Greenough, M. J. Moore, N. Vasilieva, M. Somasundaran, J. L. Sullivan, M. Farzan, H. Choe, Efficient replication of severe acute respiratory syndrome coronavirus

- in mouse cells is limited by murine angiotensin-converting enzyme 2. *J. Virol.* **78**, 11429–11433 (2004).
25. K. Kuba, Y. Imai, S. Rao, H. Gao, F. Guo, B. Guan, Y. Huan, P. Yang, Y. Zhang, W. Deng, L. Bao, B. Zhang, G. Liu, Z. Wang, M. Chappell, Y. Liu, D. Zheng, A. Leibbrandt, T. Wada, A. S. Slutsky, D. Liu, C. Qin, C. Jiang, J. M. Penninger, A crucial role of angiotensin converting enzyme 2 (ACE2) in SARS coronavirus-induced lung injury. *Nat. Med.* **11**, 875–879 (2005).
 26. S. Bertram, I. Glowacka, M. A. Muller, H. Lavender, K. Gnirss, I. Nehlmeier, D. Niemyer, Y. He, G. Simmons, C. Drosten, E. J. Soilleux, O. Jahn, I. Steffen, S. Pohlmann, Cleavage and activation of the severe acute respiratory syndrome coronavirus spike protein by human airway trypsin-like protease. *J. Virol.* **85**, 13363–13372 (2011).
 27. S. Bertram, A. Heurich, H. Lavender, S. Gierer, S. Danisch, P. Perin, J. M. Lucas, P. S. Nelson, S. Pöhlmann, E. J. Soilleux, Influenza and SARS-coronavirus activating proteases TMPRSS2 and HAT are expressed at multiple sites in human respiratory and gastrointestinal tracts. *PLOS ONE* **7**, e35876 (2012).
 28. H. Chu, C.-M. Chan, X. Zhang, Y. Wang, S. Yuan, J. Zhou, R. K.-H. Au-Yeung, K.-H. Sze, D. Yang, H. Shuai, Y. Hou, C. Li, X. Zhao, V. K.-M. Poon, S. P. Leung, M.-L. Yeung, J. Yan, G. Lu, D.-Y. Jin, G. F. Gao, J. F.-W. Chan, K.-Y. Yuen, Middle East respiratory syndrome coronavirus and bat coronavirus HKU9 both can utilize GRP78 for attachment onto host cells. *J. Biol. Chem.* **293**, 11709–11726 (2018).
 29. H. J. Hedrich, *The Laboratory Mouse* (Academic Press, 2012), 845 pp.
 30. G. K. Reznik, Comparative anatomy, physiology, and function of the upper respiratory tract. *Environ. Health Perspect.* **85**, 171–176 (1990).
 31. Y. Suzuki, J. Schafer, A. I. Farbman, Phagocytic cells in the rat olfactory epithelium after bulbectomy. *Exp. Neurol.* **136**, 225–233 (1995).
 32. Y. Suzuki, M. Takeda, A. I. Farbman, Supporting cells as phagocytes in the olfactory epithelium after bulbectomy. *J. Comp. Neurol.* **376**, 509–517 (1996).
 33. F. Vogalis, C. C. Hegg, M. T. Lucero, Ionic conductances in sustentacular cells of the mouse olfactory epithelium. *J. Physiol.* **562**, 785–799 (2005).
 34. S. Pfister, T. Weber, W. Härtig, C. Schwerdel, R. Elsaesser, I. Knuesel, J.-M. Fritschy, Novel role of cystic fibrosis transmembrane conductance regulator in maintaining adult mouse olfactory neuronal homeostasis. *J. Comp. Neurol.* **523**, 406–430 (2014).
 35. R. Choi, B. J. Goldstein, Olfactory epithelium: Cells, clinical disorders, and insights from an adult stem cell niche. *Laryngoscope Investig. Otolaryngol.* **3**, 35–42 (2018).
 36. R. B. Fletcher, D. Das, L. Gadye, K. N. Street, A. Baudhuin, A. Wagner, M. B. Cole, Q. Flores, Y. G. Choi, N. Yosef, E. Purdom, S. Dudoit, D. Rizzo, J. Ngai, Deconstructing olfactory stem cell trajectories at single-cell resolution. *Cell Stem Cell* **20**, 817–830.e8 (2017).
 37. J. E. Schwob, W. Jang, E. H. Holbrook, B. Lin, D. B. Herrick, J. N. Peterson, J. Hewitt Coleman, Stem and progenitor cells of the mammalian olfactory epithelium: Taking poetic license. *J. Comp. Neurol.* **525**, 1034–1054 (2017).
 38. M. A. Durante, S. Kurtenbach, Z. B. Sargi, J. W. Harbour, R. Choi, S. Kurtenbach, G. M. Goss, H. Matsunami, B. J. Goldstein, Single-cell analysis of olfactory neurogenesis and differentiation in adult humans. *Nat. Neurosci.* **23**, 323–326 (2020).
 39. W. Sungnak, N. Huang, C. Bécavin, M. Berg, R. Queen, M. Litvinukova, C. Talavera-López, H. Maatz, D. Reichart, F. Sampaziotis, K. B. Worlock, M. Yoshida, J. L. Barnes; HCA Lung Biological Network, SARS-CoV-2 entry factors are highly expressed in nasal epithelial cells together with innate immune genes. *Nat. Med.* **26**, 681–687 (2020).
 40. Y. J. Hou, K. Okuda, C. E. Edwards, D. R. Martinez, T. Asakura, K. H. Dinno III, T. Kato, R. E. Lee, B. L. Yount, T. M. Mascenik, G. Chen, K. N. Olivier, A. Ghio, L. V. Tse, S. R. Leist, L. E. Gralinski, A. Schäfer, H. Dang, R. Gilmore, S. Nakano, L. Sun, M. L. Fulcher, A. Livraghi-Butrico, N. I. Nicely, M. Cameron, C. Cameron, D. J. Kelvin, A. de Silva, D. M. Margolis, A. Markmann, L. Bartelt, R. Zumwalt, F. J. Martinez, S. P. Salvatore, A. Borczuk, P. R. Tata, V. Sontake, A. Kimple, I. Jaspers, W. K. O'Neal, S. H. Randell, R. C. Boucher, R. S. Baric, SARS-CoV-2 reverse genetics reveals a variable infection gradient in the respiratory tract. *Cell* **182**, 1–18 (2020).
 41. M. Deprez, L.-E. Zaragosi, M. Truchi, S. R. Garcia, M.-J. Arguel, K. Lebrigand, A. Paquet, D. Peer, C.-H. Marquette, S. Leroy, P. Barbry, A single-cell atlas of the human healthy airways. bioRxiv 884759 [Preprint]. 23 December 2019. <https://doi.org/10.1101/2019.12.21.884759>.
 42. F. A. Vieira Braga, G. Kar, M. Berg, O. A. Carpaij, K. Polanski, L. M. Simon, S. Brouwer, T. Gomes, L. Hesse, J. Jiang, E. S. Fasouli, M. Eremova, R. Vento-Tormo, C. Talavera-López, M. R. Jonker, K. Affleck, S. Palit, P. M. Strzelecka, H. V. Firth, K. T. Mahbubani, A. Cvejic, K. B. Meyer, K. Saeb-Parsy, M. Luinge, C.-A. Brandsma, W. Timens, I. Angelidis, M. Strunz, G. H. Koppelman, A. J. van Oosterhout, H. B. Schiller, F. J. Theis, M. van den Berge, M. C. Nawijn, S. A. Teichmann, A cellular census of human lungs identifies novel cell states in health and in asthma. *Nat. Med.* **25**, 1153–1163 (2019).
 43. L. R. Saraiva, F. Riveros-McKay, M. Mezzavilla, E. H. Abou-Moussa, C. J. Arayata, M. Makhlof, C. Trimmer, X. Ibarra-Soria, M. Khan, L. Van Gerven, M. Jorissen, M. Gibbs, C. O'Flynn, S. McGrane, P. Mombaerts, J. C. Marioni, J. D. Mainland, D. W. Logan, A transcriptomic atlas of mammalian olfactory mucosae reveals an evolutionary influence on food odor detection in humans. *Sci. Adv.* **5**, eaax0396 (2019).
 44. W. Sungnak, N. Huang, C. Bécavin, M. Berg, HCA Lung Biological Network, SARS-CoV-2 entry genes are most highly expressed in nasal goblet and ciliated cells within human airways. arXiv:2003.06122 [q-bio.CB] (13 March 2020).
 45. N. Zhu, D. Zhang, W. Wang, X. Li, B. Yang, J. Song, X. Zhao, B. Huang, W. Shi, R. Lu, P. Niu, F. Zhan, X. Ma, D. Wang, W. Xu, G. Wu, G. F. Gao, W. Tan; China Novel Coronavirus Investigating and Research Team, A novel coronavirus from patients with pneumonia in China, 2019. *N. Engl. J. Med.* **382**, 727–733 (2020).
 46. L. R. Saraiva, X. Ibarra-Soria, M. Khan, M. Omura, A. Scialdone, P. Mombaerts, J. C. Marioni, D. W. Logan, Hierarchical deconstruction of mouse olfactory sensory neurons: From whole mucosa to single-cell RNA-seq. *Sci. Rep.* **5**, 18178 (2015).
 47. N. Kanageswaran, M. Demond, M. Nagel, B. S. P. Schreiner, S. Baumgart, P. Scholz, J. Altmüller, C. Becker, J. F. Doerner, H. Conrad, S. Oberland, C. H. Wetzel, E. M. Neuhaus, H. Hatt, G. Gisselmann, Deep sequencing of the murine olfactory receptor neuron transcriptome. *PLOS ONE* **10**, e0113170 (2015).
 48. B. M. Colquitt, E. Markenscoff-Papadimitriou, R. Duffié, S. Lomvardas, Dnmt3a regulates global gene expression in olfactory sensory neurons and enables odorant-induced transcription. *Neuron* **83**, 823–838 (2014).
 49. Z. M. Soler, Z. M. Patel, J. H. Turner, E. H. Holbrook, A primer on viral-associated olfactory loss in the era of COVID-19. *Int. Forum Allergy Rhinol.*, 1–11 (2020).
 50. A. Zeisel, H. Hochgerner, P. Lönnerberg, A. Johnsson, F. Memic, J. van der Zwan, M. Häring, E. Braun, L. E. Borm, G. L. Manno, S. Codeluppi, A. Furlan, K. Lee, N. Skene, K. D. Harris, J. Hjerling-Leffler, E. Arenas, P. Ernfors, U. Marklund, S. Linnarsson, Molecular architecture of the mouse nervous system. *Cell* **174**, 999–1014.e22 (2018).
 51. L. S. Brown, C. G. Foster, J.-M. Courtney, N. E. King, D. W. Howells, B. A. Sutherland, Pericytes and neurovascular function in the healthy and diseased brain. *Front. Cell. Neurosci.* **13**, 282 (2019).
 52. I. Hamming, W. Timens, M. L. C. Bulthuis, A. T. Lely, G. Navis, H. van Goor, Tissue distribution of ACE2 protein, the functional receptor for SARS coronavirus. A first step in understanding SARS pathogenesis. *J. Pathol.* **203**, 631–637 (2004).
 53. P. G. Kehoe, S. Wong, N. Al Mulhim, L. E. Palmer, J. S. Miners, Angiotensin-converting enzyme 2 is reduced in Alzheimer's disease in association with increasing amyloid- β and tau pathology. *Alzheimers Res Ther* **8**, 50 (2016).
 54. M. Chen, R. R. Reed, A. P. Lane, Chronic inflammation directs an olfactory stem cell functional switch from neuroregeneration to immune defense. *Cell Stem Cell* **25**, 501–513.e5 (2019).
 55. L. W. Plasschaert, R. Žilionis, R. Choo-Wing, V. Savova, J. Knehr, G. Roma, A. M. Klein, A. B. Jaffe, A single-cell atlas of the airway epithelium reveals the CFTR-rich pulmonary ionocyte. *Nature* **560**, 377–381 (2018).
 56. C. G. D. Bihun, D. H. Percy, Morphologic changes in the nasal cavity associated with sialodacryoadenitis virus infection in the Wistar rat. *Vet. Pathol.* **32**, 1–10 (1995).
 57. C. Hopkins, P. Surda, E. Whitehead, B. N. Kumar, Early recovery following new onset anosmia during the COVID-19 pandemic—An observational cohort study. *J. Otolaryngol. Head Neck Surg.* **49**, 26 (2020).
 58. L. S. Politi, E. Salsano, M. Grimaldi, Magnetic resonance imaging alteration of the brain in a patient with coronavirus disease 2019 (COVID-19) and anosmia. *JAMA Neurol.*, 10.1001/jamaneuro.2020.2125 (2020).
 59. T. Laurendon, T. Radulesco, J. Mugnier, M. Géralt, C. Chagnaud, A.-A. El Ahmadi, A. Varoquaux, Bilateral transient olfactory bulbs edema during COVID-19-related anosmia. *Neurology*, 10.1212/WNL.0000000000009850 (2020).
 60. K. Bohmwald, N. M. S. Gálvez, M. Ríos, A. M. Kaleris, Neurologic alterations due to respiratory virus infections. *Front. Cell. Neurosci.* **12**, 386 (2018).
 61. S. L. Youngentob, J. E. Schwob, S. Saha, G. Manglapus, B. Jubelt, Functional consequences following infection of the olfactory system by intranasal infusion of the olfactory bulb line variant (OBLV) of mouse hepatitis strain JHM. *Chem. Senses* **26**, 953–963 (2001).
 62. R. L. Doty, Systemic diseases and disorders. *Handb. Clin. Neurol.* **164**, 361–387 (2019).
 63. E. M. Barnett, S. Perlman, The olfactory nerve and not the trigeminal nerve is the major site of CNS entry for mouse hepatitis virus, strain JHM. *Virology* **194**, 185–191 (1993).
 64. J. E. Schwob, S. Saha, S. L. Youngentob, B. Jubelt, Intranasal inoculation with the olfactory bulb line variant of mouse hepatitis virus causes extensive destruction of the olfactory bulb and accelerated turnover of neurons in the olfactory epithelium of mice. *Chem. Senses* **26**, 937–952 (2001).
 65. J. Netland, D. K. Meyerholz, S. Moore, M. Cassell, S. Perlman, Severe acute respiratory syndrome coronavirus infection causes neuronal death in the absence of encephalitis in mice transgenic for human ACE2. *J. Virol.* **82**, 7264–7275 (2008).
 66. E. Hemmila, C. Turbide, M. Olson, S. Jothy, K. V. Holmes, N. Beauchemin, Ceacam1a^{-/-} mice are completely resistant to infection by murine coronavirus mouse hepatitis virus A59. *J. Virol.* **78**, 10156–10165 (2004).
 67. R.-D. Jiang, M.-Q. Liu, Y. Chen, C. Shan, Y.-W. Zhou, X.-R. Shen, Q. Li, L. Zhang, Y. Zhu, H.-R. Si, Q. Wang, J. Min, X. Wang, W. Zhang, B. Li, H.-J. Zhang, R. S. Baric, P. Zhou, X.-L. Yang, Z.-L. Shi, Pathogenesis of SARS-CoV-2 in transgenic mice expressing human angiotensin-converting enzyme 2. *Cell* **182**, 1–9 (2020).

68. S.-H. Sun, Q. Chen, H.-J. Gu, G. Yang, Y.-X. Wang, X.-Y. Huang, S.-S. Liu, N.-N. Zhang, X.-F. Li, R. Xiong, Y. Guo, Y.-Q. Deng, W.-J. Huang, Q. Liu, Q.-M. Liu, Y.-L. Shen, Y. Zhou, X. Yang, T.-Y. Zhao, C.-F. Fan, Y.-S. Zhou, C.-F. Qin, Y. C. Wang, A mouse model of SARS-CoV-2 infection and pathogenesis. *Cell Host Microbe*, 10.1016/j.chom.2020.05.020 (2020).
69. L. Bao, W. Deng, B. Huang, H. Gao, J. Liu, L. Ren, Q. Wei, P. Yu, Y. Xu, F. Qi, Y. Qu, F. Li, Q. Lv, W. Wang, J. Xue, S. Gong, M. Liu, G. Wang, S. Wang, Z. Song, L. Zhao, P. Liu, L. Zhao, F. Ye, H. Wang, W. Zhou, N. Zhu, W. Zhen, H. Yu, X. Zhang, L. Guo, L. Chen, C. Wang, Y. Wang, X. Wang, Y. Xiao, Q. Sun, H. Liu, F. Zhu, C. Ma, L. Yan, M. Yang, J. Han, W. Xu, W. Tan, X. Peng, Q. Jin, G. Wu, C. Qin, The pathogenicity of SARS-CoV-2 in hACE2 transgenic mice. *Nature*, 10.1038/s41586-020-2312-y (2020).
70. L. He, M. A. Mäe, Y. Sun, L. Muhl, K. Nahar, E. V. Liébanas, M. J. Fagerlund, A. Oldner, J. Liu, G. Genové, R. Pietilä, L. Zhang, Y. Xie, S. Leptidis, G. Mocchi, S. Stritt, A. Osman, A. Anisimov, K. A. Hemantakumar, M. Räsänen, J. Björkegren, M. Vanlandewijck, K. Blomgren, E. Hansson, T. Mäkinen, X.-R. Peng, T. D. Arnold, K. Alitalo, L. I. Eriksson, U. Lendahl, C. Betsholtz, Pericyte-specific vascular expression of SARS-CoV-2 receptor ACE2—Implications for microvascular inflammation and hypercoagulopathy in COVID-19 patients. *bioRxiv* 088500 [Preprint]. 12 May 2020. <https://doi.org/10.1101/2020.05.11.088500>.
71. Y. Zhang, M. Xiao, S. Zhang, P. Xia, W. Cao, W. Jiang, H. Chen, X. Ding, H. Zhao, H. Zhang, C. Wang, J. Zhao, X. Sun, R. Tian, W. Wu, D. Wu, J. Ma, Y. Chen, D. Zhang, J. Xie, X. Yan, X. Zhou, Z. Liu, J. Wang, B. du, Y. Qin, P. Gao, X. Qin, Y. Xu, W. Zhang, T. Li, F. Zhang, Y. Zhao, Y. Li, S. Zhang, Coagulopathy and antiphospholipid antibodies in patients with Covid-19. *N. Engl. J. Med.* **382**, e38 (2020).
72. N. Poyiadji, G. Shahin, D. Noujaim, M. Stone, S. Patel, B. Griffith, COVID-19-associated acute hemorrhagic necrotizing encephalopathy: CT and MRI features. *Radiology*, 201187 (2020).
73. J. Helms, S. Kremer, H. Merdji, L. Clere-Jehl, M. Schenck, C. Kummerlen, O. Collange, C. Boulay, S. Fafi-Kremer, M. Ohana, M. Anheim, F. Meziani, Neurologic features in severe SARS-CoV-2 infection. *N. Engl. J. Med.* **382**, 2268–2270 (2020).
74. T. Coolen, V. Lolli, N. Sadeghi, A. Rovai, N. Trotta, F. S. Taccone, J. Creteur, S. Henrard, J.-C. Goffard, O. Dewitte, G. Naeije, S. Goldman, X. De Tiege, Early postmortem brain MRI findings in COVID-19 non-survivors. *medRxiv* 20090316 [Preprint]. 8 May 2020. <https://doi.org/10.1101/2020.05.04.20090316>.
75. T. Chen, D. Wu, H. Chen, W. Yan, D. Yang, G. Chen, K. Ma, D. Xu, H. Yu, H. Wang, T. Wang, W. Guo, J. Chen, C. Ding, X. Zhang, J. Huang, M. Han, S. Li, X. Luo, J. Zhao, Q. Ning, Clinical characteristics of 113 deceased patients with coronavirus disease 2019: Retrospective study. *BMJ* **368**, m1295 (2020).
76. R. Beyrouti, M. E. Adams, L. Benjamin, H. Cohen, S. F. Farmer, Y. Y. Goh, F. Humphries, H. R. Jäger, N. A. Losseff, R. J. Perry, S. Shah, R. J. Simister, D. Turner, A. Chandratheva, D. J. Werring, Characteristics of ischaemic stroke associated with COVID-19. *J. Neurol. Neurosurg. Psychiatry*, jnnp-2020-323586 (2020).
77. T. Schaller, K. Hirschtbühl, K. Burkhardt, G. Braun, M. Trepel, B. Märkl, R. Claus, Postmortem examination of patients with COVID-19. *JAMA* **323**, 2518–2520 (2020).
78. V. G. Puelles, M. Lütgehetmann, M. T. Lindenmeyer, J. P. Sperhake, M. N. Wong, L. Allweiss, S. Chilla, A. Heinemann, N. Wanner, S. Liu, F. Braun, S. Lu, S. Pfefferle, A. S. Schröder, C. Edler, O. Gross, M. Glatzel, D. Wichmann, T. Wieg, S. Kluge, K. Pueschel, M. Aepfelbacher, T. B. Huber, Multiorgan and renal tropism of SARS-CoV-2. *N. Engl. J. Med.*, 10.1056/NEJMc2011400 (2020).
79. R. Ueha, K. Kondo, R. Kagoya, S. Shichino, S. Ueha, T. Yamasoba, Background mechanisms of olfactory dysfunction in COVID-19: Expression of ACE2, TMPRSS2, and Furin in the nose and olfactory bulb in human and mice. *bioRxiv* 097352 [Preprint]. 15 May 2020. <https://doi.org/10.1101/2020.05.15.097352>.
80. M. F. Doobay, L. S. Talman, T. D. Obr, X. Tian, R. L. Davisson, E. Lazartigues, Differential expression of neuronal ACE2 in transgenic mice with overexpression of the brain renin-angiotensin system. *Am. J. Physiol. Regul. Integr. Comp. Physiol.* **292**, R373–R381 (2007).
81. K. Bilinska, P. Jakubowska, C. S. Von Bartheld, R. Butowt, Expression of the SARS-CoV-2 entry proteins, ACE2 and TMPRSS2, in cells of the olfactory epithelium: Identification of cell types and trends with age. *ACS Chem. Neurosci.* **11**, 1555–1562 (2020).
82. R. Chen, K. Wang, J. Yu, Z. Chen, C. Wen, Z. Xu, The spatial and cell-type distribution of SARS-CoV-2 receptor ACE2 in human and mouse brain. *bioRxiv* 030650 [Preprint]. 9 April 2020. <https://doi.org/10.1101/2020.04.07.030650>.
83. V. J. Munster, F. Feldmann, B. N. Williamson, N. van Doremalen, L. Pérez-Pérez, J. Schulz, K. Meade-White, A. Okumura, J. Callison, B. Brumbaugh, V. A. Avanzato, R. Rosenke, P. W. Hanley, G. Saturday, D. Scott, E. R. Fischer, E. de Wit, Respiratory disease in rhesus macaques inoculated with SARS-CoV-2. *Nature*, 10.1038/s41586-020-2324-7 (2020).
84. Z. Chen, L. Mi, J. Xu, J. Yu, X. Wang, J. Jiang, J. Xing, P. Shang, A. Qian, Y. Li, P. X. Shaw, J. Wang, S. Duan, J. Ding, C. Fan, Y. Zhang, Y. Yang, X. Yu, Q. Feng, B. Li, X. Yao, Z. Zhang, L. Li, X. Xue, P. Zhu, Function of HAb18G/CD147 in invasion of host cells by severe acute respiratory syndrome coronavirus. *J. Infect. Dis.* **191**, 755–760 (2005).
85. K. Wang, W. Chen, Y.-S. Zhou, J.-Q. Lian, Z. Zhang, P. Du, L. Gong, Y. Zhang, H.-Y. Cui, J.-J. Geng, B. Wang, X.-X. Sun, C.-F. Wang, X. Yang, P. Lin, Y.-Q. Deng, D. Wei, X.-M. Yang, Y.-M. Zhu, K. Zhang, Z.-H. Zheng, J.-L. Miao, T. Guo, Y. Shi, J. Zhang, L. Fu, Q.-Y. Wang, H. Bian, P. Zhu, Z.-N. Chen, SARS-CoV-2 invades host cells via a novel route: CD147-spike protein. *bioRxiv* 988345 [Preprint]. 14 March 2020. <https://doi.org/10.1101/2020.03.14.988345>.
86. M. M. Lamers, J. Beumer, J. van der Vaart, K. Knoops, J. Puschhof, T. I. Breugem, R. B. G. Ravelli, J. Paul van Schayck, A. Z. Mykytyyn, H. Q. Duimel, E. van Donselaar, S. Riesebosch, H. J. H. Kijpers, D. Schippers, W. J. van de Wetering, M. de Graaf, M. Koopmans, E. Cuppen, P. J. Peters, B. L. Haagmans, H. Clevers, SARS-CoV-2 productively infects human gut enterocytes. *Science*, eabc1669 (2020).
87. C. G. K. Ziegler, S. J. Allon, S. K. Nyquist, I. M. Mbanu, V. N. Miao, C. N. Tzouanas, Y. Cao, A. S. Yousef, J. Bals, B. M. Hauser, J. Feldman, C. Muus, M. H. Wadsworth II, S. W. Kazer, T. K. Hughes, B. Doran, G. J. Gatter, M. Vukovic, F. Taliaferro, B. E. Mead, Z. Guo, J. P. Wang, D. Gras, M. Plaisant, M. Ansari, I. Angelidis, H. Adler, J. M. S. Sucre, C. J. Taylor, B. Lin, A. Wharney, V. Mitsialis, D. F. Dwyer, K. M. Buchheit, J. A. Boyce, N. A. Barrett, T. M. Laidlaw, S. L. Carroll, L. Colonna, V. Tkachev, C. W. Peterson, A. Yu, H. B. Zheng, H. P. Gideon, C. G. Winchell, P. L. Lin, C. D. Bingle, S. B. Snapper, J. A. Kroppski, F. J. Theis, H. B. Schiller, L.-E. Zaragosi, P. Barbry, A. Leslie, H.-P. Kiem, J. L. Flynn, S. M. Fortune, B. Berger, R. W. Finberg, L. S. Kean, M. Garber, A. G. Schmidt, D. Lingwood, A. K. Shalek, J. Ordovas-Montanes; HCA Lung Biological Network. Electronic address: lung-network@humancellatlas.org; HCA Lung Biological Network, SARS-CoV-2 receptor ACE2 is an interferon-stimulated gene in human airway epithelial cells and is detected in specific cell subsets across tissues. *Cell* **181**, 1016–1035.e19 (2020).
88. S. P. Sajuthi, P. De Ford, N. D. Jackson, M. T. Montgomery, J. L. Everman, C. L. Rios, E. Pruesse, J. D. Nolin, E. G. Plender, M. E. Wechsler, A. C. Y. Mak, C. Eng, S. Salazar, V. Medina, E. M. Wohlford, S. Huntsman, D. A. Nickerson, S. Germer, M. C. Zody, G. Abecasis, H. M. Kang, K. M. Rice, R. Kumar, S. Oh, J. Rodriguez-Santana, E. G. Burchar, M. A. Seibold, Type 2 and interferon inflammation strongly regulate SARS-CoV-2 related gene expression in the airway epithelium. *bioRxiv* 034454 [Preprint]. 10 April 2020. <https://doi.org/10.1101/2020.04.09.034454>.
89. L. Fodouljan, J. Tuberosa, D. Rossier, B. N. Landis, A. Carleton, I. Rodriguez, SARS-CoV-2 receptor and entry genes are expressed by sustentacular cells in the human olfactory neuroepithelium. *bioRxiv* 013268 [Preprint]. 2 April 2020. <https://doi.org/10.1101/2020.03.31.013268>.
90. M. Chen, W. Shen, N. R. Rowan, H. Kulaga, A. Hillel, M. Ramanathan Jr., A. P. Lane, Elevated ACE2 expression in the olfactory neuroepithelium: Implications for anosmia and upper respiratory SARS-CoV-2 entry and replication. *bioRxiv* 084996 [Preprint]. 9 May 2020. <https://doi.org/10.1101/2020.05.08.084996>.
91. A. Haehner, J. Draf, S. Draeger, K. de With, T. Hummel, Predictive value of sudden olfactory loss in the diagnosis of COVID-19. *medRxiv* 20081356 [Preprint]. 3 May 2020. <https://doi.org/10.1101/2020.04.27.20081356>.
92. F. Shweta, K. Murugadoss, S. Awasthi, A. J. Venkatakrishnan, A. Puranik, M. Kang, B. W. Pickering, J. C. O'Horo, P. R. Bauer, R. R. Razonable, P. Vergidis, Z. Temesgen, S. Rizza, M. Mahmood, W. R. Wilson, D. Challener, P. Anand, M. Liebers, Z. Doctor, E. Silvert, H. Solomon, T. Wagner, G. J. Gores, A. W. Williams, J. Halamka, V. Soundararajan, A. D. Badley, augmented curation of unstructured clinical notes from a massive EHR system reveals specific phenotypic signature of impending COVID-19 diagnosis. *arXiv:2004.09338 [cs.LG]* (17 April 2020).
93. C. Weinreb, A. Rodriguez-Fraticelli, F. D. Camargo, A. M. Klein, Lineage tracing on transcriptional landscapes links state to fate during differentiation. *Science* **367**, eaaw3381 (2020).
94. E. Z. Macosko, A. Basu, R. Satija, J. Nemesk, K. Shekhar, M. Goldman, I. Tirosh, A. R. Bialas, N. Kamitaki, E. M. Martersteck, J. J. Trombetta, D. A. Weitz, J. R. Sanes, A. K. Shalek, A. Regev, S. A. McCarroll, Highly parallel genome-wide expression profiling of individual cells using nanoliter droplets. *Cell* **161**, 1202–1214 (2015).
95. J. Schindelin, I. Arganda-Carreras, E. Frise, V. Kaynig, M. Longair, T. Pietzsch, S. Preibisch, C. Rueden, S. Saalfeld, B. Schmid, J.-Y. Tinevez, D. J. White, V. Hartenstein, K. Eliceiri, P. Tomancak, A. Cardona, Fiji: An open-source platform for biological-image analysis. *Nat. Methods* **9**, 676–682 (2012).
96. A. K. Indra, X. Warot, J. Brocard, J.-M. Bornert, J.-H. Xiao, P. Chambon, D. Metzger, Temporally-controlled site-specific mutagenesis in the basal layer of the epidermis: Comparison of the recombinase activity of the tamoxifen-inducible Cre-ER^T and Cre-ER^{2T} recombinases. *Nucleic Acids Res.* **27**, 4324–4327 (1999).
97. S. Srinivas, T. Watanabe, C. S. Lin, C. M. William, Y. Tanabe, T. M. Jessell, F. Costantini, Cre reporter strains produced by targeted insertion of EYFP and ECFP into the ROSA26 locus. *BMC Dev. Biol.* **1**, 4 (2001).
98. L. Gadye, D. Das, M. A. Sanchez, K. Street, A. Baudhuin, A. Wagner, M. B. Cole, Y. G. Choi, N. Yosef, E. Purdom, S. Dudoit, D. Risso, J. Ngai, R. B. Fletcher, Injury activates transient olfactory stem cell states with diverse lineage capacities. *Cell Stem Cell* **21**, 775–790.e9 (2017).
99. M. B. Cole, D. Risso, A. Wagner, D. DeTomaso, J. Ngai, E. Purdom, S. Dudoit, N. Yosef, Performance assessment and selection of normalization procedures for single-Cell RNA-seq. *Cell Syst.* **8**, 315–328.e8 (2019).

100. C. S. McGinnis, L. M. Murrow, Z. J. Gartner, DoubletFinder: Doublet detection in single-cell RNA sequencing data using artificial nearest neighbors. *Cell Syst.* **8**, 329–337.e4 (2019).
101. S. L. Wolock, R. Lopez, A. M. Klein, Scrublet: Computational identification of cell doublets in single-cell transcriptomic data. *Cell Syst.* **8**, 281–291.e9 (2019).
102. D. Risso, J. Ngai, T. P. Speed, S. Dudoit, Normalization of RNA-seq data using factor analysis of control genes or samples. *Nat. Biotechnol.* **32**, 896–902 (2014).
103. D. Risso, L. Purvis, R. B. Fletcher, D. Das, J. Ngai, S. Dudoit, E. Purdom, clusterExperiment and RSEC: A bioconductor package and framework for clustering of single-cell and other large gene expression datasets. *PLoS Comput. Biol.* **14**, e1006378 (2018).
104. C. Weinreb, S. Wolock, A. M. Klein, SPRING: A kinetic interface for visualizing high dimensional single-cell expression data. *Bioinformatics* **34**, 1246–1248 (2018).
105. F. A. Wolf, P. Angerer, F. J. Theis, SCANPY: Large-scale single-cell gene expression data analysis. *Genome Biol.* **19**, 15 (2018).
106. T. Stuart, A. Butler, P. Hoffman, C. Hafemeister, E. Papalexi, W. M. Mauck III, Y. Hao, M. Stoeckius, P. Smibert, R. Satija, Comprehensive integration of single-cell data. *Cell* **177**, 1888–1902.e21 (2019).
107. L. Zappia, A. Oshlack, Clustering trees: A visualization for evaluating clusterings at multiple resolutions. *GigaScience* **7**, giy083 (2018).
108. E. Galliano, E. Franzoni, M. Breton, A. N. Chand, D. J. Byrne, V. N. Murthy, M. S. Grubb, Embryonic and postnatal neurogenesis produce functionally distinct subclasses of dopaminergic neuron. *eLife* **7**, e32373 (2018).
109. C. M. Hempel, K. Sugino, S. B. Nelson, A manual method for the purification of fluorescently labeled neurons from the mammalian brain. *Nat. Protoc.* **2**, 2924–2929 (2007).
110. I. C. Macaulay, M. J. Teng, W. Haerty, P. Kumar, C. P. Ponting, T. Voet, Separation and parallel sequencing of the genomes and transcriptomes of single cells using G&T-seq. *Nat. Protoc.* **11**, 2081–2103 (2016).
111. N. L. Bray, H. Pimentel, P. Melsted, L. Pachter, Near-optimal probabilistic RNA-seq quantification. *Nat. Biotechnol.* **34**, 525–527 (2016).
112. D. J. McCarthy, K. R. Campbell, A. T. Lun, Q. F. Wills, Scater: Pre-processing, quality control, normalization and visualization of single-cell RNA-seq data in R. *Bioinformatics* **33**, 1179–1186 (2017).
113. J. Ninkovic, L. Pinto, S. Petricca, A. Lepier, J. Sun, M. A. Rieger, T. Schroeder, A. Cvekl, J. Favor, M. Götz, The transcription factor Pax6 regulates survival of dopaminergic olfactory bulb neurons via crystallin αA . *Neuron* **68**, 682–694 (2010).
114. K. Shekhar, S. W. Lapan, I. E. Whitney, N. M. Tran, E. Z. Macosko, M. Kowalczyk, X. Adiconis, J. Z. Levin, J. Nemes, M. Goldman, S. A. McCarroll, C. L. Cepko, A. Regev, J. R. Sanes, Comprehensive classification of retinal bipolar neurons by single-cell transcriptomics. *Cell* **166**, 1308–1323.e30 (2016).
115. J. C. Burns, M. C. Kelly, M. Hoa, R. J. Morell, M. W. Kelley, Single-cell RNA-seq resolves cellular complexity in sensory organs from the neonatal inner ear. *Nat. Commun.* **6**, 8557 (2015).
116. S. McInturff, J. C. Burns, M. W. Kelley, Characterization of spatial and temporal development of Type I and Type II hair cells in the mouse utricle using new cell-type-specific markers. *Biology open* **7**, bio038083 (2018).
117. B. R. Shrestha, C. Chia, L. Wu, S. G. Kujawa, M. C. Liberman, L. V. Goodrich, Sensory neuron diversity in the inner ear is shaped by activity. *Cell* **174**, 1229–1246.e17 (2018).
118. G. La Manno, D. Gyllborg, S. Codeluppi, K. Nishimura, C. Salto, A. Zeisel, L. E. Borm, S. R. W. Stott, E. M. Toledo, J. C. Villaescusa, P. Lönnerberg, J. Ryge, R. A. Barker, E. Arenas, S. Linnarsson, Molecular diversity of midbrain development in mouse, human and stem cells. *Cell* **167**, 566–580.e19 (2016).
119. M. S. Cembrowski, M. G. Phillips, S. F. DiLisio, B. C. Shields, J. Winnubst, J. Chandrashekar, E. Bas, N. Spruston, Dissociable structural and functional hippocampal outputs via distinct subiculum cell classes. *Cell* **173**, 1280–1292.e18 (2018).
120. M. Chevéé, J. De Jong Robertson, G. H. Cannon, S. P. Brown, L. A. Goff, Variation in activity state, axonal projection, and position define the transcriptional identity of individual neocortical projection neurons. *Cell Rep.* **22**, 441–455 (2018).
121. R. A. Romanov, A. Zeisel, J. Bakker, F. Girach, A. Hellysaz, R. Tomer, A. Alpár, J. Mulder, F. Clotman, E. Keimpema, B. Hsueh, A. K. Crow, H. Martens, C. Schwindling, D. Calvigioni, J. S. Bains, Z. Máté, G. Szabó, Y. Yanagawa, M.-D. Zhang, A. Rendeiro, M. Farlik, M. Uhlén, P. Wulff, C. Beck, C. Broberger, K. Deisseroth, T. Hökfelt, S. Linnarsson, T. L. Horvath, T. Harkany, Molecular interrogation of hypothalamic organization reveals distinct dopamine neuronal subtypes. *Nat. Neurosci.* **20**, 176–188 (2017).
122. A. Furlan, G. La Manno, M. Lübke, M. Häring, H. Abdo, H. Hochgerner, J. Kupari, D. Usoskin, M. S. Airaksinen, G. Oliver, S. Linnarsson, P. Ernfors, Visceral motor neuron diversity delineates a cellular basis for nipple- and pilo-erection muscle control. *Nat. Neurosci.* **19**, 1331–1340 (2016).
123. D. Usoskin, A. Furlan, S. Islam, H. Abdo, P. Lönnerberg, D. Lou, J. Hjerling-Leffler, J. Haeggström, O. Kharchenko, P. V. Kharchenko, S. Linnarsson, P. Ernfors, Unbiased classification of sensory neuron types by large-scale single-cell RNA sequencing. *Nat. Neurosci.* **18**, 145–153 (2015).
124. M. Haring, A. Zeisel, H. Hochgerner, P. Rinwa, J. E. T. Jakobsson, P. Lönnerberg, G. La Manno, N. Sharma, L. Borgius, O. Kiehn, M. C. Lagerström, S. Linnarsson, P. Ernfors, Neuronal atlas of the dorsal horn defines its architecture and links sensory input to transcriptional cell types. *Nat. Neurosci.* **21**, 869–880 (2018).
125. A. T. Lun, K. Bach, J. C. Marioni, Pooling across cells to normalize single-cell RNA sequencing data with many zero counts. *Genome Biol.* **17**, 75 (2016).

Acknowledgments: We thank members of the Datta lab, J. Schwob, B. Sabatini, A. Schaefer, K. Franks, M. Greenberg, and V. Ruta for helpful comments on the manuscript. We thank J. Lipscombe and A. Crespo for technical support. **Funding:** S.R.D. was supported by grants RO11DC016222 and U19 NS112953 from the NIH and by the Simons Collaboration on the Global Brain, and the HMS Neurobiology Imaging Facility was supported by NIH grant P30NS072030. D.H.B. was supported by an NSF Graduate Research Fellowship. J.N. was supported by NIH grant RO1DC007235. D.R. was supported by Programma per Giovani Ricercatori Rita Levi Montalcini granted by the Italian Ministry of Education, University, and Research. K.V.d.B. is a postdoctoral fellow of the Belgian American Educational Foundation (BAEF) and was supported by the Research Foundation Flanders (FWO), grant 1246220N.D.D. was a fellow of the Berkeley Institute for Data Science, funded in part by the Gordon and Betty Moore Foundation (grant GBMF3834) and the Alfred P. Sloan Foundation (grant 2013-10-27). M.L. and M.S.G. were supported by a Leverhulme Trust Research Grant (RPG-2016-095) and a Consolidator Grant from the European Research Council (725729; FUNCOPLAN). J.M. was supported by a Medical Research Council grant (K013807) and a Medical Research Council Clinical Infrastructure Award (M008924). I.C.M. was supported by a BBSRC New Investigator Grant (BB/P022073/1) and the BBSRC National Capability in Genomics and Single Cell Analysis at Earlham Institute (BB/CCG1720/1). B.J.G. was supported by grant R01DC016859. H.M. was supported by grants R01DC014423 and R01DC016224. **Author contributions:** D.H.B., T.T., R.C., H.-J.C., R.B.F., Y.G.C., M.L., I.C.M., R.A.H., and B.J.G. designed and performed experiments. D.H.B., T.T., C.W., M.L., K.V.d.B., B.G., R.C., H.-J.C., D.D., K.S., and H.R.d.B. performed analysis. D.R., S.D., E.P., J.M., B.J.G., M.S.G., J.N., and S.R.D. designed and supervised experiments. D.H.B., T.T., C.W., M.L., H.M., D.W.L., B.J.G., M.S.G., J.N., and S.R.D. wrote the manuscript. **Competing interests:** D.W.L. is an employee of Mars Inc. All other authors declare that they have no competing interests. **Data and materials availability:** All data needed to evaluate the conclusions in the paper are present in the paper and/or the Supplementary Materials. Reanalyzed datasets are obtained from the URLs listed in the Supplementary Materials. Raw and processed datasets generated as part of this study are available from the NCBI GEO at accessions GSE148360, GSE151346, GSE153730, and GSE151709. Additional data related to this paper may be requested from the authors.

Submitted 1 May 2020

Accepted 18 June 2020

Published First Release 24 July 2020

Published 31 July 2020

10.1126/sciadv.abc5801

Citation: D. H. Brann, T. Tsukahara, C. Weinreb, M. Lipovsek, K. Van den Berge, B. Gong, R. Chance, I. C. Macaulay, H.-J. Chou, R. B. Fletcher, D. Das, K. Street, H. Roux de Bezieux, Y. G. Choi, D. Risso, S. Dudoit, E. Purdom, J. Mill, R. A. Hachem, H. Matsunami, D. W. Logan, B. J. Goldstein, M. S. Grubb, J. Ngai, S. R. Datta, Non-neuronal expression of SARS-CoV-2 entry genes in the olfactory system suggests mechanisms underlying COVID-19-associated anosmia. *Sci. Adv.* **6**, eabc5801 (2020).

COGNITIVE NEUROSCIENCE

Temporal circuit of macroscale dynamic brain activity supports human consciousness

Zirui Huang^{1*}, Jun Zhang^{2*}, Jinsong Wu³, George A. Mashour^{1,4}, Anthony G. Hudetz^{1,4}

The ongoing stream of human consciousness relies on two distinct cortical systems, the default mode network and the dorsal attention network, which alternate their activity in an anticorrelated manner. We examined how the two systems are regulated in the conscious brain and how they are disrupted when consciousness is diminished. We provide evidence for a “temporal circuit” characterized by a set of trajectories along which dynamic brain activity occurs. We demonstrate that the transitions between default mode and dorsal attention networks are embedded in this temporal circuit, in which a balanced reciprocal accessibility of brain states is characteristic of consciousness. Conversely, isolation of the default mode and dorsal attention networks from the temporal circuit is associated with unresponsiveness of diverse etiologies. These findings advance the foundational understanding of the functional role of anticorrelated systems in consciousness.

INTRODUCTION

Evidence from noninvasive functional neuroimaging studies has pointed to two distinct cortical systems that support consciousness. The default mode network (DMN) is an internally directed system that correlates with consciousness of self, and the dorsal attention network (DAT) is an externally directed system that correlates with consciousness of the environment (1–7). The DMN engages in a variety of internally directed processes such as autobiographical memory, imagination, and self-referencing (6–8). The DAT, on the other hand, mediates externally directed cognitive processes such as goal-driven attention, inhibition, and top-down guided voluntary control (2, 6, 9). Moreover, the DMN and DAT appear to be in a reciprocal relationship with each other such that they are not simultaneously active, i.e., they are “anticorrelated.” This anticorrelation is presumed to be vital for maintaining an ongoing interaction between self and environment that contributes to consciousness (5). Conversely, diminished anticorrelation between DMN and DAT activity has been reported in humans when consciousness was suppressed by general anesthesia (10, 11) and in neuropathological patients with disorders of consciousness (4, 12), supporting the hypothesis that a balance of the internally and externally directed systems is important for waking consciousness.

Despite some evidence for this temporal relationship, the anticorrelation of DMN and DAT over time has not been conclusively demonstrated. First, the anticorrelation of functional magnetic resonance imaging (fMRI) signals is generally inferred from temporally averaged functional connectivity, which does not allow a direct assessment of the temporal dynamics of networks. Second, the criticism has been raised that the anticorrelation of fMRI signals may be a by-product of global signal regression (GSR)—a necessary preprocessing step that most such studies have used (13–15). Therefore, the controversy about GSR characteristic of conventional static connectivity analysis prevents the unequivocal conclusion that the disruption of anticorrelation

between DMN and DAT is a cause of disrupted consciousness. Furthermore, even assuming anticorrelation, the dynamic relationship of DMN and DAT to other networks of critical relevance to consciousness has not been elucidated.

To fill this gap of knowledge, an analysis of dynamic brain activity is necessary. Although the brain appears to engage in an ongoing exploration of its repertoire of distinct states (16–20), i.e., dynamic shaping and reshaping of functional brain configurations, it remains largely unknown if there is a structured exploration of its repertoire that is specific to the conscious versus unconscious brain. Accordingly, we hypothesized that the alternation of DMN and DAT over time is embedded in the ongoing exploration of all functional brain networks and that a disruption of this exploration may account for the diminished DMN-DAT anticorrelation when consciousness is suppressed. We also hypothesized that, in the conscious brain, the dynamic switching of networks including the DMN and DAT occurs along a set of structured transition trajectories, what might be conceived of as a “temporal circuit,” and that this temporal circuit is disrupted during diminished consciousness.

We tested our hypotheses by analyzing resting-state fMRI (rs-fMRI) signals from a cohort of 98 participants and patients in conditions that included conscious resting state and various unresponsive states induced by pharmacological (propofol and ketamine anesthesia, with distinct molecular targets) and neuropathological [unresponsive wakefulness syndrome (UWS)] etiologies. Although these conditions involve different molecular mechanisms, neural circuits, and brain functions, they share a common behavioral end point, i.e., a general unresponsiveness to external voice commands. Here, we conservatively use the term “unresponsiveness” instead of “unconsciousness” to allow for the possibility that covert or disconnected consciousness could occur in the absence of behavioral response. Combining data from different conditions allowed us to examine both the common and specific (anesthetic agent- and neuropathology-dependent) alterations of macroscale brain dynamics. We adopted an unsupervised machine learning approach to capturing transient, momentary coactivation patterns (CAPs) (21–24). The temporal dynamics of CAP transition trajectories were then analyzed as a Markov process, and the transition probability, persistence, and accessibility of CAPs were quantified. Last, we explored the stimulus modulations of CAPs during different conditions in a subset ($n = 37$) of the main

Copyright © 2020 The Authors, some rights reserved; exclusive licensee American Association for the Advancement of Science. No claim to original U.S. Government Works. Distributed under a Creative Commons Attribution NonCommercial License 4.0 (CC BY-NC).

¹Center for Consciousness Science, Department of Anesthesiology, University of Michigan Medical School, Ann Arbor, MI 48109, USA. ²Department of Anesthesiology, Huashan Hospital, Fudan University, Shanghai 200040, PR China. ³Department of Neurosurgery, Huashan Hospital, Fudan University, Shanghai 200040, PR China. ⁴Neuroscience Graduate Program, University of Michigan, Ann Arbor, MI 48109, USA. *Corresponding author. Email: huangzu@med.umich.edu (Z.H.); snapzhang@alium.com (J.Z.)

cohort and evaluated the specificity of our results in an independent cohort of 248 participants consisting of healthy control participants and patients with psychiatric disorders (schizophrenia, bipolar disorder, and attention deficit/hyperactive disorder), who might have altered brain networks but who were nonetheless conscious.

RESULTS

We recorded fMRI data at two independent research sites in Shanghai (SHH) and Wisconsin (WI), which generated four datasets (i.e., propofol-SHH, propofol-WI, ketamine, and neuropathological patients) containing both control and test results (Fig. 1A). CAPs of brain activity, i.e., sets of voxels simultaneously activated, were extracted from the entire dataset by k -means clustering algorithm (see more details in Materials and Methods). We determined an optimized number of CAPs ($k = 8$; from a search between 2 and 30) based on the non-GSR data for our main analysis scheme, and other selections of k (both with and without GSR) served as control analysis. This was achieved by evaluating the clustering performance, trading off the interdataset similarity (fig. S1) and visually inspecting the spatial patterns corresponding to major known functional networks (fig. S2). The eight CAPs were classified as DMN+, DAT+, frontoparietal network (FPN+), sensory and motor network (SMN+), visual network (VIS+), ventral attention network (VAT+), and global network of activation and deactivation (GN+ and GN-) (Fig. 1B). The eight CAPs could be divided into four pairs of “mirror” motifs, with a strong negative spatial similarity (Pearson correlation coefficient: $r = -0.97$ to -1.00 ; Fig. 1C). For instance, the DMN+ was accompanied by codeactivation of DAT (DAT-) and vice versa for DAT+ (DMN-). The “antiphase” relationship between those mirror motifs is to be expected. Assuming that fMRI signals exhibit block correlation structure and that voxels fluctuate in their amplitude over time, then voxels will be “active” or “inactive” at different times with respect to the correlation structure and moving in blocks. In addition, the DMN+ and DAT+ were more spatially segregated (consisting of 18 and 14 clusters), distributed across widespread cortical and subcortical regions, compared to other CAPs (fig. S3). As expected, the CAPs could capture the instantaneous phase synchronizations at single-volume temporal resolution of fMRI (fig. S3).

Suppression of DMN+ and DAT+ in various forms of behavioral unresponsiveness

We first tested whether there are common associations between the occurrence rates of CAPs (i.e., dividing the number of fMRI volumes belonging to a given CAP by the total number of volumes per scan) and level of responsiveness across various conditions. We found significant positive correlations between the occurrence rates of DMN and DAT (joint DMN+ and DAT+) and level of responsiveness for all datasets together (all pooled, $\rho = 0.58$, $P < 0.0001$), and individual datasets [propofol-SHH, $\rho = 0.64$, $P < 0.0001$; propofol-WI, $\rho = 0.43$, $P = 0.0017$; ketamine, $\rho = 0.55$, $P = 0.0002$; neuropathological patients, $\rho = 0.73$, $P < 0.0001$; false discovery rate (FDR)-corrected at $\alpha < 0.05$] (Fig. 2A). The correlations for DMN+ and DAT+ alone yielded similar results. In contrast, for instance, the occurrence rates of VIS+ and VAT+ (for propofol-SHH, propofol-WI, and neuropathological patients) and GN+ and GN- (for ketamine and neuropathological patients) showed negative correlations with the level of responsiveness (see fig. S4 for scatterplots and statistics).

We next examined the differences of CAP occurrence rates between conditions. During unresponsive conditions, the occurrence rates of DMN+ and DAT+ were significantly reduced (a summary of statistics in table S1). As anticipated by the above correlation analysis, this phenomenon was reproducible in two independent datasets of propofol-induced unresponsiveness (propofol-SHH and propofol-WI) and generalizable from propofol-induced unresponsiveness to ketamine-induced unresponsiveness and to patients with minimally conscious state (MCS) and UWS (Fig. 2B). In addition, the results were robust with respect to the choice of k in the k -means clustering method and to the option of GSR or not during data preprocessing (fig. S5).

We also found specific changes of CAP occurrence rates during various unresponsive conditions. Comparing to the conscious condition, an increased prevalence of VIS+ and VAT+ was seen during propofol-induced unresponsiveness (Fig. 2C). An increased prevalence of GN+ and GN-, as well as a decreased prevalence of FPN+ and SMN+, respectively, was observed during ketamine-induced unresponsiveness (Fig. 2, D and E). The patients with UWS shared those effects with propofol and ketamine anesthesia. Last, we measured the state entropy characterizing the uniformity of the occurrence rates of different CAPs. We found that the state entropy was significantly reduced in all unresponsive conditions ($P = 0.048$ for conscious condition versus propofol-induced unresponsiveness; $P = 0.005$ for conscious condition versus ketamine-induced unresponsiveness; $P = 0.022$ for conscious condition versus patients with UWS). This suggests that the distribution of CAP occurrence rates tends to be less uniform (or imbalanced), and therefore more stereotypic, during unresponsive conditions.

Persistence and transitions between CAPs distinguish conscious from behaviorally unresponsive conditions

To advance the field beyond the typical approach of describing static patterns, we sought to delineate the temporal dynamics of these CAPs and compare fully unresponsive conditions to baseline consciousness (Fig. 3, A and B, and see movie S1 for an illustration of CAP temporal dynamics). First, we observed distinct characteristics across different conditions in terms of preferred transitions (i.e., the probability of transitioning between two distinct CAPs is higher than a null model; see more details in Materials and Methods) and nonpreferred transitions (i.e., lower than null). During the conscious condition, the CAPs seemed to follow structured transition trajectories with relatively balanced preferred and nonpreferred paths. Second, in contrast, there were fewer trajectories reaching DMN+ and DAT+, and the trajectories were monopolized by a few specific “hosts” such as VIS+ and VAT+ during propofol-induced unresponsiveness and patients with UWS and VIS+, VAT+, GN+, and GN- during ketamine-induced unresponsiveness (Fig. 3C). Last, the CAP persistence probabilities, i.e., the probability of remaining in a given CAP, for all conditions occurred significantly above the level of chance (higher than a null model). However, compared to the conscious condition, the persistence probabilities of the CAPs were overall weaker during the unresponsive conditions (Fig. 3C). Ketamine-induced unresponsiveness was associated with an increased persistence of globally activated and deactivated brain states (GN+ and GN-).

These observations were supported by examining the entropy of Markov trajectories (25, 26). This approach measured the descriptive complexity of trajectories (in bits) between each pair of CAPs (Fig. 4A).

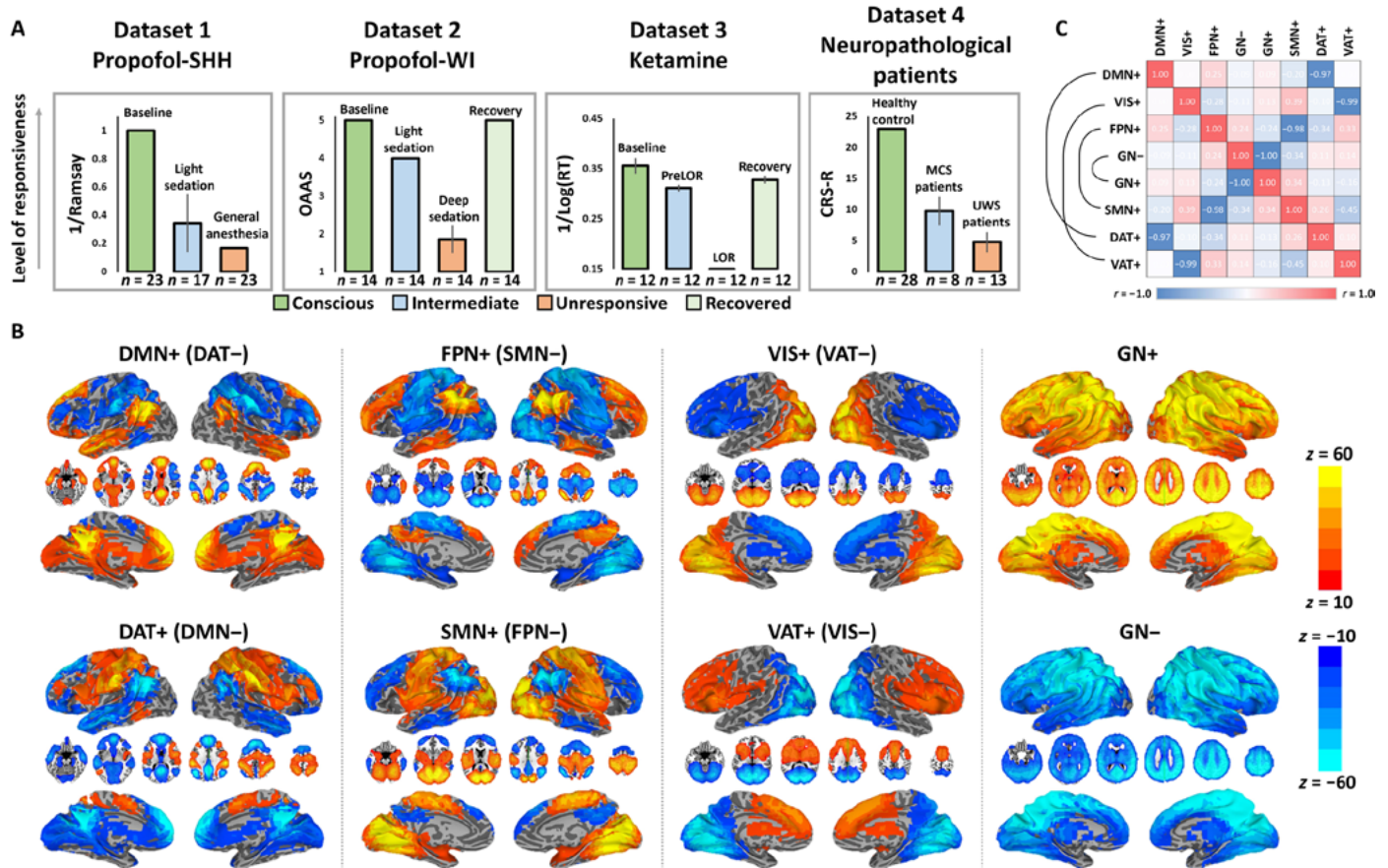


Fig. 1. Level of behavioral responsiveness across datasets and CAPs. (A) Dataset 1 (propofol-SHH) adopted Ramsay scale. Dataset 2 (propofol-WI) adopted observer's assessment of alertness/sedation (OAAS). Dataset 3 (ketamine) adopted a button press task for every 30 s. Reaction time (RT) in milliseconds with respect to each instruction was recorded. By comparing the timing of verbal instruction and actual responsiveness during and after ketamine infusion, the periods during which a participant retained responsiveness (PreLOR), loss of responsiveness (LOR), and recovery of responsiveness were determined. Dataset 4 (neurological patients) adopted Coma Recovery Scale–Revised (CRS-R). Level of responsiveness is shown by the total score of six subscales (auditory, visual, motor, verbal, communication, and arousal). MCS, minimally conscious state. Error bars indicate \pm SD. (B) Spatial maps of eight CAPs. The CAPs consist of DMN+, DAT+, FPN+, SMN+, VIS+, VAT+, GN+, and GN-. (C) The eight CAPs are composed of four pairs of mirror motifs with a strong negative spatial similarity, including DMN+ versus DAT+, VIS+ versus VAT+, FPN+ versus SMN+, and GN- versus GN+.

A lower descriptive complexity from a starting point (initial CAP) to its destination (final CAP) indicates a higher accessibility for the destination. For example, if the transition probability from CAP i to CAP j equals 1, then the entropy of trajectory from CAP i to CAP j is 0 bits, reflecting the conditional determinism (i.e., high accessibility) of that path. In contrast, if the transition probability from CAP i to CAP j equals to 0, then CAP i must first transition to other CAPs to end at CAP j . In this scenario, the entropy of trajectory from CAP i to CAP j is higher (needs more bits), thus reflecting a higher uncertainty or lower accessibility of that path. The key finding across these various conditions is that unresponsiveness was associated with an isolation (i.e., less accessibility) of DMN+ and DAT+ from the trajectory space, which is monopolized by a few giant attractors. More specifically, compared to the conscious condition, propofol-induced unresponsiveness and patients with UWS were characterized by increased accessibility of VIS+ and VAT+ and decreased accessibility of DMN+ and DAT+. Ketamine-induced unresponsiveness was characterized by increased accessibility of GN+, GN-, VIS+, and VAT+ and decreased accessibility of DMN+, DAT+, FPN+, and SMN+ (Fig. 4, B and C). The main finding regarding the decreased acces-

sibility of DMN+ and DAT+ during unresponsive states was robust with respect to the choice of k and to the option of GSR or not during data preprocessing (fig. S6).

Furthermore, the transition probability and entropy of Markov trajectory matrices estimated from individual participants showed predictive value in distinguishing conscious versus unresponsive states. We did so by constructing a feature space based on these matrices and subsequently training a classifier of support vector machine (SVM; using `sklearn.svm` with default settings) by the leave-one-participant-out cross-validation procedure. We found that the SVM classifier achieved reliable performance. The mean classification accuracies for propofol versus conscious, ketamine versus conscious, and patients with UWS versus conscious were, respectively, 0.81 ($P < 0.001$, permutation test), 0.83 ($P < 0.001$), and 0.93 ($P < 0.001$) based on the transition probability matrices and 0.77 ($P < 0.001$), 0.75 ($P = 0.028$), and 0.88 ($P < 0.001$) based on the entropy of Markov trajectory matrices (fig. S7). We considered the above machine learning analyses as exploratory in supporting our major conclusions. Future investigations may be needed such as comparing different machine learning models, parameter optimization,

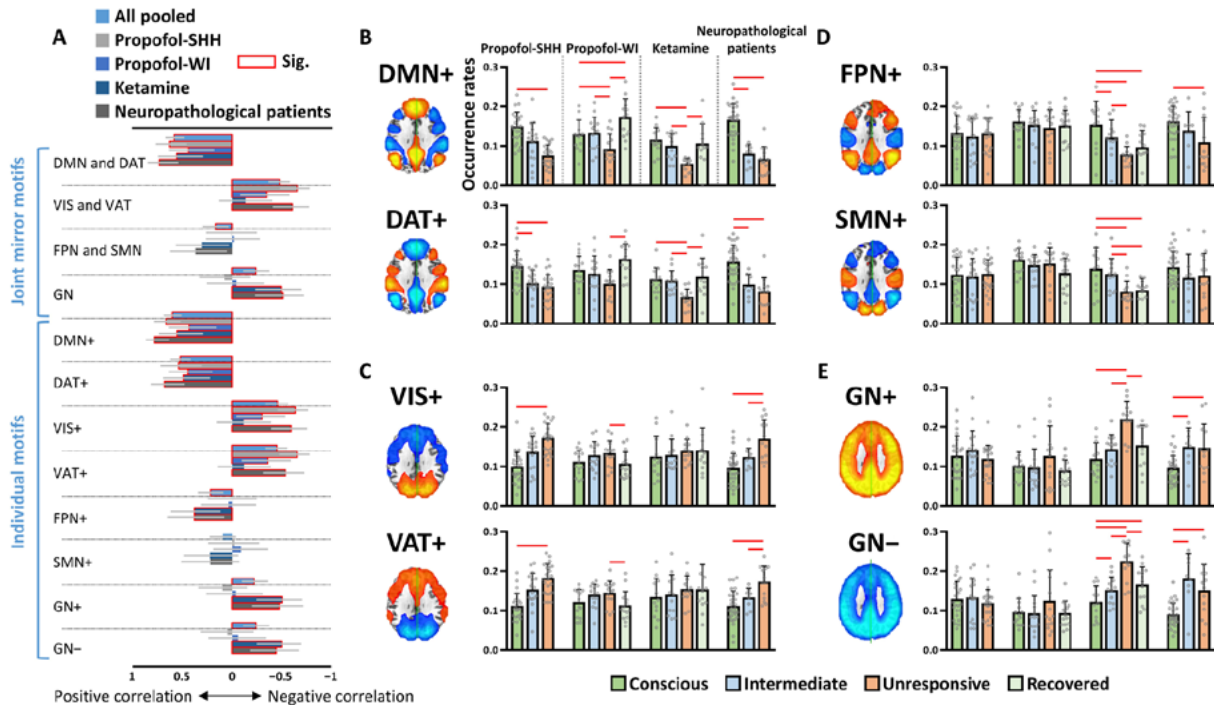


Fig. 2. Occurrence rates of CAPs. (A) Spearman rank correlations between the occurrence rates of joint mirror motifs or individual CAPs and the level of responsiveness. (B to E) The CAP occurrence rates in different conditions (conscious, intermediate, unresponsive, and recovered) and in different datasets. Intermediate conditions refer to propofol light sedation, PreLOR of ketamine induction, and patients with MCS; unresponsive conditions refer to propofol general anesthesia and deep sedation, LOR due to ketamine, and patients with UWS. Red squares in (A) and lines in (B) to (E) indicate significance at FDR-corrected $\alpha < 0.05$. See fig. S4 and table S1 for full statistics. Error bars in (A) indicate 95% confidence interval, and error bars in (B) to (E) indicate $\pm 5D$.

or multiclass classification, which are beyond the scope of the current study.

Antiphase coactivation accounts for anticorrelation

The reduced occurrence rates of antiphase coactivation of DMN+ and DAT+ are consistent with the previously reported decreased DMN-DAT anticorrelation in various unresponsive conditions (4, 10–12). First, in line with those studies, we observed significantly weakened DMN-DAT anticorrelation (GSR procedure was applied), as well as weakened within-network functional connectivity for both DMN and DAT, during propofol-induced unresponsiveness, ketamine-induced unresponsiveness, and in both MCS and UWS (Fig. 5A and see fig. S8 for results of other CAPs). We observed a strong negative correlation between the joint occurrence rates of DMN+ and DAT+ and the strength of DMN-DAT functional connectivity ($r = -0.72$, $P < 0.0001$) across all participants, suggesting that the lower the CAP prevalence in DMN+ and DAT+, the weaker the anticorrelation of DMN-DAT (Fig. 5B). As expected, positive correlations were seen between the joint occurrence rates of DMN+ and DAT+ and the within-network functional connectivity for both DMN ($r = 0.71$, $P < 0.0001$) and DAT ($r = 0.65$, $P < 0.0001$).

Note that the anticorrelation relationship between DMN and DAT, as measured by conventional static functional connectivity, was only seen when GSR was applied (fig. S8). Given that neither the identification of antiphase CAPs of DMN+ and DAT+ (Fig. S2) nor the strong association between the occurrence rates of the two CAPs and their anticorrelations relies on the GSR procedure (fig. S9), it is plausible to assume that the anticorrelation structure underlying fMRI signals is not an artifact due to GSR; instead, it is inherent

in the data and likely derives from the transient antiphase CAPs. Therefore, our results may provide a more dynamic (i.e., reflecting transient neural events) and unbiased (i.e., avoiding the controversial methodology of GSR) account for the anticorrelation phenomenon commonly seen in fMRI signals and their associations with levels of consciousness.

Stimulus modulations of CAPs and control analysis in psychiatric patients

Next, we sought to provide additional support for the functional and cognitive relevance of DMN+ and DAT+. Prior work suggests that the DMN is associated with internally focused awareness and can be suppressed when attention is shifted to external stimuli. The suppression of DMN’s activation may be triggered by the activation of other functional networks such as DAT and VAT during top-down allocation of attention and/or detection of unexpected stimuli (9). We thus hypothesized that, upon receiving external stimuli, the CAP occurrence rates of DMN+ would be attenuated, while the occurrence rates of other CAPs involved in stimulus processing would be elevated during conscious wakefulness. We also hypothesized that this modulation would be disrupted during reduced levels of responsiveness, which are presumably accompanied by reduced internal and/or external awareness. Accordingly, we investigated the effect of stimulus modulations on the CAP occurrence rates during different levels of responsiveness. We examined a subset of participants in dataset 1 (propofol-SHH) and dataset 4 (neuro-pathological patients) that received auditory stimuli (e.g., verbal names in propofol-SHH and verbal sentences in neuro-pathological patients) without any requirement of motor response (27, 28). We

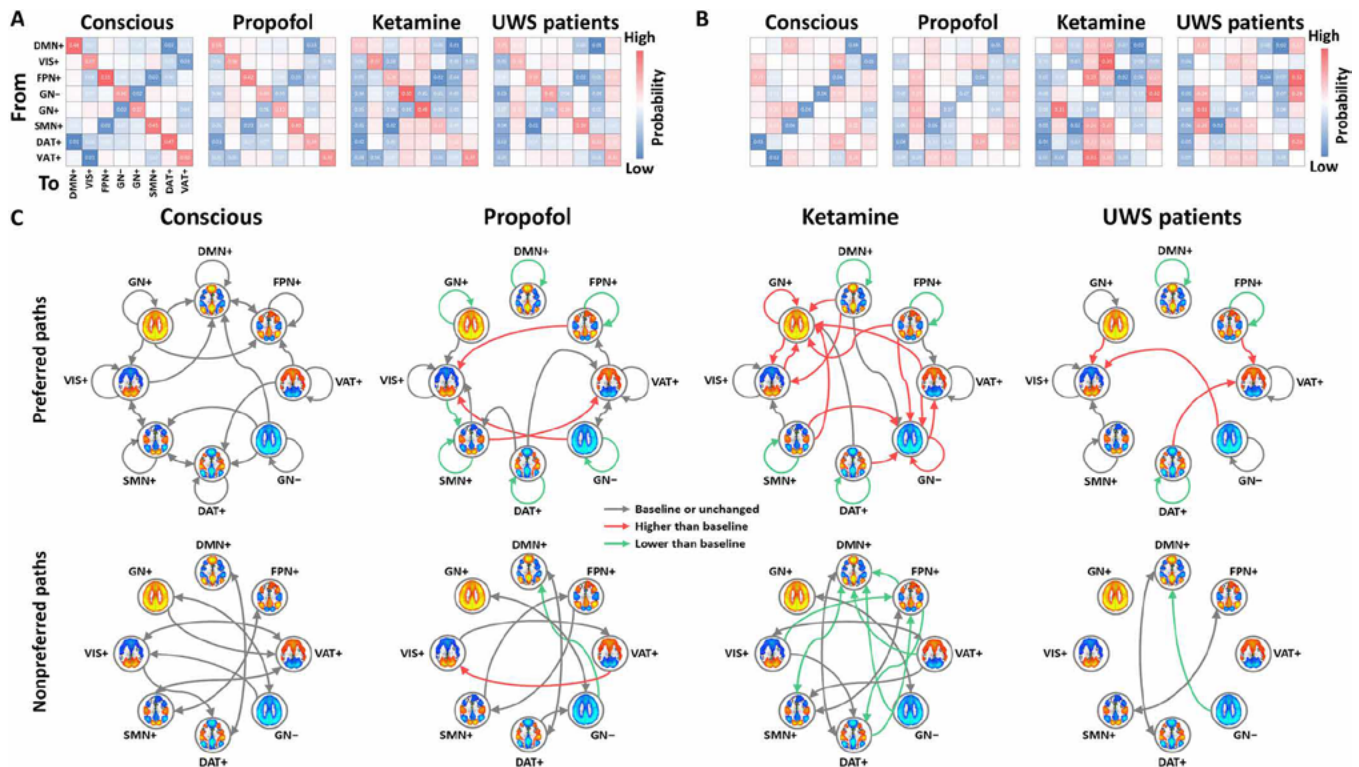


Fig. 3. Transition probabilities among CAPs. (A) Full transition probability matrix for conscious condition (conscious), propofol-induced unresponsiveness (propofol), ketamine-induced unresponsiveness (ketamine), and patients with UWS. The on-diagonal entries are referred to as the persistence probabilities. (B) Diagonal-free transition probability matrix, where the off-diagonal entries are referred to as transition probabilities by controlling for autocorrelation due to the CAP's persistence. (C) Schematic illustration of the significant preferred paths (>null) and nonpreferred paths (<null) for conscious versus null, propofol versus null, ketamine versus null, and patients with UWS versus null (all gray arrows). Red (higher than conscious condition) and green (lower than conscious condition) arrows indicate significant differences of persistence probabilities and transition probabilities comparing to baseline consciousness. The null model for each condition and the differences between conditions were generated by 1000 permutations across the entire dataset (see more details in Materials and Methods). Significance level was determined at $P < 0.001$ by considering multiple comparison corrections (99.9th and 0.1th percentile of the null distributions; two-sided).

assigned each time point of the task dataset to a particular CAP based on its maximal similarity to the CAP centroids derived from the main cohort resting-state data. The purpose of doing this was to make the results comparable and generalizable across datasets. As predicted, auditory stimuli were associated with an attenuation of CAP occurrence rates of DMN+ (as well as VIS+), with an elevated CAP occurrence rate of VAT+ in both datasets only during conscious conditions (Fig. 6, A and B). The results support that the DMN+ identified in our main cohort could be suppressed when the brain attends to external stimuli, whereas this stimulus modulation was corrupted during unresponsiveness (propofol-induced and patients with UWS).

Last, we extended our observations from pharmacological and neuropathological data to an open access dataset from a cohort of patients with psychiatric disease (29). We assessed whether the suppression of DMN+ and DAT+ is specific to the reduced level of responsiveness as opposed to disorders of cognitive function in general. Another motivation was to further understand the ketamine-specific alterations in the CAP occurrence rates, as altered states of consciousness induced by ketamine are often associated with psychoactive effects and unique brain dynamics (30–32). Using the same method applied in the task dataset (i.e., maximal similarity to the predefined CAP centroids from the main cohort), we identified eight comparable CAPs in the psychiatric cohort (Fig. 6C). There

were two main observations. First, we did not find any significant difference between healthy control participants and patients with schizophrenia, bipolar disorder, or attention deficit/hyperactive disorder in the occurrence rates of DMN+ and DAT+. Second, we found that the occurrence rates of GN+ and GN– were both significantly increased in schizophrenic patients, while the occurrence rates of FPN+ and SMN+ were both significantly decreased in patients with bipolar disorder (Fig. 6D). Patients with attention deficit/hyperactive disorder did not show any significant difference compared to healthy control participants. Therefore, altered occurrence rates of DMN+ and DAT+ are specific to unresponsiveness (likely reflecting unconsciousness in these experimental groups) and do not simply occur as a result of any brain disorder. Furthermore, the results suggest that alterations of the occurrence rates of FPN+, SMN+, GN+, and GN– induced by ketamine are similar to those found in patients with schizophrenia and bipolar disorder.

DISCUSSION

The goal of this study was to determine the spatiotemporal dynamics of prevalent functional brain networks in the conscious state and their potential modification during unresponsiveness. Our results revealed both common and distinct characteristics of brain activity in anesthetized participants and neuropathological patients as compared

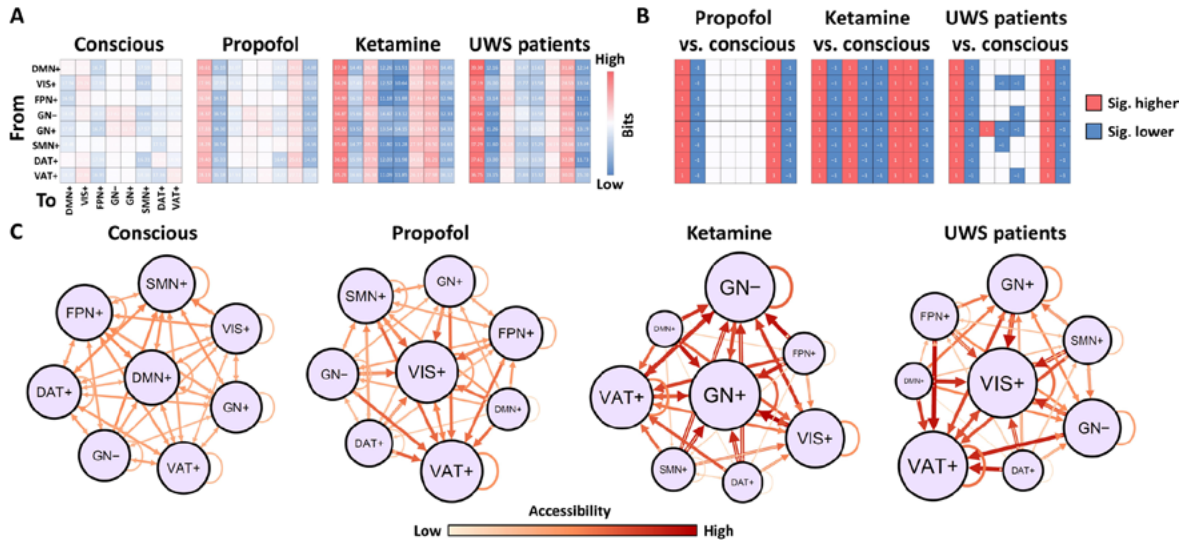


Fig. 4. Descriptive complexity of trajectories among CAPs and their in-degree accessibility. (A) Descriptive complexity of trajectories (in bits) between each pair of CAPs in the conscious condition (conscious), propofol-induced unresponsiveness (propofol), ketamine-induced unresponsiveness (ketamine), and in patients with UWS. (B) Significant differences of the descriptive complexity of trajectories for propofol versus conscious, ketamine versus conscious, and patients with UWS versus conscious. The null models were generated by 1000 permutations across the entire dataset. Significance level was determined at $P < 0.001$. (C) Schematic illustration for (A). The accessibility of each CAP is defined as the inverse of descriptive complexity. The node size is proportional to in-degree accessibility. The Gephi Force Atlas layout algorithm (<https://gephi.org>) was used.

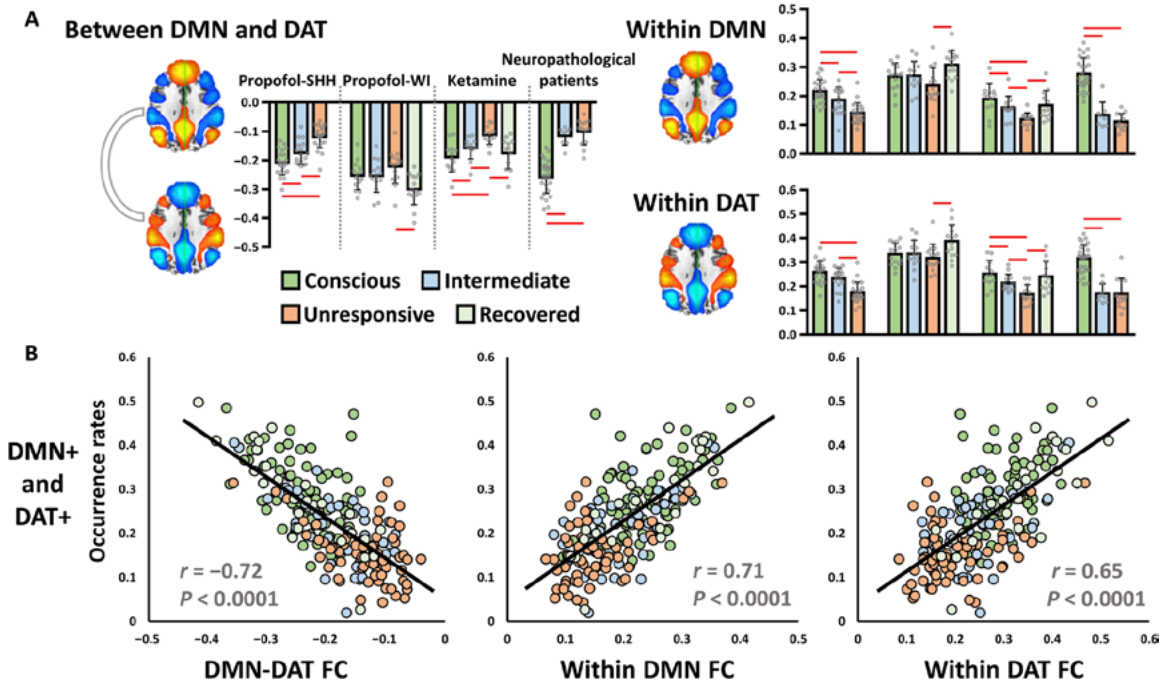


Fig. 5. Antiphasic coactivation accounts for anticorrelation. (A) Conventional static functional connectivity between DMN and DAT and within-network connectivity of DMN and DAT in different conditions (conscious, intermediate, unresponsive, and recovered) and in different datasets. Red lines indicate significance at FDR-corrected $\alpha < 0.05$. Error bars indicate \pm SD. (B) Pearson correlations between the joint occurrence rates of DMN+ and DAT+ and the strength of DMN-DAT functional connectivity (FC) (left), as well as within-network functional connectivity of DMN (middle) and DAT (right) across all participants.

to conscious conditions. The temporal prevalence of two CAPs, DMN+ and DAT+, was suppressed in both propofol- and ketamine-induced unresponsiveness as well as in patients with UWS. The changes specific to various unresponsive conditions included an increased prevalence of antiphase activation of VIS+ and VAT+

with propofol and an increased prevalence of global network activity with ketamine. Patients with UWS shared the latter two effects. We demonstrate that conscious brain activity is characterized by a set of structured dynamic transition trajectories in which the accessibility of distinct brain states is relatively balanced. In contrast, during

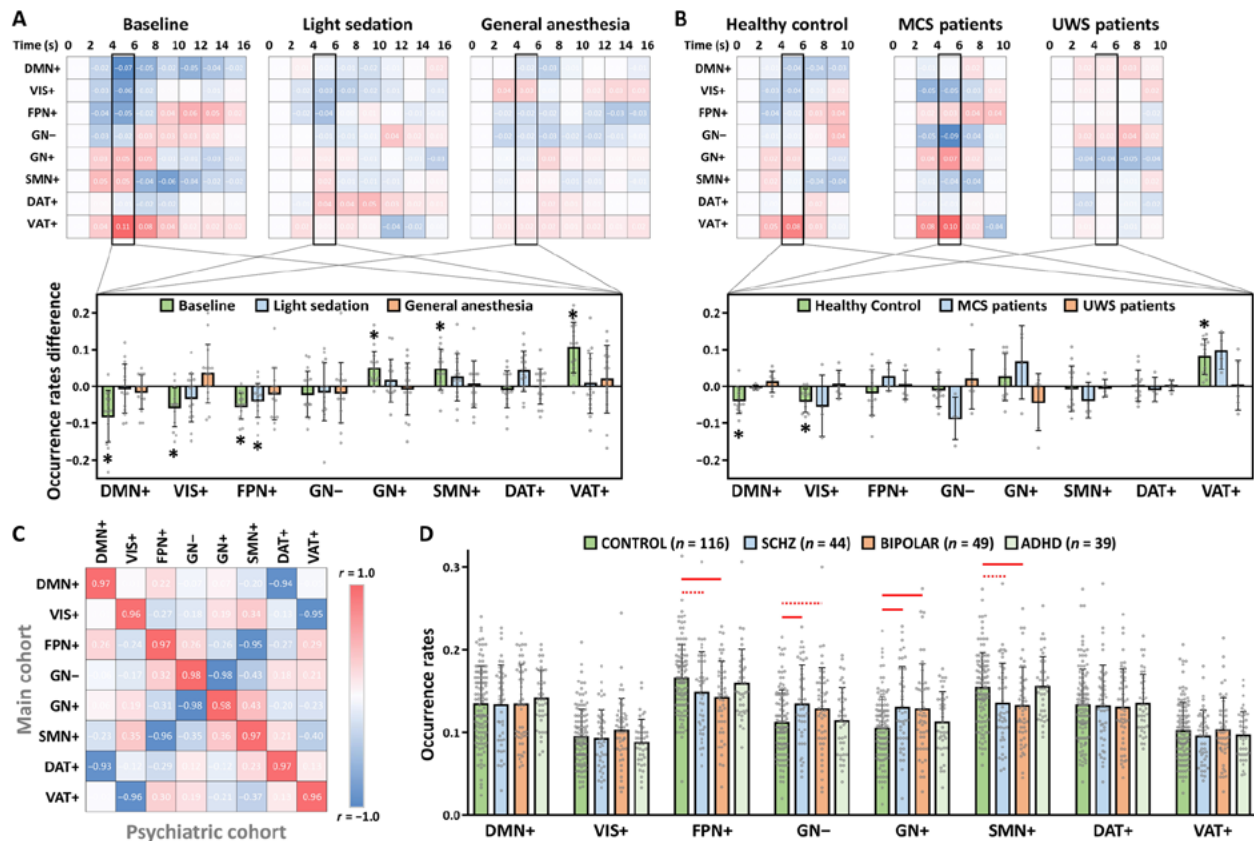


Fig. 6. Stimulus modulations of CAPs and control analysis in psychiatric patients. (A) Stimulus-induced CAP occurrence rate changes (against stimulus onset, $t = 0$) in baseline conscious condition, light sedation, and general anesthesia ($n = 15$). Student's t tests (against zero) for the CAP occurrence rate changes were performed during the peak period of stimulus-evoked fMRI signal activity (4 to 6 s). Asterisks indicate significance at $\alpha < 0.05$ after FDR correction. (B) Stimulus-induced CAP occurrence rate changes in healthy controls ($n = 12$), patients with MCS ($n = 4$), and patients with UWS ($n = 6$). (C) Spatial similarity of the eight CAPs between the main cohort and psychiatric cohort data. (D) Comparisons of the CAP occurrence rates for healthy control participants (CONTROL) versus schizophrenic (SCHZ), bipolar disorder (BIPOLAR), and attention deficit/hyperactive disorder (ADHD) patients by Student's t tests. Red solid lines indicate significant group differences at $\alpha < 0.05$ after FDR correction, and red dash lines indicate uncorrected significance at $P < 0.05$. Error bars indicate $\pm SD$.

unresponsiveness, the trajectories are substantially altered such that the DMN and DAT become isolated, and the trajectories become monopolized by the visual, ventral attention, and global networks.

Common spatiotemporal characteristics during behavioral unresponsiveness

A key finding of our study is the suppression of antiphase activation of DMN+ and DAT+ that occurred in various conditions of behavioral unresponsiveness. Given that this result was obtained with different anesthetic agents with distinct molecular targets and in nonanesthetized neuropathological patients, we are inclined to tentatively conclude that DMN+ and DAT+ are two fundamental signatures of consciousness. Our results provide a dynamic account of the suppression of DMN+ and DAT+ prevalence during unresponsiveness. First, the sequential maintenance of the CAPs (measured by their persistence probabilities) was overall weaker in the unresponsive conditions compared to the conscious condition. This suggests that, during unresponsiveness, the brain states of DMN+ and DAT+ were less stable. Second, during unresponsiveness, the DMN+ and DAT+ were dissociated from the reciprocal relationship of CAPs that were instead monopolized by VIS+, VAT+, GN+, and GN- (e.g., Fig. 3C). That is, it became difficult, along with the increased complexity of trajectories

(less accessible), for the other CAPs to transition to DMN+ or DAT+ (e.g., Fig. 4C). This finding provides new understanding, in terms of spatiotemporal brain dynamics, of how the previously known anticorrelation of DMN and DAT is diminished in unconsciousness (4, 10–12).

According to prior evidence from functional neuroimaging of disorders of consciousness (4, 12) and anesthesia (10, 11), an anticorrelated activity of the DMN and DAT is associated with internal versus external awareness (sometimes also referred to as disconnected and connected consciousness, respectively). In addition, a behavioral and neuroimaging experiment in healthy volunteers reported a periodic shift from internal to external awareness associated with the periodic neural activity in the DMN and DAT (8). Consequently, in our results, the suppression of both DMN+ and DAT+ may indicate a lack of both forms of awareness (internal and external) during unresponsiveness. The observation that the degree of suppression of the DMN+ and DAT+ was similar across the pharmacological and neuropathological unresponsive conditions suggests that internal and external awareness may be tightly interacting and the give-and-take relationship of the two systems may be particularly important for normal levels of consciousness.

This interpretation is further supported by the results of stimulus modulation at different levels of responsiveness. Upon receiving

auditory stimuli, the CAP occurrence rate of DMN+ was attenuated, while the occurrence rate of VAT+ (involved in auditory stimulus processing) was elevated only during conscious conditions. This is consistent with our expectation that the DMN+, associated with internal awareness, is suppressed when attention is shifted to external stimuli. The occurrence rate of stimulus-related attenuation of the DMN+ was not found in the unresponsive conditions (propofol-induced and patients with UWS). Although the DAT+ occurrence rate was not increased by the auditory stimulus, this may be expected. The DAT mediates top-down guided voluntary allocation of attention, whereas the VAT is involved in detecting unattended or unexpected stimuli and triggering shifts of attention (9). As the stimulus applied in our study did not require voluntary execution, it did not, as would be predicted, activate the DAT+ system.

Distinct spatiotemporal characteristics during behavioral unresponsiveness

In addition to the common effects across unresponsive conditions, we observed some specific changes of CAP prevalence and transition dynamics. During propofol-induced unresponsiveness, VIS+ and VAT+ played a dominant role, where the prevalence of both CAPs was increased compared to the conscious condition. They served as attractors into which other CAPs transformed (e.g., Figs. 3C and 4C). As the VIS+ and VAT+ are at a relatively low or intermediate level of hierarchical cortical functional organization (33), we speculate that propofol may shift the hierarchical cortical functional organization to a lower order. However, the validity of this speculation will require more detailed investigations such as measuring the functional gradient of networks under propofol anesthesia.

During ketamine-induced unresponsiveness, GN+ and GN– increased their prevalence and persistence probabilities compared to the conscious condition and served as attractors. The changes were analogous to those of schizophrenic patients (e.g., Fig. 6D). Prior studies have reported global hyperconnectivity of fMRI signals in schizophrenic patients (34), as well as shared phenomenology between schizophrenic symptoms and ketamine's dissociative/psychoactive effects (30, 32). All participants receiving ketamine reported having dreams, and 8 of 12 participants in our study could recall their hallucinations (e.g., flying on a cloud, weird smells, taking an elevator, and thick mist) after recovery from anesthesia. Therefore, we speculate that the dominance of GN+ and GN– in the dynamic brain states may be associated with psychoactive effects.

In patients with UWS, the alterations of brain state dynamics seemed to be situated in between propofol and ketamine anesthesia. If we assume that the arousal of patients with UWS was relatively preserved, unlike the suppression of arousal in propofol-induced unresponsive participants, then the GN+ and GN– in UWS may reflect, to some extent, arousal fluctuations (35, 36).

Spatial characteristics of CAPs

We identified six CAPs encompassing the DMN+, DAT+, FPN+, SMN+, VIS+, and VAT+ that resembled canonical resting-state networks in agreement with previous studies (24, 37, 38). We also identified two other CAPs with globally activated and deactivated patterns (GN+ and GN–), which have been related to arousal or vigilance fluctuations in the context of the global brain signal (35, 36). GN+ and GN– were present without applying GSR (e.g., fig. S2). Note that, compared to other CAPs, the DMN+ and DAT+ showed the highest within-network anatomical segregation as they consisted

of 18 and 14 clusters, respectively, distributed across widespread cortical and subcortical regions (e.g., fig. S3). We speculate that spatial segregation is relevant for the higher-order abstract representations necessary for conscious processing. This is supported by evidence that the DMN and DAT are at a high position of a representational hierarchy, with a widespread backbone, relatively far from the sensory and motor systems in terms of both functional connectivity and anatomical distance (33). This hierarchical disposition is thought to allow the two systems to process transmodal information in a way that is unconstrained by immediate sensory input.

Methodologic strengths and limitations

Our approach has unique strengths. First, the *k*-means clustering method can capture transient, temporally localized coactivations, which reflect the underlying brain activity in a rather direct way when compared to conventional time-averaged analysis. The clustering procedure itself does not perform any transformation of the data, holds a minimal set of assumptions and constraints, and is free from the controversial aspects of GSR (21). The method thus allowed us to reframe the known neural phenomenon—i.e., diminished, temporally averaged DMN-DAT anticorrelation in unresponsiveness—into a dynamic picture of brain activity where the DMN and DAT are embedded in a chain of transient explorations among distinct brain states. Second, the temporal dynamics of brain states were analyzed as a Markov process. This method allowed us to quantify temporal dependencies of brain states and their trajectories, leading us to form the concept of a temporal circuit. Third, we combined an unsupervised machine learning approach (*k*-means clustering) with a supervised machine learning approach (i.e., maximal similarity to predefined cluster centroids), when comparing our results from the main cohort with another cohort. This method, with relatively low computational cost, may have the potential for “big data” analysis rendering the observations comparable and generalizable across multiple datasets or research sites. This idea may be analogous to the seed-based (supervised) functional connectivity analysis with a priori knowledge of seed regions.

A few limitations of our study are recognized. First, coactivation at the temporal resolution of 2 s is, at best, an indirect measure of large-scale brain connectivity. Second, the neural origin of transient CAPs remains unclear. Third, the richness of mental content and cognitive process seems far beyond the repertoire of CAPs we can detect. The functional association and the causal relationship between CAPs and cognitive functions remain unclear. Fourth, the relationship of CAP transitions to the fast transient topographical patterns of electroencephalography (EEG) (39) and magnetoencephalography (40), such as “microstates” on the order of 100 ms, remains to be determined. However, recent studies of EEG during anesthetic-induced unresponsiveness have used *k*-means clustering and Markov analysis, suggesting that addressing the neurophysiologic time scale with these techniques is tractable (41, 42). Fifth, the choice of *k* (the number of CAPs) for clustering analysis was somewhat challenging. Arguably, any reasonable choice would far underestimate the actual diversity of meaningful brain states. The choice of *k*, in general, is limited by the experimental approach and fMRI methodology. Sixth, we found that the reduced occurrence rates of DMN+ and DAT+ were accompanied by the decreased trajectory accessibility of the two CAPs during unresponsiveness. This coincidence may be expected. For instance, if other CAPs do not prefer to transition to DMN+ or DAT+, then the occurrence rates of the two CAPs

(regardless of its own repetitions or persistence) will be likely lower than that of others. In this sense, the occurrence rates and transition probabilities may offer two views of the same temporal dynamics, whereas the information gained from the two quantities is partially overlapped. Furthermore, if we assume that the transition probabilities between CAPs are caused by certain neural mechanisms, then the occurrence rates are just statistical descriptions resulting from the transition probabilities. The precise neural mechanisms and the regulation of state transitions may be an important question for future investigations. Last, although our observations yield predictions that can guide future work, an important caveat is that the specific characteristics of CAPs in different states of consciousness were derived from rs-fMRI signals without subjective report of mental content. Therefore, the exact associations between those CAPs and conscious contents remain to be systematically studied.

CONCLUSIONS

This study suggests that human consciousness relies on a specific temporal circuit of dynamic brain activity characterized by balanced reciprocal accessibility of functional brain states. The disruption of this temporal circuit, exhibiting limited access to the DMN and DAT, appears to be a common signature of unresponsiveness of diverse etiologies.

MATERIALS AND METHODS

The fMRI data were recorded at two independent research sites (Shanghai and Wisconsin), which generated four datasets containing both control and test results. Dataset 1 included 23 participants during baseline conscious condition, propofol light sedation, and propofol general anesthesia collected in Shanghai, hereafter referred to as propofol-SHH. Dataset 2 included 14 participants during baseline conscious condition, propofol light sedation, propofol deep sedation, and recovery, which was collected in Wisconsin, hereafter referred to as propofol-WI. Dataset 3 included 12 participants during baseline conscious condition, ketamine induction period before loss of responsiveness (PreLOR), loss of responsiveness (LOR) period, and recovery of responsiveness period, hereafter referred to as ketamine. Dataset 4 includes 28 healthy controls (conscious condition), 8 patients diagnosed in an MCS, and 13 patients diagnosed in an UWS/vegetative state. This dataset, with patients of disorders of consciousness, was referred to as neuropathological patients. To minimize misdiagnosis, these states were defined by validated, objective scales as opposed to clinical interpretation alone.

Dataset 1: Propofol-SHH

The dataset has been previously published using analyses different from those applied here (28, 43). The study was approved by the Institutional Review Board (IRB) of Huashan Hospital, Fudan University. Informed consent was obtained from all participants ($n = 26$; right-handed; male/female, 12/14; age, 27 to 64 years), who were undergoing an elective transsphenoidal approach for pituitary microadenoma resection. The pituitary microadenomas were diagnosed by their size (<10 mm in diameter without growing out of the sella) based on radiological examinations and plasma endocrinal parameters. The participants were American Society of Anesthesiologists (ASA) physical status I or II, with no history of brain dysfunction, vital organ dysfunction, or administration of neuropsychiatric drugs. They had

no contraindication to an MRI examination, such as vascular clips or metallic implants. Among them, 3 participants had to be excluded from the study and further data analysis because of excessive movements, resulting in 23 participants for the following analysis.

Participants fasted for at least 8 hours from solid foods and 2 hours from liquids before the study. Vital signs including blood pressure, electrocardiography, pulse oximetry (SpO_2), and partial pressure of carbon dioxide were continuously monitored during the fMRI study. The participants received propofol light sedation (17 of 23) and general anesthesia ($n = 23$), during which intravenous anesthetic propofol was infused through an intravenous catheter placed into a vein of the right hand or forearm. Propofol was administered using a target-controlled infusion (TCI) pump to obtain constant effect-site concentration, as estimated by the pharmacokinetic model of propofol (Marsh model). Remifentanyl ($1.0 \mu\text{g}/\text{kg}$) and succinylcholine ($1.5 \text{mg}/\text{kg}$) were administered to facilitate endotracheal intubation under general anesthesia. TCI concentrations were increased in $0.1 \mu\text{g}/\text{ml}$ steps beginning at $1.0 \mu\text{g}/\text{ml}$ until reaching the appropriate effect-site concentration. A 5-min equilibration period was allowed to ensure equilibration of propofol distribution between compartments.

The TCI propofol was maintained at a stable effect-site concentration for light sedation ($1.3 \mu\text{g}/\text{ml}$) and for general anesthesia ($4.0 \mu\text{g}/\text{ml}$). Behavioral responsiveness was assessed by the Ramsay scale. The participants were asked to strongly squeeze the hand of the investigator. The participant was considered fully conscious if the response to verbal command (“strongly squeeze my hand!”) was clear and strong (Ramsay 1 and 2), in mild sedation if the response to verbal command was clear but slow (Ramsay 3 and 4), and in deep sedation or general anesthesia if there was no response to verbal command (Ramsay 5 and 6). For each assessment, the Ramsay scale verbal commands were repeated twice. The participants continued to breathe spontaneously, with supplemental oxygen via nasal cannula, during conscious resting state and light sedation. During general anesthesia, the participants were ventilated with intermittent positive pressure ventilation, setting a tidal volume at 8 to 10 ml/kg, a respiratory rate of 10 to 12 beats/min, and maintaining partial pressure of end tidal CO_2 at 35 to 45 mmHg. Two certified anesthesiologists were present throughout the study and assured that resuscitation equipment was always available. Participants wore earplugs and headphones during the fMRI scanning.

rs-fMRI data acquisition consisted of three 8-min scans in baseline conscious condition, light sedation, and general anesthesia. The participant’s head was fixed in the scan frame and padded with spongy cushions to minimize head movement. The participants were asked to relax and assume a comfortable supine position with their eyes closed during scanning (an eye patch was applied). They were instructed not to concentrate on anything in particular during the resting-state scan. A Siemens 3T scanner (Siemens MAGNETOM, Germany) with a standard eight-channel head coil was used to acquire gradient-echo echo-planar imaging (EPI) images of the whole brain [33 slices; repetition time/echo time (TR/TE), 2000/30 ms; slice thickness, 5 mm; field of view, 210 mm; flip angle, 90° ; image matrix, 64×64]. High-resolution anatomical images were also acquired for rs-fMRI coregistration.

Dataset 2: Propofol-WI

The dataset has been previously published using analyses different from those applied here (44). The IRB of Medical College of Wisconsin (MCW) approved the experimental protocol. Fifteen healthy participants (male/female, 9/6; age, 19 to 35 years) received propofol sedation.

The OAAS (observer's assessment of alertness/sedation) was applied to measure the levels of behavioral responsiveness. During baseline conscious and recovery conditions, participants responded readily to verbal commands (OAAS score, 5). During light sedation, participants showed lethargic response to verbal commands (OAAS score, 4). During deep sedation, participants showed no response to verbal commands (OAAS score, 2 and 1). The corresponding target plasma concentrations vary across participants (light sedation, 0.98 ± 0.18 $\mu\text{g/ml}$; deep sedation, 1.88 ± 0.24 $\mu\text{g/ml}$) because of the variability in individual sensitivity to anesthetics. At each level of sedation, the plasma concentration of propofol was maintained at equilibrium by continuously adjusting the infusion rate to maintain the balance between accumulation and elimination of the drug. The infusion rate was manually controlled and guided by the output of a computer simulation developed for target-controlled drug infusion (STANPUMP) based on the pharmacokinetic model of propofol. Standard ASA monitoring was conducted during the experiment, including electrocardiogram, noninvasive blood pressure cuff, pulse oximetry, and end-tidal carbon dioxide gas monitoring. Supplemental oxygen was administered prophylactically via nasal cannula. One participant had to be excluded from the study and further data analysis because of excessive movements, resulting in 14 participants for the following analysis.

rs-fMRI data acquisition consisted of four 15-min scans in baseline conscious condition, light and deep sedation, and recovery. A 3T Signa GE 750 scanner (GE Healthcare, Waukesha, WI, USA) with a standard 32-channel transmit/receive head coil was used to acquire gradient-echo EPI images of the whole brain (41 slices; TR/TE, 2000/25 ms; slice thickness, 3.5 mm; field of view, 224 mm; flip angle, 77°; image matrix, 64×64). High-resolution anatomical images were also acquired for rs-fMRI coregistration.

Dataset 3: Ketamine

The study was approved by the IRB of Huashan Hospital, Fudan University. Informed consent was obtained from all participants. Twelve right-handed participants were recruited (male/female, 7/5; age, 32 to 66 years), who were undergoing an elective transsphenoidal approach for resection of a pituitary microadenoma. The patient inclusion, anesthesia procedure, fMRI setting-up and scanning parameters, and vital sign monitoring were the same as those of propofol-SHH.

Ketamine was infused through an intravenous catheter placed into a vein of the left forearm. Continuous fMRI scanning was conducted throughout the whole experiment for about 1 hour, ranging from 44 to 62 min (means \pm SD, 54.6 ± 5.9 min). A 10-min baseline conscious condition was first acquired (except for two participants in which baseline condition was for 6 and 11 min). Then, 0.05 mg/kg per min of ketamine was infused for 10 min (0.5 mg/kg in total), and 0.1 mg/kg per min was infused for another 10 min (1.0 mg/kg in total), except for two participants who only received 0.1 mg/kg per min infusion for 10 min. After that, the ketamine infusion was discontinued, and participants regained their responsiveness spontaneously.

Behavioral responsiveness (button press) was assessed throughout the entire fMRI scan. Specifically, participants were asked to press a button using their right index finger after hearing a verbal instruction "press the button." The instruction was programmed to play every 30 s using E-Prime 2.0 (Psychology Software Tools, Pittsburgh, PA) and was delivered via earphones designed for an MRI environment. The volume of the headphones was adjusted for participant comfort.

By comparing the timing of verbal instruction and actual responsiveness during and after ketamine infusion, the periods during which a participant retained responsiveness (PreLOR), LOR, and recovery of responsiveness were determined. The duration (means \pm SD in minutes) for each period across participants was 9.8 ± 1.0 for baseline conscious condition, 12.5 ± 4.5 for PreLOR, 18.2 ± 7.6 for LOR, and 14.1 ± 6.0 for recovery. In addition, reaction time with respect to each instruction was recorded for quantitative analysis of behavioral responsiveness.

Dataset 4: Neuropathological patients

The dataset has been previously published using analyses different from those applied here (27, 43). The study was approved by the IRB of Huashan Hospital, Fudan University. Informed consent was obtained from the patients' legal representatives and from the healthy participants. The dataset included 21 patients (male/female, 18/3) with disorders of consciousness and 28 healthy control participants (male/female, 14/14). The patients were assessed using the Coma Recovery Scale-Revised (45) on the day of fMRI scanning. Of those assessed, 13 patients were diagnosed as having UWS, and 8 patients were diagnosed as being in MCS. None of the healthy controls had a history of neurological or psychiatric disorders nor were they taking any kind of medication.

rs-fMRI data were acquired on a Siemens 3T scanner (Siemens MAGNETOM, Germany). A standard eight-channel head coil was used to acquire gradient-echo EPI images of the whole brain (33 slices; TR/TE, 2000/35 ms; slice thickness, 4 mm; field of view, 256 mm; flip angle, 90°; image matrix, 64×64). Two hundred EPI volumes (6 min and 40 s) and high-resolution anatomical images were acquired.

Data preprocessing

Preprocessing steps were implemented in AFNI (Analysis of Functional NeuroImages; <http://afni.nimh.nih.gov/>). (i) The first two frames of each fMRI run were discarded; (ii) slice timing correction; (iii) rigid head motion correction/realignment within and across runs; frame-wise displacement (FD) of head motion was calculated using frame-wise Euclidean norm (square root of the sum squares) of the six-dimensional motion derivatives (46). A frame and its each previous frame were tagged as zeros (ones, otherwise) if the given frame's derivative value has a Euclidean norm above 0.4 mm of FD (44); (iv) coregistration with high-resolution anatomical images; (v) spatial normalization into Talairach stereotaxic space; (vi) using AFNI's function 3dTproject, the time-censored data were high-pass filtered above 0.008 Hz. At the same time, various undesired components (e.g., physiological estimates and motion parameters) were removed via linear regression. The undesired components included linear and nonlinear drift, time series of head motion and its temporal derivative, binarized FD time series (output data included zero values at censored time points), and mean time series from the white matter and cerebrospinal fluid; (vii) spatial smoothing with 6-mm full width at half maximum isotropic Gaussian kernel; (viii) the time course per voxel of each run was normalized to zero mean and unit variance, accounting for differences in variance of non-neural origin (e.g., distance from head coil). GSR was not applied for our main analysis, as we were motivated to provide a dynamic and unbiased account for the anticorrelation phenomenon commonly seen in conventional static functional connectivity with GSR procedure. However, to evaluate the robustness of our results against different processing schemes, we also performed control analyses both with and without the GSR procedure.

CAP analysis

We adopted an unsupervised machine learning approach using k -means clustering algorithm. It is a procedure for classifying a set of objects (e.g., fMRI volumes) into different categories (e.g., patterns) such that within category differences are smaller than across category differences. Accordingly, we classified fMRI volumes into k clusters based on their spatial similarity and thus produced a set of CAPs or brain states (22, 24). Hence, the original fMRI (three-dimensional + time) data were translated into a one-dimensional time series of discrete CAP labels.

The above analysis was performed on the concatenated data of 69,010 fMRI volumes acquired from all 98 participants. There were 7.1% of the total volumes tagged as zeros based on the above motion censoring procedure, which were not included in the following analysis. Then, k -means clustering was performed to partition the all fMRI volumes of the matrix (64,118 volumes \times 6088 voxels) into k clusters, which returned a $64,118 \times 1$ vector containing cluster indices (i.e., CAP labels) for each fMRI volume. The distance between two fMRI volumes was defined as one minus their Pearson's correlation coefficient of the intensity values across voxels (22, 24). The computational load of the k -means clustering increases quickly with the number of fMRI volumes. As a trade-off between computational cost and spatial resolution, the preprocessed fMRI data were down-sampled to the spatial resolution of 6 mm by 6 mm by 6 mm while preserving the original temporal resolution (2 s) before k -means clustering.

After clustering, the fMRI volumes assigned to the same cluster were simply averaged, resulting in k maps that we defined as CAPs. These CAPs were then normalized by the SE (within cluster and across fMRI volumes) to generate z -statistic maps, which quantify the degree of significance to which the CAP map values (for each voxel) deviate from zero (22). The spatial characteristics of those CAPs were examined by counting the number of spatial clusters as a function of threshold (z values; ranging from 1 to 100). A single spatial cluster was defined as the nearest-neighbor clustering (faces touching) encompassing at least six voxels, where positive and negative voxels in each CAP were calculated separately. In addition, we calculated the instantaneous phase synchrony for each CAP. For each voxel's time series, the instantaneous phase traces were calculated using Hilbert transform. The phase synchrony across voxels as a function of time was quantified by the Kuramoto order parameter. Then, the phase synchrony values were sorted into k bins according to the time series of CAP labels. The phase synchrony values within each bin were averaged yielding the mean phase synchrony for each CAP.

For each participant or each condition, the occurrence rate of each CAP was quantified by the ratio of the number of volumes that appeared versus the total number of volumes per scan. A challenge for clustering analysis is the choice of k , i.e., the number of CAPs to be extracted from the data. We evaluated the clustering performance using a few indices including Silhouette, Calinski-Harabasz, Davies-Bouldin, and Dunn for the data with and without GSR (fig. S1). Broadly speaking, higher values of the Silhouette, Calinski-Harabasz, and Dunn and a lower value of the Davies-Bouldin indicate a better separation of clusters and more tightness inside the clusters. In line with a previous study by Liu *et al.* (22), who used the dataset from the 1000 Functional Connectomes Project, we also observed that different clustering evaluation criteria yielded inconsistent recommendations. We next sought to adopt an alternative strategy by

identifying a k with the best reliability of consistently identifying conscious conditions across datasets and the best distinction of conscious versus unresponsive conditions. Specifically, we determined an optimized k (from a search between 2 and 30) by trading off the interdataset similarity (measured by Euclidean distance) of the averaged CAP occurrence rate distributions in each dataset. We derived an index, $(CC + UU)/(2 \times CU)$, as the ratio of interdataset similarity among conscious conditions (CC) and among unresponsive conditions (UU) versus the interdataset similarity among conscious and unresponsive conditions (CU) across the four datasets. We found that $k = 8$ (non-GSR) yielded a high interdataset similarity among conscious conditions and among unresponsive conditions, with a low interdataset similarity among conscious and unresponsive conditions. In addition, to further evaluate the choice of k , we inspected the spatial patterns in terms of consistency and redundancy from $k = 2$ to $k = 16$ with a step of two (fig. S2).

Transition matrix

For each condition, we concatenated all participants' CAP time series and computed the transition probability between each pair of CAPs. These transition probability matrices can be described by a Markov process, where the probability of CAP j (at time $t + 1$) is determined by the CAP i (at time t). That is, we defined transition probability between two CAPs to be the probability of transitioning from state CAP i to CAP j , given that the current state is CAP i . Those probabilities were encoded in a transition matrix with row sums equal to 1 and the ij th elements of the matrix equal to the number of transitions from CAP i to CAP j divided by the number of occurrences of CAP i . We referred to the diagonal entries in the full transition probability matrix as the persistence probabilities, i.e., the probability of remaining in a given CAP. We referred to the off-diagonal transition probability matrix as the transition probabilities, i.e., the probability of transitioning between two distinct CAPs. The off-diagonal transition probability matrix was calculated by removing repeating CAPs in the time series to control for autocorrelation due to the CAP's persistence (24). Note that the censored time point of head motion and the joint point between participants were tagged with zeros, such that the transition from a CAP to zero or from zero to a CAP was discarded in the above calculation. This may minimize the head motion effect and avoid the contamination of noncontinued data derived from concatenation.

Entropy of Markov trajectories

On the basis of the above off-diagonal transition probability matrices, we quantified the entropy of Markov trajectories (25, 26). This approach measured the descriptive complexity of trajectories (in bits) between each pair of CAPs, e.g., routes starting from a particular CAP and ending to another. A lower descriptive complexity from a starting point (initial CAP) to its destination (final CAP) indicates a higher accessibility for the destination. More specifically, the entropy of Markovian trajectories is considered as a finite irreducible Markovian chain with transition matrix P and associated entropy rate $H(X) = -\sum_{i,j} \mu_i P_{ij} \log P_{ij}$, where μ is the stationary distribution given by the solution of $\mu = \mu P$. A trajectory T_{ij} of the Markov chain is a path with initial state i , final state j , and no intervening states equal to j . The entropy $H(T_{ii})$ of the random trajectory originating and terminating in state i is given by $H(T_{ii}) = H(X)/\mu_i$. Therefore, the entropy of the random trajectory T_{ij} is the product of the expected number of steps $1/\mu_i$ to return to state i and the entropy rate $H(X)$

per step for the stationary Markov chain. The entropies $H(T_{ij})$ is given by $H = K - K' + H_{\Delta}$, where H is the matrix of trajectory entropies $H_{ij} = H(T_{ij})$; $K = (I - P + A)^{-1} (H^* - H_{\Delta})$; K' is a matrix in which the ij th element K'_{ij} equals the diagonal element K_{ij} of K ; A is the matrix of stationary probabilities with entries $A_{ij} = \mu_j$; H^* is the matrix of single-step entropies with entries $H_{ij}^* = H(P_i) = -\sum_k P_{ik} \log P_{ik}$; and H_{Δ} is a diagonal matrix with entries $(H_{\Delta})_{ii} = H(X)/\mu_i$. For further details, see the seminar work by Ekroot and Cover (25), and the MATLAB code is available at https://github.com/stdimitr/Entropy_of_Markov_Trajectories.

Conventional static functional connectivity analysis

We defined functional networks based on the identified CAPs. As a CAP may include antiphase coactivations (e.g., voxels with positive or negative values), presumably representing two anticorrelation networks, we thus only extracted the positive voxels within each CAP and binarized them to form a mask of a given network. Within-network connectivity was defined as the averaged Pearson correlation coefficients (Fisher's z -transformed) between all pairs of voxels within the network, and between-network connectivity was calculated by averaging the Pearson correlation coefficient between all pairs of voxels from different networks (i.e., excluding within-network voxel pairs). Both measurements were calculated for data with and without GSR procedure.

Stimulus modulation

A subset of participants in propofol-SHH ($n = 15$) and neuropathological patients ($n = 22$; 12 healthy controls, 4 MCS, and 6 UWS) received auditory stimuli. For propofol-SHH, an event-related design was adopted with 60 names delivered in a pseudorandom order [see more details in (28)]. Each audio clip (0.5 s) was followed by intertrial intervals (ITIs) ranging unpredictably from 15.5 to 25.5 s (2-s step). The participants were required to pay attention and passively listen to the names without behavioral response or judgment. Three 18-min fMRI scans were acquired for each level of responsiveness (baseline conscious condition, light sedation, and general anesthesia). For neuropathological patients, an event-related design was applied with 160 sentences delivered in a pseudorandom order [see more details in (27)]. Each audio clip (2 s) was followed by ITIs ranging unpredictably from 8.0 to 12.0 s (2-s step). All participants were instructed to silently answer the questions. Four 18-min fMRI scans were acquired for each participant.

After applying the same fMRI data preprocessing pipeline, we assigned each time point of the task dataset to a particular CAP based on its maximal similarity to the predefined CAP centroids from the main cohort data. The purpose of doing this was to make the results comparable and generalizable across datasets. This also avoided the potential stimulus-evoked contamination in the definition of CAPs, if otherwise resting state and task state were combined during k -means clustering. The CAP occurrence rate was calculated across trials for each time point following stimulus onset ($t = 0$) within the time window of 0 to 16 s for propofol-SHH and 0 to 10 s for neuropathological patients. The CAP occurrence rates for each time point (per condition and per participant) was corrected by subtracting the CAP occurrence rate at $t = 0$, yielding a relative change against the stimulus onset.

Psychiatric dataset

The data were obtained from the OpenfMRI database. It is a shared neuroimaging dataset from the University of California, Los Angeles

Consortium from Neuropsychiatric Phenomics (29). The original dataset included 272 participants encompassing healthy individuals ($n = 130$) and individuals with psychiatric disorders including schizophrenia ($n = 50$), bipolar disorder ($n = 49$), and attention deficit/hyperactivity disorder ($n = 43$). Participants were excluded if they had no T1 images or resting-state data, the overall head motion range was above 3 mm, or the data had insufficient degree of freedom after band-pass filtering and motion scrubbing. This resulted in 116, 44, 49, and 39 participants for healthy individuals, schizophrenia, bipolar disorder, and attention deficit/hyperactivity disorder, respectively, in our analysis (248 in total).

As mentioned above, using maximal similarity to the predefined CAP centroids, we classified individual fMRI volumes into eight CAPs informed by the k -means clustering approach from main cohort data. Accordingly, this produced a time series of discrete CAP labels per participant. The occurrence rates of each CAP per participant were calculated.

Statistical analysis

We performed Spearman rank correlations between the occurrence rates of joint mirror motifs and individual CAPs, with the level of responsiveness. Conscious and recovery conditions were ranked at 3, intermediate conditions (propofol light sedation, PreLOR of ketamine induction, and patients with MCS) were ranked at 2, and unresponsive conditions (propofol general anesthesia and deep sedation, LOR due to ketamine, and patients with UWS) were ranked as 1. In addition, Student's t tests (paired sample for propofol-SHH, propofol-WI, and ketamine; unpaired sample for neuropathological patients; two-sided) on the CAP occurrence rates were performed between conditions in each dataset. FDR correction ($\alpha < 0.05$) was applied to correct for multiple comparisons.

To examine whether the persistence probabilities significantly deviated from uniformly random sequences, we generated null CAP time series by 1000 permutations, randomly and uniformly exchanging CAP positions in time, across the entire dataset. This null model was only used for assessing the statistical significance of CAP persistence for each condition alone (e.g., conscious state) but not for between conditions (see below). Because of the strong autocorrelation of fMRI signals, the CAP persistence probability shall be expected to be significantly higher than the null distribution. Therefore, this permutation test served as a proof of principle, which is not of interest in this study. To examine whether the transition probabilities and entropies of Markov trajectories significantly deviated from uniformly random sequences for a given condition (e.g., conscious state) and to examine the differences between conditions (e.g., conscious versus propofol) for transition probabilities, entropies of Markov trajectories, and persistence probability, we generated another null CAP time series by controlling the autocorrelation of fMRI signals (24). That is, we preserved dwell times (approximately preserved autocorrelative properties) but otherwise permuted CAP cluster labels 1000 times across the entire dataset. Accordingly, the transition probabilities, entropies of Markov trajectories, and persistence probabilities for each surrogate condition (corresponding to the null time series) were calculated 1000 times to form null distributions for each condition. The deviation of each condition from null (except for the persistence probability that was tested by the first null model) and the deviation of differences between conditions from the null differences were determined at the significance level of $P < 0.001$ by considering multiple comparison corrections

(99.9th and 0.1th percentile of the null distributions; two-sided). Considering that our focus was the common and specific alterations between conscious and various unresponsive conditions, we did not assess the intermediate conditions (e.g., propofol light sedation, PreLOR during ketamine induction, and patients with MCS) and recovery conditions. We also collapsed the conscious conditions across the four datasets, and collapsed propofol-induced unresponsiveness of propofol-SHH and propofol-WI, to reduce the complexity of comparisons. These yielded four conditions with one conscious and three unresponsive conditions: propofol, ketamine, and patients with UWS.

For conventional static functional connectivity analysis, group-level *t* tests (two-sided) on the functional connectivity values were performed, and significance was determined at FDR-corrected $\alpha < 0.05$. For stimulus modulation analysis, Student's *t* tests (against zero; $\alpha < 0.05$, FDR corrected; two-sided) for the CAP occurrence rate changes were performed during the peak period of stimulus-evoked fMRI signal activity (4 to 6 s) at the group level. For psychiatric dataset, comparisons of the CAP occurrence rates for healthy individuals versus schizophrenia, healthy individuals versus bipolar disorder, and healthy individuals versus attention deficit/hyperactivity disorder were performed at the group level by independent sample *t* tests (two-sided; $\alpha < 0.05$, FDR corrected).

SUPPLEMENTARY MATERIALS

Supplementary material for this article is available at <http://advances.sciencemag.org/cgi/content/full/6/11/eaaz0087/DC1>

Fig. S1. *k*-means clustering approach and evaluations of *k*.

Fig. S2. CAPs identified from *k* = 2 to *k* = 16 with and without GSR.

Fig. S3. Spatial characteristics of the CAPs.

Fig. S4. Scatterplots and statistics for the Spearman rank correlations between the occurrence rate of joint mirror motifs or individual CAPs and the level of responsiveness.

Fig. S5. CAP occurrence rates of different conditions from *k* = 4 to *k* = 12 with and without GSR.

Fig. S6. In-degree CAP accessibility of different conditions from *k* = 4 to *k* = 12 with and without GSR.

Fig. S7. Classifying conscious versus unresponsive states using SVM.

Fig. S8. Conventional static functional connectivity.

Fig. S9. The association between CAP occurrence rates and anticorrelations from *k* = 4 to *k* = 12 with and without GSR.

Table S1. A summary of statistics for Fig. 2 (B to E).

Movie S1. CAP temporal dynamics.

[View/request a protocol for this paper from Bio-protocol.](#)

REFERENCES AND NOTES

- M. D. Fox, A. Z. Snyder, J. L. Vincent, M. Corbetta, D. C. Van Essen, M. E. Raichle, The human brain is intrinsically organized into dynamic, anticorrelated functional networks. *Proc. Natl. Acad. Sci. U.S.A.* **102**, 9673–9678 (2005).
- M. Corbetta, G. L. Shulman, Control of goal-directed and stimulus-driven attention in the brain. *Nat. Rev. Neurosci.* **3**, 201–215 (2002).
- A. Fornito, B. J. Harrison, A. Zalesky, J. S. Simons, Competitive and cooperative dynamics of large-scale brain functional networks supporting recollection. *Proc. Natl. Acad. Sci. U.S.A.* **109**, 12788–12793 (2012).
- C. Di Perri, M. A. Bahri, E. Amico, A. Thibaut, L. Heine, G. Antonopoulos, V. Charland-Verville, S. Wannez, F. Gomez, R. Hustinx, L. Tshibanda, A. Demertzi, A. Soddu, S. Laureys, Neural correlates of consciousness in patients who have emerged from a minimally conscious state: A cross-sectional multimodal imaging study. *Lancet Neurol.* **15**, 830–842 (2016).
- R. L. Carhart-Harris, K. J. Friston, The default-mode, ego-functions and free-energy: A neurobiological account of Freudian ideas. *Brain* **133**, 1265–1283 (2010).
- M. E. Raichle, The brain's default mode network. *Annu. Rev. Neurosci.* **38**, 433–447 (2015).
- A. Demertzi, A. Soddu, S. Laureys, Consciousness supporting networks. *Curr. Opin. Neurobiol.* **23**, 239–244 (2013).
- A. Vanhaudenhuyse, A. Demertzi, M. Schabus, Q. Noirhomme, S. Bredart, M. Boly, C. Phillips, A. Soddu, A. Luxen, G. Moonen, S. Laureys, Two distinct neuronal networks mediate the awareness of environment and of self. *J. Cogn. Neurosci.* **23**, 570–578 (2011).
- S. Vossel, J. J. Geng, G. R. Fink, Dorsal and ventral attention systems: Distinct neural circuits but collaborative roles. *Neuroscientist* **20**, 150–159 (2014).
- P. Boveroux, A. Vanhaudenhuyse, M.-A. Bruno, Q. Noirhomme, S. Lauwick, A. Luxen, C. Degueldre, A. Plenevaux, C. Schnakers, C. Phillips, J.F. Brichant, V. Bonhomme, P. Maquet, M. D. Greicius, S. Laureys, M. Boly, Breakdown of within- and between-network resting state functional magnetic resonance imaging connectivity during propofol-induced loss of consciousness. *Anesthesiology* **113**, 1038–1053 (2010).
- V. Bonhomme, A. Vanhaudenhuyse, A. Demertzi, M.A. Bruno, O. Jaquet, M. A. Bahri, A. Plenevaux, M. Boly, P. Boveroux, A. Soddu, J. F. Brichant, P. Maquet, S. Laureys, Resting-state network-specific breakdown of functional connectivity during ketamine alteration of consciousness in volunteers. *Anesthesiology* **125**, 873–888 (2016).
- Z. D. Threlkeld, Y. G. Bodien, E. S. Rosenthal, J. T. Giacino, A. Nieto-Castanon, O. Wu, S. Whitfield-Gabrieli, B. L. Edlow, Functional networks reemerge during recovery of consciousness after acute severe traumatic brain injury. *Cortex* **106**, 299–308 (2018).
- K. Murphy, R. M. Birn, D. A. Handwerker, T. B. Jones, P. A. Bandettini, The impact of global signal regression on resting state correlations: Are anti-correlated networks introduced? *Neuroimage* **44**, 893–905 (2009).
- J. S. Anderson, T. J. Druzgal, M. Lopez-Larson, E.K. Jeong, K. Desai, D. Yurgelun-Todd, Network anticorrelations, global regression, and phase-shifted soft tissue correction. *Hum. Brain Mapp.* **32**, 919–934 (2011).
- K. Murphy, M. D. Fox, Towards a consensus regarding global signal regression for resting state functional connectivity MRI. *Neuroimage* **154**, 169–173 (2017).
- P. Barttfeld, L. Uhrig, J. D. Sitt, M. Sigman, B. Jarraya, S. Dehaene, Signature of consciousness in the dynamics of resting-state brain activity. *Proc. Natl. Acad. Sci. U.S.A.* **112**, 887–892 (2015).
- A. Demertzi, E. Tagliazucchi, S. Dehaene, G. Deco, P. Barttfeld, F. Raimondo, C. Martial, D. Fernández-Espejo, B. Rohaut, H. U. Voss, N. D. Schiff, A. M. Owen, S. Laureys, L. Naccache, J. D. Sitt, Human consciousness is supported by dynamic complex patterns of brain signal coordination. *Sci. Adv.* **5**, eaat7603 (2019).
- D. Golkowski, S. K. Larroque, A. Vanhaudenhuyse, A. Plenevaux, M. Boly, C. Di Perri, A. Ranft, G. Schneider, S. Laureys, D. Jordan, V. Bonhomme, R. Ilg, Changes in whole brain dynamics and connectivity patterns during sevoflurane- and propofol-induced unconsciousness identified by functional magnetic resonance imaging. *Anesthesiology* **130**, 898–911 (2019).
- A. G. Hudetz, X. Liu, S. Pillay, Dynamic repertoire of intrinsic brain states is reduced in propofol-induced unconsciousness. *Brain Connect.* **5**, 10–22 (2015).
- E. Tagliazucchi, D. R. Chialvo, M. Siniatchkin, E. Amico, J.F. Brichant, V. Bonhomme, Q. Noirhomme, H. Laufs, S. Laureys, Large-scale signatures of unconsciousness are consistent with a departure from critical dynamics. *J. R. Soc. Interface* **13**, 20151027 (2016).
- X. Liu, N. Zhang, C. Chang, J. H. Duyn, Co-activation patterns in resting-state fMRI signals. *Neuroimage* **180**, 485–494 (2018).
- X. Liu, C. Chang, J. H. Duyn, Decomposition of spontaneous brain activity into distinct fMRI co-activation patterns. *Front. Syst. Neurosci.* **7**, 101 (2013).
- X. Liu, J. H. Duyn, Time-varying functional network information extracted from brief instances of spontaneous brain activity. *Proc. Natl. Acad. Sci. U.S.A.* **110**, 4392–4397 (2013).
- E. J. Cornblath, A. Ashourvan, J. Z. Kim, R. F. Betzel, R. Ciric, G. L. Baum, X. He, K. Ruparel, T. M. Moore, R. C. Gur, R. E. Gur, R. T. Shinohara, D. R. Roalf, T. D. Satterthwaite, D. S. Bassett, Context-dependent architecture of brain state dynamics is explained by white matter connectivity and theories of network control. *bioRxiv*, 412429 (2018).
- L. Ekroo, T. M. Cover, The entropy of Markov trajectories. *IEEE Trans. Inf. Theory.* **39**, 1418–1421 (1993).
- S. I. Dimitriadis, C. I. Salis, Mining time-resolved functional brain graphs to an EEG-based chronnectomic brain aged index (CBAI). *Front. Hum. Neurosci.* **11**, 423 (2017).
- Z. Huang, R. Dai, X. Wu, Z. Yang, D. Liu, J. Hu, L. Gao, W. Tang, Y. Mao, Y. Jin, X. Wu, B. Liu, Y. Zhang, L. Lu, S. Laureys, X. Weng, G. Northoff, The self and its resting state in consciousness: An investigation of the vegetative state. *Hum. Brain Mapp.* **35**, 1997–2008 (2014).
- Z. Huang, J. Zhang, J. Wu, X. Liu, J. Xu, J. Zhang, P. Qin, R. Dai, Z. Yang, Y. Mao, A. G. Hudetz, G. Northoff, Disrupted neural variability during propofol-induced sedation and unconsciousness. *Hum. Brain Mapp.* **39**, 4533–4544 (2018).
- R. A. Poldrack, E. Congdon, W. Triplett, K. J. Gorgolewski, K. H. Karlsgodt, J. A. Mumford, F. W. Sabb, N. B. Freimer, E. D. London, T. D. Cannon, R. M. Bilder, A phenotype-wide examination of neural and cognitive function. *Sci. Data* **3**, 160110 (2016).
- P. E. Visides, T. Bel-Bahar, A. Nelson, K. Chilton, E. Smith, E. Janke, V. Tarnal, P. Picton, R. E. Harris, G. A. Mashour, Subanaesthetic ketamine and altered states of consciousness in humans. *Br. J. Anaesth.* **121**, 249–259 (2018).
- D. Li, G. A. Mashour, Cortical dynamics during psychedelic and anesthetized states induced by ketamine. *Neuroimage* **196**, 32–40 (2019).
- G. Scott, R. L. Carhart-Harris, Psychedelics as a treatment for disorders of consciousness. *Neurosci. Conscious.* **2019**, niz003 (2019).
- D. S. Margulies, S. S. Ghosh, A. Goulas, M. Falkiewicz, J. M. Huntenburg, G. Langs, G. Bezdin, S. B. Eickhoff, F. X. Castellanos, M. Petrides, E. Jefferies, J. Smallwood, Situating

- the default-mode network along a principal gradient of macroscale cortical organization. *Proc. Natl. Acad. Sci. U.S.A.* **113**, 12574–12579 (2016).
34. G. J. Yang, J. D. Murray, G. Repovs, M. W. Cole, A. Savic, M. F. Glasser, C. Pittenger, J. H. Krystal, X. J. Wang, G. D. Pearlson, D. C. Glahn, A. Anticevic, Altered global brain signal in schizophrenia. *Proc. Natl. Acad. Sci. U.S.A.* **111**, 7438–7443 (2014).
 35. X. Liu, J. A. De Zwart, M. L. Schölvinck, C. Chang, F. Q. Ye, D. A. Leopold, J. H. Duyn, Subcortical evidence for a contribution of arousal to fMRI studies of brain activity. *Nat. Commun.* **9**, 395 (2018).
 36. C. Chang, D. A. Leopold, M. L. Schölvinck, H. Mandelkow, D. Picchioni, X. Liu, F. Q. Ye, J. N. Turchi, J. H. Duyn, Tracking brain arousal fluctuations with fMRI. *Proc. Natl. Acad. Sci. U.S.A.* **113**, 4518–4523 (2016).
 37. B. T. Yeo, F. M. Krienen, J. Sepulcre, M. R. Sabuncu, D. Lashkari, M. Hollinshead, J. L. Roffman, J. W. Smoller, L. Zölle, J. R. Polimeni, B. Fischl, H. Liu, R. L. Buckner, The organization of the human cerebral cortex estimated by intrinsic functional connectivity. *J. Neurophysiol.* **106**, 1125–1165 (2011).
 38. J. D. Power, A. L. Cohen, S. M. Nelson, G. S. Wig, K. A. Barnes, J. A. Church, A. C. Vogel, T. O. Laumann, F. M. Miezin, B. L. Schlaggar, S. E. Petersen, Functional network organization of the human brain. *Neuron* **72**, 665–678 (2011).
 39. C. M. Michel, T. Koenig, EEG microstates as a tool for studying the temporal dynamics of whole-brain neuronal networks: A review. *Neuroimage* **180**, 577–593 (2018).
 40. J. A. Roberts, L. L. Gollo, R. G. Abeyesuriya, G. Roberts, P. B. Mitchell, M. W. Woolrich, M. Breakspear, Metastable brain waves. *Nat. Commun.* **10**, 1056 (2019).
 41. P. E. Vlisides, D. Li, M. Zierau, A. P. Lapointe, K. I. Ip, A. M. McKinney, G. A. Mashour, Dynamic cortical connectivity during general anesthesia in surgical patients. *Anesthesiology* **130**, 885–897 (2019).
 42. D. Li, P. E. Vlisides, M. B. Kelz, M. S. Avidan, G. A. Mashour; ReCCognition Study Group, Dynamic cortical connectivity during general anesthesia in healthy volunteers. *Anesthesiology* **130**, 870–884 (2019).
 43. Z. Huang, J. Zhang, J. Wu, P. Qin, X. Wu, Z. Wang, R. Dai, Y. Li, W. Liang, Y. Mao, Z. Yang, J. Zhang, A. Wolff, G. Northoff, Decoupled temporal variability and signal synchronization of spontaneous brain activity in loss of consciousness: An fMRI study in anesthesia. *Neuroimage* **124**, 693–703 (2016).
 44. Z. Huang, X. Liu, G. A. Mashour, A. G. Hudetz, Timescales of intrinsic BOLD signal dynamics and functional connectivity in pharmacologic and neuropathologic states of unconsciousness. *J. Neurosci.* **38**, 2304–2317 (2018).
 45. J. T. Giacino, K. Kalmar, J. Whyte, The JFK coma recovery scale-revised: Measurement characteristics and diagnostic utility. *Arch. Phys. Med. Rehabil.* **85**, 2020–2029 (2004).
 46. J. D. Power, K. A. Barnes, A. Z. Snyder, B. L. Schlaggar, S. E. Petersen, Spurious but systematic correlations in functional connectivity MRI networks arise from subject motion. *Neuroimage* **59**, 2142–2154 (2012).
- Acknowledgments:** We thank G. Northoff, X. Wu, and P. Qin who shared the neuropathological data. We also appreciate assistance of X. Liu, K. Lauer, C. Roberts, S. Liu, S. Gollapudy, and W. Gross in performing the anesthetic procedures at the MCW and of Y. Chen, J. Xu, X. Li, Z. Yang, and J. Zhang in performing the anesthetic procedures at the Huashan Hospital. **Funding:** This study was supported by Medical Guidance Supporting Project from Shanghai Municipal Science and Technology Commission No. 17411961400 (to J.Z.), Shanghai Municipal Science and Technology Major Project No. 2018SHZDZX01 (to J.Z.), and ZJLab. This study was also supported by a grant from the National Institute of General Medical Sciences of the NIH under award R01-GM103894 (to A.G.H.). The content is solely the responsibility of the authors and does not necessarily represent the official views of the NIH. **Author contributions:** Z.H., J.Z., and A.G.H. designed the study. J.Z. and J.W. conducted the experiment, performed the anesthetic procedures, and collected the data of propofol-SHH and ketamine. A.G.H. collected the data of propofol-WI. Z.H. conducted the experiment and collected the task fMRI data in neuropathological patients. Z.H. and A.G.H. conceptualized the data analyses. Z.H. analyzed the entire dataset and prepared the figures. Z.H., G.A.M., and A.G.H. interpreted the data and edited the manuscript. Z.H., J.Z., G.A.M., and A.G.H. wrote the manuscript. **Competing interests:** The authors declare that they have no competing interests. **Data and materials availability:** All data needed to evaluate the conclusions in the paper are present in the paper and the Supplementary Materials. Additional data related to this paper may be requested from the authors. The psychiatric dataset is available at OpenfMRI (<https://openfMRI.org/dataset/ds000030/>).
- Submitted 5 August 2019
 Accepted 16 December 2019
 Published 11 March 2020
 10.1126/sciadv.aaz0087
- Citation:** Z. Huang, J. Zhang, J. Wu, G. A. Mashour, A. G. Hudetz, Temporal circuit of macroscale dynamic brain activity supports human consciousness. *Sci. Adv.* **6**, eaaz0087 (2020).

Congratulations
to Christopher Zimmerman, Ph.D.
Postdoctoral Fellow
Princeton Neuroscience Institute



Meet the Winner

Eppendorf & Science Prize for Neurobiology

Congratulations to Christopher Zimmerman on winning the 2020 Eppendorf & Science Prize for his work on the neural circuits that govern thirst and drinking behavior. Dr. Zimmerman discovered that sensory signals originating throughout the body come together within individual neurons in the brain to produce the sense of thirst. He demonstrated that this new class of body-to-brain signals predicts changes in hydration before they occur and, as a result, adjusts our level of thirst preemptively. Dr. Zimmerman's research has revealed fundamental principles of ingestive behavior and provided neural mechanisms to explain aspects of everyday human experience.

The annual US\$25,000 Eppendorf & Science Prize for Neurobiology honors scientists, like Dr. Zimmerman, for their outstanding contributions to neurobiological research. Christopher Zimmerman is the 19th recipient of this international award. Due to coronavirus (COVID-19), the 2020 winner and finalists will be honored at the Prize Ceremony in November 2021 in Chicago.

You could be next to win this prize.

If you are 35 years of age or younger and currently performing neurobiological research, you could be next to win the 2021 Prize.

Deadline for entries is June 15, 2021.

Learn more at: www.eppendorf.com/prize

NEUROIMMUNOLOGY

T cell engagement of cross-presenting microglia protects the brain from a nasal virus infection

E. Ashley Moseman^{1,2,*†}, Alexa C. Blanchard^{1*}, Debasis Nayak³, Dorian B. McGavern^{1†}

The neuroepithelium is a nasal barrier surface populated by olfactory sensory neurons that detect odors in the airway and convey this information directly to the brain via axon fibers. This barrier surface is especially vulnerable to infection, yet respiratory infections rarely cause fatal encephalitis, suggesting a highly evolved immunological defense. Here, using a mouse model, we sought to understand the mechanism by which innate and adaptive immune cells thwart neuroinvasion by vesicular stomatitis virus (VSV), a potentially lethal virus that uses olfactory sensory neurons to enter the brain after nasal infection. Fate-mapping studies demonstrated that infected central nervous system (CNS) neurons were cleared noncytolytically, yet specific deletion of major histocompatibility complex class I (MHC I) from these neurons unexpectedly had no effect on viral control. Intravital imaging studies of calcium signaling in virus-specific CD8⁺ T cells revealed instead that brain-resident microglia were the relevant source of viral peptide–MHC I complexes. Microglia were not infected by the virus but were found to cross-present antigen after acquisition from adjacent neurons. Microglia depletion interfered with T cell calcium signaling and antiviral control in the brain after nasal infection. Collectively, these data demonstrate that microglia provide a front-line defense against a neuroinvasive nasal infection by cross-presenting antigen to antiviral T cells that noncytolytically cleanse neurons. Disruptions in this innate defense likely render the brain susceptible to neurotropic viruses like VSV that attempt to enter the CNS via the nose.

INTRODUCTION

Viral infections of the central nervous system (CNS) can be devastating when not properly contained (1, 2). Because the CNS contains irreplaceable postmitotic cells, it is protected by several physical barriers that limit pathogen access into the CNS, including the blood–brain barrier (BBB), blood cerebrospinal fluid barrier (BCSFB), and skull, among others. In addition, immune responses in this compartment are heavily regulated (3). Viruses, in turn, use several approaches to bypass these barriers such as direct infection of the BBB, invasion of peripheral nerves followed by transport into the CNS, and “trojan horse” entry via surveying immune cells (4). One especially vulnerable route that viruses use to invade the CNS is via olfactory sensory neurons (OSNs) within the nasal cavity.

OSNs lie within the mucosal upper airway surface, which is constantly exposed to environmental pathogens. However, the olfactory epithelium (OE) lining the nasal turbinates is unique in that this mucosal surface provides access for viruses to enter the CNS. Unlike the neighboring respiratory epithelium, the OE contains thousands to millions of OSNs (depending on the species) that are the predominant cell type within the olfactory neuroepithelial surface. Although the OSN cell bodies lie beneath a layer of supporting or sustentacular cells, they extend a ciliated dendrite into the mucus lined airway space. Odorant information gathered from the external environment is conveyed via OSN axons within the turbinates through the specialized cribriform plate at the front of the skull and into the olfactory bulb (OB) of the brain (5). However, this anatomical arrangement

also results in OSNs serving as a direct single-cell route for neuroinvasion. Pathogens that infect OSNs can be shuttled intracellularly along OSN axons directly into the brain. The intracellular passage via OSNs into the brain allows invading pathogens to “tunnel under the castle wall” and evade classical CNS barriers that typically shield the brain. Thus, the olfactory route of infection is especially vulnerable to neurotropic viruses (6, 7).

The immune response to viruses must be appropriately balanced between pathogen clearance and limiting tissue damage. This balance is especially important in the CNS because most neurons are unable to regenerate, and damage can result in permanent damage to neural networks (1). Although virus-induced cytopathology poses a serious concern to the CNS, immune-mediated cellular damage via perforin/granzyme poses a similar threat to neuronal integrity. Therefore, noncytolytic viral clearance via cytokines, especially interferons (IFNs), are believed to play an important role in CNS viral control (8–10). Type I IFN (IFN-I) is critical to the innate defense against most viruses (11) and also plays an important role in priming adaptive immune responses (12, 13). On the other hand, IFN γ , which is primarily produced by lymphocytes [CD8⁺, CD4⁺, and natural killer (NK) cells], plays a dominant role in the control of CNS viral infections (14–17). Tumor necrosis factor- α (TNF α) has also been shown to facilitate noncytolytic clearance (18–20).

Upper airway infections are a ubiquitous part of human life, and although many viruses infect the respiratory system (e.g., influenza, rhinovirus, coronavirus, and respiratory syncytial virus), several of these viruses can also infect the OE. In this study, we used vesicular stomatitis virus (VSV) as a model for nasal infection because of its ability to target the OE preferentially over the respiratory epithelium (21)—a preference shared by herpes simplex virus (HSV) (22). Several other viruses can also infect the OE, including mouse hepatitis virus (MHV) (23), parainfluenza (24), Japanese encephalitis virus (JEV) (25), and influenza virus (6, 26). Whereas seasonal influenza is typically an infection of respiratory epithelium (27), some more

Copyright © 2020
The Authors, some
rights reserved;
exclusive licensee
American Association
for the Advancement
of Science. No claim
to original U.S.
Government Works

¹Viral Immunology and Intravital Imaging Section, National Institute of Neurological Disorders and Stroke, National Institutes of Health, Bethesda, MD, USA. ²Department of Immunology, Duke University School of Medicine, Durham, NC, USA. ³Discipline of Bioscience and Biomedical Engineering, Indian Institute of Technology Indore, MP, India.

*These authors contributed equally to this work.

†Corresponding author. Email: mcgavern@mail.nih.gov (D.B.M.); ashley.moseman@duke.edu (E.A.M.)

pathogenic strains are clearly able to target OSNs (26). Highly pathogenic avian influenza H5N1 prefers to replicate within the OE (28).

We undertook this study to better understand the mechanisms by which a cytopathic virus that infects the OE is contained and ultimately prohibited from spreading throughout the CNS. Intranasal VSV infection can induce a potent encephalitis that varies in outcome depending on the age and strain of the infected animal (29). After nasal infection, VSV is transported from the airway via the OE into the CNS, where it is initially observed within the OB (30). Virus replication is usually halted at the glomerular layer of the OB where OSN projections enter (10); however, the virus can sometimes move into deeper regions of the OB and throughout the CNS. VSV that escapes this OSN-glomerular junction is believed to use retrograde axon transport and the ventricular system to move caudally in the CNS (31). It is known that IFN-I (32, 33), B cells (33, 34), and antiviral T cells (29, 35) all play a role in containing VSV. In this study, we monitored the *in vivo* activities of CD8⁺ T cells in the anatomical site where VSV is typically contained within the OB (glomeruli) and probed for the most functionally relevant source(s) of antigen presentation that result in noncytolytic VSV control in neurons. Unexpectedly, an innate immune cell that is never infected by the virus (microglia) served as a key player in the control of virus in neurons.

RESULTS

Virus infection of the olfactory epithelium leads to rapid neuroinvasion

To more precisely understand how neurotropic viruses invade the CNS after infection of the OE, we inoculated mice intranasally with VSV expressing DsRed (VSV-DsRed). This approach enabled us to monitor the distribution and spread of the virus in olfactory tissue. Confocal imaging of coronal whole head sections (fig. S1) revealed 24 hours after intranasal infection that there was widespread viral replication within OSNs in the OE (Fig. 1, A and C). After intranasal inoculation, VSV moves from the OE into the OB where it is typically halted at the glomerular layer (10). At day 6 after infection, we observed robust VSV-DsRed signal in outer nerve layer, which are peripheral nerves that project into the OB (Fig. 1, B and D). We also observed virus in the OB glomerular layer, indicating invasion of the brain parenchyma (Fig. 1, B and D). Quantification of viral titers in the OB revealed that VSV was very efficient at gaining access to the brain via this intranasal route (Fig. 1E). Viral titers reached $\sim 10^4$ plaque-forming units (PFU) at 24 hours and climbed to $\sim 10^5$ PFU on day 6 before being extinguished by day 8.

To protect the CNS, noncytolytic viral clearance is often favored in this compartment (36). However, because VSV is a cytopathic virus, it was unclear whether this lifecycle could be halted once initiated. To determine whether a cytopathic virus could be cleared noncytolytically from the brain, we generated a recombinant of VSV expressing iCre-recombinase (VSV-iCre). We then conducted fate-mapping studies by infecting floxed Stop TdTomato reporter (Stop^{fl/fl} TdTomato) mice with this recombinant virus. We observed dense patches of TdTomato⁺ cells with a definitive neuronal morphology in the OB at late time points (>40 days) (Fig. 1F and fig. S2), long after infectious virus was cleared from this compartment (Fig. 1E). These data indicate that VSV can be noncytolytically cleared from the OB, although it does not exclude the possibility that some cells are cytolytically cleared as well.

Intranasal VSV infection induces a robust immune response in the olfactory system

Except for patches of bone marrow within the turbinate bones, the naïve OE as shown in coronal head sections (fig. S1A) contains few hematopoietic cells (Fig. 2A); however, after nasal infection, widespread VSV replication within the OE provoked robust inflammatory cell infiltration. CD45⁺ leukocytes were observed in the OE as early as day 2, and infiltration elevated massively by day 6 after infection (Fig. 2A). At this time point, virus and leukocytes were found in OE and in the airways. This was associated with substantial OE degradation and dissociation from the lamina propria (Fig. 2, A and B).

Under steady state, the OB is defended in part by resident microglia; however, the arrival of VSV into this compartment via OSNs is associated with a large influx of peripherally derived immune cells that surrounded infected glomeruli (Fig. 2, A and C to E). This response was dominated by neutrophils and NK cells during the first 3 days, which were superseded by CD8⁺ T cells and Ly6C^{hi} monocytes at day 6 after infection (Fig. 2E). CD4⁺ T cells also arrived at this time point. At day 8 after infection, T cell and monocyte numbers increased further within the OB (Fig. 2E). To track the recruitment of virus-specific CD8⁺ T cells to the OB, we seeded mice intravenously with 3000 mCerulean⁺ OT-I and then infected them intranasally with VSV-ovalbumin (OVA). VSV-specific CD8⁺ T cells were primed and proliferated in the draining cervical lymph nodes and spleen and increased steadily over time in the OB (Fig. 2F). These data demonstrate that the OB mounts a robust immunological defense against intranasal VSV infection.

T cells and antiviral effector molecules protect against fatal VSV encephalitis

VSV titers in the OB are controlled between days 6 and 8 after infection (Fig. 1E), which coincided with the arrival of antiviral T cells (Fig. 2, E and F). We therefore sought to better understand the role of these T cells in preventing the fatal spread of VSV from olfactory glomeruli throughout the brain. We used survival rather than viral titers as an initial screen because we wanted to identify components of the OB antiviral defense that prevent induction of fatal disease after intranasal infection. Consistent with a previous study that used Balb/c mice (nu/nu) to demonstrate a role for T cells in controlling VSV (29), we found that a fraction of C57BL/6J mice depleted of either CD8⁺ or CD4⁺ T cells developed fatal VSV encephalitis (Fig. 3A). In addition, depletion of both T cell subsets induced fatal disease in nearly all mice infected intranasally with VSV. Consistent with this observation, we found increased viral titers in the OB (Fig. 3B) and caudal brain (Fig. 3C) of T cell-depleted mice at day 8 after infection. In addition, although VSV-green fluorescent protein (GFP) was largely confined to the outer nerve layer and glomeruli of control mice (Fig. 3, D and F), T cell depletion promoted movement of VSV-GFP to other brain regions, including the rostral migratory stream and brainstem (Fig. 3, D and F). T cell depletion also allowed VSV-GFP to invade deeper layers of the OB, such as the mitral cell layer (Fig. 3E).

We next examined the effector mechanisms involved in preventing fatal VSV encephalitis. Mice deficient in TNF α , IFN γ , or perforin (PRF1) all showed modest reductions in survival comparable with that observed in mice depleted with anti-CD8 or CD4 antibodies (Fig. 3G). None of these knockout mice phenocopied the incidence of fatal disease observed in mice receiving anti-CD8/4-depleting

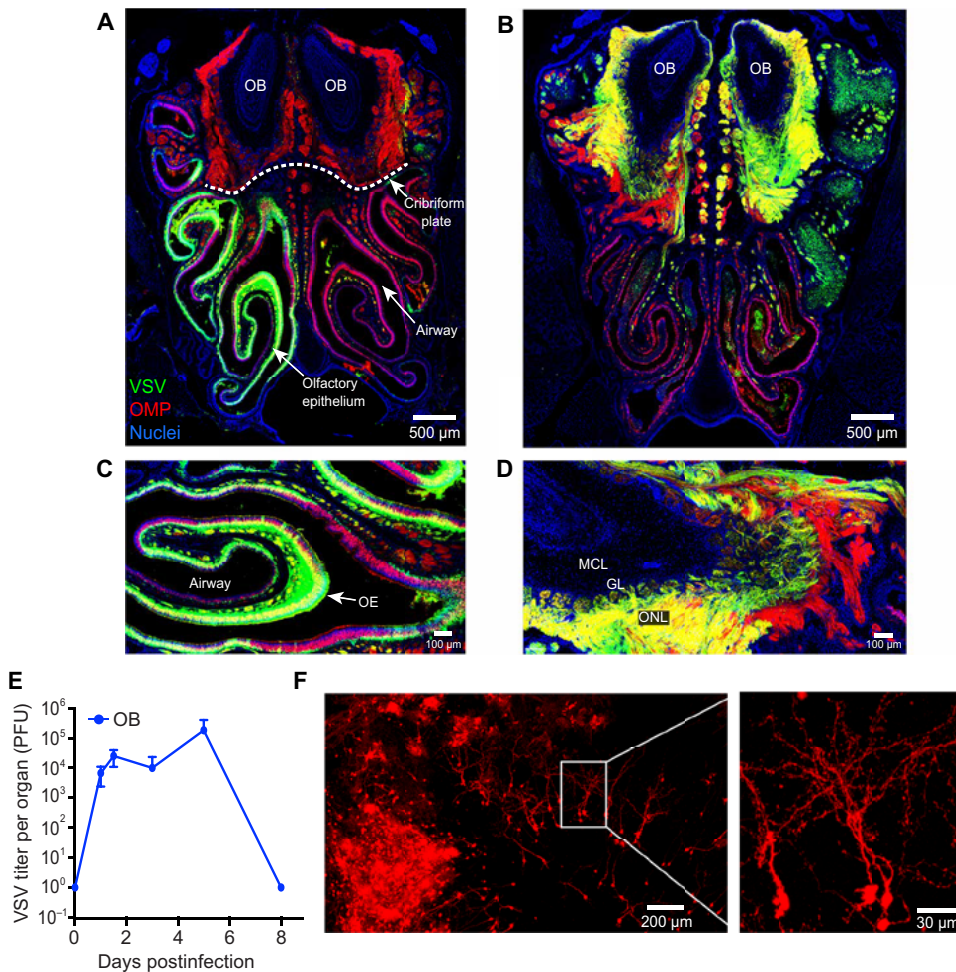


Fig. 1. VSV rapidly travels from the nasal turbinates into the OB where it is controlled noncytolytically. (A and B) Representative confocal micrographs of coronal head sections (see fig. S1) show the nasal airway, OE, cribriform plate (white dotted line), and OBs from OMP-GFP mice on days 1 (A) and 6 (B) after intranasal VSV-DsRed (green) infection (OMP-GFP in red, nuclei shown in blue). (C and D) Higher magnification images show the virus invading the OE at day 1 (C) and OB via the outer nerve layer at day 6 (D). Anatomical structures such as the airway, OE, olfactory nerve layer (ONL), glomerular layer (GL), and mitral cell layer (MCL) are annotated in these images. (E) Time course of viral titers represented as PFU per OB after intranasal VSV infection (means \pm SD; $n = 4$ to 5 mice per time point; data representative of three independent experiments). (F) Confocal micrographs of a cleared OB from a VSV-iCre infected *Stop^{fl/fl}tdTomato* reporter mouse 50 days after intranasal infection.

antibodies (Fig. 3A). To determine whether expression of the IFN γ R was required on infected cells, we inoculated floxed IFN γ R with VSV-iCre (Fig. 3H). This, however, did not reduce survival, indicating that IFN γ R is not required on infected cells to elicit antiviral control. Collectively, these data suggest that there are redundant effector mechanisms controlling VSV within the OB.

Antiviral CTLs have slowed motility within the infected OB

Although it is likely, based on our depletion studies, that CD4⁺ and CD8⁺ T cells exert complementary antiviral programs after infection (Fig. 3A), we decided to focus in more detail on the CD8⁺ T cell compartment because their major histocompatibility complex class I (MHC I) restriction offered the possibility of studying a broader selection of potential target cells. We initially examined VSV-specific versus bystander CD8⁺ T cell dynamics in the living OB at day 6 or 7 after infection. We selected these time points because viral titers in

the OB declined rapidly between days 6 and 8 after infection (Fig. 1E), and we wanted to understand the mechanism by which this occurred. One day before VSV-OVA infection, B6 mice were seeded with 3000 mCerulean⁺ OT-I cells that served as the virus-specific CD8⁺ T cell population. Bystander cells were generated by seeding a separate group of B6 mice with orange fluorescent protein–positive (OPF⁺) P14 cells, which are specific to the glycoprotein of lymphocytic choriomeningitis virus (LCMV) (37). These mice were then infected intraperitoneally with LCMV Armstrong, and at day 7, effector OPF⁺ P14 cells were harvested from the spleen and transferred into VSV-GFP-OVA–infected mice 1 day before imaging. mCerulean⁺ OT-I (VSV-specific) and OPF⁺ P14 (bystander) cells were imaged simultaneously by intravital two-photon microscopy (TPM) through a thinned skull preparation (38, 39) made above the OB. This technique allowed us for the first time to analyze antiviral T cell behavior in the virally infected OB. After VSV-GFP-OVA infection, virus-specific CD8⁺ T cells moved rapidly along, between, and across infected axon tracts in the outer nerve layer and within the glomeruli (Fig. 4, A and B, and movies S1 and S2). Quantification of T cell track velocities in two-photon time lapses revealed that virus-specific CD8⁺ T cells had reduced track velocities relative to bystander T cells imaged in the same OB (Fig. 4, C and D). In addition, virus-specific CD8⁺ T cells also had a lower motility coefficient and higher arrest coefficient (Fig. 4D), all suggesting that these cells were encountering antigen locally (40).

CTLs engage cognate antigen on an uninfected brain-resident cell population

To more accurately assess antigen encounters by virus-specific CD8⁺ T cells in vivo, we devised an approach to monitor T cell calcium flux by TPM. T cell recognition of cognate peptide MHC complexes results in a rapid increase in intracellular calcium levels (41). We therefore generated OT-I and P14 cells expressing mTomato (to label the plasma membrane) and GCaMP6s—a fluorescent calcium concentration indicator protein (13). Six days after intranasal infection with VSV-OVA, calcium flux was visible in virus-specific CD8⁺ T cells that had infiltrated and were surveying the OB (Fig. 5, A, B, and D, and movie S3). Calcium flux was rarely observed in infiltrating bystander P14 CD8⁺ T cells, indicating that T cell calcium flux is a good surrogate for cognate peptide MHC recognition (Fig. 5B) (13). We also observed that calcium fluxing virus-specific OT-I CD8⁺ T cells had reduced instantaneous velocities

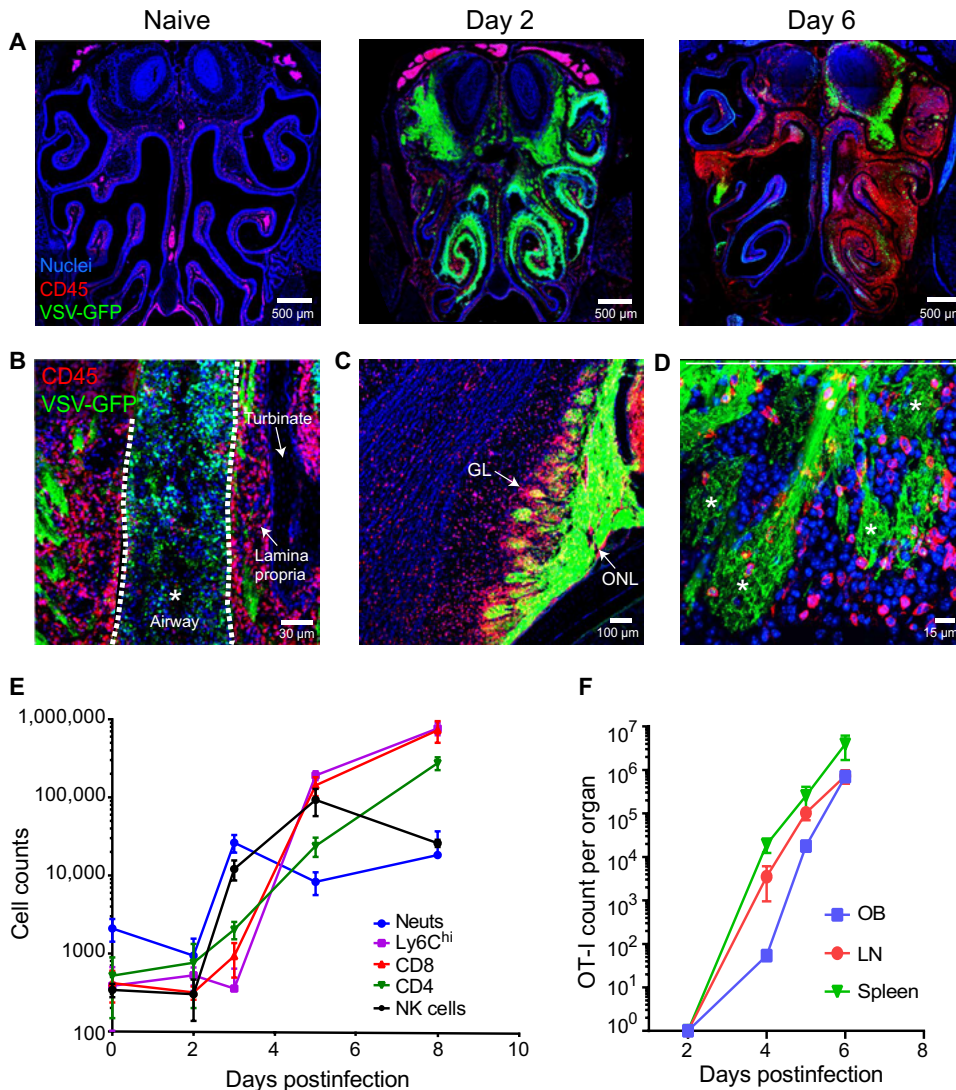


Fig. 2. Intranasal VSV infection drives massive immune cell infiltration into the OE and OB. (A) Representative confocal images of coronal head sections (see fig. S1) show the distribution of CD45⁺ leukocytes (red) in OE/OB-uninfected mice relative to days 2 and 6 after intranasal VSV-GFP (green) infection. Cell nuclei are shown in blue. (B) Confocal micrograph depicting CD45⁺ infiltration into the VSV-eGFP-infected olfactory turbinates 6 days after infection. Note that the airway space denoted with white asterisk and white dotted lines is filled with cells and virus. (C) A confocal micrograph from a day 6 infected OB shows VSV-GFP in the glomerular layer (GL) and outer nerve layer (ONL). (D) Confocal micrograph of day 6 VSV-eGFP-infected OSN terminals. Asterisks denote individual glomeruli within the OB. (E) Graph depicts the kinetics of inflammatory cell infiltration into the VSV-infected OB. The following markers were used to identify the different immune subsets after first gating on living, CD45⁺ cells: neutrophils (Ly6C^{int}, Ly6C^{hi}, CD11b⁺) and monocytes (Ly6C^{hi}, CD11b^{hi}); NK cells (NK1.1⁺, TCRβ^{neg}), CD4 T cells (TCRβ⁺, CD4⁺, CD8⁻), and CD8 T cells (TCRβ⁺, CD4⁺, CD8⁺) (means ± SD; n = 4 to 5 mice time point; data representative of three independent experiments). (F) Kinetics of adoptively transferred antigen-specific CD8⁺ OT-I T cell expansion in the OB, draining mandibular and superficial cervical LNs, and spleen after intranasal VSV infection. OT-I cells were defined as living, CD45.1⁺, CD8⁺, mTomato⁺ (means ± SD; n = 4 to 5 mice per time point; two independent experiments).

relative to the cells that were not fluxing (Fig. 5C), which is consistent with studies showing that T cell antigen recognition is associated with decreased motility (40).

We next classified virus-specific CD8⁺ T cell interactions in the virally infected OB into two groups based on velocity. “Kinetic” interactions were defined by continued T cell motility while fluxing calcium, whereas “stable” interactions were characterized by a relative

loss of motility (<2 μm/min) during calcium flux (Fig. 5, E and F, and movie S3) (42). Most antigen encounters (65%) by virus-specific CD8⁺ T cells were defined as kinetic interactions. These cells did not arrest during peptide MHC recognition but paused briefly before continuing their migration through the OB (Fig. 5, E and F, and movie S3). Virus-specific CD8⁺ T cells also engaged in more stable interactions where the T cell would fully arrest and then flux calcium; however, this was only observed in 35% of the antigen encounters (Fig. 5, E and F, and movie S3). Stable interactions typically resulted in more calcium fluxes (Fig. 5G) and longer flux durations relative to the kinetic interactions (fig. S3).

Having defined the dynamics of virus-specific CD8⁺ T cell interactions in the infected OB, we next sought to define target cell identity. In our imaging studies, we often noted that T cells would flux calcium upon engagement of “autofluorescent” cells (Fig. 5, A and D, and movie S3). Morphologically, these autofluorescent cells did not match the size, shape, or spatial distribution of VSV-GFP infected cells that we typically observed in the OB. Because hematopoietic cells massively infiltrated the OB after VSV infection (Fig. 2), we posited that an infiltrating cell population might be responsible for presenting local antigen to virus-specific CD8⁺ T cells. To address this possibility, we generated bone marrow chimeras in which the CNS-resident compartment lacked MHC I, whereas the infiltrating hematopoietic compartment was MHC I sufficient. The percentage of donor-derived hematopoietic cells in the blood of these mice was 99.2 ± 0.4%, demonstrating near-complete chimerism. The overall frequency of cytotoxic lymphocyte (CTL) calcium flux dropped significantly in mice lacking MHC I on the CNS-resident compartment, indicating that antigen presentation to virus-specific CD8⁺ T cells relied primarily on a radiation-resistant brain cell population rather than infiltrating hematopoietic cells (Fig. 5H). VSV

is known to infect neurons, but MHC I is expressed at very low levels on these cells (43, 44). We nevertheless set out to evaluate the importance CTL-neuronal interactions in controlling an intranasal VSV infection. To address this question, we generated a conditional β₂-microglobulin (β₂M) mouse in which the exons 2 and 3 are flanked by loxP sites (floxed β₂M) (fig. S4A). β₂M is an essential component of the MHC I surface complex, and thus, removal

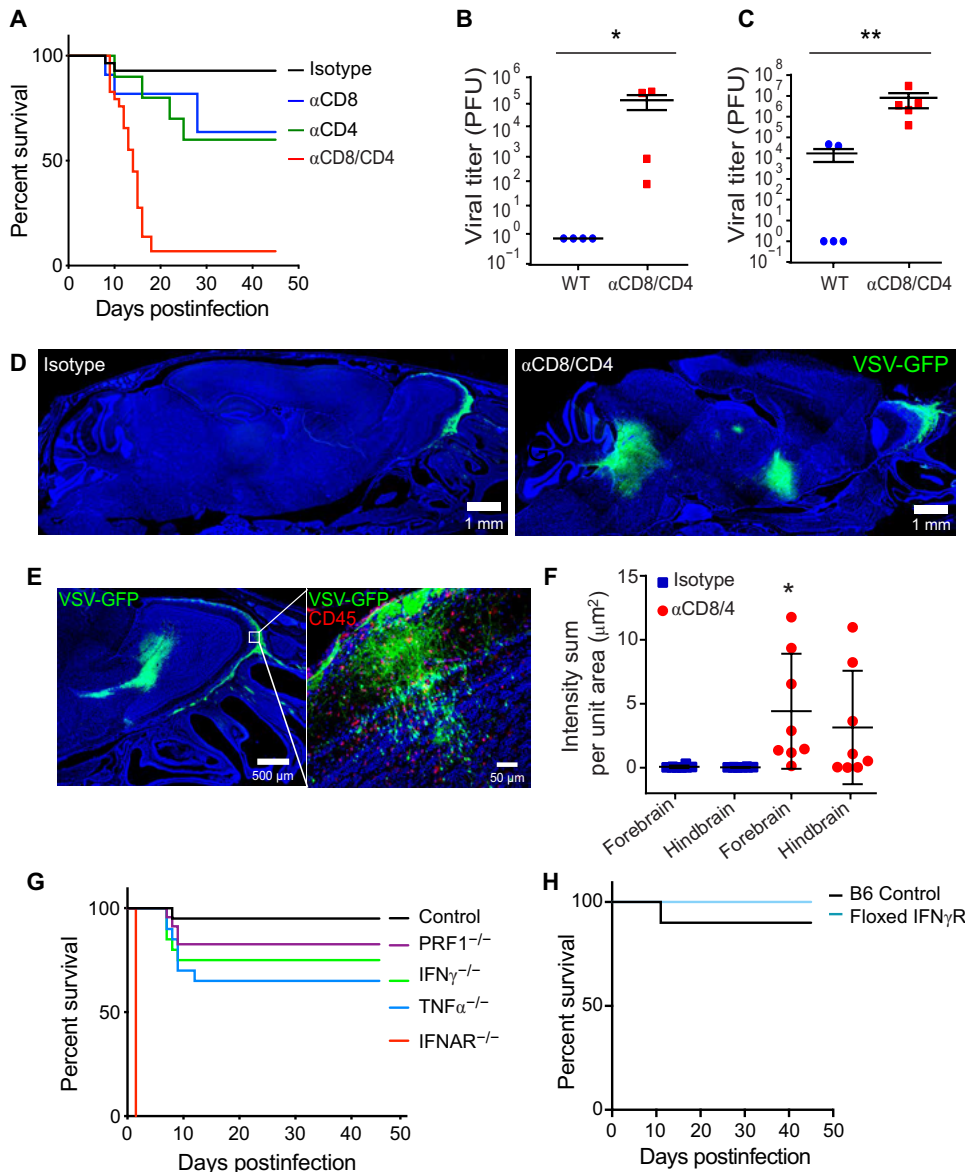


Fig. 3. T cells prevent fatal VSV neuroinvasion after intranasal infection. (A) Survival curves of isotype control, α CD4-, α CD8-, or α CD8/ α CD4-treated mice after intranasal VSV infection ($n = 28$ mice for isotype; $n = 10$ for α CD4 depleted, $P = 0.0183$; $n = 11$ for α CD8 depleted, $P = 0.0263$; $n = 31$ mice for α CD8/4 depleted, $P < 0.0001$; two independent experiments). (B and C) Viral titers from the OB (B) and remaining cerebrum (C) of isotype control or T cell-depleted mice 8 days after intranasal VSV infection ($n = 4$ mice per group; two independent experiments; $*P = 0.0286$, $**P = 0.008$). Black lines denote means \pm SD. (D) Representative confocal micrographs of sagittal brain sections (see fig. S1B) from an isotype control (left) or T cell-depleted mouse (right) 8 days after intranasal VSV-eGFP infection. (E) Representative confocal micrographs of viral escape from the glomerular layer within T cell-depleted OBs after VSV-eGFP infection. (F) Quantification of VSV-eGFP signal in the forebrain and hindbrains of isotype control or T cell-depleted animals ($n = 8$ per group; three independent experiments; $*P = 0.02$). Black lines denote means \pm SD. (G) Survival curves for VSV-OVA-infected control, antibody-treated mice, and genetically deficient mouse strains ($n = 40$ mice for control; $n = 20$ for $\text{TNF}\alpha^{-/-}$, $P < 0.0021$; $n = 9$ for $\text{IFNAR}^{-/-}$, $P < 0.0001$; $n = 20$ for $\text{IFN}\gamma^{-/-}$, $P = 0.02$; $n = 23$ for $\text{PRF1}^{-/-}$; $P = 0.1039$; data are pooled from six independent experiments). (H) Survival curves for control and floxed $\text{IFN}\gamma\text{R}$ mice infected intranasally with VSV-iCre ($n = 10$ mice for control; $n = 9$ mice for floxed $\text{IFN}\gamma\text{R}$; $P = 0.3657$; two independent experiments).

severely impairs presentation of class I peptides (45). We infected “conditional $\beta_2\text{M}$ ” mice with VSV-iCre to remove the possibility that infected cells engage in direct antigen presentation to CD8^+ T cells. Infection with VSV-iCre resulted in deletion of $\beta_2\text{M}$ from the

genome of infected cells (fig. S4B). However, unexpectedly, VSV-iCre-infected floxed $\beta_2\text{M}$ mice survived intranasal infection at the rate of control animals (Fig. 5I), indicating that the antiviral pressure exerted by CD8^+ T cells, which is required in part for survival, does not involve direct interactions with virus-infected cells.

Microglia within the infected OB are activated and present antigen to CTLs

Microglia are radiation-resistant CNS-resident myeloid cells, and although they are not believed to be potent antigen-presenting cells in the naïve state (46), we characterized the surface expression of antigen-presenting molecules on microglia during VSV infection (Fig. 6, A and B). Six days after VSV infection, microglia in the OB showed evidence of activation characterized by robust up-regulation of MHC I, CD80, and CD86 as well as a very modest increase in CD40 and MHC II relative to naïve microglia (Fig. 6, A and B). These changes in antigen-presenting molecules suggested that microglia were capable of presenting viral antigen to CD8^+ T cells.

We next sought to directly observe in vivo whether microglia were presenting antigen to virus-specific CD8^+ T cells. To accomplish this, we adoptively transferred naïve mTomato^+ GCaMP6s^+ OT-I cells into bone marrow chimeras in which $\text{CX3CR1}^{\text{gfp/+}}$ were reconstituted with wild-type (WT) bone marrow ($99.6 \pm 0.31\%$ blood chimerism). In these chimeras, radioresistant microglia are GFP positive, whereas all peripherally derived hematopoietic cells as well as perivascular and meningeal macrophages are GFP negative. Six days after intranasal infection with VSV-OVA, we used intravital microscopy to identify calcium flux induced by antiviral CD8^+ T cell engagement in the OB (movie S4). We then quantified the frequency of CD8^+ T cell antigen recognition (calcium flux) occurring in contact with microglia versus unlabeled space within the OB. This study revealed that $\sim 72\%$ of CD8^+ T cell calcium flux occurred in contact with a $\text{CX3CR1}^{\text{gfp/+}}$ microglia (Fig. 6, C and D, and movie S4), suggesting that microglia are indeed presenting cognate peptide MHC I complexes to virus-specific T cells. The interaction partner for the remaining CTL calcium flux events ($\sim 28\%$) is not known; however, we noted that the within the OB of the bone

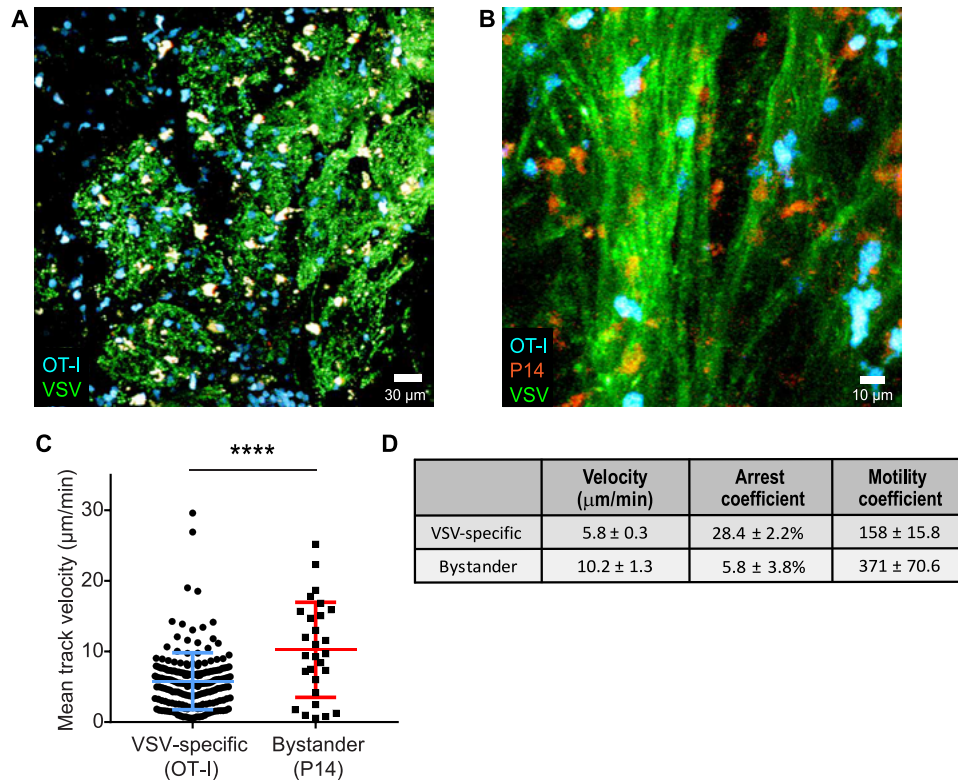


Fig. 4. Antiviral CTLs exhibit decreased motility within the virally infected OB. (A) Representative image from an intravital imaging experiment depicting adoptively transferred virus-specific OT-I T cells (cyan) within the VSV-GFP (green)-infected OB glomerular layer at day 7 after infection. (B) Representative image from a two-photon imaging experiment showing VSV-specific OT-I T cells (blue) and LCMV-specific P14 T cells (red) traveling along VSV-eGFP (green)-infected nerve fibers in the OB outer nerve layer. Mice were coinfecting with VSV-eGFP and VSV-OVA for this experiment. (C) Mean track velocity of VSV-specific OT-I T cells and LCMV-specific P14 T cells in day 7 VSV-infected OB ($n = 4$ mice; 305 OT-I T cells and 57 P14 T cells; **** $P < 0.0001$). Colored horizontal lines denote means \pm SD. (D) Motility analysis comparing average track velocities, arrest coefficients, and motility coefficients for VSV-specific OT-I T cells relative to bystander LCMV-specific P14 T cells within the infected OB at day 7 (from the same experiments as above; $n = 4$ mice; average velocity, $P < 0.0001$; arrest coefficient, $P = 0.003$; motility coefficient, $P < 0.0001$).

marrow chimeras, $23.4 \pm 3.9\%$ of the microglia were nonfluorescent (i.e., donor-derived). These cells might also have induced T cell calcium flux.

Microglia acquire infected OSN debris and orchestrate neuroprotective CTL activity

Our calcium imaging data suggested that microglia play an important role in presenting antigen to antiviral CD8⁺ T cells after VSV neuroinvasion. Neurons are the only known target of VSV after nasal infection; however, we decided to evaluate whether microglia were also infected. We sought evidence for microglia infection in two ways—by inoculating WT mice with VSV-GFP (fig. S5A) and by inoculating Stop^{fl/fl} TdTomato mice with VSV-iCre (fig. S5B). Using either approach, flow cytometric analyses of the OB from infected mice revealed no evidence of microglia infection despite an abundance of virus in CD45-negative cells (presumably neurons) (fig. S5, A and B).

The absence of direct microglia infection led us to investigate alternative mechanisms of antigen acquisition and presentation by microglia. VSV can cause damage to the neurons it infects, and microglia are known to phagocytose cellular debris. We therefore evaluated whether microglia acquired antigen from VSV-infected

OSNs. We labeled OSNs within the OE by injecting fluorescent cholera toxin B (CTB) intranasally into olfactory marker protein-GFP (fig. S5C) or CX3CR1^{gfp/+} mice (Fig. 7A) (47). Ten hours later, after CTB was transported along OSN axons into OB glomeruli (fig. S5C), we infected mice with VSV and, 6 days later, observed evidence of CX3CR1^{gfp/+} cells with intracellular CTB obtained from the labeled OSNs (Fig. 7A). These cells had the morphological characteristics of microglia, and this was confirmed flow cytometrically, which revealed that ~5% of microglia in the OB contained CTB (i.e., OSN debris) 6 days after infection (Fig. 7, B and C). Processing the entire OB for flow cytometry, however, did not allow us to specifically analyze the anatomically relevant microglia in the glomerular layer of the OB, which is where VSV (Fig. 2C) and CTB (fig. S5C) enter via OSN axons. We therefore quantified uptake histochemically, allowing us to focus on this anatomical site. We found 6 days after VSV infection that ~40% of Iba-1⁺ myeloid cells in OB glomeruli contained intracellular CTB derived from OSNs (Fig. 7D). For these studies, CTB served as a surrogate for an OSN-derived antigen. We next wanted to address whether microglia could also acquire virus particles. This was accomplished by infecting mice with VSV-PeGFP—a viral recombinant in which the phosphoprotein (P) is fused to enhanced GFP (eGFP) enabling detection of the virion itself (48). Six days after

infection with VSV-PeGFP, we determined that ~10% of Iba-1⁺ myeloid cells in OB glomeruli contained VSV-PeGFP (Fig. 7E). Collectively, these data indicate that microglia can directly acquire antigens from virally infected OSNs.

Having demonstrated that microglia could acquire OSN-derived antigens *in vivo*, we next asked whether their specific removal affected cognate antigen recognition of virus-specific CD8⁺ T cells in the infected OB. To deplete microglia, we first generated CX3CR1-Cre-ER \times Rosa Stop^{fl/fl} diphtheria toxin receptor (DTR) mice and treated them with tamoxifen to drive DTR expression in myeloid cells. After tamoxifen cessation, we waited an additional 60 days before DT treatment to allow for peripheral monocyte turnover (49). This is a commonly used approach that allows microglial depletion while preserving CX3CR1-expressing monocytes and antiviral T cells. These mice were then seeded with naive mTomato⁺ GCaMP6s⁺ OT-I cells and infected intranasally with VSV-OVA. Six days later, we observed that virus-specific CD8⁺ T cell calcium flux was significantly reduced in the microglia-depleted mice (Fig. 7F), indicating compromised viral antigen presentation when OB microglia but not monocytes were reduced (fig. S6, A and B). Because the microglia depletion efficiency varied between animals, we tested

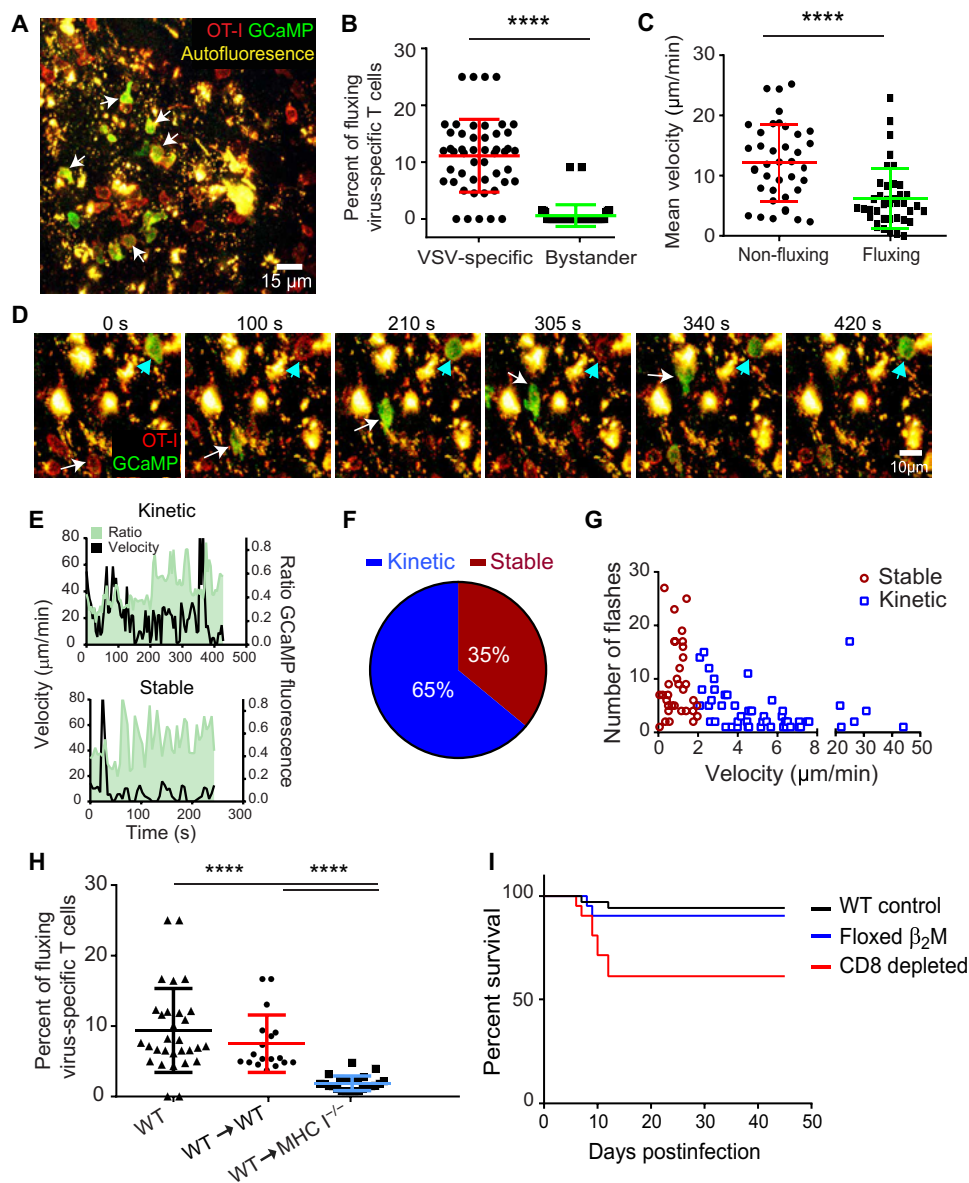


Fig. 5. Antiviral CTLs engage antigen on an uninfected CNS-resident cell type. (A) A representative image from a two-photon imaging experiment shows OT-I mTomato⁺ GfCaMP6s⁺ T cells in day 6 VSV-OVA infected OB. (B) Calcium flux frequency of VSV-specific OT-I mTomato⁺ GfCaMP6s⁺ T cells compared with calcium flux frequency in bystander LCMV-specific P14 mTomato⁺ GfCaMP6s⁺ T cells within VSV-OVA-infected OB (*n* = 4 mice; six time periods sampled per mouse; 24 OT-I T cells, 20 P14 T cells; *****P* < 0.0001). Colored horizontal lines denote means ± SD. (C) Mean velocities of calcium fluxing versus non fluxing OT-I mTomato⁺ GfCaMP6s⁺ T cells within VSV-OVA-infected OB (*n* = 3 mice; 39 OT-I T cells; *****P* < 0.0001). Colored horizontal lines denote means ± SD. (D) A representative time lapse from an intravital imaging experiment shows two different OT-I⁺ mTomato⁺ GfCaMP6s⁺ T cells fluxing calcium (green) upon interaction with autofluorescent cells (yellow) within the VSV-OVA-infected OB at day 6. The white arrow denote a T cell engaged in a kinetic fluxing behavior, whereas the cyan arrowhead denote a stably arrested T cell fluxing calcium. (E) Calcium and motility profiles for representative OT-I kinetic (top, velocity of >2 μm/min) and stable (bottom, <2 μm/min) interactions. (F) Frequency of kinetic and stable calcium flux events in virus-specific OT-I T cells within the OB 6 days after VSV-OVA infection [(*n* = 4 mice; 99 OT-I T cells total: 64 kinetic (>2 μm/min) and 35 stable (<2 μm/min)]. (G) Number of calcium flux events as a function of velocity during kinetic and stable virus-specific OT-I T cells interactions in OB at day 6 (*n* = 4 mice; 99 OT-I T cells total, same as above; *P* = 0.001). (H) Calcium flux frequency of OT-I mTomato⁺ GfCaMP6s⁺ T cells within WT nonchimeric, control bone marrow chimeric, and MHC I-deficient bone marrow chimeric mice (*n* = 4 mice; 6 time points sampled per movie; *****P* < 0.0001). Horizontal lines denote means ± SD. (I) Survival curves for WT (*n* = 33 mice), floxed β₂M (*n* = 19 mice), and αCD8 depleted WT mice (*n* = 13 mice) intranasally infected with VSV-iCre (*P* = 0.0016 for WT versus αCD8, *P* = 0.2825 for WT versus β₂M, *P* = 0.0347 floxed β₂M versus αCD8).

whether there was any relationship between the frequency of CD8⁺ T cell calcium flux and the percentage of microglia remaining in the OB. We observed a strong positive correlation (*r* = 0.75, *P* < 0.0013) between these two variables, further emphasizing the importance of microglia in fostering cognate antigen recognition and calcium flux in antiviral CD8⁺ T cells (Fig. 7G).

Last, we assessed the degree to which microglia contributed to the antiviral defense against an intranasal VSV infection. For this study, we used a more convenient alternative method to deplete microglia. Specifically, C57BL/6J mice were fed chow containing the CSF1R antagonist pexidartinib (PLX3397) for 1 month (50). This treatment decreased the number of microglia in the OB by 66% without reducing the recruitment of CD8⁺ or CD8⁺ OT-I T cells in day 7 VSV-OVA-infected mice (fig. S6). Despite the preservation of CD8⁺ T cells, VSV infection of PLX3397-treated animals resulted in frequent viral escape at day 7 after infection with elevated brain viral titers compared with control animals (Fig. 7H). Moreover, viral escape in PLX3397-treated mice was accompanied by reduced survival (Fig. 7I), which mirrored that observed in mice depleted of CD8⁺ T cells (Fig. 3G). Collectively, these data suggest that microglia can acquire and cross-present locally derived viral antigen to brain-infiltrating CD8⁺ T cells that exert antiviral pressure and contain VSV in the OB.

DISCUSSION

OSNs in the upper airway are responsible for relaying information about airborne odorants, but their contact with circulating air makes them a target for many pathogens. OSN infection provides a direct single-cell route into the CNS that bypasses the BBB and BCSFB. In this study, we sought previously unknown insights into how the propagation of a cytopathic nasal pathogen is thwarted as it enters and attempts to spread throughout the CNS. Nasal VSV infection induced massive leukocyte infiltration into the OE. The virus nevertheless managed to travel via OSN axons through the cribriform plate and into the OB. Within the OB, fate-mapping studies revealed that VSV was controlled noncytolytically

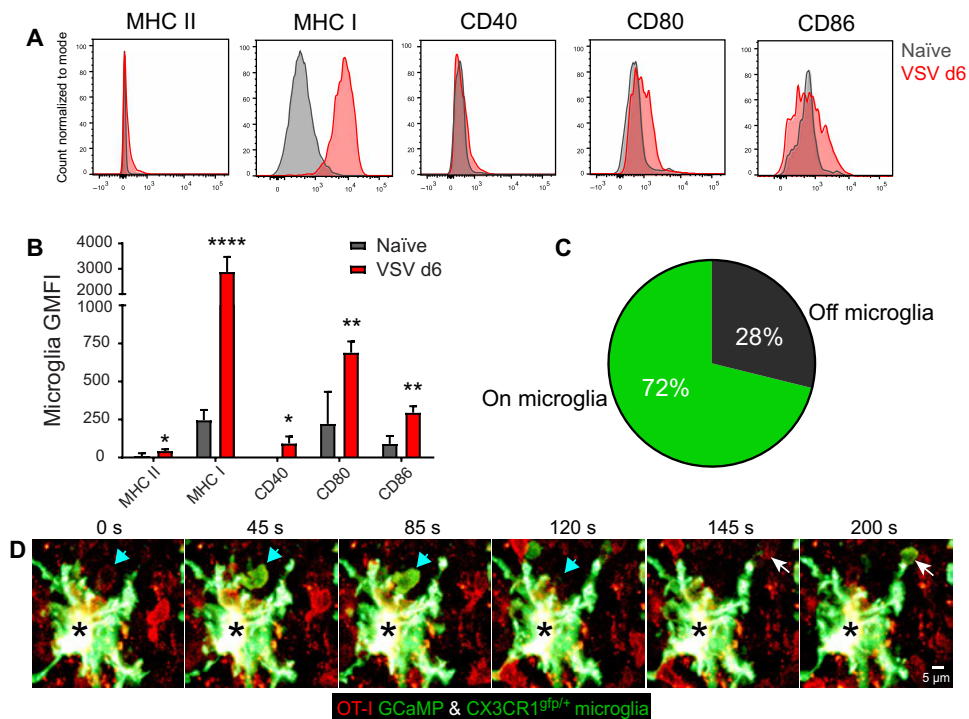


Fig. 6. Microglia elicit antigen-specific calcium flux from antiviral CTLs. (A) Representative flow cytometric histograms of OB microglia show surface molecule expression 6 days after VSV infection (red) compared with naïve OB microglia (gray). Microglia were defined as Thy1.2⁺, CD11b⁺, Ly6G⁻, and CD45int. (B) Quantification of surface molecule geometric mean fluorescent intensity (GMFI) on OB microglia 6 days after VSV infection versus naïve OB microglia. GMFI data for each surface marker are plotted as the means \pm SD after subtracting the isotype control antibody GMFI ($n = 4$ mice per group; two independent experiments; * $P < 0.05$, ** $P < 0.01$, **** $P < 0.0001$). (C) Pie chart representing the frequency of all VSV-specific OT-I T cell calcium flux events observed by TPM in contact or not in contact with CX3CR1^{9fp/+} OB microglia in day 6 after VSV-OVA-infected bone marrow chimeric mice (i.e., CX3CR1^{9fp/+} mice with C57BL/6J bone marrow) ($n = 5$ mice; 9 movies; 61 time points; four independent experiments; $P < 0.0001$). (D) A representative time lapse from a two-photon imaging experiment shows an OT-I mTomato⁺ GCaMP6s⁺ T cells in a day 6 VSA-OVA-infected CX3CR1^{9fp/+} bone marrow chimera. Arrows (white and cyan) denote two virus-specific OT-I T cells fluxing calcium upon engagement of a single CX3CR1^{9fp/+} microglia (black asterisks) in the infected OB.

after infecting neurons in glomeruli as well as deeper neuronal layers. This containment depended in part on antiviral T cells and a combination of effector molecules (perforin, IFN γ , TNF α). However, specific removal of MHC I from virus-infected cells using floxed β_2 M mice demonstrated that direct engagement of neurons by CD8⁺ T cells was not required for viral control. This unexpected observation led us to perform intravital imaging studies of cognate antigen recognition by virus-specific CD8⁺ T cells in infected glomeruli. These studies revealed that microglia displayed cognate peptide-MHC I, promoting CTL antigen recognition and calcium flux. Microglia were not infected by VSV but instead acquired antigen from adjacent neurons, which was then cross-presented to the infiltrating virus-specific CTLs. These interactions were functionally important, because microglia depletion markedly reduced cognate antigen recognition by CTLs, impeding viral containment within the OB and promoting the development of fatal encephalitis.

After nasal inoculation, virus is rapidly transported from the airway via the OSNs into the CNS where it is seen primarily within the OB. Viral replication is usually halted at the OSN-glomerular junction (10). Previous studies have shown that T cells play an important role in the control and clearance of VSV after CNS infection (29, 35). In

addition, IFN γ , TNF α , interleukin-12, and nitric oxide synthase 1 were all shown to participate in the antiviral defense against VSV (51–55), yet it is presently unclear how T cell effector functions are regulated in the CNS. Regulation of T cell effector functions is important because adult neurogenesis is reserved for specialized compartments [such as the OE (56, 57)]; thus, when neurons are lost in the CNS during adulthood, they typically are not replaced. Because of this, it is postulated that the CNS favors the use of noncytolytic viral clearance—a well-described cytokine-mediated mechanism of eradicating an intracellular pathogen without killing the cell (18, 58). Cytokines such as IFN γ , TNF α , and IFN-I are all capable of purging viruses noncytolytically, and this mode of viral clearance has been described for many different pathogens, including hepatitis B virus (59), LCMV (60, 61), influenza virus (62, 63), MHV (64), and Sindis virus (65).

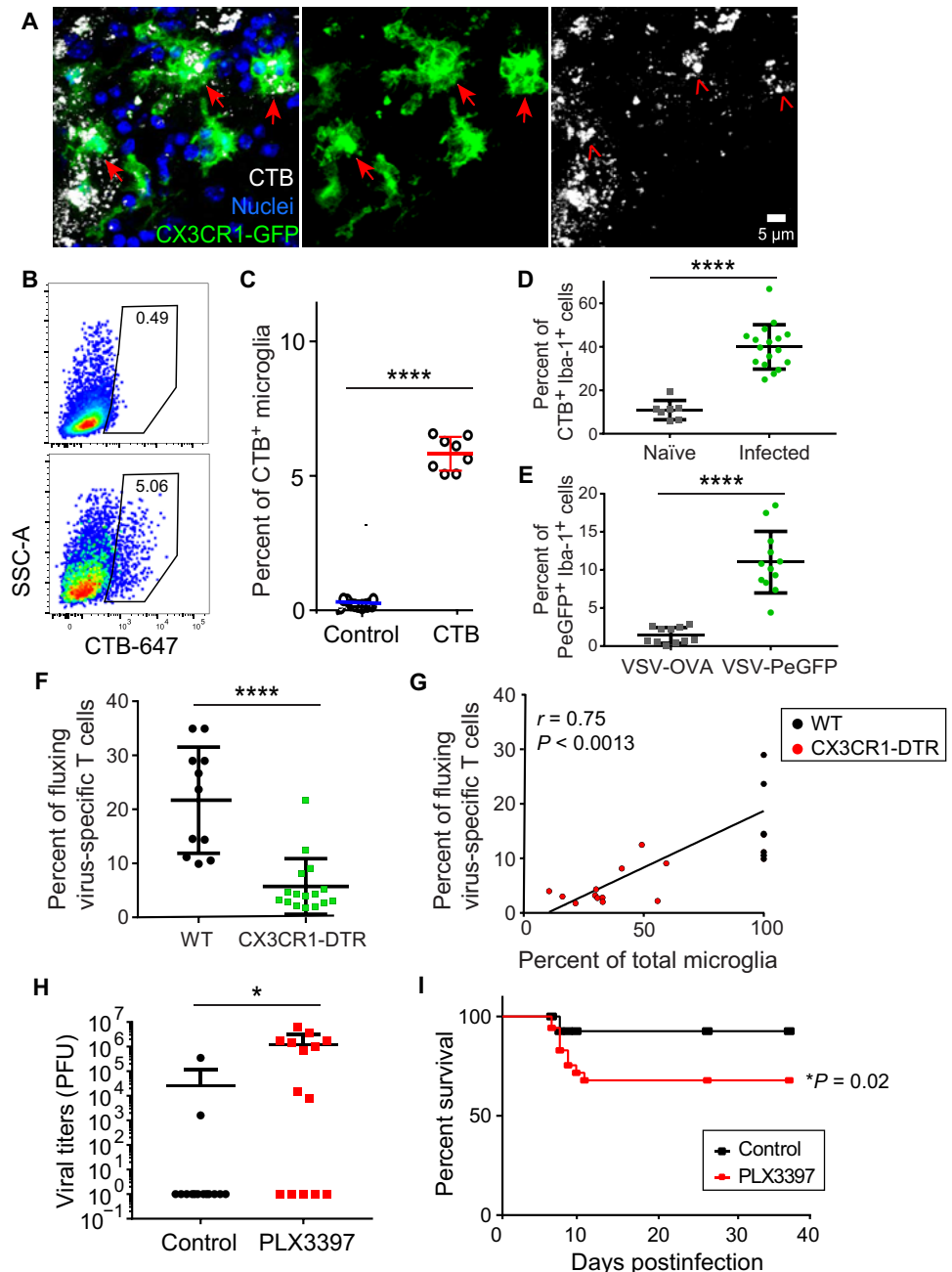
VSV is a cytopathic pathogen that is highly lytic in vitro (66); however, its interaction with the CNS appears to be more nuanced, as mice infected with VSV can sometimes harbor virus for several weeks before succumbing (Fig. 3A). Although we cannot exclude a role for CTLs using cytolytic effector molecules like perforin to control this virus (Fig. 3G), our fate mapping studies in VSV-iCre-infected Stop^{fl/fl} TdTomato reporter mice revealed ample evidence of previously infected OB neurons that were cleared

noncytolytically. These results are consistent with a previous study showing that neurotropic MHV can be noncytolytically cleared from OB interneurons after infection (64). Antiviral cytokines like IFN γ and TNF α are known to play a direct role in noncytolytic viral clearance from the CNS (8, 9, 65) and peripheral tissues (18, 19, 60). We observed that both IFN γ - and TNF α -deficient mice have impaired survival after intranasal VSV infection, which is consistent with studies showing an important role for these cytokines in controlling other CNS infections. For example, IFN γ is known to help control measles virus (14), herpes virus (16), MHV (67), Borna virus (68), and recombinant vaccinia virus (69), whereas TNF α has a protective role against West Nile virus (WNV) (70), JEV (71), tick-borne encephalitis virus (72), and HSV (73). In our study, VSV-iCre allowed us to distinguish the direct effects of IFN γ on infected cells from other potential functions exerted by this cytokine, such as the activation and recruitment of immune cells (74–76). We observed that IFN γ R expression by infected cells plays no direct antiviral role in mediating survival after intranasal VSV inoculation. Whether TNF receptor is required on infected cells in this model is presently unclear.

MHC I is important for different phases of normal brain development and for controlling ongoing plasticity (77, 78). However,

Fig. 7. Microglia acquire and present antigen from virus-infected neurons to drive protective antiviral CTL responses. (A) Representative confocal micrographs of OB microglia (green) containing fragments of OSNs labeled with CTB (white) 10 hours before VSV infection. Images were captured at day 6 after infection. (B) Representative fluorescence-activated cell sorting plots of microglia (Thy1.2⁺, Cd11b⁺, Ly6C/G⁺, and CD45int) from CTB-treated control (top) or day 6 VSV-infected mice (bottom).

(C) Quantification of CTB containing microglia frequencies. Values are normalized to VSV-infected mice without CTB to control for autofluorescence (7 mice per group; two independent experiments; **** $P < 0.001$). Horizontal lines denote means \pm SD. (D) Frequency of microglia containing CTB within the OB glomerular layer of day 6 VSV-infected mice as determined by quantification of confocal images. Values are normalized to VSV-infected mice without CTB to control for autofluorescence ($n = 4$ mice per group; $n = 17$ fields for day 6, seven fields for naïve; **** $P < 0.001$). Horizontal lines denote means \pm SD. (E) Frequency of GFP⁺ microglia within the OB glomerular layer 6 days after VSV-PeGFP infection as determined by quantification of confocal images. Nonfluorescent VSV-OVA was used as a control ($n = 3$ mice per group; $n = 12$ fields for VSV-PeGFP, $n = 11$ fields for VSV-OVA; **** $P < 0.0001$). Horizontal lines denote means \pm SD. (F) Intravital calcium flux frequency of VSV-specific OT-I mTomato⁺ GCaMP6s⁺ T cells in WT control versus CX3CR1-CreER x ROSA Stop^{fl/fl} DTR microglia-depleted mice on day 6 after VSV-OVA infection ($n = 6$ control mice per group, 11 movies; $n = 7$ microglia-depleted mice per group, 16 movies; **** $P < 0.001$). Horizontal lines denote means \pm SD. (G) Calcium flux frequency of VSV-specific OT-I mTomato⁺ GCaMP6s⁺ T cells in control or CX3CR1-CreER x ROSA Stop^{fl/fl} DTR microglia-depleted animals as a function of microglia depletion efficiency (Pearson's $r = 0.753$, $P < 0.0013$). (H) Viral titers in the brains of control versus PLX3397-treated animals on day 7 after VSV infection (14 mice per group from three pooled independent experiments; * $P = 0.0265$). Horizontal lines denote means \pm SD. (I) Survival curve for control versus PLX3397-treated VSV-infected mice ($n = 36$ mice for control; $n = 35$ mice for PLX3397; $P = 0.0201$).



MHC I expression is often undetectable on most CNS neurons (43, 44, 79), and its ability to engage in physiologically relevant levels of antigen presentation is a source of continued debate. The classical paradigm suggests that activated CTLs enter virally infected tissues and recognize cognate viral peptides presented in MHC I molecules displayed on the infected cell surface. After some viral infections, neuronal MHC I does appear to play a role in containing virus through CTL pressure, and these interactions can facilitate release of immune effector molecules and eventual neuronal damage (80). During HSV infection, CTL-derived IFN γ is believed to contribute to noncytolytic maintenance of viral latency within infected neurons (16, 81). In addition, perforin and granzyme B also participate in the noncytolytic control of this virus in neurons by degrad-

ing the HSV-1 immediate early protein (82). By contrast, CNS neurons infected by WNV are believed to be targeted directly by CTLs that use perforin-mediated cytolytic mechanisms to purge virally infected neurons (83). It is presently unclear why some CTL engagements of infected neurons result in cytopathology, whereas others do not. This could be linked to the amount of MHC I expressed by different neuronal subtypes.

Although CTLs have the capacity to engage at least some virus-infected neuronal populations, our results in VSV-iCre-infected floxed β_2M mice demonstrate that MHC I expression on infected neurons does not play a role in protecting mice from fatal encephalitis (Fig. 5I). CTLs are, however, important in preventing fatal disease after intranasal VSV infection (Fig. 5I), and our intravital imaging

studies of cognate antigen recognition by antiviral CTLs in the OB uncovered that microglia served as the target of at least 70% of these interactions. This was especially unexpected because we found no evidence, using two sensitive methods, that microglia were infected by VSV (fig. S5A and B). These results suggested that microglia were, in fact, acquiring antigen from adjacent neurons and cross-presenting the material via MHC I to CTLs. This conclusion is supported by our data showing that microglia within the OB engulfed the neuronal tracer CTB and fluorescent protein–tagged VSV particles—a process that supplies potentially cross-presentable MHC I antigen. Cross-presentation is thought to be important during naïve CTLs priming within secondary lymphoid organs; however, it can also occur in peripheral tissues, particularly tumors (84). In addition, both neonatal and adult microglia were previously shown to cross-present exogenous antigen (85), demonstrating that these cells do indeed have the capacity to cross-present.

Recent studies have begun to shed light on the roles microglia play in host defense and immunopathology after CNS virus infection (86–93). Depletion studies have revealed that microglia participate in the antiviral defense against pseudorabies virus (88), JEV (87), MHV (89), Theiler's murine encephalomyelitis virus (90), VSV (91), and WNV (87, 92). For example, Wheeler *et al.* (89) found that many microglia-depleted mice fail to control MHV, resulting in compromised survival after intracerebral infection. This study also noted that microglia-depleted animals had impaired CD4⁺ T cell accumulation and function within the CNS. This is noteworthy because unlike microglia from VSV-infected brains (Fig. 6A) (94), MHV infection induces a marked up-regulation of MHC II on microglia. These two models of virus infection appear to showcase an important functional divergence in the ability of microglia to support either MHC I- or MHC II-restricted T cell responses in the virally infected CNS. The importance of separating MHC I and II presentation to effector T cells in the CNS is not known; however, this is the case after VSV infection, because OB-infiltrating myeloid cells express very high levels of MHC II, whereas microglia do not (94).

Although we did not focus on virus-specific CD4⁺ T cell interactions in this study, our findings demonstrate a role for cross-presenting microglia in displaying cognate peptide–MHC I complexes to CTLs. We had intended to provide a more direct role for MHC I expression on microglia by conditionally deleting β_2M from these cells. However, VSV infection of CX3CR1-Cre-ER \times floxed β_2M mice resulted in near-complete NK cell-mediated deletion of the MHC I class negative microglia similar to what was described previously in inflamed floxed β_2M mice (95). Nevertheless, our intravital imaging studies revealed that microglia supported most of the CTL calcium flux activity in the OB, and cognate antigen recognition was markedly reduced in their absence. CTL calcium flux in the infected OB correlated positively with the number of microglia remaining in depleted mice. In addition, microglia depletion promoted both viral escape into the brain and increased the incidence of fatal encephalitis. Antigen presentation by uninfected microglia to infiltrating CTLs is likely a mechanism the CNS uses to elicit antiviral activity but protect neurons from direct CTL contact and potential lysis. It is also important to note that most CTL interactions with microglia were short lived (kinetic) rather than stable. It is postulated that these short-lived interactions favor CTL usage of antiviral molecules (e.g., cytokines) rather than killing behavior (42). This would provide a mechanism to control virus in adjacent neurons without engaging them.

In conclusion, this study relied on intravital microscopy to analyze cognate antigen recognition by CTLs as a nasal virus attempted to enter the brain via infection of the peripheral nervous system (i.e., OSNs). Because VSV primarily infects neurons, it was unclear how CTLs would exert their antiviral pressure on a cell population that expresses little to no MHC I. However, our studies uncovered cross-presenting microglia as the main innate immune cell type responsible for driving protective, noncytolytic CTL responses against a cytopathic CNS viral infection. These findings have important implications for our understanding of antiviral immunity, because they indicate that microglia need not be infected to present antigen on MHC I and participate in the eradication of virus from neurons. Evolutionarily, it makes sense for microglia to serve as an intermediary in the defense against a neuronal infection. Microglia are a renewable cell population, whereas most neurons are not. We therefore postulate that the CNS is designed to minimize direct engagement of infected neurons by CTLs and favor release of noncytolytic antiviral cytokines through interactions with cross-presenting intermediaries. Microglia play an important role in synaptic pruning and CNS homeostasis, and their proximity to neurons makes them an ideal candidate for this task. Given the role of microglia in cross-presenting viral antigen, factors that result in their distraction or depletion are likely to render the CNS more susceptible to infection.

MATERIALS AND METHODS

Mice

C57BL/6J (B6), B6.129(Cg)-Gt(ROSA)26Sor^{tm4}(ACTB-tdTomato,-EGFP)^{Luo}/J (mTomato), C57BL/6-Tg(TcraTcrb)1100Mjb/J (OT-I), C57BL/6-Prfl^{tm1Sdz}/J (PRF^{-/-}), B6.Cg-Gt(ROSA)26Sor^{tm14}(CAG-tdTomato)Hze/J (Stop^{fl/fl} TdTomato), B6.129P2(Cg)-Cx3cr1^{tm2.1}(cre/ERT2)^{Litt}/WganJ (CX3CR1-Cre-ER), C57BL/6-Gt(ROSA)26Sor^{tm1}(HBEGF)^{Awai}/J (ROSA Stop^{fl/fl} DTR), C57BL/6N-Ifngr1^{tm1.1Rds}/J (IFNR^{fl/fl}) B6.129P-Cx3cr1^{tm1Litt}/J (CX3CR1^{gfp/gfp}), B6.129S7-Ifng^{tm1Ts}/J (IFN^{-/-}), and B6.129S-Tnf^{tm1Gkl}/J (TNF α ^{-/-}) mice were purchased from the Jackson Laboratory and either used or bred in house. F1 crosses were made between CX3CR1-Cre-ER and ROSA Stop^{fl/fl} DTR mice as well as B6 and CX3CR1^{gfp/gfp} mice. H-2K^bD^{b/-/-} (96), IFNAR^{-/-} (32) (provided by Jonathan Sprent, formerly at The Scripps Research Institute), P14 (37), OFP⁺ P14 (97), mTomato⁺ P14, mTomato⁺ GCaMP6s⁺ P14, mCerulean⁺ OT-I (97), mTomato⁺ OT-I, CD45.1, and actin-GCaMP6s mTomato OT-I (13) and were bred and maintained under specific pathogen-free conditions at the National Institutes of Health (NIH). OMP-GFP (98) mice were provided by Leo Belluscio, NINDS, and backcrossed onto a C57BL/6J background. All mice in this study were handled in accordance with the guidelines set forth by the NIH Animal Care and Use Committee.

Viruses and plaque assays

LCMV, VSV-OVA serotype Indiana (provided by Leo Lefrancois, formerly at the University of Connecticut) (99), VSV-eGFP (100), VSV-DsRed, VSV-iCre, and VSV-PeGFP (48) were propagated on BHK21 cells. Infectivity of VSV preparations was quantified by plaque assay on green monkey kidney cells (Vero). VSV titers from brains of infected mice were determined similarly. Briefly, animals were perfused with saline, brains were immersed in 1 ml of 2% FBS RPMI containing zirconia silica beads and homogenized with a FastPrep 24-5G (MP Biomedical). Homogenates were spun for 3 min at 15,000g, and supernatants were serially diluted for quantification

on Vero cells. One-hundred microliters of diluted homogenate was added to Vero monolayers in flat bottom 24-well plates and incubated for ~3 hours. One-hundred microliters of 0.75% methylcellulose in DMEM (containing 10% FBS, 1% glutamine, and 1% Pen/Strep) were added to each well and incubated for 44 to 48 hours at 37°C in a 5% CO₂ incubator. Cells were subsequently fixed with 4% neutral buffered formalin and stained with crystal violet, and plaques were enumerated.

VSV-iCre generation

The pFL-VSVBsiWI plasmid (48) was modified with insertion of Ova-IRES-iCre (101) sequence (pFL-VSV-Ova-IRES-iCre) flanked by BsiWI site at G-L junction of the plasmid. The recombinant VSV expressing OVA and iCre recombinase was recovered by co-transfection of full-length plasmids along with supporting plasmids pN, pP, and pL (carrying the coding sequences of the N, P, and L proteins of VSV) in BHK-21 cells as per the protocol published earlier (48). The recombinant virus (rVSV-OVA-iCre) was plaque purified and viral stocks were prepared using BHK-21 cells. Lastly, a Western blot was performed to confirm expression of Ova and iCre proteins in cell lysates from BHK-21 cells infected with rVSV-OVA-iCre.

Infections

Eight- to 10-week-old mice were infected intranasally by injecting 10 µL of viral diluent in each nostril. For survival, titering, immunohistochemical, flow cytometric, and microarray experiments, mice were infected with 1×10^5 PFU of VSV per nostril. For intravital imaging experiments, mice were infected with 4×10^5 PFU per nostril to ensure more uniform OB infection. For experiments involving LCMV, mice were infected i.p. with 2×10^5 PFU of LCMV Armstrong.

Transgenic mouse generation

Floxed beta-2 microglobulin (β_2M) knock-in mice (floxed β_2M) were generated by Cyagen Biosciences. Homology arms were derived from BAC clones RP23-285J7 and RP23-299B11 from the C57BL/6 library and LoxP sites were inserted into genomic positions flanking exons 2 and 3 of the beta microglobulin gene (fig. S4). Homologous recombination was performed in C57BL/6 ES cells before transfer into C57BL/6 embryos. Positive founder lines were backcrossed one additional generation onto the C57BL/6J background before intercrossing.

SUPPLEMENTARY MATERIALS

immunology.sciencemag.org/cgi/content/full/5/48/eabb1817/DC1

Materials and Methods

Fig. S1. Diagrams of sectioning planes through the mouse head.

Fig. S2. Parenchymal cells within the OB and brain survive VSV infection after intranasal inoculation.

Fig. S3. Virus-specific CTLs flux calcium for longer durations while undergoing stable interactions.

Fig. S4. Generation of floxed β_2M transgenic mice.

Fig. S5. VSV does not infect microglia and CTB traffics from OSNs to OB glomeruli.

Fig. S6. Quantification of microglia and infiltrating cells in the OB using different microglia depletion methods.

Movie S1. Virus-specific CTLs rapidly migrate across VSV infected axon tracts within the infected outer nerve layer.

Movie S2. Virus-specific CTLs survey the infected glomerular layer with the OB.

Movie S3. Antiviral CTLs engage cognate antigen and flux calcium within the infected OB.

Movie S4. Antiviral CTLs flux calcium upon contact with microglia.

References (102, 103)

[View/request a protocol for this paper from Bio-protocol.](#)

REFERENCES AND NOTES

- P. A. Swanson II, D. B. McGavern, Viral diseases of the central nervous system. *Curr. Opin. Virol.* **11**, 44–54 (2015).
- K. L. Tyler, Acute Viral Encephalitis. *N. Engl. J. Med.* **379**, 557–566 (2018).
- J. V. Forrester, P. G. McMenamin, S. J. Dando, CNS infection and immune privilege. *Nat. Rev. Neurosci.* **19**, 655–671 (2018).
- D. B. McGavern, S. S. Kang, Illuminating viral infections in the nervous system. *Nat. Rev. Immunol.* **11**, 318–329 (2011).
- A. W. Barrios, G. Nunez, P. Sanchez Quinteiro, I. Salazar, Anatomy, histochemistry, and immunohistochemistry of the olfactory subsystems in mice. *Front. Neuroanat.* **8**, 63 (2014).
- D. van Riel, R. Verdijk, T. Kuiken, The olfactory nerve: A shortcut for influenza and other viral diseases into the central nervous system. *J. Pathol.* **235**, 277–287 (2015).
- I. Mori, Y. Nishiyama, T. Yokochi, Y. Kimura, Olfactory transmission of neurotropic viruses. *J. Neurovirol.* **11**, 129–137 (2005).
- G. K. Binder, D. E. Griffin, Interferon-gamma-mediated site-specific clearance of alphavirus from CNS neurons. *Science* **293**, 303–306 (2001).
- R. Burdeinick-Kerr, D. Govindarajan, D. E. Griffin, Noncytolytic clearance of sindbis virus infection from neurons by gamma interferon is dependent on Jak/STAT signaling. *J. Virol.* **83**, 3429–3435 (2009).
- C. N. Detje, T. Meyer, H. Schmidt, D. Kreuz, J. K. Rose, I. Bechmann, M. Prinz, U. Kalinke, Local type I IFN receptor signaling protects against virus spread within the central nervous system. *J. Immunol.* **182**, 2297–2304 (2009).
- F. McNab, K. Mayer-Barber, A. Sher, A. Wack, A. O'Garra, Type I interferons in infectious disease. *Nat. Rev. Immunol.* **15**, 87–103 (2015).
- J. Crouse, U. Kalinke, A. Oxenius, Regulation of antiviral T cell responses by type I interferons. *Nat. Rev. Immunol.* **15**, 231–242 (2015).
- E. A. Moseman, T. Wu, J. C. de la Torre, P. L. Schwartzberg, D. B. McGavern, Type I interferon suppresses virus-specific B cell responses by modulating CD8^T cell differentiation. *Sci. Immunol.* **1**, eaah3565 (2016).
- C. E. Patterson, D. M. P. Lawrence, L. A. Echols, G. F. Rall, Immune-mediated protection from measles virus-induced central nervous system disease is noncytolytic and gamma interferon dependent. *J. Virol.* **76**, 4497–4506 (2002).
- A. Tishon, H. Lewicki, A. Andaya, D. McGavern, L. Martin, M. B. A. Oldstone, CD4 T cell control primary measles virus infection of the CNS: Regulation is dependent on combined activity with either CD8 T cells or with B cells: CD4, CD8 or B cells alone are ineffective. *Virology* **347**, 234–245 (2006).
- T. Liu, K. M. Khanna, B. N. Carriere, R. L. Hendricks, Gamma interferon can prevent herpes simplex virus type 1 reactivation from latency in sensory neurons. *J. Virol.* **75**, 11178–11184 (2001).
- E. M. Cantin, D. R. Hinton, J. Chen, H. Openshaw, Gamma interferon expression during acute and latent nervous system infection by herpes simplex virus type 1. *J. Virol.* **69**, 4898–4905 (1995).
- L. G. Guidotti, F. V. Chisari, Noncytolytic control of viral infections by the innate and adaptive immune response. *Annu. Rev. Immunol.* **19**, 65–91 (2001).
- P. N. Gilles, G. Fey, F. V. Chisari, Tumor necrosis factor alpha negatively regulates hepatitis B virus gene expression in transgenic mice. *J. Virol.* **66**, 3955–3960 (1992).
- H. Lauterbach, E. I. Zuniga, P. Truong, M. B. Oldstone, D. B. McGavern, Adoptive immunotherapy induces CNS dendritic cell recruitment and antigen presentation during clearance of a persistent viral infection. *J. Exp. Med.* **203**, 1963–1975 (2006).
- B. Lundh, K. Kristensson, E. Norrby, Selective infections of olfactory and respiratory epithelium by vesicular stomatitis and Sendai viruses. *Neuropathol. Appl. Neurobiol.* **13**, 111–122 (1987).
- M. Shivkumar, R. Milho, J. S. May, M. P. Nicoll, S. Efstathiou, P. G. Stevenson, Herpes simplex virus 1 targets the murine olfactory neuroepithelium for host entry. *J. Virol.* **87**, 10477–10488 (2013).
- E. M. Barnett, S. Perlman, The olfactory nerve and not the trigeminal nerve is the major site of CNS entry for mouse hepatitis virus, strain JHM. *Virology* **194**, 185–191 (1993).
- I. Mori, T. Komatsu, K. Takeuchi, K. Nakakuki, M. Sudo, Y. Kimura, Parainfluenza virus type 1 infects olfactory neurons and establishes long-term persistence in the nerve tissue. *J. Gen. Virol.* **76**, 1251–1254 (1995).
- S. L. Park, Y.-J. S. Huang, A. C. Lyons, V. B. Ayers, S. M. Hettenbach, D. S. McVey, K. R. Burton, S. Higgs, D. L. Vanlandingham, North American domestic pigs are susceptible to experimental infection with Japanese encephalitis virus. *Sci. Rep.* **8**, 7951 (2018).
- I. Mori, F. Goshima, Y. Imai, S. Kohsaka, T. Sugiyama, T. Yoshida, T. Yokochi, Y. Nishiyama, Y. Kimura, Olfactory receptor neurons prevent dissemination of neurovirulent influenza A virus into the brain by undergoing virus-induced apoptosis. *J. Gen. Virol.* **83**, 2109–2116 (2002).
- J. M. van den Brand, K. J. Stittelaar, G. van Amerongen, L. Reperant, L. de Waal, A. D. Osterhaus, T. Kuiken, Comparison of temporal and spatial dynamics of seasonal H3N2, pandemic H1N1 and highly pathogenic avian influenza H5N1 virus infections in ferrets. *PLOS ONE* **7**, e42343 (2012).

28. E. J. Schrauwen, S. Herfst, L. M. Leijten, P. van Run, T. M. Bestebroer, M. Linster, R. Bodewes, J. H. Kreijtz, G. F. Rimmelzwaan, A. D. Osterhaus, R. A. Fouchier, T. Kuiken, D. van Riel, The multibasic cleavage site in H5N1 virus is critical for systemic spread along the olfactory and hematogenous routes in ferrets. *J. Virol.* **86**, 3975–3984 (2012).
29. B. S. Huneycutt, Z. Bi, C. J. Aoki, C. S. Reiss, Central neuropathogenesis of vesicular stomatitis virus infection of immunodeficient mice. *J. Virol.* **67**, 6698–6706 (1993).
30. C. S. Reiss, I. V. Plakhov, T. Komatsu, Viral replication in olfactory receptor neurons and entry into the olfactory bulb and brain. *Ann. N. Y. Acad. Sci.* **855**, 751–761 (1998).
31. T. E. Cornish, D. E. Stallknecht, C. C. Brown, B. S. Seal, E. W. Howerth, Pathogenesis of experimental vesicular stomatitis virus (New Jersey serotype) infection in the deer mouse (*Peromyscus maniculatus*). *Vet. Pathol.* **38**, 396–406 (2001).
32. U. Müller, U. Steinhoff, L. F. Reis, S. Hemmi, J. Pavlovic, R. M. Zinkernagel, M. Aguet, Functional role of type I and type II interferons in antiviral defense. *Science* **264**, 1918–1921 (1994).
33. U. Steinhoff, U. Müller, A. Schertler, H. Hengartner, M. Aguet, R. M. Zinkernagel, Antiviral protection by vesicular stomatitis virus-specific antibodies in alpha/beta interferon receptor-deficient mice. *J. Virol.* **69**, 2153–2158 (1995).
34. E. A. Moseman, M. Iannacone, L. Bosurgi, E. Tonti, N. Chevrier, A. Tumanov, Y.-X. Fu, N. Hacohen, U. H. von Andrian, B cell maintenance of subcapsular sinus macrophages protects against a fatal viral infection independent of adaptive immunity. *Immunity* **36**, 415–426 (2012).
35. C. S. Reiss, C. Aoki, Vesicular stomatitis virus: Immune recognition, responsiveness, and pathogenesis of infection in mice. *Rev. Med. Virol.* **4**, 129–140 (1994).
36. D. E. Griffin, T. Metcalf, Clearance of virus infection from the CNS. *Curr. Opin. Immunol.* **1**, 216–221 (2011).
37. H. Pircher, K. Bürki, R. Lang, H. Hengartner, R. M. Zinkernagel, Tolerance induction in double specific T-cell receptor transgenic mice varies with antigen. *Nature* **342**, 559–561 (1989).
38. G. Yang, F. Pan, C. N. Parkhurst, J. Grutzendler, W.-B. Gan, Thinned-skull cranial window technique for long-term imaging of the cortex in live mice. *Nat. Protoc.* **5**, 201–208 (2010).
39. M. Manglani, D. B. McGavern, Intravital imaging of neuroimmune interactions through a thinned skull. *Curr. Protoc. Immunol.* **120**, 24.2.21–24.2.12 (2018).
40. H. D. Moreau, F. Lemaître, K. R. Garrod, Z. Garcia, A.-M. Lennon-Dumenil, P. Bouso, Signal strength regulates antigen-mediated T-cell deceleration by distinct mechanisms to promote local exploration or arrest. *Proc. Natl. Acad. Sci. U.S.A.* **112**, 12151–12156 (2015).
41. M. Oh-hora, A. Rao, Calcium signaling in lymphocytes. *Curr. Opin. Immunol.* **20**, 250–258 (2008).
42. D. R. Fooksman, S. Vardhana, G. Vasiliver-Shamis, J. Liese, D. A. Blair, J. Waite, C. Sacristán, G. D. Vitoria, A. Zanin-Zhorov, M. L. Dustin, Functional anatomy of T cell activation and synapse formation. *Annu. Rev. Immunol.* **28**, 79–105 (2010).
43. E. Joly, L. Mucke, M. B. Oldstone, Viral persistence in neurons explained by lack of major histocompatibility class I expression. *Science* **253**, 1283–1285 (1991).
44. E. Joly, M. B. Oldstone, Neuronal cells are deficient in loading peptides onto MHC class I molecules. *Neuron* **8**, 1185–1190 (1992).
45. B. H. Koller, P. Marrack, J. W. Kappler, O. Smithies, Normal development of mice deficient in beta 2M, MHC class I proteins, and CD8⁺ T cells. *Science* **248**, 1227–1230 (1990).
46. D. Nayak, T. L. Roth, D. B. McGavern, Microglia development and function. *Annu. Rev. Immunol.* **32**, 367–402 (2014).
47. F. W. van Ginkel, R. J. Jackson, Y. Yuki, J. R. McGhee, Cutting edge: The mucosal adjuvant cholera toxin redirects vaccine proteins into olfactory tissues. *J. Immunol.* **165**, 4778–4782 (2000).
48. S. C. Das, D. Nayak, Y. Zhou, A. K. Pattnaik, Visualization of intracellular transport of vesicular stomatitis virus nucleocapsids in living cells. *J. Virol.* **80**, 6368–6377 (2006).
49. C. N. Parkhurst, G. Yang, I. Ninan, J. N. Savas, J. R. Yates III, J. J. Lafaille, B. L. Hempstead, D. R. Littman, W.-B. Gan, Microglia promote learning-dependent synapse formation through brain-derived neurotrophic factor. *Cell* **155**, 1596–1609 (2013).
50. M. R. Elmore, A. R. Najafi, M. A. Koike, N. N. Dagher, E. E. Spangenberg, R. A. Rice, M. Kitazawa, B. Matusow, H. Nguyen, B. L. West, K. N. Green, Colony-stimulating factor 1 receptor signaling is necessary for microglia viability, unmasking a microglia progenitor cell in the adult brain. *Neuron* **82**, 380–397 (2014).
51. Z. Bi, M. Barna, T. Komatsu, C. S. Reiss, Vesicular stomatitis virus infection of the central nervous system activates both innate and acquired immunity. *J. Virol.* **69**, 6466–6472 (1995).
52. Z. Bi, C. S. Reiss, Inhibition of vesicular stomatitis virus infection by nitric oxide. *J. Virol.* **69**, 2208–2213 (1995).
53. T. Komatsu, D. D. Ireland, N. Chen, C. S. Reiss, Neuronal expression of NOS-1 is required for host recovery from viral encephalitis. *Virology* **258**, 389–395 (1999).
54. T. Komatsu, Z. Bi, C. S. Reiss, Interferon- γ induced type I nitric oxide synthase activity inhibits viral replication in neurons. *J. Neuroimmunol.* **68**, 101–108 (1996).
55. T. Komatsu, M. Barna, C. S. Reiss, Interleukin-12 promotes recovery from viral encephalitis. *Viral Immunol.* **10**, 35–47 (1997).
56. C. T. Leung, P. A. Coulombe, R. R. Reed, Contribution of olfactory neural stem cells to tissue maintenance and regeneration. *Nat. Neurosci.* **10**, 720–726 (2007).
57. J. E. Schwob, Neural regeneration and the peripheral olfactory system. *Anat. Rec.* **269**, 33–49 (2002).
58. L. G. Guidotti, F. V. Chisari, Cytokine-induced viral purging—role in viral pathogenesis. *Curr. Opin. Microbiol.* **2**, 388–391 (1999).
59. L. G. Guidotti, R. Rochford, J. Chung, M. Shapiro, R. Purcell, F. V. Chisari, Viral clearance without destruction of infected cells during acute HBV infection. *Science* **284**, 825–829 (1999).
60. L. G. Guidotti, P. Borrow, A. Brown, H. McClary, R. Koch, F. V. Chisari, Noncytotoxic clearance of lymphocytic choriomeningitis virus from the hepatocyte. *J. Exp. Med.* **189**, 1555–1564 (1999).
61. J. Herz, K. R. Johnson, D. B. McGavern, Therapeutic antiviral T cells noncytotoxically clear persistently infected microglia after conversion into antigen-presenting cells. *J. Exp. Med.* **212**, 1153–1169 (2015).
62. N. S. Heaton, R. A. Langlois, D. Sachs, J. K. Lim, P. Palese, B. R. tenOever, Long-term survival of influenza virus infected club cells drives immunopathology. *J. Exp. Med.* **211**, 1707–1714 (2014).
63. R. E. Dumm, J. K. Fiege, B. M. Waring, C. T. Kuo, R. A. Langlois, N. S. Heaton, Non-lytic clearance of influenza B virus from infected cells preserves epithelial barrier function. *Nat. Commun.* **10**, 779 (2019).
64. D. L. Wheeler, J. Athmer, D. K. Meyerholz, S. Perlman, Murine olfactory bulb interneurons survive infection with a neurotropic coronavirus. *J. Virol.* **91**, e01099–e01017 (2017).
65. R. Burdeinick-Kerr, D. E. Griffin, Gamma interferon-dependent, noncytolytic clearance of sindbis virus infection from neurons in vitro. *J. Virol.* **79**, 5374–5385 (2005).
66. G. Faulkner, M. Dubois-Dalq, E. Hooghe-Peters, H. F. McFarland, R. A. Lazzarini, Defective interfering particles modulate VSV infection of dissociated neuron cultures. *Cell* **17**, 979–991 (1979).
67. B. D. Pearce, M. V. Hobbs, T. S. McGraw, M. J. Buchmeier, Cytokine induction during T-cell-mediated clearance of mouse hepatitis virus from neurons in vivo. *J. Virol.* **68**, 5483–5495 (1994).
68. J. Hausmann, A. Pagenstecher, K. Baur, K. Richter, H.-J. Rziha, P. Staeheli, CD8 T cells require gamma interferon to clear borna disease virus from the brain and prevent immune system-mediated neuronal damage. *J. Virol.* **79**, 13509–13518 (2005).
69. T. M. Kündig, H. Hengartner, R. M. Zinkernagel, T cell-dependent IFN-gamma exerts an antiviral effect in the central nervous system but not in peripheral solid organs. *J. Immunol.* **150**, 2316–2321 (1993).
70. B. Shrestha, B. Zhang, W. E. Purtha, R. S. Klein, M. S. Diamond, Tumor necrosis factor alpha protects against lethal West Nile virus infection by promoting trafficking of mononuclear leukocytes into the central nervous system. *J. Virol.* **82**, 8956–8964 (2008).
71. D. Hayasaka, K. Shirai, K. Aoki, N. Nagata, D. S. Simantini, K. Kitaura, Y. Takamatsu, E. Gould, R. Suzuki, K. Morita, TNF- α acts as an immunoregulator in the mouse brain by reducing the incidence of severe disease following Japanese encephalitis virus infection. *PLOS ONE* **8**, e71643 (2013).
72. M. M. Tun, K. Aoki, M. Senba, C. C. Buerano, K. Shirai, R. Suzuki, K. Morita, D. Hayasaka, Protective role of TNF- α , IL-10 and IL-2 in mice infected with the Oshima strain of Tick-borne encephalitis virus. *Sci. Rep.* **4**, 5344 (2014).
73. Y. Sergerie, S. Rivest, G. Boivin, Tumor necrosis factor- α and interleukin-1 β play a critical role in the resistance against lethal herpes simplex virus encephalitis. *J. Infect. Dis.* **196**, 853–860 (2007).
74. X. Zhang, D. R. Hinton, D. J. Cua, S. A. Stohlman, M. M. Lai, Expression of interferon- γ by a coronavirus defective-interfering RNA vector and its effect on viral replication, spread, and pathogenicity. *Virology* **233**, 327–338 (1997).
75. M. T. Liu, D. Armstrong, T. A. Hamilton, T. E. Lane, Expression of Mig (monokine induced by interferon- γ) is important in T lymphocyte recruitment and host defense following viral infection of the central nervous system. *J. Immunol.* **166**, 1790–1795 (2001).
76. A. A. Lin, P. K. Tripathi, A. Sholl, M. B. Jordan, D. A. Hildeman, Gamma interferon signaling in macrophage lineage cells regulates central nervous system inflammation and chemokine production. *J. Virol.* **83**, 8604–8615 (2009).
77. G. S. Huh, L. M. Boulanger, H. Du, P. A. Riquelme, T. M. Brotz, C. J. Shatz, Functional requirement for class I MHC in CNS development and plasticity. *Science* **290**, 2155–2159 (2000).
78. B. M. Elmer, A. K. McAllister, Major histocompatibility complex class I proteins in brain development and plasticity. *Trends Neurosci.* **35**, 660–670 (2012).
79. G. F. Rall, CNS neurons: The basis and benefits of low class I major histocompatibility complex expression. *Curr. Top. Microbiol. Immunol.* **232**, 115–134 (1998).
80. G. Chevalier, E. Suberbielle, C. Monnet, V. Duplan, G. Martin-Blondel, F. Farrugia, G. Le Masson, R. Liblau, D. Gonzalez-Dunia, Neurons are MHC class I-dependent targets for CD8 T cells upon neurotropic viral infection. *PLOS Pathog.* **7**, e1002393 (2011).
81. T. Liu, K. M. Khanna, X. Chen, D. J. Fink, R. L. Hendricks, CD8⁺ T cells can block herpes simplex virus type 1 (HSV-1) reactivation from latency in sensory neurons. *J. Exp. Med.* **191**, 1459–1466 (2000).

82. J. E. Knickelbein, K. M. Khanna, M. B. Yee, C. J. Baty, P. R. Kinchington, R. L. Hendricks, Noncytotoxic lytic granule-mediated CD8⁺ T cell inhibition of HSV-1 reactivation from neuronal latency. *Science* **322**, 268–271 (2008).
83. B. Shrestha, M. A. Samuel, M. S. Diamond, CD8⁺ T cells require perforin to clear West Nile virus from infected neurons. *J. Virol.* **80**, 119–129 (2006).
84. F. M. Cruz, J. D. Colbert, E. Merino, B. A. Kriegsman, K. L. Rock, The biology and underlying mechanisms of cross-presentation of exogenous antigens on MHC-I molecules. *Annu. Rev. Immunol.* **35**, 149–176 (2017).
85. C. Beauvillain, S. Donnou, U. Jarry, M. Scotet, H. Gascan, Y. Delneste, P. Guermonprez, P. Jeannin, D. Couez, Neonatal and adult microglia cross-present exogenous antigens. *Glia* **56**, 69–77 (2008).
86. M. J. Vasek, C. Garber, D. Dorsey, D. M. Durrant, B. Bollman, A. Soung, J. Yu, C. Perez-Torres, A. Frouin, D. K. Wilton, K. Funk, B. K. DeMasters, X. Jiang, J. R. Bowen, S. Mennerick, J. K. Robinson, J. R. Garbow, K. L. Tyler, M. S. Suthar, R. E. Schmidt, B. Stevens, R. S. Klein, A complement-microglial axis drives synapse loss during virus-induced memory impairment. *Nature* **534**, 538–543 (2016).
87. S. Seitz, P. Clarke, K. L. Tyler, Pharmacologic depletion of microglia increases viral load in the brain and enhances mortality in murine models of flavivirus-induced encephalitis. *J. Virol.* **92**, e00525–e00518 (2018).
88. R. Fekete, C. Cserép, N. Lénárt, K. Tóth, B. Orsolits, B. Martinecz, E. Méhes, B. Szabó, V. Németh, B. Gönci, B. Sperlág, Z. Boldogkői, Á. Kittel, M. Baranyi, S. Ferenczi, K. Kovács, G. Szalay, B. Rózsa, C. Webb, G. G. Kovacs, T. Hortobágyi, B. L. West, Z. Környei, Á. Dénes, Microglia control the spread of neurotropic virus infection via P2Y12 signalling and recruit monocytes through P2Y12-independent mechanisms. *Acta Neuropathol.* **136**, 461–482 (2018).
89. D. L. Wheeler, A. Sariol, D. K. Meyerholz, S. Perlman, Microglia are required for protection against lethal coronavirus encephalitis in mice. *J. Clin. Invest.* **128**, 931–943 (2018).
90. I. Waltl, C. Käufer, I. Gerhauser, C. Chhatbar, L. Ghita, U. Kalinke, W. Löscher, Microglia have a protective role in viral encephalitis-induced seizure development and hippocampal damage. *Brain Behav. Immun.* **74**, 186–204 (2018).
91. C. Chhatbar, C. N. Detje, E. Grabski, K. Borst, J. Spanier, L. Ghita, D. A. Elliott, M. J. C. Jordão, N. Mueller, J. Sutton, C. K. Prajeeth, V. Gudi, M. A. Klein, M. Prinz, F. Bradke, M. Stangel, U. Kalinke, Type I interferon receptor signaling of neurons and astrocytes regulates microglia activation during viral encephalitis. *Cell Rep.* **25**, 118–129.e4 (2018).
92. K. E. Funk, R. S. Klein, CSF1R antagonism limits local restimulation of antiviral CD8⁺ T cells during viral encephalitis. *J. Neuroinflammation* **16**, 22 (2019).
93. C. Garber, A. Soung, L. L. Vollmer, M. Kanmogne, A. Last, J. Brown, R. S. Klein, T cells promote microglia-mediated synaptic elimination and cognitive dysfunction during recovery from neuropathogenic flaviviruses. *Nat. Neurosci.* **22**, 1276–1288 (2019).
94. P. M. D'Agostino, C. Kwak, H. A. Vecchiarelli, J. G. Toth, J. M. Miller, Z. Masheeb, B. S. McEwen, K. Bulloch, Viral-induced encephalitis initiates distinct and functional CD103⁺ CD11b⁺ brain dendritic cell populations within the olfactory bulb. *Proc. Natl. Acad. Sci. U.S.A.* **109**, 6175–6180 (2012).
95. M. D. Bern, B. A. Parikh, L. Yang, D. L. Beckman, J. Poursine-Laurent, W. M. Yokoyama, Inducible down-regulation of MHC class I results in natural killer cell tolerance. *J. Exp. Med.* **216**, 99–116 (2019).
96. B. Pérarnau, M. F. Saron, B. R. San Martin, N. Bervas, H. Ong, M. J. Soloski, A. G. Smith, J. M. Ure, J. E. Gairin, F. A. Lemonnier, Single H2K^b, H2D^b and double H2K^bD^b knockout mice: Peripheral CD8⁺ T cell repertoire and anti-lymphocytic choriomeningitis virus cytolytic responses. *Eur. J. Immunol.* **29**, 1243–1252 (1999).
97. S. Gossa, D. Nayak, B. H. Zinselmeyer, D. B. McGavern, Development of an immunologically tolerated combination of fluorescent proteins for *in vivo* two-photon imaging. *Sci. Rep.* **4**, 6664 (2014).
98. S. M. Potter, C. Zheng, D. S. Koos, P. Feinstein, S. E. Fraser, P. Mombaerts, Structure and emergence of specific olfactory glomeruli in the mouse. *J. Neurosci.* **21**, 9713–9723 (2001).
99. S. K. Kim, D. S. Reed, S. Olson, M. J. Schnell, J. K. Rose, P. A. Morton, L. Lefrançois, Generation of mucosal cytotoxic T cells against soluble protein by tissue-specific environmental and costimulatory signals. *Proc. Natl. Acad. Sci. U.S.A.* **95**, 10814–10819 (1998).
100. K. Chandran, N. J. Sullivan, U. Felbor, S. P. Whelan, J. M. Cunningham, Endosomal proteolysis of the Ebola virus glycoprotein is necessary for infection. *Science* **308**, 1643–1645 (2005).
101. D. R. Shimshek, J. Kim, M. R. Hübner, D. J. Spergel, F. Buchholz, E. Casanova, A. F. Stewart, P. H. Seeburg, R. Sprengel, Codon-improved Cre recombinase (iCre) expression in the mouse. *Genesis* **32**, 19–26 (2002).
102. B. H. Zinselmeyer, J. Dempster, D. L. Wokosin, J. J. Cannon, R. Pless, I. Parker, M. J. Miller, Chapter 16. Two-photon microscopy and multidimensional analysis of cell dynamics. *Methods Enzymol* **461**, 349–378 (2009).
103. E. A. Susaki, K. Tainaka, D. Perrin, H. Yukinaga, A. Kuno, H. R. Ueda, Advanced CUBIC protocols for whole-brain and whole-body clearing and imaging. *Nat. Protoc.* **10**, 1709–1727 (2015).

Acknowledgments: We thank A. Hoofring in the NIH Medical Arts Design Section for generating the illustration shown in fig. S1. **Funding:** This research was supported by the intramural program at the NIH. **Author contributions:** A.C.B. and E.A.M. performed all the experiments and analyzed data. D.N. generated VSV recombinants. D.B.M. provided the funding. E.A.M. and D.B.M. wrote the manuscript. **Competing interests:** The authors declare that they have no competing interests. **Data and materials availability:** All data needed to evaluate the conclusions are present in the paper or the Supplementary Materials.

Submitted 5 February 2020
 Accepted 17 April 2020
 Published 5 June 2020
 10.1126/sciimmunol.abb1817

Citation: E. A. Moseman, A. C. Blanchard, D. Nayak, D. B. McGavern, T cell engagement of cross-presenting microglia protects the brain from a nasal virus infection. *Sci. Immunol.* **5**, eabb1817 (2020).

INFECTIOUS DISEASES

Human antibodies neutralize enterovirus D68 and protect against infection and paralytic disease

Matthew R. Vogt^{1*}, Jianing Fu^{2*}, Nurgun Kose³, Lauren E. Williamson⁴, Robin Bombardi³, Ian Setliff⁵, Ivelin S. Georgiev^{3,4}, Thomas Klose², Michael G. Rossmann^{2†}, Yury A. Bochkov⁶, James E. Gern^{6,7}, Richard J. Kuhn², James E. Crowe Jr.^{1,3,4,5‡}

Enterovirus D68 (EV-D68) causes outbreaks of respiratory illness, and there is increasing evidence that it causes outbreaks of acute flaccid myelitis (AFM). There are no licensed therapies to prevent or treat EV-D68 infection or AFM disease. We isolated a panel of EV-D68-reactive human monoclonal antibodies that recognize diverse antigenic variants from participants with prior infection. One potently neutralizing cross-reactive antibody, EV68-228, protected mice from respiratory and neurologic disease when given either before or after infection. Cryo-electron microscopy studies revealed that EV68-228 and another potently neutralizing antibody (EV68-159) bound around the fivefold or threefold axes of symmetry on virion particles, respectively. The structures suggest diverse mechanisms of action by these antibodies. The high potency and effectiveness observed *in vivo* suggest that antibodies are a mechanistic correlate of protection against AFM disease and are candidates for clinical use in humans with EV-D68 infection.

INTRODUCTION

Enterovirus D68 (EV-D68) is a reemerging picornavirus. This family of single-stranded positive-sense RNA genome, nonenveloped viruses shares a characteristic capsid. Sixty copies each of four viral proteins (VP1, VP2, VP3, and VP4) are arranged in pseudo $T = 3$ icosahedral symmetry forming five-, three-, and twofold axes of symmetry (1). EV-D68 has caused outbreaks of respiratory disease throughout the world (2–4). Clusters of acute flaccid myelitis (AFM), a poliomyelitis-like illness, were noted during a large outbreak of EV-D68–induced respiratory illness in the United States in 2014 (5). AFM outbreaks have occurred worldwide and have been well characterized in the United States, with large peaks in incidence during the August to October months every other year since 2014 (6). These biennial AFM outbreaks have been associated with EV-D68 circulation in the population, and strong evidence of causality for enteroviruses and AFM has built over time (7–9). Understanding this causal association has increased the urgency of defining the molecular and cellular basis for EV-D68 pathogenesis and host response (10). Genetic diversification of EV-D68 has accelerated in recent years, resulting in the appearance of different viral clades with distinct genotypes designated A, B (with subclades B1, B2, and B3), C, and D (previously described as A2) (11). It remains unclear whether the emergence of these new clades is associated with reduced immunity of the general population against EV-D68 infection or with increased occurrence of AFM. However, it is clear that EV-D68 has become a public health threat worldwide. Therefore, comprehensive studies of EV-D68 and the mechanisms

by which the human immune system controls EV-D68 infection and AFM disease are needed.

The role of antibodies in protection against EV-D68 infection and disease is uncertain. Numerous seroepidemiological studies have shown nearly universal seroprevalence of neutralizing antibodies for EV-D68 in adult human sera (12). Two studies that more closely investigated EV-D68 seroepidemiology in children noted a nadir of population antibody prevalence around 1 year of age, with a gradual rise in the presence of EV-D68 neutralizing antibodies through childhood (13, 14). Polyclonal human immune globulin pooled for intravenous use [intravenous immunoglobulin (IVIG)] contains EV-D68 neutralizing antibodies (15) and is capable of protecting mice from lethal experimental challenge causing AFM-like infections (16). Although both children and adults are susceptible to infection of the respiratory mucosa with EV-D68, AFM occurs almost exclusively in children (6). Likely, the pathogenesis of EV-D68 infection associated with AFM mimics some of the mechanisms by which the related picornavirus poliovirus causes infection of the nervous system during poliomyelitis. For poliovirus, vaccination induces serum neutralizing antibodies that are imperfect at blocking infection of the gastrointestinal mucosa but prevent progression to poliomyelitis (17). To determine whether antibodies play a critical role in preventing EV-D68–associated AFM, we sought to characterize the different classes of antibodies made by humans in response to natural infection. Using human B cell hybridoma technology, we isolated a panel of naturally occurring human monoclonal antibodies (mAbs) that recognize EV-D68. After characterizing their neutralization and binding properties *in vitro*, we focused on two mAbs for structural studies to determine their epitopes on the virion and one mAb for subsequent *in vivo* studies of prevention and treatment of EV-D68 infection in mice.

RESULTS

Isolation of human hybridomas secreting antibodies to EV-D68

After obtaining written informed consent, 12 participants who had previous documented EV-D68 respiratory tract infections during

Copyright © 2020
The Authors, some
rights reserved;
exclusive licensee
American Association
for the Advancement
of Science. No claim
to original U.S.
Government Works

¹Department of Pediatrics (Infectious Diseases), Vanderbilt University Medical Center, Nashville, TN, USA. ²Department of Biological Sciences and Purdue Institute of Inflammation, Immunology, and Infectious Disease, Purdue University, West Lafayette, IN, USA. ³Vanderbilt Vaccine Center, Vanderbilt University Medical Center, Nashville, TN, USA. ⁴Department of Pathology, Microbiology, and Immunology, Vanderbilt University Medical Center, Nashville, TN, USA. ⁵Program in Chemical and Physical Biology, Vanderbilt University, Nashville, TN, USA. ⁶Department of Pediatrics, University of Wisconsin-Madison, Madison, WI, USA. ⁷Department of Medicine, University of Wisconsin-Madison, Madison, WI, USA.

*These authors contributed equally to this work.

†Deceased.

‡Corresponding author. Email: james.crowe@vmc.org

the 2014 outbreak in the United States donated blood, from which we isolated peripheral blood mononuclear cells (PBMCs). The participants were 12 to 15 years old when infected and 16 to 18 years old at time of blood collection. Each participant had a history of EV-D68-associated respiratory disease, and none had symptoms of AFM (table S1). The collected PBMCs were transformed *in vitro* by inoculation with Epstein-Barr virus to generate memory B cell-derived lymphoblastoid cell lines (LCLs), which secrete antibodies. LCL culture supernatants were used in an indirect enzyme-linked immunosorbent assay (ELISA) to screen for the presence of EV-D68-reactive immunoglobulin Gs (IgGs). We selected cultures with antibodies that bound to laboratory-grown live virus preparations of EV-D68 generated from 2014 clinical isolates but that did not bind to a similarly prepared uninfected cell supernatant. After electrofusion of LCLs secreting EV-D68-specific antibodies with a nonsecreting myeloma cell line, the resulting hybridoma cells were single cell-sorted to generate clonal hybridomas secreting fully human mAbs (table S2).

Binding and neutralization properties of EV-D68-reactive mAbs

We sought to determine how many major antigenic sites on the virus surface are bound by human mAbs made in response to natural infection. To identify groups of antibodies that recognized similar epitopes, we determined whether the mAbs could compete with the binding of each of the other mAbs to live virus in an indirect ELISA. For competition-binding experiments, virus was coated directly onto an ELISA plate and then incubated with high concentrations of one unlabeled mAb. Next, mAbs labeled by biotinylation were added at a lower concentration, and the ability of the second mAb to bind the virus in the presence of the first mAb was determined. We then used a Pearson correlation with the inhibition data to determine the relatedness of the antibody binding patterns to each other and identified four main competition-binding groups (Fig. 1), which we termed groups 1 to 4. We used each mAb to stain a Western blot of EV-D68 preparations and found that nearly all mAbs in competition-binding groups 2 and 3 bound to linear epitopes in the VP1 protein, whereas only a single other mAb bound to any protein in the virus preparation (fig. S1).

During the 2014 EV-D68 outbreak in the United States, nearly all viral isolates were of the newly emergent B1 clade, with fewer detections of virus from the closely related B2 or distantly related D clades (18). All but one of the participants for this study were infected with B1 clade isolates (table S1). Since 2014, B3 clade viruses have dominated, and B1 clade

viruses are no longer circulating (19); in 2018, all EV-D68 isolates sequenced by the U.S. Centers for Disease Control and Prevention were from the B3 clade (20). We first measured the *in vitro* neutralization capability of each mAb in a 50% cell culture infectious dose (CCID₅₀) assay using a B1 clade EV-D68 isolate (Fig. 2A). Twenty-eight mAbs demonstrated neutralization with a half maximal inhibitory concentration (IC₅₀) below 50 μg/ml, with mAb EV68-159 exhibiting the strongest neutralization at an IC₅₀ value of 0.32 ng/ml (fig. S2). We further tested the 21 most potently neutralizing mAbs against a D clade isolate and found that 11 mAbs neutralized that virus, with 7 of those exhibiting at least a 10-fold decrease in potency by IC₅₀ value for the heterologous virus. The Fermon strain is an isolate from 1962 and is so distantly related to modern EV-D68 isolates that it does not fit into the clade classification scheme (18). Nine mAbs neutralized the Fermon laboratory reference strain but less potently than they inhibited the contemporary B1 clade virus.

Recognizing that neutralization assays may underestimate cross-reactivity, we used the same indirect ELISA approach described above to generate half maximal effective concentrations (EC₅₀) of purified mAb for binding to representative EV-D68 isolates from the B1, B2,

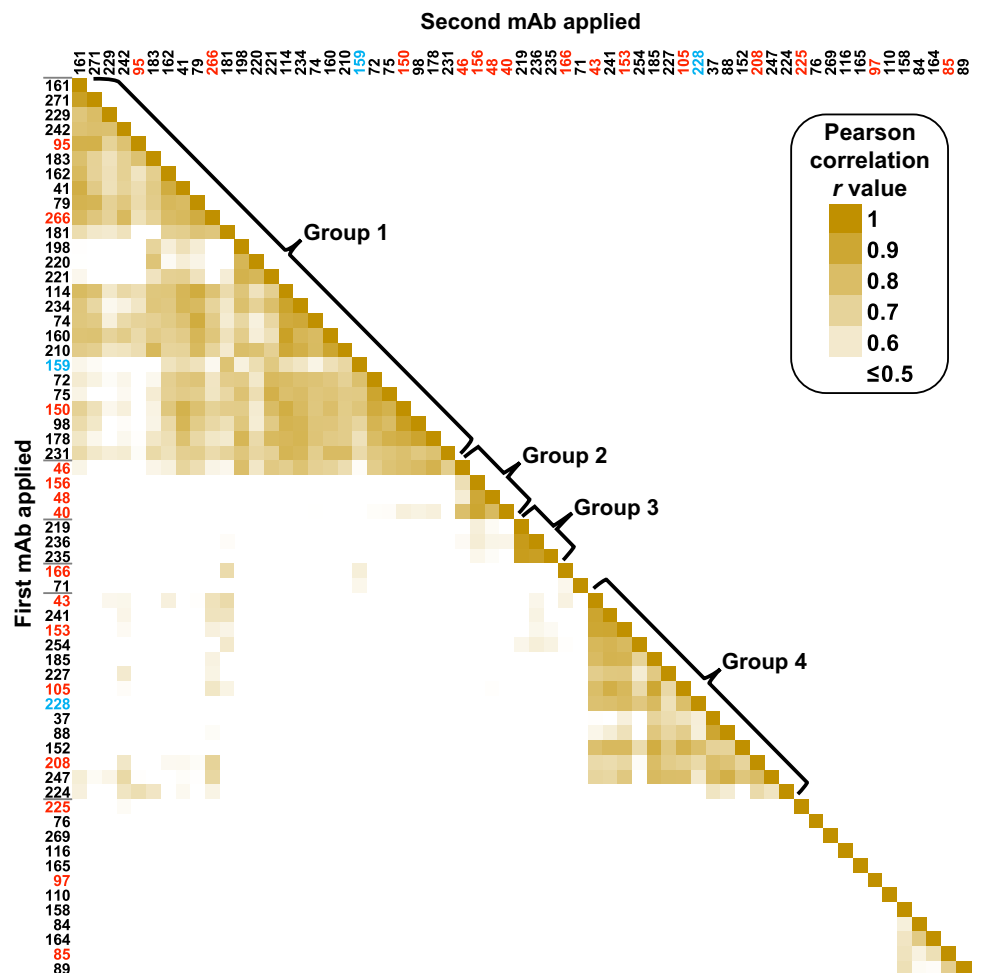


Fig. 1. Competition-binding groups of mAbs from EV-D68-immune human participants. Relatedness scores were generated from competition-binding ELISAs with a B1 clade EV-D68 isolate and used to cluster mAbs into four competition-binding groups designated 1 to 4. Clone numbers listed in red or blue are potentially neutralizing mAbs, with blue clone names indicating the two mAbs studied in detail in later figures.

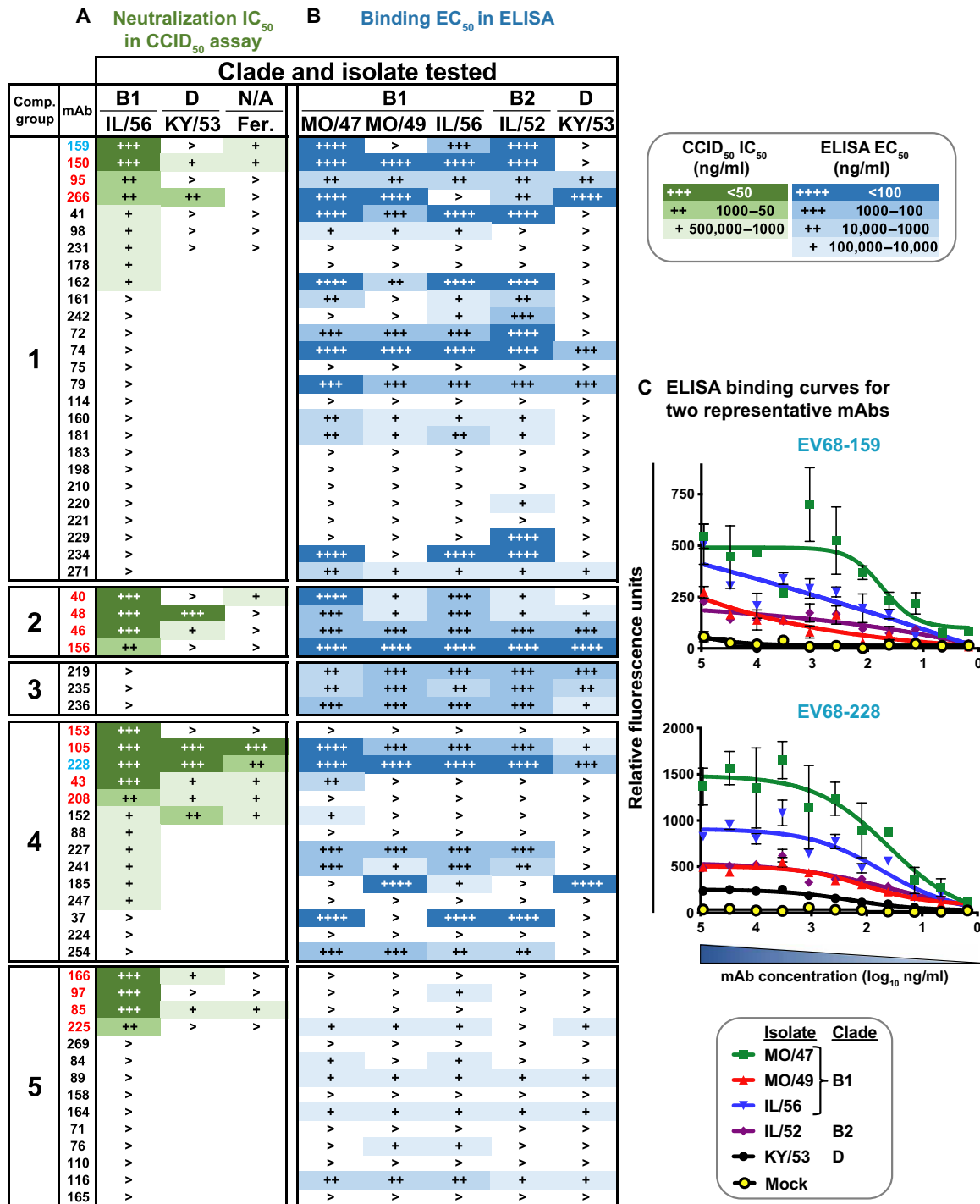


Fig. 2. Neutralization potency and binding capacity of human mAbs. (A) MAbs were ranked within competition-binding group (Comp. group; group 5 indicates the residual collection of singletons) by IC₅₀ value in a CCID₅₀ neutralization assay using a B1 clade isolate. We also tested neutralization of a D clade and Fermon (Fer.) isolate for the 21 most potent neutralizing mAbs. “>” denotes neutralization was not detected when tested in concentrations up to 50 μg/ml. Blank cells indicate not tested. Clone numbers listed in red or blue are potentially neutralizing mAbs, with blue clone names indicating the two mAbs studied in detail in later figures. (B) Binding strength to live virus isolates or a mock virus preparation is denoted using EC₅₀ values generated using (C) indirect ELISA with purified mAb dilutions to fit sigmoidal dose response curves. “>” indicates EC₅₀ value exceeds the maximum concentration tested of 100 μg/ml, suggesting poor or no binding.

or D clades (Fig. 2, B and C, and fig. S3). Of the mAbs with EC₅₀ values for binding of ≤1 μg/ml to B1 clade isolates, all bound to a B2 clade isolate, whereas about half also bound to a D clade isolate

(Fig. 2B and fig. S2). An additional class of mAbs was observed that bound weakly in general but cross-reacted to viruses from all clades tested.

Structural studies of two neutralizing anti-EV-D68 antibodies

To date, structural studies of antibody–EV-D68 interactions have been limited to murine mAbs (21). We selected two potentially neutralizing human mAbs, the clade-specific mAb EV68-159 and the highly cross-reactive mAb EV68-228, to make immune complexes with Fabs and a B1 clade EV-D68 isolate for cryo–electron microscopy (cryo-EM) studies. The final density maps attained a resolution of 2.9 Å (EV68-159) or 3.1 Å (EV68-228) (Fig. 3A, figs. S4 and S5, and table S3). The structures revealed two distinct binding sites: EV68-159 attached around the threefold axes of symmetry, whereas EV68-228 bound around the fivefold axes between depressions that form the canyon regions (Fig. 3 and fig. S6). Thus, for each Fab, a total of 60 copies bound to the virus particle. The Fab variable domains, which interacted with the viral surface, displayed strong densities similar to the viral capsid proteins, and an atomic model of each Fab was built together with the four viral capsid proteins. In contrast, the Fab constant domains, which are located further from the viral surface, displayed weaker densities and were excluded from atomic model building. The backbone of the polypeptide chains and most of amino acid side chains are well ordered in the density maps, demonstrating the critical features of the binding interface between virus particle and Fab molecule.

For both models, the viral surface residues that were facing and within a 4-Å distance from the Fab were identified as the footprint (Fig. 3C, fig. S7, and table S4). The footprints show that both Fab molecules sit within one protomer. In the EV-D68:Fab EV68-159 complex, each Fab masked a viral surface area around 990 Å². At the binding interface (Fig. 4), essential interactions were found between the EV68-159 light chain and three residues on the C terminus of VP1: Glu²⁷¹ and Arg²⁷² (Fig. 5A) and Asp²⁸⁵ (Fig. 5B). Residues Glu²⁷¹ and Arg²⁷² formed hydrogen bonds with complementarity-determining region 3 (CDR3) and CDR1. Arg²⁷² and Asp²⁸⁵ formed salt bridges with CDR3 and CDR2 residues, respectively. The heavy chain of EV68-159 contributed 77% of the masked surface areas. A series of hydrogen bonds was found between the heavy-chain CDR2 and CDR3 and the VP3 N-terminal loop before the B–β strand (βB) (Fig. 5C).

In the EV-D68:Fab EV68-228 complex, each Fab masked about 1170 Å² of the viral capsid surface. Similar to EV68-159, the heavy chain of the EV68-228 Fab dominated the interaction with the viral capsid by masking around 84% of the surface area. The binding interface (Fig. 4) was stabilized mainly by hydrogen bonds formed between the heavy-chain CDRs and the VP1 βB as well as the VP3 C terminus (Fig. 5D). The light chain CDR1 interacted with the VP2 EF loop. In addition, hydrogen bonds formed between the heavy-chain

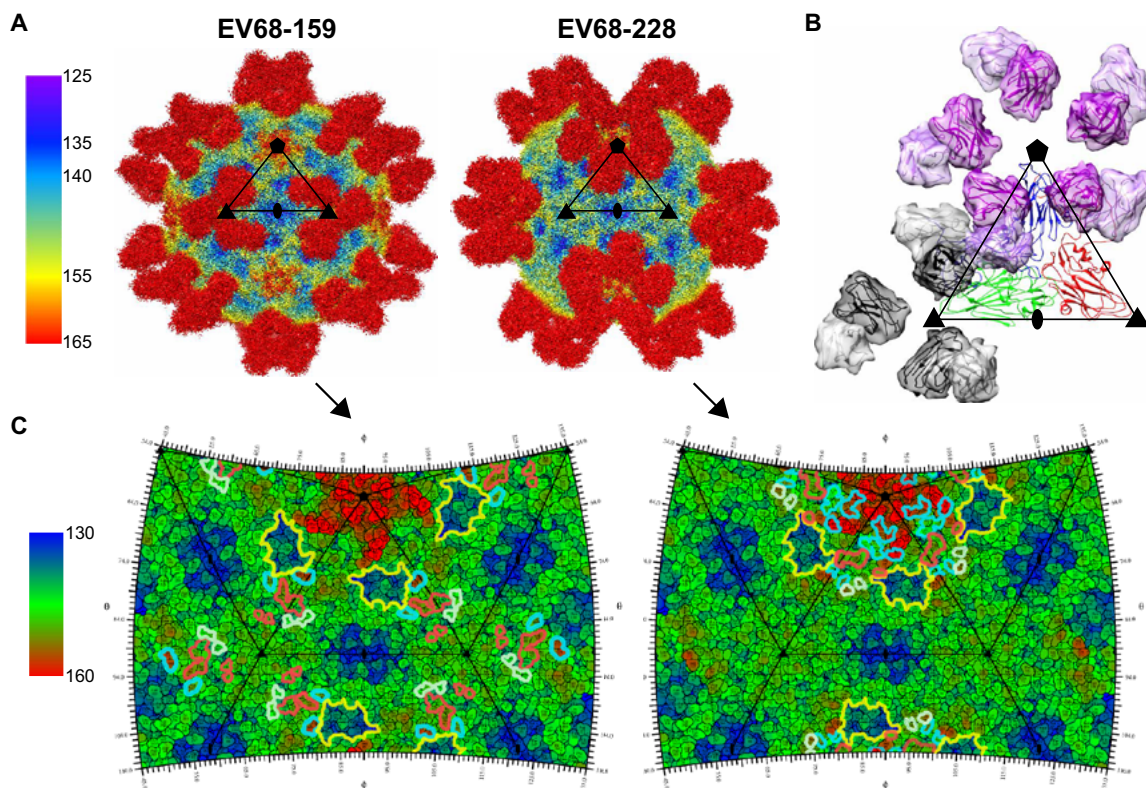


Fig. 3. Structural feature comparison between two immune complexes. (A) Radially colored cryo-EM maps of EV-D68:Fab EV68-159 (left) or EV-D68:Fab EV68-228 (right). Each map is projected down a twofold axis of symmetry. The five-, three-, and twofold axes of each asymmetric unit are depicted using a triangle outline labeled with one pentagon, two small triangles, and one oval, respectively. (B) Binding position comparison on an asymmetric unit. Viral proteins are colored in blue (VP1), green (VP2), and red (VP3). Fab molecules are colored in gray (EV68-159) or purple (EV68-228), and the heavy or light chains are shown in the same colors with dark or light intensities, respectively. (C) Footprints of EV68-159 Fab (left) or EV68-228 Fab (right). Radially colored 2D projections of the viral surface were created with Radial Interpretation of Viral Electron density Maps (RIVEM) software. Virus surface residues facing any atoms from the Fab molecules within a distance of 4 Å are outlined in light blue (VP1), light green (VP2), and light red (VP3). The canyon region is outlined in yellow. Scale bars in (A) and (C) indicate radial distance measured in angstrom.

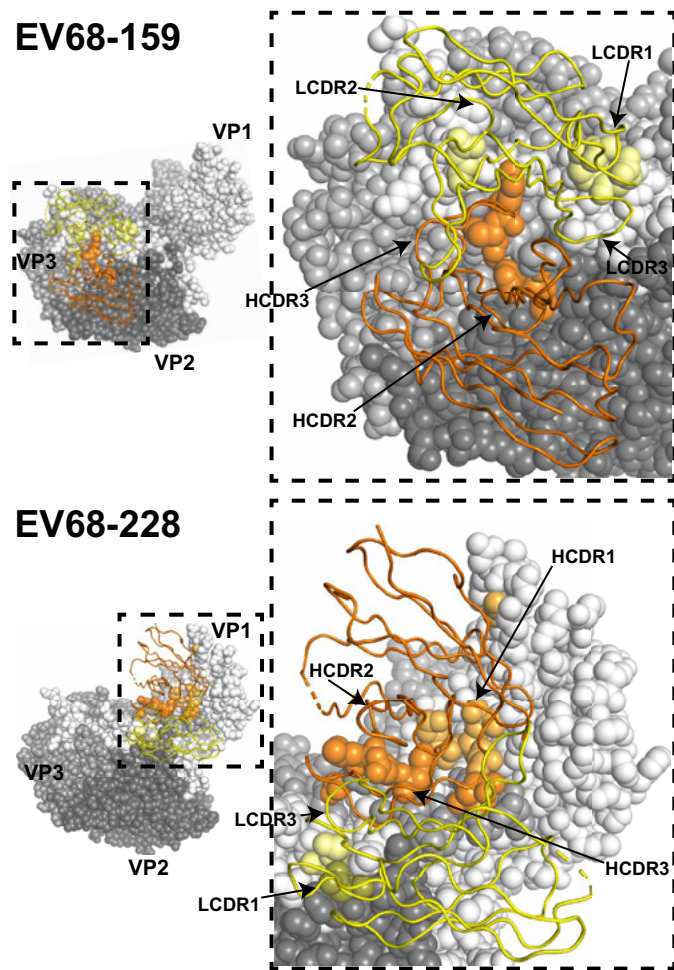


Fig. 4. Close-up view of the binding interfaces of EV68-159 and EV68-228. The viral capsid is shown as surface, and the Fab is shown in a cartoon representation. VP1, VP2, and VP3 are colored in white, dark gray, and silver, respectively. Heavy or light chains are colored in orange or yellow, respectively. Viral residues making interactions are colored on the basis of the heavy and light chains, and the color intensities vary based on which of the VPs. The heavy- and light-chain CDRs (HCCR and LCCR, respectively) involved in the binding interfaces are shown with arrows.

framework region 3 and the VP1 DE loop. Furthermore, a salt bridge between the light chain CDR3 and the VP1 C terminus was observed. Overall, the EV68-228 Fab bound the viral surface around the fivefold axes and recognized the classical picornavirus neutralizing immunogenic sites (NIm) NIm-IB (VP1 DE loop) and NIm-II (VP2 EF loop) (22).

Bulky side chains were found at the interface for both Fabs and act to stabilize the structures through hydrophobic interaction networks (fig. S8). Furthermore, disulfide bonds also were detected around CDR1 and CDR3 in heavy and light chains. Another pair of cysteines, Cys¹⁰¹ and Cys¹⁰⁶, was found within the CDR3 of the EV68-228 heavy chain and was at the correct distance and orientation to form a disulfide bond (Fig. 5D). Specifically, when the contour levels were reduced, the densities of the two cysteine side chains connected. As described above for the EV-D68:Fab EV68-228 complex, hydrogen bonds were observed between the heavy-chain CDR3 and the VP3 C-terminal residues adjacent to the canyon involving

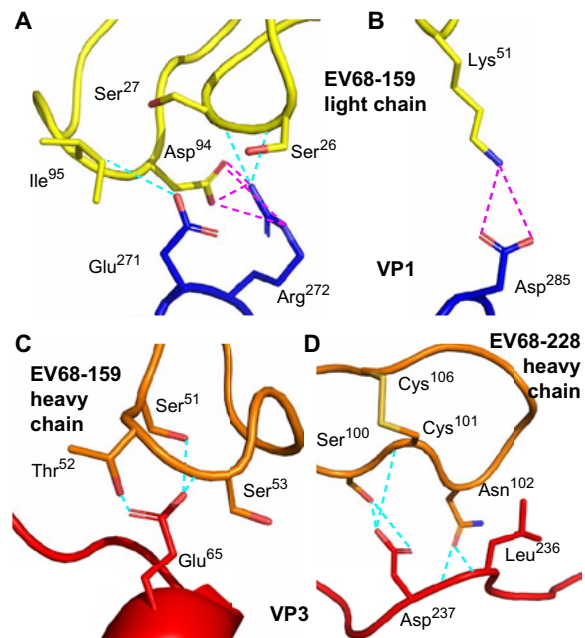


Fig. 5. Molecular detail of virion-Fab interactions. Representative interaction at the binding interface of EV-D68:Fab EV68-159 (A to C) and EV-D68:Fab EV68-228 (D). Hydrogen bonds are colored in cyan, and salt bridges are colored in magenta.

Cys¹⁰¹, forming both a hydrogen bond and a disulfide bond. These cysteine residues play critical roles in stabilizing both Fab structure and the virus-Fab binding interface.

Prophylactic and therapeutic effects of neutralizing antibodies in mouse models

We next sought to determine whether the potentially neutralizing and highly cross-reactive human mAb EV68-228 could prevent or treat infection and disease in small animal models of EV-D68 infection. We tested for this antiviral activity *in vivo* using two different established models of infection causing either respiratory or AFM-like neurologic disease in AG129 strain mice that are deficient in receptor for interferon α/β and γ (23, 24). First, we tested whether antibodies could reduce viremia and lung virus replication in the respiratory model of infection. MAb EV68-228 administered systemically as prophylaxis a day before virus inoculation provided sterilizing immunity in the blood (Fig. 6A) and lungs (Fig. 6B) at each of the concentrations tested, whereas human IVIG only sterilized the blood. Induction of proinflammatory cytokine secretion was inhibited in the lungs of EV68-228-treated mice (Fig. 7, A to C). When used as a treatment given at increasing times after virus inoculation, again, all treatments were highly effective at sterilizing the blood (Fig. 6C) but only EV68-228 had efficacy in the lungs (Fig. 6D). We similarly observed reduced proinflammatory cytokine levels in the lungs of EV68-228-treated mice (Fig. 7, D to F).

Next, we assessed the effect of passive transfer of antibodies in a neurologic model of infection that mimics AFM disease. EV68-228 prophylaxis provided sterilizing immunity of the blood (Fig. 8A) and complete protection from death (Fig. 8B) or development of any neurologic disease (Fig. 8C), whereas IVIG treatment protected only partially. Given therapeutically, EV68-228 treatment sterilized the blood within 24 hours of administration (Fig. 8D) at each of the

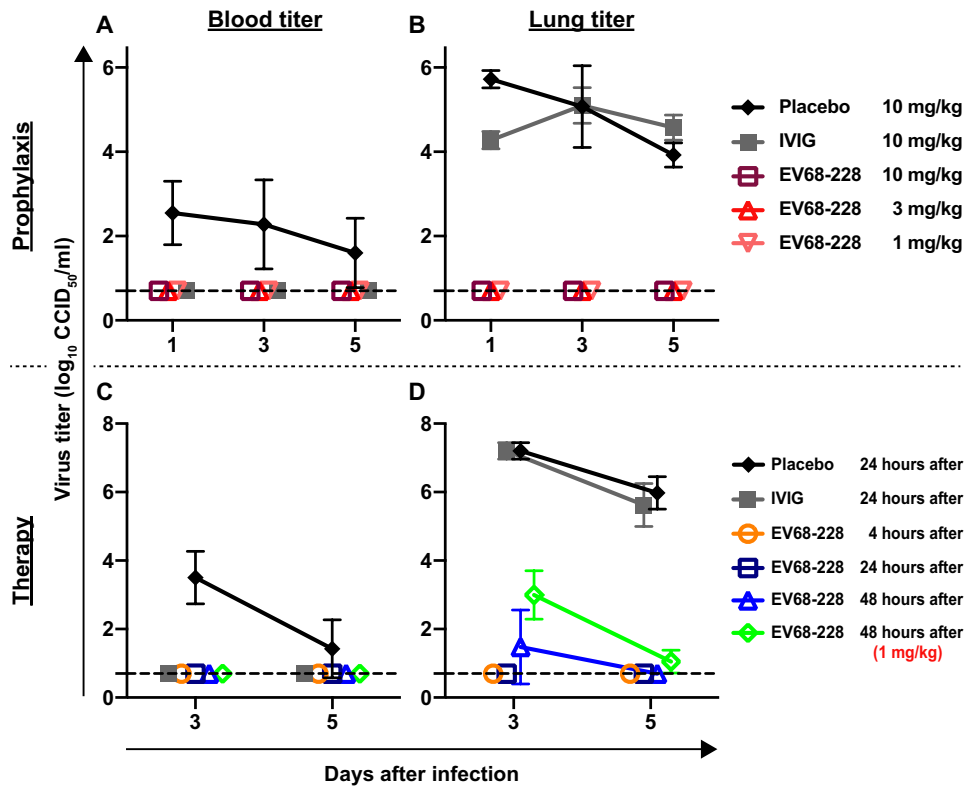


Fig. 6. MAb EV68-228 protects mice from EV-D68-induced respiratory disease, when used as either prophylaxis or therapy. Four-week-old AG129 strain mice ($n = 4$ per time point) were inoculated with mouse-adapted B1 clade EV-D68 intranasally, antibody was administered intraperitoneally, and viral titers for indicated tissue were measured by a CCID₅₀ assay. (A and B) Mice were inoculated with virus 24 hours after indicated dose of antibody, and then viral titers were measured at indicated time points. (C and D) Mice were inoculated with virus followed by 10 mg/kg (except where indicated) of antibody 4, 24, or 48 hours later, and then viral titers were measured.

time points given. EV68-228 improved survival (Fig. 8E) and neurologic disease when given as late as 48 hours after infection; when given at 72 hours after infection, the mouse that survived improved clinically (Fig. 8F and table S5).

DISCUSSION

These studies reveal diverse features of the human B cell response to EV-D68 infection. We attempted to be unbiased in our approach to isolating these mAbs, using live virus isolates as the screening antigen. The diversity in antibody phenotypes that we recovered may be a result of this strategy, as we observed a broad range of cross-reactivity among clades of EV-D68, both with binding and neutralization. Strong binding to live virus particles did not necessarily predict high neutralizing potency. Of the competition-binding groups observed, only groups 2 and 3 exhibited uniformity in phenotype. mAbs in both groups were cross-reactive, but group 2 mAbs neutralized virus, whereas group 3 mAbs did not. Nearly all of the group 2 and 3 mAbs bound to VP1 in western blot (figs. S1 and S2), suggesting that they bind to linear epitopes. The competition-binding studies used full-length IgG molecules, so the competition seen is functional as would occur in human tissues and does not necessarily indicate that there are only four structurally distinct epitopes on the viral surface.

The lack of western blot reactivity of EV68-159 and EV68-228 correlates with the findings in the structural studies that show both

epitopes span all three major viral surface proteins. The conformation-dependent nature of the epitopes of these two potentially neutralizing mAbs is notable because recent diagnostic advances using peptide microarray (8) and phage library (9) technologies scanned for antibodies in the cerebrospinal fluid of patients with AFM that recognize linear epitopes. Detection of antibodies recognizing linear epitopes currently can be used in valuable diagnostic tools; however, our studies reveal that these tests are at best only partially informative about the quality of antibody response these patients make in response to enterovirus infection. The structures also suggest the molecular basis for antibody-mediated neutralization. By contacting all three structural proteins within a protomer, both mAbs appear capable of inhibiting dynamic structural transitions necessary for infection, which are poorly understood.

The disulfide bond in the CDR3 of EV68-228 heavy chain is a structural moiety we have now observed in broadly neutralizing antiviral human mAbs for a number of viruses, including both hepatitis C (25) and influenza A virus (26). The intervening four to five amino acids between cysteines form a smaller structured loop at the most distal tip of the full CDR3 loop, stabilizing the CDR3 in a preconfigured state optimal for binding the viral antigen. For EV68-228 specifically, the Cys¹⁰¹ also directly interacts with VP3 via a hydrogen bond, so the cysteine participates in both CDR3 loop stabilization and interaction with target.

The three VP1 residues that interact with EV68-159 light chain (Glu²⁷¹, Arg²⁷², and Asp²⁸⁵) and Glu⁵⁹ on the N-terminal loop of VP3, which interacts with EV68-159 heavy chain, are adjacent to the sialic acid receptor-binding site (27), suggesting that the EV68-159 Fab may block virus from binding sialic acid receptors. In particular, these three VP1 residues are located on a 22-amino acid VP1 C-terminal peptide that is bound by antibodies found in the cerebrospinal fluid of patients with AFM (8, 9). Furthermore, the interaction of the EV68-159 Fab heavy chain with the VP3 N-terminal loop may prevent the virus from uncoating, because the N termini of the four VPs contribute to capsid stability (28). EV68-228 may prevent the virus from uncoating by binding VP1 βB, inhibiting the externalization of the N terminus of VP1 that is required for entry. In addition, the antibody footprint includes residues on the C terminus of VP3, which is not part of a classical NIm. These residues are adjacent to the canyon receptor-binding site, suggesting that mAb EV68-228 also may block virus binding to receptors.

Last, at a time when poliovirus types 2 and 3 have been eradicated, AFM is on the rise, and the role of EV-D68 in causing epidemics of this paralytic disease is increasingly evident. Given how well prophylaxis with human mAb EV68-228 works in vivo, these data suggest that an effective EV-D68 vaccine might prevent AFM disease.

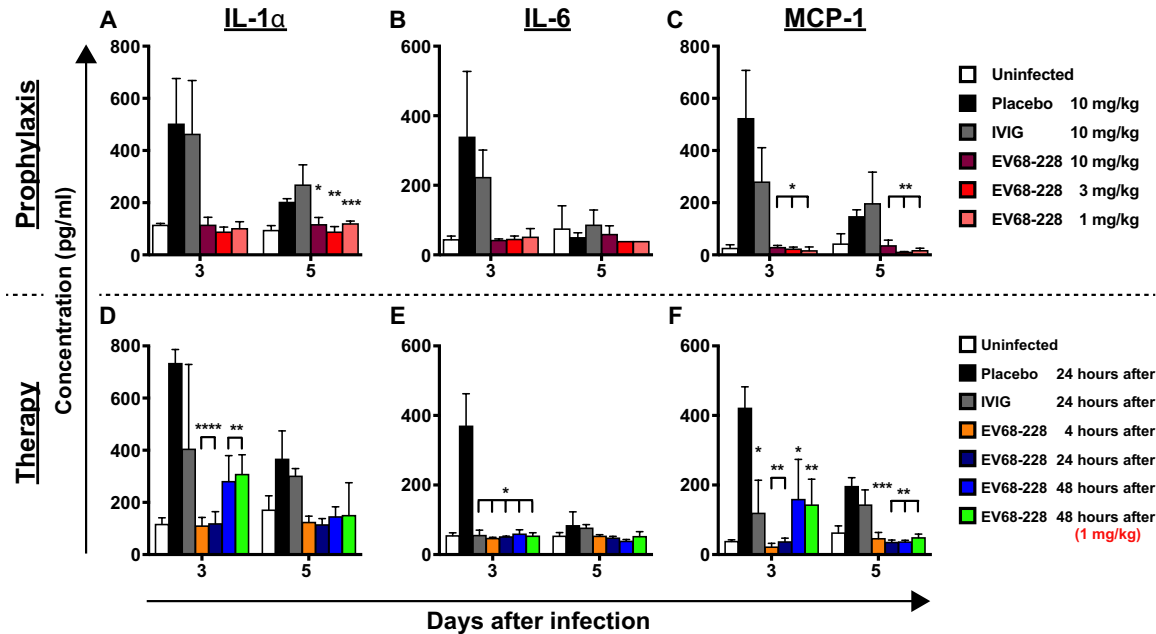


Fig. 7. MAb EV68-228 decreases lung inflammation in EV-D68-infected mice. Four-week-old AG129 mice ($n = 4$ per time point) (A to C) were inoculated with virus intranasally 24 hours after indicated dose of antibody or (D to F) were inoculated with virus intranasally followed by 10 mg/kg (except where indicated) of antibody 4, 24, or 48 hours later, and then cytokines were measured at indicated time points. Cytokines were quantified from lung homogenates using an ELISA. Values from the treatment groups were compared with the placebo group for each time point using a one-way ANOVA with Dunnett’s T3 multiple comparisons test ($*P < 0.05$, $**P < 0.01$, $***P < 0.001$, and $****P < 0.0001$). IL, interleukin; MCP, monocyte chemoattractant protein.

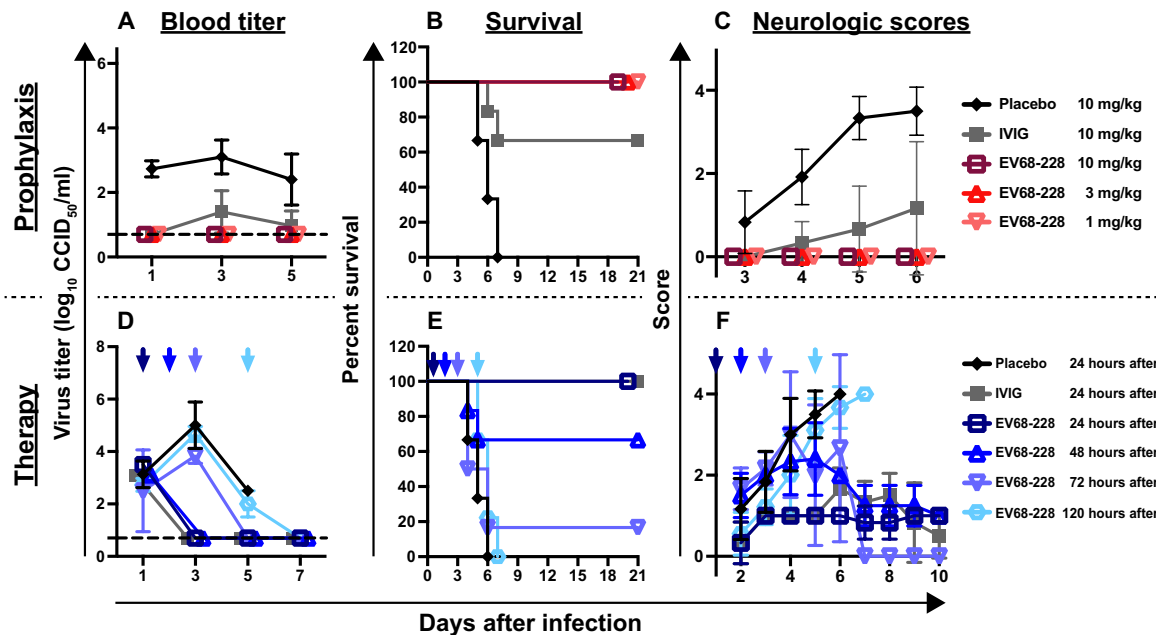


Fig. 8. MAb EV68-228 protects mice from EV-D68-induced neurologic disease, when used as either prophylaxis or therapy. Ten-day-old mice were inoculated with mouse-adapted B1 clade EV-D68 intraperitoneally, antibody was administered intraperitoneally, and viral titers for indicated tissue were measured by a CCID₅₀ assay. (A to C) Mice were inoculated with virus 24 hours after indicated dose of antibody, then (A) viral titers were measured ($n = 3$ per time point), (B) survival was monitored, and (C) neurologic scores ($n = 6$ per time point) were recorded at indicated time points. Higher scores indicate more severe motor impairment. (D to F) Mice were inoculated with virus followed by a 10 mg/kg dose of antibody, then (D) viral titers were measured ($n = 3$ per time point), (E) survival was monitored, and (F) neurologic scores ($n = 6$ per time point, except $n = 9$ for 120 hours after) were recorded. Colored vertical arrows indicate time of treatment.

Recent studies indicate that virus-like particle (29, 30) and inactivated EV-D68 (31) vaccine candidates are immunogenic and protective against infection in mice. However, a study of cotton rats vaccinated

with inactivated EV-D68 suggested that they may have suffered worse respiratory disease upon subsequent EV-D68 infection (32). Although this finding could suggest the possibility of antibody-dependent

enhancement (ADE) of EV-D68 infection, in mice, we did not observe ADE caused by polyclonal antibodies or mAbs, within the range of antibody concentrations we tested. In addition, the prospect of using mAb EV68-228 as a therapy early during EV-D68 infection is appealing, especially because this antibody potentially neutralizes a diverse set of viral isolates without obvious autoreactive binding to human cell materials (Fig. 2C). Although IVIG protected mice from AFM-like disease due to EV-D68 in prior *in vivo* studies (16), so far, IVIG has not been shown to confer benefit for humans with AFM (33). However, IVIG is a complex mixture of polyclonal antibodies with only a small fraction that recognize EV-D68. mAb prophylaxis or therapy for EV-D68-associated AFM is more promising than IVIG due to the high specificity, high potency, and lower antibody dose that can be used. It is possible, however, that a cocktail of mAbs directed at multiple epitopes may be more protective than mAb monotherapy. A mAb cocktail theoretically would provide a higher barrier to emergence of mAb-resistant virus, but we did not observe resistance *in vivo* (Figs. 6 and 8). Even under conditions optimized for selecting EV68-228-resistant viruses *in vitro*, we could only identify virus genomes with mutations of unclear significance (table S6). In the absence of a reverse genetics system for making recombinant viruses with these mutations, we were unable to verify specifically whether these mutations caused escape from neutralization. Therefore, we find emergence of resistance during potential therapeutic use unlikely. These experiments also provide hope for therapeutic efficacy in patients with severe respiratory disease due to EV-D68, which is the clinical syndrome that brought the 2014 EV-D68 outbreak to the attention of public health authorities before recognition of the association with AFM (3). Overall, the studies we present here show that natural EV-D68 infection of humans induces B cells encoding broad and potentially neutralizing antibodies that can prevent or treat infection and disease in both the respiratory tract and the nervous system.

MATERIALS AND METHODS

Study design

We designed this study to try to identify any antibodies that humans can make in response to EV-D68 infection. Therefore, we used live virus isolates in an indirect ELISA screen to identify B cells secreting EV-D68-binding antibodies and then electrofused those B cells with myeloma cells to create mAb secreting hybridomas. We then characterized the neutralization and binding properties of these individual mAbs *in vitro* using CCID₅₀, ELISA, and cryo-EM-based techniques. We pursued *in vivo* experiments to generate preclinical data supporting the development of mAb EV68-228 as a prophylactic and/or therapeutic agent in humans. For this purpose, we studied the effectiveness of mAb EV68-228 at protecting mice from EV-D68 infection as compared with human IVIG, which is widely used to treat humans with AFM based on theoretical benefit, but this IVIG treatment, so far, has not been proven to be effective. An advantage of the AG129 murine model of infection is that we could measure the effect of antibody treatment in both respiratory and neurologic models of infection.

Cell lines

RD cells (human, female origin) were obtained from the American Type Culture Collection (ATCC CCL-136). RD cells were cultured in 5% CO₂ at 37°C in Dulbecco's modified Eagle medium (DMEM; Thermo Fisher Scientific) supplemented with 10% heat-inactivated fetal bovine serum (HI-FBS; HyClone), 1 mM sodium pyruvate, and

1% penicillin-streptomycin-amphotericin B (Thermo Fisher Scientific). For structural studies, RD cells were cultured in DMEM (Sigma-Aldrich) supplemented with 10% HI-FBS (Sigma-Aldrich) and non-essential amino acids (Life Technologies). The ExpiCHO (hamster, female origin) cell line was purchased from Thermo Fisher Scientific and cultured according to the manufacturer's protocol. The HMMA2.5 line is a nonsecreting mouse-human heteromyeloma cell line (sex information is not available) that was generated by fusing a murine myeloma cell line with a human myeloma cell line (34). This cell line was cultured as described previously (35). All cell lines were tested on a monthly basis for *Mycoplasma* and found to be negative in all cases.

Viruses

See table S7 for a list of the virus isolates used in this study. EV-D68 isolates were propagated for two generations in RD cell monolayer cultures for use in the ELISAs described below. RD cell monolayers were inoculated with a given virus isolate and monitored until 70 to 90% cell death was observed. This cell culture flask was then frozen to -80°C and thawed, and the contents scraped and collected into a 50-ml conical tube. This preparation was sonicated three times for 20 s in an inverted-cup sonicator at maximum power settings (Fisherbrand), vortexed for 30 s, and then sonicated two more times for 20 s. Cell debris was pelleted, and the virus-containing supernatant was spun over a 30% sucrose in phosphate-buffered saline (PBS) (w/v) cushion at 10°C for 4 hours at 100,000g. Supernatant was discarded, and the pellet was allowed to soak in 0.01% (w/v) bovine serum albumin (BSA) in NTE buffer [20 mM tris, 120 mM NaCl, and 1 mM EDTA (pH 8.0)] overnight at 4°C. The resuspended pellet was then clarified further by centrifugation at 10,000g for 10 min before storage of virus aliquots at -80°C until ready for use.

For structural studies, the US/MO/14-18947 isolate was used. Virus was passaged in RD cells and stored at -80°C before large-scale propagation. RD cells were grown to 80% confluency and were infected with EV-D68 at a multiplicity of infection of 0.01. Two days after infection, the cells were collected together with the supernatant and spun down. The cell pellets were collected and, after multiple freeze/thaw cycles, spun down to remove cell debris. All supernatants were combined and pelleted at 210,000g for 2 hours. The pellets were incubated and resuspended in 250 mM Hepes (pH 7.5) and 250 mM NaCl buffer and then supplemented with final concentrations of 5 mM MgCl₂, deoxyribonuclease (0.01 mg/ml; Sigma-Aldrich), trypsin (0.8 mg/ml), 15 mM EDTA, and 1% (w/v) *n*-lauryl-sarcosine. The sample was then pelleted at 210,000g for 2 hours, resuspended, and loaded onto a potassium tartrate gradient (10 to 40%, w/v) for the last round of ultracentrifugation at 160,000g for 2 hours. The purified virus sample, which was observed as a blue band in the middle of the tube, was extracted and buffered exchanged into 20 mM tris, 120 mM NaCl, and 1 mM EDTA (pH 8.0) (NTE buffer) to remove potassium tartrate.

Detection of virus load by CCID₅₀ assay

Titration of virus stocks or virus in murine blood or lung samples was performed by CCID₅₀ assay in RD cell culture monolayers. Briefly, increasing 10-fold dilutions of the samples were applied to RD cell monolayers in triplicate wells (50 µl) of a 96-well plate, incubated for 5 days in 5% CO₂ at 33°C, then fixed with 1% paraformaldehyde, and stained with crystal violet. Wells with any cytopathic effect were scored as positive for virus, and titers were determined using a formula based on the Spearman-Kärber equation (36); the limit of detection was 136 CCID₅₀/ml.

Virus neutralization assay

Virus neutralization assays were performed in a CCID₅₀ format using the indicated viruses, essentially as described previously for poliovirus (37). Virus was incubated with increasing concentrations of mAb in duplicate for 1 hour at 33°C, and then each suspension was added to a monolayer of RD cells in technical quadruplicate wells (50 μ l) of a 96-well plate. After 5 days incubation in 5% CO₂ at 33°C, cells were fixed with 1% paraformaldehyde and stained with crystal violet. Wells with any cytopathic effect were scored as positive for virus, and IC₅₀s were determined using a formula based on the Spearman-Kärber equation (36); the limits of detection were 57 μ g/ml to 4.8 pg/ml.

Mouse models

Ten-day-old (neurologic model) or 4-week-old (respiratory model) male and female AG129 mice (deficient in receptors for interferon α/β and γ) were obtained from a specific pathogen-free colony maintained at the Utah Science Technology and Research (USTAR) building at Utah State University. The mice were bred and maintained on irradiated Teklad Rodent Diet (Harlan Teklad) and autoclaved tap water at the USTAR building of Utah State University. This study was conducted in accordance with the approval of the Institutional Animal Care and Use Committee of Utah State University dated 2 March 2019 (expires 1 March 2022). The work was performed in the Association for Assessment and Accreditation of Laboratory Animal Care (AAALAC)-accredited Laboratory Animal Research Center of Utah State University. The U.S. Government (National Institutes of Health) approval was renewed 9 March 2018 [U.S. Public Health Service assurance no. D16-00468(A3801-01)] in accordance with the National Institutes of Health Guide for the Care and Use of Laboratory Animals (revision, 2011).

Antibody and control treatments were diluted in PBS and administered by intraperitoneal injection at indicated time points before or after EV-D68 inoculation. Guanidine HCl (Sigma-Aldrich) served as a positive control for treatment (24), started 4 hours after infection, and continued twice daily for 5 days. A suspension of mouse adapted EV-D68 was administered by intraperitoneal injection [neurologic model; 10^{6.5} CCID₅₀ in a 100- μ l volume of minimum essential medium (MEM)] or intranasal instillation (respiratory model; 10^{4.5} CCID₅₀ in a 90- μ l volume of MEM). Mice were weighed before treatment and daily thereafter. Mice were euthanized humanely at indicated time points after infection for measurement of lung virus titers, blood virus titers, or lung cytokine concentrations, as indicated. For the neurologic model, all mice were observed daily for morbidity, mortality, and neurological scores (NSs) through day 21. NSs were recorded as follows: NS0, no observable paralysis; NS1, abnormal splay of hindlimb but normal or slightly slower gait; NS2, hindlimb partially collapsed and foot drags during use for forward motion; NS3, rigid paralysis of hindlimb and hindlimb is not used for forward motion; and NS4, rigid paralysis in hindlimbs and no forward motion. Any animals observed with a score of NS4 were euthanized humanely.

Lung cytokine/chemokine evaluations

Each sample of lung homogenate was tested for cytokines and chemokines using quantitative chemiluminescent ELISA-based assays according to the manufacturer's instructions (Quansys Biosciences Q-Plex Array, Logan, UT). The Quansys multiplex ELISA is a quantitative test in which 16 distinct capture antibodies are applied to each well of a 96-well plate in a defined array.

Generation of human mAbs

Participants were identified from the Childhood Onset of Asthma birth cohort (38) who had laboratory-documented EV-D68 upper respiratory tract infections (39). After written informed consent was obtained, peripheral blood was collected and stored at room temperature until PBMCs could be purified using SepMate tubes (STEMCELL Technologies) per the manufacturer's protocol and then cryopreserved in 10% (v/v) dimethyl sulfoxide in FBS and stored in the vapor phase of liquid nitrogen. LCLs were generated as described previously (40) from memory B cells within the PBMCs by mixing with Epstein-Barr virus, cell cycle checkpoint kinase 2 inhibitor (Sigma-Aldrich), CpG (Sigma-Aldrich), and cyclosporin A (Sigma-Aldrich) in Medium A (STEMCELL Technologies). One week later, LCLs were counted and then expanded on a feeder layer of gamma-irradiated, human PBMCs from an unrelated donor. In one more week, LCL supernatants were screened for the presence of EV-D68-reactive IgG by indirect ELISA using live EV-D68 virus as the antigen, comprising cell culture grown EV-D68 virus generated from a 2014 clinical isolate. LCLs from wells containing virus-reactive antibodies were fused to HMM2.5 myeloma cells by electrofusion, as previously described (35). After the fusion reaction, hybridoma lines were cultured in a selection medium containing hypoxanthine, aminopterin, and thymidine medium supplements (Sigma-Aldrich) and ouabain (Sigma-Aldrich) in 384-well plates before screening of supernatants for antibody production. Two weeks later, supernatants from the resulting hybridoma cell lines were screened by indirect ELISA with live virus as antigen, and cell lines from wells with EV-D68-reactive antibodies were expanded in culture and then cloned by single-cell flow cytometric sorting into 384-well cell culture plates. These cloned cells were expanded in Medium E until about 50% confluent in 12-well tissue culture-treated plates (Corning) and their supernatants screened for virus binding by ELISA. Wells with the highest signal in ELISA were selected as the mAb-producing hybridoma cell lines for further use.

mAb isotype and gene sequence analysis

The isotype and subclass of secreted antibodies were determined using mouse anti-human IgG1, IgG2, IgG3, or IgG4 antibodies conjugated with horseradish peroxidase (Southern Biotech). Antibody heavy- and light-chain variable region genes were sequenced from RNA obtained from hybridoma lines that had been cloned biologically by flow cytometric sorting. Total RNA was extracted using the RNeasy Mini Kit (QIAGEN). A modified 5' rapid amplification of complementary DNA (cDNA) ends approach was used (41). Briefly, 5 μ l of total RNA was mixed with cDNA synthesis primer mix (10 μ M each) and incubated for 2 min at 70°C, followed by a decrease in the incubation temperature to 42°C to anneal the synthesis primers (1 to 3 min). After incubation, a mixture containing 5 \times first-strand buffer (Clontech), dithiothreitol (20 mM), 5' template switch oligo (10 μ M), deoxynucleotide triphosphate (dNTP) solution (10 mM each), and 10 \times SMARTScribe Reverse Transcriptase (Clontech) was added to the primer-annealed total RNA reaction and incubated for 60 min at 42°C. The first-strand synthesis reaction was purified using the Ampure Size Select Magnetic Bead Kit at a ratio of 1.8 \times (Beckman Coulter). After purification, a single polymerase chain reaction (PCR) amplification reaction containing 5 μ l of first-strand cDNA, 2 \times Q5 High-Fidelity Master Mix (New England Biolabs), dNTP (10 mM each), forward universal primer (10 μ M), and reverse primer mix (0.2 μ M each in heavy-chain mix and 0.2 μ M each in light-chain mix)

was subjected to thermal cycling with the following conditions: initial denaturation for 90 s followed by 30 cycles of denaturation at 98°C for 10 s, annealing at 60°C for 20 s, and extension at 72°C for 40 s, followed by a final extension step at 72°C for 4 min. All primer sequences used in this protocol were described previously (41). The first PCR reaction was purified using the AMPure Size Select Magnetic Bead Kit at a ratio of 0.6× (Beckman Coulter). Amplicon libraries were then prepared according to the Multiplex SMRT Sequencing protocol (Pacific Biosciences) and sequenced on a Sequel platform instrument (Pacific Biosciences). Raw sequencing data were demultiplexed, and circular consensus sequences were determined using the SMRT Analysis tool suite (Pacific Biosciences). The identities of gene segments, CDRs, and mutations from germline genes were determined by alignment using the ImMunoGeneTics database (42).

Antibody production and purification

For hybridoma-derived mAb, hybridoma cells were grown to exhaustion in Hybridoma-SFM (1×) serum-free medium (Gibco). For recombinant mAb production, cDNA encoding the genes of heavy and light chains was synthesized and cloned into a DNA plasmid expression vector encoding a full-length IgG1 protein (43) and transformed into *Escherichia coli* cells. mAb proteins were produced after transient transfection of ExpiCHO cells following the manufacturer's protocol. The resulting secreted IgGs were purified from filtered culture supernatants by fast protein liquid chromatography on an ÄKTA instrument using a Protein G column (GE Healthcare Life Sciences). Purified mAbs were buffer-exchanged into PBS, filtered using sterile 0.45- μm -pore size filter devices (Millipore), concentrated, and stored in aliquots at -80°C until use. An aliquot of each mAb also was biotinylated directly in 96-well format using the EZ-Link NHS-PEG₄-Biotin Kit (Thermo Fisher Scientific) with a 20-fold molar excess of biotin to mAb, followed by buffer exchange back to PBS using a desalting plate (Zeba, 7-kDa cutoff). Hybridoma-derived mAbs were used in *in vitro* experiments, and recombinant mAbs were used in *in vivo* experiments. Pooled human IgG was purchased as IVIG (Carimune, CSL Behring, King of Prussia, PA). RSV90 is a recombinant human IgG1 mAb produced in our laboratory that was used as a negative control, placebo mAb in mouse experiments. Polyclonal anti-VP1, -VP2, and -VP3 antibodies used in western blot were purchased from Genetex.

Fab fragment production

Fab fragments were generated and purified via Pierce Fab Preparation Kit (Thermo Fisher Scientific). The Immobilized Papain vial spin column and Zeba Spin Desalting Column were equilibrated with digestion buffer [35 mg of cysteine-HCl per 10 ml of supplied Fab Digestion Buffer (pH \sim 7.0)] before use. The NAb Protein A Plus Spin Column was equilibrated with PBS buffer before use. The original IgG samples were passed through the Zeba Spin Desalting Column, and 0.5 ml of the prepared IgG samples were applied on the Immobilized Papain vial and incubated at 37°C for 5 hours Fab digestion. Then, the final Fab fragments were buffer-exchanged to PBS and stored at 4°C.

EV-D68-specific ELISA

Wells of medium binding, black fluorescent immunoassay microtiter plates (Greiner Bio-One) were coated with virus stocks diluted in 100 mM bicarbonate/carbonate buffer (pH 9.6) and incubated at 4°C overnight. Plates were blocked with 2% BSA in Dulbecco's PBS (DPBS) containing 0.05% Tween 20 for 1 hour. For mAb screening assays, hybridoma culture supernatants were added to the wells and

incubated for 2 hours at ambient temperature. The bound antibodies were detected using Fc-specific goat anti-human IgG conjugated with horseradish peroxidase (Southern Biotech) and QuantaBlu fluorogenic peroxidase substrate (Thermo Fisher Scientific). After 20 min, 100 mM glycine (pH 10.5) was added to quench the reaction, and the emission was measured at 420 nm after excitation at 325 nm using a Synergy H1 microplate reader (BioTek). For dose-response and cross-reactivity assays, serial dilutions of purified mAbs were applied to the wells in duplicate technical replicates, and mAb binding was detected as above; the experiments were performed at least three times. For the competition ELISA, microtiter plates were first coated with virus, and then a purified mAb was added at 100 $\mu\text{g}/\text{ml}$ and allowed to incubate at 33°C for 3 hours. Then, a biotinylated mAb was spiked into this mixture at a final concentration of 5 $\mu\text{g}/\text{ml}$ and allowed to incubate at ambient temperature for 1.5 hours. After a wash and 30 min of incubation with avidin peroxidase (Thermo Fisher Scientific), biotinylated mAb binding was detected as above.

Western blot

B1 clade virus preparation was mixed with denaturing and reducing loading buffer, boiled at 100°C for 5 min, and then run on an SDS-polyacrylamide gel electrophoresis gel along with Novex Sharp Pre-stained Protein Standard (Thermo Fisher Scientific). Protein was transferred to a membrane, blocked in blocking buffer (LI-COR), and then cut into strips so that individual lanes could be stained with purified mAb in blocking buffer. An IRDye 800CW-conjugated goat anti-human secondary antibody (LI-COR) was used to detect mAb binding. Strips were reassembled to visualize molecular weight and imaged on an Odyssey CLx near-infrared imager (LI-COR).

Cryo-EM sample preparation and data collection

For both EV-D68:Fab EV68-159 and EV-D68:Fab EV68-228 complexes, purified EV-D68 viruses and Fabs were mixed at a molar ratio of 1:200. After incubating at room temperature for 45 to 60 min, 3.5 μl of virus-Fab mixture sample was added to a glow-discharged 400-mesh lacey carbon film copper grid (Ted Pella Inc.). Grids were plunge-frozen (Cryoplunge 3 system, Gatan) in liquid ethane after being blotted for 3.5 s in 75 to 80% humidity. Cryo-EM datasets were collected on a 300-kV Titan Krios microscope (Thermo Fisher Scientific). For the EV-D68:Fab EV68-228 dataset, movies were collected using the program Legicon (44) with a K3 direct detection camera (Gatan) at a magnification of \times 64,000, resulting in a super-resolution pixel size of 0.662 Å, with a defocus range from 0.7 to 2 μm . A total electron dose of 44.2 electrons/Å² was recorded in 2.6 s and split into 50 frames. The EV-D68:Fab EV68-159 dataset was acquired with a K2 Summit direct electron detector (Gatan) at a nominal magnification of \times 81,000, resulting in a superresolution pixel size of 0.874 Å and a defocus range from 0.7 to 3.5 μm . A total electron dose of 31.4 electrons/Å² over 12 s of exposure was split into 60 frames. Overall, 462 movies and 732 movies were acquired for the EV-D68:Fab EV68-228 and EV-D68:Fab EV68-159 datasets, respectively.

Image processing

For both datasets, motion correction was performed on the raw movie frames via MotionCor2 (45) as implemented in Appion (46) during data collection. The contrast transfer function was estimated on the aligned frames with CTFFIND4 (47). Particle-picking templates were generated using the Appion Manual Picker (46), and templates

for auto picking were obtained through two-dimensional (2D) classification in XMIPP (48). These templates were then used for autopicking in FindEM (49), and particles were extracted using RELION. These particles were then subjected to multiple rounds of 2D and 3D classifications in RELION (50). This resulted in 20,194 and 30,554 particles for the EV-D68:Fab EV68-228 and EV-D68:Fab EV68-159 datasets, which were selected for final 3D icosahedral reconstructions using the program JSPR following the gold-standard refinement method (51). The final resolutions for both maps were estimated on the basis of a gold-standard Fourier shell correlation cutoff of 0.143 (52). Map sharpening was performed in RELION (50) after processing. Data collection parameters and related items are summarized in table S3.

Model building, refinement, and analysis

The same methods were used for the atomic structures of both EV-D68:Fab EV68-159 and EV-D68:Fab EV68-228. The x-ray crystallography model of the EV-D68 Fermon strain [Protein Data Bank (PDB) code: 4WM8] was selected as a starting reference for model building and was manually fitted into the density maps using the program Chimera (53). Using the initial fitting as a basis, the models were rebuilt in Coot (54) and refined using real-space refinement in PHENIX (55) to correct for outliers and poorly fitted rotamers. Chimera (53), Coot (54), and CCP4i2-PISA (56) were used to determine the binding interface residues. The final atomic models were validated in MolProbity (57). Refinement statistics are described in table S3.

Selection of neutralization escape mutant virus

A clade B1 EV-D68 isolate was passaged under selection with increasing amounts of purified mAb in RD cells. After incubating mAb and virus for 1 hour at 33°C, this mixture was added to a cell monolayer for 2 hours at 33°C. The monolayer was then rinsed thrice, and mAb-containing medium was added back. This culture was incubated at 33°C until at least 70% cytopathic effect was observed (cells lifted off of plate), at which point the cells and supernatant together were collected and frozen to -80°C. This sample was thawed and sonicated in the same microfuge tube in an inverted-cup sonicator at maximum power for 3 × 20 s, vortexed for 30 s at maximum power, and sonicated again for 2 × 20 s. Cellular debris was clarified for 10 min at 10,000g. Then, the virus-containing supernatant was mixed 1:1 with fresh medium containing mAb at higher concentration. Over three passages, mAb concentration was increased from 5 to 50 to 500 ng/ml. Viral RNA was harvested using TRI Reagent and Direct-zol RNA MiniPrep kit (Zymo Research). In triplicate, we generated cDNA templates, from which a 3080-base pair amplicon covering the P1 region of the viral genome was generated with the PrimeScript One Step RT-PCR Kit version 2 (Takara) and primers 5'-CCTCCGGC-CCCTGAAT (forward) and 5'-CCATTGAATCCCTGGCCCTT (reverse). Then, we used a Pacific Biosciences next-generation sequencing platform to generate sequences of each of the three replicates. Two thousand reads of each sequencing run were used to quantitate the percentage of reads in which each mutation was observed. Mutations were determined as compared with a wild-type consensus sequence of all of the reads from the negative control selection mAb selection.

Quantification and statistical analysis

Technical and biological replicates are indicated in the methods and figure legends. Error bars in figures represent SD. Statistical analyses were performed using Prism v8 (GraphPad).

Competition-binding assay

ELISA fluorescence values were normalized to a percentage of maximal binding determined from a control well without an irrelevant prior competing mAb added. The Pearson correlation of each biotinylated mAb to each other biotinylated mAb was calculated using the median inhibition percentage from three different experiments using the *corr* method of the Pandas Python package (58). Hierarchical clustering was then performed on these Pearson correlations using *clustermap* from the Seaborn Python package. The clustering information was exported in newick format and imported into Interactive Tree of Life v4 (59), which was used to display the hierarchically clustered heatmap before importation into Excel (Microsoft) for final display.

Antibody ELISA binding experiments

EC₅₀ values for mAb binding were determined after log transformation of antibody concentration using four-parameter sigmoidal dose-response nonlinear regression analysis constrained to a bottom value of zero and top value less than the maximal fluorescent value of the mAb with the highest saturation fluorescence value.

Virus assays

MAb IC₅₀ values were calculated using a formula based on the Spearman-Kärber equation (36). Viral titers in murine plasma and lungs were compared using a one-way analysis of variance (ANOVA) and Dunnett's multiple comparisons test, with a single pooled variance. A value of *P* < 0.05 was considered significant.

Lung cytokine/chemokine evaluations

For each cytokine/chemokine, the concentrations from treated mice were compared with placebo-treated mice using a Brown-Forsythe one-way ANOVA test and Dunnett's T3 multiple comparisons test, with individual variances computed for each comparison. This analysis was chosen because we did not assume equal standard deviations for each measurement.

In vivo protection studies

Survival curves were generated using the Kaplan-Meier method and curves compared using the log-rank test (Mantel-Cox). Neurologic scores were compared using a chi-square test.

SUPPLEMENTARY MATERIALS

immunology.sciencemag.org/cgi/content/full/5/49/eaba4902/DC1

Fig. S1. Western blot data.

Fig. S2. Detailed characteristics of human mAbs.

Fig. S3. Indirect ELISA data for all mAbs.

Fig. S4. Representative densities from the EV-D68: Fab EV68-228 electron density map.

Fig. S5. Estimates of immune complex map resolutions.

Fig. S6. Comparison of the Fab binding sites.

Fig. S7. Road maps showing an enlarged view of the Fab footprints.

Fig. S8. Bulky side chains of the EV68-228 Fab heavy chain.

Table S1. Characteristics of participants who provided PBMCs.

Table S2. Sequence characteristics of human mAbs.

Table S3. Cryo-EM data acquisition parameters and refinement statistics.

Table S4. Structural contact amino acid residues of EV-D68 and respective Fabs.

Table S5. Neurologic scores of individual mice treated with antibody after EV-D68 inoculation.

Table S6. Neutralization escape amino acid mutations.

Table S7. EV-D68 isolates used.

Table S8. Raw data file (Excel spreadsheet).

[View/request a protocol for this paper from Bio-protocol.](#)

REFERENCES AND NOTES

1. Y. Liu, J. Sheng, A. Fokine, G. Meng, W. H. Shin, F. Long, R. J. Kuhn, D. Kihara, M. G. Rossmann, Structure and inhibition of EV-D68, a virus that causes respiratory illness in children. *Science* **347**, 71–74 (2015).

2. Centers for Disease Control and Prevention (CDC), Clusters of acute respiratory illness associated with human enterovirus 68—Asia, Europe, and United States, 2008–2010. *MMWR Morb. Mortal. Wkly. Rep.* **60**, 1301–1304 (2011).
3. C. M. Midgley, J. T. Watson, W. A. Nix, A. T. Curns, S. L. Rogers, B. A. Brown, C. Conover, S. R. Dominguez, D. R. Feikin, S. Gray, F. Hassan, S. Hoferka, M. A. Jackson, D. Johnson, E. Leshem, L. Miller, J. B. Nichols, A. C. Nyquist, E. Obringer, A. Patel, M. Patel, B. Rha, E. Schneider, J. E. Schuster, R. Selvarangan, J. F. Seward, G. Turabelidze, M. S. Oberste, M. A. Pallansch, S. I. Gerber; EV-D68 Working Group, Severe respiratory illness associated with a nationwide outbreak of enterovirus D68 in the USA (2014): A descriptive epidemiological investigation. *Lancet Respir. Med.* **3**, 879–887 (2015).
4. R. Poelman, I. Schuffenecker, C. Van Leer-Buter, L. Josset, H. G. Niesters, B. Lina; ESCV-ECDC EV-D68 study group, European surveillance for enterovirus D68 during the emerging North-American outbreak in 2014. *J. Clin. Virol.* **71**, 1–9 (2015).
5. J. J. Sejvar, A. S. Lopez, M. M. Cortese, E. Leshem, D. M. Pastula, L. Miller, C. Glaser, A. Kambhampati, K. Shioda, N. Aliabadi, M. Fischer, N. Gregoricus, R. Lanciotti, W. A. Nix, S. K. Sakthivel, D. S. Schmid, J. F. Seward, S. Tong, M. S. Oberste, M. Pallansch, D. Feikin, Acute flaccid myelitis in the United States, August–December 2014: Results of nationwide surveillance. *Clin. Infect. Dis.* **63**, 737–745 (2016).
6. A. Lopez, A. Lee, A. Guo, J. L. Konopka-Anstadt, A. Nisler, S. L. Rogers, B. Emery, W. A. Nix, S. Oberste, J. Routh, M. Patel, Vital signs: Surveillance for acute flaccid myelitis – United States, 2018. *MMWR Morb. Mortal. Wkly. Rep.* **68**, 608–614 (2019).
7. K. Messacar, E. J. Asturias, A. M. Hixon, C. Van Leer-Buter, H. G. M. Niesters, K. L. Tyler, M. J. Abzug, S. R. Dominguez, Enterovirus D68 and acute flaccid myelitis—evaluating the evidence for causality. *Lancet Infect. Dis.* **18**, e239–e247 (2018).
8. N. Mishra, T. F. F. Ng, R. L. Marine, K. Jain, J. Ng, R. Thakkar, A. Caciula, A. Price, J. A. Garcia, J. C. Burns, K. T. Thakur, K. L. Hertzler, J. A. Routh, J. L. Konopka-Anstadt, W. A. Nix, R. Tokarz, T. Briese, M. S. Oberste, W. I. Lipkin, Antibodies to enteroviruses in cerebrospinal fluid of patients with acute flaccid myelitis. *MBio* **10**, e01903–19 (2019).
9. R. D. Schubert, I. A. Hawes, P. S. Ramachandran, A. Ramesh, E. D. Crawford, J. E. Pak, W. Wu, C. K. Cheung, B. D. O'Donovan, C. M. Tato, A. Lyden, M. Tan, R. Sit, G. A. Sowa, H. A. Sample, K. C. Zorn, D. Banerji, L. M. Khan, R. Bove, S. L. Hauser, A. A. Gelfand, B. L. Johnson-Kerner, K. Nash, K. S. Krishnamoorthy, T. Chitnis, J. Z. Ding, H. J. McMillan, C. Y. Chiu, B. Briggs, C. A. Glaser, C. Yen, V. Chu, D. A. Wadford, S. R. Dominguez, T. F. F. Ng, R. L. Marine, A. S. Lopez, W. A. Nix, A. Soldatos, M. P. Gorman, L. Benson, K. Messacar, J. L. Konopka-Anstadt, M. S. Oberste, J. L. DeRisi, M. R. Wilson, Pan-viral serology implicates enteroviruses in acute flaccid myelitis. *Nat. Med.* **25**, 1748–1752 (2019).
10. D. M. Morens, G. K. Folkers, A. S. Fauci, Acute flaccid myelitis: Something old and something new. *MBio* **10**, e00521–19 (2019).
11. J. Sun, X.-Y. Hu, X.-F. Yu, Current understanding of human enterovirus D68. *Viruses* **11**, 490 (2019).
12. M. R. Vogt, J. E. Crowe Jr., Current understanding of humoral immunity to enterovirus D68. *J. Pediatric Infect. Dis. Soc.* **7**, 549–553 (2018).
13. S. Sun, F. Gao, Y. Hu, L. Bian, X. Wu, Y. Su, R. Du, Y. Fu, F. Zhu, Q. Mao, Z. Liang, A cross-sectional seroepidemiology study of EV-D68 in China. *Emerg. Microbes Infect.* **7**, 99 (2018).
14. E. Kamau, H. Harvala, S. Blomqvist, D. Nguyen, P. Horby, R. Pebody, P. Simmonds, Increase in enterovirus D68 infections in young children, United Kingdom, 2006–2016. *Emerg. Infect. Dis.* **25**, 1200–1203 (2019).
15. Y. Zhang, D. D. Moore, W. A. Nix, M. S. Oberste, W. C. Weldon, Neutralization of enterovirus D68 isolated from the 2014 US outbreak by commercial intravenous immune globulin products. *J. Clin. Virol.* **69**, 172–175 (2015).
16. A. M. Hixon, P. Clarke, K. L. Tyler, Evaluating treatment efficacy in a mouse model of enterovirus D68-associated paralytic myelitis. *J. Infect. Dis.* **216**, 1245–1253 (2017).
17. N. Nathanson, The pathogenesis of poliomyelitis: What we don't know. *Adv. Virus Res.* **71**, 1–50 (2008).
18. Y. Tan, F. Hassan, J. E. Schuster, A. Simenauer, R. Selvarangan, R. A. Halpin, X. Lin, N. Fedorova, T. B. Stockwell, T. T. Lam, J. D. Chappell, T. V. Hartert, E. C. Holmes, S. R. Das, Molecular evolution and intracade recombination of enterovirus D68 during the 2014 outbreak in the United States. *J. Virol.* **90**, 1997–2007 (2016).
19. R. Dyrda, M. Mastafa, E. B. Hodcroft, R. A. Neher, J. Albert, Intra- and interpatient evolution of enterovirus D68 analyzed by whole-genome deep sequencing. *Virus Evol.* **5**, vez007 (2019).
20. S. A. Kujawski, C. M. Midgley, B. Rha, J. Y. Lively, W. A. Nix, A. T. Curns, D. C. Payne, J. A. Englund, J. A. Boom, J. V. Williams, G. A. Weinberg, M. A. Staat, R. Selvarangan, N. B. Halasa, E. J. Klein, L. C. Sahni, M. G. Michaels, L. Shelley, M. McNeal, C. J. Harrison, L. S. Stewart, A. S. Lopez, J. A. Routh, M. Patel, M. S. Oberste, J. T. Watson, S. I. Gerber, Enterovirus D68-associated acute respiratory illness – New Vaccine Surveillance Network, United States, July–October, 2017 and 2018. *MMWR Morb. Mortal. Wkly. Rep.* **68**, 277–280 (2019).
21. Q. Zheng, R. Zhu, L. Xu, M. He, X. Yan, D. Liu, Z. Yin, Y. Wu, Y. Li, L. Yang, W. Hou, S. Li, Z. Li, Z. Chen, Z. Li, H. Yu, Y. Gu, J. Zhang, T. S. Baker, Z. H. Zhou, B. S. Graham, T. Cheng, S. Li, N. Xia, Atomic structures of enterovirus D68 in complex with two monoclonal antibodies define distinct mechanisms of viral neutralization. *Nat. Microbiol.* **4**, 124–133 (2019).
22. M. G. Rossmann, E. Arnold, J. W. Erickson, E. A. Frankengerger, J. P. Griffith, H.-J. Hecht, J. E. Johnson, G. Kamer, M. Luo, A. G. Mosser, R. R. Rueckert, B. Shery, G. Vriend, Structure of a human common cold virus and functional relationship to other picornaviruses. *Nature* **317**, 145–153 (1985).
23. W. J. Evans, B. L. Hurst, C. J. Peterson, A. J. Van Wettere, C. W. Day, D. F. Smee, E. B. Tarbet, Development of a respiratory disease model for enterovirus D68 in 4-week-old mice for evaluation of antiviral therapies. *Antivir. Res.* **162**, 61–70 (2019).
24. B. L. Hurst, W. J. Evans, D. F. Smee, A. J. Van Wettere, E. B. Tarbet, Evaluation of antiviral therapies in respiratory and neurological disease models of enterovirus D68 infection in mice. *Virology* **526**, 146–154 (2019).
25. A. I. Flyak, S. Ruiz, M. D. Colbert, T. Luong, J. E. Crowe Jr., J. R. Bailey, P. J. Bjorkman, HCV broadly neutralizing antibodies use a CDRH3 disulfide motif to recognize an E2 glycoprotein site that can be targeted for vaccine design. *Cell Host Microbe* **24**, 703–716.e3 (2018).
26. S. Bangaru, S. Lang, M. Schotsaert, H. A. Vanderven, X. Zhu, N. Kose, R. Bombardi, J. A. Finn, S. J. Kent, P. Gilchuk, H. L. Turner, A. Garcia-Sastre, S. Li, A. B. Ward, I. A. Wilson, J. E. Crowe Jr., A site of vulnerability on the influenza virus hemagglutinin head domain trimer interface. *Cell* **177**, 1136–1152.e18 (2019).
27. Y. Liu, J. Sheng, J. Baggen, G. Meng, C. Xiao, H. J. Thibaut, F. J. van Kuppeveld, M. G. Rossmann, Sialic acid-dependent cell entry of human enterovirus D68. *Nat. Commun.* **6**, 8865 (2015).
28. D. J. Filman, R. Syed, M. Chow, A. J. Macadam, P. D. Minor, J. M. Hogle, Structural factors that control conformational transitions and serotype specificity in type 3 poliovirus. *EMBO J.* **8**, 1567–1579 (1989).
29. C. Zhang, X. Zhang, W. Zhang, W. Dai, J. Xie, L. Ye, H. Wang, H. Chen, Q. Liu, S. Gong, L. Geng, Z. Huang, Enterovirus D68 virus-like particles expressed in *Pichia pastoris* potentially induce neutralizing antibody responses and confer protection against lethal viral infection in mice. *Emerg. Microbes Infect.* **7**, 3 (2018).
30. W. Dai, C. Zhang, X. Zhang, P. Xiong, Q. Liu, S. Gong, L. Geng, D. Zhou, Z. Huang, A virus-like particle vaccine confers protection against enterovirus D68 lethal challenge in mice. *Vaccine* **36**, 653–659 (2018).
31. C. Zhang, X. Zhang, W. Dai, Q. Liu, P. Xiong, S. Wang, L. Geng, S. Gong, Z. Huang, A mouse model of enterovirus D68 infection for assessment of the efficacy of inactivated vaccine. *Viruses* **10**, 58 (2018).
32. M. C. Patel, W. Wang, L. M. Pletneva, S. V. Rajagopala, Y. Tan, T. V. Hartert, M. S. Boukhvalova, S. N. Vogel, S. R. Das, J. C. Blanco, Enterovirus D-68 infection, prophylaxis, and vaccination in a novel permissive animal model, the cotton rat (*Sigmodon hispidus*). *PLOS ONE* **11**, e0166336 (2016).
33. K. Messacar, T. L. Schreiner, K. Van Haren, M. Yang, C. A. Glaser, K. L. Tyler, S. R. Dominguez, Acute flaccid myelitis: A clinical review of US cases 2012–2015. *Ann. Neurol.* **80**, 326–338 (2016).
34. M. R. Posner, H. Elboim, D. Santos, The construction and use of a human-mouse myeloma analogue suitable for the routine production of hybridomas secreting human monoclonal antibodies. *Hybridoma* **6**, 611–625 (1987).
35. X. Yu, P. A. McGraw, F. S. House, J. E. Crowe Jr., An optimized electrofusion-based protocol for generating virus-specific human monoclonal antibodies. *J. Immunol. Methods* **336**, 142–151 (2008).
36. M. A. Ramakrishnan, Determination of 50% endpoint titer using a simple formula. *World J. Virol.* **5**, 85–86 (2016).
37. W. C. Weldon, M. S. Oberste, M. A. Pallansch, Standardized methods for detection of poliovirus antibodies. *Methods Mol. Biol.* **1387**, 145–176 (2016).
38. R. F. Lemanske Jr., The childhood origins of asthma (COAST) study. *Pediatr. Allergy Immunol.* **13**, 38–43 (2002).
39. Y. A. Bochkov, K. Grindle, F. Vang, M. D. Evans, J. E. Gern, Improved molecular typing assay for rhinovirus species A, B, and C. *J. Clin. Microbiol.* **52**, 2461–2471 (2014).
40. S. A. Smith, J. E. Crowe Jr., Use of human hybridoma technology to isolate human monoclonal antibodies. *Microbiol. Spectr.* **3**, AID-0027-2014 (2015).
41. M. A. Turchaninova, A. Davydov, O. V. Britanova, M. Shugay, V. Bikos, E. S. Egorov, V. I. Kirgizova, E. M. Merzlyak, D. B. Staroverov, D. A. Bolotin, I. Z. Mamedov, M. Izraelson, M. D. Logacheva, O. Kladova, K. Plevova, S. Pospisilova, D. M. Chudakov, High-quality full-length immunoglobulin profiling with unique molecular barcoding. *Nat. Protoc.* **11**, 1599–1616 (2016).
42. V. Giudicelli, M. P. Lefranc, IMGT/junctionanalysis: IMGT standardized analysis of the V-J and V-D-J junctions of the rearranged immunoglobulins (IG) and T cell receptors (TR). *Cold Spring Harb Protoc* **2011**, 716–725 (2011).
43. G. R. McLean, A. Nakouzi, A. Casadevall, N. S. Green, Human and murine immunoglobulin expression vector cassettes. *Mol. Immunol.* **37**, 837–845 (2000).
44. C. Suloway, J. Pulokas, D. Fellmann, A. Cheng, F. Guerra, J. Quispe, S. Stagg, C. S. Potter, B. Carragher, Automated molecular microscopy: The new Legimon system. *J. Struct. Biol.* **151**, 41–60 (2005).

45. S. Q. Zheng, E. Palovcak, J. P. Armache, K. A. Verba, Y. Cheng, D. A. Agard, MotionCor2: Anisotropic correction of beam-induced motion for improved cryo-electron microscopy. *Nat. Methods* **14**, 331–332 (2017).
46. G. C. Lander, S. M. Stagg, N. R. Voss, A. Cheng, D. Fellmann, J. Pulokas, C. Yoshioka, C. Irving, A. Mulder, P. W. Lau, D. Lyumkis, C. S. Potter, B. Carragher, Appion: An integrated, database-driven pipeline to facilitate EM image processing. *J. Struct. Biol.* **166**, 95–102 (2009).
47. A. Rohou, N. Grigorieff, CTFFIND4: Fast and accurate defocus estimation from electron micrographs. *J. Struct. Biol.* **192**, 216–221 (2015).
48. C. O. Sorzano, R. Marabini, J. Velazquez-Muriel, J. R. Bilbao-Castro, S. H. Scheres, J. M. Carazo, A. Pascual-Montano, XMIPP: A new generation of an open-source image processing package for electron microscopy. *J. Struct. Biol.* **148**, 194–204 (2004).
49. A. M. Roseman, FindEM—A fast, efficient program for automatic selection of particles from electron micrographs. *J. Struct. Biol.* **145**, 91–99 (2004).
50. S. H. Scheres, RELION: Implementation of a Bayesian approach to cryo-EM structure determination. *J. Struct. Biol.* **180**, 519–530 (2012).
51. F. Guo, W. Jiang, Single particle cryo-electron microscopy and 3-D reconstruction of viruses. *Methods Mol. Biol.* **1117**, 401–443 (2014).
52. S. H. Scheres, S. Chen, Prevention of overfitting in cryo-EM structure determination. *Nat. Methods* **9**, 853–854 (2012).
53. E. F. Pettersen, T. D. Goddard, C. C. Huang, G. S. Couch, D. M. Greenblatt, E. C. Meng, T. E. Ferrin, UCSF Chimera—A visualization system for exploratory research and analysis. *J. Comput. Chem.* **25**, 1605–1612 (2004).
54. P. Emsley, B. Lohkamp, W. G. Scott, K. Cowtan, Features and development of Coot. *Acta Crystallogr. D Biol. Crystallogr.* **66**, 486–501 (2010).
55. P. D. Adams, P. V. Afonine, G. Bunkoczi, V. B. Chen, I. W. Davis, N. Echols, J. J. Headd, L. W. Hung, G. J. Kapral, R. W. Grosse-Kunstleve, A. J. McCoy, N. W. Moriarty, R. Oeffner, R. J. Read, D. C. Richardson, J. S. Richardson, T. C. Terwilliger, P. H. Zwart, PHENIX: A comprehensive Python-based system for macromolecular structure solution. *Acta Crystallogr. D Biol. Crystallogr.* **66**, 213–221 (2010).
56. L. Potterton, J. Agirre, C. Ballard, K. Cowtan, E. Dodson, P. R. Evans, H. T. Jenkins, R. Keegan, E. Krissinel, K. Stevenson, A. Lebedev, S. J. McNicholas, R. A. Nicholls, M. Noble, N. S. Pannu, C. Roth, G. Sheldrick, P. Skubak, J. Turkenburg, V. Uski, F. von Delft, D. Waterman, K. Wilson, M. Winn, M. Wojdyr, CCP4i2: The new graphical user interface to the CCP4 program suite. *Acta Crystallogr. D Struct. Biol.* **74**, 68–84 (2018).
57. V. B. Chen, W. B. Arendall III, J. J. Headd, D. A. Keedy, R. M. Immormino, G. J. Kapral, L. W. Murray, J. S. Richardson, D. C. Richardson, in *International Tables for Crystallography* (Springer, 2012), vol. F, chap. 21.6, pp. 694–701.
58. W. McKinney, in *Proceedings of the Python in Science Conferences*, S. van der Walt, J. Millman, Eds. (SciPy, 2010), pp. 51–56.
59. I. Letunic, P. Bork, Interactive Tree Of Life (iTOL) v4: Recent updates and new developments. *Nucleic Acids Res.* **47**, W256–W259 (2019).
- Acknowledgments:** We thank M. Jensen, R. Sutton, R. Nargi, E. Armstrong, M. Goff, W. Reichard, L. Shakhmourad, T. Cooper, M. Jenkins, P. Gilchuk, and R. Carnahan for laboratory support in generation or characterization of antibodies. M. Schildts and T. Tan assisted with data about virus isolates and sequences. S. Das contributed discussion and provided the Fermon virus isolate. We thank C. Tisler, D. J. Jackson, and R. F. Lemanske Jr. for coordinating human participants and sample acquisition. We also thank the Purdue Cryo-EM Facility. Vanderbilt University Medical Center used the nonclinical and preclinical services program offered by the National Institute of Allergy and Infectious Diseases, coordinated by Eunchung Park. Contract murine studies supported by NIAID were performed by B. Hurst and B. Tarbet at Utah State University. **Funding:** M.R.V. was supported by the Pediatric Infectious Diseases Society–St. Jude Children’s Research Hospital Fellowship Program in Basic Research. This work was supported by NIH grant T32 HL069765 (to L.E.W.), U19 AI117905 (to J.E.C.), P01 HL070831 and U19 AI104317 (to J.E.G.), and R01 AI011219 and CSGID contract HHSN272201700060C (to R.J.K.). The content is solely the responsibility of the authors and does not necessarily represent the official views of the NIH. **Author contributions:** M.R.V., J.F., R.B., M.G.R., R.J.K., and J.E.C. planned the studies. M.R.V., J.F., N.K., L.E.W., R.B., and T.K. conducted experiments. Y.A.B. and J.E.G. obtained human specimens. M.R.V., J.F., R.B., I.S., I.S.G., T.K., R.J.K., and J.E.C. interpreted the studies. M.R.V. and J.E.C. wrote the first draft of the paper. M.R.V., M.G.R., J.E.G., and J.E.C. obtained funding. All authors reviewed, edited, and approved the paper. **Competing interests:** J.E.C. is on the Scientific Advisory Boards of CompuVax and Meissa Vaccines, is a recipient of previous unrelated research grants from Moderna and Sanofi, and is founder of IDBiologics Inc. J.E.G. serves as consultant for MedImmune, Regeneron, Ena Therapeutics, and Meissa Vaccines. Vanderbilt University has applied for a patent concerning antibodies discussed in this paper; M.R.V. and J.E.C. are cited as inventors. All other authors declared that they have no competing interests. **Data and materials availability:** The (EV-D68 virus + EV68-159 Fab) and the (EV-D68 virus + EV68-228 Fab) cryo-EM structures have been deposited to the PDB and Electron Microscopy Data Bank (EMDB) under accession numbers: PDB 6WDS and EMD-21647 and PDB 6WDT and EMD-21648, respectively. All relevant data are included within the manuscript. Further information and requests for resources and reagents should be directed to and will be fulfilled by the lead contact, J.E.C. (james.crowe@vumc.org). Materials described in this paper are available for distribution under the Association of University Technology Managers (AUTM) Uniform Biological Material Transfer Agreement (UBMTA).

Submitted 8 December 2019
 Accepted 12 June 2020
 Published 3 July 2020
 10.1126/sciimmunol.aba4902

Citation: M. R. Vogt, J. Fu, N. Kose, L. E. Williamson, R. Bombardi, I. S. Georgiev, T. Klose, M. G. Rossmann, Y. A. Bochkov, J. E. Gern, R. J. Kuhn, J. E. Crowe Jr., Human antibodies neutralize enterovirus D68 and protect against infection and paralytic disease. *Sci. Immunol.* **5**, eaba4902 (2020).

ARTIFICIAL INTELLIGENCE

Beyond imitation: Zero-shot task transfer on robots by learning concepts as cognitive programs

Miguel Lázaro-Gredilla*, Dianhuan Lin, J. Swaroop Guntupalli, Dileep George*

Humans can infer concepts from image pairs and apply those in the physical world in a completely different setting, enabling tasks like IKEA assembly from diagrams. If robots could represent and infer high-level concepts, then it would notably improve their ability to understand our intent and to transfer tasks between different environments. To that end, we introduce a computational framework that replicates aspects of human concept learning. Concepts are represented as programs on a computer architecture consisting of a visual perception system, working memory, and action controller. The instruction set of this cognitive computer has commands for parsing a visual scene, directing gaze and attention, imagining new objects, manipulating the contents of a visual working memory, and controlling arm movement. Inferring a concept corresponds to inducing a program that can transform the input to the output. Some concepts require the use of imagination and recursion. Previously learned concepts simplify the learning of subsequent, more elaborate concepts and create a hierarchy of abstractions. We demonstrate how a robot can use these abstractions to interpret novel concepts presented to it as schematic images and then apply those concepts in very different situations. By bringing cognitive science ideas on mental imagery, perceptual symbols, embodied cognition, and deictic mechanisms into the realm of machine learning, our work brings us closer to the goal of building robots that have interpretable representations and common sense.

INTRODUCTION

Humans are good at inferring the concepts conveyed in a pair of images and then applying them in a completely different setting—for example, the concept of stacking red and green objects in Fig. 1A applied to the different settings in Fig. 1 (B to D). The human-inferred concepts are at a sufficiently high level to be effortlessly applied in situations that look very different, a capacity so natural that it is used by IKEA and LEGO to make language-independent assembly instructions. In contrast, robots are currently programmed by tediously specifying the desired object locations and poses or by imitation learning where the robot mimics the actions from a demonstration (1–4). By relying on brittle stimulus-response mapping from image frames to actions, the imitation-learning policies often do not generalize to variations in the environment, which might include changes in size, shape, and/or appearance of objects; their relative positions; background clutter; and lighting conditions (5).

If, like people, a robot could extract the conceptual representation from pairs of images given as training examples (Fig. 1A) and then apply the concept in markedly different situations and embodiments, then it would greatly increase their adaptability to new situations and to unstructured environments. A shared conceptual structure with humans would also simplify communicating tasks to a robot at a high level and help to improve their conceptual repertoire with further interactions.

A concept is a redescription of everyday experience into a higher level of abstraction (6, 7). One way to characterize the pictures in Fig. 1 is a pixel-by-pixel description of the changes from the input image to the output, a description that will not generalize to new situations. Concepts enable a higher level of description that generalizes to new situations and ground (8, 9) verbal expressions like “stack green objects on the right” with real-world referents. In contrast to the visuospatial concepts like the one in Fig. 1A that are easy and immediate even for children (10), numerical concepts like the one shown in Fig. 1E are neither easy nor immediate for people. The concepts that are easy and

immediate, and form the basis of common sense in humans, are a very small subset of all potential concepts.

Here, we hypothesize that human concepts are programs, termed cognitive programs (11), implemented on a biased Turing machine (12) [e.g., a “Human Turing Machine” (13)] whose architectural constraints and biases are fundamentally different from the prevalent von Neumann style (14) architectures. Under this hypothesis, the inductive biases encoded in the architecture and instruction set of this computer explain why visuospatial concepts like those in Fig. 1A are easy and intuitive for humans, whereas the numeric concept shown in Fig. 1E is more difficult and unintuitive. In this view, concepts arise from the sequencing of elemental operations (15) on a cognitive computer according to a probabilistic language of thought (16, 17), and their generalization to new situations arises out of skillful deployment of visual attention, imagination, and actions.

Our current work builds on several key ideas from both cognitive and systems neuroscience—such as visual routines (18), perceptual symbol systems (6), image schemas (7, 19, 20), deictic mechanisms (21), and mental imagery (22)—and brings them into the foray of machine learning. Following the ideas of perceptual symbol systems (6) and image schemas (23), we treat concepts as simulations in a sensorimotor system with imageable spatial information forming its fundamental building block (20). To this end, we developed a computer architecture called visual cognitive computer (VCC) and represented concepts as programs on this computer. The main components of VCC include a vision hierarchy (VH) (24), a dynamics model for interactions between objects (25), an attention controller, an imagination blackboard, a limb controller, a set of primitives, and program induction. We evaluated our architecture on its ability to represent and infer visuospatial concepts that cognitive scientists consider to be the fundamental building blocks (20). By building a working computational model and by evaluating it on real-world robotics applications, we brought several of these ideas, which exist purely as descriptive theories, into a concrete framework useful for hypothesis testing and applications.

Given input-output examples indicating concepts (Fig. 1A), we induced programs in this architecture and executed those programs on

Copyright © 2019
The Authors, some
rights reserved;
exclusive licensee
American Association
for the Advancement
of Science. No claim
to original U.S.
Government Works

Vicarious AI, CA, USA.

*Corresponding author. Email: miguel@vicarious.com (M.L.-G.); dileep@vicarious.com (D.G.)

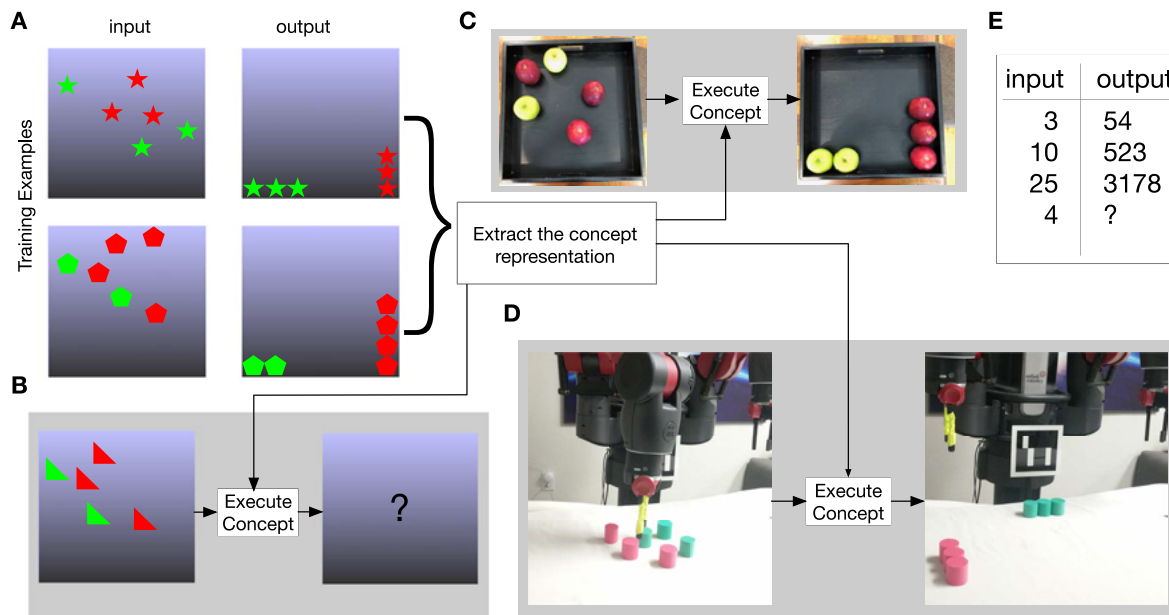


Fig. 1. People can easily understand the concept conveyed in pairs of images, a capability that is exploited by LEGO and IKEA assembly diagrams. (A) People interpret the concept conveyed by these images as stacking red objects vertically on the right and green objects horizontally at the bottom. **(B)** Given a novel image, people can predict what the result of executing the concept would be. **(C)** Concepts inferred from schematic images as in (A) can be applied in real-world settings. **(D)** Enabling robots to understand concepts conveyed in image pairs will significantly simplify communicating tasks to robots. **(E)** Not all concepts conveyed as input-output pairs are as readily apparent to humans as the visual and spatial reasoning tasks.

different robots to perform the desired tasks (Fig. 1, B to D). In contrast to imitation learning where a robot mimics a demonstration in the same setting, we show that the cognitive programs induced on our proposed architecture learned the underlying concepts and generalized well to markedly new settings without explicit demonstrations. Cognitive programs exhibited schematic-to-real transfer similar to the capability of humans to understand concepts from schematic drawings and then apply them in situations that look very different (26).

Cognitive programs on a VCC

In this section, we describe the architecture of VCC, introduce the tabletop world where it is evaluated, and provide an overview of program induction on VCC. VCC is a mechanistic consolidation of visual perception, a dynamics model, actions, attention control, working memories, and deictic mechanisms into a computer architecture. The design process for VCC started with architectural sketches provided in previous works (11, 13) based on cognitive (6, 18) and neuroscience (15, 22) considerations. These architectural sketches provided functional requirements, rough block diagrams, and descriptive theories as a starting point but no computational models. This initial architecture was then refined and extended by codesigning it with an instruction set from the viewpoint of succinctness and completeness in program induction (17, 27).

Figure 2A shows the architecture of VCC that includes the embodiment of the agent. The agent has a hand that can move objects either in the real world or in imagination and an eye whose center can be positioned within an input scene using fixation movements. The VH can parse input scenes containing multiple objects and can imagine objects, similar to the generative model we developed in (24) where top-down attention is used to segment out objects from background clutter. Parsed objects of a scene are stored in the object-indexing memory and are ordered according to their distance from the center of fixation. The dynamics model combined with the VH lets VCC predict the effect

of imagined movements and write those results into the imagination blackboard. The attention controller is used selectively and, in a top-down manner, attends to objects based on their category or color. Top-down attention also acts as an internal pointing mechanism (21) to reference objects in the imagination blackboard. An external agent—a teacher, for instance—can interact with the VCC agent by showing it images and by directing its attention with a pointer (28).

In addition to the imagination blackboard, VCC has other structured working memories for object indexing, color indexing, and fixation history. The working memories are structured in how they represent their content, and their locality to their controllers enforces structured access; the instructions that can read from and write to specific memories are prespecified. Figure 2B lists the instruction set of VCC and their mapping to the different controllers. The VCC instruction set was heavily influenced by the primacy of objects and spatial primitives in human cognition (29) and by the elemental operations that have been previously proposed (11, 15). See the Supplementary Materials for implementation details of the instruction set.

One critical design consideration for VCC is the ease of program induction. As an effect of having working memories that are local and specific to instructions rather than as generic registers in a von Neumann architecture, the program induction search is vastly simplified because of the fewer unbound variables in a candidate program (see fig. S1 for input and output working memory mappings of some of the instructions). Looping constructs `loop_start` and `loop_end` are constrained to loop over the currently attended objects in a scene. The instructions `set_color_attn`, `set_shape_attn`, `fixate_location`, and `imagine_object` have arguments that determine their effect. During program induction, the arguments to be used for a particular input-output pair can be explicitly searched or predicted from the inputs by using neural networks that are trained for that purpose. In addition, the arguments to the `fixate_location` command

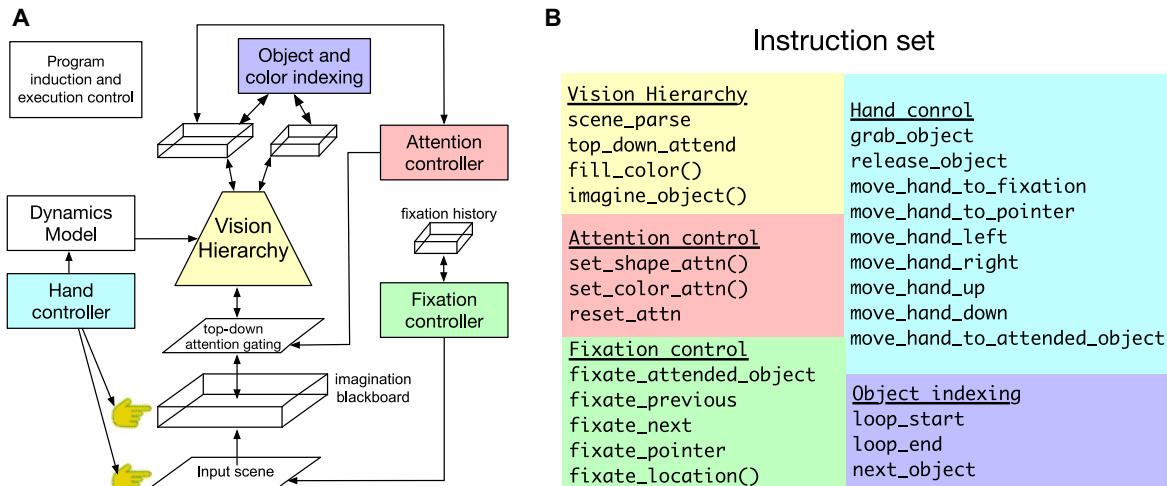


Fig. 2. Architecture and the full instruction set of the VCC. (A) Building blocks of VCC and their interactions. VH parses an input scene into objects and can attend to objects and imagine them. The hand controller has commands for moving the hand to different locations in the scene, and the fixation controller commands position the center of the eye. Object indexing commands iterate through the objects currently attended to. The attention controller can set the current attention based on object shape or color. **(B)** The full instruction set of VCC. Parentheses denote instructions with arguments. All concepts are represented using learned sequences of these 24 primitive instructions.

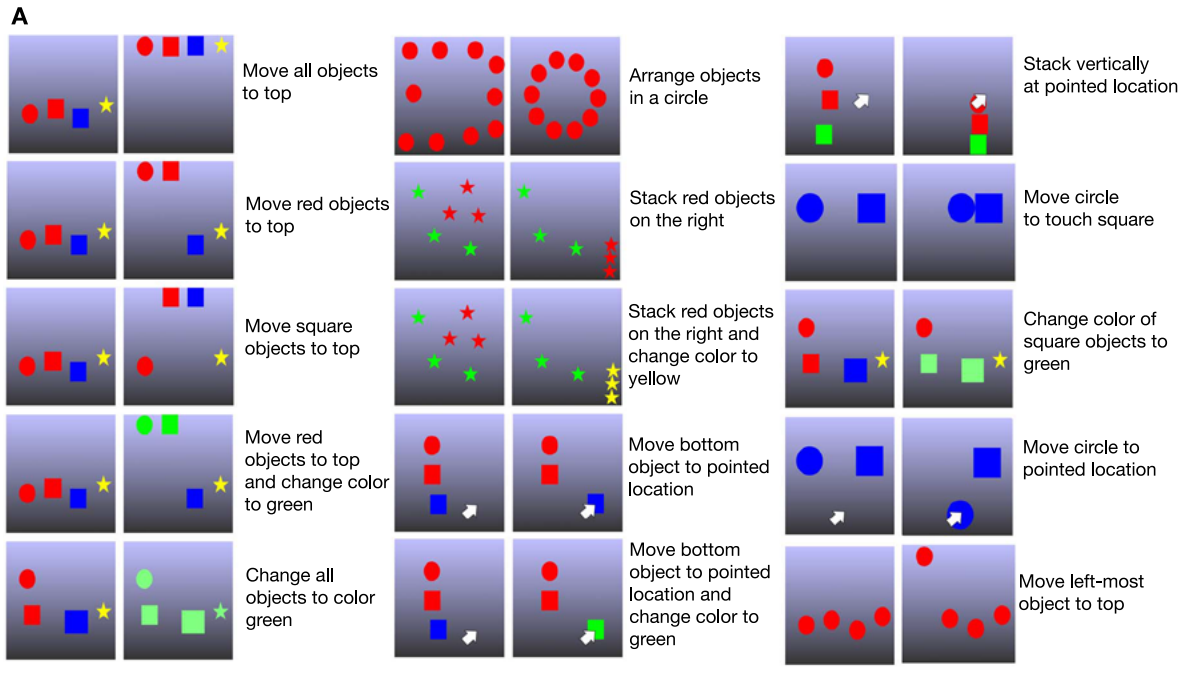
can be set externally by a teacher by the use of a pointer. A learner that takes advantage of “fixation guidance” from a teacher or accurate predictions of instruction arguments from a neural network can speed up induction by reducing the search space.

To guide the design and evaluation of VCC, we used visual concepts in “tabletop world” (TW) corresponding to the spatial arrangement of objects on a tabletop (Fig. 3A). TW allowed us to focus on imageable objects and spatial primitives that are considered to be the first conceptual building blocks (20) and provided a rich set of concepts to rigorously test concept representation and generalization while having simplified dynamics and perceptual requirements compared with the full complexity of the real world. Object motions in TW are limited to sliding along the surface of the table, and they stop moving when they collide with other objects or with the boundary of the workspace. How an agent generalizes its acquired concepts depends on the regularities of the world it is exposed to and on the regularities in its interaction with the world. By being a proper subset of the real world, TW enabled representation and discovery of concepts from schematic images while still having real-world counterparts. The infinite number of physical realizations of each TW concept enabled testing for strong generalization on a physical robot.

Figure 3B shows a simple, manually written cognitive program for a concept, serving to illustrate the representational properties of the VCC. The concept involves making the object close to the center touch the other object in the scene. Because the fixation is centered by default, the centered object is highlighted on the first call to `top_down_attend`. After moving the hand toward that object and grabbing it, `next_object` command is used to switch the attention to the other object. Moving the grabbed object toward the other object until collision achieves the desired goal of making the objects touch. Stopping the object when it comes into contact with another object requires access to the details of the outer contours of the object, a detail that is available only at the bottom of the VH. In contrast to architectures like auto-encoders that map a visual input to a fixed encoding in a feed-forward manner (30), the imagination buffer of VCC allows for the details of the object to be represented and accessed from the real world as required. As anticipated in (6), this allows the VH to be part of an interactive querying

of the world as part of a program rather than representing a scene in one feed-forward pass for downstream tasks. In our current work, we assumed that the VH and dynamics are already learned as described in our earlier works (24, 25).

The problem of learning to represent concepts is this: Given a set of input-output image pairs representing a concept, induce a program that will produce the correct output image when executed on the VCC with the corresponding input image. To solve this problem, we combined insights from recent developments in program induction (31–37) with the architectural advantages of VCC. Each program can be assigned a probability based on a model for the space of programs. To efficiently find a program for a given set of input-output pairs, our induction method relies on searching for programs in decreasing order of probability, where the probabilities are determined on the basis of generative models trained on already found programs and discriminative models that are conditioned on current inputs (Fig. 4A). We used Markov chains of instruction-to-instruction transitions (blue arrows in Fig. 4A) as generative models. This was augmented with subroutine discovery, which replaces a sequence of atomic instructions with a new instruction that can then be used in the Markov chain. Updating the generative model can be understood in the explore-compress (E-C) framework (34) where induction alternates between an exploration phase and a compression phase. During exploration, an existing generative model was used to guide the search of new programs, and during compression, all the programs found so far were used to update the generative model. The generative model works as an input-agnostic prior for the space of future programs given the concepts learned earlier. During search, this prior was combined with “argument predictions”: predictions from discriminative models (neural networks) (32) about the value that the argument of each instruction will take, given that the instruction is part of the program. This prediction is specific to instructions (green arrows in Fig. 4A) and conditional on the specific input-output pairs that the program is being induced for. If a teacher is available, then fixation guidance can be used as an additional signal to predict the arguments of certain instructions. In addition, run-time exceptions generated from the VCC, represented as solid red circles in Fig. 4A, were used to prune the search space. See Materials and Methods for more details.



B
Make central object touch the other object

```

1 scene_parse()
2 top_down_attend()
3 move_hand_to_attended_object()
4 grab_object()
5 next_object()
6 top_down_attend()
7 move_hand_to_attended_object()
8 release_object()
    
```

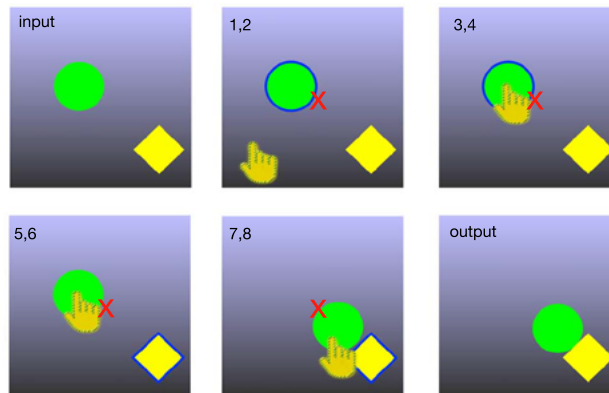


Fig. 3. Concepts and their representation as cognitive programs. (A) Input-output examples for 15 different tabletop concepts. In our work, we tested on 546 different concepts (see the Supplementary Materials for the full list). (B) A manually written program for a concept that requires moving the central object to touch the other object. The images on the right show different stages during the execution of the program, with the corresponding line numbers indicated. The attended object is indicated by a blue outline.

Although the VCC instructions are named to be meaningful to humans to help with interpretation, the agent is unaware of the meanings of these actions or how the different working memories and indexing mechanisms can be leveraged to represent concepts. By learning programs, the agent has to discover how to exploit the actions and properties of the VCC to represent various concepts.

RESULTS

Our experiments show that concepts could be induced as cognitive programs and that this enabled transfer from diagrammatic representations to execution on a robot without any explicit demonstration. We evaluated the performance of VCC on 546 different concepts, for which manually written programs varied in number of instructions from 4 to 23 (Fig. 4). We investigated how model-based search, input-conditional argument prediction, and fixation guidance affect the speed

or learning. Using a combination of the best models, argument prediction, and fixation guidance, 535 of the 546 concepts could be learned with a search budget of 1 million programs, and 526 of them could be learned with a search budget of 0.5 million programs. The induced concepts readily generalized to settings where we varied the number and size of objects, their appearance, and the color and texture of the background. They could also be readily transferred to novel situations on multiple robots to execute tasks in the real world.

Induced programs

Figure 4 (B to D) shows three examples from the 535 induced programs that demonstrate how program induction used VCC properties to represent concepts. The first example (Fig. 4B) requires to move the left-most object to the top. The learned program used the property that VCC’s object-indexing memory orders objects by their distance from the center of fixation. Although “the left-most object” is not an attribute

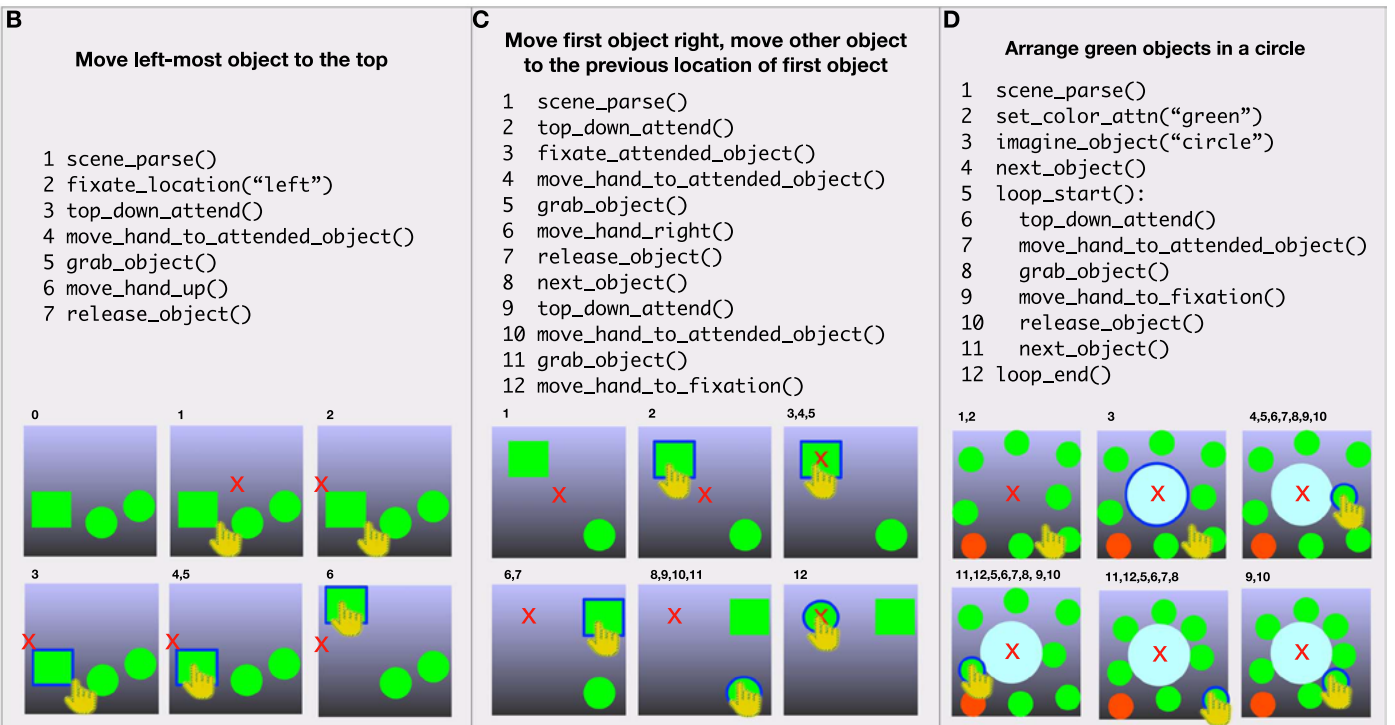
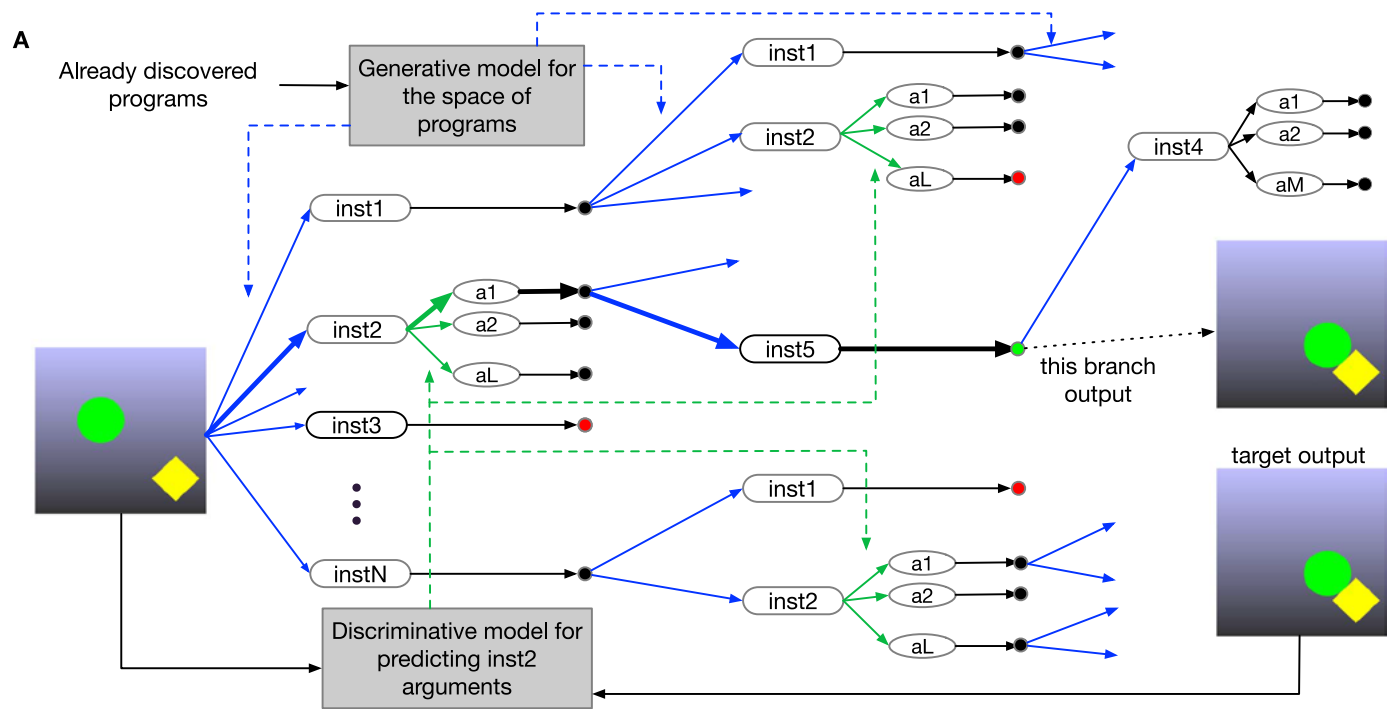


Fig. 4. Program search and discovered programs. (A) Program induction searches in an exponential space represented as a tree, where each node (solid circle) is a program. Blue branches are instruction-to-instruction transition probabilities modeled using a generative model, and green branches are instruction-to-argument probabilities predicted using discriminative neural nets trained on input-output images. The probability of a program depends on the weights of the branches leading to its node. Solid red circles are programs that generated an exception in the VCC, and the green node is a correct program. (B to D) Three examples of discovered programs and visualizations of their execution steps. Digits next to the visualizations correspond to program line numbers.

directly encoded in VCC, that concept was represented as a combination of other primitive actions.

Figure 4C shows an example where induction discovered the use of a deictic mechanism. The concept required moving the central object to the right edge and moving the other object to the position previously occupied by the first object. Achieving this requires holding the position of the previous object in working memory. Induction discovered that the fixation center can be used as a pointer to index and hold object locations in memory. The discovered program moves the center of the eye to the first object after attending to it and grabbing it. Because the eye fixation remains at the initial position of the first object when the object is moved away, the second object can be moved to the correct position by simply moving it to the fixated location. The concept of arranging small circles into a big circle (Fig. 4D) requires the agent to imagine an object that does not exist (the big circle) and then push other objects toward this imagined object while it is maintained in the working memory. This is an example where teaching by demonstration is likely to face challenges because the intermediate stages of that demonstration would provide only scant cues about the final goal of arranging objects in a circle.

Induction dynamics

We tested the efficacy of program induction under a wide variety of settings. For model-based search, we compared an order-0 model that only considers the relative frequencies of instructions to an order-1 model that learns the transition probabilities of instructions in programs. In each case, we tested the effect of learning subroutines. We tested the effect of combining the order-1 model with neural network-based predictions for the arguments of each instruction. We also tested the effect of fixation guidance where pointing action by a teacher was used to set the fixation location in the learning agent.

Iteratively discovering the programs by modifying the model that is driving the search process and augmenting that model with input-conditioned argument predictions are both important for discovering the complex concepts with longer programs. Figure 5 (A to D) shows the length distributions of the programs induced after each E-C iteration for different settings, for a search budget of 1 million programs. The histogram of the number of programs of different lengths is plotted along with a ground-truth distribution. (The ground truth is derived on the basis of manually writing programs for each of the concepts. The discovered program for any particular concept need not match the ground-truth program in implementation or length). When argument prediction was not available, program induction relied on searching exhaustively in the argument space. Without argument prediction, no programs with a length of more than 12 instructions were induced, whereas with input-conditioned prediction of arguments programs with a length of up to 18 instructions were induced. Overall, without argument prediction, only 150 of the 546 concepts were induced, whereas argument prediction and subroutines enabled the discovery of 526 of 546 concepts. Iterative refinement of the model using the discovered programs at each stage resulted in more programs being discovered in the next iteration of search. Figure 5 (A to C) shows the length distributions of programs discovered after each E-C iteration. The distributions of the discovered programs shifted right with each iteration, successively discovering longer programs that were missed in the previous iteration. The progression of concepts learned during multiple E-C iterations demonstrates the advantage of learning to learn (38) in program induction.

A teacher can help the agent learn faster by guiding the agent's attention by pointing. We tested the effect of having a teacher guide

the fixation of the agent for concepts that require using the `fixate_location()` function similar to the joint attention mechanism hypothesized in cognitive science (28). This was achieved by setting the argument of the `fixate_location()` function to the location pointed by the teacher. In contrast to other instructions, the arguments for the `fixate_location()` function were not predictable from the input-output image pairs, and program induction relied on searching the argument space in the absence of any other guidance. The effect of offering fixation guidance was most significant at search budget of 0.4 million, as shown in Fig. 5E. In this setting, using fixation guidance increased the number of discovered programs from 148 to 524. Although fixation guidance from a teacher was applied here in a very limited setting, this shows that prespecified joint attention mechanisms with a teacher hold promise for significantly speeding up induction.

Overall, using model-based search using an order-1 model and argument prediction were the most important factors that determined how quickly the programs could be learned. Figure 5 (E to H) shows the effect of various factors as the search budget was varied from 0.25 to 3 million programs. When an order-1 model was used, induction of subroutines played a smaller role in the induction of new programs: Although subroutines that reduced the description length were obtained after each compression iteration, they provided only a modest help in the future discovery of programs. To give a sense of the required computational effort, we note that searching 1 million programs took around 10 min when using a single core.

Modeling the sequential relationship between the instructions of learned concepts significantly helped with program induction, compared with modeling just the instruction frequencies. We tested an order-0 model that ignored the sequential dependencies and an order-1 Markov model between the instructions as the models used in the E-C iterations. Of 546 concepts and with a search budget of 1 million programs, the order-0 model was not able to induce any new concept when subroutines were disabled and only 7 new concepts when they were enabled (39). In contrast, an order-1 model was able to learn 525 of the 546 concepts for the same search budget (Fig. 6B). Figure 6A shows the transition matrix of the order-1 Markov model after iterations 0, 2, and 4. The transition matrix learned additional relevant modifications, with each iteration that enabled more concepts to be learned in future iterations.

Most concepts were learned correctly with just a few input-output examples and generalized well to markedly different images depicting the same concepts. Figure 6C shows the learning curve for concepts discovered in the first E-C iteration (107 concepts, including 16 bootstrapping ones). The learning curve flattens out after five examples. Figure 6D shows an example of the confusion caused when the number of examples is fewer. Although the concept required moving the yellow triangle to the middle, in the first two examples, this could be achieved just by moving to the middle whichever triangle was closest to the center. The generalization of the induced concepts to new situations was tested using concept images generated with different numbers of objects and visual transformations, examples of which are shown in Fig. 7A. The test images were generated by varying the backgrounds, object foregrounds, number and kinds of objects, and their placements within the image. For each concept, we tested on 50 different test images generated by sampling from these parameters. More examples of test images are shown in fig. S4. All the induced concepts generalized to a 100% of these new settings.

Transfer to robots

Induced concepts transferred readily from the schematic inputs to the real-world execution on two different robots: a Baxter from Rethink

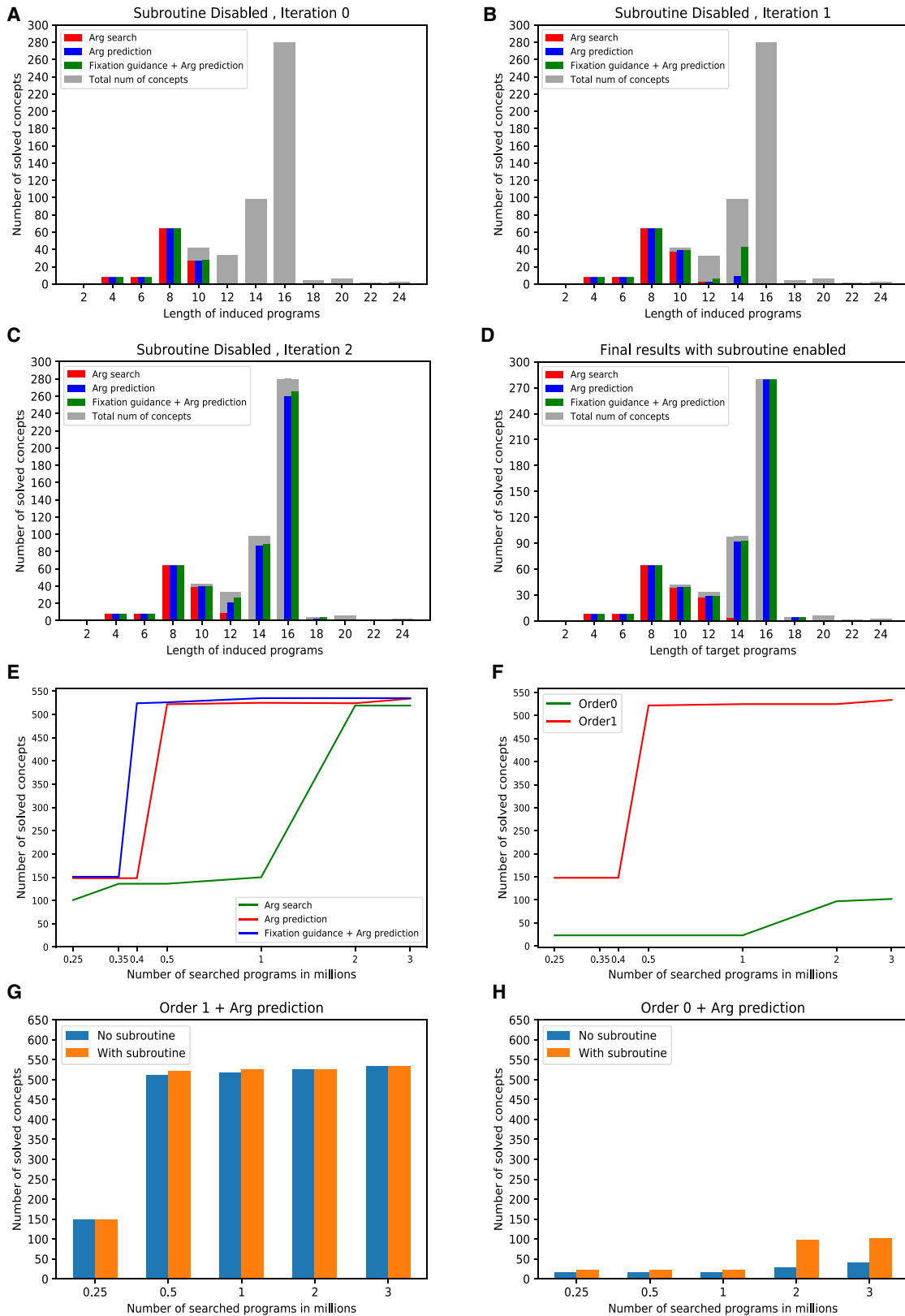


Fig. 5. Program induction details. (A to C) Length distribution of induced programs for the first three E-C iterations. X axis bins correspond to program lengths (number of atomic instructions). The gray bars represent the total number of programs of that length according to a set of manually written programs comprising all concepts. (D) Distribution at the end of all iterations. (E and F) Number of induced programs for different search budgets and for different model options. (G and H) Effect of subroutines.

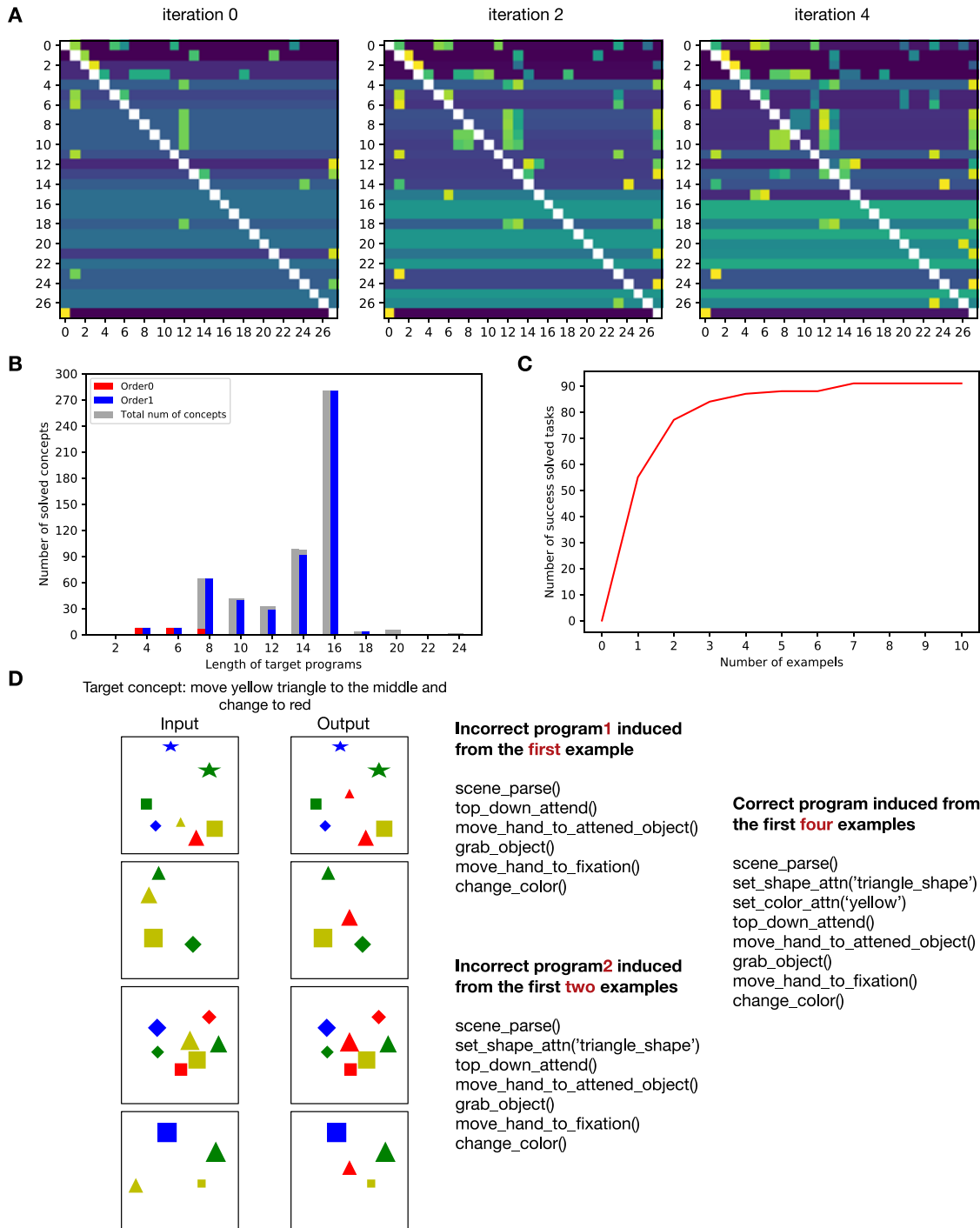
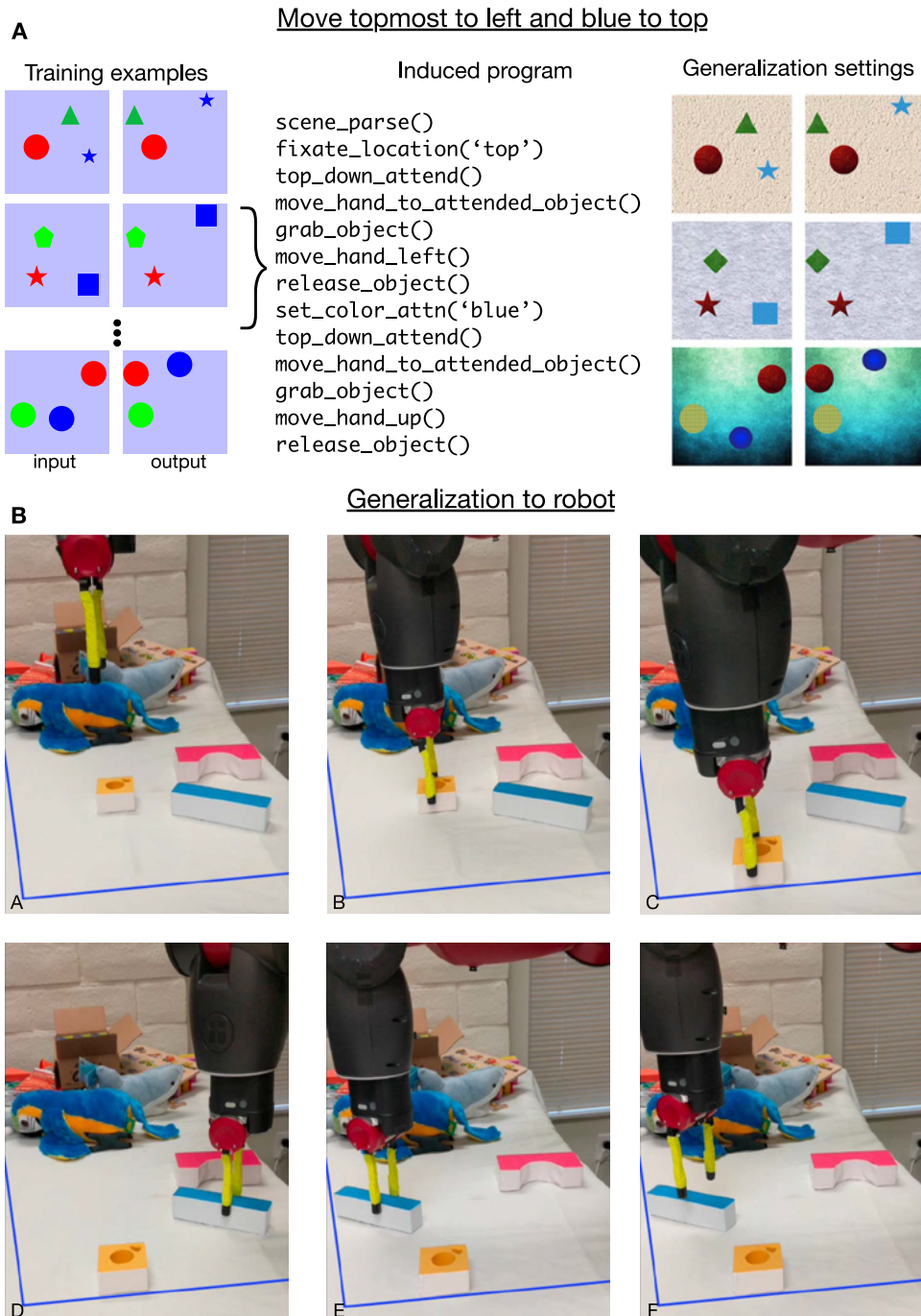


Fig. 6. Program induction and generalization. (A) The instruction-to-instruction transition matrix after different E-C iterations. (B) Length distribution of programs induced using order-0 versus order-1 model. (C) Training curve. Most concepts are solved with just a few examples. (D) An example showing wrongly induced programs when only three training examples from a concept are presented, where accidental patterns in the data can explain the examples. In this case, the correct concept was induced with four examples.

Robotics and a UR5 from Universal Robots. The primitive instructions for perception and action, such as capturing the input scene and controlling the hand, were implemented using the respective robots' interface, while the rest of the VCC instructions remained the same. We tested the transfer of five different induced concepts on the two robots, and each concept was tested in several different scenarios by changing the

number and types of objects, their positions, the number of distractor objects, and the appearance of the backgrounds. In each case, the initial state of the test scenarios was constructed such that running the induced program on the input image would produce the right output in VCC's imagination.

Figures 7 and 8 show the robots at different stages of the execution of the concepts for a sampling of the settings we tested on. The concepts



of objects were significantly different. Out of the total test scenarios that were tried, the robot UR5 succeeded in executing the concepts in more than 90% of the trials. The failures were caused by the objects slipping out of the gripper during a grasp or during placement. On Baxter, the success rate was lower (at about 70%) due to a blurry camera, a less effective gripper, and imprecise motion in our aging robot.

We also show how a complex concept that could not be induced directly could be broken into two different concepts and executed consecutively on the robot to achieve the more complex task. The final task requires moving the yellow object on the table to the left and the green object on the table to the right, which can be achieved as a combination of the first set of movements with the second. We show an application where the concept can be used to separate lemons from limes (Fig. 8B). The reader is encouraged to view the robot demonstration videos available as the Supplementary Materials.

DISCUSSION

Getting robots to perform tasks without explicit programming is one of the goals in artificial intelligence and robotics. Imitation learning, a predominant approach to this end, seeks to teach the robots via demonstration. To demonstrate the actions required for a task, a robot could be physically guided or operated remotely (1, 40). Robot operation is very time consuming, so one-shot approaches that try to learn executable policies from a single demonstration have been developed (2, 4, 41). The main drawbacks of imitation learning approaches are their focus on rote mimicry without understanding the intent of a demonstration and their tendency to latch onto surface statistics and idiosyncrasies of the demonstration (19) rather than its conceptual content, resulting in limited generalization to new settings. Recent work (3) has sought to build an intermediate representation from a demonstration that would allow generalization to more settings but still relied on having a demonstration avail-

able for each variation of a task, in addition to having a large annotated background set for the family of variations.

are executed correctly despite the variations to the number of objects, their sizes, positions, and variations in the background, as long as the information relevant for the concept is present in the input. In Fig. 8A, we show the stacking concept executed in three different settings. The different stacking concepts were executed correctly with the objects properly in contact in their final states, even when the sizes and types

By focusing on the discovery of conceptual understanding from pairs of images, our work is very different from the traditional setting of imitation learning. No demonstrations are available, and the agent has to discover the conceptual content and transformation that are

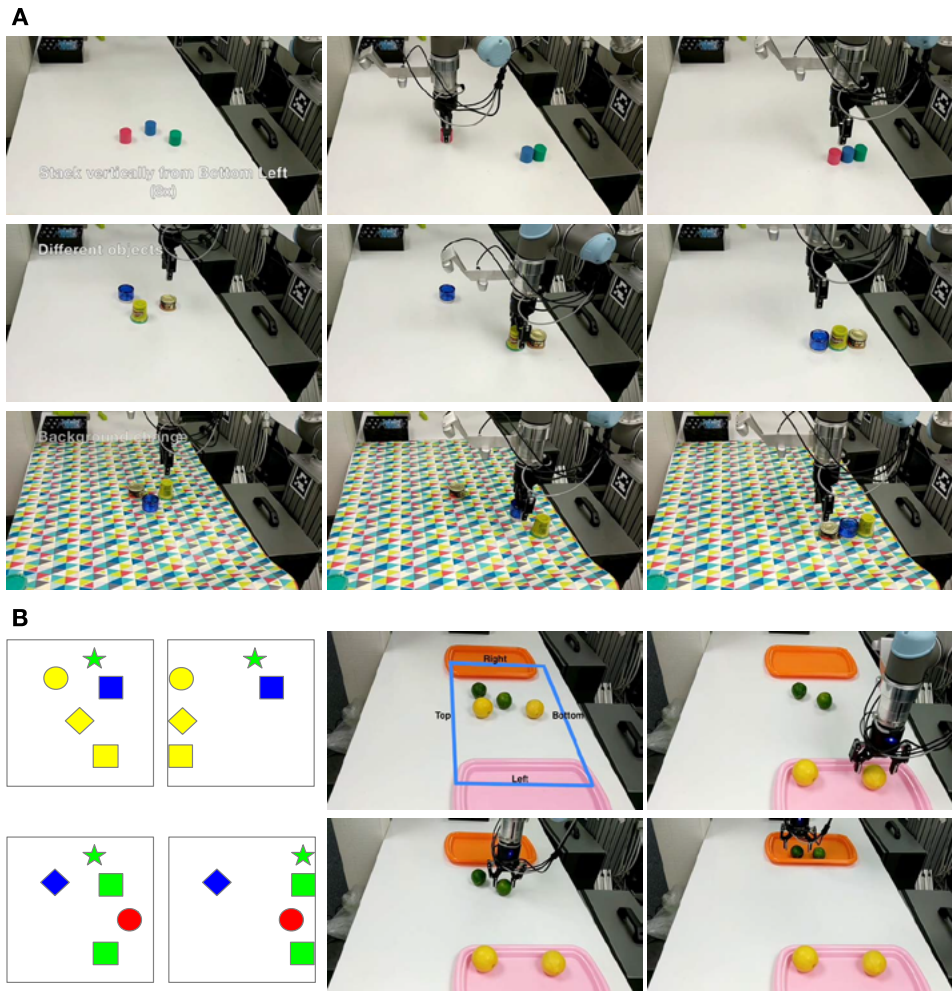


Fig. 8. Learned concepts transferred to different real-world settings. (A) Each row shows the starting state, an intermediate state, and the ending state for three different execution scenarios for a concept that requires stacking objects on the bottom left. The middle row shows execution on different objects, and the bottom row shows execution on a different background. (B) Execution frames from an application that separates limes from lemons. This task is achieved by the sequential composition of two concepts. (Left) The two concepts used (top and bottom) and (right) execution of these concepts in sequence to achieve the task.

represented by the image pairs. Moreover, the discovered representations need to transfer to very different settings, including markedly different visual appearances and different robot embodiments. Such transfer requires visual analogy making (42, 43) as opposed to rote imitation. Although we took inspiration from earlier works on learning programs to describe the contents of images and videos (38, 44, 45), those works focused on settings where the content to be described was fully observable in the images or video demonstration. Our setting is very different and significantly more challenging because of the need to discover hidden variables underlying the concepts, the number of steps involved in going from an input image to the output, and the need for strong schematic-to-real generalization in settings significantly different from the training distribution.

The sequential and programmatic nature of conceptual representations has been well recognized in cognitive science and neuroscience, with Ullman's seminal paper on visual routines (18) and its implementations (46–52), and in prevalent cognitive architectures (53, 54) that use sequential representations. Although sharing the motivations of se-

quential representations and chunking, our work is a significant departure from the traditional cognitive architectures of ACT-R and SOAR in emphasizing the perceptual, motor, and interactive nature of concept representations. In having a VH that is not a passive feed-forward transducer, but an active system that can be manipulated and reconfigured (11), our architecture follows the guidelines of perceptual symbol systems (6) rather than pure symbol manipulation. VCC and cognitive programs can also be thought of as a concrete computational instantiation of image schemas (55), an influential idea in cognitive science that emphasizes the grounded and embodied nature of concepts. The programs that we learn on VCC can be considered “patterns of sensorimotor experience” that constitute a concept, forming the basis for communication and grounded language (56). Our work is also consistent with the idea of a probabilistic language of thought (57) where complex representations are formed from small repertoire of primitives (16, 17). Representing concepts as programs makes them naturally compositional as required for a language of thought (57), and programs provide explainability that has been lacking in current black-box policy learning methods.

The tremendous success of deep learning (58, 59) along with discoveries of its limitations has rekindled the age-old debate about innate biases versus tabula rasa learning (60). Bucking the recent trend of tabula rasa learning with large training sets, our work here focused on learning programs on a biased computer architecture whose biases were inspired

by cognitive science and neuroscience and by computational considerations. We carefully considered the question of what is a good architectural starting point (26) for the learning of concepts: What should be the design of the processor (13)? What should be the elemental operations (22)? We believe that the seeming arbitrariness and ambiguity of the starting point is part of the challenge in bringing these ideas into a computational model and need to be confronted directly (61). We tackled this challenge by treating this as analogous to the design process of a microprocessor where choices need to be made regarding the nature of registers, memory, and instruction set. As described earlier, cognitive and neurosciences provided significant guidance, which were then refined from the view point of program induction. Although it is unlikely that all the detailed choices we made in this first iteration are the ones that will give rise to human-like concepts, many aspects of VCC regarding the interaction of VH, imagery, working memory, attention, action, and program induction are likely to remain in future iterations. Through further theorizing and experimenting the design of the VCC will be expanded and refined. We believe that this iterative

refinement of architectural priors, inductive biases, and learning algorithms is an essential part of building systems that work like the human mind (26).

A particularly important design choice is that of VH and top-down attention. Rather than follow the prevailing machine-learning view of treating vision as re-encoding the input for “downstream tasks” (62), we treat the VH as a mechanism for structured interaction with the world. In this view, the encoding of the world is not just at the top of the hierarchy, and all details need not be represented at the top of the VH in a loss-less manner as in deep neural network generative models. The VH in our model is lossy, and the details can be accessed at the input on demand, consistent with neuroscience ideas of using the primary visual cortex as a high-resolution buffer for mental imagery (22) and with the ideas of selective tuning of attention (63, 64). In this design, the pattern of accessing the detail at the bottom, or the more abstract representation at the top, becomes part of the representation of the concept. Top-down attention also serves to achieve binding (65)—for example, between the color and shape of an object—by using attention as an internal pointing mechanism (21).

Many of the existing datasets that measure conceptual and abstract reasoning have drawbacks that prevent them from being used in a study for acquiring and representing concepts as sensorimotor programs. Raven’s progressive matrices (RPMs) (66) are often used as a test for conceptual representation. Instead of using RPM, we chose to use TW because the properties of the world that give rise to generalization are systematic and well understood. In contrast, in RPMs, the source of generalization can encompass the full experience of a young adult, including all the generalizations that arise from a fully developed VH that can reason about occlusions and transparency. Standard RPMs are also restricted to being evaluated as a multiple-choice question. TW was also inspired by the tasks introduced in (21) for deictic mechanisms but goes beyond those in terms of complexity, analogy making, and transfer to real-world execution. In contrast to datasets that measure pixel-accurate image reconstructions in simplistic settings (67), use of the TW recognizes the schematic nature of concepts (20) and enables the evaluation of sensorimotor representations for their generalization to settings that are different from the training distribution, including different real-world settings involving robots.

One common approach in program synthesis is to combine a domain-specific language with a context-free grammar, such that the whole space of syntactically valid programs is derivable (all programs that are generated would compile, and all programs that solve a task would be generated with nonzero probability) (20, 68). To achieve this, a popular choice is to use functional programming with type checking, which guarantees successful execution of programs generated according to the grammar. In contrast, we found that an imperative programming language was more suited for our purpose and subjectively more adequate to describe the thought process associated with a concept. This does not guarantee error-free execution when sampling from a Markov model, and some programs are rejected: The machine itself becomes part of the model, conditioning on valid programs (as in rejection sampling) and effectively pruning the search space. We took inspiration from the recent work (33) in bringing the machine itself into program synthesis.

We are excited about the future research directions that our work opens up. A richer set of primitive instructions that supports an interplay of bottom-up and top-down attention and uses the part-based representation of the VH could enable a wider variety of concepts. Perhaps some of the primitives could be learned by having an agent interact with the environment using mechanisms we elaborated earlier (69).

The use of joint attention by pointing can be expanded in scope to direct top-down attention, not just fixation. Attributes of an object—width, height, number of corners, etc.—could themselves be represented as sensorimotor programs that are learned with experience in the real world but evaluated purely in imagination during execution. Expanding the dynamics model to include three-dimensional (3D) objects and combining it with occlusion reasoning and surface representation abilities of the VH could result in a large number of real-world concepts being learned as cognitive programs.

MATERIALS AND METHODS

Program induction

We are provided with a set of collections of input-output pairs of images, with each collection corresponding to some unknown concept, and we wish to infer the programs that describe each of those concepts. A naïve way to perform this inference is via brute force, but this becomes unfeasible with increasing program lengths. However, it can be useful as an initial step to discover the simplest of concepts to form a bootstrapping set. To discover more sophisticated programs, we fitted a probabilistic model to the programs in the bootstrapping set and then used that model to guide the search starting from the most probable program and searching in the order of decreasing probability. Once some effort threshold was hit (for instance, number of programs considered), we collected the found programs, refitted the probabilistic model, and repeated. This approach is referred to as the E-C framework in (34), where compression stands for fitting a probabilistic model to data. The key for this approach to work properly is the probabilistic model.

We modeled programs (both instructions and arguments) as an observed Markov chain. The model for the instructions is learned from the already discovered concepts, whereas the emission model is conditional on the input-output pairs of examples and is learned separately. As we will see next, the whole induction process depends only on two free parameters: a modeling parameter ϵ (the pseudocount) and an exploration parameter M (maximum number of explored nodes).

The probabilistic model

We start by considering programs as a sequence of instructions, without arguments. A program x is a sequence of atomic instructions $x = [x_1, x_2, \dots, x_L]$, where the last instruction is always $x_L = e$, a special end-of-program marker. The probability of a single program is

$$\log p(x) = \log p(x_1) + \sum_{i=1}^{L-1} \log p(x_{i+1}|x_i)$$

where $p(x_{i+1}|x_i)$ is the transition probability from instruction x_i to instruction x_{i+1} and $p(x_1)$ are the initial probabilities. To compute the probability of multiple programs $\{x^{(i)}\}$ that we consider independent, we can just add the log probabilities of each of them. We can express this compactly by defining $X \equiv e x^{(1)} x^{(2)} \dots$ as a sequence that simply concatenates the programs (in any order) and prepends an end-of-program marker. Then, the joint probability of multiple sequences is simply

$$\log p(X) = \sum_{i=1}^{N-1} \log p(X_{i+1}|X_i) \quad (1)$$

where N is the total length of all the programs combined, including the initial marker. From a compression perspective, $-\log p(X)$ corresponds to the description length (in nats) of the collection of programs under this model. Parameter fitting for this model amounts to determining the transition matrix T_x , where $[T_x]_{rs} = p(s|r)$. We use the maximum likelihood estimator with a small pseudocount ϵ to avoid overfitting.

We can further enhance the model using subroutines. Subroutines are sequences of instructions and can be incorporated into the model by adding a dictionary D with subroutine definitions and allowing instructions to index not only atomic instructions but also subroutines. A program with atomic instructions x can now be expressed in compressed form c by identifying the subroutines it contains and replacing them with a single instruction containing the appropriate subroutine call. The joint probability of all the programs X , its compressed representations C , and the subroutine dictionary D is then

$$\begin{aligned} \log p(X, C, D) &= \log p(X|C, D) + \log p(C) + \log p(D) \\ &= \log p(C) + \log p(D) \end{aligned} \quad (2)$$

where the last equality follows from X being deterministically obtained from C and D , and therefore, $\log p(X|C, D)$ equals 0 for valid expansions X of C . The two terms in the right-hand side (r.h.s.) can each be encoded as concatenated sequences (as we did for X) and computed using Eq. 1.

To fit this model for a given X , we maximize Eq. 2 with respect to the transition matrix T_c (which is shared for both programs and subroutines), the compressed representation C , and the dictionary D . This joint optimization is, in general, a difficult problem. We opt for a greedy method: We consider the increase in $\log p(X, C, D)$ that inserting each new possible subroutine in the dictionary (and updating C and T_c accordingly) would produce and insert the one that achieves the maximum gain. Then, we repeat the process until no positive increase is achievable, adding one subroutine at a time. We only consider as potential subroutine sequences of instructions that appear multiple times in the programs. In contrast to maximum likelihood estimation, the maximum a posteriori estimation of D includes the prior and provides a trade-off in which subroutines are only deemed useful if they appear often enough.

We now turn to modeling the arguments of the instructions of a program. Each program x has an accompanying set of parameters $y = [y_1, y_2, \dots, y_L]$ of the same length as x . Thus, each instruction has exactly one parameter, which can take one value among a discrete set of choices. Those choices are different for each instruction and are given by the syntax of the language. For a given dictionary, the probability of a full program (including now arguments) is

$$\begin{aligned} \log p(y, x, c|D) &= \log p(x|c, D) + \sum_{j=1}^{L_c-1} \log p(c_{j+1}|c_j) \\ &\quad + \sum_{i=1}^{L_c-1} \log p(y_{i+1}|x_{i+1}) \\ &= \log p(x|c, D) + \sum_{j=1}^{L_c-1} \left[\sum_{h=1}^{n_{j+1}} \log p(y_{j+1h}|x_{j+1h}) + \log p(c_{j+1}|c_j) \right] \\ &= \sum_{j=1}^{L_c-1} \log p(y_{j+1}|c_{j+1}) + \log p(c_{j+1}|c_j) \end{aligned} \quad (3)$$

where we have collected all the arguments that are used in a subroutine c_j into a single variable $y_j = [y_{j1} \dots y_{j_{n_j}}]$ and removed $\log p(X|C, D) = 0$ (due to determinism) from the equation. We have already estimated all the quantities in the above expression except for the conditional probability of the arguments $\log p(y_j|x_j)$ of a given atomic instruction, which will be described in a subsequent section on argument prediction.

The exploration

To discover the concept that explains a particular input-output collection, we start by expressing the probability of a compressed program as a Markov chain

$$\log p(z) = \sum_{j=1}^{L_c-1} \log p(z_{j+1}|z_j)$$

where $z_j \equiv (c_j, y_j)$ and the transition probability T_z can be easily derived by combining T_c and $p(y_j|c_j)$. We thus have a Markov model over “program portions” z_j , which can be either individual instructions or subroutines.

The Markov model induces an exploration tree: Each node has as children all the possible program portions and is connected to them through arcs with cost $-\log p(z_{\text{child}}|z_{\text{parent}})$. Each node corresponds to a program, and its description length can be obtained by adding the weights of the arcs on the path from the root. A best-first traversal of the tree (always expanding the nodes that have less accumulated cost from the root) visits the programs in order of decreasing probability. Each visited compressed program z can be expanded into its atomic version x and run on the VCC, checking whether the produced outputs match the provided ones. We stop the process after we find a valid program (the concept is discovered) or the number of visited nodes exceeds some effort parameter M .

To alleviate the memory demands of best-first search, we use iterative deepening where depth-first search (DFS) is run with a limit on the description length, the limit is gradually increased, and the process is repeated. The nodes (programs) visited on each iteration that were not visited in the previous iteration are then run on the VCC. This visits the nodes in approximately a best-first order: Within each search bracket, the node ordering is arbitrary, but the brackets are ordered. The smaller the brackets, the tighter the approximation to best-first search. VCC states are cached during the DFS traversal to prevent redundant instruction executions, and the successors of any node that produced an “invalid” execution on VCC are pruned away from further search.

Because the number of explored programs is relatively low, we first run a best-first search that identifies the maximum description length of the shortest M programs (without running them), and then, we run DFS using the identified description length as the cutoff. During the DFS, we run the programs, taking advantage of the optimizations described in the previous paragraph. The DFS is run until completion even if the sought-for concept is found earlier, because it does not guarantee that the shortest description of the concept will be found first.

Argument prediction

The differences and similarities between the input and output images that are used as examples for each concept provide information about what to pay attention to. We use this information to predict the argument for the following three functions: `set_shape_attn`, `set_color_attn`, and `fill_color`. Given that the argument of each function can take several potential values and each function

can appear multiple times in a program with its argument taking a different value, this becomes a multilabel problem. We build a logistic regression model for each function and argument pair.

To get training data for argument prediction, we enumerate all valid programs up to length 6 (including `scene_parse`), where valid programs are those that can be executed on input images without any failure. From the set of valid programs, we filter out uninformative programs whose output images are the same as the corresponding input. We also remove programs where the presence of an instruction with its assigned argument does not lead to different output compared with the program without that instruction.

For each program, we generate 10 examples. Each example is converted to a 3D binary array A with shape (21, 15, 15), where 21 is the number of input channels and 15 corresponds to the height and width of the discretized images. The first 10 channels are based on the input images, as shown in the first column of fig. S2. Each element is set to 1 or 0, depending on whether the feature associated with that channel is present at that location or not, respectively. The next 10 channels are based on the difference between input and output images, both using the same binary encoding, which results in the elements of these channels having -1 , 0 , and 1 as possible values. This is shown in the third column of fig. S2. The difference between output and input highlights what has changed between both images. For example, when the green color disappears, a -1 value is registered in the third column at the corresponding location and for the green color channel. In contrast, the blue square remains in the same position; thus, it becomes zero when we subtract the input from the output. The last channel summarizes the differences across the 10 previous features (channels). Thus, an element corresponding to row r and column c of channel 21 is computed as $A_{21rc} = \sum_{f=11}^{20} |A_{frc}| \geq 1$. That is, a value of 1 at a given position means that the object at that position has changed regardless of whether it was added or removed. This feature combines color change and movement change into one single indicator.

We use a convolutional neural network (CNN) to capture spatial invariance, because the object experiencing a change can be anywhere in an image. Figure S3 shows the architecture of the model. To capture the similarities among examples, we sum the max pooling results from all examples and feed it into a sigmoid function. Given that the last layer is simply performing a summation, we only need to train the convolutional weights of the CNN. The model is trained using the ADAM optimizer and L1 regularization with a weight of 0.01. There are other two functions with arguments that are not supported by this model and for which we do not perform predictions: One of them is `fixate_location` and the other one is `imagine_shape`.

We also use the result of argument prediction to predict the existence of an instruction in a concept. Specifically, if, for a given instruction, the sum of probabilities of all the values that its argument can take is below 0.55, then it is assumed that the instruction is not present in the concept and excluded from the search process.

Execution on robots

We tested the transfer of induced concepts to real world by executing programs on two different robots in different settings: a Baxter robot from Rethink Robotics and a UR5 from Universal Robots. To execute the programs on these robots, we extended VCC with an additional robot interface that implemented input scene capture and hand actions. Scene capture was achieved through a camera attached to the respective robot's end effector, a gripper. A color image with red, green, and blue channels of the scene was captured by this camera and passed on to the

scene parser of the emulator, which created the VCC's initial state. Moving a hand to any location within the workspace and grasping and releasing objects were implemented on robot using a simple Cartesian controller that moved the hand to a given x , y position on a table in a plane at a specified height above the table top. Grasping and releasing an object involved moving the gripper down and closing and opening the gripper. Instead of dragging the object along the table, we moved the object slightly above the table but otherwise respected the same collision constraints as our TW, including the boundary. The interface also mapped any position in VCC's workspace onto x , y coordinates in the robot frame of reference. Program execution took place in the VCC and called scene capture and hand action functions implemented in the robot interface when available. Executing any specific program involved giving the induced concept as a list of primitives with arguments when available and running VCC with robot interface. We used the same visual scene parser for execution on robots as we did for the VCC. We tested six different concepts, including a complex concept that involved executing two concepts in sequence. We used colored foam blocks of different shapes, fruits, and household items as objects and executed programs under different variations of background, number, and shapes and types of objects and with or without distractor objects.

Mapping locations from VCC workspace to robot reference frame requires accurate calibration of camera pose with respect to the robot, and moving robot arm to a specific location requires accurate execution of arm movement. Our UR5 robot had an external RealSense camera attached to the gripper with an accurate calibration. For Baxter, an in-built camera inside the gripper was used instead for scene capture. This camera has low resolution and some burned pixels with an approximate calibration. Because of these limitations, executions were typically accurate and more successful on UR5 compared with Baxter. Movement execution was also faster on UR5 compared with Baxter. Failed runs of program execution were primarily due to grasp failures. These happened more frequently on Baxter, so we tested most of the variations on UR5, which has better movement accuracy.

SUPPLEMENTARY MATERIALS

robotics.sciencemag.org/cgi/content/full/4/26/aav3150/DC1

Text

Fig. S1. Schematic showing local bounded working memory mappings in VCC for an example program.

Fig. S2. Features extracted from example images used for argument prediction.

Fig. S3. Argument prediction network architecture.

Fig. S4. Examples of valid test input images for three different concepts.

Table S1. List of primitive functions.

Movie S1. The concept of moving yellow objects toward the left and green objects toward the right is taught through schematic images and transferred for execution on robot to separate lemons from limes.

Movie S2. A robot executing the concept of arranging objects in a circle under various settings.

Movie S3. Robots executing the concept of stacking objects on the bottom left in a variety of settings.

Movie S4. Robots executing the concept of moving the yellow object to the bottom left corner and the green object to the top right corner in a variety of settings.

Movie S5. Robots executing the concept of stacking objects vertically in place in a variety of settings.

REFERENCES AND NOTES

1. B. Akgun, M. Cakmak, K. Jiang, A. L. Thomaz, Keyframe-based learning from demonstration. *Int. J. Soc. Robot.* **4**, 343–355 (2012).
2. Y. Duan, M. Andrychowicz, B. C. Stadie, J. Ho, J. Schneider, I. Sutskever, P. Abbeel, W. Zaremba, One-shot imitation learning, in *Advances in Neural Information Processing Systems (NIPS, 2017)*, pp. 1087–1098.

3. D.-A. Huang, S. Nair, D. Xu, Y. Zhu, A. Garg, L. Fei-Fei, S. Savarese, J. C. Niebles, Neural task graphs: Generalizing to unseen tasks from a single video demonstration. arXiv:1807.03480 [cs.CV] (10 July 2018).
4. C. Finn, T. Yu, T. Zhang, P. Abbeel, S. Levine, One-shot visual imitation learning via meta-learning. arXiv:1709.04905 [cs.LG] (14 September 2017).
5. H.-Y. F. Tung, A. W. Harley, L.-K. Huang, K. Fragkiadaki, Reward learning from narrated demonstrations. arXiv:1804.10692 [cs.CV] (27 April 2018).
6. L. W. Barsalou, Perceptual symbol systems. *Behav. Brain Sci.* **22**, 577–609 (1999).
7. J. M. Mandler, How to build a baby: II. Conceptual primitives. *Psychol. Rev.* **99**, 587–604 (1992).
8. A. Cangelosi, A. Greco, S. Harnad, *Simulating the Evolution of Language* (Springer, 2002), pp. 191–210.
9. S. Harnad, The symbol grounding problem. *Physica D* **42**, 335–346 (1990).
10. M. Amalric, L. Wang, P. Pica, S. Figueira, M. Sigman, S. Dehaene, The language of geometry: Fast comprehension of geometrical primitives and rules in human adults and preschoolers. *PLOS Comput. Biol.* **13**, e1005273 (2017).
11. J. K. Tsotsos, W. Kruijine, Cognitive programs: Software for attention's executive. *Front. Psychol.* **5**, 1260 (2014).
12. A. M. Turing, On computable numbers, with an application to the entscheidungsproblem. *Proc. Lond. Math. Soc.* **s2-42**, 230–265 (1937).
13. A. Zylberberg, S. Dehaene, P. R. Roelfsema, M. Sigman, The human turing machine: A neural framework for mental programs. *Trends Cogn. Sci.* **15**, 293–300 (2011).
14. J. Von Neumann, *The Computer and the Brain* (Yale Univ. Press, 2012).
15. P. R. Roelfsema, Elemental operations in vision. *Trends Cogn. Sci.* **9**, 226–233 (2005).
16. I. Yildirim, R. A. Jacobs, Learning multisensory representations for auditory-visual transfer of sequence category knowledge: A probabilistic language of thought approach. *Psychon. Bull. Rev.* **22**, 673–686 (2015).
17. M. C. Overlan, R. A. Jacobs, S. T. Piantadosi, Learning abstract visual concepts via probabilistic program induction in a language of thought. *Cognition* **168**, 320–334 (2017).
18. S. Ullman, *High-level Vision: Object Recognition and Visual Cognition* (MIT Press, 1996), vol. 2.
19. J. Johnson, B. Hariharan, L. van der Maaten, J. Hoffman, L. Fei-Fei, C. L. Zitnick, R. Girshick, *Inferring and Executing Programs for Visual Reasoning* (ICCV, 2017), pp. 3008–3017.
20. J. M. Mandler, C. P. Cánovas, On defining image schemas. *Lang. Cogn.* **6**, 510–532 (2014).
21. D. H. Ballard, M. M. Hayhoe, P. K. Pook, R. P. Rao, Deictic codes for the embodiment of cognition. *Behav. Brain Sci.* **20**, 723–742 (1997).
22. P. R. Roelfsema, F. P. de Lange, Early visual cortex as a multiscale cognitive blackboard. *Annu. Rev. Vis. Sci.* **2**, 131–151 (2016).
23. G. Lakoff, R. E. Núñez, Where mathematics comes from: How the embodied mind brings mathematics into being. *AMC* **10**, 12 (2000).
24. D. George, W. Leirach, K. Kansky, M. Lázaro-Gredilla, C. Laan, B. Marthi, X. Lou, Z. Meng, Y. Liu, H. Wang, A. Lavin, D. S. Phoenix, A generative vision model that trains with high data efficiency and breaks text-based CAPTCHAs. *Science* **358**, eaag2612 (2017).
25. K. Kansky, T. Silver, D. A. Mély, M. Eldawy, M. Lázaro-Gredilla, X. Lou, N. Dorfman, S. Sidor, S. Phoenix, D. George, Schema networks: Zero-shot transfer with a generative causal model of intuitive physics, in *International Conference on Machine Learning (ICML, 2017)*, pp. 1809–1818.
26. B. M. Lake, T. D. Ullman, J. B. Tenenbaum, S. J. Gershman, Building machines that learn and think like people, in *Behavioral and Brain Sciences* (2016), pp. 1–101.
27. S. Gulwani, J. Hernández-Orallo, E. Kitzelmann, S. H. Muggleton, U. Schmid, B. Zorn, Inductive programming meets the real world, in *Communications of the ACM* (Association for Computing Machinery, 2015), vol. 58, pp. 90–99.
28. M. Tomasello, Acquiring linguistic constructions, in *Child and Adolescent Development* (2008), p. 263.
29. J. C. Macbeth, D. Gromann, M. M. Hedblom, Image Schemas and Conceptual Dependency Primitives: A Comparison. Technical Report.
30. D. P. Kingma, M. Welling, Auto-encoding variational Bayes. arXiv:1312.6114 [stat. ML] (20 December 2013).
31. S. Gulwani, Dimensions in program synthesis, in *Proceedings of the 12th International ACM SIGPLAN Symposium on Principles and Practice of Declarative Programming (PPDP'10)* (ACM, 2010), pp. 13–24.
32. M. Balog, A. L. Gaunt, M. Brockschmidt, S. Nowozin, D. Tarlow, DeepCoder: Learning to write programs. arXiv:1611.01989 [cs.LG] (7 November 2016).
33. X. Chen, C. Liu, D. Song, Towards synthesizing complex programs from input-output examples. arXiv:1706.01284 [cs.LG] (5 June 2017).
34. E. Dechter, J. Malmaud, R. P. Adams, J. B. Tenenbaum, Bootstrap learning via modular concept discovery, in *Proceedings of the 23rd International Joint Conference on Artificial Intelligence (IJCAI)* (IJCAI, 2013), pp. 1302–1309.
35. A. Graves, G. Wayne, I. Danihelka, Neural Turing machines. arXiv:1410.5401 [cs.NE] (10 December 2014).
36. D. Lin, E. Dechter, K. Ellis, J. Tenenbaum, S. Muggleton, Bias reformulation for one-shot function induction, in *Proceedings of the 23rd European Conference on Artificial Intelligence* (IOS Press, 2014), pp. 525–530.
37. K. Ellis, L. Morales, M. S. Meyer, A. Solar-Lezama, J. B. Tenenbaum, Dreamcoder: Bootstrapping domain-specific languages for neurally-guided Bayesian program learning, in *Neural Abstract Machines and Program Induction Workshop at NIPS 2018* (NIPS, 2018).
38. B. M. Lake, R. Salakhutdinov, J. B. Tenenbaum, Human-level concept learning through probabilistic program induction. *Science* **350**, 1332–1338 (2015).
39. We also tested the effect of increasing the search budget. When increasing it to 3 million programs, 41 concepts are discovered without subroutines and an additional 61 when using subroutines. The effect of subroutines in concept discovery is much more marked in the case of the order-0 model because subroutines are the only mechanism that makes memory available to the model.
40. D. Whitney, E. Rosen, E. Phillips, G. Konidaris, S. Tellex, Comparing robot grasping teleoperation across desktop and virtual reality with ROS reality, in *International Symposium on Robotics Research* (Springer International, 2017), pp. 1–16.
41. Y. Wu, Y. Demiris, Towards one shot learning by imitation for humanoid robots, in *2010 IEEE International Conference on Robotics and Automation (ICRA)* (IEEE, 2010), pp. 2889–2894.
42. D. Hofstadter, M. Mitchell, The Copycat Project: A model of mental fluidity and analogy-making, in *Advances in Connectionist and Neural Computation Theory*, K. J. Holyoak, J. A. Barnden, Eds. (Ablex, 1995).
43. R. M. French, D. Hofstadter, Tabletop: An emergent, stochastic model of analogy-making, in *Proceedings of the 13th Annual Conference of the Cognitive Science Society* (Lawrence Erlbaum Associates, 1991), pp. 175–182.
44. Y. Ganin, T. Kulkarni, I. Babuschkin, S. M. A. Eslami, O. Vinyals, Synthesizing Programs for Images using Reinforced Adversarial Learning. arXiv:1804.01118 [cs.CV] (3 April 2018).
45. J. Tremblay, T. To, A. Molchanov, S. Tyree, J. Kautz, S. Birchfield, Synthetically trained neural networks for learning human-readable plans from real-world demonstrations. arXiv:1805.07054 [cs.RO] (10 July 2018).
46. M. P. Johnson, P. Maes, T. Darrell, Evolving visual routines. *Artif. Life* **1**, 373–389 (1994).
47. A. K. McCallum, Learning visual routines with reinforcement learning, in *AAAI Fall Symposium 1996* (Massachusetts Institute of Technology, 1996), pp. 82–86.
48. I. Horswill, Visual routines and visual search: A real-time implementation and an automata-theoretic analysis, in *International Joint Conference on Artificial Intelligence* (Citeseer, 1995), pp. 56–63.
49. S. Rao, Visual routines and attention, thesis, Massachusetts Institute of Technology (1998).
50. G. Salgian, D. H. Ballard, Visual routines for autonomous driving, *International Conference on Computer Vision* (1998), pp. 876–882.
51. G. Pezzulo, G. Calvi, Toward a perceptual symbol system, in *Proceedings of the Sixth International Conference on Epigenetic Robotics: Modeling Cognitive Development in Robotic Systems*. Lund University Cognitive Science Studies, vol. 118.
52. I. Kotseruba, J. K. Tsotsos, STAR-RT: Visual attention for real-time video game playing. arXiv:1711.09464 [cs.CV] (26 November 2017).
53. R. A. Andersen, C. A. Buneo, Sensorimotor integration in posterior parietal cortex. *Adv. Neurol.* **93**, 159–177 (2003).
54. A. Newell, *SOAR: A Cognitive Architecture in Perspective* (Springer, 1992), pp. 25–79.
55. J. M. Lawler, Metaphors we live by. *Language* **59**, 201–207 (1983).
56. O. Kolodny, S. Edelman, The evolution of the capacity for language: The ecological context and adaptive value of a process of cognitive hijacking. *Philos. Trans. R. Soc. Lond. B Biol. Sci.* **373**, 20170052 (2018).
57. N. D. Goodman, J. B. Tenenbaum, T. Gerstenberg, “Concepts in a probabilistic language of thought,” (Technical Report 010, Center for Brains, Minds and Machines, 2014).
58. Y. LeCun, Y. Bengio, G. Hinton, Deep learning. *Nature* **521**, 436–444 (2015).
59. J. Schmidhuber, Deep learning in neural networks: An overview. *Neural Netw.* **61**, 85–117 (2015).
60. G. Marcus, Deep learning: A critical appraisal. arXiv:1801.00631 [cs.AI] (2 January 2018).
61. G. Marcus, A. Marblestone, T. Dean, The atoms of neural computation. *Science* **346**, 551–552 (2014).
62. D. L. K. Yamins, J. J. DiCarlo, Using goal-driven deep learning models to understand sensory cortex. *Nat. Neurosci.* **19**, 356–365 (2016).
63. J. K. Tsotsos, *A Computational Perspective on Visual Attention* (MIT Press, 2011).
64. A. Rosenfeld, J. K. Tsotsos, Bridging cognitive programs and machine learning. arXiv:1802.06091 [cs.LG] (16 February 2018).
65. C. von der Malsburg, The what and why of binding: The modeler's perspective. *Neuron* **24**, 95–104 (1999).
66. J. C. Raven, *Raven's Progressive Matrices* (Western Psychological Services, 1938).
67. I. Higgins, N. Sonnerat, L. Matthey, A. Pal, C. P. Burgess, M. Bosnjak, M. Shanahan, M. Botvinick, D. Hassabis, A. Lerchner, Scan: Learning hierarchical compositional visual concepts. arXiv:1707.03389 (2017).
68. S. H. Muggleton, D. Lin, A. Tamaddoni-Nezhad, Meta-interpretive learning of higher-order dyadic datalog: Predicate invention revisited. *Mach. Learn.* **100**, 49–73 (2015).

69. N. Hay, M. Stark, A. Schlegel, C. Wendelken, D. Park, E. Purdy, T. Silver, D. S. Phoenix, D. George, Behavior is everything: Towards representing concepts with sensorimotor contingencies, in *AAAI Conference on Artificial Intelligence* (AAAI Press, 2018).
70. The starting probabilities are now expressed as transitioning probabilities from e . Also, note that, because we know $X_1 = e$ deterministically, $\log p(X_1) = 0$, and therefore, it no longer appears in the expression.

Acknowledgments: We thank the anonymous reviewers for their insightful comments that helped to improve the paper. We thank C. Wendelken, N. Hay, and D. S. Phoenix for reviewing the manuscripts. We thank the Vicarious RCN team for the RCN implementation we used and the Vicarious robotics team for the robot interfaces. **Funding:** This research was funded by Vicarious AI. **Author contributions:** D.G. conceived of the model, implemented the VCC, and designed the experiments. M.L.-G., D.G., and D.L. designed and implemented the program induction algorithms. D.L. and D.G. generated the datasets. D.L. implemented the neural nets, ran the program induction experiments, and generated the plots. J.S.G. implemented the robot interfaces, performed the robot experiments, and generated the

videos. D.G., J.S.G., and D.L. generated the figures. D.G. and M.L.-G. wrote the paper with the assistance of D.L. and J.S.G. **Competing interests:** Vicarious AI has filed a U.S. Patent Office application (number 62/727,162) related to this work. The authors declare that they have no competing financial interests. **Data and materials availability:** Program induction code and datasets used in the experiments will be made available at www.vicarious.com. All other data needed to evaluate the conclusions in the paper are present in the paper and/or the Supplementary Materials.

Submitted 5 September 2018

Accepted 19 November 2018

Published 16 January 2019

10.1126/scirobotics.aav3150

Citation: M. Lázaro-Gredilla, D. Lin, J. S. Guntupalli, D. George, Beyond imitation: Zero-shot task transfer on robots by learning concepts as cognitive programs. *Sci. Robot.* **4**, eaav3150 (2019).

ARTIFICIAL INTELLIGENCE

Toward high-performance, memory-efficient, and fast reinforcement learning—Lessons from decision neuroscience

Jee Hang Lee^{1,2*}, Ben Seymour^{3,4,5*†}, Joel Z. Leibo⁶, Su Jin An¹, Sang Wan Lee^{1,2,7†}

Recent insights from decision neuroscience raise hope for the development of intelligent brain-inspired solutions to robot learning in real dynamic environments full of noise and unpredictability.

Recent successes in building agents with superhuman performance have led to reinforcement learning (RL), becoming a dominant theoretical framework to understand decision-making through interaction with the world (1). However, recent RL algorithms still have major limitations, such as lack of the ability to develop goal-directed policies or reliance on large amounts of experience to learn (2). These limits impede the ability to rapidly adapt in dynamic environments where tasks or contexts frequently change.

In contrast, humans have a remarkable ability to rapidly adapt to environmental changes with limited experience. Recent findings in decision neuroscience suggest that the brain uses not only multiple control systems for RL but also a flexible metacontrol mechanism to select among control options, each different trait associated with prediction performance, cognitive load, and learning speed (3). Understanding how the brain implements these options could lead to brain-inspired RL algorithms that can work in real control problems for robots (4). Here, we discuss recent findings on human RL that may address several key challenges in robotics: performance-efficiency-speed trade-offs, conflicting demands in multirobot settings, and the exploration-exploitation dilemma.

First, accumulating evidence in decision neuroscience indicates that humans take advantage of two different behavior control strategies: (i) stimulus-driven habitual and (ii) goal-directed cognitive control (3). Habitual control is automatic and fast, despite being fragile in a volatile environment, and

is well accounted for by model-free RL, which incrementally learns the values of actions through trial and error without a model of the environment. Conversely, goal-directed control can rapidly adapt to changes in the environment, but it is cognitively demanding. It guides actions by learning a model of the environment and uses this knowledge base to quickly adapt to changes in environmental structure, such as learning latent (hidden) causes within state-action space.

This computational distinction between model-based and model-free RL suggests an inevitable compromise between them. Model-free RL is slow to learn but is fast to achieve a goal once a policy is learned and automatized. Model-based RL provides more accurate predictions than model-free RL in general but is computationally much heavier. Each strategy provides a complementary solution regarding accuracy, speed, and cognitive load, highlighting a trade-off between prediction performance and computational efficiency.

Second, RL algorithms usually require a large amount of experience to adequately learn causal relationships in the presence of different environmental factors (incremental learning). Humans, however, learn fast—often after a single exhibition of an event never experienced before (“one-shot learning”) (5). Recent neuroscience studies (5, 6) found that, when interactions with the environment are limited, humans have a strong tendency to increase their learning rates; they strive for quickly making sense of unknown parts of the environment, even when

this compromises safety. These results suggest that the brain directly implements computation to find a trade-off between performance and speed.

Third, accumulating evidence supports the notion that the prefrontal cortex implements metacontrol to flexibly choose between different learning strategies, such as between model-based and model-free RL (7, 8) and between incremental and one-shot learning (5). In a new environment, metacontrol accentuates performance by favoring model-based RL. Because this is computationally expensive, the brain resorts to model-free RL when it finds little benefit from further learning: Either the environment is sufficiently stable to make precise predictions or highly unstable such that predictions from model-based RL become less reliable than those from model-free RL. In other situations, metacontrol prioritizes speed. When the uncertainty in the estimated cause-effect relationships is high, the brain tends to transition to one-shot learning to quickly resolve uncertainty in predicting outcomes. However, when the agent is equally uncertain about all possible causal relationships, it resorts to incremental learning to ensure safe learning. Together, they suggest that brain-like metacontrol can deal with performance-efficiency-speed trade-offs.

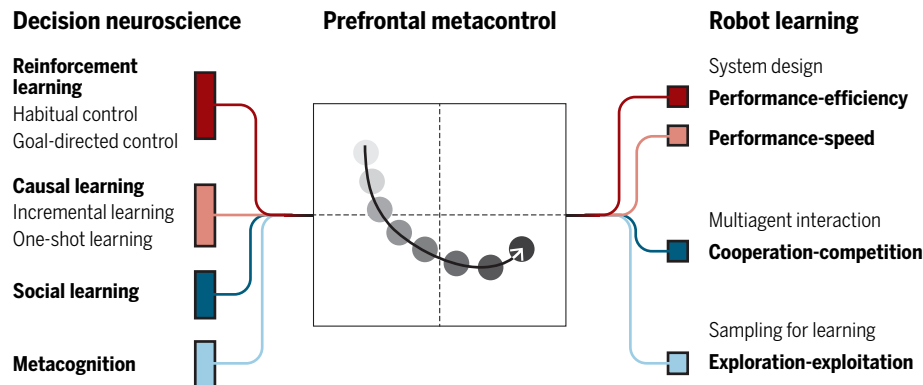
Fourth, human RL may account for social phenomena that have been important in human evolution. In human societies where multiple agents are interacting, there are social dilemmas that have partially competitive and partially aligned incentives (9). Approaches using model-based RL successfully achieve cooperation in more complex temporally extended settings [e.g., (10, 11)]. These models often work in two stages: First, there is a planning stage where the agent uses its model of the game’s rules to simulate a large number of games with itself and learns separate cooperation and defection policies by

Copyright © 2019
The Authors, some
rights reserved;
exclusive licensee
American Association
for the Advancement
of Science. No claim
to original U.S.
Government Works

¹Department of Bio and Brain Engineering, KAIST, Daejeon, Republic of Korea. ²KAIST Institute for Health Science and Technology, Daejeon, Republic of Korea. ³Computational and Biological Learning Laboratory, Department of Engineering, University of Cambridge, Trumpington Street, Cambridge CB2 1PZ, UK. ⁴Brain Information Communication Research Laboratory Group, Advanced Telecommunications Research Institute International, Kyoto, Japan. ⁵Center for Information and Neural Networks, National Institute of Information and Communications Technology, 1-4 Yamadaoka, Suita, Osaka 565-0871, Japan. ⁶DeepMind, London, UK. ⁷KAIST Institute for Artificial Intelligence, Daejeon, Republic of Korea.

*These authors contributed equally to this work.

†Corresponding author. Email: bjs49@cam.ac.uk (B.S.); sangwan@kaist.ac.kr (S.W.L.)



Brain-inspired solutions to robot learning. Neuroscientific views on various aspects of learning and cognition converge and create a new idea called prefrontal metacontrol, which can inspire researchers to design learning agents that can address various key challenges in robotics such as performance-efficiency-speed, cooperation-competition, and exploration-exploitation trade-offs.

independently learning toward both selfish and cooperative objectives. Then, in the execution phase, a tit-for-tat policy is constructed and applied using the previously learned cooperate and defect policies. Other approaches have sought to break down the strict separation between planning and execution stages and instead work in a fully online manner, such as the LOLA (Learning with Opponent-Learning Awareness) algorithm (12). In addition to assuming perfect knowledge of the game rules, this model also assumes that agents can differentiate through one another's learning process. This allows agents to learn to teach because they can isolate the effects of their actions on the learning of others.

Last, conventional RL algorithms tend to be optimistic (or overconfident), especially when sampling from a part of the environment they have not sufficiently learned. Learning without an estimate of prediction performance may lead to suboptimal policies (local minima problem), especially in complex and dynamic environments.

Humans appear to get around this problem by using metacognition—the ability to evaluate one's own performance to estimate a level of confidence and/or uncertainty (13, 14). For example, low task difficulty or low environmental noise would make the learning agent confident, leading to more decisive actions, whereas losing confidence would lead to a more cautious and defensive strategy (15). Metacognitive learning thus allows

for rapid adaptation to the context change while maintaining robustness against environmental noise. Such a strategy has potential for augmenting robot decision-making in several ways—for instance, in resolving exploration-exploitation trade-offs by overseeing how lack of confidence should drive the desire to learn.

In conclusion, the integration of findings from human decision neuroscience can offer valuable insights into action control systems for robots, leading to safer, more capable, and more efficient learning. Such an interdisciplinary approach should also yield insights for neuroscience, providing a robust test base for developing new theories of human decision computation.

REFERENCES AND NOTES

1. D. Silver, J. Schrittwieser, K. Simonyan, I. Antonoglou, A. Huang, A. Guez, T. Hubert, L. Baker, M. Lai, A. Bolton, Y. Chen, T. Lillicrap, F. Hui, L. Sifre, G. van den Driessche, T. Graepel, D. Hassabis, Mastering the game of Go without human knowledge. *Nature* **550**, 354–359 (2017).
2. B. M. Lake, T. D. Ullman, J. B. Tenenbaum, S. J. Gershman, Building machines that learn and think like people. *Behav. Brain Sci.* **40**, e253 (2017).
3. N. D. Daw, Y. Niv, P. Dayan, Uncertainty-based competition between prefrontal and dorsolateral striatal systems for behavioral control. *Nat. Neurosci.* **8**, 1704–1711 (2005).
4. S. Elfving, B. J. Seymour, Parallel reward and punishment control in humans and robots: Safe reinforcement learning using the MaxPain algorithm, in *7th Joint IEEE International Conference on Development and Learning and on Epigenetic Robotics (ICDL-EpiRob 2017)* (2018), vol. 2018, pp. 140–147.

5. S. W. Lee, J. P. O'Doherty, S. Shimojo, Neural computations mediating one-shot learning in the human brain. *PLOS Biol.* **13**, e1002137 (2015).
6. T. E. J. Behrens, M. W. Woolrich, M. E. Walton, M. F. S. Rushworth, Learning the value of information in an uncertain world. *Nat. Neurosci.* **10**, 1214–1221 (2007).
7. S. W. Lee, S. Shimojo, J. P. O'Doherty, Neural computations underlying arbitration between model-based and model-free learning. *Neuron* **81**, 687–699 (2014).
8. J. X. Wang, Z. Kurth-Nelson, D. Kumaran, D. Tirumala, H. Soyer, J. Z. Leibo, D. Hassabis, M. Botvinick, Prefrontal cortex as a meta-reinforcement learning system. *Nat. Neurosci.* **21**, 860–868 (2018).
9. P. Kollock, Social dilemmas: The anatomy of cooperation. *Annu. Rev. Soc.* **24**, 183–214 (1998).
10. M. Kleiman-Weiner, M. K. Ho, J. L. Austerweil, M. L. Littman, J. B. Tenenbaum, Coordinate to cooperate or compete: Abstract goals and joint intentions in social interaction, in *Proceedings of the 38th Annual Meeting of the Cognitive Science Society* (2016), pp. 1679–1684.
11. A. Lerer, A. Peysakhovich, Maintaining cooperation in complex social dilemmas using deep reinforcement learning, <https://arxiv.org/abs/1707.01068> (2017).
12. J. Foerster, R. Y. Chen, M. Al-Shedivat, S. Whiteson, P. Abbeel, I. Mordatch, Learning with opponent-learning awareness, in *Proceedings of the 17th International Conference on Autonomous Agents and MultiAgent Systems (International Foundation for Autonomous Agents and Multiagent Systems, 2018)*, pp. 122–130.
13. S. M. Fleming, H. C. Lau, How to measure metacognition. *Front. Hum. Neurosci.* **8**, 443 (2014).
14. Y.-L. Boureau, P. Sokol-Hessner, N. D. Daw, Deciding how to decide: Self-control and meta-decision making. *Trends Cogn. Sci.* **19**, 700–710 (2015).
15. P. Domenech, E. Koechlin, Executive control and decision-making in the prefrontal cortex. *Curr. Opin. Behav. Sci.* **1**, 101–106 (2015).

Acknowledgments: B.S. is funded by the Wellcome Trust (no. 097490) and Arthritis Research UK (no. 21357). J.H.L., S.J.A., and S.W.L. are supported by (i) the ICT R&D program of MSIP/IITP (no. 2016-0-00563, Research on Adaptive Machine Learning Technology Development for Intelligent Autonomous Digital Companion), (ii) the Institute of Information and Communications Technology Planning and Evaluation (IITP) grant funded by the Korean government (no. 2017-0-00451, Development of BCI based Brain and Cognitive Computing Technology for Recognizing User's Intentions using Deep Learning), (iii) IITP grant funded by the Korean government (MSIT) (no. 2018-0-00677, Development of Robot Hand Manipulation Intelligence to Learn Methods and Procedures for Handling Various Objects with Tactile Robot Hands), (iv) Samsung Research Funding Center of Samsung Electronics under project number SRFC-TC1603-06, and (v) the research fund of the KAIST (Korea Advanced Institute of Science and Technology; grant code: G04150045).

10.1126/scirobotics.aav2975

Citation: J. H. Lee, B. Seymour, J. Z. Leibo, S. J. An, S. W. Lee, Toward high-performance, memory-efficient, and fast reinforcement learning—Lessons from decision neuroscience. *Sci. Robot.* **4**, eaav2975 (2019).



CAREER PLANNING

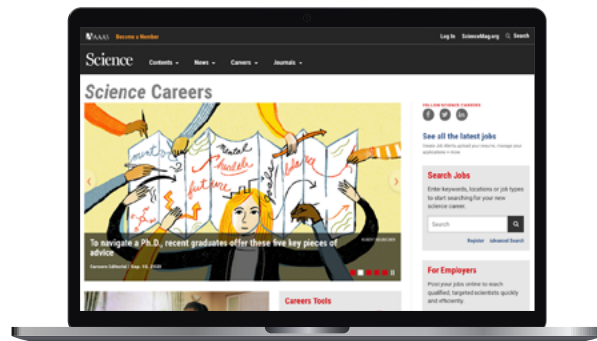
Science Careers helps you advance your career. Learn how!

- Register for a free online account on [ScienceCareers.org](https://www.sciencecareers.org).
- Search thousands of job postings and find your perfect job.
- Sign up to receive e-mail alerts about job postings that match your criteria.
- Upload your resume into our database and connect with employers.
- Watch one of our many webinars on different career topics such as job searching, networking, and more.
- Download our career booklets, including Career Basics, Careers Beyond the Bench, and Developing Your Skills.
- Complete an interactive, personalized career plan at “my IDP”
- Visit our Employer Profiles to learn more about prospective employers.
- Read relevant career advice articles from our library of thousands.

Visit [ScienceCareers.org](https://www.sciencecareers.org) today — all resources are free

ScienceCareers

FROM THE JOURNAL SCIENCE  AAAS



SCIENCECAREERS.ORG

ADDICTION

μ -Opioid receptor–induced synaptic plasticity in dopamine neurons mediates the rewarding properties of anabolic androgenic steroids

Leonardo Bontempi^{1*} and Antonello Bonci^{2*}

Anabolic androgenic steroids (AAS) have medical utility but are often abused, and the effects of AAS on reward circuits in the brain have been suggested to lead to addiction. We investigated the previously reported correlations between AAS and the endogenous μ -opioid system in the rewarding properties of AAS in mice. We found that a single injection of a supraphysiological dose of natural or synthetic AAS strengthened excitatory synaptic transmission in putative ventral tegmental area (VTA) dopaminergic neurons. This effect was associated with the activation of μ -opioid receptors (MORs) and an increase in β -endorphins released into the VTA and the plasma. Irreversible blockade of MORs in the VTA counteracted two drug-seeking behaviors, locomotor activity and place preference. These data suggest that AAS indirectly stimulate a dopaminergic reward center of the brain through activation of endogenous opioid signaling and that this mechanism mediates the addictive effects of AAS.

INTRODUCTION

Anabolic androgenic steroids (AAS) consist of synthetic derivatives of the primary male sex hormone, testosterone. AAS abuse can lead to physical and psychological dependence and is especially abused by males in first adulthood to enhance athletic performance or for cosmetic purposes (1–4). The use of AAS by teenagers has also been a primary public health concern because of their potential side effects during a period where brain remodeling and behavioral maturation occur. This, as well as other epidemiological reports, supports studies that link early initiation of AAS misuse with increased risk of psychiatric conditions, indiscriminate and unprovoked aggression, steroid dependence, and the use of other illicit drugs (5, 6). However, whether and why AAS induce physical and psychological dependence is still a matter of debate.

The rewarding properties of AAS have been commonly associated with the improvement of physical appearance, muscular strength, and athletic performance. However, in addition to their influence on somatic features, a growing body of work in adult rodents shows that androgen compounds might have rewarding and reinforcing effects (7). These effects are observed using different behavioral paradigms, such as conditioned place preference (CPP) or self-administration (8–11). In particular, self-administration of testosterone causes autonomic depression in a similar manner as observed with opioids and is blocked by naltrexone, an opioid antagonist (11). Furthermore, AAS seem to interact with the endogenous opioid system in both humans and rodents, suggesting that some of the AAS effects in the brain might be mediated by opioids (11, 12). In particular, chronic administration of AAS increases the concentration of the endogenous μ -opioid receptor (MOR) agonist β -endorphin in several brain regions including the dopamine (DA) system of the ventral tegmental area [VTA; (13)].

The VTA mediates reward prediction, positive reinforcement, motivation, and reward/drugs-seeking behavior (14, 15). All drugs

of abuse interact with DA neurons to increase their activity and the level of DA in brain regions, such as the nucleus accumbens (16). Moreover, drugs of abuse also induce long-term alterations in glutamatergic synaptic transmission on DA neurons, which represents a learning mechanism that is both sufficient and necessary to develop and maintain drug addiction or stress-related behavior (17–20). Current hypotheses are that AAS might enhance DAergic activity because testosterone place preference is DA dependent (8, 10). However, there is now insufficient evidence of a direct action by androgens and the mechanisms by which AAS modulate DA neuron activity and synaptic transmission.

Along this line of thought, the first aim of this work was to assess the long-lasting effect of a high dose of the synthetic androgen nandrolone and the endogenous androgen testosterone, two of the most abused AAS, on the physiology of putative DA neurons. The second aim was to understand the mechanism by which AAS interact with the VTA, focusing on the interaction between AAS and the endogenous MOR agonist β -endorphin. Last, we attempted to demonstrate how these mechanisms are involved in the rewarding properties of AAS.

RESULTS

Single administration of AAS induces synaptic plasticity on putative DA neurons

Several lines of evidence show that a single exposure of drugs of abuse is capable of rapidly causing long-lasting neuroadaptive changes onto VTA DA neurons (17, 21–23). Synaptic plasticity on DA neurons plays a pivotal role in the development of drug addiction (24). Moreover, it also affects the individual susceptibility to relapse, which is one of the most critical parts in the treatment of drug addiction (24). Thus, studying the long-lasting effect and the mechanisms by which drugs of abuse interact with the VTA are crucial to understand the neurobiology of drug addiction and to discover new therapeutic targets to treat drug dependence. On these bases, we used whole-cell electrophysiological recordings from acute brain slices containing the VTA from male mice treated, 24 hours before the recording, with a single intraperitoneal injection of either vehicle or a supraphysiological concentration of either nandrolone or testosterone. The dose was chosen on the basis of previous studies

Copyright © 2020
The Authors, some
rights reserved;
exclusive licensee
American Association
for the Advancement
of Science. No claim
to original U.S.
Government Works

¹Intramural Research Program, Synaptic Plasticity Section, National Institute on Drug Abuse, Baltimore, MD 21224, USA. ²Global Institutes on Addictions, Miami, FL 33132 USA.

*Corresponding author. Email: leonardo.bontempi@it.it (L.B.); anto.bonci@gia.miami (A.B.)

to simulate a similar amount of AAS abused by people (25–28). First, we measured the firing rate of putative DA neurons. Putative DA neurons were recorded medial to the medial nucleus of the optic tract and identified by morphology, tonic spike rate, and presence of a hyperpolarization-induced I_h current. There was no change in the frequency of firing of putative DA neurons at resting (fig. S1, A and B). Moreover, also the membrane capacitance, resistance, and resting membrane potential—after hyperpolarization potential I_h current and neurons firing after different depolarizing steps—were unaltered (fig. S1, C to H). These data suggested that a single injection of AAS did not induce any alteration of the intrinsic properties of putative DA neurons. Next, we studied the long-lasting effect of

AAS on glutamatergic synaptic plasticity. First, we pharmacologically isolated spontaneous miniature excitatory postsynaptic currents (mEPSCs; Fig. 1A). Mean amplitude and frequency distribution of mEPSC were significantly increased in nandrolone- and testosterone-treated animals compared to vehicle-treated mice, as indicated by a shift in the cumulative probability distributions (Fig. 1, B and C). The observed increase in amplitude and frequency of mEPSC may be attributable to increased AMPA receptors (AMPA) function and/or number. To assess synaptic strength, we calculated the ratio of AMPAR-mediated synaptic currents (AMPA EPSCs) to *N*-methyl-D-aspartate receptor (NMDAR)-mediated synaptic currents (NMDAR EPSCs). In animals treated with either nandrolone

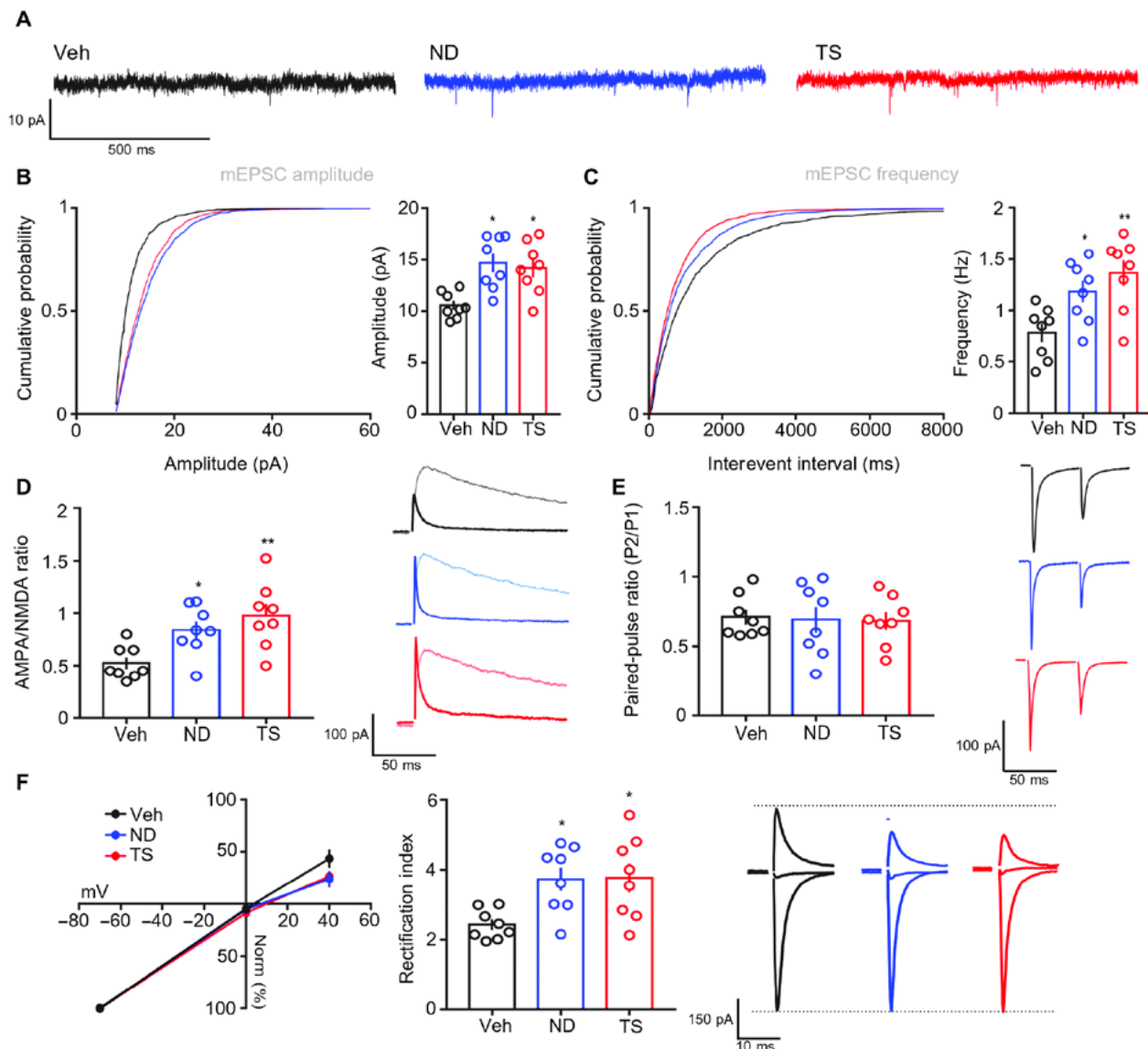


Fig. 1. AAS strengthen excitatory synaptic transmission on putative DA neurons. (A to C) Representative traces (A) and analysis of mEPSC frequency (B) and amplitude (C) in putative VTA DA neurons of mice treated with a single injection of either testosterone (TS; 10 mg/kg), nandrolone (ND; 10 mg/kg), or vehicle (Veh). Cumulative distributions of amplitude and frequency were analyzed by using Kolmogorov-Smirnov test: $P < 0.01$ versus Veh. (D) AMPAR/NMDAR ratio of mice treated with AAS as described in (A) to (C). (E) Paired-pulse ratio obtained at 50-ms interpulse interval from mice treated as described in (A) to (C). (F) *I*-*V* (current-voltage relation) plot of pharmacological isolated AMPAR EPSC (left). All EPSCs were normalized to the EPSC amplitude measured at -70 mV. Rectification index (middle) of AMPAR EPSCs was calculated as the ratio between the amplitude of EPSC obtained at -70 and $+40$ mV. In (A) to (F), values are means \pm SEM of $n = 8$ neurons recorded from four mice per condition, analyzed by one-way ANOVA with Bonferroni post hoc test: $*P < 0.05$, $**P < 0.01$ versus Veh. Representative traces are shown (right).

or testosterone, there was a significant increase of AMPAR/NMDAR ratio (Fig. 1D). To understand whether this change in AMPAR/NMDAR was associated to either an increase of AMPAR EPSC or decrease of NMDAR EPSC or both, we performed an input-output experiment pharmacologically isolating either AMPAR or NMDAR EPSC. We reported a significant increase of AMPAR EPSC in mice treated with AAS compared to vehicle-treated mice (fig. S2A). On the contrary, we reported no change in NMDAR EPSC in any experimental condition (fig. S2B), suggesting that the increase of AMPAR/NMDAR ratio might be attributed to an increase of AMPAR function or expression. To verify possible presynaptic alterations, we performed a paired-pulse stimulation experiment to test changes in glutamate release probability. There were no substantial changes in the paired-pulse ratio neither in nandrolone- nor in testosterone-treated mice (Fig. 1E). These data might suggest that there was no presynaptic alteration after treatment with AAS, even though we cannot completely rule out this hypothesis. Drug-evoked potentiation of synaptic transmission is usually, in part, mediated through an exchange of GluR2-containing and GluR2-lacking AMPAR, leading to EPSCs that are sensitive to polyamines and have a rectifying current-voltage relationship (29). Thus, we measured EPSC at -70 , 0 , and $+40$ mV to calculate the rectification index ($EPSC_{-70mV}/EPSC_{+40mV}$). In mice treated with either nandrolone or testosterone, the rectification index was significantly higher than control mice, suggesting the presence of GluR2-lacking AMPAR (Fig. 1F). Last, we tested possible alterations of inhibitory γ -aminobutyric acid (GABA) transmission on putative DA neurons. Neither the treatment with nandrolone nor testosterone showed a long-lasting effect on GABAergic transmission. As a matter of fact, there were no significant differences in neither the frequency nor the amplitude of the miniature inhibitory postsynaptic current (mIPSC; fig. S3, A to C). In summary, these results showed that a single injection of AAS induces long-term alteration of glutamatergic synaptic transmission on putative DA neurons.

AAS-induced synaptic plasticity is not mediated by androgen receptor activation

Next, we wanted to describe the mechanism by which AAS modulate glutamatergic synaptic transmission on putative VTA DA neurons. We started our study by investigating the canonical target for androgens: the intracellular androgen receptor. This receptor is expressed in many brain regions, especially in the hypothalamus (30). Androgen receptor expression is reported also in other limbic regions such as the VTA, even though, the physiological role of this receptor in this region remains unknown (31, 32). Thus, we pretreated mice with a subcutaneous injection of the selective androgen receptor antagonist flutamide 60 min before the administration of either AAS or the vehicle. The pretreatment with flutamide did not affect neither the frequency nor the amplitude of mEPSC in testosterone- or nandrolone-treated mice (Fig. 2, A to C). To understand whether treatment with flutamide affected the strength of glutamatergic synaptic transmission, we evaluated the AMPAR/NMDAR ratio. In addition, in this situation, we showed that flutamide did not block the increase of the AMPAR/NMDAR ratio in AAS-treated mice (Fig. 2D). We also reported that pretreatment with flutamide might not affect the presynaptic glutamate release because it did not impair the pair-pulse ratio in any experimental group (Fig. 2E). In the end, we showed that pretreatment with flutamide did not affect also the rectification of AMPAR EPSC in mice treated with AAS (Fig. 2F). These data suggested that AAS induced the alter-

ation of glutamatergic synaptic transmission on putative VTA DA neurons through a noncanonical mechanism without engaging the androgen receptor.

AAS increases the plasma and VTA concentration of β -endorphin

Several studies in humans and rodents suggest that AAS may modulate brain activity, enhancing the endogenous opioid system. It has previously been demonstrated that chronic treatment with nandrolone increases the level of β -endorphin in the VTA (13), whereas chronic treatment with testosterone increases the concentration of β -endorphin in the hypothalamus, pituitary gland, and plasma (33–35), suggesting that AAS might boost the synthesis or release of endogenous MOR agonists. We decided to investigate whether an acute administration of AAS was sufficient to modulate the plasma and VTA concentration of β -endorphin (Fig. 3A). The results showed that a single injection of either nandrolone or testosterone induced a significant increase of plasma and VTA concentration of β -endorphin (Fig. 3B). The effect was evident 5 to 15 min after the injection with AAS, whereas the level of β -endorphin returned to the basal level after 1 hour. Together, these results showed that AAS were capable of quickly increasing the concentration of the endogenous MOR agonist β -endorphin in both plasma and VTA. β -Endorphin might represent a promising target by which AAS modulate synaptic transmission on DA neurons.

Blockade of MOR counteracts AAS-induced synaptic plasticity

The rewarding properties of exogenous and endogenous opioids, such as β -endorphin, are well demonstrated, and it is also shown that acute treatment with opioids induces synaptic plasticity in DA neurons (36, 37). Thus, we assumed that AAS might indirectly modulate synaptic transmission in DA neurons, increasing the concentration of β -endorphin and consequently activating MORs. On these bases, we performed intracerebroventricular (ICV) injections of the selective, irreversible MOR antagonist β -funaltrexamine (β -FNA) 24 hours before the injection of either AAS or vehicle (Fig. 4A). Our results showed that pretreatment with β -FNA blocked AAS-induced increase of mEPSC frequency and amplitude. β -FNA did not affect mEPSC amplitude and frequency in vehicle-treated mice (Fig. 4, B to D). We then investigated whether β -FNA was able to block the strength of glutamatergic synapses on putative DA neurons. Our result showed that the irreversible blockade of MOR was capable of dampening the increase of the AMPAR/NMDAR ratio induced by treatment with AAS (Fig. 4E). We also found that pretreatment with β -FNA appeared to have no effect on presynaptic glutamate release because the excitatory prepulse ratio was unaltered in any of the experimental conditions used (Fig. 4F). Rather, pretreatment with β -FNA blocked AAS-induced increases in the AMPAR EPSC rectification index but did not affect the AMPAR rectification index in vehicle-treated mice (Fig. 4G). These data indicate that AAS are capable of modulating synaptic strength on putative DA neurons through a MOR-dependent mechanism that may be attributed to an increase in β -endorphin levels in the VTA.

We then sought to test this hypothesis. As presented above, AAS rapidly increased the level of β -endorphin, which returned to basal level after almost 1 hour. Thus, to test whether inhibiting MOR activity also blocked AAS-induced synaptic plasticity when β -endorphin returns to basal level, we performed an ICV injection of β -FNA 1 hour after the administration of AAS (fig. S4A). Our results showed that,

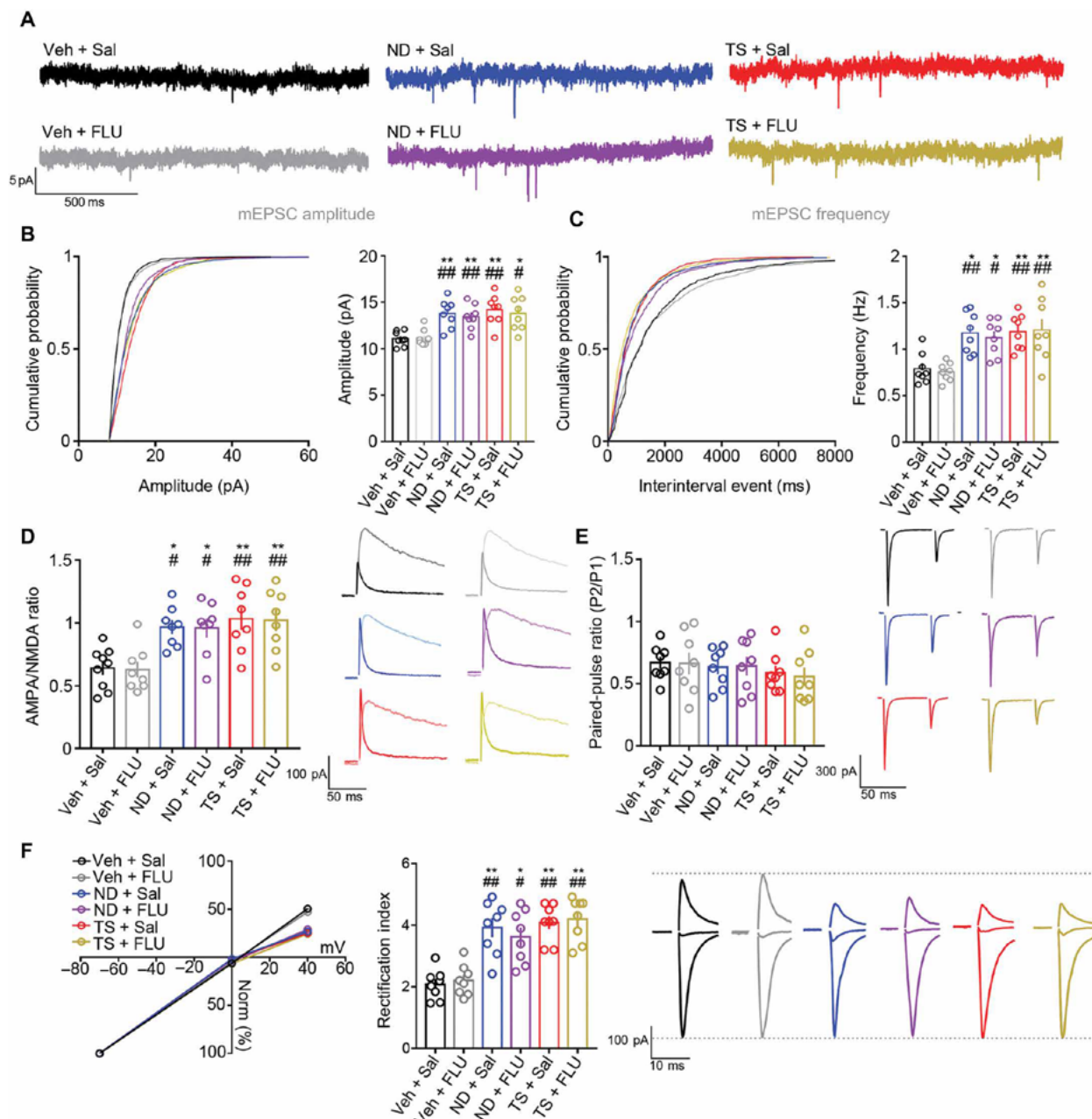


Fig. 2. Androgen receptor antagonist flutamide did not affect AAS-induced synaptic plasticity. (A to C) Representative traces (A) and analysis of mEPSC frequency (B) and amplitude (C) in putative VTA DA neurons of mice pretreated with flutamide (FLU; 20 mg/kg, sc) or saline (Sal) 1 hour before a single intraperitoneal injection of either testosterone (TS; 10 mg/kg), nandrolone (ND; 10 mg/kg), or vehicle. Cumulative distributions of amplitude and frequency were analyzed by using Kolmogorov-Smirnov test: $P < 0.01$ for the ND/TS+ conditions versus the Veh conditions. (D) AMPAR/NMDAR ratio in putative DA neuron of mice treated as described in (A) to (C). (E) Paired-pulse ratio obtained at 50-ms interpulse interval in putative DA neurons of mice treated as described in (A) to (C). (F) *I-V* plot of pharmacological isolated AMPAR EPSC (left). All EPSCs were normalized to the EPSC amplitude measured at -70 mV. Rectification index (middle) of AMPAR EPSCs was calculated as the ratio between the amplitude of EPSC obtained at -70 and $+40$ mV. Representative traces are shown (right). In (A) to (F), values are means \pm SEM of $n = 8$ neurons recorded from four mice per condition, analyzed by one-way ANOVA with Bonferroni post hoc test: * $P < 0.05$; # $P < 0.05$; ** $P < 0.01$; ### $P < 0.01$ versus Veh + Sal or Veh + FLU, respectively.

in this experimental setting, β -FNA did not block AAS-induced increase of mEPSC frequency and amplitude in putative DA neurons (fig. S4, B to D). Moreover, injection of β -FNA 1 hour after the AAS injection did not affect either the AAS-induced increase in the AMPAR/NMDAR ratio (fig. S4E) or the rectification index of AMPAR EPSCs (fig. S4F) on putative DA neurons. These results suggested that AAS-induced increases in β -endorphin levels in the VTA might

be necessary to enhance excitatory synaptic transmission on putative DA neurons.

AAS-induced locomotion and place preference requires activation of VTA MOR

The VTA is a brain region centrally involved in the development and expression of a variety of behaviors associated with drug use

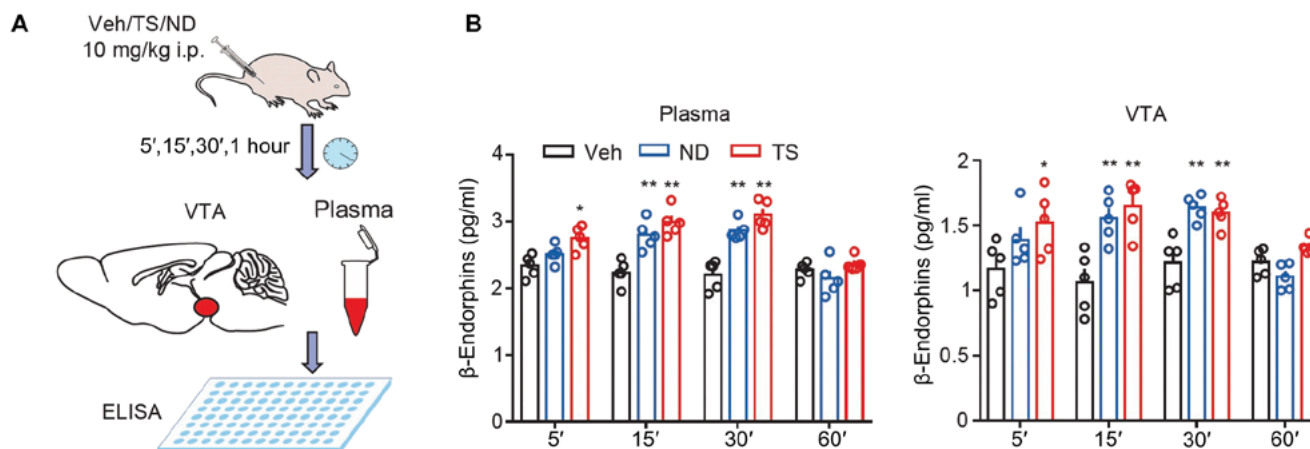


Fig. 3. AAS induce rapid increase of plasma and VTA β -endorphin levels. (A) Schematic of experiment: Mice were injected with either testosterone (TS; 10 mg/kg), nandrolone (ND; 10 mg/kg), or vehicle (Veh). After different time points (5', 15', 30' and 60'), either VTA or plasma was isolated and processed for β -endorphin quantification through ELISA. (B) Quantification of β -endorphin level in the VTA (left) and plasma (right) of mice treated as described (A). Values are means \pm SEM; five mice in each condition were analyzed by one-way ANOVA with Bonferroni post hoc test: * $P < 0.05$; ** $P < 0.01$ versus Veh. i.p., intraperitoneally.

such as increased locomotor activity and drug-seeking behavior (38). To determine whether AAS modulate locomotor activity, mice were injected with a single administration of either testosterone, nandrolone, or vehicle, and the locomotor activity was monitored for 1 hour. Our results showed that both testosterone and nandrolone significantly increased the locomotor activity 10 to 15 min after the injection (Fig. 5A). The locomotor activity remained high for almost 45 min, which might resemble a similar time course shown with the increase of β -endorphin level. To test whether the increase of the locomotor activity was due to activation of VTA MOR, we pretreated mice with an intra-VTA injection of the irreversible MOR antagonist β -FNA (Fig. 5B and fig. S5) and found that this blocked the increase in locomotor activity in both nandrolone- and testosterone-treated mice (Fig. 5C). These results suggest that the acute increase in locomotor activity induced by AAS was dependent on VTA MOR activation.

Several papers show the rewarding and reinforcing effect of both testosterone and nandrolone using either CPP or self-administration paradigms (6–8). To determine whether AAS also induced place preference in our experimental conditions, we performed CPP experiments in mice conditioned with either testosterone or nandrolone (Fig. 6A) and found that both steroids were capable of inducing a strong and significant CPP in mice (Fig. 6B), demonstrating the rewarding effect of AAS. Next, we investigated whether the development of CPP was dependent on VTA MOR activation. We took advantage of the irreversible antagonist β -FNA to induce a chronic pharmacological blockade of VTA MOR. However, to minimize the number of β -FNA injections in the VTA, we assessed the duration of MOR inactivation after a single microinjection of β -FNA in the VTA (fig. S6A). MORs are expressed on presynaptic GABAergic terminals, and their activation reduces GABA release on DA neurons. To verify when MOR activity was restored after β -FNA injection, we analyzed the effect of the MOR agonist [D-Ala², N-MePhe⁴, Gly-ol]-enkephalin (DAMGO) on putative DA neurons GABAergic synaptic transmission. DAMGO did not modify the frequency of mIPSC 1 or 2 days after β -FNA injection (fig. S6, B to F) but did significantly by 3 days after (fig. S6, G and H). These data suggested that the intra-VTA injection of β -FNA could block the activity of VTA MOR for 48 hours. Thus, we microinjected β -FNA in the VTA (fig. S7)

every 2 days, 20 hours before the AAS conditioning session (Fig. 6, C and D). Our results showed that irreversible chronic blockade of VTA MOR dampened the development of both nandrolone and testosterone place preference (Fig. 6, E and F). To finally confirm that β -FNA injection did not affect the result of the CPP due to its possible aversive effect, we performed another CPP experiment, wherein the AAS and vehicle conditioning sessions were inverted and β -FNA was injected in the VTA (fig. S8) 20 hours before the vehicle conditioning session (fig. S9A). Our result showed that also in this situation, β -FNA was still capable to block the development of AAS-induced place preference (fig. S9, B and C). Together, these data indicate that the rewarding effect of AAS is mediated by VTA MOR activation, likely due to an increase of β -endorphins in the VTA.

DISCUSSION

AAS abuse remains a poorly understood and underappreciated social problem despite the risk of addiction and side effects. According to several studies, about 30 to 32% of subjects using AAS will suffer from dependence; this may lead to severe side effects such as increased aggressive behavior and depression, which is associated with a high risk of suicide (39, 40). Thus, studying how AAS modulate the function of brain regions usually involved in drug addiction and the mechanisms underlying the rewarding properties of AAS might be of pivotal importance to find therapeutic targets capable of counteracting AAS abuse and side effects.

A major hypothesis in the pathogenesis of addictive behavior points at drug-induced plasticity within the VTA DA system as one of the major causes of compulsive drug-seeking and relapse behavior (24, 34). All drugs of abuse typically increase the excitatory transmission on DA neurons, and it is demonstrated how these long-term alterations of synaptic transmission are related to the behavioral effects of addictive drugs (that is, CPP or drug sensitization or reinstatement of drug self-administration). Some studies also report that AAS might interact with the DAergic system because AAS place preference is DA dependent, and chronic treatment with AAS induces alteration of DA receptors in many brain regions (8–10).

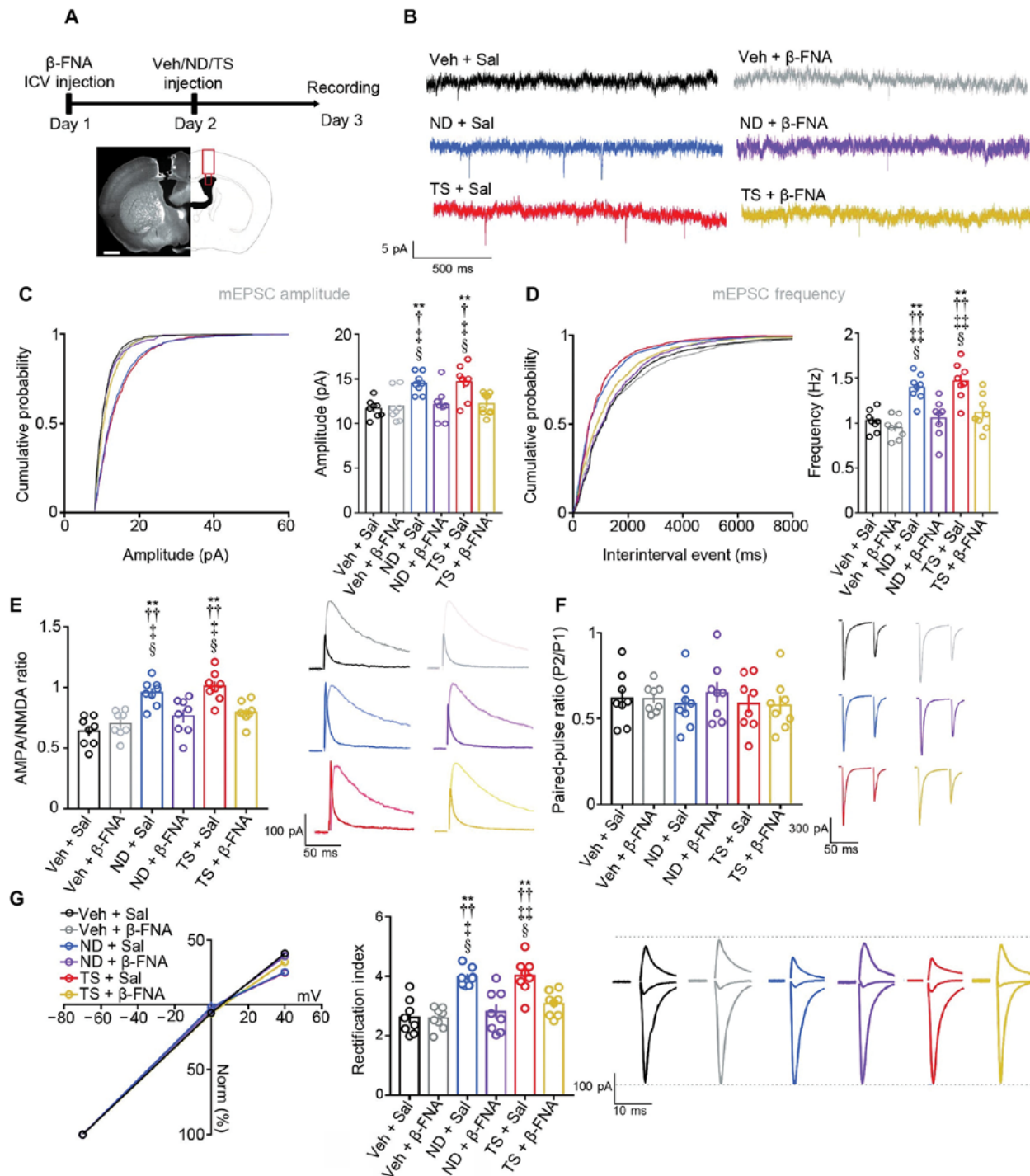


Fig. 4. AAS-induced synaptic plasticity on putative DA neurons is mediated by MOR activation. (A) Coronal section depicting cannula implantation in the left lateral ventricle and schematic of experiment: Mice received an ICV injection of the irreversible MOR antagonist β -FNA (0.2 μ g in 0.2 μ l of saline) or saline (Sal) 24 hours before injecting either testosterone (TS; 10 mg/kg), nandrolone (ND; 10 mg/kg), or vehicle (Veh). Scale bar, 1 mm. Whole-cell patch-clamp recordings were performed 24 hours after the treatment with either AAS or Veh. (B to D) Representative traces (B) and analysis of mEPSC frequency (C) and amplitude (D) recorded in putative VTA DA neurons of mice treated as described (A). Cumulative distributions of amplitude and frequency were analyzed by using Kolmogorov-Smirnov test: $P < 0.01$ for ND + β -FNA and TS + β -FNA versus ND + Sal, TS + Sal, Veh + Sal, and Veh + β -FNA. (E) AMPAR/NMDAR ratio in putative DA neurons of mice treated as described (A). (F) Paired-pulse ratio obtained at 50-ms interpulse interval. (G) *I-V* plot and rectification index in putative DA neurons of mice treated as described (A). *I-V* plot of pharmacologically isolated AMPAR EPSC (left). All EPSCs were normalized to the EPSC amplitude measured at -70 mV. Rectification index (middle) of AMPAR EPSCs was calculated as the ratio between the amplitude of EPSC obtained at -70 and $+40$ mV. Representative traces (right). In (C) to (F), values are means \pm SEM of $n = 8$ neurons recorded from four mice per condition, analyzed by one-way ANOVA with Bonferroni post hoc test: ** $P < 0.01$ versus Veh + Sal; † $P < 0.05$ and †† $P < 0.01$ versus Veh + β -FNA; ‡ $P < 0.05$; ‡‡ $P < 0.01$ versus ND + β -FNA; § $P < 0.05$; §§ $P < 0.01$ versus TS + β -FNA.

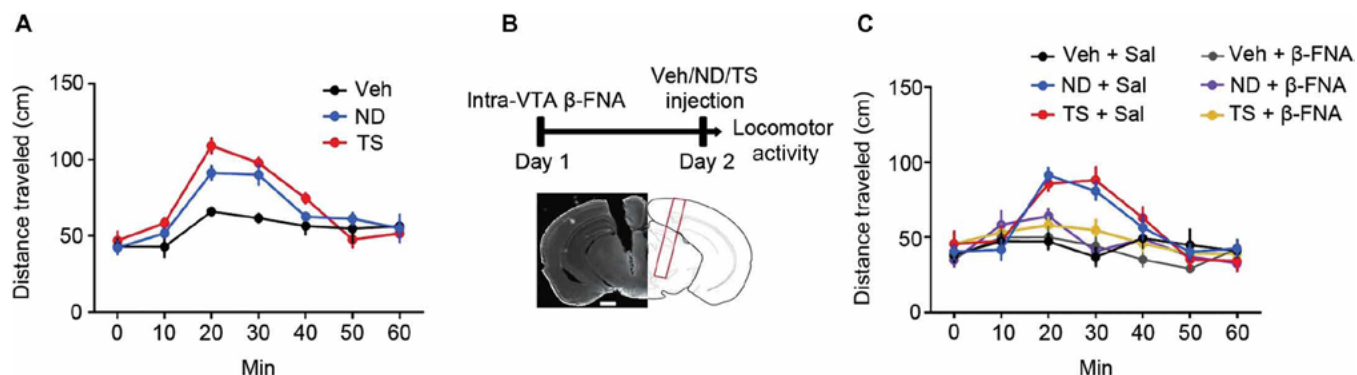


Fig. 5. AAS-induced locomotor activity required VTA MOR activation. (A) Locomotor activity in mice treated with a single intraperitoneal injection with either testosterone (TS; 10 mg/kg), nandrolone (ND; 10 mg/kg), or vehicle (Veh). Values are means \pm SEM (nine mice per group), analyzed by one-way ANOVA with Bonferroni post hoc test: $P < 0.01$ ND versus Veh and $P < 0.001$ TS versus Veh at 15 min; $P < 0.01$ ND versus Veh and $P < 0.001$ TS versus Veh at 30 min. (B) Coronal section depicting intra-VTA cannula implantation. (C) Locomotor activity in mice pretreated with an intra-VTA injection of β -FNA (0.2 μ g in 0.2 μ l of saline) or saline (0.2 μ l; Sal), 24 hours before a single intraperitoneal injection with either TS, ND, or Veh as described in (A). Values are means \pm SEM of seven mice per group, analyzed by one-way ANOVA with Bonferroni post hoc test: $P < 0.01$ for ND + Sal versus TS + β -FNA, TS + Sal versus Veh + Sal, and TS + Sal versus Veh + β -FNA; $P < 0.001$ for ND + Sal versus Veh + β -FNA and $P < 0.0001$ for ND + Sal versus Veh + Sal at 15 min; $P < 0.05$ for TS + Sal versus TS + β -FNA; $P < 0.01$ for ND + Sal versus Veh + β -FNA; $P < 0.001$ for ND + Sal versus Veh + Sal, ND + Sal versus ND + β -FNA, and TS + Sal versus Veh + β -FNA; $P < 0.0001$ for TS + Sal versus Veh + Sal and TS + Sal versus ND + β -FNA at 30 min.

In this study, we found that AAS can directly affect the physiology of DA neurons. Our results revealed that a single administration of two of the most common AAS was capable of strengthening the excitatory synaptic transmission on putative VTA DA neurons. We reported an increase of mEPSC amplitude and frequency as well as an increase of the AMPAR/NMDAR ratio due to an increase of AMPAR EPSC and increase of the rectification index of AMPAR EPSC. These data demonstrated that AAS, as well as other drugs of abuse, were capable of strengthening excitatory transmission on putative DA neurons. We also found that this effect was not mediated by androgen receptor activation, which suggests the involvement of noncanonical mechanisms. Administration of AAS in humans induces a feeling of pleasure within 15 to 20 min of administration, which indicates the presence of a fast, nongenomic action (41). Previous studies suggest several receptors as potential targets for the nongenomic effect of androgens. These include GABA receptors, the sigma-1 receptor (σ_1 R), and a putative membrane receptor for androgens (42, 43). Moreover, several studies report that the nongenomic action of androgens might also be linked to the endogenous opioid system (12). Fifty percent of people abusing AAS meet the diagnostic criteria for opioid use disorder (12). Furthermore, self-administration of testosterone in rodents is blocked by the presence of the opioid antagonist naltrexone. Pretreatment with testosterone induces CPP to subthreshold doses of morphine, and chronic treatment with nandrolone increases the level of β -endorphin in the VTA (11–13). In our study, we also showed that a single injection of either testosterone or nandrolone quickly increased the VTA and plasma level of β -endorphin. This increase of β -endorphin supports the assumption that androgens might affect neuronal activity by enhancing the endogenous opioid system activity, even though the mechanisms and the body regions by which androgens promote the release of β -endorphin are not yet known and require further investigation.

The rewarding effect of β -endorphin and its role in natural and drug reward are well described (36, 37). However, the involvement of the endogenous β -endorphin in drug-induced synaptic plasticity is still a matter of debate. Another study shows that a raise in the endogenous level of β -endorphin might be linked to the rewarding

properties of ultraviolet light (43). Thus, although it is not completely demonstrated, it would not be unexpected if β -endorphin played a role in the rewarding properties of AAS as well. We showed that preexposure to the selective irreversible MOR antagonist β -FNA dampened the AAS-induced synaptic plasticity in putative VTA DA neurons, demonstrating that activation of MOR was required for AAS action in the VTA. MOR can regulate DA neuron activity and synaptic transmission either through a presynaptic mechanism, reducing GABA release or promoting glutamate release (44), or through a postsynaptic mechanism because they are also expressed in DA neurons (45). Moreover, some authors report that opioids induce synaptic plasticity on DA neurons, regulating the release of other neuromodulators such as orexin (23). Our study does not uncover whether AAS-dependent synaptic plasticity and behavioral effects are mediated by presynaptic or postsynaptic VTA MOR or whether other neuromodulators are involved. This, too, will require further investigation.

Taking advantage of the CPP paradigm to study whether the rewarding effect of AAS was dependent on VTA MOR activation, our results further showed that the irreversible inhibition of MOR in the VTA was sufficient to block AAS-induced place preference and locomotor activity. Another study shows that systemic injection with naloxone blocks testosterone self-administration, suggesting that the endogenous opioids system might be involved in the rewarding properties of this natural hormone. Along this line, our findings provide evidence that AAS-induced enhancement of μ -opioid signaling is involved in the physiological, long-lasting alterations in the VTA commonly seen after exposure to drugs of abuse and that are implicated in the development of drug-seeking behavior. Overall, we did not report any substantial difference between testosterone and nandrolone in any experiment. This suggests that, regarding the aspects studied in this paper, they probably work through the same mechanisms and induce the same effect.

Although our results need to be replicated in other behavioral paradigms, the same mechanism (that of MOR-mediated glutamatergic synaptic transmission on putative VTA DA neurons) may be involved in the rewarding properties of AAS. The interaction between

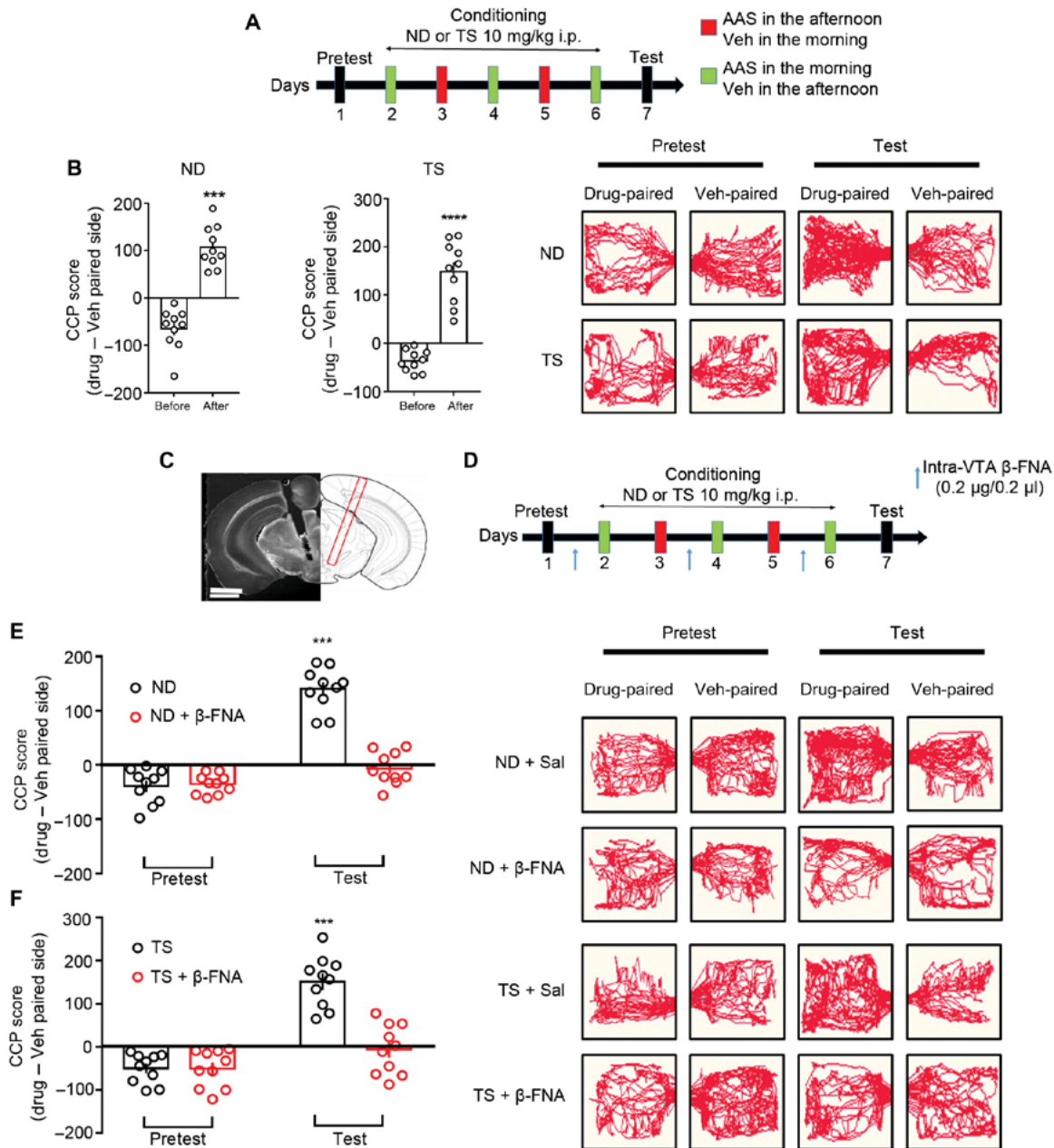


Fig. 6. Irreversible blockade of VTA MOR counteracted AAS-induced place preference. (A) Schematic of experiment: During the pretest, mice were allowed to explore all compartments and were monitored for 15 min to assess any preference for a certain compartment. During conditioning, mice were injected in the morning during days 2, 4, and 6 and in the afternoon during days 3 and 5 with either testosterone (TS; 10 mg/kg) or nandrolone (ND; 10 mg/kg) and were confined to the not preferred compartment. In the afternoon of days 2, 4, and 6 or in the morning of days 3 and 5, mice were treated with vehicle (Veh) and were confined to the preferred side. The test day occurred in the middle of the day, and the mice were allowed to explore all compartments for 15 min. (B) Conditioned place preference (CPP) in mice conditioned as described (A). CPP score was calculated, subtracting the time spent in the drug-paired side to the Veh-paired side. Values are means ± SEM (10 mice per group). Two-tailed paired Student's *t* test; ****P* < 0.001, *****P* < 0.0001. (C) Coronal section depicting intra-VTA cannula implantation (scale bar: 2mm). (D) Schematic of experiment: The experiment was performed as shown previously (A), except for the fact that β-FNA (0.2 μg in 0.2 μl of Sal) was injected in the VTA every 48 hours to maintain VTA MOR blocked for the whole duration of the experiment. The injection occurred on day 1 after the pretest and on days 3 and 5 after the conditioning session to not allow the association between any possible aversive effect of β-FNA with any compartment of the CPP apparatus. (E and F) CPP in mice conditioned as described (D). Values are means ± SEM (10 mice per group); two-tailed paired *t* test comparing the time spent on the drug-paired side before and after conditioning. ****P* < 0.001, *****P* < 0.0001.

AAS and endogenous opioid system might be of pivotal importance here, given the co-abuse of AAS and opioids. AAS have been previously defined as a gateway drug to opioid dependence. It is also plausible that if AAS addiction is wired through opioid signaling,

then people suffering of AAS addiction might be treated with the same approved medication used for opioid abuse, such as buprenorphine. Moreover, further investigations about the plasma concentration of endogenous opioids or of brain opioid receptor binding should also

be performed in people abusing AAS. Ultimately, understanding the connection between androgens and opioids could be crucial toward understanding the development of side effects, such as aggressive behavior or depression, commonly seen with chronic abuse of AAS.

MATERIALS AND METHODS

Animals

Male mice (8 to 10 weeks old) were group housed in a colony maintained under a 12-hour light/dark cycle with food and water available ad libitum. All experiments were carried out during the mouse dark cycle. All analyses were performed on mice whose genotype was unknown to the experimenter. All procedures were conducted in accordance with the Guide for the Care and Use of Laboratory Animals of the National Institutes of Health.

Drugs

Testosterone was purchased from Cayman Chemicals (Ann Arbor, MI, USA; catalog no. 15645). Nandrolone was purchased from Sigma-Aldrich (St. Louis, MO, USA; catalog no. N7252). Flutamide, β -FNA, DAMGO, and 6,7-Dinitroquinoxaline-2,3-dione (DNQX) disodium salt were purchased from Tocris (Minneapolis, MN; catalog nos. 4094, 0926, 1171, and 2312). D-aminophosphovalerate (D-APV), tetrodotoxin citrate (TTX), and picrotoxin were purchased from Abcam (Cambridge, MA; catalog nos. ab120003, ab120055, and ab120315). Testosterone and nandrolone were dissolved in 45% (2-hydroxypropyl)- β -cyclodextrin (Sigma-Aldrich, catalog no. H107). Flutamide and β -FNA were dissolved in 0.9% NaCl solution (saline). DAMGO, DNQX, D-APV, TTX, and picrotoxin were dissolved in water.

Electrophysiology

Male mice were treated with a single intraperitoneal injection of either vehicle or testosterone (10 mg/kg) or nandrolone (10 mg/kg). After 24 hours, mice were anesthetized with Euthazol and decapitated. Brains were quickly removed and placed in ice-cold low-sodium artificial cerebrospinal fluid (ACSF). For pharmacological experiments with antagonist, mice were pretreated with flutamide (20 mg/kg) or β -FNA ICV injection (2 μ g in 0.2 μ l of saline) 1 or 24 hours before the injection of AAS, respectively. Horizontal sections (250 μ m) containing the VTA were prepared in ice-cold ACSF using a vibrating blade microtome (Leica VT1200, Buffalo Grove, IL, USA). Right after cutting, slices were recovered for 10 min at 32°C and then transferred to holding ACSF at room temperature. Cutting and recovery were performed with ACSF containing the sodium substitute N-methyl-D-glucamine (NMDG) (45): 92 mM NMDG, 20 mM Hepes (pH 7.35), 25 mM glucose, 30 mM sodium bicarbonate, 1.2 mM sodium phosphate, 2.5 mM potassium chloride, 5 mM sodium ascorbate, 3 mM sodium pyruvate, 2 mM thiourea, 10 mM magnesium, 14 mM sulfate, and 0.5 mM calcium chloride (46). The ACSF used for holding slices before recording was identical but contained 92 mM sodium chloride instead of NMDG and contained 1 mM magnesium chloride and 2 mM calcium chloride. The ACSF used to perfuse slices during recording contained 125 mM sodium chloride, 2.5 mM potassium chloride, 1.25 mM sodium phosphate, 1 mM magnesium chloride, 2.4 mM calcium chloride, 26 mM sodium bicarbonate, and 11 mM glucose. All ACSF solutions were saturated with 95% O₂ and 5% CO₂. For recording, a single slice was transferred to a heated chamber (32°C) and perfused with normal ACSF (2.5 ml min⁻¹) using a peristaltic pump (World Precision Instruments, Sarasota, FL, USA).

Visualization of putative VTA DA neurons was performed with an upright microscope equipped for differential interference contrast microscopy (BX51WI, Olympus, Waltham, MA, USA). Putative DAergic neurons in the VTA were located medial to the medial nucleus of the optic tract and identified by morphology, tonic spike rate, and presence of a hyperpolarization-induced I_h current, which can be a reasonable predictor of DAergic identity in mice (47). Whole-cell patch-clamp recordings were made using a MultiClamp 700B amplifier (1 kHz low-pass Bessel filter and 10 kHz digitization) with pClamp 10.3 software (Molecular Devices, San Jose, CA, USA). Voltage-clamp recordings of excitatory synaptic transmission were made using glass pipets with resistance of 1.5 to 3 megohms, filled with internal solution containing the following: 117 mM cesium methanesulfonate, 20 mM Hepes, 0.4 mM EGTA, 2.8 mM NaCl, 5 mM Tetraethylammonium chloride (TEA-Cl), 2.5 mM Mg-ATP (adenosine triphosphate), and 0.25 mM Na-GTP (guanosine triphosphate); pH 7.2 to 7.3 and 280 to 285 mOsm. Spermine (0.1 mM) was added to the internal solution for measuring the current-voltage relationship of AMPAR currents. For inhibitory transmission, GABA-A mIPSCs were recorded with glass microelectrodes (1.5 to 3 megohms) containing the following: 128 mM KCl, 20 mM NaCl, 10 mM Hepes, 1 mM MgCl₂, 1 mM EGTA, 0.3 mM CaCl₂, 2 mM Mg-ATP, and 0.25 mM Na-GTP (280 to 285 mOsm) to detect mIPSC as large inward currents at -65 mV. Input and series resistance was continually monitored online; if either parameter changed by more than 20%, data were not included in the analysis. Membrane potentials were not corrected for junction potentials (estimated to be 10 mV). Excitatory afferents were stimulated at 0.1 Hz with a bipolar stimulating electrode placed 100 to 300 μ m rostral to the recording electrode. Excitatory paired-pulse ratios were acquired at -70 mV by having a second afferent stimulus of equal intensity at 50 ms after the initial stimulus. The ratio was calculated from the peak amplitude of the second and the first stimuli. The experiments looking at AMPAR/NMDAR ratios were carried out by evoking the dual-component EPSC at +40 mV, and then D-APV (50 μ M) was bath applied to isolate AMPAR EPSC. NMDAR responses were calculated by digital subtraction of the average response in the presence of D-APV from the response isolated in its absence. To yield the AMPAR/NMDAR ratio, the peak of the AMPAR EPSC was divided by the peak of the NMDAR EPSC. We measured the rectification of AMPAR-mediated currents by pharmacologically isolating AMPAR EPSC at a holding potential ranging from -70 to +40 mV and then normalizing the peak amplitude of each holding potential to the current at -70 mV. mEPSCs were pharmacologically isolated by having picrotoxin (100 μ M) and tetrodotoxin (20 nM) present throughout the experiment and sampled at 1 kHz while clamping the cells at -70 mV. mIPSCs were isolated by having NBQX (2,3-dihydroxy-6-nitro-7-sulfamoylbenzo[f]quinoxaline) (10 μ M) and D-APV (50 μ M) and tetrodotoxin (20 nM) and were clamped at -65 mV. Two hundred events per cell were acquired and detected using a threshold of 8 pA. Analyses of mEPSC and mIPSC were performed offline and verified by eye using the MiniAnalysis program (v6.0, Synaptosoft). For current-clamp recordings looking at cell excitability, electrodes were filled with the following: 135 mM K-gluconate, 10 mM Hepes, 4 mM KCl, 4 mM Mg-ATP, and 0.3 mM Na-GTP; pH 7.2 to 7.3 and 280 to 285 mOsm. We measured cell excitability with incremental steps of current injections and monitored the number of spikes fired during a fixed current injection (2 s). All values were obtained after cells had reached a stable response, and then averages of three cycles for each cell were taken.

No more than one to two cells per animal were used for each experimental setting.

Surgery and cannula implantation

Mice were anesthetized using ketamine (1 ml of 100 mg/ml solution) mixed with xylazine (0.1 ml of 100 mg/ml solution) in injectable saline (8.9 ml) and intraperitoneally administered in a volume of 0.1 ml/10 g of mouse weight. For the assessment of the MOR irreversible blockade by β -FNA, a solution containing β -FNA (0.2 μ g) diluted in saline solution and 50% (v/v) of fluorescent microspheres (Thermo Fisher Scientific, Waltham, MA, USA; catalog no. F10720) was injected in the VTA [AP (anterior-posterior), -2.9 ; ML (medio-lateral), ± 1.6 ; DV (dorso-ventral), -4.6] in a volume of 0.2 μ l. Fluorescent beads were used to detect the site of injection during the patch-clamp recording, ensuring that the drug has been delivered to the VTA. Slices without detectable fluorescence in the VTA were excluded. For the pharmacological studies with β -FNA, mice were implanted with guide cannulas above the VTA (AP, -2.9 ; ML, ± 1.6 ; DV, -3.6 ; the microneedle protruded 1 mm from the cannula tip) or the left lateral ventricle for ICV injection (AP, -0.6 ; ML, -1.2 ; DV, -1.8). For VTA cannula implantation, two holes were drilled through the skull for simultaneous placement of guide cannulas. A third hole was drilled about 2 mm anterior to the guide cannula holes; this hole was enlarged for the placement of an anchor screw, which provided an additional surface area for the skull cap to adhere. Dental cement was applied to the exposed cranium with the aim of securing the guide cannulas and the anchor screw in place. After about 4 hours of recovery, all animals were returned to their reverse light/dark cycle holding room and given free access to food and water.

Behavioral analyses

Locomotor activity was performed in a circular locomotor box with a 40-cm diameter. The day before the experiment, mice were habituated to the apparatus for 30 min. On the next day, mice were injected with either vehicle, testosterone (10 mg/kg), or nandrolone (10 mg/kg) and returned to the same locomotor box. Locomotor activity was monitored for 1 hour. For experiments with intra-VTA cannula microinjection, mice were allowed to recover from the surgery for at least 2 weeks. Mice received an intra-VTA injection of β -FNA (0.2 μ g in 0.2 μ l of saline) 24 hours before the test. Locomotor activity was monitored using the Noldus EthoVision software.

The CPP apparatus consisted of three chambers. The conditioning compartments consisted of a grid rod-style floor white compartment and a mesh-style floor black compartment connected to a neutral central small compartment (Med Associates Inc., St. Albans, VT, USA). On the first day, mice were allowed to explore the chambers for 15 min. The time spent in each chamber was recorded to determine any preference for one compartment. During conditioning days 2, 4, and 6, mice received an intraperitoneal injection in the morning of either nandrolone (10 mg/kg) or testosterone (10 mg/kg) and were confined in the less preferred compartment for 30 min. In the afternoon, they received a vehicle injection and were confined in the preferred compartment. On days 3 and 5, the session order was inverted. The test occurred on day 7, where the mice were allowed to explore all compartments for 15 min. During another experimental setting, mice were treated with an intra-VTA injection of either β -FNA (0.2 μ g in 0.2 μ l of saline) or saline (0.2 μ l of saline). The microinjection was performed every 48 hours to irreversibly block the VTA MOR for the entire duration of the experiment (during both

AAS and vehicle conditioning sessions). The injection of β -FNA is performed 20 hours before the next conditioning session to avoid any association between β -FNA injection and the chambers of the CPP apparatus. Time spent in the drug-paired chamber minus time spent in the saline-paired chamber was assessed.

ELISA assay

Tissue samples containing the VTA or plasma were obtained from mice injected with either testosterone (10 mg/kg), nandrolone (10 mg/kg), or vehicle at different time points (5, 15, 30, and 60 min). Tissue samples were weighted and homogenized in cold 1 \times phosphate-buffered saline (PBS) (pH 7.4), and the supernatant was collected after centrifuging for 20 min at 2000 to 3000 rpm. For plasma extraction, whole blood was collected into EDTA-coated Eppendorf (10% 0.5 M sterile EDTA of the expected blood volume into a 2-ml Eppendorf tube). Samples were incubated at room temperature for 10 to 20 min and then centrifuged for 20 min at 2000 to 3000 rpm. Enzyme-linked immunosorbent assay (ELISA) for β -endorphin (BioVision, Milpitas, CA, USA; catalog no. E4458) was performed following the manufacturer's instruction.

Immunohistochemistry and histological analysis

After behavioral testing, all mice were deeply anesthetized and transcardially perfused with cold 4% paraformaldehyde solution (PFA; Sigma-Aldrich, catalog no. P6148). Coronal sections containing the VTA (100 μ m) were directly mounted on slides with Fluoroshield mounting medium with DAPI (4',6-diamidino-2-phenylindole) (Abcam, catalog no. ab104135). After histological verification, mice with incorrect cannula implantation were excluded from data analysis. For patch-clamp experiments, after recording, horizontal slices were put in cold 4% PFA overnight. The following day, the slices were washed three times (15 min each) in 1 \times PBS and mounted on slides. Sections were imaged with an upright confocal laser scanning microscope (Olympus FV-1000).

Statistical analysis

Electrophysiology data were analyzed with Clampex and MiniAnalysis. Behavior data were analyzed with EthoVision. Quantitative data are presented as the means \pm SEM performed by GraphPad Prism 6 software (InStat, GraphPad Software). All comparisons relate test to control data from littermate animals collected during the same time period. Statistical significance was assessed by *t* test and one-way analysis of variance (ANOVA). The significant differences were identified by post hoc analysis using the Bonferroni post hoc method for multiple comparisons. Assessments were considered significant with $P < 0.05$.

SUPPLEMENTARY MATERIALS

stke.sciencemag.org/cgi/content/full/13/647/eaba1169/DC1

Fig. S1. Intrinsic properties of putative DA neurons were not affected by AAS treatment.

Fig. S2. Treatment with AAS increased AMPAR EPSCs, but not NMDAR EPSCs, in putative DA neurons.

Fig. S3. GABAergic synaptic transmission in putative DA neurons was not affected 24 hours after AAS treatment.

Fig. S4. Blockade of VTA MOR 60 min after AAS injection did not affect AAS-induced synaptic plasticity in putative DA neurons.

Fig. S5. Histological verification of VTA cannula placement used for locomotor experiments.

Fig. S6. β -FNA irreversibly blocked VTA MOR activity for 48 hours.

Fig. S7. Histological verification of VTA cannula placement used for CPP experiments.

Fig. S8. Histological verification of VTA cannula placement used for CPP experiments with inverted AAS and vehicle conditioning sessions.

Fig. S9. β -FNA blocked AAS-induced place preference also when the daily AAS and vehicle conditioning sessions were inverted.

[View/request a protocol for this paper from Bio-protocol.](#)

REFERENCES AND NOTES

- G. Kanayama, K. J. Brower, R. I. Wood, J. I. Hudson, H. G. Pope Jr., Anabolic-androgenic steroid dependence: An emerging disorder. *Addiction* **104**, 1966–1978 (2009).
- B. Jacka, B. Larence, J. Copeland, L. Burns, M. Farrell, E. Jackson, L. Degenhardt, Health care engagement behaviors of men who use performance- and image-enhancing drugs in Australia. *Subst. Abus.* **41**, 139–145 (2020).
- C. Mullen, B. J. Whalley, F. Schifano, J. S. Baker, Anabolic androgenic steroid abuse in the United Kingdom: An update. *Br. J. Pharmacol.* **177**, 2180–2198 (2020).
- E. Pereira, S. J. Moyses, S. A. Ignácio, D. K. Mendes, D. Silva, E. Carneiro, A. Hardy, E. Rosa, P. Bettega, A. Johann, Prevalence and profile of users and non-users of anabolic steroids among resistance training practitioners. *BMC Public Health* **19**, 1650 (2019).
- J. G. Oberlander, L. P. Henderson, The Sturm und Drang of anabolic steroid use: Angst, anxiety, and aggression. *Trends Neurosci.* **35**, 382–392 (2012).
- D. Piacentino, G. D. Kotzalidis, A. Casale, M. R. Aromatario, C. Pomara, P. Girardi, G. Sani, Anabolic-androgenic steroid use and psychopathology in athletes. *Curr. Neuropharmacol.* **13**, 101–121 (2015).
- E. Mhillaj, M. G. Morgese, P. Tucci, M. Bove, S. Schiavone, L. Trabace, Effects of anabolic-androgens on brain reward function. *Front. Neurosci.* **9**, 295 (2015).
- F. J. Martinez-Rivera, E. J. Natal-Albelo, N. A. Martinez, R. A. Orozco-Vega, O. A. Muñoz-Seda, J. L. Barreto-Estrada, The effect of the anabolic steroid, nandrolone, in conditioned place preference and D1 dopamine receptor expression in adolescent and adult mice. *Behav. Processes* **113**, 81–85 (2015).
- J. Parrilla-Carrero, O. Figueroa, A. Lugo, R. García-Sosa, P. Brito-Vargas, B. Cruz, M. Rivera, J. L. Barreto-Estrada, The anabolic steroids testosterone propionate and nandrolone, but not 17 α -methyltestosterone, induce conditioned place preference in adult mice. *Drug Alcohol Depend.* **100**, 122–127 (2009).
- M. G. Packard, J. P. Schroeder, G. M. Alexander, Expression of testosterone conditioned place preference is blocked by peripheral or intra-accumbens injection of α -flupenthixol. *Horm. Behav.* **34**, 39–47 (1998).
- K. D. Peters, R. I. Wood, Androgen dependence in hamsters: Overdose, tolerance, and potential opioidergic mechanisms. *Neuroscience* **130**, 971–981 (2005).
- F. Nyberg, M. Hallberg, Interactions between opioids and anabolic androgenic steroids: Implications for the development of addictive behavior. *Int. Rev. Neurobiol.* **102**, 189–206 (2012).
- P. Johansson, A. Ray, Q. Zhou, W. Huang, K. Karlsson, F. Nyberg, Anabolic androgenic steroids increase β -endorphin levels in the ventral tegmental area in the male rat brain. *Neurosci. Res.* **27**, 185–189 (1997).
- M. Morales, E. B. Margolis, Ventral tegmental area: Cellular heterogeneity, connectivity and behaviour. *Nat. Rev. Neurosci.* **18**, 73–85 (2017).
- M. Pignatelli, A. Bonci, Role of dopamine neurons in reward and aversion: A synaptic plasticity perspective. *Neuron* **86**, 1145–1157 (2015).
- G. Di Chiara, A. Imperato, Drugs abused by humans preferentially increase synaptic dopamine concentrations in the mesolimbic system of freely moving rats. *Proc. Natl. Acad. Sci. U.S.A.* **85**, 5274–5278 (1988).
- M. A. Ungless, J. L. Whistler, R. C. Malenka, A. Bonci, Single cocaine exposure in vivo induces long-term potentiation in dopamine neurons. *Nature* **411**, 583–587 (2001).
- M. Pignatelli, G. K. E. Umanah, S. P. Ribeiro, R. Chen, S. S. Karuppagounder, H. J. Yau, S. Eacker, D. L. Dawson, T. M. Dawson, A. Bonci, Synaptic plasticity onto dopamine neurons shapes fear learning. *Neuron* **93**, 425–440 (2017).
- C. Lüscher, R. C. Malenka, Drug-evoked synaptic plasticity in addiction: From molecular changes to circuit remodeling. *Neuron* **69**, 650–663 (2011).
- L. Bontempi, P. Savoia, F. Bono, C. Fiorentini, C. Missale, Dopamine D3 and acetylcholine nicotinic receptor heteromerization in midbrain dopamine neurons: Relevance for neuroplasticity. *Eur. Neuropsychopharmacol.* **27**, 313–324 (2017).
- D. Mao, K. Gallagher, D. S. McGehee, Nicotine potentiation of excitatory inputs to ventral tegmental area dopamine neurons. *J. Neurosci.* **31**, 6710–6720 (2011).
- B. E. Bernier, L. R. Whitaker, H. Morikawa, Previous ethanol experience enhances synaptic plasticity of NMDA receptors in the ventral tegmental area. *J. Neurosci.* **31**, 5205–5212 (2011).
- C. Baimel, S. L. Borgland, Orexin signaling in the VTA gates morphine-induced synaptic plasticity. *J. Neurosci.* **35**, 7295–7303 (2015).
- N. D. Volkow, M. Morales, The brain on drugs: From reward to addiction. *Cell* **162**, 712–725 (2015).
- A. S. Clark, D. M. Barber, Anabolic-androgenic steroids and aggression in castrated male rats. *Physiol. Behav.* **56**, 1107–1113 (1994).
- P. J. Perry, K. H. Andersen, W. R. Yates, Illicit anabolic steroid use in athletes: A case series analysis. *Am. J. Sports Med.* **18**, 422–428 (1990).
- B. A. Costine, J. G. Oberlander, M. C. Davis, C. A. A. Penatti, D. M. Porter, R. N. Leaton, L. P. Henderson, Chronic anabolic androgenic steroid exposure alters corticotropin releasing factor expression and anxiety-like behaviors in the female mouse. *Psychoneuroendocrinology* **35**, 1473–1485 (2010).
- E. Kalinine, E. R. Zimmer, K. C. Zenki, I. Kalinine, V. Kazlauskas, C. B. Haas, G. Hansel, A. R. Zimmer, D. O. Souza, A. P. Müller, L. V. Portela, Nandrolone-induced aggressive behavior is associated with alterations in extracellular glutamate homeostasis in mice. *Horm. Behav.* **66**, 383–392 (2014).
- K. L. Conrad, K. J. Tseng, J. L. Uejima, M. J. Reimers, L. Heng, Y. Shaham, M. Marinelli, M. E. Wolf, Formation of accumbens GluR2-lacking AMPA receptors mediates incubation of cocaine craving. *Nature* **454**, 118–121 (2009).
- K. A. Walters, M. C. Edwards, D. Tesic, A. S. L. Caldwell, M. Jimenez, J. T. Smith, D. J. Handelsman, The role of central androgen receptor actions in regulating the hypothalamic-pituitary-ovarian axis. *Neuroendocrinology* **106**, 389–400 (2018).
- M. F. Kritzer, Selective colocalization of immunoreactivity for intracellular gonadal hormone receptors and tyrosine hydroxylase in the ventral tegmental area, substantia nigra, and retrorubral fields in the rat. *J. Comp. Neurol.* **379**, 247–260 (1997).
- M. F. Kritzer, L. M. Creutz, Region and sex differences in constituent dopamine neurons and immunoreactivity for intracellular estrogen and androgen receptors in mesocortical projections in rats. *J. Neurosci.* **28**, 9525–9535 (2008).
- N. Pluchino, F. Ninni, E. Casarosa, A. Giannini, S. Merlini, A. Cubeddu, M. Luisi, V. Cela, A. R. Genazzani, Sex differences in brain and plasma β -endorphin content following testosterone, dihydrotestosterone and estradiol administration to gonadectomized rats. *Neuroendocrinology* **89**, 411–423 (2009).
- O. F. X. Almeida, K. E. Nikolarakis, A. Herz, Significance of testosterone in regulating hypothalamic content and in vitro release of β -endorphin and dynorphin. *J. Neurochem.* **49**, 742–747 (1987).
- L. J. Forman, M. F. Harwell, J. Cater, Beta-endorphin in the male rat pituitary: Testosterone influences the effect of cocaine. *Brain Res. Bull.* **25**, 65–68 (1990).
- M. Amalric, E. J. Cline, J. L. Martinez, F. E. Bloom, G. F. Koob, Rewarding properties of β -endorphin as measured by conditioned place preference. *Psychopharmacology* **91**, 14–19 (1987).
- I. Roth-Deri, T. Green-Sadan, G. Yadid, β -Endorphin and drug-induced reward and reinforcement. *Prog. Neurobiol.* **86**, 1–21 (2008).
- R. Rinaldi, Dopamine and reward seeking: The role of ventral tegmental area. *Rev. Neurosci.* **25**, 621–630 (2014).
- M. F. Fromm, R. B. Kim, *Doping in Sports Biochemical Principles, Effects and Analysis* (Springer Science & Business Media, 2010), vol. 195.
- R. I. Wood, Anabolic-androgenic steroid dependence? Insights from animals and humans. *Front. Neuroendocrinol.* **29**, 490–506 (2008).
- P. Thomas, Y. Pang, J. Dong, A. H. Berg, Identification and characterization of membrane androgen receptors in the ZIP9 zinc transporter subfamily: II. Role of human ZIP9 in testosterone-induced prostate and breast cancer cell apoptosis. *Endocrinology* **155**, 4250–4265 (2014).
- M. Wang, Neurosteroids and GABA-A receptor function. *Front. Neurosci.* **2**, 44 (2011).
- G. L. Fell, K. C. Robinson, J. Mao, C. J. Woolf, D. E. Fisher, Skin β -endorphin mediates addiction to UV light. *Cell* **157**, 1527–1534 (2014).
- M. Chen, Y. Zhao, H. Yang, W. Luan, J. Song, D. Cui, G. Dong, B. Lai, L. Ma, P. Zheng, Morphine disinhibits glutamatergic input to VTA dopamine neurons and promotes dopamine neuron excitation. *eLife* **4**, e09275 (2015).
- E. B. Margolis, G. O. Hjelmstad, W. Fujita, H. L. Fields, Direct bidirectional μ -opioid control of midbrain dopamine neurons. *J. Neurosci.* **34**, 14707–14716 (2014).
- J. T. Ting, B. R. Lee, P. Chong, G. Soler-Llavina, C. Cobbs, C. Koch, H. Zeng, E. Lein, Preparation of acute brain slices using an optimized N-Methyl-D-glucamine protective recovery method. *J. Vis. Exp.* **132**, 53825 (2018).
- M. J. Wanat, A. Bonci, Dose-dependent changes in the synaptic strength on dopamine neurons and locomotor activity after cocaine exposure. *Synapse* **62**, 790–795 (2008).

Acknowledgments: We are thankful to M. Pignatelli for assistance with electrophysiology experiments. We thank M. Lalama for assistance in the editing of the manuscript. We thank A. Mateja for expert statistical assistance. **Funding:** This research was supported by the Intramural Research Program of the National Institute on Drug Abuse (NIDA). **Author contributions:** L.B. designed and performed experiments. Both authors wrote the manuscript. **Competing interests:** The authors declare that they have no competing interests. **Data and materials availability:** All data needed to evaluate the conclusions in the paper are present in the paper or the Supplementary Materials.

Submitted 5 November 2019
 Accepted 14 August 2020
 Published 1 September 2020
 10.1126/scisignal.aba1169

Citation: L. Bontempi, A. Bonci, μ -Opioid receptor-induced synaptic plasticity in dopamine neurons mediates the rewarding properties of anabolic androgenic steroids. *Sci. Signal.* **13**, eaba1169 (2020).

HOST-MICROBE INTERACTIONS

A dynamic mouse peptidome landscape reveals probiotic modulation of the gut-brain axis

Pei Zhang^{1,2*}, Xiaoli Wu^{3*}, Shan Liang^{3,4*}, Xianfeng Shao^{1,5*}, Qianqian Wang¹, Ruibing Chen⁵, Weimin Zhu¹, Chen Shao^{1†}, Feng Jin^{3†}, Chenxi Jia^{1‡}

Copyright © 2020
The Authors, some
rights reserved;
exclusive licensee
American Association
for the Advancement
of Science. No claim
to original U.S.
Government Works

Certain probiotics have beneficial effects on the function of the central nervous system through modulation of the gut-brain axis. Here, we describe a dynamic landscape of the peptidome across multiple brain regions, modulated by oral administration of different probiotic species over various times. The spatiotemporal and strain-specific changes of the brain peptidome correlated with the composition of the gut microbiome. The hippocampus exhibited the most sensitive response to probiotic treatment. The administration of heat-killed probiotics altered the hippocampus peptidome but did not substantially change the gut microbiome. We developed a literature-mining algorithm to link the neuropeptides altered by probiotics with potential functional roles. We validated the probiotic-regulated role of corticotropin-releasing hormone by monitoring the hypothalamic-pituitary-adrenal axis, the prenatal stress-induced hyperactivity of which was attenuated by probiotics treatment. Our findings provide evidence for modulation of the brain peptidome by probiotics and provide a resource for further studies of the gut-brain axis and probiotic therapies.

INTRODUCTION

The human intestines contain a complex community of microorganisms that are increasingly recognized as an important contributor to the regulation of the physiology, metabolism, and immunity of the host (1, 2). Emerging evidence suggests that the gut microbiota is associated with many neurological processes, including neurotransmission, neurogenesis, neuroinflammation, and neuroendocrine signaling, which further influences the host's psychology and social behavior (1–4). Dysbiosis of the gut microbiome possibly contributes to many behavioral and mental diseases, such as autism spectrum disorders (5), Alzheimer's disease (6), Parkinson's disease (7), depression (8, 9), and anxiety (10, 11). Brain and gut communicate bidirectionally through the gut-brain axis by three major communication pathways: the vagus nerve, the immune response, and the microbial metabolites (8). Although important roles of the gut-brain axis have been identified, the underlying mechanisms are still unclear.

Probiotics are live microorganisms that offer health benefits to the host (12). Many previous studies in rodent models suggest that probiotics administration can relieve some anxiety, depression, and autism-like behaviors through the gut-brain axis (12). Bravo *et al.* (13) reported that chronic treatment of healthy mice with *Lactobacillus rhamnosus* reduced anxiety-related behaviors and also induced region-dependent changes in transcripts encoding the metabotropic γ -aminobutyric acid receptor GABA_{B1b}, and a mouse strain effect was observed in a follow-up study (14). Hsiao *et al.* (15) demonstrated that ingestion of *Bacteroides fragilis* ameliorated abnormalities in

gut permeability and autism-related behavior in mice. Buffington *et al.* (16) found that *Lactobacillus reuteri* restored oxytocin production in the hypothalamus and corrected the social deficits of offspring in a mouse model of maternal diet-induced obesity. Liang *et al.* (17) showed that treatment of rats with *Lactobacillus helveticus* NS8 improved chronic stress-induced depression and cognitive dysfunction. In addition to these findings from rodent models, a clinical trial showed that subchronic administration of a probiotic formulation containing *L. helveticus* R0052 and *Bifidobacterium longum* R0175 alleviated psychological distress (11). Although many reports have indicated the beneficial consequences of probiotics as well as connections between microbiome, gut, and brain, it is still challenging to elucidate the underlying mechanisms, largely because of lack of in-depth molecular knowledge about this complex system.

Neuropeptides and peptide hormones are diverse classes of biological modulators. They are highly enriched in the central nervous system (CNS) and involved in most physiological and psychological processes, including reproduction, feeding, energy homeostasis, pain, memory, mood, anxiety, reward pathways, arousal, and sleep-wake cycles (18–25). Several reports have indicated that neuropeptides are involved in gut-brain communication (26, 27). If the gut microbiome can modulate the expression and secretion of peptides in the CNS, the downstream physiological processes and behavior of the hosts will be modulated or influenced (26). The changes can either benefit the fitness of the hosts or cause neurological disorders. Given the importance of the regulatory roles of brain peptides and previous findings in the brain-gut axis, we ask (i) whether the administration of probiotics can alter the brain peptidome and (ii) whether the brain peptidome and the gut microbiome are correlated.

Here, using a mass spectrometry (MS)-based peptidomics approach, we describe a dynamic landscape wherein the brain peptidome was influenced by probiotics administration and pinpoint the regulatory signature of peptidome changes. We found that remodeling of the brain peptidome by probiotics treatment exhibited spatiotemporal and probiotics strain-specific patterns, which were highly correlated with the composition of the gut microbiome. Collectively, these data open an avenue to investigate these signaling molecules

¹State Key Laboratory of Proteomics, Beijing Proteome Research Center, Beijing Institute of Lifeomics, National Center for Protein Sciences (The PHOENIX Center, Beijing), Beijing 102206, China. ²School of Life Sciences, Hebei University, Hebei Province, Baoding 071002, China. ³Key Laboratory of Mental Health, Institute of Psychology, Chinese Academy of Sciences, Beijing 100101, China. ⁴Key Laboratory of Microbial Physiological and Metabolic Engineering, Institute of Microbiology, Chinese Academy of Sciences, Beijing 100101, China. ⁵Department of Genetics, School of Basic Medical Sciences, Tianjin Medical University, Tianjin 300070, China.

*These authors contribute equally to this work.

†Corresponding author. Email: cja@mail.ncpsb.org (C.J.); jinfeng@psych.ac.cn (F.J.); shaochen@mail.ncpsb.org (C.S.)

‡Lead contact.

in the gut-brain axis by using high-throughput techniques and are a rich resource for the neuroscience and microbiology communities.

RESULTS

One-hour peptidomics enables accurate and rapid analysis of brain peptides

To systematically investigate the effects of gut microbiota on brain peptides, we subjected seven groups of naturally colonized adult male mice to four different 1-month treatment regimens and three different 2-month treatment regimens (Fig. 1A). The 1-month treatment regimens included mice fed plain water or water mixed with the probiotics *L. helveticus* NS8 (17), heat-killed NS8, or *Lactobacillus fermentum* NS9 (28), hereafter referred to as C, NS8, NS8h, or NS9 treatment, respectively. The 2-month treatment regimens included animals given only plain water (CC), water with NS8 for 1 month followed by plain water for 1 month (NS8C), or water with NS8 for 2 months (NS8NS8). After animals were euthanized, endogenous peptides across four brain regions (hypothalamus, hippocampus, striatum, and pituitary) were analyzed by MS-based peptidomics, and the gut microbiomes were assessed by 16S ribosomal RNA (rRNA) sequencing (Fig. 1A). This experimental design separates the effects of treatment into several variable factors, including different probiotic strains, treatment time, and brain regions as well as live versus heat-killed probiotics.

Extremely low concentrations of endogenous peptides, high dynamic range of peptide abundance, and relatively large sample cohorts are major challenges for peptidome analysis. To overcome these challenges, we established a “1-hour peptidomics” workflow (Fig. 1B) with the capability to identify 2598 modification-specific peptides (a peptide contains specific types and sites of modifications) from the tiny mouse hypothalamus by single-run liquid chromatography–tandem MS (LC-MS/MS), including neuropeptides, peptide hormones,

and other endogenous peptides. The high quality of quantitative results using this method was demonstrated by mass accuracy, confidence score, reproducibility, and quantitative accuracy, among other factors [figs. S1 (A to E) and S2 (A and B)].

The 1-hour peptidomics approach was further benchmarked across multiple brain regions by the analysis of 12 mice from the dataset of C group, resulting in the identification of 2290, 1162, 1262, and 4620 modification-specific peptides from hypothalamus, hippocampus, striatum, and pituitary, respectively (Fig. 2A and data file S1). The pituitary gland contained the largest number of endogenous peptides with the highest dynamic range of abundance. Our results also show that some peptides displayed highly dynamic expression in different regions. For example, neuropeptide Y (NPY) ranked among the top 30 in abundance in hippocampus, hypothalamus, and striatum but ranked as low in abundance in the pituitary. We also plotted the cumulative abundance of peptides in the hypothalamus (Fig. 2B) and summarized the families represented in the top 75% of these peptides (Fig. 2C and table S1). There were six peptides that accounted for the first 25% of the total accumulative intensity, and three of these have well-studied functions, namely, little-SAAS, big-LEN, and somatostatin-28(1-12) (Fig. 2B). This finding highlights the challenge of brain peptide analytics due to the high dynamic range of peptide abundance. Collectively, the 1-hour peptidomics approach enabled high-throughput analysis of brain peptides and generated a brain region–resolvable resource with 6315 identified modification-specific peptides in total.

Probiotics treatment induces remodeling of the brain peptidome

To evaluate the effect of probiotics treatment, we performed label-free quantitative analysis on the peptidomics data between the NS8 and C groups. After treatment, 366 of 2230 quantifiable brain peptides

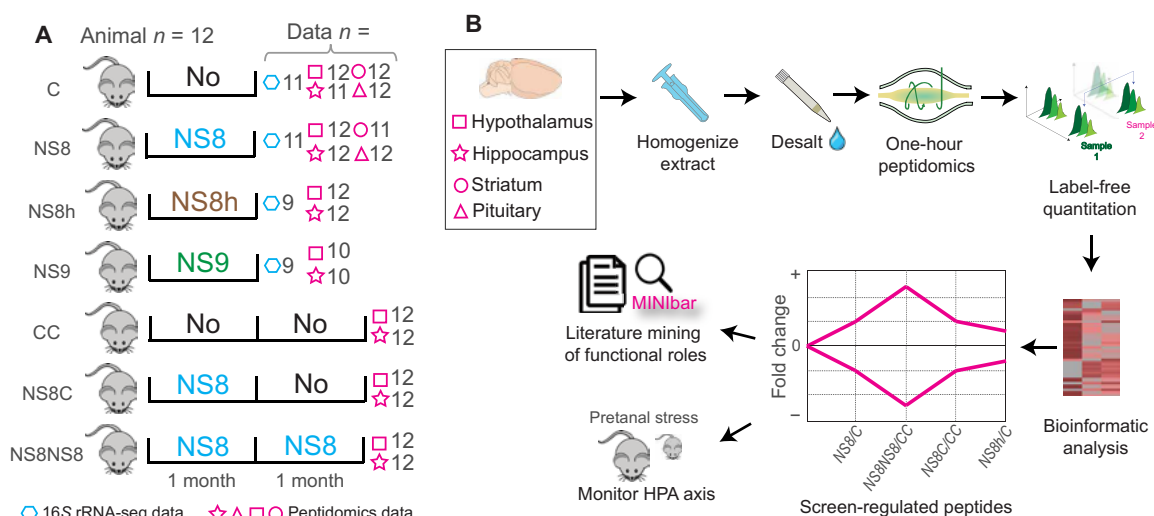


Fig. 1. Experimental design and integrated peptidomics workflow. (A) Seven groups of mice ($n = 12$ animals in each group) were differentially treated with plain water (C), *L. helveticus* NS8 (NS8), *L. fermentum* NS9 (NS9), or heat-killed NS8 (NS8h) for 1 or 2 months as shown. After treatment, gut microbiome composition (16S rRNA sequencing) and brain peptidomics data were generated for each group. The n value for each omics dataset is indicated next to the symbol for that dataset. For data analysis, all the data in each group were combined. The n value for data in some omics sets is less than the number of animals in each experiment ($n = 12$) because of failed sample preparation or data acquisition. C, 1-month control; NS8, 1-month NS8 treatment; NS8h, 1-month heat-killed NS8 treatment; NS9, 1-month NS9 treatment; CC, 2-month control; NS8C, 1-month NS8 treatment and 1-month nontreatment; NS8NS8, 2-month NS8 treatment. (B) Integrated workflow for in-depth analysis of brain peptidomes.

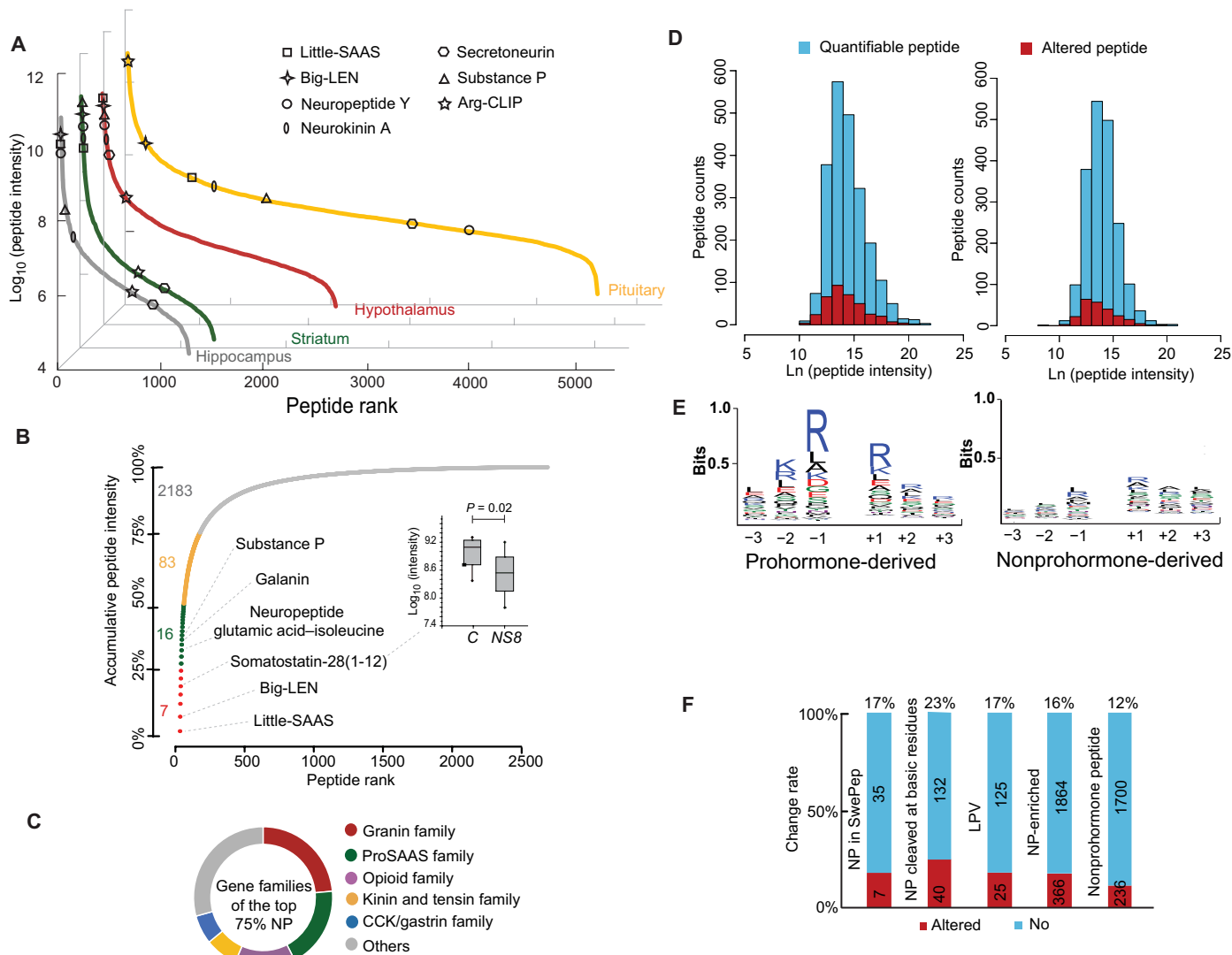


Fig. 2. Benchmarking the 1-hour peptidomics approach and peptidome changes upon probiotics administration. (A) Dynamic range of brain peptides based on peptide intensities across four brain regions in control animals given plain water for 1 month (group C). Values for some peptides are noted, and the complete list of identified peptides is in data file S1. (B) Cumulative abundance of peptides in the hypothalamus of group C from the highest to the lowest abundance. The box plot inset shows the change in somatostatin-28(1-12) abundance induced by probiotics treatment. (C) Families to which the top 75% of neuropeptides (by accumulative intensity) in the hypothalamus of group C animals belong. (D) Histogram illustrating the quantifiable and significantly altered peptides in hypothalamus after 1-month of NS8 treatment compared to 1 month of no treatment (NS8/C) including the prohormone-derived (left) and nonprohormone-derived peptides (right). Unique sequences and abundance data are shown in data file S2. (E) Logo plot illustrating the motifs present in the terminal regions flanking peptides corresponding to the quantifiable peptides in (D) and data file S2. (F) Rate of NS8-induced change of neuropeptide-derived peptides compared to control. CCK, cholecystokinin; NP, neuropeptide; LPV, longest peptide variants. Significance of altered peptides was calculated by a two-tailed *t* test ($P < 0.05$).

(unique sequences) were found to have significant changes in abundance (data file S2), and the peptide intensity and count information were further clustered into a histogram (Fig. 2D, left). Some of the C- and N-terminal linear sequence motifs of the quantifiable peptides displayed a feature characteristic of neuropeptides, the dibasic cleavage site KR or the monobasic cleavage site R (Fig. 2E, left), which are consistent with the cleavage rules of the enzymatic processing of neuropeptides (29). In addition to neuropeptides derived from prohormones, there are thousands of endogenous peptides derived from nonprohormone proteins, which were simultaneously acquired in the LC-MS/MS data. To compare the response sensitiv-

ities of neuropeptides and other endogenous peptides on probiotics treatment, we constructed a customized database based on UniProt mouse protein entries by removing the prohormone proteins and then conducted quantitative analysis using the LC-MS/MS data against this database. We obtained a set of nonprohormone peptides without enriched motifs (Fig. 2E, right, and data file S2) that was similar to a previous report on rat brain peptides (30). The histograms of peptide intensity and count information (Fig. 2D) show that the prohormone-derived peptide group had a higher rate of change in response to probiotic treatment than the nonprohormone-derived peptide group. This result indicates that neuropeptides acting as

important signaling molecules are more sensitive than nonprohormone peptides in response to probiotics treatments. Furthermore, we calculated the percentages of altered peptides due to probiotic treatment on three types of biological molecules, including (i) peptides in the SwePep database (31), (ii) the longest peptide variants (LPV) (30), and (iii) the neuropeptides produced at the cleavage site of basic residues (K/R in positions -1 , $+1$, and $+2$) (29). These three types of biomolecules exhibited more neuropeptide-enriched features, and their rates of change were much higher than those of nonprohormone peptides (Fig. 2F). These results reveal that the probiotics treatment caused significant changes of neuropeptides and that the sensitivity of the response to treatment depended on the type of regulatory molecule.

Gut microbiome assessment reveals potential interaction with the brain peptidome

To discover the possible cause of brain peptide change through the gut-brain axis, we investigated the intestinal microbiome by analyzing the 16S rRNA datasets of groups C, NS8, and NS8h. For all groups, we obtained typical mouse microbiomes dominated by the phyla of Bacteroidetes and Firmicutes (fig. S3A). Although there was no significant intergroup difference by analysis of α diversity (fig. S3B), the principal coordinates analysis (PCoA) of β diversity indicated that the NS8 group differed more from the C and NS8h groups than the C and NS8h groups differed from one another (Fig. 3A, left). The NS8h group did not show statistically significant change in the gut microbiome compared to the C group. Next, we carried out principal components analysis (PCA) of the peptidome datasets from the hypothalamus and hippocampus (Fig. 3A, middle and right). In the hypothalamus, the change trend of the peptidome was observed as similar as that of the microbiome. Only the live NS8 treatment caused change of the brain peptidome, but the heat-killed NS8 treatment did not. Also, a brain region-specific effect was observed. In the PCA plot of hippocampus peptides, both of NS8 and NS8h groups were separated from the C group, indicating that treatment by heat-killed and live NS8 altered the hippocampus peptidome.

Four of the 115 annotated bacterial genera, belonging to the Lachnospiraceae and Ruminococcaceae families, were significantly altered by NS8 treatment (Fig. 3B). Previous reports showed that change of these two families occurs in multiple sclerosis (32), depression (33), and autism (34). Subsequently, we chose the four significantly altered bacterial genera, [*Eubacterium*] *xylanophilum* group, *Anaerotruncus*, *Ruminiclostridium* 5, and *Ruminococcaceae* UCG-013, to perform Spearman's rank correlation analysis with peptidome datasets across all samples (Fig. 3C, and data file S3 illustrate representative correlated peptides in hypothalamus). Vasoactive intestinal peptide (VIP) showed distinct correlation with *Anaerotruncus* (Fig. 3D). VIP is a 28-amino acid peptide that binds to class II heterotrimeric guanine nucleotide-binding protein-coupled receptors, playing an important role in the regulation of energy metabolism and circadian rhythm (35). *Anaerotruncus* is a bacterial genus belonging to the family Ruminococcaceae, which is also associated with energy metabolism. These results indicate possible regulatory connections between these bacterial genera and brain peptides through the gut-brain axis.

We observed that the treatment with live NS8 caused remarkable, correlated changes in the gut microbiome and hypothalamus peptidome (Fig. 3, A and B). This suggests that change of the microbiome composition is a possible pathway through which probiotics modulate brain peptides. To investigate the peptides associated with microbi-

ome change, we clustered those exclusively altered in the NS8 group (Fig. 3E and data file S4) and then grouped them into neuropeptide families (Fig. 3F). Granin, opioid, proSAAS, somatostatin (SMS), and F&Y amide families ranked at the top, suggesting potential functional responses of these groups of peptides to the changes in gut microbiota. In addition, the NS8h group showed a different pattern of peptide abundances from those of the C group (Fig. 3E).

Brain peptide changes upon probiotics treatment display region-specific patterns

To provide a bird's-eye view of brain peptide expression profile upon probiotics treatment, we aggregated peptidomics information by the family to which neuropeptide belongs (36) and further clustered them into a circular peptide map across four brain regions (Fig. 4A and data file S5). Peptides in the pituitary gland were dominated by the granin and opioid families, both of which were less prevalent in the other three brain regions. By calculating the percentage of the altered peptides in each family (Fig. 4B), the cocaine- and amphetamine-regulated transcript family in hypothalamus showed a change rate of 33%.

To perform a comparative analysis of the response to probiotics treatment across brain regions, we evaluated two quantifiable values of brain peptides: change rate (ratio of altered to quantifiable peptide number) and fold change. The quantitative peptidomics data of the NS8 treatment group compared to that of the C group (NS8/C) of the four brain regions were aggregated into histograms showing peptide count versus intensity (Fig. 4C). The fold changes of increased or decreased brain peptides were further summarized into boxplots (Fig. 4C). The peptides in hippocampus showed the highest change rate at 33% and also the highest amount of increase, indicating the most sensitive response among the four regions under investigation. In contrast, the change rate of peptides in striatum was minimal, and the fold changes of the decreased peptides were the smallest. To some extent, the NS8 treatment suppressed the expression of some peptides in the striatum.

Next, we investigated the colocalization and coregulation of brain peptides across multiple regions. The peptidomics data of NS8/C were summarized into a multipanel, region-resolved bar graph (Fig. 4D and data file S6). Seventy-three percent of identified peptides were exclusively expressed in a single region, and almost 99% of the peptides that increased in abundance and 96% of the peptides that decreased in abundance displayed single region-specific distribution. Subsequently, we performed Spearman's rank correlation analysis between brain peptides and the change in gut bacterial genera, across different brain regions using the datasets of the C and NS8 groups. Representative peptides correlated with the four bacterial genera, including neuropeptides with functions in appetite regulation (Fig. 4, E and F), including the anorexigenic peptides α -melanocyte-stimulating hormone (α -MSH), β -MSH, neuromedin-B, and somatostatin-28(1-12), and the orexigenic peptides NPY and orexin (37). In addition, VIP and neuromedin-B displayed similar correlation pattern in two brain regions. The correlation between gut bacteria and brain peptides suggests possible modulatory relationships.

Multiple factors drive remodeling of the hypothalamus peptidome

To generate a global view of brain peptide change in the seven experimental groups (Fig. 1A), we processed hypothalamus peptidomics data by PCA and plotted the centric values of each group in a

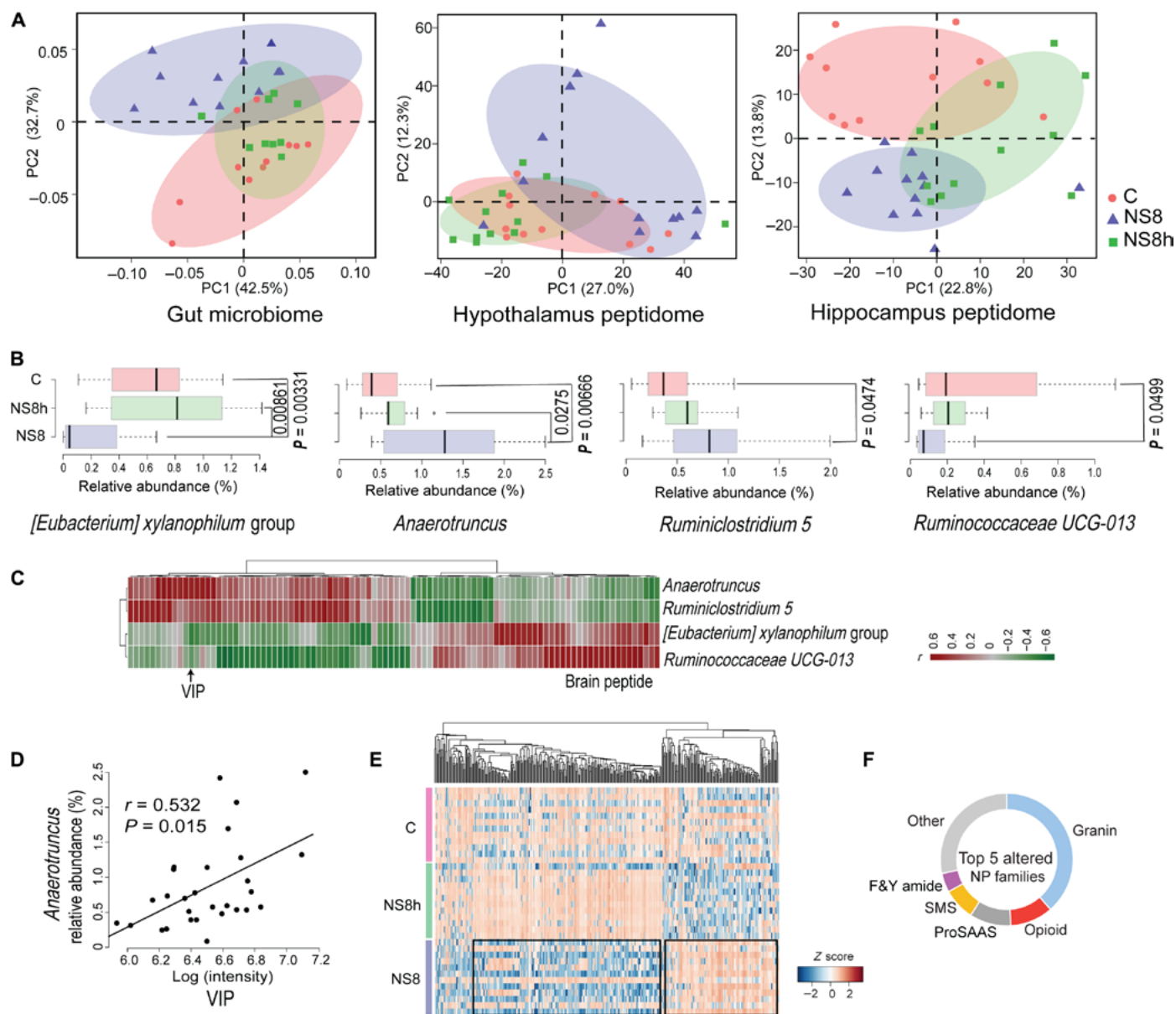


Fig. 3. Correlation between changes in the brain peptidome and gut microbiome upon 1-month treatment with the probiotic NS8 and heat-killed NS8. (A) PCoA plot of gut microbiome and PCA plots of the hypothalamus and hippocampus peptidomes after 1 month of treatment with live (NS8) or heat-killed (NS8h) NS8 compared to control animals (C). (B) Relative abundance of four bacterial genera in groups C, NS8, and NS8h. Two-tailed t test. (C) Heatmap showing the matrix of Spearman's correlation coefficient (*r*) of significantly altered bacterial genera and representative brain peptides in hypothalamus. $r < -0.5$ or $r > 0.5$ for at least one of the four bacterial genera. Details are available in data file S3. (D) Scatter plot showing the relationship between the abundance of vasoactive intestinal peptide (VIP) against the relative abundance of *Anaerotruncus* in the gut microbiome. (E) Hierarchical clustering of changes in the hypothalamus peptidome C, NS8h, and NS8 treatment groups. One-way analysis of variance (ANOVA), $P < 0.05$. The peptides exclusively altered in the NS8 group as compared to the C and NS8h groups are boxed, and complete data is included in data file S4. (F) Neuropeptide families of the hypothalamus peptidome that were exclusively altered in the NS8 group.

ternary diagram (Fig. 5A). The group CC was clearly separated from the C group, suggesting an effect of age that is independent of probiotic treatment. The 1-month treatment group NS8 was separated from the 1-month control group C along a different direction, and then the 2-month treatment group NS8NS8 was further separated from NS8 because of the combined effects of age and NS8 treatment. In addition, the NS9 and NS8h groups separated from group C in different directions by the effects of different probiotics strain

and live versus heat-killed bacteria, respectively. It should be noted that we only addressed the major effects. These results vividly illustrate the dynamic landscape of peptidome remodeling under various treatment conditions, which also raises questions about (i) whether the peptide change by probiotics treatment was time dependent; (ii) the extent of the effect of age on peptide change of adult mice; and (iii) whether differences between strains of probiotics result in different phenotypes of peptide change.

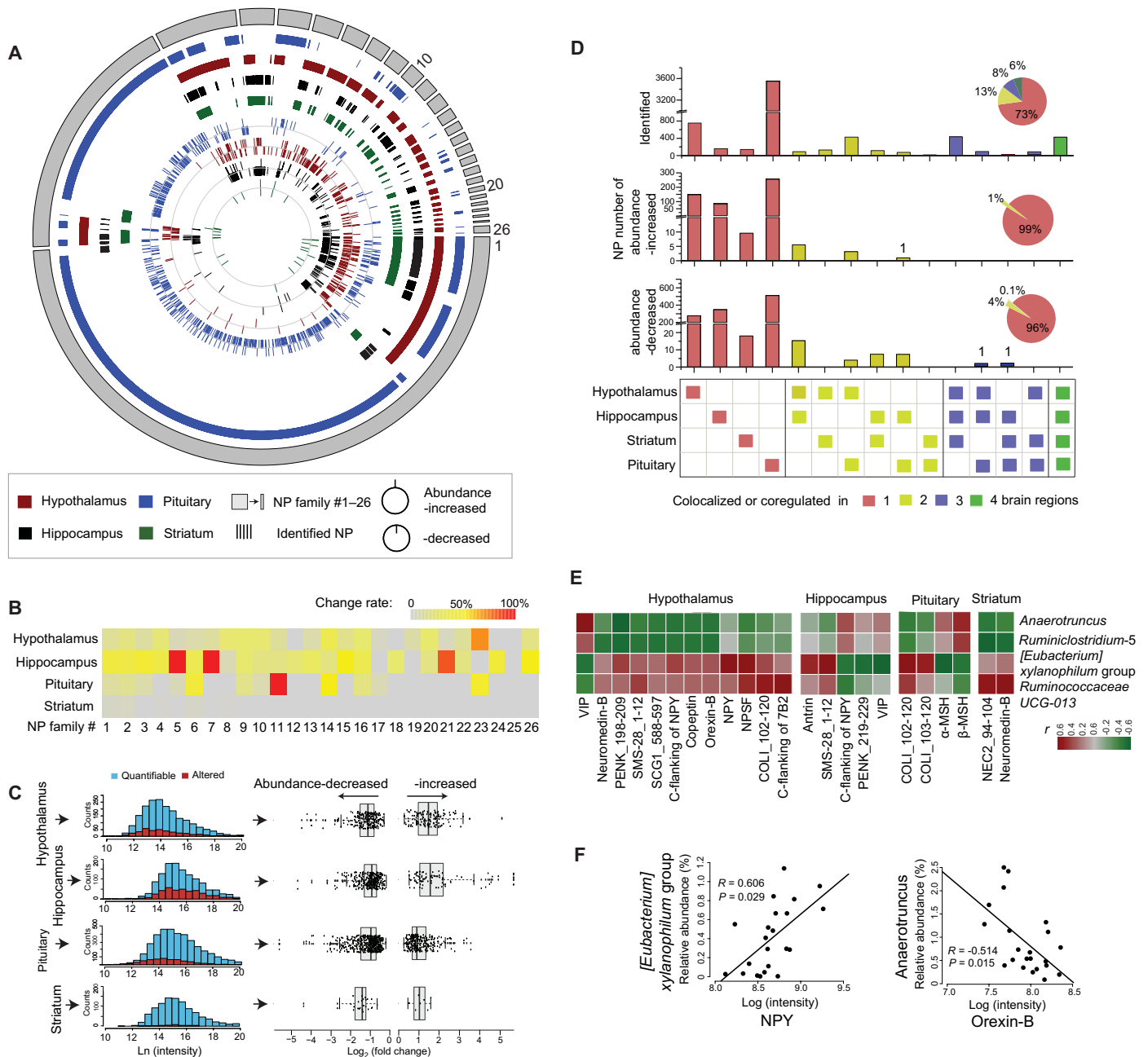
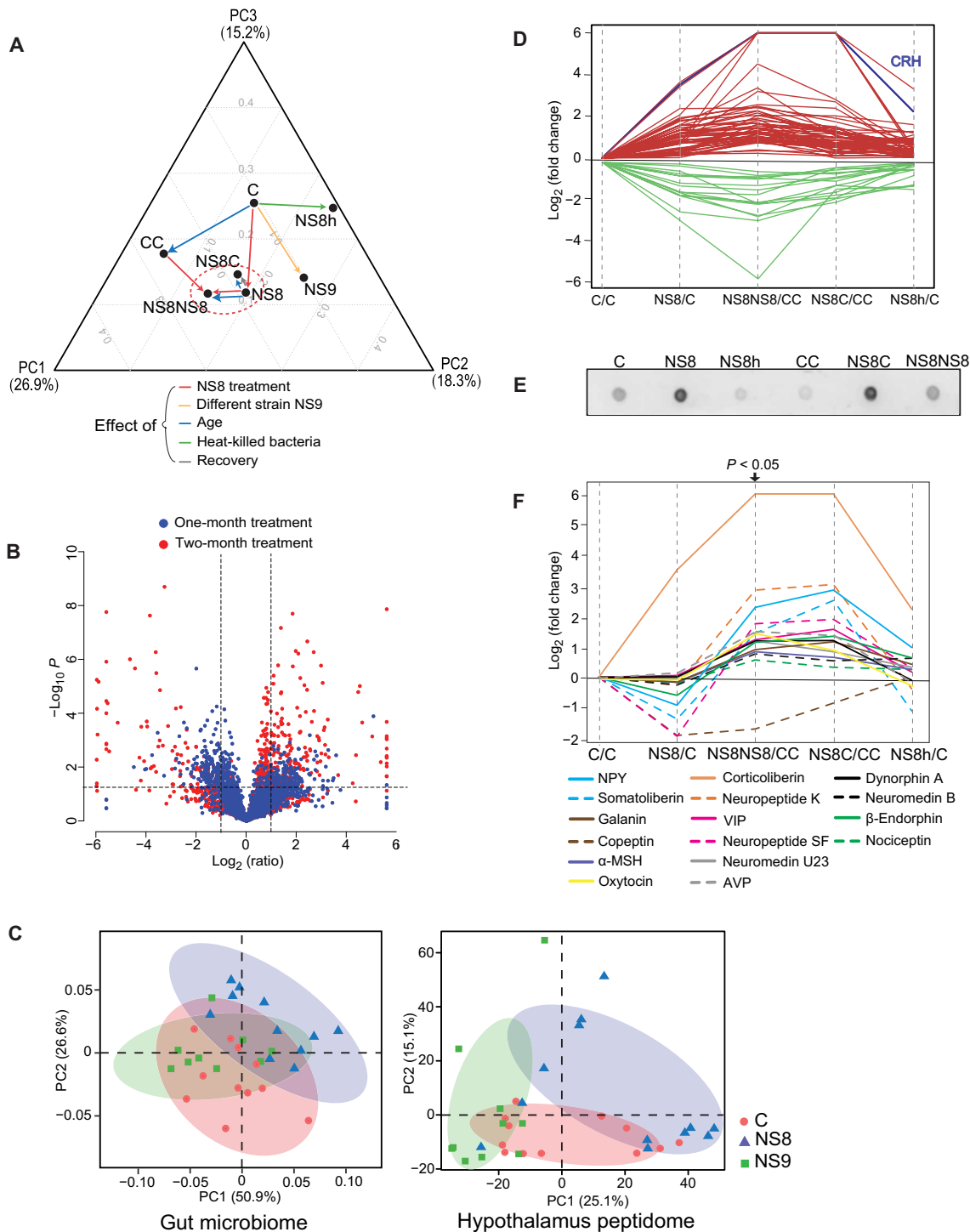


Fig. 4. Regional brain distribution and change of peptides in NS8-treated versus control animals. (A) Circular brain peptidome maps depict the qualitative, quantitative, and region-specific information in the peptidomes from control (group C) animals (details in data file S5). The outer ring indicates the neuropeptide families; the middle four rings are qualitative information of brain peptides in the four regions of the brain; the inner four rings are quantitative information for each of the four brain regions. The 26 neuropeptide families are listed in table S1. (B) Heatmap shows the change rate (altered/quantifiable peptides in a family) of brain peptide families in NS8-treated mice compared to control mice. (C) Histograms illustrate the quantifiable brain peptides that were altered in the four brain regions in NS8-treated mice compared to group C. Box plots show the fold change of the altered brain peptides (modification-specific peptides). (D) Bar graphs show the number of peptides that were identified, increased, or decreased in each brain region. Subsets of peptides that were present in multiple regions (colocalized) or showed similar changes in abundance in multiple regions (colocalization) are noted in the matrix below the graphs. The pie charts summarize the percentage of brain peptides that were coregulated in one, two, three, or all four brain regions. The details are shown in data file S6. (E) Heatmap shows the matrix of Spearman's correlation coefficient (r) of significantly altered bacterial genera and representative brain peptides across four brain regions. $r < -0.5$ or $r > 0.5$ for at least one of the four bacterial genera. (F) Scatter plots show the relationships between the abundances of neuropeptide Y (NPY) and orexin-B and the *[Eubacterium] xylanophilum* group and *Anaerotruncus* in the gut microbiome. The data were processed from quantitative data of NS8-treated versus control (NS8/C) in four brain regions. Significance of altered peptides was calculated by a two-tailed t test ($P < 0.05$), and peptides that increased or decreased in abundance were determined by mean differences.

Fig. 5. Changes in hypothalamus peptides across treatment conditions.

(A) Ternary PCA plot of the brain peptidome changes across the seven experimental groups C, NS8, NS8h, NS9, CC, NS8C, and NS8NS8. The colored arrows indicate treatment groups through which pairwise comparisons can identify changes specific to probiotic treatment, different probiotic strains, the 1-month age difference between animals, live versus heat-killed probiotic, and recovery from 1-month treatment with live NS8. **(B)** Volcano plots of altered brain peptides for 1- and 2-month treatment with NS8 compared to water-only controls (NS8/C and NS8NS8/CC). Two-tailed *t* test, $P < 0.05$. **(C)** PCoA plot of gut microbiome and PCA plot of hypothalamus peptidome for groups C, NS8, and NS9. **(D)** Screening curve showing putative probiotics-altered peptides that increased (red) or decreased (green) with NS8 treatment compared to control. CRH is highlighted in blue (data file S7, first sheet). **(E)** Dot blot validation of CRH abundance under the six indicated conditions. **(F)** Changes in the abundances of representative neuropeptides after 1-month (NS8) and 2-month (NS8NS8) NS8 treatment regimens relative to (I) the control groups as indicated (data file S7, second sheet). Peptides were selected by significance of a two-tailed *t* test for NS8NS8/CC, $P < 0.05$. AVP, arginine vasopressin; α -MSH, α -melanocyte-stimulating hormone.



To answer the first question, the peptidomic datasets of NS8/C and NS8NS8/CC were plotted into a two-layer volcano graph (Fig. 5B). The 2-month treatment results showed more remarkable changes than those of the 1-month treatment groups, indicating that the probiotics-induced change of the peptidome depended on the duration of treatment. To answer the second question, we performed differential analysis on the C and CC groups of peptidomics data.

The 1-month age difference between the adult mice at the end points of each experiment was responsible for a 29% of change rate (fig. S4), which is much higher than the 16% change rate resulting from NS8 treatment (Fig. 2F). This result indicates that animal development and age is a non-negligible factor in the effect of probiotics treatment on brain peptide changes. To answer the third question, we performed PCoA analysis of the microbiome and PCA analysis of the peptidome

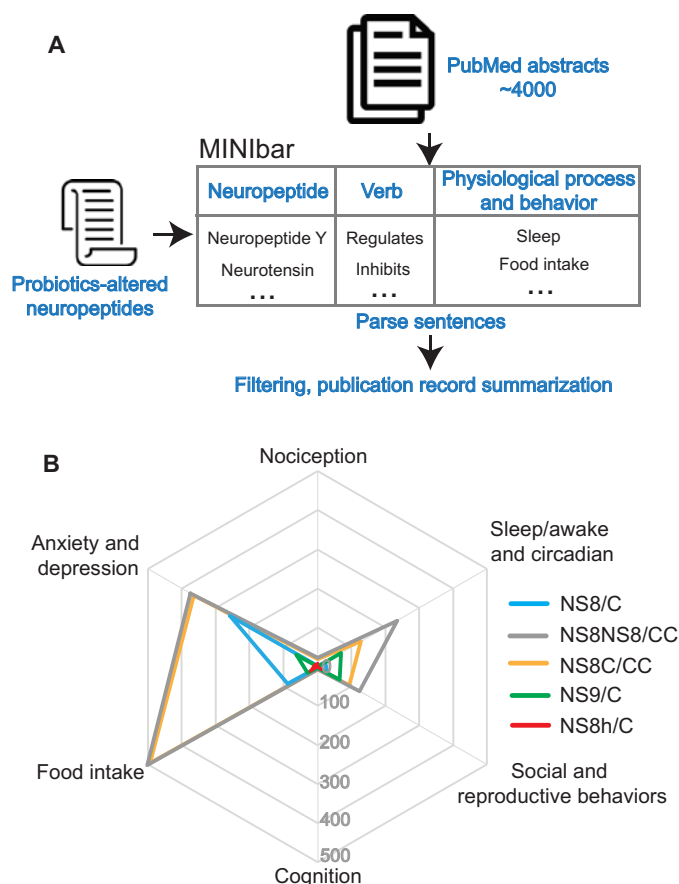


Fig. 6. The MINibar algorithm for text mining of behaviors related to specific neuropeptides in published abstracts. (A) Schematic showing how PubMed abstracts were mined to identify physiological processes and behaviors regulated by specific neuropeptides altered by probiotic treatment. (B) Radar diagram showing possible connections between probiotic treatments and behaviors predicted from publication mining. The five probiotic treatment conditions are linked with the six behaviors on the basis of numbers of publications reporting regulatory roles of neuropeptides on behaviors. Details are shown in data file S9.

of groups C, NS8, and NS9 (Fig. 5C). *L. helveticus* NS8 and *L. fermentum* NS9 are different species of *Lactobacillus* and exhibit distinct beneficial consequences mediated by distinct metabolic mechanisms (17, 28, 38). From the PCoA analysis of the gut microbiome data (Fig. 5C), we found that the NS9 treatment caused a much smaller change in the gut microbiome than did NS8 treatment. A similar effect was observed in PCA analysis of the hypothalamus peptidome. Subsequently, we carried out hierarchical clustering on the peptidomics data, which illustrates the peptide changes with the same and opposite trends by the treatments resulting from the strain-specific effect (fig. S5).

Probiotics-altered brain peptides show similar patterns of change

To narrow down the candidates of probiotics-altered brain peptides, we selected the peptides that changed in certain patterns under different treatment conditions. We hypothesized that a peptide altered by probiotics treatment would follow one of the trends shown in the peptide screening plot (Fig. 1B) and that the heat-killed probiotics

would be less effective than the live ones. For peptides that exhibited probiotics-dependent increase during the first month of treatment, the abundance would continue to increase during the second month of treatment and decrease during the second month of plain water only (Fig. 1B). Similarly, there should be a mirror trend for the peptides that exhibited a probiotics-dependent decrease in abundance during the first month of treatment—continuing to decrease in the second month of treatment and increasing during the subsequent month of plain water only. It should be noted that peptides could show a different trend in change due to probiotics treatment, such as an increase or decrease during the first month of treatment that remained unchanged after an additional month on plain water without continuing to change in abundance or reverse its change in abundance.

By using this screening strategy, we obtained 71 peptide candidates that followed the trends defined in the peptide screening plot (Figs. 1B and 5D and data file S7) in hypothalamus, including an increase in the well-studied neuropeptide corticotropin-releasing hormone (CRH) (Fig. 5, D and E), which is at the top of hypothalamus-pituitary-adrenal (HPA) axis. This increase in CRH might be induced by immune responses to the probiotics treatment (39). In addition to the peptides that followed the rules of clustering we established (Fig. 5D), many neuropeptides with important reported functions exhibited change only after the second month of NS8 treatment (Fig. 5F and data file S7), including oxytocin. Previously, Buffington *et al.* (16) found that *L. reuteri* reversed social deficits in the offspring of mice born to mothers on high-fat diet and proposed a model that *L. reuteri* improved social behavior by increasing oxytocin production and related functions. The dynamic variation of these functional molecules in our dataset suggests that chronic probiotics treatment might alter physiological processes and behaviors.

Literature mining reveals the functional roles of probiotics-altered neuropeptides

We constructed an algorithmic strategy called MINibar (Mining neuropeptide and related behavior) to mine PubMed for the functional roles and behaviors of neuropeptides altered in abundance by probiotics treatment (Fig. 6A). Five treatment conditions with altered neuropeptides were aligned with possible related physiological processes and behaviors by the numbers of publications supporting each association (Fig. 6B). For example, the 2-month NS8 treatment identified changes in 12 neuropeptides that are highly associated with anxiety and depression, as evidenced by 374 publications (Fig. 6B). This result is consistent with a previous report that NS8 improves stress-induced anxiety and depression-like behavior (17). In addition, food intake, social and reproductive behaviors, and sleep-wake and circadian cycles were also associated with the neuropeptides altered by probiotics treatment (Fig. 6B). These literature-based results provide evidence of association of NS8-altered peptides with phenotypic behaviors and also suggest potential applications for NS8.

NS8 treatment attenuates the increases in CRH and adrenocorticotrophic hormone induced by prenatal stress

To explore the possible functional consequences of probiotics-induced increases in CRH (Fig. 5, D and E), we investigated the effect of probiotics on prenatal stress-induced increases in CRH and adrenocorticotrophic hormone (ACTH), key elements of the HPA axis. Exposure to prenatal stress causes a hyperreactive response in the HPA axis in mice (40). Clinical studies have reported that the exposure of women to valproic acid (VPA) during pregnancy increases

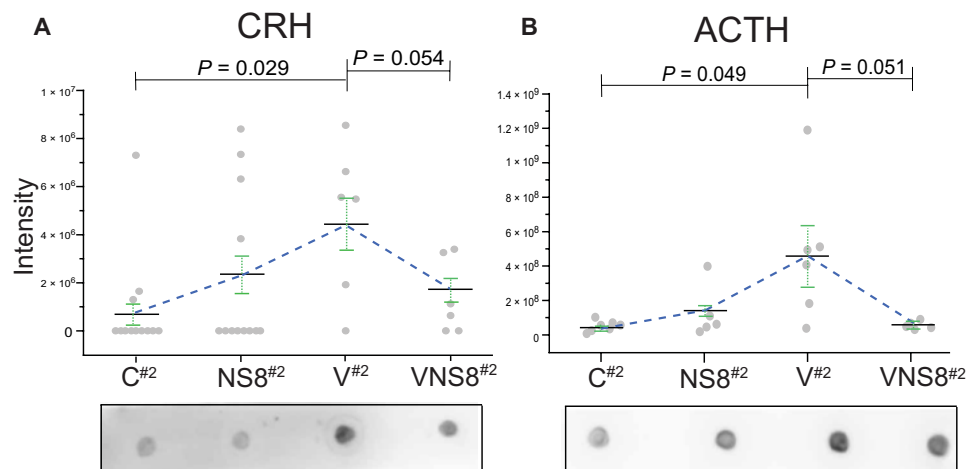


Fig. 7. Monitoring the brain peptide change of HPA axis upon prenatal stress and NS8 treatment. (A) Column scatter plot shows peptidomic intensities of CRH in the hypothalamus of control (C^{#2}, $n = 12$) and NS8-treated (NS8^{#2}, $n = 12$) offspring of untreated mothers and in the hypothalamus of control (V^{#2}, $n = 6$) and NS8-treated (VNS8^{#2}, $n = 6$) offspring of VPA-treated mothers. Below the graph, dot blots for CRH in peptides extracted from the hypothalamus of the indicated mice are shown. Blots are representative of independent experiments with samples from three different mice. (B) Column scatter plot shows peptidomic intensities of ACTH in the pituitary of control (C^{#2}, $n = 7$) and NS8-treated (NS8^{#2}, $n = 5$) offspring of untreated mothers and in the hypothalamus of control (V^{#2}, $n = 6$) and NS8-treated (VNS8^{#2}, $n = 5$) offspring of VPA-treated mothers. Below the graph, dot blots for ACTH in peptides extracted from the hypothalamus of the indicated mice are shown. Blots are representative of independent experiments with samples from three different mice. Data are means \pm SEM. Significance was calculated by a two-tailed t test.

the risk of autism in their offspring (41, 42), and in utero exposure of rodents to VPA is a robust model of autism (42). To investigate the effect of VPA exposure and probiotics treatment on CRH and ACTH cascades in offspring, we conducted a second set of animal experiments including four groups of offspring. Female mice were treated with VPA during pregnancy, and then their offspring mice were split into two groups. One group was treated with NS8 for 1 month (group VNS8^{#2}), and another was not treated (group V^{#2}). In parallel, two groups of offspring from females not treated with VPA with and without probiotics treatment were used as controls (groups NS8^{#2} and C^{#2}, respectively). Analysis of the hypothalamus and pituitary peptidomes for all four groups showed increased abundance of CRH in the hypothalamus of the V^{#2} group compared to the C^{#2} group, but the amount of increase was reduced in the VNS8^{#2} group (Fig. 7A). ACTH in the pituitary followed the same trend (Fig. 7B). Immunoblotting supported the results from the peptidomic analysis (Fig. 7, A and B). These data indicate that in utero VPA exposure influenced the CRH and ACTH signaling cascades, and this could be attenuated by postnatal probiotic treatment. Our results demonstrate that CRH can also be altered by NS8. The other peptides screened by our approach (Fig. 5D) therefore merit further in-depth analysis to elucidate their connection with the probiotics and for the potential for probiotics to affect behavioral or physiological functions regulated by those neuropeptides.

DISCUSSION

Previous studies have revealed that the gut and brain communicate with each other and that probiotics have beneficial effects on the function of the nervous system and host behavior (1, 8). Neuropeptides are a diverse class of signaling molecules that are associated with most

physiological processes. Here, we performed an in-depth analysis on the effect of probiotics administration on the brain peptidome. Our study has shown that the brain peptidome was remodeled in spatiotemporal- and probiotic strain-specific patterns that correlated with changes in the gut microbiome. Our comprehensive brain peptidome dataset illustrates the likely important role of these biomolecules in the gut-brain axis.

Neuropeptides, a major component of total brain peptides, are generated from prohormones (precursor proteins) by a series of enzymatic cleavage steps (43). One prohormone may produce many mature neuropeptides with diverse activities and functions. Although transcriptomic and proteomic approaches allow large-scale analysis of biomolecules, the analytical capability and scale are only accurate at the level of transcripts and prohormones, respectively, instead of the bioactive, mature neuropeptides. In comparison, a peptidomic approach allows direct analysis of the endogenous neuropeptides, which enables the detection of posttranslational modifications to the starting peptide sequence and more accurately reflects physiological prohormone processing. We established a 1-hour peptidomics approach for accurate and rapid analysis of large sample cohorts, the utility and efficiency of which are demonstrated by the high quality of the benchmark dataset. Previous reports showed that certain physiological and environmental changes, such as circadian (44), time-of-day (45), and high-salt or high-fat diet (46, 47), modulate the production of brain peptides. These variable factors have been minimized in this study, with probiotic administration being the major factor altering brain peptides between the control and the probiotic treatment groups. So far, no large-scale brain proteomics investigations of the gut-brain axis have been published. Chen *et al.* (48) reported that the intestinal microbiome and brain metabolome were associated across life span and established a two-layer strategy to analyze the correlation. In addition to metabolites and neuropeptides, a range of bioactive molecules, such as proteins, RNAs, lipids, and others, are worthy of being investigated for new insights into their regulatory roles in the gut-brain axis.

We observed significant correlation between some species of gut bacteria and brain peptides. The bacteria belonged to Lachnospiraceae and Ruminococcaceae, two dominant bacterial families associated with energy metabolism and body weight regulation (49, 50). Gomez-Arango *et al.* (51) investigated the relationship between gut microbiome and metabolic hormones in overweight and obese pregnant women and found that Lachnospiraceae and Ruminococcaceae are strongly correlated with adipokine. Decreased abundance in the relative representation of both of these bacterial families in the gut microbiome is associated with long-term weight gain, with Ruminococcaceae especially exhibiting a protective effect (52). Colonization of a Lachnospiraceae bacterium in obese mice promoted the development of diabetes (53). Our results indicate that many

neuropeptides are correlated with the two bacterial families, including VIP, orexin-B, NPY, α -MSH, neuromedin-B, and somatostatin-28. Most of these neuropeptides are involved in the regulation of energy homeostasis and food intake (37), and publications implicating food intake and related physiological processes ranked highest in our literature mining for those probiotics-altered neuropeptides. Future investigations should be directed to understand the molecular mechanisms by which gut microbes alter these processes through the modulation of neuropeptides.

Another important finding in our study is that the treatment with heat-killed probiotics caused remarkable change of the peptidome profile in the hippocampus. Thermal-processed and nonviable probiotics are called paraprobiotics (54). These dead probiotics, which contain active components like peptidoglycan fragments and DNA that can modulate immune functions, are suitable for commercial development of therapeutic products because of the advantages of easier storage and longer product shelf life. Ou *et al.* (55) reported that heat-killed lactic acid bacteria enhanced immunomodulatory ability by switching the immune response. In our results, there was no significant change at the level of genus by heat-killed NS8 treatment, and PCoA analysis showed no separation, indicating that heat-killed NS8 did not change the microbiome composition. Overall, our results provide peptidome-level evidence that heat-killed probiotics can affect the gut-brain axis without affecting the composition of the gut microbiome.

In our previous reports, treatment with NS8 improved behavioral and cognitive impairments induced by chronic restraint stress in rats (17), and administration of NS9 restored antibiotics-induced psychological aberrations (28). In this study, we observed that the two probiotics *L. helveticus* NS8 and *L. fermentum* NS9, both belonging to the *Lactobacillus* family, exhibited strain-specific effects for regulation of the brain peptidome. It has been accepted that the mechanisms and actions of probiotics are strain specific, and each strain presents a specific health benefit. Buffington *et al.* (16) reported that *L. reuteri* treatment restored social deficits of mice, but *Lactobacillus johnsonii* had no effect. Wall *et al.* (56) evaluated the administration of *Bifidobacterium breve* strains NCIMB 702258 and DPC 6330, observing altered fatty acid composition in mouse brains. The most significantly altered fatty acids in that study, arachidonic acid and docosahexaenoic acid, play important roles in neurogenesis and neurotransmission. In our study, administration of NS8 and NS9 resulted in distinct changes to the gut microbiome and brain peptidome. Our data reveal the peptide-level signature of strain-specific effects, which might be one of the reasons why different probiotics strains offer diverse beneficial and therapeutic consequences.

Our current study provides strong evidence to support that probiotics can alter the brain peptidome. It has been proposed that probiotics might change the microbiota composition or directly modulate the pathways involved in the conversation between gut and brain, including the host's immune system, vagus nerve, and/or metabolites (12, 39, 57, 58). The former model involves regulation through the microbiota-gut-brain axis, whereas the latter involves direct action through the gut-brain axis. Our results show that probiotics can modulate the brain peptidome through both mechanisms. Live NS8 altered the gut microbiota, but heat-killed NS8 treatment altered the brain peptidome without changing the gut microbiome, demonstrating possible direct action through the gut-brain axis. Several genera of gut bacteria were highly correlated with specific brain peptides, suggesting functional connections. Thus, probiotics administration

might alter the brain peptidome through both the gut-brain axis and the microbiota-gut-brain axis.

There are many gut peptide hormones (59) involved in modulation of the gut-brain axis. Gut microbes increase the proliferation of enteroendocrine L cells that release glucagon-like peptide 1 (GLP-1) and peptide YY (PYY), both of which play appetite-regulatory roles (60). Also, the gut microbes generate short-chain fatty acids that stimulate the secretion of GLP-1 and PYY (61). These peptide hormones enter the circulatory system and affect the brain. Among the brain peptides identified in this study, some of them are also produced in the gut. One example is VIP, which is produced in many organs, including the brain and gut (35), and this peptide in the hypothalamus showed significant correlation with *Anaerotruncus* in our results. The microbes may interact directly with intestinal cells to promote the production of VIP that enters the circulation and disseminates to the brain, or they may indirectly modulate VIP production in the brain. Addressing these possibilities merits further investigation.

In conclusion, our study reveals that oral administration of probiotics can alter the brain peptidome through the gut-brain axis, and the brain peptidome correlated with the composition of the gut microbiome. We provide a dynamic peptidome landscape across different brain regions, treatment times, and strains of probiotics, as well as a paraprobiotics. Overall, these information-rich datasets paint a quantitative picture of brain peptides in relation to gut bacteria as well as related physiological processes and behaviors, demonstrating the power of our 1-hour peptidomics approach to elucidate the molecular mechanisms of the gut-brain axis and highlighting the therapeutic potentials of probiotics.

MATERIALS AND METHODS

Bacteria and animals

The *L. helveticus* NS8 and *L. fermentum* NS9 strains (17, 28) were inoculated into MRS (De Man, Rogosa and Sharpe agar) medium at 37°C for 18 hours each. Then, the bacteria were collected by centrifugation at 3000 rpm for 5 min and washed twice with phosphate-buffered saline (PBS) buffer. The pellet was resuspended in drinking water at a concentration of 10⁹ colony-forming units/ml to feed the animals for probiotic treatment. The heat-killed probiotics were prepared by keeping at 121°C for 30 min.

Two-month-old male specific pathogen-free C57BL/6J mice (Vital River Laboratories Co. Ltd.) were individually housed during the experiment under standard laboratory conditions (17). A regular diet was supplied with 0.3% salt, 5% fat, 22% protein, and 58% carbohydrates (Vital River Laboratories Co. Ltd). After 2 weeks of accommodation, mice were randomly divided into seven groups for treatment ($n = 12$ each group, details shown in the legend of Fig. 1). Specifically, the NS8 and NS8NS8 groups were fed with probiotics NS8 respectively for 1 and 2 months. The NS9 and NS8h groups were treated with NS9 and heat-killed NS8, respectively. The NS8C group was treated with NS8 in the first month and not treated in the second month. As controls, the C and CC groups were fed with regular water. The mice accessed the probiotics-containing water *ad libitum* over the treatment period as previously reported (16, 17, 62), which was changed daily to minimize dosage variation. The body weight of mice was measured monthly, and no significant change of body weight of mice caused by probiotics treatment was observed. At the end of treatment, the mice were randomly taken out from cages at 9:00 a.m.

to minimize the effect of time difference on brain peptide change (44, 45) and then quickly euthanized for sample collection.

For the prenatal stress experiment (63), the pregnant C57BL/6 J mice at embryonic day 12 (Vital River Laboratories Co. Ltd.) were subcutaneously injected with VPA or PBS (600 mg/kg). Their offspring mice were weaned at postnatal day 21 and divided into four groups (details shown in the legend of Fig. 7). The four offspring groups at postnatal day 35 were respectively treated with water or probiotics for an additional 2 months until euthanized. The animals' care was in accordance with institutional guidelines of National Center for Protein Sciences–Beijing and Institute of Psychology, Chinese Academy of Sciences.

Sample preparation

Mice were anesthetized with isoflurane before being decapitated. Brains were immediately dissected, and the brain region boundaries were carefully checked according to The Mouse Brain Library (www.mbl.org/). The tissues were heated using a microwave oven at 800 W for 9 s (64, 65) and stored at -80°C until further use. For peptide extraction, the tissues were manually homogenized with a glass-glass Dounce grinder. The homogenized samples were combined and centrifuged at 20,000g for 10 min at 4°C to remove the insoluble pellet. This extraction step was repeated three times. Extracts were combined and dried down in a SpeedVac vacuum concentrator. Crude peptide sample was further desalted by C18 ZipTip and resuspended in 5 μl of 0.1% formic acid aqueous solution for LC-MS/MS analysis.

LC-MS/MS analysis

The LC-MS/MS experiments were performed on an Orbitrap Q Exactive HF mass spectrometer (Thermo Fisher Scientific) coupled with an online EASY-nLC 1200 nano–high-performance liquid chromatography (HPLC) system (Thermo Fisher Scientific). The peptide mixtures were separated on a reversed-phase nano-HPLC C18 column [precolumn: 3 μm , 2 cm by 100 μm inner diameter (ID); analytical column: 1.9 μm , 12 cm by 150 μm ID] at a flow rate of 600 nl/min with a 65-min gradient: 3 to 7% solvent B for 1 min, 7 to 12% for 8 min, 12 to 22% for 33 min, 22 to 32% for 10 min, 32 to 55% for 10 min, and 55 to 90% for 3 min (solvent A, water; solvent B, acetonitrile; 0.1% formic acid). The electrospray voltage was 2.2 kV. Peptides were analyzed by data-dependent MS/MS acquisition mode with a resolution of 120,000 at full-scan mode and 15,000 at MS/MS mode. The full scan was processed in the Orbitrap from mass/charge ratio 250 to 1800; the top 20 most intense ions in each scan were automatically selected for higher-energy collisional dissociation (HCD) fragmentation with normalized collision energy of 29% and measured in Orbitrap. Typical mass spectrometric conditions were as follows: Automatic gain control targets were 3×10^6 ions for full scans and 2×10^5 for MS/MS scans; the maximum injection time was 80 ms for full scans and 80 ms for MS/MS scans; and dynamic exclusion was used for 13 s. Each sample was analyzed with one technical replicate because of limited sample volume.

Peptide identification and quantification by PEAKS Studio

Raw data were processed with PEAKS Studio version 8.5 against our purpose-made neuropeptide database (aggregation and filtration of publicly accessible databases: Neuropeptides.nl (36), SwePep (31), Neuropred.com (29), and Neuropedia.com (66)) or a customized UniProt protein database (downloaded on 23 November 2017, encompassing 87,215 protein sequence entries). Mass tolerance for

searches was set to a maximum of 10 parts per million for peptide masses and 0.02 Da for HCD fragment ion masses. Enzyme was set to none. The pyroglutamylation (N-terminal Q, E), oxidation (M), amidation (C terminus), phosphorylation (S, T), and acetylation (K) were set as variable modifications. The identified peptides were filtered by these criteria: (i) false discovery rate $< 1\%$, (ii) identified in ≥ 4 biological replicates, and (iii) containing ≥ 5 amino acids. For peptides with five and six amino acids, further curation was performed by inspecting whether the fragment ions contained a sequence tag of ≥ 3 consecutive b or y ions. The C-terminal amidated peptides without a preceding glycine were considered as false-positive assignments and removed (67). The label-free quantitation based on extracted ion chromatograms was performed using the PEAKS Q module. Only peptides with valid quantitative values of $\geq 70\%$ in at least one group were kept. The sample degradation was examined by inspecting the percentage of basic-cleavage-site-containing peptides (data file S8). The quantitative information was exported as .csv files for further bioinformatics processing.

16S rRNA gene sequencing and analysis

The bacterial genomic DNA was extracted from mouse fecal pellets using the MO BIO PowerSoil Kit. The V3 and V4 regions of the 16S rRNA gene were amplified by polymerase chain reaction (PCR) and sequenced in the Illumina MiSeq 2500 platform. The 2×250 -base pair paired-end protocol was used with individually barcoded universal primers containing adapters for pooling and direct sequencing of PCR products. A quality filter was applied to the resulting merged reads. Reads with Q value of < 25 were discarded. The 16S rRNA gene sequences were clustered into operational taxonomic units (OTUs) at a similarity cutoff value of 97% using the Uclust algorithm. The taxonomies were determined by mapping OTUs to the SILVA database (68). The α diversity and β diversity were generated with the Quantitative Insights Into Microbial Ecology (QIIME) pipeline (69) and calculated on the basis of unweighted UniFrac distance matrices.

Dot blotting

Dot blotting was carried out for orthogonal validation of quantification results from LC-MS. The normalization factor of each sample was calculated according to total ion chromatograph (70) by PEAKS Studio, and the sample loading amount is equal to volume divided by normalization factors. The peptide samples were spotted directly onto nitrocellulose membranes, which were then blocked with 5% nonfat dry milk in tris-buffered saline (TBS) with 0.05% Tween 20. The membrane was incubated in primary antibodies overnight at 4°C . The rabbit polyclonal anti-CRH (Abcam, ab8901) and anti-ACTH (Abcam, ab74976) antibodies were diluted to 1:500. After washing three times for 5 min with 0.05% TBST, the membranes were incubated with peroxidase-conjugated goat anti-rabbit secondary antibody (ZSGB-Bio, 2301) for 1 hour at room temperature. Reactivity was visualized using enhanced chemiluminescence substrate (CWBio, CW0048M). Each experiment was repeated three times.

Data analysis

R scripts were used for all data analyses and visualizations in this study. For peptidomics data analysis, peptides with valid quantitative values (PEAKS quality score > 0.2) were filtered for downstream analysis. The raw abundance values were \log_2 -transformed. Missing values were then replaced with a constant value of zero. Differentially expressed peptides between groups were identified by a two-tailed

t test with unequal variances. The criterion to identify significant differences was $P < 0.05$. Expression patterns of peptides in C, NS8, and NS8h groups were further analyzed by a hierarchical clustering method with Euclidean distance and average linkage in R.

Amino acid sequence logo plots were drawn by IceLogo 1.2, which was scaled on the amino acid frequencies found in *Mus musculus*.

Neuropeptides were classified by the families of the genes encoding them, and there were 25 gene families, of which 17 were classified by the neuropeptide database [www.neuropeptides.nl (36)], and the remaining 8 named by corresponding precursors.

To identify significant changes in bacteria abundance, we investigated the genus levels of bacteria. Different expression of genus between C group and NS8 group were identified by a two-tailed *t* test with unequal variances. *P* values of <0.05 were considered significant. To uncover the links between brain peptidome and gut microbiome, Spearman's correlation coefficients (*r* values) were calculated between peptides and the four significantly altered bacteria genera. Those with *r* values > 0.5 or < -0.5 were considered significant.

Literature mining

A neuropeptide text mining algorithm was implemented in R scripts (listed in data file S9). Detailed procedure is as follows.

1) PubMed entries with Medical Subject Headings terms containing the words mouse, neuropeptide, and hypothalamus were selected as corpus. Each entry in the corpus contains PubMed Identifier, article title, and abstract. Abstracts were segmented into sentences by R package natural language processing (NLP).

2) To obtain behavior-related sentences, we compiled a small behavioral dictionary (data file S9) used for screening sentences with the matching tokens. The resulting sentences were further extracted and compiled into a target statement library. The R package coreNLP split sentences in the target statement library to words, performed part-of-speech tagging, and extracted sentence syntactic structure and grammatical relations.

3) The sentences containing a list of target verbs (data file S9) and conforming the grammatical structure of (neuropeptide) subject-verb-object (behavior) were extracted. Target verbs can indicate how neuropeptides regulate behavior and in what way.

4) Last, the sentences were grouped into six behavioral categories: anxiety and depression, food intake, sleep/awake and circadian, social and reproductive behaviors, nociception, and cognition. The number of publications in each group was counted.

SUPPLEMENTARY MATERIALS

stke.sciencemag.org/cgi/content/full/13/642/eabb0443/DC1

Fig. S1. Data quality of the 1-hour peptidomics approach in analysis of hypothalamus peptides.

Fig. S2. Quality control of the quantitative peptidomics.

Fig. S3. Gut microbiome compositions resulting from 16S rRNA analysis.

Fig. S4. Histogram illustrates the total quantifiable and significantly altered hypothalamus peptides (unique sequences) of the CC/C dataset resulting from 1-month development of mice.

Fig. S5. Hierarchical clustering shows the brain peptide change in hypothalamus among the C, NS8, and NS9 groups.

Table S1. Neuropeptide families.

Data file S1. Identified peptides from four brain regions (corresponding to Fig. 2A) (Excel file).

Data file S2. Detailed information of peptides shown in Fig. 2D (Excel file).

Data file S3. Detailed information of correlation analysis shown in Fig. 3C (Excel file).

Data file S4. Detailed information of clustering analysis shown in Fig. 3E (Excel file).

Data file S5. Detailed information of peptidome shown in Fig. 4A (Excel file).

Data file S6. Detailed information of peptidome shown in Fig. 4D (Excel file).

Data file S7. Detailed information of peptidome shown in Fig. 5, D and F (Excel file).

Data file S8. Percentage of basic-cleavage-site-containing peptides (Excel file).

Data file S9. Detailed information of MINIBar script (Excel file).

[View/request a protocol for this paper from Bio-protocol.](#)

REFERENCES AND NOTES

- G. Sharon, T. R. Sampson, D. H. Geschwind, S. K. Mazmanian, The central nervous system and the gut microbiome. *Cell* **167**, 915–932 (2016).
- H. E. Vuong, J. M. Yano, T. C. Fung, E. Y. Hsiao, The microbiome and host behavior. *Annu. Rev. Neurosci.* **40**, 21–49 (2017).
- R. Diaz Heijtz, S. Wang, F. Anuar, Y. Qian, B. Bjorkholm, A. Samuelsson, M. L. Hibberd, H. Forsberg, S. Pettersson, Normal gut microbiota modulates brain development and behavior. *Proc. Natl. Acad. Sci. U.S.A.* **108**, 3047–3052 (2011).
- C. de la Fuente-Nunez, B. T. Meneguetti, O. L. Franco, T. K. Lu, Neuromicrobiology: How microbes influence the brain. *ACS Chem. Neurosci.* **9**, 141–150 (2018).
- H. E. Vuong, E. Y. Hsiao, Emerging roles for the gut microbiome in autism spectrum disorder. *Biol. Psychiatry* **81**, 411–423 (2017).
- T. Harach, N. Marunguang, N. Duthilleul, V. Cheatham, K. D. Mc Coy, G. Frisoni, J. J. Neher, F. Fak, M. Jucker, T. Lasser, T. Bolmont, Reduction of Abeta amyloid pathology in APPPS1 transgenic mice in the absence of gut microbiota. *Sci. Rep.* **7**, 41802 (2017).
- A. Parashar, M. Udayabanu, Gut microbiota: Implications in Parkinson's disease. *Parkinsonism Relat. Disord.* **38**, 1–7 (2017).
- J. A. Foster, K. A. McVey Neufeld, Gut-brain axis: How the microbiome influences anxiety and depression. *Trends Neurosci.* **36**, 305–312 (2013).
- S. Liang, X. Wu, X. Hu, T. Wang, F. Jin, Recognizing depression from the microbiota–gut–brain axis. *Int. J. Mol. Sci.* **19**, 1592 (2018).
- K.-A. Neufeld, N. Kang, J. Bienenstock, J. A. Foster, Effects of intestinal microbiota on anxiety-like behavior. *Commun. Integr. Biol.* **4**, 492–494 (2011).
- M. Messaoudi, R. Lalonde, N. Violle, H. Javelot, D. Desor, A. Nejdi, J. F. Bisson, C. Rougeot, M. Pichelin, M. Cazaubiel, J. M. Cazaubiel, Assessment of psychotropic-like properties of a probiotic formulation (*Lactobacillus helveticus* R0052 and *Bifidobacterium longum* R0175) in rats and human subjects. *Br. J. Nutr.* **105**, 755–764 (2011).
- X. Liu, S. Cao, X. Zhang, Modulation of gut microbiota-brain axis by probiotics, prebiotics, and diet. *J. Agric. Food Chem.* **63**, 7885–7895 (2015).
- J. A. Bravo, P. Forsythe, M. V. Chew, E. Escaravage, H. M. Savignac, T. G. Dinan, J. Bienenstock, J. F. Cryan, Ingestion of *Lactobacillus* strain regulates emotional behavior and central GABA receptor expression in a mouse via the vagus nerve. *Proc. Natl. Acad. Sci. U.S.A.* **108**, 16050–16055 (2011).
- K. A. McVey Neufeld, S. Kay, J. Bienenstock, Mouse strain affects behavioral and neuroendocrine stress responses following administration of probiotic *Lactobacillus rhamnosus* JB-1 or traditional antidepressant fluoxetine. *Front. Neurosci.* **12**, 294 (2018).
- E. Y. Hsiao, S. W. McBride, S. Hsien, G. Sharon, E. R. Hyde, T. McCue, J. A. Codelli, J. Chow, S. E. Reisman, J. F. Petrosino, P. H. Patterson, S. K. Mazmanian, Microbiota modulate behavioral and physiological abnormalities associated with neurodevelopmental disorders. *Cell* **155**, 1451–1463 (2013).
- S. A. Buffington, G. V. DiPrisco, T. A. Auchtung, N. J. Ajami, J. F. Petrosino, M. Costa-Mattioli, Microbial reconstitution reverses maternal diet-induced social and synaptic deficits in offspring. *Cell* **165**, 1762–1775 (2016).
- S. Liang, T. Wang, X. Hu, J. Luo, W. Li, X. Wu, Y. Duan, F. Jin, Administration of *Lactobacillus helveticus* NS8 improves behavioral, cognitive, and biochemical aberrations caused by chronic restraint stress. *Neuroscience* **310**, 561–577 (2015).
- L. D. Fricker, J. Lim, H. Pan, F.-Y. Che, Peptidomics: Identification and quantification of endogenous peptides in neuroendocrine tissues. *Mass Spectrom. Rev.* **25**, 327–344 (2006).
- A. N. van den Pol, Neuropeptide transmission in brain circuits. *Neuron* **76**, 98–115 (2012).
- L. Li, J. V. Sweedler, Peptides in the brain: Mass spectrometry-based measurement approaches and challenges. *Annu. Rev. Anal. Chem.* **1**, 451–483 (2008).
- H. Ye, J. Wang, Z. Tian, F. Ma, J. Dowell, Q. Bremer, G. Lu, B. Baldo, L. Li, Quantitative mass spectrometry reveals food intake-induced neuropeptide level changes in rat brain: Functional assessment of selected neuropeptides as feeding regulators. *Mol. Cell. Proteomics* **16**, 1922–1937 (2017).
- F. Petruzzello, S. Falasca, P. E. Andren, G. Rainer, X. Zhang, Chronic nicotine treatment impacts the regulation of opioid and non-opioid peptides in the rat dorsal striatum. *Mol. Cell. Proteomics* **12**, 1553–1562 (2013).
- C. Jia, L. Hui, W. Cao, C. B. Lietz, X. Jiang, R. Chen, A. D. Catherman, P. M. Thomas, Y. Ge, N. L. Kelleher, L. Li, High-definition de novo sequencing of crustacean hyperglycemic hormone (CHH)-family neuropeptides. *Mol. Cell. Proteomics* **11**, 1951–1964 (2012).
- C. Jia, C. B. Lietz, H. Ye, L. Hui, Q. Yu, S. Yoo, L. Li, A multi-scale strategy for discovery of novel endogenous neuropeptides in the crustacean nervous system. *J. Proteomics* **91**, 1–12 (2013).

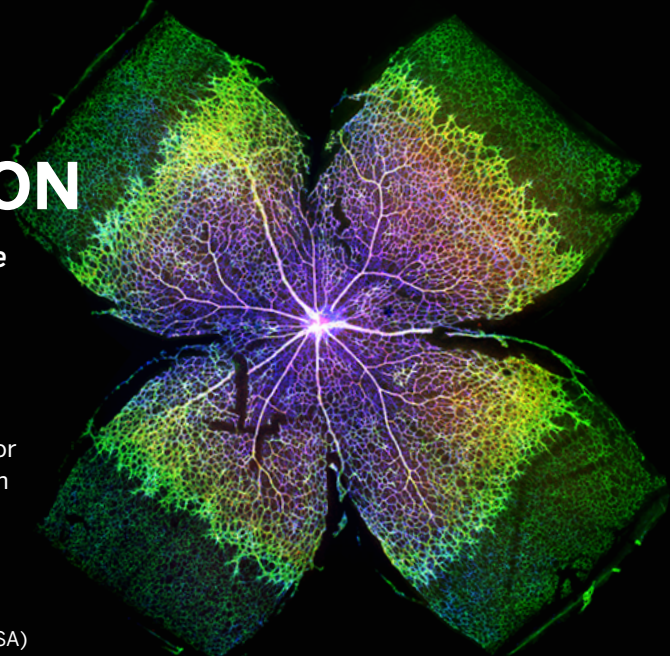
25. M. P. Nusbaum, D. M. Blitz, E. Marder, Functional consequences of neuropeptide and small-molecule co-transmission. *Nat. Rev. Neurosci.* **18**, 389–403 (2017).
26. P. Holzer, Neuropeptides, Microbiota, and Behavior. *Int. Rev. Neurobiol.* **131**, 67–89 (2016).
27. A. Farzi, A. M. Hassan, G. Zenz, P. Holzer, Diabetes and mood disorders: Multiple links through the microbiota-gut-brain axis. *Mol. Aspects Med.* **66**, 80–93 (2019).
28. T. Wang, X. Hu, S. Liang, W. Li, X. Wu, L. Wang, F. Jin, *Lactobacillus fermentum* NS9 restores the antibiotic induced physiological and psychological abnormalities in rats. *Benef. Microbes* **6**, 707–717 (2015).
29. B. R. Southey, A. Amare, T. A. Zimmerman, S. L. Rodriguez-Zas, J. V. Sweedler, NeuroPred: A tool to predict cleavage sites in neuropeptide precursors and provide the masses of the resulting peptides. *Nucleic Acids Res.* **34**, W267–W272 (2006).
30. A. Secher, C. D. Kelstrup, K. W. Conde-Frieboes, Analytic framework for peptidomics applied to large-scale neuropeptide identification. *Nat. Commun.* **7**, 11436 (2016).
31. M. Falth, K. Skold, M. Norrman, M. Svensson, D. Fenyo, P. E. Andren, SwePep, a database designed for endogenous peptides and mass spectrometry. *Mol. Cell. Proteomics* **5**, 998–1005 (2006).
32. H. Tremlett, D. W. Fadrosh, A. A. Faruqi, F. Zhu, J. Hart, S. Roalstad, J. Graves, S. Lynch, E. Waubant, Gut microbiota in early pediatric multiple sclerosis: A case-control study. *Eur. J. Neurol.* **23**, 1308–1321 (2016).
33. P. Zheng, B. Zeng, C. Zhou, M. Liu, Z. Fang, X. Xu, L. Zeng, J. Chen, S. Fan, X. Du, X. Zhang, D. Yang, Y. Yang, H. Meng, W. Li, N. D. Melgiri, J. Licinio, H. Wei, P. Xie, Gut microbiome remodeling induces depressive-like behaviors through a pathway mediated by the host's metabolism. *Mol. Psychiatry* **21**, 786–796 (2016).
34. B. L. Williams, M. Hornig, T. Buie, M. L. Bauman, M. Cho Paik, I. Wick, A. Bennett, O. Jabado, D. L. Hirschberg, W. I. Lipkin, Impaired carbohydrate digestion and transport and mucosal dysbiosis in the intestines of children with autism and gastrointestinal disturbances. *PLOS ONE* **6**, e24585 (2011).
35. C. M. White, S. Ji, H. Cai, S. Maudsley, B. Martin, Therapeutic potential of vasoactive intestinal peptide and its receptors in neurological disorders. *CNS Neurol. Disord. Drug Targets* **9**, 661–666 (2010).
36. J. P. Burbach, Neuropeptides from concept to online database www.neuropeptides.nl. *Eur. J. Pharmacol.* **626**, 27–48 (2010).
37. J. J. Hillebrand, D. de Wied, R. A. Adan, Neuropeptides, food intake and body weight regulation: A hypothalamic focus. *Peptides* **23**, 2283–2306 (2002).
38. J. Luo, T. Wang, S. Liang, X. Hu, W. Li, F. Jin, Ingestion of *Lactobacillus* strain reduces anxiety and improves cognitive function in the hyperammonemia rat. *Sci. China Life Sci.* **57**, 327–335 (2014).
39. T. A. Oelschlaeger, Mechanisms of probiotic actions - A review. *Int. J. Med. Microbiol.* **300**, 57–62 (2010).
40. Z. Jafari, J. Mehla, B. E. Kolb, M. H. Mohajerani, Prenatal noise stress impairs HPA axis and cognitive performance in mice. *Sci. Rep.* **7**, 10560 (2017).
41. A. Arnou, Valproic acid in pregnancy: How much are we endangering the embryo and fetus? *Reprod. Toxicol.* **28**, 1–10 (2009).
42. C. Nicolini, M. Fahnstock, The valproic acid-induced rodent model of autism. *Exp. Neurol.* **299**, 217–227 (2018).
43. J. E. Lee, Neuropeptidomics: Mass spectrometry-based identification and quantitation of neuropeptides. *Genomics Inform.* **14**, 12–19 (2016).
44. N. G. Hatcher, N. Atkins Jr., S. P. Annangudi, A. J. Forbes, N. L. Kelleher, M. U. Gillette, J. V. Sweedler, Mass spectrometry-based discovery of circadian peptides. *Proc. Natl. Acad. Sci. U.S.A.* **105**, 12527–12532 (2008).
45. N. Atkins Jr., S. Ren, N. Hatcher, P. W. Burgoon, J. W. Mitchell, Functional peptidomics: Stimulus- and time-of-day-specific peptide release in the mammalian circadian clock. *ACS Chem. Neurosci.* **9**, 2001–2008 (2018).
46. C. D. Dotson, M. C. Geraedts, S. D. Munger, Peptide regulators of peripheral taste function. *Semin. Cell Dev. Biol.* **24**, 232–239 (2013).
47. C. K. Frese, A. J. Boender, S. Mohammed, A. J. Heck, R. A. Adan, A. F. Altelar, Profiling of diet-induced neuropeptide changes in rat brain by quantitative mass spectrometry. *Anal. Chem.* **85**, 4594–4604 (2013).
48. T. Chen, Y. You, G. Xie, X. Zheng, A. Zhao, J. Liu, Q. Zhao, S. Wang, F. Huang, C. Rajani, C. Wang, S. Chen, Y. Ni, H. Yu, Y. Deng, X. Wang, Strategy for an association study of the intestinal microbiome and brain metabolome across the lifespan of rats. *Anal. Chem.* **90**, 2475–2483 (2018).
49. K. Lippert, L. Kedenko, L. Antonioli, I. Kedenko, C. Gemeier, M. Leitner, A. Kautzky-Willer, B. Paulweber, E. Hackl, Gut microbiota dysbiosis associated with glucose metabolism disorders and the metabolic syndrome in older adults. *Benef. Microbes* **8**, 545–556 (2017).
50. V. A. Poroyko, A. Carreras, A. Khalyfa, A. A. Khalyfa, V. Leone, E. Peris, I. Almendros, A. Gileles-Hillel, Z. Qiao, N. Hubert, R. Farre, E. B. Chang, D. Gozal, Chronic sleep disruption alters gut microbiota, induces systemic and adipose tissue inflammation and insulin resistance in mice. *Sci. Rep.* **6**, 35405 (2016).
51. L. F. Gomez-Arango, H. L. Barrett, H. D. McIntyre, L. K. Callaway, M. Morrison, M. Dekker Nitert, Connections between the gut microbiome and metabolic hormones in early pregnancy in overweight and obese women. *Diabetes* **65**, 2214–2223 (2016).
52. C. Menni, M. A. Jackson, T. Pallister, C. J. Steves, T. D. Spector, A. M. Valdes, Gut microbiome diversity and high-fibre intake are related to lower long-term weight gain. *Int. J. Obes.* **41**, 1099–1105 (2017).
53. K. Kameyama, K. Itoh, Intestinal colonization by a *Lachnospiraceae* bacterium contributes to the development of diabetes in obese mice. *Microbes Environ.* **29**, 427–430 (2014).
54. C. N. de Almada, C. N. Almada, R. C. R. Martinez, A. S. Sant'Ana, Paraprobiotics: Evidences on their ability to modify biological responses, inactivation methods and perspectives on their application in foods. *Trends Food Sci. Tech.* **58**, 96–114 (2016).
55. C.-C. Ou, S.-L. Lin, J.-J. Tsai, M.-Y. Lin, Heat-killed lactic acid bacteria enhance immunomodulatory potential by skewing the immune response toward Th1 polarization. *J. Food Sci.* **76**, M260–M267 (2011).
56. R. Wall, T. M. Marques, O. O'Sullivan, R. P. Ross, F. Shanahan, E. M. Quigley, T. G. Dinan, B. Kiely, G. F. Fitzgerald, P. D. Cotter, F. Fouchy, C. Stanton, Contrasting effects of *Bifidobacterium breve* NCIMB 702258 and *Bifidobacterium breve* DPC 6330 on the composition of murine brain fatty acids and gut microbiota. *Am. J. Clin. Nutr.* **95**, 1278–1287 (2012).
57. W. R. Wikoff, A. T. Anfora, J. Liu, P. G. Schultz, S. A. Lesley, E. C. Peters, G. Siuzdak, Metabolomics analysis reveals large effects of gut microflora on mammalian blood metabolites. *Proc. Natl. Acad. Sci. U.S.A.* **106**, 3698–3703 (2009).
58. M. Matsumoto, R. Kibe, T. Ooga, Y. Aiba, E. Sawaki, Y. Koga, Y. Benno, Cerebral low-molecular metabolites influenced by intestinal microbiota: A pilot study. *Front. Syst. Neurosci.* **7**, 9 (2013).
59. K. Tatemoto, V. Mutt, Isolation of two novel candidate hormones using a chemical method for finding naturally occurring polypeptides. *Nature* **285**, 417–418 (1980).
60. M. Covasa, R. W. Stephens, R. Todorean, C. Cobuz, Intestinal sensing by gut microbiota: Targeting gut peptides. *Front. Endocrinol.* **10**, 82 (2019).
61. T. U. Greiner, F. Bäckhed, Microbial regulation of GLP-1 and L-cell biology. *Mol. Metab.* **5**, 753–758 (2016).
62. M. Sgritta, S. W. Dooling, S. A. Buffington, E. N. Momin, M. B. Francis, R. A. Britton, M. Costa-Mattioli, Mechanisms underlying microbial-mediated changes in social behavior in mouse models of autism spectrum disorder. *Neuron* **101**, 246–259.e6 (2019).
63. J.-W. Kim, H. Seung, K. C. Kim, E. L. T. Gonzales, H. A. Oh, S. M. Yang, M. J. Ko, S.-H. Han, S. Banerjee, C. Y. Shin, Agmatine rescues autistic behaviors in the valproic acid-induced animal model of autism. *Neuropharmacology* **113**, 71–81 (2017).
64. F.-Y. Che, J. Lim, H. Pan, R. Biswas, L. D. Fricker, Quantitative neuropeptidomics of microwave-irradiated mouse brain and pituitary. *Mol. Cell. Proteomics* **4**, 1391–1405 (2005).
65. M. Svensson, K. Sköld, P. Svenningsson, P. E. Andren, Peptidomics-based discovery of novel neuropeptides. *J. Proteome Res.* **2**, 213–219 (2003).
66. Y. Kim, S. Bark, V. Hook, N. Bandeira, NeuroPedia: Neuropeptide database and spectral library. *Bioinformatics* **27**, 2772–2773 (2011).
67. K. D. B. Anapindi, E. V. Romanova, B. R. Southey, J. V. Sweedler, Peptide identifications and false discovery rates using different mass spectrometry platforms. *Talanta* **182**, 456–463 (2018).
68. C. Quast, E. Pruesse, P. Yilmaz, J. Gerken, T. Schweer, P. Yarza, J. Peplies, F. O. Glockner, The SILVA ribosomal RNA gene database project: Improved data processing and web-based tools. *Nucleic Acids Res.* **41**, D590–D596 (2013).
69. J. G. Caporaso, J. Kuczynski, J. Stombaugh, K. Bittinger, F. D. Bushman, E. K. Costello, N. Fierer, A. G. Pena, J. K. Goodrich, J. I. Gordon, G. A. Huttley, S. T. Kelley, D. Knights, J. E. Koenig, R. E. Ley, C. A. Lozupone, D. McDonald, B. D. Muegge, M. Pirrung, J. Reeder, J. R. Sevinsky, P. J. Turnbaugh, W. A. Walters, J. Widmann, T. Yatsunenko, J. Zaneveld, R. Knight, QIIME allows analysis of high-throughput community sequencing data. *Nat. Methods* **7**, 335–336 (2010).
70. X. Wang, S. Shen, S. S. Rasam, J. Qu, MS1 ion current-based quantitative proteomics: A promising solution for reliable analysis of large biological cohorts. *Mass Spectrom. Rev.* **38**, 461–482 (2019).
71. J. Ma, T. Chen, S. Wu, C. Yang, M. Bai, K. Shu, K. Li, G. Zhang, Z. Jin, F. He, H. Hermjakob, Y. Zhu, iProX: An integrated proteome resource. *Nucleic Acids Res.* **47**, D1211–D1217 (2019).

Acknowledgments: We thank L. Li (University of Wisconsin-Madison) and H. Hermjakob (EMBL-EBI) for proofreading the manuscript and the MS facility of the National Center for Protein Science–Beijing (PHOENIX Center) for instrument accessing. Y. Duan is acknowledged for discussion. **Funding:** This work was supported by grants from the National Key R&D Program of China (nos. 2017YFA0505702 and 2016YFA0501302 to C.J.), the National Science Foundation of China (no. 21675006 to C.J.), Key Research Program of China (BWS17J025 to C.J.), and NS Bio Japan (20170403 to F.J.). **Author contributions:** C.J., F.J., and C.S. designed the project. X.S., S.L., X.W., and P.Z. conducted animal experiments under C.J.'s supervision. X.S., C.J., and P.Z. conducted sample preparation and LC-MS/MS analysis. P.Z., C.J., and C.S. conducted data processing and bioinformatics analysis. C.J. conceived and P.Z. wrote the MINBar script. Q.W. performed dot blotting. C.J., C.S., and P.Z. wrote the manuscript. All the

authors have approved the final manuscript. **Competing interests:** The authors declare that they have no competing interests. **Data and materials availability:** The MS proteomics data have been deposited to the ProteomeXchange Consortium (<http://proteomecentral.proteomexchange.org>) through the iProX partner repository (71) with the dataset identifier PXD015323. The 16S rRNA sequence data have been deposited in the National Center for Biotechnology Information (NCBI) database with accession code PRJNA612927. All other data needed to evaluate the conclusions in the paper are present in the paper or the Supplementary Materials.

Submitted 25 January 2020
 Accepted 10 June 2020
 Published 28 July 2020
 10.1126/scisignal.abb0443

Citation: P. Zhang, X. Wu, S. Liang, X. Shao, Q. Wang, R. Chen, W. Zhu, C. Shao, F. Jin, C. Jia, A dynamic mouse peptidome landscape reveals probiotic modulation of the gut-brain axis. *Sci. Signal.* **13**, eabb0443 (2020).



THIS IS NOT SCIENCE FICTION
 This is captivating, impactful Science

Contact us today to discuss pricing options for adding any of these journals to your collection of Science resources.

Institutional Licensing
ScienceMag.org/request | scienceonline@aaas.org
 1-866-265-4152 (USA) | +1-202-326-6730 (outside USA)

Science
AAAS

Science
 Advances

Science
 Immunology

Science
 Robotics

Science
 Signaling

Science
 Translational
 Medicine

ALZHEIMER'S DISEASE

Prospective longitudinal atrophy in Alzheimer's disease correlates with the intensity and topography of baseline tau-PET

Renaud La Joie^{1*}, Adrienne V. Visani¹, Suzanne L. Baker², Jesse A. Brown¹, Viktoriya Bourakova¹, Jungho Cha¹, Kiran Chaudhary¹, Lauren Edwards¹, Leonardo Iaccarino¹, Mustafa Janabi², Orit H. Lesman-Segev¹, Zachary A. Miller¹, David C. Perry¹, James P. O'Neil², Julie Pham¹, Julio C. Rojas¹, Howard J. Rosen¹, William W. Seeley¹, Richard M. Tsai¹, Bruce L. Miller¹, William J. Jagust^{2,3}, Gil D. Rabinovici^{1,2,3,4}

Copyright © 2020 The Authors, some rights reserved; exclusive licensee American Association for the Advancement of Science. No claim to original U.S. Government Works

β -Amyloid plaques and tau-containing neurofibrillary tangles are the two neuropathological hallmarks of Alzheimer's disease (AD) and are thought to play crucial roles in a neurodegenerative cascade leading to dementia. Both lesions can now be visualized in vivo using positron emission tomography (PET) radiotracers, opening new opportunities to study disease mechanisms and improve patients' diagnostic and prognostic evaluation. In a group of 32 patients at early symptomatic AD stages, we tested whether β -amyloid and tau-PET could predict subsequent brain atrophy measured using longitudinal magnetic resonance imaging acquired at the time of PET and 15 months later. Quantitative analyses showed that the global intensity of tau-PET, but not β -amyloid-PET, signal predicted the rate of subsequent atrophy, independent of baseline cortical thickness. Additional investigations demonstrated that the specific distribution of tau-PET signal was a strong indicator of the topography of future atrophy at the single patient level and that the relationship between baseline tau-PET and subsequent atrophy was particularly strong in younger patients. These data support disease models in which tau pathology is a major driver of local neurodegeneration and highlight the relevance of tau-PET as a precision medicine tool to help predict individual patient's progression and design future clinical trials.

INTRODUCTION

Alzheimer's disease (AD) is characterized by the co-occurrence of β -amyloid (A β) deposition into extracellular plaques and neurofibrillary tangles composed of aggregated hyperphosphorylated tau (1). The aggregation of A β and tau is thought to play a crucial role in a neurodegenerative cascade that results in the loss of neurons and synapses (2). The development of radiotracers binding to A β plaques (3) and paired helical filaments of tau that comprise neurofibrillary tangles (4) allows the visualization and quantification of AD pathology in living patients using positron emission tomography (PET). Those imaging biomarkers offer an opportunity to improve patient diagnosis and to study the development of AD pathophysiology by describing the relationships between protein aggregation, neurodegeneration, and cognitive impairment.

Cross-sectional neuroimaging studies have demonstrated that lower brain volumes are more strongly associated with tau-PET than with A β -PET burden in patients with mild cognitive impairment and dementia (5). Moreover, studies examining the topography of neuroimaging biomarkers have indicated that the pattern of neurodegeneration [i.e., regions with low cortical volume/thickness (6, 7) or glucose hypometabolism (8, 9)] greatly resembles the pattern of elevated tau-PET, but not A β -PET, signal. However, the spatial extent of tau-PET signal appears to exceed the extent of neurode-

generation (6, 8), suggesting that tau-PET elevation might precede and potentially predict neurodegeneration. Converging evidence also suggests that the intensity and topography of tau-PET, but not A β -PET, are strongly associated with the severity of each patient's specific clinical deficits (10). In addition, earlier age of onset seems to be associated with higher tau-PET signal (8, 11), potentially accounting for the higher rates of brain atrophy observed in patients with early-onset AD compared to their older counterparts (12–14).

Because tau-PET imaging is a relatively novel technique, most previous studies have been based on cross-sectional data, which lead to technical and conceptual limitations. First, cross-sectional studies define neurodegeneration as low volume/metabolism because they cannot directly measure decline in volume/metabolism over time. Resulting metrics are then biased by preexisting interindividual variability in cerebral anatomy and function (15). Second, cross-sectional designs do not allow direct observation of a chronological sequence of biomarker abnormalities. More recently, retrospective longitudinal studies [in which longitudinal magnetic resonance imaging (MRI) data were acquired before tau-PET acquisition] have also highlighted a close association between tau-PET and neurodegeneration (16, 17) but might be biased by the nonlinear nature of atrophy over the disease course (18, 19).

In the present observational study, we prospectively assessed and compared the associations between baseline A β and tau-PET burden [using [¹¹C]Pittsburgh compound B (PIB) and [¹⁸F]florbetapir (FTP), respectively] and subsequent longitudinal atrophy in a group of patients at the early clinical stages of AD. Our primary hypothesis was that the tau deposition detected with FTP-PET drives, and therefore precedes, regional neurodegeneration in early symptomatic AD. From a precision medicine perspective, we were interested

¹Memory and Aging Center, Department of Neurology, Weill Institute for Neurosciences, University of California, San Francisco, San Francisco, CA, USA. ²Molecular Biophysics and Integrated Bioimaging Division, Lawrence Berkeley National Laboratory, Berkeley, CA, USA. ³Helen Wills Neuroscience Institute, University of California, Berkeley, Berkeley, CA, USA. ⁴Department of Radiology and Biomedical Imaging, University of California, San Francisco, San Francisco, CA, USA.

*Corresponding author. Email: renaud.lajoie@ucsf.edu

in testing PET imaging's ability to predict neuroimaging changes at the individual patient level. On the basis of the cross-sectional evidence described above, we hypothesized that higher baseline FTP-PET, but not PIB-PET, would be associated with higher atrophy rates and that the topography of FTP-PET binding would predict the pattern of subsequent atrophy at the individual patient level. We had two secondary aims. First, we tested whether baseline PIB and FTP-PET data could help predict patients' clinical deterio-

ration, measured with the clinical dementia rating scale sum of boxes (CDR-SB), a measure of disease severity based on functional decline (20). Last, we investigated whether the previously highlighted association between earlier age of onset and greater atrophy rates could be explained by baseline differences in tau burden.

RESULTS

Description of the cohort

The current study included 32 patients in early clinical stages of AD (mild cognitive impairment or mild dementia, and a positive PIB-PET scan). All patients underwent structural MRI and PET with both PIB and FTP at the baseline visit, and a second structural MRI at a follow-up visit (median time interval, 15 months). Two Siemens 3-T MRI scanners were used in this study (see Materials and Methods and Discussion). Demographics are presented in Table 1. The sample was heterogeneous and included six patients fulfilling criteria for logopenic variant primary progressive aphasia (21) and three patients meeting criteria for posterior cortical atrophy (22). Patients were between 49 and 83 years old at the time of PET scan [20 patients (63%) being under 65 years old].

At the group level, longitudinal atrophy is greater in regions with high baseline FTP binding

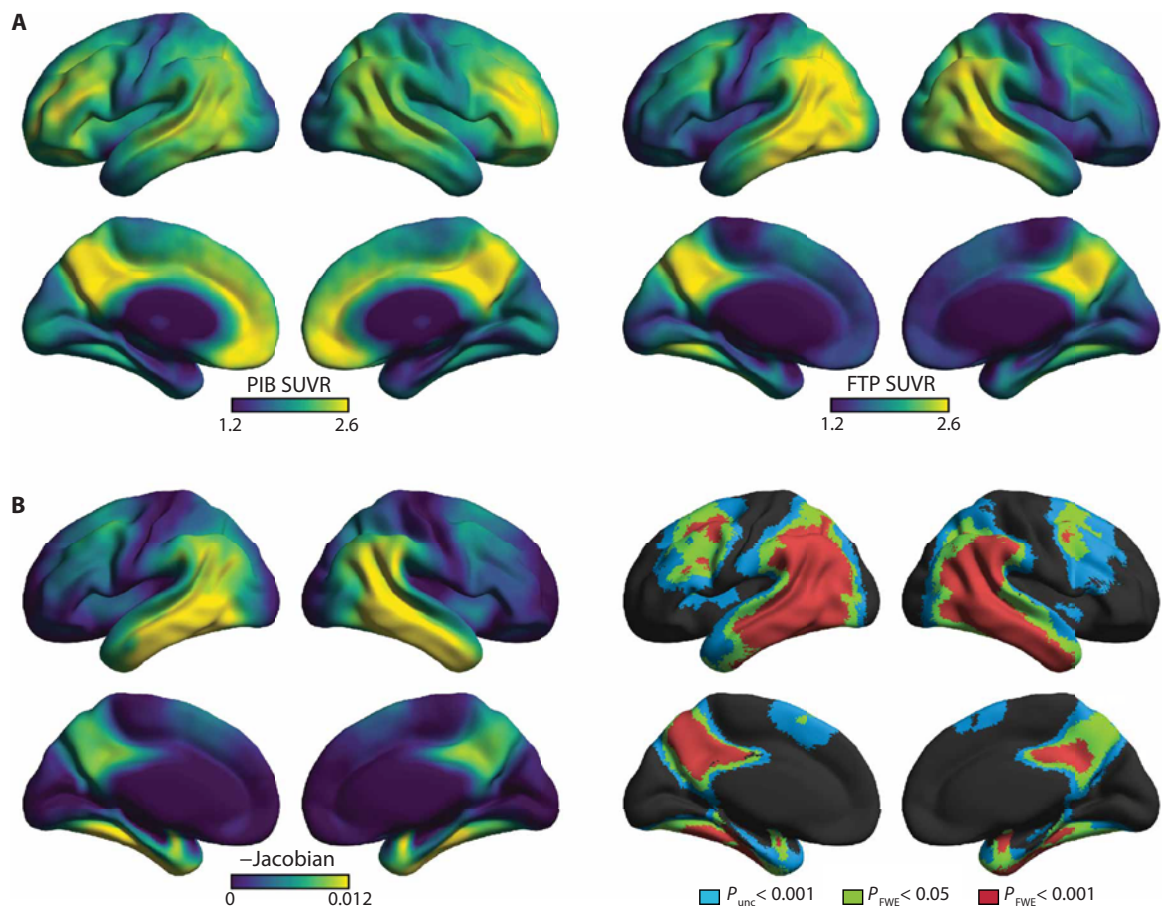
For each patient, baseline PET scans were processed to calculate standardized uptake value ratio (SUVR) maps [see (23) and Materials

Table 1. Patients included in the analyses. For continuous variables, mean \pm SD [min, max] is indicated. MMSE, mini-mental state examination; CDR-SB, clinical dementia rating scale sum of boxes.

| | |
|-------------------------------------------------------|------------------------|
| Sex: $n_{\text{female}}/n_{\text{male}}$ | 21/11 |
| Age at baseline | 64 \pm 9 [49, 83] |
| Education | 17 \pm 3 [12, 24] |
| APOE4 alleles: $n_0/n_1/n_2$ (n_{missing}) | 14/13/3 (2) |
| MMSE at baseline | 24 \pm 4 [14, 30] |
| CDR-SB at baseline | 3.8 \pm 2 [0, 8] |
| Baseline to follow-up MRI (months) | 15 \pm 3 [10, 24] |
| Baseline MRI to FTP-PET (months) | 1.8 \pm 2.2 [0, 7.7] |
| Baseline MRI to PIB-PET (months) | 1.6 \pm 2.3 [0, 7.7] |

Fig. 1. Voxelwise patterns at the group level.

(A) Group-average PET SUVR maps at baseline. (B) Voxelwise pattern of longitudinal cortical atrophy. Left: Average of 32 reversed GM-masked and smoothed reversed Jacobian maps (higher value means higher rate of atrophy). Right: Statistical map corresponding to a voxelwise one-sample t test including the 32 individual maps, showing areas of significant atrophy (reversed Jacobians > 0) based on three increasingly conservative thresholds [$P_{\text{uncorrected}} < 0.001$, family-wise error (FWE)-corrected $P_{\text{FWE}} < 0.05$ and $P_{\text{FWE}} < 0.001$ at the voxel level; all three with $P_{\text{FWE}} < 0.05$ at the cluster level]. All maps are available for visualization at <https://neurovault.org/collections/WLDODMCY/>.



and Methods for more details]. The two MRI scans were processed using a specific longitudinal pipeline (24) to derive a three-dimensional (3D) map of Jacobians representing annualized atrophy (Jacobians were reversed so that positive values indicate tissue shrinkage over time). All maps were masked to restrict the investigations to the cortical gray matter (GM) (fig. S1) and analyzed in native or template space, depending on the analysis. We first created group-average images of PIB, FTP, and longitudinal atrophy using images warped to template space (Fig. 1).

PIB binding predominated in medial areas (prefrontal and posterior cingulate/precuneus regions); signal was also elevated in lateral frontal and temporo-parietal cortices (Fig. 1A). FTP binding was maximal at the temporo-parietal junction and the posterior cingulate/precuneus and moderate in dorsal frontal, occipital, and infero-medial temporal cortices (Fig. 1A).

The pattern of longitudinal atrophy is shown in Fig. 1B as the group-average reversed Jacobian map (higher values indicating higher atrophy rates) and as a statistical map based on a one-sample t test performed on the 32 Jacobian maps. Atrophy was maximal in temporo-parietal areas, posterior cingulate/precuneus, and dorsal frontal areas, surviving stringent family-wise error (FWE) correction ($P_{FWE} < 0.001$) in those regions where baseline FTP-PET signal was particularly elevated.

Patients with high baseline FTP-PET binding develop more severe cortical atrophy

We investigated the relationships between baseline cortical alterations (PIB SUVR, FTP SUVR, and cortical thickness) and the severity of subsequent atrophy across patients. Figure 2 shows the associations between baseline global (mean of entire cortex) measures of PIB-SUVR, FTP-SUVR, and cortical thickness [values were derived from FreeSurfer 5.3, Z-scored based on normative dataset (25), and reversed so higher values indicate lower baseline thickness] and overall cortical atrophy (average reversed cortical Jacobian values). Longitudinal cortical atrophy was strongly associated with baseline FTP ($r_{FTP-atrophy} = 0.670$, 95% confidence interval (CI) [0.388, 0.841], $P < 0.001$), in contrast with weaker correlations with baseline cortical PIB ($r_{PIB-atrophy} = 0.291$, 95% CI [-0.029, 0.546], $P = 0.07$) and baseline global cortical thickness ($r_{thickness-atrophy} = 0.281$, 95% CI [-0.067, 0.586], $P = 0.12$). Pairwise comparisons of correla-

tions (based on bootstrapping of correlation coefficient pairs with 5000 permutations) showed that longitudinal atrophy was more strongly correlated with FTP than PIB ($\Delta r = 0.379$, 95% CI [0.121, 0.594], $P = 0.004$), but the difference between $r_{FTP-atrophy}$ and $r_{thickness-atrophy}$ was not significant at $\alpha = 0.05$ ($\Delta r = 0.390$, 95% CI [-0.119, 0.821], $P = 0.11$).

When including all three baseline predictors in a single multiple regression model to predict subsequent longitudinal atrophy, FTP remained significant (standardized $\beta = 0.696$, $t = 4.2$, $P < 0.001$ versus $\beta = -0.083$, $t = -0.5$, $P = 0.58$ for PIB and $\beta = 0.173$, $t = 1.3$, $P = 0.22$ for thickness; see table S1), and this full model did not perform better than a model including FTP only to predict longitudinal atrophy (table S1).

Voxelwise FTP-PET patterns predict maps of subsequent atrophy at the individual patient level

We next assessed whether the topography of PIB and FTP binding could help predict the pattern of atrophy at the individual patient level, using a voxelwise approach. For each patient, the topographical similarity between 3D maps of PET binding and atrophy was quantified using a voxelwise spatial correlation approach restricted to a cortical mask, as previously described (26) and illustrated in Fig. 3A (see fig. S1 for details on the preprocessing). Resulting spatial correlation coefficients (baseline PIB to longitudinal atrophy and baseline FTP to longitudinal atrophy) were then z -transformed to allow analysis at the group level (see Fig. 3B). Across the 32 patients, spatial correlation between baseline PIB and subsequent atrophy was minimal: mean $z(r) = 0.183$, 95% CI [0.131, 0.226] (percentile bootstrap CI based on 5000 permutations), indicating 3% [2%, 5%] shared variance on average. In contrast, the spatial correlation between baseline FTP and longitudinal atrophy was high: mean $z(r) = 0.780$, 95% CI [0.682, 0.859], indicating 43% [35%, 48%] shared variance on average. Spatial correlation with longitudinal atrophy was significantly higher for baseline FTP than PIB [paired t test conducted on the $z(r)$ values: $t(31) = 14.9$, $P < 0.001$]. Note that correlations were higher for FTP than for PIB in all 32 patients, as shown in Fig. 3B.

Baseline tau-PET predicts longitudinal atrophy independent of baseline thickness

Our finding that baseline FTP-SUVR correlates with subsequent atrophy could be confounded by the fact that these regions are usually

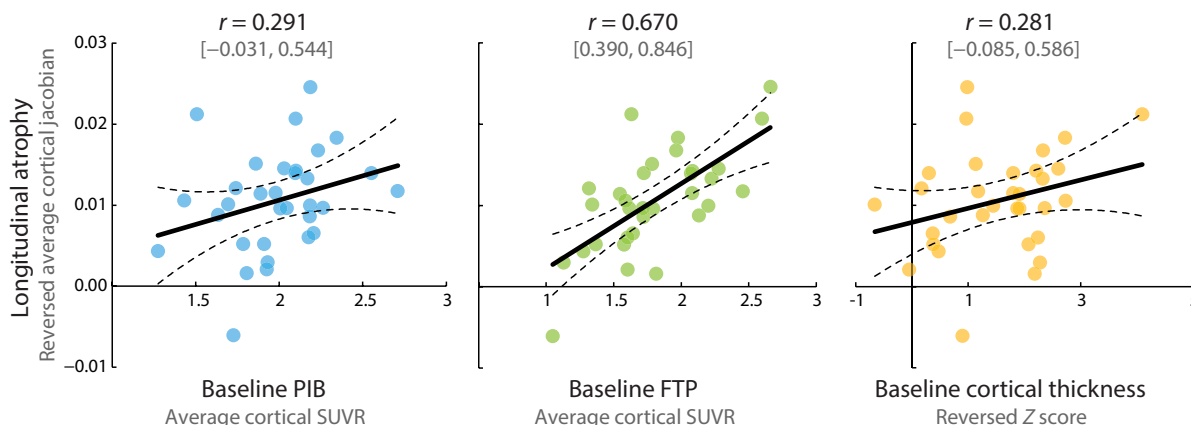


Fig. 2. Bivariate associations between baseline measures and subsequent atrophy across the 32 patients. Ninety-five percent confidence intervals (95% CI) were computed using bootstrapping with 5000 permutations. Details about the statistical analyses, including a multiple regression with all three baseline predictors, are available in Results and table S1.

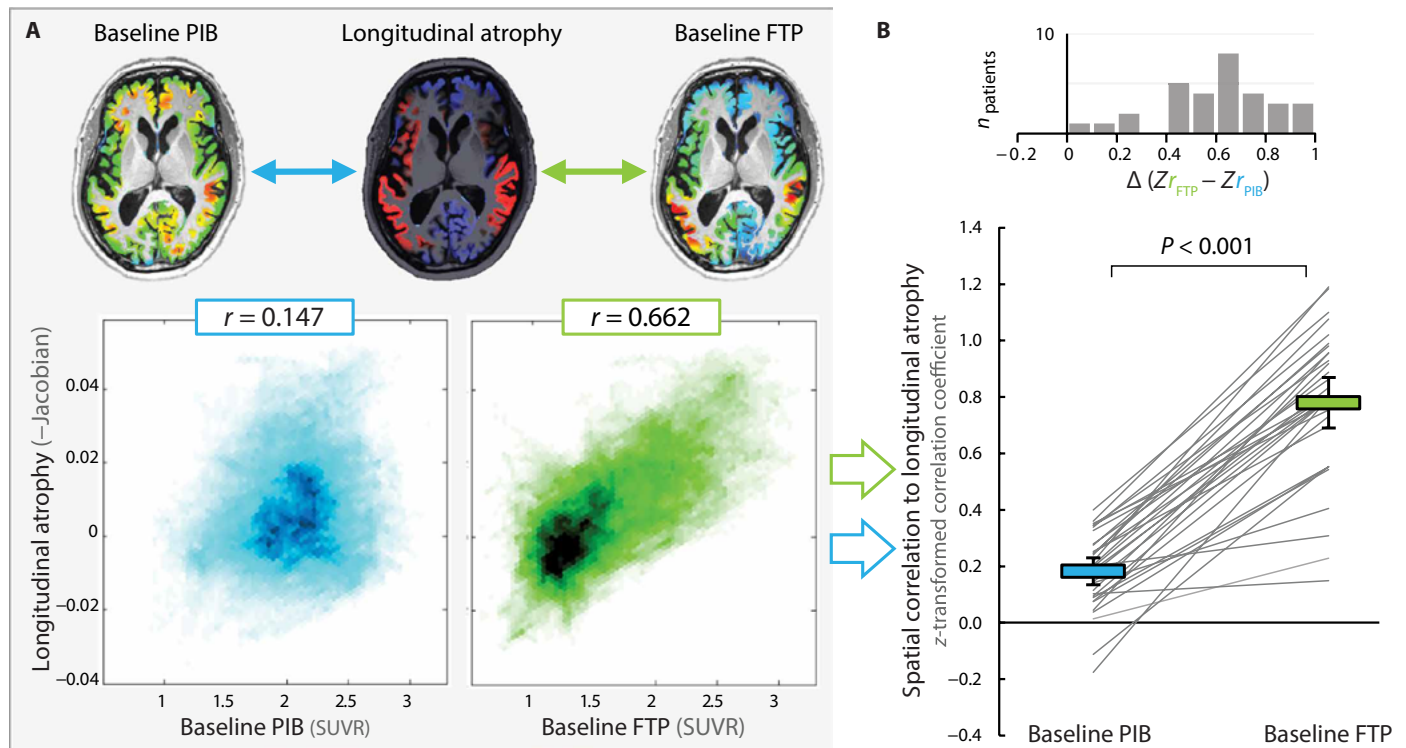


Fig. 3. Voxelwise spatial correlations between baseline PET patterns and the topography of subsequent atrophy. (A) Analyses conducted at the individual patient level to quantify the similarity between patterns of PET SUVR at baseline and maps of longitudinal atrophy (reversed Jacobians). The images used for illustration correspond to a patient with close-to-average values. For each patient, correlations were assessed on all voxels of the cortex (see fig. S1 for details about specific image preprocessing steps). (B) Group-level analyses. Resulting correlation coefficients were z-transformed to be analyzed at the group level. Gray lines show individual patients, whereas colored bars indicate average z-transformed coefficients (with 95% CI). P value corresponds to two-tailed paired t test. The top panel shows the histogram of the difference between z-transformed spatial correlation coefficients between PIB and atrophy and FTP and atrophy across all 32 patients, highlighting that the latter was higher than the former in all 32 cases.

already atrophic at baseline and that atrophy tends to accelerate locally. In addition, low cortical thickness at baseline could reduce the PET signal due to partial volume effects and introduce additional noise in the measurements. We therefore conducted additional analyses to assess the potential confounding effect of “baseline atrophy” on the association between FTP-PET and subsequent atrophy at a regional level. This set of analyses was conducted using regions of interests, enabling the use of partial volume corrected (PVC) PET data. Each patient’s cortex was segmented into 68 regions of interest (ROIs) using FreeSurfer 5.3, and the average cortical thickness was extracted from the baseline MRI for each ROI. For each patient, cortical thickness values were converted to a Z score (based on normative data, see Materials and Methods) to be used as indicators of baseline neurodegeneration. Average baseline FTP-SUVR_{PVC} and Jacobian values were also extracted from each ROI (see fig. S2 for details on the preprocessing and Fig. 4A to visualize group averages).

The spaghetti plots in Fig. 4B show that, for most patients, regions with higher baseline FTP-SUVR_{PVC} and, to a smaller extent, lower baseline cortical thickness had higher atrophy rates. Linear mixed-effect models (LMEMs) were used to test the respective contribution of each baseline measure to longitudinal atrophy. All ROIs from all patients were included in LMEMs ($68 \times 32 = 2176$ entries), with random slopes and intercepts for both ROI and patient factors (see table S2 for further details on model specifications and results). Separate LMEMs were first conducted for each predic-

tor, and both were significant ($P < 0.001$; see Fig. 4B, bottom right panel), although FTP_{PVC} was a stronger predictor ($t = 12.6$, marginal $R^2 = 0.444$, conditional $R^2 = 0.785$) than baseline thickness ($t = 5.1$, marginal $R^2 = 0.057$, conditional $R^2 = 0.610$). However, when entering both predictors in the same model (Fig. 4B, bottom line), only FTP_{PVC} was significant ($t = 11.9$, $P < 0.001$ versus $t = -1.7$, $P = 0.09$ for thickness). In addition, this full model roughly explained the same amount of variance (marginal $R^2 = 0.426$, conditional $R^2 = 0.800$) as the model including baseline FTP_{PVC} only and had a slightly decreased Akaike information criterion (AIC) value ($-15,579$ versus $-15,498$; see table S2), indicating that adding baseline thickness only minimally improved the overall model fit. The conclusions of the LMEMs were very similar when using non-PVC PET data and when including baseline PIB-SUVR in the model (see fig. S3).

Baseline tau-PET is more strongly associated with follow-up than baseline cortical thickness

We hypothesized that baseline tau PET will correlate more strongly with cortical thickness measured at follow-up than at baseline, consistent with a conceptual model in which tau deposition precedes neurodegeneration. Figure 5A shows that, at the group level, baseline tau burden (global cortical FTP-SUVR_{PVC}) correlated more strongly with global cortical thinning (reversed Z-scored thickness) measured at follow-up than baseline ($r = 0.431$, 95% CI [0.166,

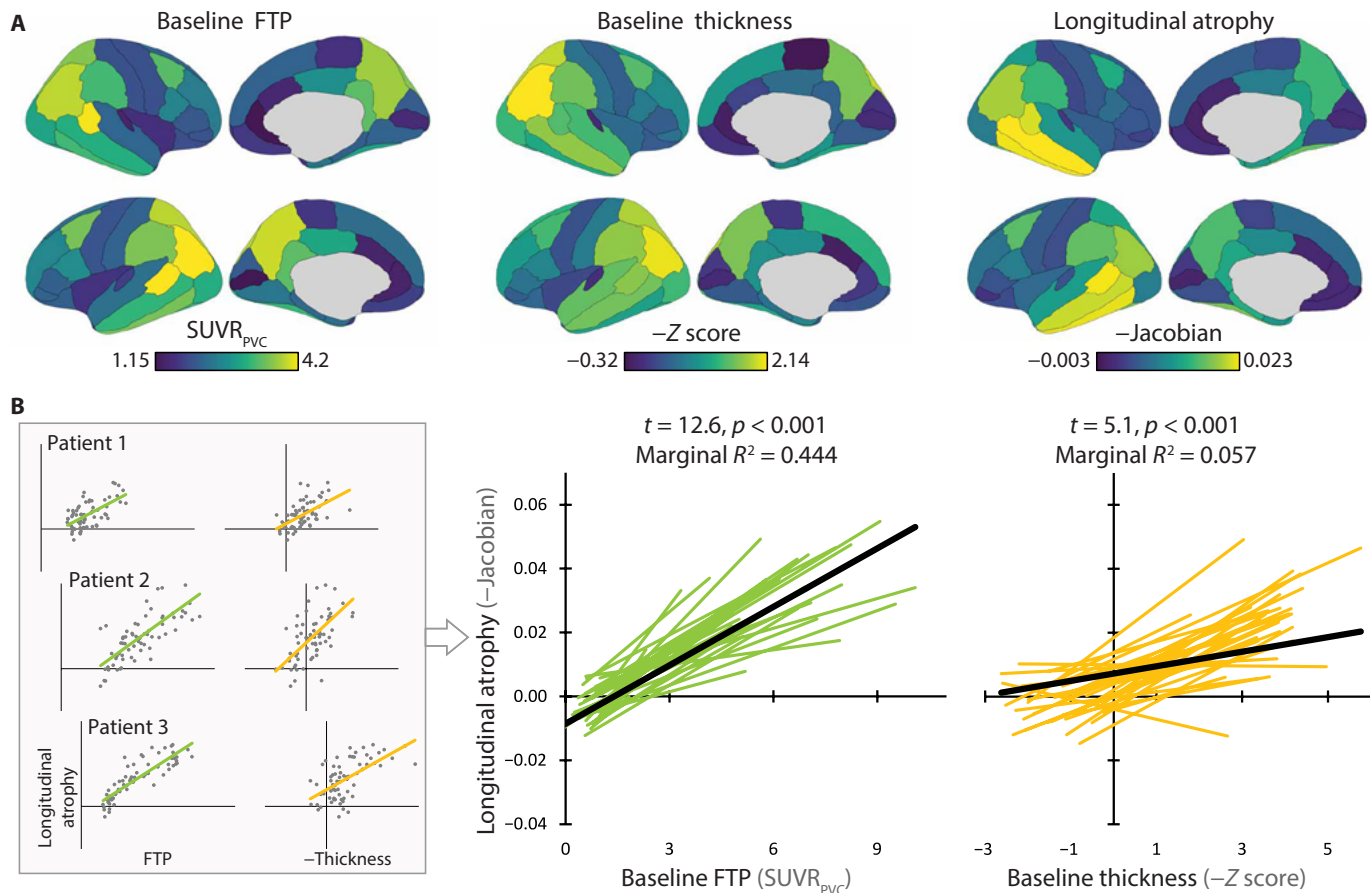


Fig. 4. Relative contribution of baseline partial volume corrected FTP-PET and baseline thickness patterns to predict the topography of subsequent atrophy using FreeSurfer-defined cortical regions of interest. (A) Group average values in the 68 FreeSurfer cortical regions of interest (ROIs). The color scale was adapted to the range of values of each modality to best illustrate regional variations. $SUVR_{PVC}$, partial volume corrected standardized uptake value ratio. (B) Spatial associations between patterns of baseline FTP- $SUVR_{PVC}$, thickness, and longitudinal atrophy were conducted for each patient on the basis of the 68 ROIs, as illustrated in the left panel. The spaghetti plots on the right illustrate the 32 regression lines obtained at the patient level for each pair of variables. The statistical indices on top of each spaghetti plot indicate the results of linear mixed-effect models (LMEMs) to predict reverse Jacobians; separate models were run with each of the two baseline variables as a predictor. A full model that included both predictors together is described in Results and table S2.

0.663] versus $r = 0.168$, 95% CI [−0.150, 0.480], $\Delta r = 0.263$, bootstrapped 95% CI [0.026, 0.517], $P = 0.026$).

We also tested the spatial similarity between baseline tau-PET and cortical thinning measured at each time point (Fig. 5B). The method was similar to that presented in Fig. 3, except that the patient-level analysis was conducted using ROIs rather than voxelwise, enabling the calculation of Z score thickness values as mentioned above (see fig. S2). Across the 32 patients, baseline FTP_{PVC} spatially correlated with concurrent cortical thickness: mean spatial correlation $z(r) = 0.787$, 95% CI [0.681, 0.876], indicating 43% [35%, 50%] shared variance on average. Yet, the spatial correlation was higher between baseline FTP_{PVC} and follow-up thickness patterns: mean $z(r) = 0.833$, 95% CI [0.727, 0.921], indicating 47% [39%, 53%]; paired t test on the $z(r)$ values: $t(31) = 2.86$, $P = 0.008$.

Longitudinal precuneus atrophy parallels clinical decline

The CDR-SB was used to measure clinical progression; to control for variations in clinical follow-up duration (mean = 15.0 months, min = 11.1, max = 23.7), changes in CDR-SB were annualized [(follow-up – baseline)/time interval]. On average, CDR-SB increased by 1.6 ± 2.0 points per year [one-sample t test: $t(31) = 4.52$, $P < 0.001$].

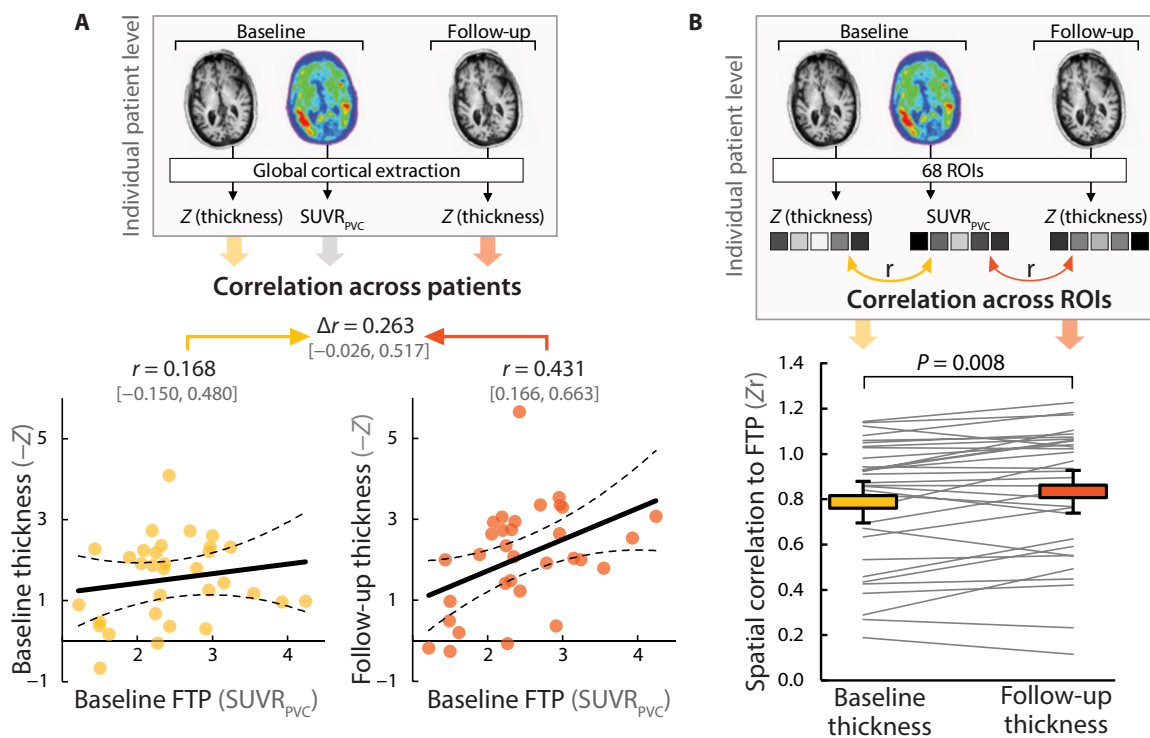
Annualized CDR-SB increase was poorly correlated with global cortical measures of baseline PIB $SUVR$ ($r = -0.125$, $P = 0.51$), FTP $SUVR$ ($r = -0.041$, $P = 0.80$), cortical thickness ($r = 0.006$, $P = 0.95$), or longitudinal atrophy ($r = 0.095$, $P = 0.65$; see fig. S4 for 95% CI and scatter plots). Voxelwise analyses showed that increase in CDR-SB over time was associated with longitudinal atrophy in the precuneus/posterior cingulate area (surviving FWE correction at the voxel level; see fig. S4). In contrast, no regional association was found in any of the three baseline predictors (based on the $P_{uncorrected} < 0.001$ threshold).

Earlier disease onset is associated with higher tau burden and thus more rapid atrophy

Older age at baseline was associated with lower baseline abnormalities (fig. S5), although the correlation only reached statistical significance (at $\alpha = 0.05$) for baseline FTP- $SUVR$ ($r = -0.572$, $P = 0.002$), but not baseline PIB- $SUVR$ ($r = -0.313$, $P = 0.07$) and baseline thickness ($r = -0.224$, $P = 0.12$; see Fig. 6A for 95% CI and scatter plots). In addition, older patients had lower rates of atrophy (correlation between age and reversed average cortical Jacobian: $r = -0.542$, $P = 0.006$; Fig. 6A). When including both patient's age

Fig. 5. Association between baseline FTP-PET and cortical thickness at baseline and follow-up.

(A) Association between baseline global cortical PVC FTP-SUVR values and cortical thickness at baseline (yellow) and follow-up (orange) across patients. Cortical thickness measures were Z-scored on the basis of normative data and reversed, so higher values indicate more neurodegeneration. Ninety-five percent CIs are based on bootstrap with 5000 permutations. **(B)** Spatial similarity between FTP-SUVR_{PVC} and low cortical thickness at each time point was assessed at the single patient level using a correlation approach based on FreeSurfer ROIs (top panel). Cortical thickness was extracted from 68 FreeSurfer



cortical ROIs, transformed into a Z score using normative data, and reversed to higher values to indicate more neurodegeneration; FTP-SUVR_{PVC} values were extracted from each ROI. Correlations were Fisher z-transformed to be analyzed at the group level (bottom panel). Each gray line represents a single patient, and color bars illustrate group averages with bootstrap 95% CIs. *P* value corresponds to a paired *t* test, showing that patterns of baseline FTP binding are more similar to patterns of low cortical thickness at follow-up than baseline.

and baseline cortical FTP-SUVR in a multiple regression model, FTP remained highly predictive of longitudinal atrophy (standardized $\beta = 0.536$, $P = 0.003$), while the effect of age was reduced (standardized $\beta = -0.235$, $P = 0.16$). Mediation analyses further showed that the relationship between patient's age and longitudinal rate of atrophy was at least partly mediated by baseline cortical FTP-SUVR (Fig. 6A). No mediation effect was found using baseline PIB-SUVR or baseline cortical thickness (see fig. S6). Voxelwise analyses showed that both FTP-SUVR and longitudinal atrophy decreased with greater patient age throughout the brain (Fig. 6B) and most strongly in the fronto-parietal areas where correlations reached statistical significance ($P_{\text{unc}} < 0.001$ at the voxel level with $P_{\text{FWE}} < 0.05$ at the cluster level; see fig. S7).

Last, the spatial similarity between baseline FTP-SUVR maps and patterns of subsequent atrophy (quantified at the individual patient level using the voxelwise spatial correlation method described in Fig. 3) decreased with age ($r = -0.471$, $P = 0.005$) (see Fig. 6B). Spatial correlation values went from an estimated $z(r) \sim 0.9$ at age 55 ($R^2 = 52\%$ shared variance) to $z(r) \sim 0.63$ at age 75 ($R^2 = 31\%$ shared variance). The spatial correlation between baseline PIB and longitudinal atrophy was low regardless of patient's age ($r = -0.253$, $P = 0.13$; see fig. S5 for 95% CI and scatter plots).

DISCUSSION

In this prospective longitudinal neuroimaging study conducted in patients at early clinical stages of AD, we investigated the associations between baseline PET measures of tau and A β burden and

subsequent neurodegeneration measured as MRI atrophy over time. In line with our original hypotheses, we found that baseline tau PET, but not A β -PET, predicted the degree and spatial distribution of cortical atrophy over the subsequent year.

The association between baseline FTP-PET and subsequent atrophy, and notably the topographical similarity between the two patterns, was a strong and robust finding. The association was found at both the group (Figs. 1 and 2) and the individual patient levels (Figs. 3 and 4) and using complementary voxelwise (Fig. 3) and ROI-based (Fig. 4 and 5 and fig. S3) approaches. The predictive value of the baseline tau-PET pattern on future atrophy remained substantial even after adjusting for baseline cortical thickness, with tau-PET explaining $\sim 40\%$ of unique variance in longitudinal atrophy. Last, although cross-sectional relationships can be found between tau-PET and concurrent neurodegeneration, we showed that tau-PET more closely resembles neurodegeneration at a future time point (Fig. 5). Together, these longitudinal results expand on previous findings from postmortem and cross-sectional studies, by providing prospective evidence that the aggregation of tau predicts future neurodegeneration in patients with biomarker-confirmed AD. These results support a sequential relationship between tau fibrillar aggregates and downstream degeneration. This directionality is in line with a recent longitudinal tau-PET study from our group showing that, at the clinical stage of AD, tau pathology and brain atrophy progress in different regions, likely reflecting a phase shifting, with tau elevation locally preceding atrophy (27).

Multiple studies (28–31) previously reported that baseline cerebrospinal fluid (CSF) concentration of tau was associated with

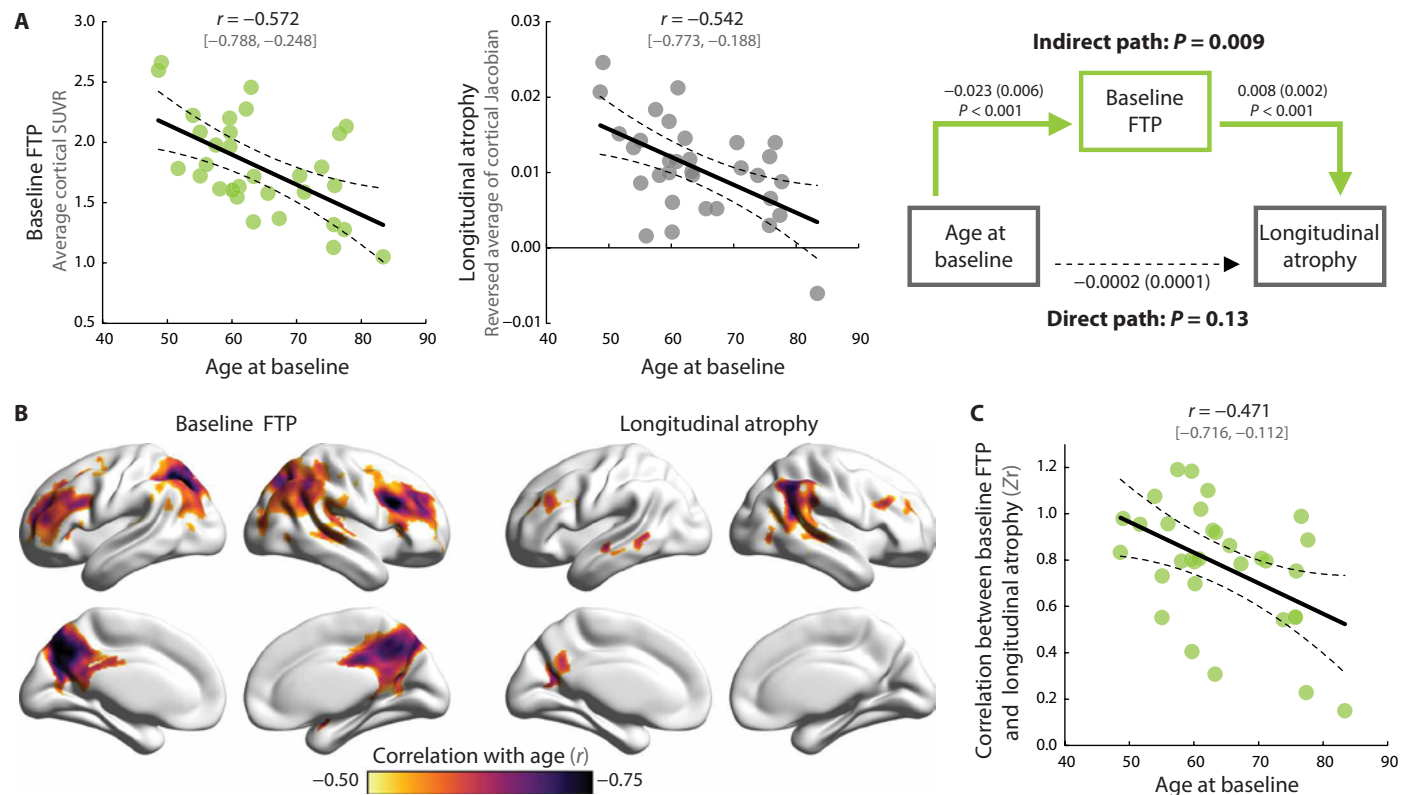


Fig. 6. Effect of patient age on baseline tau pathology and subsequent atrophy. (A) Association between patient age and global cortical FTP-SUVR at baseline and longitudinal atrophy; see fig. S5 for associations between age and other variables. Mediation analysis showed that baseline cortical FTP-SUVR mediated the effect of age on longitudinal atrophy; see fig. S6 for the (nonsignificant) mediation models conducted with baseline PIB and baseline thickness instead of baseline FTP. (B) Voxelwise analyses showing the regional associations between increasing patient's age and lower FTP-SUVR or atrophy rates (see fig. S7 for unthresholded maps and <https://neurovault.org/collections/WLDODMCY/> to access the 3D maps). (C) Association between patient's age and the topographical similarity between patterns of baseline FTP-SUVR and subsequent atrophy measured using voxelwise spatial correlation (as described in Fig. 3); see fig. S5 for similar plot with PIB.

higher atrophy rates in heterogeneous groups of patients, although contradicting results exist (32, 33). Our finding of an association between global cortical FTP and global cortical atrophy (Fig. 2A) confirms that this relationship is not driven by the inclusion of AD (high biomarker, high atrophy) and controls or non-AD (low biomarker, low atrophy) patients, but exists within a group of patients with biomarker-confirmed AD. The replicability of the tau biomarker/subsequent atrophy association across biomarker types (fluid versus imaging) is also consistent with the relationships found between PET and CSF measures of tau (23, 34, 35). The topographical information embedded in the PET data constitutes a major advantage compared to CSF markers. We demonstrated that tau-PET is not only predictive of how much but also of where atrophy will occur, which has major implications for patient prognosis and clinical trials.

Our findings suggest that tau-PET could be useful for the design of clinical trials and could increase the ability to detect a treatment effect even over a relatively short time frame (36, 37). First, tau-PET could be used to enrich trials with patients with tau-PET signal predictive of upcoming atrophy or to stratify patients in trials based on the degree of expected atrophy in the upcoming year. Second, tau-PET could help determine how (i.e., where) atrophy should be measured to maximize study sensitivity. A major issue of using MRI to monitor disease progression is the interindividual heterogeneity

in atrophy patterns (38), even when selecting patients with a classic amnesic phenotype as in the Alzheimer's Disease Neuroimaging Initiative (12, 39). A given generic ROI (e.g., the hippocampus) would not optimally capture every patient's brain atrophy [e.g., patients with "hippocampal-sparing" (38, 40)]. Alternative options exist to maximize detection of AD atrophy using data-driven ROIs (41) or adapting the ROI to specific phenotypes (42), but our data suggest that PET could be used to create patient-tailored, FTP-informed ROIs for atrophy detection. This approach could capture tau-mediated neurodegeneration in every patient in a more optimal manner, agnostic of any a priori assumptions. Alternatively, the tight relationship between tau and atrophy might imply that, in regions with elevated tau-PET signal, the pathological cascade leading to neurodegeneration has already been triggered and that neurodegeneration processes are now uncoupled from tau pathology. In that case, anti-tau therapies could be more effective in preventing atrophy in regions with low to mild tau-PET signal, whereas atrophy in high tau-PET regions would be difficult to modify with anti-tau therapies.

Clinical decline measured with the CDR-SB was associated with atrophy in the precuneus but was not correlated with baseline FTP-PET. This weak relationship might be related to methodological factors: the small sample size, the intrinsic noise of measuring clinical progression based on two time points, or the use of memory-centric

CDR-SB in a clinically diverse cohort like ours that includes language, and visuospatial-predominant AD phenotypes. Alternatively, the lack of correlation with FTP could also reflect the indirect relationship between tau pathology and clinical deficits that is thought to be at least partly mediated by brain degeneration (10).

In contrast to tau-PET, neither the burden nor topography of A β -PET was a strong predictor of future atrophy. This is consistent with multiple reports that A β -PET has no or weak relationships with the patterns of neurodegeneration or clinical deficits at symptomatic stages (8, 43), although associations might be found at earlier (preclinical) stage (44). The quantitative and topographical dissociation between A β and neurodegeneration is also consistent with autopsy data (45, 46). To our knowledge, the relationships between baseline volume or thickness and future atrophy have not been thoroughly investigated, but studies have suggested that atrophy accelerates over time, before decelerating in later stages (18, 19). This nonlinear relationship might explain why we could not identify consistent and robust relationships between baseline MRI findings and subsequent atrophy.

Baseline tau-PET accounted for ~40 to 50% of the severity and topography of subsequent atrophy in our cohort. Future investigations will be needed to study additional predictors of atrophy [e.g., inflammation (47), nonlocal effects of pathology (48, 49), or additional brain pathologies (50)] to further our understanding of the complex mechanisms underlying neurodegeneration in AD.

Our analyses identified patient's age as an important factor regarding not only the severity of tau burden and brain atrophy but also the relationship between pathology and longitudinal atrophy. First, we replicated previous findings that later age of disease onset is associated with lower tau-PET burden (8, 11) and longitudinal atrophy rates (12–14). Moreover, we showed that the spatial association between FTP and longitudinal atrophy sharply decreased with patient's age (Fig. 5), in line with a recent cross-sectional study (51). Together, these results are consistent with the idea that early-onset AD might constitute a more pure form of AD in which neurodegeneration is mainly driven by AD pathology, whereas later-onset clinical AD is multifactorial, associated with distinctive risk factors, and related to more frequent co-morbidities and co-pathologies (52, 53). Previous clinicopathological studies showed that the relationship between AD neuropathology and dementia decreased in older patients (54). Together, growing evidence suggests that potential disease-modifying drugs that specifically target AD neuropathology may benefit patients with earlier-onset AD more than older patients.

A number of study features and limitations should be highlighted to appropriately interpret our results. First, note that PET signal is only a proxy for underlying pathology, and although postmortem studies suggest that FTP binds to paired helical filaments of tau (55, 56), "off target" signal unrelated to tau in the basal ganglia (57, 58) and in some tau-negative conditions (59, 60) raises questions about specificity. Second, the sample size was modest, though similar to previous cross-sectional tau-PET/atrophy association studies. The use of complementary robust statistical approaches, and the inspection of all scatter plots and images, showed that results were not influenced by outliers. Third, the patients included in our study constitute an academic-based cohort of diverse and relatively young patients, which may limit generalizability. Note that the results remained unchanged when excluding non-amnesic variants (language or visuospatial phenotypes of AD; see fig. S8).

Fourth, our cohort encompassed early clinical stages of AD, and the results cannot be extrapolated to earlier (i.e., preclinical) or more severe stages of the disease, when neurodegeneration might be associated or driven by distinct mechanisms. Fifth, because of the recent development of FTP, patients only had one follow-up MRI after the baseline visit, and additional time points would enable a more precise characterization of atrophy trajectories. Future studies will be needed to determine the prognostic value of baseline tau-PET over longer follow-up. Similarly, clinical decline was evaluated on the basis of two time points only, and more data would be needed to improve signal to noise; the limited available time points, together with the heterogeneity of the cohort, might account for the lack of associations between baseline tau-PET and clinical decline. Last, our patients underwent MRI scanning on two different Siemens 3-T scanners, which might have added noise to the estimation of longitudinal atrophy. However, further analyses showed that the present results were found independently of MRI scanning protocol (fig. S9).

In summary, our study illustrates the potential of PET imaging to identify the pathological drivers of neurodegeneration in AD and to help predict individual patients' future evolution. These results outline the robust local relationships between accumulation of tau-containing paired helical filament and neurodegeneration, emphasizing tau as a relevant target for disease-modifying drugs at this early clinical stage (61). Additional studies will be needed to extend our approach to larger cohorts, notably considering additional disease stages, older age of onset, and longer follow-up duration.

MATERIALS AND METHODS

Experimental design

The main objective of this study was to test whether amyloid and tau-PET could predict future brain atrophy in patients at symptomatic stages of AD. Data were derived from an ongoing longitudinal observational study including repeated MRI, PIB-PET, and FTP-PET in patients with a clinical diagnosis of AD at the mild cognitive impairment or dementia stage. No power analysis was performed before the study, but the sample size is within the range of previous papers assessing relationships between tau-PET and brain volume in symptomatic patients (6–7, 17). Data preprocessing steps were performed using automated pipeline agnostic of the baseline tau- and amyloid-PET data. Quality control of the preprocessing steps was done blind to the baseline PET measures. No outlier was detected, and all data were included in all analyses and plotted on each figure.

Patients

All patients underwent a comprehensive clinical evaluation (10) at the University of California, San Francisco (UCSF) Memory and Aging Center. We selected patients who (i) had a clinical diagnosis of AD [at either the mild cognitive impairment or dementia stage (62, 63)], (ii) had undergone 3-T structural MRI, FTP-PET, and PIB-PET at their baseline visit, (iii) had a positive PIB-PET [based on visual read (64)], and (iv) had a follow-up 3-T MRI at least 9 months after the first visit. By 1 December 2018, 36 patients fulfilled these criteria, but 4 were excluded because of movement artifacts on an MRI and/or failure of the longitudinal MRI pipeline. The remaining 32 patients were included in the analyses.

Written informed consent was obtained from all patients or their surrogates. The study was approved by the University of California (San Francisco and Berkeley) and Lawrence Berkeley National Laboratory institutional review boards for human research.

Image acquisition

T1-weighted magnetization-prepared rapid gradient echo MRI sequences were acquired at UCSF, on either a 3-T Siemens Tim Trio or a 3-T Siemens Prisma Fit scanner. Both scanners had very similar acquisition parameters (sagittal slice orientation; slice thickness, 1.0 mm; slices per slab, 160; in-plane resolution, 1.0×1.0 mm; matrix, 240×256 ; repetition time, 2300 ms; inversion time, 900 ms; flip angle, 9°), although echo time slightly differed (Trio, 2.98 ms; Prisma, 2.9 ms).

PET data were acquired on a Siemens Biograph PET/computer tomography (CT) scanner at the Lawrence Berkeley National Laboratory. Both radiotracers were synthesized and radiolabeled at the Lawrence Berkeley National Laboratory's Biomedical Isotope Facility. Here, we analyzed PET data that were acquired from 50 to 70 min after the injection of ~ 15 mCi of PIB (four 5-min frames) and 80 to 100 min after the injection of ~ 10 mCi of FTP (four 5-min frames). A low-dose CT scan was performed for attenuation correction before PET acquisition, and PET data were reconstructed using an ordered subset expectation maximization algorithm with weighted attenuation and smoothed with a 4-mm Gaussian kernel with scatter correction (calculated image resolution, $6.5 \times 6.5 \times 7.25$ mm based on Hoffman phantom).

SUVr calculation

Each patient's baseline MRI was segmented using FreeSurfer 5.3 (<https://surfer.nmr.mgh.harvard.edu/>) and Statistical Parametric Mapping 12 (SPM12; Wellcome Department of Imaging Neuroscience, Institute of Neurology, London, UK) to create tracer-specific PET reference regions. PET frames were realigned, averaged, and coregistered onto their corresponding MRI. SUVr images were created using FreeSurfer-defined cerebellar GM for PIB-PET. For FTP, FreeSurfer segmentation was combined with the SUIT template (65) (which was reverse-normalized to each patient individual space using SPM12) to only include inferior cerebellum voxels, therefore avoiding contamination from off-target binding in the dorsal cerebellum (58, 66).

Longitudinal pipeline and voxelwise analyses

For each patient, the baseline and follow-up MRIs were processed using SPM12 pairwise longitudinal registration (24), creating a within-patient midpoint average MRI and a 3D Jacobian rate map reflecting an annualized measure of volumetric change. In this original Jacobian map, negative values indicate contraction over time (e.g., classically in the brain), whereas positive values indicate expansion (e.g., in the ventricles). The Jacobian maps were reversed (i.e., multiplied by -1), so higher values in the cortex indicate greater atrophy. PIB and FTP-SUVr images were moved from baseline MRI space to the midpoint average MRI space using SPM12's deformation toolbox, to be aligned with the Jacobian rate map.

The mid-point average MRI was then segmented into GM, white matter, and CSF. The tissue segments were used to derive a binary GM mask, which was later masked to exclude basal ganglia [because of FTP off-target binding (57) and relative sparing in AD] and cerebellum (i.e., PET reference region) using the Hammers atlas (67), resulting in a binary cerebral cortical mask (see fig. S1 for illustration).

The reversed Jacobian rate map and the PET-SUVr images were finally smoothed within this mask using AFNI 3dBlurInMask command and applying differential kernels (4 mm for PET and 8 mm for Jacobians), so all three images had equivalent final smoothness (fig. S1). These images were used to calculate spatial correlations between patterns of atrophy (Jacobian values) and PET binding (Fig. 3).

PIB, FTP, and Jacobian maps from all patients were warped to Montreal Neurological Institute space using the deformation parameters estimated during the midpoint average MRI segmentation step and averaged to create across patient averages for PIB SUVr, FTP SUVr, and Jacobians (Fig. 1). Template-warped Jacobian maps were entered in a voxelwise one-sample t test to detect areas of significant atrophy (reversed Jacobians > 0) over time (Fig. 1). All voxelwise results were presented using an uncorrected voxel threshold of $P < 0.001$ combined with a corrected cluster threshold of $P_{FWE} < 0.05$; voxels that reached more conservative voxel-level thresholds ($P_{FWE} < 0.05$ and $P_{FWE} < 0.001$) were also highlighted.

FreeSurfer segmentation and ROI analyses

To quantify baseline cortical neurodegeneration (i.e., in a cross-sectional design), we used the FreeSurfer segmentation outputs derived from the previous step (see the "SUVr calculation" section) and based on the first MRI. The average thickness measure of each of the 68 cortical ROIs was extracted from each patient's FreeSurfer directory and converted into a Z score based on the code and the data provided by Potvin *et al.* (25). Briefly, patients' thickness values were converted into Z scores denoting the deviation from their expected values, as calculated based on the patient's characteristics (age, sex, estimated total intracranial volume, scanner manufacturer, and magnetic field strength) and a normative multicentric sample of 2713 healthy controls aged 18 to 94 years. This approach was previously used to quantify cortical thickness in AD (68).

To assess the correlation between the patterns of baseline GM and subsequent atrophy (i.e., are regions that shrink over time already abnormally small at baseline?), we extracted the average SPM12-generated Jacobian values from each of the 68 FreeSurfer ROIs for each patient. Average FTP-PET SUVr values were extracted from all 68 ROIs using a PVC algorithm based on geometric transfer matrix technique [see (58, 66)]. LMEMs were run including all ROIs from all patients (including random slopes and intercepts for both factors), with longitudinal atrophy (Jacobian values) as the dependent variable, and baseline thickness Z score and/or FTP-SUVr_{PVC} as predictors.

Statistical analyses

All statistical analyses were conducted using MATLAB 2015a (MathWorks Inc., www.mathworks.com/) and the Robust correlation toolbox (69) to calculate Pearson correlation estimates and percentile bootstrap CI (from which P values were derived). Jamovi (www.jamovi.org) was used to conduct multiple regressions, analyses of variance (ANOVAs), mediation analyses, and LMEMs using dedicated modules. Details about each specific analysis are provided with the description of the analyses in Results or the Supplementary Materials.

Imaging results were displayed on 3D brain surfaces using BrainNet Viewer (70) and ggseg (<https://lcbc-uo.github.io/ggseg/>). Data file S1 contains most of the data used in the analyses presented in the article.

SUPPLEMENTARY MATERIALS

stm.sciencemag.org/cgi/content/full/12/524/eaau5732/DC1

Fig. S1. Image processing pipeline related to the voxelwise spatial correlation analyses presented in Fig. 3.

Fig. S2. Image processing pipeline related to the ROI analyses shown in Figs. 4 and 5.

Fig. S3. LMEMs using FreeSurfer-defined cortical ROIs and non-PVC SUVR data (related to Fig. 4 and table S2).

Fig. S4. Associations between neuroimaging measures and clinical decline.

Fig. S5. Association between patient's age and global neuroimaging measures (related to Fig. 6).

Fig. S6. Summary of bivariate associations and mediation models between global cortical neuroimaging measures at baseline, global cortical longitudinal atrophy, and age (related to Fig. 6).

Fig. S7. Voxelwise associations between patient's age, baseline FTP-PET, and longitudinal atrophy (related to Fig. 6).

Fig. S8. Analyses of the influence of atypical AD phenotypes on the main results.

Fig. S9. Analyses of the influence of MRI scanner switch on the main results.

Table S1. Details of linear regression models presented in Fig. 2.

Table S2. Details of LMEMs shown in Fig. 4.

Data file S1. Data used for the analyses presented in the manuscript.

[View/request a protocol for this paper from Bio-protocol.](#)

REFERENCES AND NOTES

- B. T. Hyman, C. H. Phelps, T. G. Beach, E. H. Bigio, N. J. Cairns, M. C. Carrillo, D. W. Dickson, C. Duyckaerts, M. P. Frosch, E. Masliah, S. S. Mirra, P. T. Nelson, J. A. Schneider, D. R. Thal, B. Thies, J. Q. Trojanowski, H. V. Vinters, T. J. Montine, National Institute on Aging—Alzheimer's Association guidelines for the neuropathologic assessment of Alzheimer's disease. *Alzheimers Dement.* **8**, 1–13 (2012).
- C. Duyckaerts, B. Delatour, M.-C. Potier, Classification and basic pathology of Alzheimer disease. *Acta Neuropathol.* **118**, 5–36 (2009).
- W. E. Klunk, H. Engler, A. Nordberg, Y. Wang, G. Blomqvist, D. P. Holt, M. Bergström, I. Savitcheva, G.-F. Huang, S. Estrada, B. Ausén, M. L. Debnath, J. Barletta, J. C. Price, J. Sandell, B. J. Lopresti, A. Wall, P. Koivisto, G. Antoni, C. A. Mathis, B. Långström, Imaging brain amyloid in Alzheimer's disease with Pittsburgh Compound-B. *Ann. Neurol.* **55**, 306–319 (2004).
- D. T. Chien, S. Bahri, A. K. Szardenings, J. C. Walsh, F. Mu, M.-Y. Su, W. R. Shankle, A. Elizarov, H. C. Kolb, Early clinical PET imaging results with the novel PHF-tau radioligand [F-18]-T807. *J. Alzheimers Dis.* **34**, 457–468 (2013).
- H. Cho, J. Y. Choi, M. S. Hwang, J. H. Lee, Y. J. Kim, H. M. Lee, C. H. Lyoo, Y. H. Ryu, M. S. Lee, Tau PET in Alzheimer disease and mild cognitive impairment. *Neurology* **87**, 375–383 (2016).
- L. Iaccarino, G. Tammewar, N. Ayakta, S. L. Baker, A. Bejanin, A. L. Boxer, M. L. Gorno-Tempini, M. Janabi, J. H. Kramer, A. Lazaris, S. N. Lockhart, B. L. Miller, Z. A. Miller, J. P. O'Neil, R. Ossenkoppele, H. J. Rosen, D. R. Schonhaut, W. J. Jagust, G. D. Rabinovici, Local and distant relationships between amyloid, tau and neurodegeneration in Alzheimer's Disease. *Neuroimage Clin.* **17**, 452–464 (2018).
- I. M. Nasrallah, Y. J. Chen, M.-K. Hsieh, J. S. Phillips, K. Ternes, G. E. Stockbower, Y. Sheline, C. T. McMillan, M. Grossman, D. A. Wolk, ¹⁸F-flortaucipir PET/MRI correlations in nonamnestic and amnestic variants of Alzheimer disease. *J. Nucl. Med.* **59**, 299–306 (2018).
- R. Ossenkoppele, D. R. Schonhaut, M. Schöll, S. N. Lockhart, N. Ayakta, S. L. Baker, J. P. O'Neil, M. Janabi, A. Lazaris, A. Cantwell, J. Vogel, M. Santos, Z. A. Miller, B. M. Bettcher, K. A. Vossel, J. H. Kramer, M. L. Gorno-Tempini, B. L. Miller, W. J. Jagust, G. D. Rabinovici, Tau PET patterns mirror clinical and neuroanatomical variability in Alzheimer's disease. *Brain* **139**, 1551–1567 (2016).
- J. Dronse, K. Fliessbach, G. N. Bischof, B. von Reutern, J. Faber, J. Hammes, G. Kuhnert, B. Neumaier, O. A. Onur, J. Kukulja, T. van Eimeren, F. Jessen, G. R. Fink, T. Klockgether, A. Drzezga, In vivo Patterns of tau pathology, amyloid- β burden, and neuronal dysfunction in clinical variants of Alzheimer's disease. *J. Alzheimers Dis.* **55**, 465–471 (2017).
- A. Bejanin, D. R. Schonhaut, R. La Joie, J. H. Kramer, S. L. Baker, N. Sosa, N. Ayakta, A. Cantwell, M. Janabi, M. Lauriola, J. P. O'Neil, M. L. Gorno-Tempini, Z. A. Miller, H. J. Rosen, B. L. Miller, W. J. Jagust, G. D. Rabinovici, Tau pathology and neurodegeneration contribute to cognitive impairment in Alzheimer's disease. *Brain* **140**, 3286–3300 (2017).
- M. J. Pontecorvo, M. D. Devous, M. Navitsky, M. Lu, S. Salloway, F. W. Schaefer, D. Jennings, A. K. Arora, A. McGeehan, N. C. Lim, H. Xiong, A. D. Joshi, A. Siderowf, M. A. Mintun; 18F-AV-1451-A05 investigators, Relationships between flortaucipir PET tau binding and amyloid burden, clinical diagnosis, age and cognition. *Brain* **140**, 748–763 (2017).
- C. M. Fiford, G. R. Ridgway, D. M. Cash, M. Modat, J. Nicholas, E. N. Manning, I. B. Malone, G. J. Biessels, S. Ourselin, O. T. Carmichael, M. J. Cardoso, J. Barnes; Alzheimer's Disease Neuroimaging Initiative, Patterns of progressive atrophy vary with age in Alzheimer's disease patients. *Neurobiol. Aging* **63**, 22–32 (2018).
- H. Cho, S. Jeon, S. J. Kang, J.-M. Lee, J.-H. Lee, G. H. Kim, J. S. Shin, C. H. Kim, Y. Noh, K. Im, S. T. Kim, J. Chin, S. W. Seo, D. L. Na, Longitudinal changes of cortical thickness in early- versus late-onset Alzheimer's disease. *Neurobiol. Aging* **34**, 1921.e9–1921.e15 (2013).
- D. Holland, R. S. Desikan, A. M. Dale, L. K. McEvoy; Alzheimer's Disease Neuroimaging Initiative, Rates of decline in Alzheimer disease decrease with age. *PLOS ONE* **7**, e42325 (2012).
- L. E. M. Wisse, S. R. Das, C. Davatzikos, B. C. Dickerson, S. X. Xie, P. A. Yushkevich, D. A. Wolk, Defining SNAP by cross-sectional and longitudinal definitions of neurodegeneration. *Neuroimage Clin.* **18**, 407–412 (2018).
- M. R. LaPoint, J. P. Chhatwal, J. Sepulcre, K. A. Johnson, R. A. Sperling, A. P. Schultz, The association between tau PET and retrospective cortical thinning in clinically normal elderly. *Neuroimage* **157**, 612–622 (2017).
- S. R. Das, L. Xie, L. E. M. Wisse, R. Ittyerah, N. J. Tustison, B. C. Dickerson, P. A. Yushkevich, D. A. Wolk; Alzheimer's Disease Neuroimaging Initiative, Longitudinal and cross-sectional structural magnetic resonance imaging correlates of AV-1451 uptake. *Neurobiol. Aging* **66**, 49–58 (2018).
- K. K. Leung, J. W. Bartlett, J. Barnes, E. N. Manning, S. Ourselin, N. C. Fox, Cerebral atrophy in mild cognitive impairment and Alzheimer disease: Rates and acceleration. *Neurology* **80**, 648–654 (2013).
- M. R. Sabuncu, R. S. Desikan, J. Sepulcre, B. T. T. Yeo, H. Liu, N. J. Schmansky, M. Reuter, M. W. Weiner, R. L. Buckner, R. A. Sperling, B. Fischl; Alzheimer's Disease Neuroimaging Initiative, The dynamics of cortical and hippocampal atrophy in Alzheimer disease. *Arch. Neurol.* **68**, 1040–1048 (2011).
- J. M. Cedarbaum, M. Jaros, C. Hernandez, N. Coley, S. Andrieu, M. Grundman, B. Vellas; Alzheimer's Disease Neuroimaging Initiative, Rationale for use of the Clinical Dementia Rating Sum of Boxes as a primary outcome measure for Alzheimer's disease clinical trials. *Alzheimers Dement.* **9**, S45–S55 (2013).
- M. L. Gorno-Tempini, A. E. Hillis, S. Weintraub, A. Kertesz, M. Mendez, S. F. Cappa, J. M. Ogar, J. D. Rohrer, S. Black, B. F. Boeve, F. Manes, N. F. Dronkers, R. Vandenberghe, K. Rascovsky, K. Patterson, B. L. Miller, D. S. Knopman, J. R. Hodges, M. M. Mesulam, M. Grossman, Classification of primary progressive aphasia and its variants. *Neurology* **76**, 1006–1014 (2011).
- S. J. Crutch, J. M. Schott, G. D. Rabinovici, M. Murray, J. S. Snowden, W. M. van der Flier, B. C. Dickerson, R. Vandenberghe, S. Ahmed, T. H. Bak, B. F. Boeve, C. Butler, S. F. Cappa, M. Ceccaldi, L. C. de Souza, B. Dubois, O. Felician, D. Galasko, J. Graff-Radford, N. R. Graff-Radford, P. R. Hof, P. Krolak-Salmon, M. Lehmann, E. Magnin, M. F. Mendez, P. J. Nestor, C. U. Onyike, V. S. Pelak, Y. Pijnenburg, S. Primativo, M. N. Rossor, N. S. Ryan, P. Scheltens, T. J. Shakespeare, A. S. González, D. F. Tang-Wai, K. X. X. Yong, M. Carrillo, N. C. Fox; Alzheimer's Association ISTAART Atypical Alzheimer's Disease and Associated Syndromes Professional Interest Area, Consensus classification of posterior cortical atrophy. *Alzheimers Dement.* **13**, 870–884 (2017).
- R. La Joie, A. Bejanin, A. M. Fagan, N. Ayakta, S. L. Baker, V. Bourakova, A. L. Boxer, J. Cha, A. Karydas, G. Jerome, A. Maass, A. Mensing, Z. A. Miller, J. P. O'Neil, J. Pham, H. J. Rosen, R. Tsai, A. V. Visani, B. L. Miller, W. J. Jagust, G. D. Rabinovici, Associations between [¹⁸F] AV1451 tau PET and CSF measures of tau pathology in a clinical sample. *Neurology* **90**, e282–e290 (2018).
- J. Ashburner, G. R. Ridgway, Symmetric diffeomorphic modeling of longitudinal structural MRI. *Front. Neurosci.* **6**, 197 (2013).
- O. Potvin, L. Dieumegarde, S. Duchesne; Alzheimer's Disease Neuroimaging Initiative, Normative morphometric data for cerebral cortical areas over the lifetime of the adult human brain. *Neuroimage* **156**, 315–339 (2017).
- A. Bejanin, R. La Joie, B. Landeau, S. Belliard, V. de La Sayette, F. Eustache, B. Desgranges, G. Chételat, Distinct interplay between atrophy and hypometabolism in Alzheimer's versus semantic dementia. *Cereb. Cortex* **29**, 1889–1899 (2019).
- T. M. Harrison, R. La Joie, A. Maass, S. L. Baker, K. Swinnerton, L. Fenton, T. J. Melling, L. Edwards, J. Pham, B. L. Miller, G. D. Rabinovici, W. J. Jagust, Longitudinal tau accumulation and atrophy in aging and Alzheimer disease. *Ann. Neurol.* **85**, 229–240 (2019).
- L.-O. Wahlund, K. Blennow, Cerebrospinal fluid biomarkers for disease stage and intensity in cognitively impaired patients. *Neurosci. Lett.* **339**, 99–102 (2003).
- W. J. P. Hennenman, H. Vrenken, J. Barnes, I. C. Sluiter, N. A. Verwey, M. A. Blankenstein, M. Klein, N. C. Fox, P. Scheltens, F. Barkhof, W. M. van der Flier, Baseline CSF p-tau levels independently predict progression of hippocampal atrophy in Alzheimer disease. *Neurology* **73**, 935–940 (2009).
- R. Tarawneh, D. Head, S. Allison, V. Buckles, A. M. Fagan, J. H. Ladenson, J. C. Morris, D. M. Holtzman, Cerebrospinal fluid markers of neurodegeneration and rates of brain atrophy in early Alzheimer disease. *JAMA Neurol.* **72**, 656–665 (2015).

31. A. M. Fjell, K. B. Walhovd, C. Fennema-Notestine, L. K. McEvoy, D. J. Hagler, D. Holland, J. B. Brewer, A. M. Dale; Alzheimer's Disease Neuroimaging Initiative, CSF Biomarkers in prediction of cerebral and clinical change in mild cognitive impairment and Alzheimer's disease. *J. Neurosci.* **30**, 2088–2101 (2010).
32. N. Schuff, N. Woerner, L. Boreta, T. Kornfield, L. M. Shaw, J. Q. Trojanowski, P. M. Thompson, C. R. Jack, M. W. Weiner; Alzheimer's Disease Neuroimaging Initiative, MRI of hippocampal volume loss in early Alzheimer's disease in relation to ApoE genotype and biomarkers. *Brain* **132**, 1067–1077 (2009).
33. J. D. Sluimer, F. H. Bouwman, H. Vrenken, M. A. Blankenstein, F. Barkhof, W. M. van der Flier, P. Scheltens, Whole-brain atrophy rate and CSF biomarker levels in MCI and AD: A longitudinal study. *Neurobiol. Aging* **31**, 758–764 (2010).
34. N. Mattsson, M. Schöll, O. Strandberg, R. Smith, S. Palmqvist, P. S. Insel, D. Hägerström, T. Ohlsson, H. Zetterberg, J. Jögi, K. Blennow, O. Hansson, ¹⁸F-AV-1451 and CSF T-tau and P-tau as biomarkers in Alzheimer's disease. *EMBO Mol. Med.* **9**, 1212–1223 (2017).
35. J. P. Chhatwal, A. P. Schultz, G. A. Marshall, B. Boot, T. Gomez-Isla, J. Dumurgier, M. LaPoint, C. Scherzer, A. D. Roe, B. T. Hyman, R. A. Sperling, K. A. Johnson, Temporal T807 binding correlates with CSF tau and phospho-tau in normal elderly. *Neurology* **87**, 920–926 (2016).
36. J. M. Schott, J. W. Bartlett, J. Barnes, K. K. Leung, S. Ourselin, N. C. Fox, Reduced sample sizes for atrophy outcomes in Alzheimer's disease trials: Baseline adjustment. *Neurobiol. Aging* **31**, 1452–1462.e2 (2010).
37. D. M. Cash, J. D. Rohrer, N. S. Ryan, S. Ourselin, N. C. Fox, Imaging endpoints for clinical trials in Alzheimer's disease. *Alzheimers Res. Ther.* **6**, 87 (2014).
38. J. L. Whitwell, D. W. Dickson, M. E. Murray, S. D. Weigand, N. Tosakulwong, M. L. Senjem, D. S. Knopman, B. F. Boeve, J. E. Parisi, R. C. Petersen, C. R. Jack, K. A. Josephs, Neuroimaging correlates of pathologically defined subtypes of Alzheimer's disease: A case-control study. *Lancet Neurol.* **11**, 868–877 (2012).
39. X. Zhang, E. C. Mormino, N. Sun, R. A. Sperling, M. R. Sabuncu, B. T. T. Yeo; Alzheimer's Disease Neuroimaging Initiative, Bayesian model reveals latent atrophy factors with dissociable cognitive trajectories in Alzheimer's disease. *Proc. Natl. Acad. Sci. U.S.A.* **113**, E6535–E6544 (2016).
40. M. E. Murray, N. R. Graff-Radford, O. A. Ross, R. C. Petersen, R. Duara, D. W. Dickson, Neuropathologically defined subtypes of Alzheimer's disease with distinct clinical characteristics: A retrospective study. *Lancet Neurol.* **10**, 785–796 (2011).
41. B. A. Gutman, Y. Wang, I. Yanovsky, X. Hua, A. W. Toga, C. R. Jack, M. W. Weiner, P. M. Thompson, Empowering imaging biomarkers of Alzheimer's disease. *Neurobiol. Aging* **36** (Suppl. 1), S69–S80 (2015).
42. S. D. Edland, M. C. Ard, J. Sridhar, D. Cobia, A. Martersteck, M. M. Mesulam, E. J. Rogalski, Proof of concept demonstration of optimal composite MRI endpoints for clinical trials. *Alzheimers Dement.* **2**, 177–181 (2016).
43. R. La Joie, A. Perrotin, L. Barré, C. Hommet, F. Mézence, M. Ibazizene, V. Camus, A. Abbas, B. Landeau, D. Guilloteau, V. de La Sayette, F. Eustache, B. Desgranges, G. Chételat, Region-specific hierarchy between atrophy, hypometabolism, and β -amyloid (A β) load in Alzheimer's disease dementia. *J. Neurosci.* **32**, 16265–16273 (2012).
44. G. Chételat, V. L. Villemagne, P. Bourgeat, K. E. Pike, G. Jones, D. Ames, K. A. Ellis, C. Szoek, R. N. Martins, G. J. O'Keefe, O. Salvado, C. L. Masters, C. C. Rowe; Australian Imaging Biomarkers and Lifestyle Research Group, Relationship between atrophy and β -amyloid deposition in Alzheimer disease. *Ann. Neurol.* **67**, 317–324 (2010).
45. E. Falke, J. Nisanov, T. W. Mitchell, D. A. Bennett, J. Q. Trojanowski, S. E. Arnold, Subicular dendritic arborization in Alzheimer's disease correlates with neurofibrillary tangle density. *Am. J. Pathol.* **163**, 1615–1621 (2003).
46. T. Gómez-Isla, R. Hollister, H. West, S. Mui, J. H. Growdon, R. C. Petersen, J. E. Parisi, B. T. Hyman, Neuronal loss correlates with but exceeds neurofibrillary tangles in Alzheimer's disease. *Ann. Neurol.* **41**, 17–24 (1997).
47. A.-C. Dupont, B. Largeau, M. J. Santiago Ribeiro, D. Guilloteau, C. Tronel, N. Arlicot, Translocator protein-18 kDa (TSPO) Positron Emission Tomography (PET) imaging and its clinical impact in neurodegenerative diseases. *Int. J. Mol. Sci.* **18**, E785 (2017).
48. P. Bourgeat, G. Chételat, V. L. Villemagne, J. Fripp, P. Raniga, K. Pike, O. Acosta, C. Szoek, S. Ourselin, D. Ames, K. A. Ellis, R. N. Martins, C. L. Masters, C. C. Rowe, O. Salvado, β -amyloid burden in the temporal neocortex is related to hippocampal atrophy in elderly subjects without dementia. *Neurology* **74**, 121–127 (2010).
49. E. Klupp, T. Grimmer, M. Tahmasian, C. Sorg, I. Yakushev, B. H. Yousefi, A. Drzezga, S. Förster, Frontal hypometabolism in Alzheimer disease is related to longitudinal amyloid accumulation in remote brain regions. *J. Nucl. Med.* **56**, 399–404 (2015).
50. K. A. Josephs, D. W. Dickson, N. Tosakulwong, S. D. Weigand, M. E. Murray, L. Petrucelli, A. M. Liesinger, M. L. Senjem, A. J. Spychalla, D. S. Knopman, J. E. Parisi, R. C. Petersen, C. R. Jack, J. L. Whitwell, Rates of hippocampal atrophy and presence of post-mortem TDP-43 in patients with Alzheimer's disease: A longitudinal retrospective study. *Lancet Neurol.* **16**, 917–924 (2017).
51. J. L. Whitwell, J. Graff-Radford, N. Tosakulwong, S. D. Weigand, M. M. Machulda, M. L. Senjem, A. J. Spychalla, P. Vemuri, D. T. Jones, D. A. Drubach, D. S. Knopman, B. F. Boeve, N. Ertekin-Taner, R. C. Petersen, V. J. Lowe, C. R. Jack, K. A. Josephs, Imaging correlations of tau, amyloid, metabolism, and atrophy in typical and atypical Alzheimer's disease. *Alzheimers Dement.* **14**, 1005–1014 (2018).
52. A. A. J. Gerritsen, C. Bakker, F. R. J. Verhey, M. E. de Vugt, R. J. F. Melis, R. T. C. M. Koopmans, 4C study team, Prevalence of comorbidity in patients with young-onset Alzheimer disease compared with late-onset: A comparative cohort study. *J. Am. Med. Assoc.* **17**, 318–323 (2016).
53. G. D. Rabinovici, M. C. Carrillo, M. Forman, S. DeSanti, D. S. Miller, N. Kozauer, R. C. Petersen, C. Randolph, D. S. Knopman, E. E. Smith, M. Isaac, N. Mattsson, L. J. Bain, J. A. Hendrix, J. R. Sims, Multiple comorbid neuropathologies in the setting of Alzheimer's disease neuropathology and implications for drug development. *Alzheimers Dement.* **3**, 83–91 (2017).
54. B. D. James, D. A. Bennett, P. A. Boyle, S. Leurgans, J. A. Schneider, Dementia from Alzheimer disease and mixed pathologies in the oldest old. *JAMA* **307**, 1798–1800 (2012).
55. M. Marquie, E. E. Verwer, A. C. Meltzer, S. J. W. Kim, C. Agüero, J. Gonzalez, S. J. Makaretz, M. Siao Tick Chong, P. Ramanan, A. C. Amaral, M. D. Normandin, C. R. Vanderburg, S. N. Gomperts, K. A. Johnson, M. P. Frosch, T. Gómez-Isla, Lessons learned about [F-18]-AV-1451 off-target binding from an autopsy-confirmed Parkinson's case. *Acta Neuropathol. Commun.* **5**, 75 (2017).
56. K. Sander, T. Lashley, P. Gami, T. Gendron, M. F. Lythgoe, J. D. Rohrer, J. M. Schott, T. Revesz, N. C. Fox, E. Årstad, Characterization of tau positron emission tomography tracer [¹⁸F]AV-1451 binding to postmortem tissue in Alzheimer's disease, primary tauopathies, and other dementias. *Alzheimers Dement.* **12**, 1116–1124 (2016).
57. J. Y. Choi, H. Cho, S. J. Ahn, J. H. Lee, Y. H. Ryu, M. S. Lee, C. H. Lyoo, Off-target ¹⁸F-AV-1451 binding in the basal ganglia correlates with age-related iron accumulation. *J. Nucl. Med.* **59**, 117–120 (2018).
58. S. L. Baker, A. Maass, W. J. Jagust, Considerations and code for partial volume correcting [¹⁸F]-AV-1451 tau PET data. *Data Brief* **15**, 648–657 (2017).
59. S. N. Lockhart, N. Ayakta, J. R. Winer, R. La Joie, G. D. Rabinovici, W. J. Jagust, Elevated ¹⁸F-AV-1451 PET tracer uptake detected in incidental imaging findings. *Neurology* **88**, 1095–1097 (2017).
60. R. M. Tsai, A. Bejanin, O. Lesman-Segev, R. LaJoie, A. Visani, V. Bourakova, J. P. O'Neil, M. Janabi, S. Baker, S. E. Lee, D. C. Perry, L. Bajorek, A. Karydas, S. Spina, L. T. Grinberg, W. W. Seeley, E. M. Ramos, G. Coppola, M. L. Gorno-Tempini, B. L. Miller, H. J. Rosen, W. Jagust, A. L. Boxer, G. D. Rabinovici, ¹⁸F-flortaucipir (AV-1451) tau PET in frontotemporal dementia syndromes. *Alzheimers Res. Ther.* **11**, 13 (2019).
61. L. Bakota, R. Brandt, Tau biology and tau-directed therapies for Alzheimer's disease. *Drugs* **76**, 301–313 (2016).
62. G. M. McKhann, D. S. Knopman, H. Chertkow, B. T. Hyman, C. R. Jack Jr., C. H. Kawas, W. E. Klunk, W. J. Koroshetz, J. J. Manly, R. Mayeux, R. C. Mohs, J. C. Morris, M. N. Rossor, P. Scheltens, M. C. Carrillo, B. Thies, S. Weintraub, C. H. Phelps, The diagnosis of dementia due to Alzheimer's disease: Recommendations from the National Institute on Aging-Alzheimer's Association workgroups on diagnostic guidelines for Alzheimer's disease. *Alzheimers Dement.* **7**, 263–269 (2011).
63. M. S. Albert, S. T. DeKosky, D. Dickson, B. Dubois, H. H. Feldman, N. C. Fox, A. Gamst, D. M. Holtzman, W. J. Jagust, R. C. Petersen, P. J. Snyder, M. C. Carrillo, B. Thies, C. H. Phelps, The diagnosis of mild cognitive impairment due to Alzheimer's disease: Recommendations from the National Institute on Aging-Alzheimer's Association workgroups on diagnostic guidelines for Alzheimer's disease. *Alzheimers Dement.* **7**, 270–279 (2011).
64. G. D. Rabinovici, H. J. Rosen, A. Alkalay, J. Kornak, A. J. Furst, N. Agarwal, E. C. Mormino, J. P. O'Neil, M. Janabi, A. Karydas, M. E. Growdon, J. Y. Jang, E. J. Huang, S. J. Dearmond, J. Q. Trojanowski, L. T. Grinberg, M. L. Gorno-Tempini, W. W. Seeley, B. L. Miller, W. J. Jagust, Amyloid vs FDG-PET in the differential diagnosis of AD and FTL. *Neurology* **77**, 2034–2042 (2011).
65. J. Diedrichsen, J. H. Balsters, J. Flavell, E. Cussans, N. Ramnani, A probabilistic MR atlas of the human cerebellum. *Neuroimage* **46**, 39–46 (2009).
66. A. Maass, S. Landau, S. L. Baker, A. Hornig, S. N. Lockhart, R. La Joie, G. D. Rabinovici, W. J. Jagust; Alzheimer's Disease Neuroimaging Initiative, Comparison of multiple tau-PET measures as biomarkers in aging and Alzheimer's disease. *Neuroimage* **157**, 448–463 (2017).
67. A. Hammers, R. Allom, M. J. Koeppe, S. L. Free, R. Myers, L. Lemieux, T. N. Mitchell, D. J. Brooks, J. S. Duncan, Three-dimensional maximum probability atlas of the human brain, with particular reference to the temporal lobe. *Hum. Brain Mapp.* **19**, 224–247 (2003).
68. H. Girard, O. Potvin, S. Nugent, C. Dallaire-Thérout, S. Cunnane, S. Duchesne; Alzheimer's Disease Neuroimaging Initiative, Faster progression from MCI to probable AD for carriers of a single-nucleotide polymorphism associated with type 2 diabetes. *Neurobiol. Aging* **64**, 157.e11–157.e17 (2018).
69. C. R. Pernet, R. Wilcox, G. A. Rousselet, Robust correlation analyses: False positive and power validation using a new open source matlab toolbox. *Front. Psychol.* **3**, 606 (2012).

70. M. Xia, J. Wang, Y. He, BrainNet Viewer: A network visualization tool for human brain connectomics. *PLOS ONE* **8**, e68910 (2013).

Acknowledgments: We thank the patients and their caregivers for their participation in the study. Avid Radiopharmaceuticals enabled use of the [18 F]flortaucipir tracer by providing precursor but did not provide direct funding and was not involved in data analysis or interpretation. **Funding:** Alzheimer's Association (AARF-16-443577 to R.L.J.), National Institute on Aging grants (R01-AG045611 to G.D.R.; P50-AG023501 to B.L.M. and G.D.R.; P01-AG19724 to W.J.J., B.L.M., and G.D.R.), Tau Consortium (to G.D.R. and W.J.J.), and State of California Department of Health Services Alzheimer's Disease Research Centre of California grant (04-33516 to B.L.M.). **Author contributions:** Study conceptualization: R.L.J. and G.D.R.; data acquisition and quality control: R.L.J., A.V.V., S.L.B., V.B., K.C., L.E., M.J., O.H.L.-S., Z.A.M., D.C.P., J.P.O., J.P., J.C.R., H.J.R., R.M.T., B.L.M., W.J.J., and G.D.R.; data processing and methodology: R.L.J., A.V.V., S.L.B., J.A.B., V.B., J.C., L.E., L.I., O.H.L.-S., and W.W.S.; data analysis: R.L.J.; writing the original draft: R.L.J.; reviewing and editing manuscript: all authors; supervision: G.D.R.; project administration and resources: K.C.; funding acquisition: R.L.J., B.L.M., W.J.J., and G.D.R. **Competing interests:** D.C.P. receives support from the NIH (K23AG045289). J.C.R. receives support from the NIH (R01 AG038791 PI, Adam Boxer) and travel funds from Eli Lilly. S.L.B. consults for Genentech. W.W.S. receives research support from NIH/NIA and has received consulting fees from Merck Inc., Biogen Idec, and Bristol-Myers Squibb. H.J.R. receives research support from the NIH/National Institute on Aging, R01 AG032306 (PI), P01 AG019724 (Core leader), AG045333 (PI), and AG023501 (Core leader). R.M.T. receives research support from the University of California. R.M.T. also consulted for ExpertConnect and Grifols. B.L.M. receives research support from the NIH/NIA and the Centers for Medicare & Medicaid Services (CMS) as grants for the Memory and Aging Center. As an additional disclosure, B.L.M. serves as Medical

Director for the John Douglas French Foundation; Scientific Director for the Tau Consortium; Director/Medical Advisory Board of the Larry L. Hillblom Foundation; Scientific Advisory Board Member for the National Institute for Health Research Cambridge Biomedical Research Centre and its subunit, the Biomedical Research Unit in Dementia (UK); and Board Member for the American Brain Foundation (ABF). W.J.J. has served as a consultant to BioClinica, Genentech, and Novartis Pharmaceuticals. G.D.R. receives research support from Avid Radiopharmaceuticals, GE Healthcare, and Life Molecular Imaging and has received consulting fees or speaking honoraria from Axon Neurosciences, Roche, Eisai, Genentech, Merck. The other authors declare that they have no competing interests. **Data and materials availability:** Most data associated with this study are available in the main text, supplementary data file, or on neurovault for group-level voxelwise images (<https://neurovault.org/collections/WLDODMCY/>). Individual MRI and PET images data will be shared with external investigators upon submission of a proposal and under a data transfer agreement.

Submitted 3 August 2018
Resubmitted 13 September 2019
Accepted 13 November 2019
Published 1 January 2020
10.1126/scitranslmed.aau5732

Citation: R. La Joie, A. V. Visani, S. L. Baker, J. A. Brown, V. Bourakova, J. Cha, K. Chaudhary, L. Edwards, L. Iaccarino, M. Janabi, O. H. Lesman-Segev, Z. A. Miller, D. C. Perry, J. P. O'Neil, J. Pham, J. C. Rojas, H. J. Rosen, W. W. Seeley, R. M. Tsai, B. L. Miller, W. J. Jagust, G. D. Rabinovici, Prospective longitudinal atrophy in Alzheimer's disease correlates with the intensity and topography of baseline tau-PET. *Sci. Transl. Med.* **12**, eaau5732 (2020).

GENE THERAPY

Gene therapy delivering a paraoxonase 1 variant offers long-term prophylactic protection against nerve agents in mice

Venkaiah Betapudi*, Reena Goswami, Liliya Silayeva[†], Deborah M. Doctor, Nageswararao Chilukuri[‡]

Chemical warfare nerve agents are organophosphorus chemical compounds that induce cholinergic crisis, leaving little or no time for medical intervention to prevent death. The current chemical treatment regimen may prevent death but does not prevent postexposure complications such as brain damage and permanent behavioral abnormalities. In the present study, we have demonstrated an adeno-associated virus 8 (AAV8)-mediated paraoxonase 1 variant IF-11 (PON1-IF11) gene therapy that offers asymptomatic prophylactic protection to mice against multiple lethal doses of G-type chemical warfare nerve agents, namely, tabun, sarin, cyclosarin, and soman, for up to 5 months in mice. A single injection of liver-specific adeno-associated viral particles loaded with PON1-IF11 gene resulted in expression and secretion of recombinant PON1-IF11 in milligram quantities, which has the catalytic power to break down G-type chemical warfare nerve agents into biologically inactive products *in vitro* and *in vivo* in rodents. Mice containing milligram concentrations of recombinant PON1-IF11 in their blood displayed no clinical signs of toxicity, as judged by their hematological parameters and serum chemistry profiles. Our study unfolds avenues to develop a one-time application of gene therapy to express a near-natural and circulating therapeutic PON1-IF11 protein that can potentially protect humans against G-type chemical warfare nerve agents for several weeks to months.

INTRODUCTION

Chemical warfare nerve agents (CWNAs) are colorless, odorless, and tasteless organophosphorus (OP) compounds being used as invisible lethal weapons in war zones and civilian societies worldwide (1–3). These toxic chemical compounds and their closely related pesticides are used in the form of gas, vapor, and liquid (4, 5). The first nerve agent, tabun (GA), was synthesized by Gerhard Schrader in Germany in 1936 potentially for agricultural purposes, but the modern world is believed to have stockpiles of several nerve agents categorized into G series (GA, GD, GF, and GB), V series (VE, VG, VM, VP, VR, and VX), insecticides (malathion and parathion), and many more (5, 6). These dangerous chemicals are frequently used in modern wars and terrorist attacks (7–9). Pesticides are relatively less toxic than nerve agents but are believed to be responsible for nearly a quarter million annual deaths in developing countries and pose a greater threat to public health because of their widespread use for domestic and agricultural purposes (10).

OP chemicals enter the bloodstream through the skin, food, and drink, as well as by inhalation, cross the blood-brain barrier, and irreversibly inhibit acetylcholinesterase (AChE; EC 3.1.1.7), a key enzyme of the central nervous system, to disrupt normal communication between brain and muscles, causing miosis, hypersalivation, lacrimation, involuntary urination and defecation, seizures, and rapid death from respiratory failure (11, 12). Medical intervention with the available synthetic chemical regimen including atropine sulfate, 2-pyridine aldoxime methyl chloride (2-PAM), and diazepam is a

common practice to offer relief and remission and to prevent death (13). Because these synthetic chemical therapeutics do not offer relief from postexposure complications such as convulsions, performance deficits, and permanent brain damage, pretreatment with pyridostigmine bromide (PB) appears advantageous to military and medical personnel (14). However, PB use has been suspected to be associated with Gulf War illness and to cause other medical issues such as diarrhea, vomiting, cold sweats, and blurred vision (15). Therefore, an alternative approach could be pretreatment with a natural or recombinant protein-based therapeutic capable of scavenging/hydrolyzing nerve agents into biologically inactive products before their escaping from blood circulation. Among protein-based scavengers of nerve agents, butyrylcholinesterase (BChE; EC 3.1.1.8), OP hydrolase (OPH; EC 3.1.8.1), and paraoxonase 1 (PON1; EC 3.1.8.1) appear promising in offering prophylactic protection in animal models. However, BChE binds OP compounds at a one-to-one ratio; therefore, this enzyme is required in large quantities to afford protection against CWNAs (16, 17). Both OPH and PON1 in their native forms or their variants hydrolyze nerve agents in a catalytic manner and are promising bioscavengers to offer prophylactic protection against OP nerve agents. However, their short circulating half-lives, immunogenicity behavior, degradation, and rapid clearance from the bloodstream have become serious issues in developing them into prophylactics against CWNAs (18–20). Also, nanocapsulation, polysialylation, PEGylation, and polycarboxybetaine conjugation of these protein-based bioscavengers failed to resolve the issues of their poor circulation stability and immunogenicity (21–24). Therefore, in this study, we adopted a gene therapy approach to express bioscavengers in the bloodstream to offer long-term protection against multiple lethal dosages of CWNAs. Previously, we demonstrated gene therapy as a viable approach by expressing human and mouse BChE, wild-type PON1, and its variants VIID11 and IF11 using adenoviral vectors in mice; however, their expression in the circulation lasted for less than 8 days because of the immunogenic

Copyright © 2020
The Authors, some
rights reserved;
exclusive license
American Association
for the Advancement
of Science. No claim
to original U.S.
Government Works

Medical Toxicology Research Division, Biochemistry & Physiology Department, Agent Mitigation, United States Army Medical Research Institute of Chemical Defense, 8350 Ricketts Point Road, Aberdeen Proving Ground, MD 21010-5400, USA.

*Present address: Research and Development Division, Countering Weapons of Mass Destruction, U.S. Department of Homeland Security, 1120 Vermont Ave., Washington, DC 20005, USA.

[†]Present address: ADS Federal, 4401 N. Fairfax Dr., Suite 321, Arlington, VA 22203, USA.

[‡]Corresponding author. Email: nageswararao.chilukuri.civ@mail.mil

nature of adenoviral vectors (23, 25). Here, we tested a relatively nontoxic adeno-associated virus 8 (AAV8) vector to express PON1 variant, namely, IF11 (PON1-IF11) in mouse systemic circulation for extended periods of time, and to offer protection against lethal dosages of all G-type CWNA. We selected PON1-IF11 for this study because this enzyme, compared to four other variants, displayed the highest racemic catalytic efficiencies for G-type CWNA and also the highest preference to the hydrolysis of the more toxic isomer than the nontoxic isomer (23). Now, we report that a one-time administration of AAV8 carrying PON1-IF11 gene (AAV8-PON1-IF11) resulted in high expression and secretion of PON1-IF11 recombinant protein in the circulation and conferred asymptomatic protection against multiple lethal dosages of all G-type CWNA for at least 5 months. Our study unfolds avenues to develop AAV8-based prophylactics for agricultural workers and soldiers as well as for animals working in military, medical, and homeland security operations.

RESULTS

PON1-IF11 expression in mouse blood using AAV8-vectored gene therapy and characterization of the enzyme

We tested three different promoters to accomplish the long-term and high expression of recombinant PON1-IF11 at therapeutic concentrations in the bloodstream of mice using the AAV8 vector: (i) a liver-specific thyroxine-binding globulin (TBG) promoter (26); (ii) a muscle-specific synthetic promoter consisting of fragments of the cytomegalovirus immediate early promoter (CMV), chimeric chicken- β -actin promoter, and ubiquitin C enhancer element (CASI) (27); and (iii) the ubiquitous CMV promoter in AAV8 viral vectors (fig. S1). AAV8 with TBG vector was chosen because it was found to be the most efficient for liver-targeted gene delivery expression (26). Synthetic CASI promoter was chosen because of the report by Balazs *et al.* (27) suggesting that milligram concentrations of HIV neutralized immunoglobulin production in mice. Purity of AAV8-PON1-IF11 particles was tested by subjecting them to polyacrylamide gel electrophoresis (PAGE) and Coomassie blue staining (fig. S2). Mice were transduced by giving a single tail vein injection of viral particles at a dosage of $\sim 9 \times 10^{12}$ GC (gene copies) per mouse. The active recombinant PON1-IF11 enzyme expression in mouse circulation was determined over a period of 150 days using paraoxon as the substrate. The activity profiles of PON1-IF11 in mouse plasma are shown in Fig. 1A. Relative to the enzyme activity in the plasma of mice injected with AAV8 vector lacking PON1-IF11 gene (control), sera from mice injected with AAV8-PON1-IF11 vectors containing CMV and CASI promoters showed substantially low concentrations of PON1-IF11 protein (Fig. 1A). In contrast, the plasma from mice injected with AAV8-PON1-IF11 vector containing TBG promoter displayed high levels of PON1-IF11 enzyme activity through the entire 5-month experimental duration. After AAV8-TBG-PON1-IF11 vector delivery into the mouse tail vein, PON1-IF11 expression began to rise on day 3, reached to peak concentrations on day 21, and then declined slightly to steady-state concentrations, which were maintained through the 150-day experimental duration. PON1-IF11 protein concentrations in mouse plasma were found to be 1.5 to 2.5 mg/ml on day 21 and 1.0 to 1.5 mg/ml thereafter through the 5-month duration. These mice containing milligram concentrations of PON1-IF11 in their bloodstreams for over 5 months displayed no visible symptoms of toxicity by daily visual examination of their behavior. These results show that a single tail vein injection

of AAV8-TBG-PON1-IF11 vector is capable of inducing production of PON1-IF11 recombinant protein in milligram quantity in the mouse systemic circulation.

To determine whether the AAV8-TBG-PON1-IF11 vector-expressed recombinant PON1-IF11 was full length and intact, pooled plasma samples from mice expressing recombinant PON1-IF11 on days 3, 7, 14, 21, 28, 35, 42, and 56 were analyzed by Western blotting with polyclonal rabbit anti-PON1-G3C9 antibody. The PON1-G3C9 antibodies cross-react with PON1-IF11 because both variants differ only by eight amino acids and maintain 98% structural similarity. These antibodies recognized a doublet of ~ 42 - and ~ 45 -kDa PON1-IF11 proteins in all the plasma samples collected from mice on days 3 to 56 after transduction (Fig. 1B). Purified bacterial PON1-IF11 with a 37-kDa molecular weight and plasma from mice injected with AAV8 vector-lacking PON1-IF11 gene were included to serve as positive and negative controls in this experiment, respectively. The fact that the AAV8-TBG-PON1-IF11-transduced recombinant PON1-IF11 in mouse plasma is a doublet with ~ 42 and ~ 45 kDa relative to a single band of 37 kDa for the bacterial PON1-IF11 protein suggests that the recombinant PON1-IF11 expressed in mouse is glycosylated. This is in agreement with our previous study in which the PON1-IF11 protein expressed *in vitro* in mammalian cells and in the mouse systemic circulation transduced with adenoviral vector PON1-IF11 also revealed a doublet with ~ 42 and ~ 45 kDa (23). One more notable observation is that despite PON1-IF11 expression in milligram quantity, no smaller molecular weight bands were observed on immunoblots, suggesting its existence as full-length protein in mouse blood without any proteolysis into smaller molecular weight species. These results demonstrate that the recombinant PON1-IF11 expressed in mouse blood by AAV8-mediated gene therapy is full length and intact and circulates without undergoing proteolysis for at least 56 days.

Because an ideal and successful CWNA medical countermeasure should be nontoxic, nonimmunogenic, and intramuscularly injectable to the host, we tested whether an intramuscular injection of AAV8-PON1-IF11 vectors would transduce PON1-IF11 expression in mouse blood. Similar to tail vein injections, mice were transduced by giving a single intramuscular injection of AAV8-PON1-IF11 vectors at a dosage of $\sim 5 \times 10^{12}$ GC per mouse. The expression of the active recombinant PON1-IF11 enzyme in mouse blood was determined on day 27. Very little PON1-IF11 was noted in the plasma samples of mice injected with AAV8-PON1-IF11 vectors carrying CMV and CASI promoters (Fig. 1C). In contrast, the plasma sample from mice injected with AAV8-PON1-IF11 vector containing TBG promoter contained PON1-IF11 at a concentration of 1.2 mg/ml. These results suggest that the AAV8-TBG-PON1-IF11 vectors can be given to mice through the desired intramuscular injection route for expressing recombinant PON1-IF11 in systemic circulation.

Because AAV8-PON1-IF11 vectors with CMV and CASI promoters produced relatively low concentrations of PON1-IF11 in the mouse bloodstream, plasmids used for generating these AAV8 vectors were subjected to quality control by transiently expressing them in liver-specific HepG2 cells. Paraoxon hydrolysis assays using transfected cell growth medium revealed readily measurable PON1-IF11 activity under both CMV and CASI promoters, ruling out the possibility of defective AAV8 plasmid constructs (Fig. 1D).

In vitro hydrolysis of G-type CWNA by PON1-IF11 in mouse blood

In our previous study with recombinant PON1-IF11 expressed *in vitro* in mammalian cells and *in vivo* in mouse blood using adenovirus,

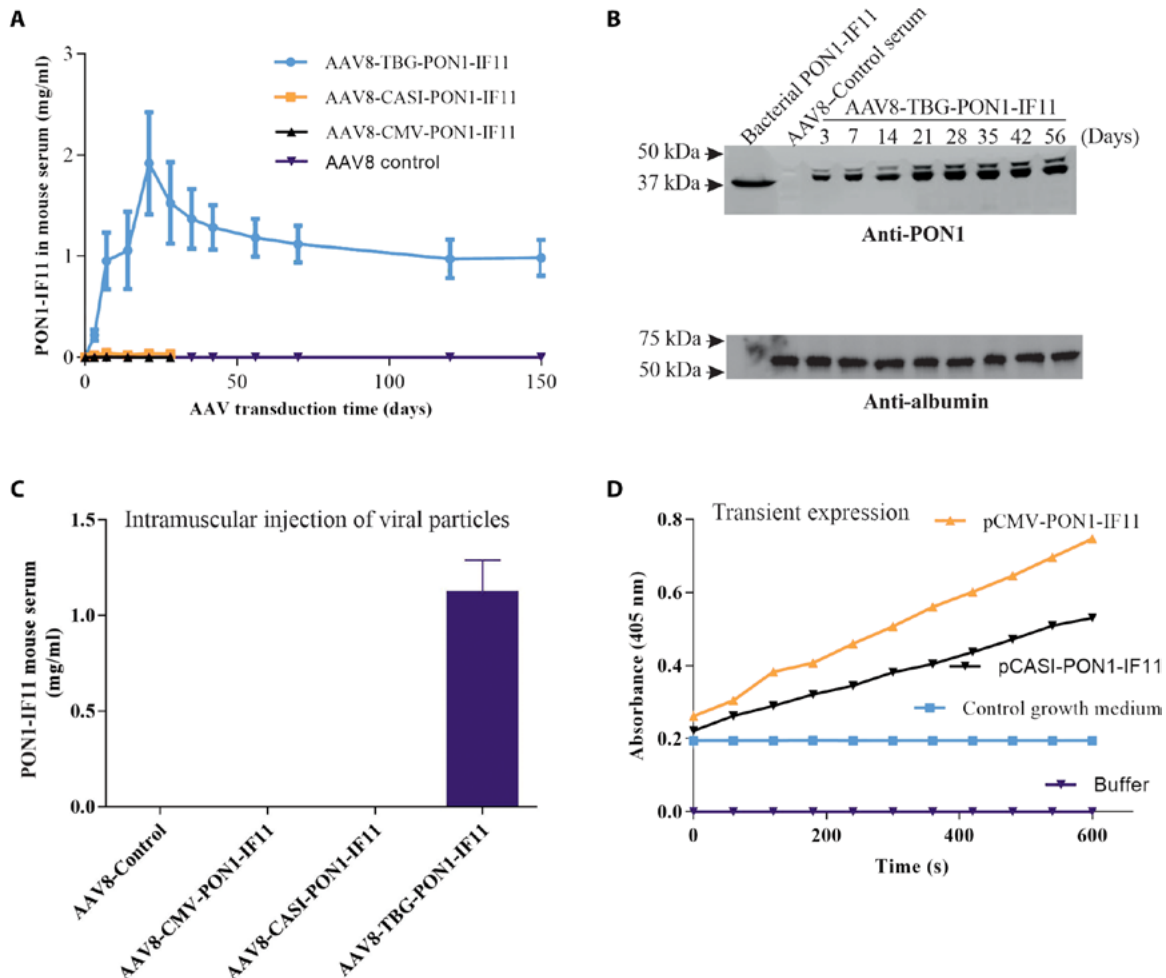


Fig. 1. Long-term expression of PON1-IF11 in mouse blood. (A) Tail vein injection of viral particles and high level expression of PON1-IF11 under the liver-specific TBG promoter. (B) Western blot analysis of mouse plasma and long-term expression of PON1-IF11 under TBG promoter. (C) Intramuscular injection of viral particles and PON1-IF11 enzyme activity in mouse plasma. (D) Transient expression of PON1-IF11 under CMV and CASI promoters in the liver-specific cells.

we reported that recombinant PON1-IF11 is most active against G-type CWNAs, namely, soman (GD; $K_{cat}/K_m = 23 \times 10^6 \text{ M min}^{-1}$) followed by cyclosarin (GF; $K_{cat}/K_m = 9.2 \times 10^6 \text{ M min}^{-1}$), sarin (GB; $K_{cat}/K_m = 2.5 \times 10^6 \text{ M min}^{-1}$), and tabun (GA; $K_{cat}/K_m = 1.1 \times 10^6 \text{ M min}^{-1}$) (23). To determine whether the PON1-IF11 transduced by AAV8-TBG-PON1-IF11 vector in mouse blood would display a similar activity profile, we performed an indirect micro-Ellman assay (28). In this assay, control and test plasma samples were incubated with G-type CWNAs for 30 min at room temperature, and the intact nerve agent was determined by titration with recombinant human AChE in a micro-Ellman reaction. In the micro-Ellman reaction, AChE hydrolyzes acetylthiocholine (ATC) to produce thiocholine, which reacts with 5,5'-dithiobis-(2-nitrobenzoic acid) (DTNB) to produce a yellow-colored compound with λ_{max} at 405 nm. Thus, no absorbance at 405 nm indicates background (Fig. 2A, lane marked Buffer), whereas a gradual increase leading to a steady-state value in absorbance indicates AChE activity (Fig. 2A, lane marked AChE). To determine how this assay works for plasma samples, we performed a micro-Ellman assay to test hydrolysis of GD by control mouse plasma spiked with varying amounts of (0.1 to 2.0 μg) purified bacterial PON1-IF11. We incubated the plasma with GD at room tem-

perature for 30 min, and then a 20 μl of the reaction mixture was assayed in the micro-Ellman assay. As shown in Fig. 2B for lanes marked 1.0 μg and 2.0 μg , absorbance at 405 nm rapidly climbed and plateaued within 2 min, suggesting complete hydrolysis of GD by bacterial PON1-IF11 in these reactions. In contrast, in plasma samples spiked with 0.1, 0.2, and 0.5 μg of PON1-IF11, absorbance at 405 nm is directly proportional to the amount of PON1-IF11 in the reaction mixture (Fig. 2B). Next, the micro-Ellman assay was performed to test activity of AAV8-TBG-PON1-IF11 plasma sample to hydrolyze GD (Fig. 2C), GF (Fig. 2D), GB (Fig. 2E), and GA (Fig. 2F). Control plasma samples incubated with or without GD, GF, GB, and GA were included as negative and positive controls, respectively. As shown in Fig. 2C, control plasma samples lacking GD developed color and showed maximum absorbance at 405 nm; however, when incubated with GD, the reaction showed no absorbance at 405 nm because there was no GD hydrolysis in this sample. However, the plasma from mice injected with AAV8-TBG-PON1-IF11 vector showed time-dependent increase in absorbance at 405 nm, which reached the negative control sample after 60 min, suggesting complete hydrolysis of GD by AAV8 vector-expressed PON1-IF11 ($P < 0.0001$; Fig. 2C). Similarly, the PON1-IF11-expressing plasma

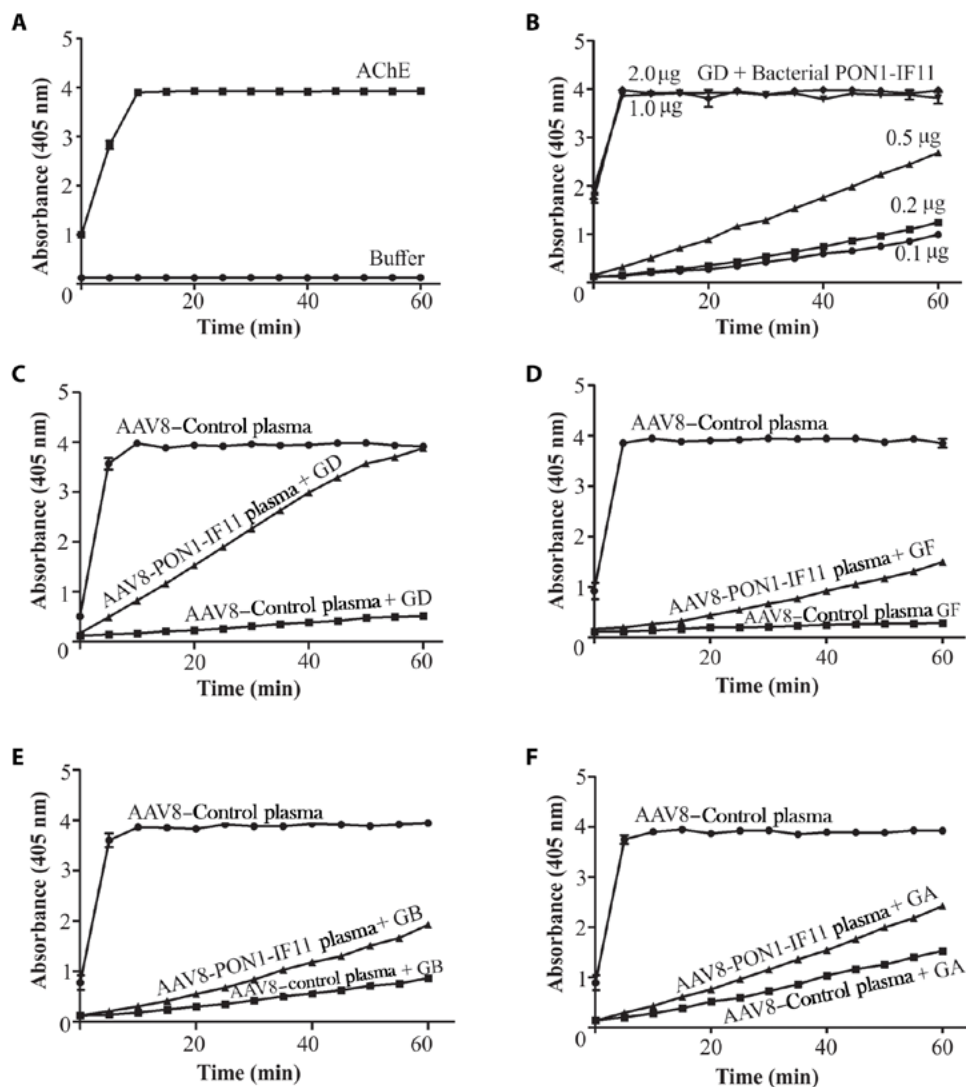


Fig. 2. In vitro hydrolysis of G-type nerve agents by plasma from mice injected with AAV8-TBG-PON1-IF11. (A) Micro-Ellman assay using AChE and no nerve agent. (B) Purified bacterial PON1-IF11 protein and hydrolysis of GD in vitro. (C) Mouse plasma and hydrolysis of GD in vitro. (D) Mouse plasma and hydrolysis of GF in vitro. (E) Mouse plasma and hydrolysis of GB in vitro. (F) Mouse plasma and hydrolysis of GA in vitro.

sample displayed steady development of yellow color and absorbance at 405 nm to varying amounts with GF ($P < 0.0001$; Fig. 2D), GB ($P < 0.0001$; Fig. 2E), and GA ($P < 0.0001$; Fig. 2F). The auto-hydrolysis rate is somewhat low for GD and GF and high for GB and GA (lanes marked AAV8-Control plasma + GD, GF, GB, and GA in Fig. 2, C, D, E, and F, respectively). This is probably due to the instability of GA and GB in aqueous solutions and hydrolysis of G agents by carboxylesterase in mouse plasma. Collectively, these studies suggest that AAV8-TBG-PON1-IF11 vector-expressed PON1-IF11 in mouse blood is capable of hydrolyzing G-type CWNA with the fastest hydrolysis rate for GD followed by GF, GB, and GA.

In vivo prophylactic efficacy of PON1-IF11 against G-type CWNAs

Having established that the mice injected with AAV8-TBG-PON1-IF11 vector are expressing biologically active PON1-IF11 protein in

systemic circulation in milligram amounts for up to 5 months, the next logical study was to assess its prophylactic efficacy against G-type CWNAs in vivo. For these studies, a new set of 17 animals were injected with AAV8-TBG-PON1-IF11 vector at a concentration of 1.5×10^{13} GC per mouse via the tail vein. On day 21, the mice were found to be expressing PON1-IF11 from 0.37 to 2.5 mg/ml in their plasma (Table 1 and table S1). On day 24, the mice were subcutaneously challenged with a dosage of $5 \times LD_{50}$ (median lethal dose) GD and then monitored for CWNA exposure symptoms, such as Straub tail and tremors, and for 24-hour survival. Similarly, a control naïve animal was exposed to ensure the toxic potency of GD. The control animal died within 1 to 2 min of exposure to GD, whereas the 17 mice injected with AAV8-TBG-PON1-IF11 did not show any signs of GD exposure and scored a 100% 24-hour survival rate (Table 1). On days 28, 30, and 35 after GD exposure, these mice were exposed to a subcutaneous dose of $5 \times LD_{50}$ GF, GB, and GA. Upon exposure to GB, one mouse died. Blood analysis before the challenges showed low expression of PON1-IF11 (0.37 mg/ml) in the circulation. The rest of the mice, expressing PON1-IF11 concentrations at 0.75 mg/ml and higher, resisted successive challenges with the dosage of $5 \times LD_{50}$ GF, GB, and GA and survived symptom-free (Table 1 and the Supplementary Materials).

Because one of our goals has been to lend experimental evidence to the concept that a catalytic enzyme/bioscavenger such as PON1-IF11 is not consumed by binding to CWNAs in the circulation and remains circulating to offer asymptomatic protection against future exposures, first, we measured the plasma concentration of PON1-IF11 in these mice on day 42 and then exposed G-type CWNAs as described above. We found the PON1-IF11 concentrations to vary between 2.4 and 4.4 mg/ml in these mice (Table 1 and table S1). One mouse was removed from the study as it was losing body weight from not eating because of a hind leg injury, an event unrelated to the CWNA exposure. The remaining 15 mice were exposed to a dosage of $5 \times LD_{50}$ GD, GF, GB, and GA on days 49, 50, 51, and 52, respectively. None of these mice displayed any signs of CWNA toxicity and scored 100% survival rates. On day 69, these mice were exposed to a dosage of $6 \times LD_{50}$ CWNA cocktail containing a dosage of $1.5 \times LD_{50}$ GD, GF, GB, and GA and evaluated for CWNA toxic signs and 24-hour survival rates. Once again, all 15 mice tolerated the $6 \times LD_{50}$ cocktail of all G-type nerve agents, showed no signs of CWNA toxicity, and scored 100% survival rate. Thus, 15 mice with PON1-IF11 concentrations of 0.75 mg/ml or

Table 1. Animal survival against nerve agent challenges.

| Number of mice | Postviral transduction (days) | PON1-IF11 in blood (mg/ml) | Nerve agent (5 LD ₅₀) | Animals with toxic signs (%) | Survival (%) |
|----------------|-------------------------------|----------------------------|----------------------------------------------------|------------------------------|--------------|
| 17 | 24 | 0.37 – 2.5 | GD | 0 | 100 |
| 17 | 28 | 0.37 – 2.5 | GF | 0 | 100 |
| 17 | 30 | 0.37 – 2.5 | GB | 6 | 94 |
| 16 | 35 | 0.37 – 2.5 | GA | 0 | 100 |
| 15 | 49 | 2.4 – 4.4 | GD | 0 | 100 |
| 15 | 50 | 2.4 – 4.4 | GF | 0 | 100 |
| 15 | 51 | 2.4 – 4.4 | GB | 0 | 100 |
| 15 | 52 | 2.4 – 4.4 | GA | 0 | 100 |
| 15 | 65 | 2.4 – 4.4 | (GD + GF + GB + GA) total of 6 LD ₅₀ | 0 | 100 |

higher were afforded asymptomatic protection to a total of eight $5 \times \text{LD}_{50}$ exposures of GD, GF, GB, and GA and one $6 \times \text{LD}_{50}$ exposure to a mixture of all four G-type CWNA over a 42-day period. At the time of every CWNA challenge experiment, a naïve control animal was exposed to the same G-type nerve agent preparation to ensure toxicity; death of control animal occurred within 1 min of exposure in all cases. Collectively, these data suggest that PON1-IF11 catalytic bioscavenger, when present in the systemic circulation at a therapeutic concentration, offered asymptomatic protection against multiple lethal dosages of G-type CWNA. Also, our data suggest that a catalytic bioscavenger like PON1-IF11 does not get consumed by CWNA and remains circulating at effective concentration in animals.

Circulating PON1-IF11 concentration in mouse blood and protection efficacy against G-type CWNA

Because PON1-IF11 shows different catalytic efficacies in detoxifying various G-type CWNA in vitro and in vivo (23), understanding the relationship between its concentration in the systemic circulation and the degree of protection offered against a dosage of 2 to $5 \times \text{LD}_{50}$ G-type CWNA is also warranted. Therefore, in this experiment, 20 mice were injected with different numbers of AAV8-TBG-PON1-IF11 vector particles ($1 \times 10^{9-12}$ GC per mouse) so that the mice contained varying concentrations of PON1-IF11 (ranging from 0.030 to 1.05 mg/ml) in their bloodstreams (table S2). These animals were used to establish a relationship between the plasma PON1-IF11 concentrations and protection against a dosage of 2 to $5 \times \text{LD}_{50}$ GD, GF, GB, and GA. In view of the possibility of changing PON1-IF11 concentrations in the blood during the study, before the day of CWNA challenge, plasma samples were collected, and PON1-IF11 concentration was determined for each animal. Animals were challenged with a particular LD_{50} dose of a specific G-type CWNA and observed for cholinergic signs/tremors and 24-hour survival. The experiment began with the animals being challenged with a dosage of $2 \times \text{LD}_{50}$ GD through subcutaneous injection. One naïve animal was challenged with the CWNA as a positive control to account for the toxicity of the nerve agent. Moribund mice were euthanized immediately. The following day, surviving animals were exposed to a dosage of $3 \times \text{LD}_{50}$ GD, and this process was repeated until the data on the cholinergic signs and 24-hour survival rates were determined for 2, 3, 4, and $5 \times \text{LD}_{50}$ dosages of GD, GF, GB, and GA, respectively.

The data are shown in Fig. 3A for GD, Fig. 3B for GF, Fig. 3C for GB, and Fig. 3D for GA. The results showed that ~ 40 to $80 \mu\text{g}$ of PON1-IF11 protein in 1 ml of plasma are required to provide asymptomatic protection against a dosage of 2 to $5 \times \text{LD}_{50}$ GD and plasma (~ 60 to $120 \mu\text{g}/\text{ml}$) for a dosage of 2 to $5 \times \text{LD}_{50}$ GF (Fig. 3B). Much higher concentrations of PON1-IF11 were required to offer the same protection against GB and GA, and they were ~ 120 to $500 \mu\text{g}$ and ~ 150 to $700 \mu\text{g}/\text{ml}$ of plasma, respectively. On the basis of the weight of the mouse being around 33 g, we suggest that a PON1-IF11 concentration of $\sim 1.2 \text{ mg}/\text{kg}$ body weight would provide protection against GD versus $\sim 2.0 \text{ mg}/\text{kg}$ body weight for GF, $\sim 4.0 \text{ mg}/\text{kg}$ body weight for GB, and $\sim 9.0 \text{ mg}/\text{kg}$ body weight for GA. These studies also indicated that PON1-IF11 is most efficacious against GD followed by GF, GB, and GA in offering protection.

Toxicity of PON1-IF11 to the mouse

One of the requirements of a successful prophylactic against CWNA toxicity is that it not only is efficacious but also should be nontoxic protein to the recipient. This is the first time that PON1-IF11, a prophylactic candidate against G-type CWNA, has ever been produced in milligram quantities in vivo in mice blood for more than 5 months. Therefore, we analyzed the toxicity of PON1-IF11 overexpression in mouse blood for extended periods of time. Blood samples ($n = 3$) were examined for serum chemistry parameters (Table 2) and hematology panels (Table 3). Animals were euthanized, and tissues including brain, liver, heart, diaphragm, kidney, pancreas, lung, urinary bladder, prostate gland, epididymis, and skeletal muscle were examined for any gross histological changes by hematoxylin and eosin staining. The slides were processed by trained technicians and read by a board-certified veterinary pathologist. These studies were also performed in mice that survived nine exposures to a dosage of $5 \times \text{LD}_{50}$ G-type CWNA ($n = 3$) and age-matched controls ($n = 3$). Results of necropsy, together with hematology and serum chemistry panels, did not reveal any signs of pathology or gross abnormalities in these experimental animals. A few minor changes were noticed: In particular, one animal in PON1-IF11 group displayed higher numbers of neutrophils and monocytes and lower numbers of lymphocytes and platelets relative to other animals in the same group and others, and the three animals in CWNA-exposed PON1-IF11 animals displayed higher numbers of reticulocytes relative to control group

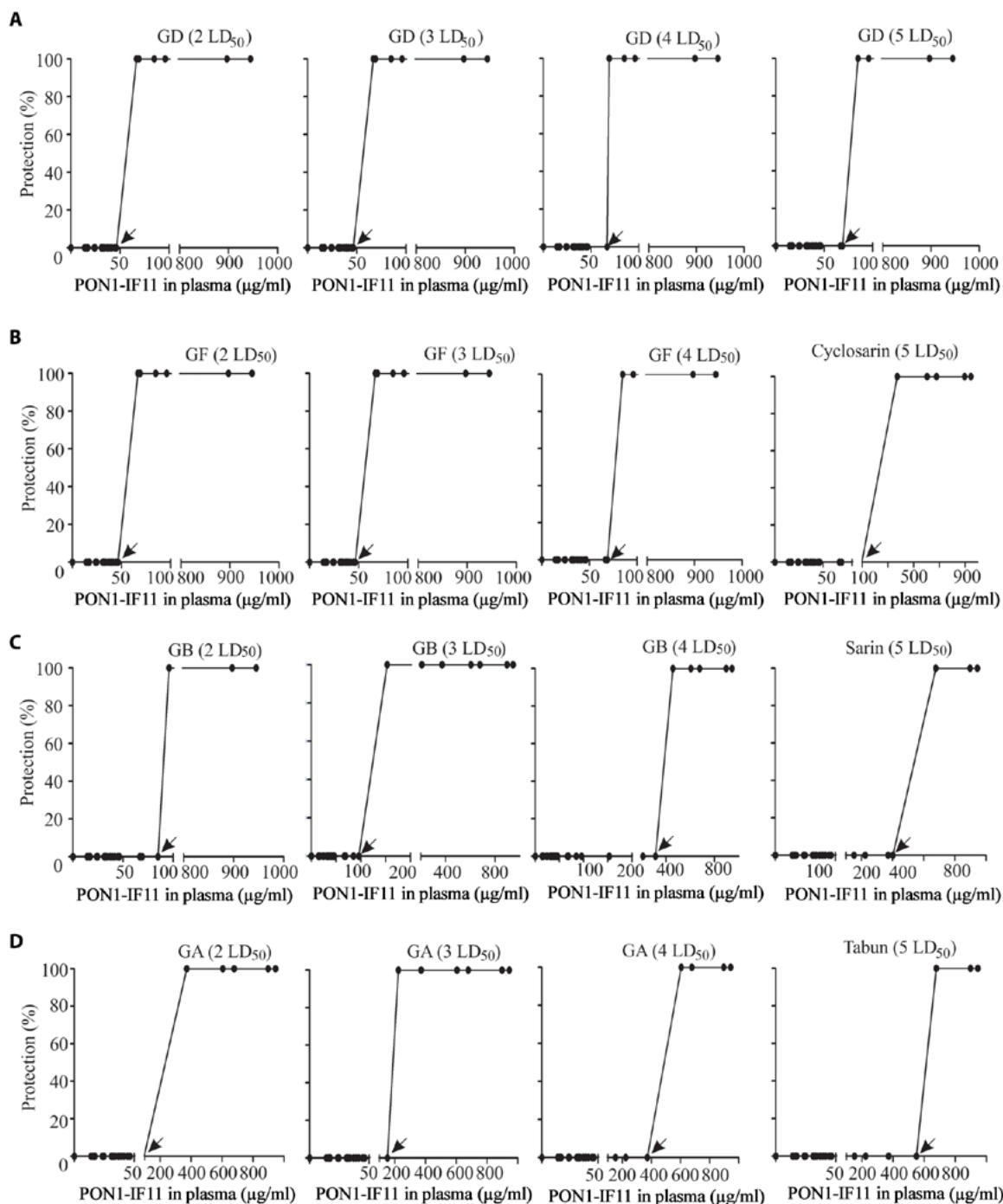


Fig. 3. PON1-IF11 protein concentration in mouse blood circulation and G-type CWNA dosage relationship. Twenty mice expressing variable amounts of PON1-IF11 protein ranging from 0.030 to 1.05 mg/ml plasma were challenged with a dosage of 2 to 5 × LD₅₀ of G-type nerve agents. Arrows indicate that animals require more than that particular amount of circulating PON1-IF11 to survive against nerve agent. **(A)** Circulating PON1-IF11 concentration and protection against GD. **(B)** Circulating PON1-IF11 concentration and protection against GF. **(C)** Circulating PON1-IF11 concentration and protection against GB. **(D)** Circulating PON1-IF11 concentration and protection against GA. Zero percent protection indicates death of the animals, whereas 100% protection indicates that the animal is alive without any observable signs of CWNA toxicity.

and PON1-IF11-expressing animals and a 40% increase in lactate dehydrogenase and creatinine kinase levels in PON1-IF11-expressing animals relative to controls. Otherwise, no abnormalities were observed in the rest of the hematology and serum chemistry panels between age-matched controls, PON1-IF11-overexpressing animals,

and animals that survived multiple G-type CWNA challenges (Tables 2 and 3). Collectively, these results suggest that mice expressing milligram levels of PON1-IF11 for at least 5 months showed little evidence of toxicity, suggesting that PON1-IF11 is relatively non-toxic to mouse.

Table 2. Effect of long-term expression of PON1-IF11 on mouse hematology parameters.* WBC, white blood cell; NEU, neutrophil; LYM, lymphocyte; MONO, monocyte; EOS, eosinophil; BASO, basophil; RBC, red blood cell; HGB, hemoglobin; HCT, hematocrit; MCV, mean cell volume; MCH, mean cell hemoglobin; MCHC, mean cell hemoglobin concentration; RDW-CV, red cell distribution width-CV; RDW-SD, red cell distribution width-SD; PLT, platelets; MPV, mean platelet volume; PCT, plateletcrit; P-LCR, platelet large cell ratio; PDW, platelet distribution width; RET, reticulocytes; IRF, immature reticulocyte fraction; LFR, low fluorescence ratio; MFR, median fluorescence ratio; HFR, high fluorescence ratio.

| Parameter | Control | PON1-IF11 | PON1-IF11-CWNAs |
|-------------------|-----------|-----------|-----------------|
| WBC (K/ μ l) | 2.04–4.76 | 1.89–5.52 | 3.36–4.59 |
| NEU (K/ μ l) | 0.43–0.69 | 0.23–0.84 | 0.42–0.62 |
| NEU (%) | 12.4–21.7 | 12.2–31.0 | 10.3–13.4 |
| LYM (K/ μ l) | 1.48–3.78 | 0.50–4.35 | 2.70–3.79 |
| LYM (%) | 73.0–79.4 | 25.6–78.8 | 80.4–82.6 |
| MONO (K/ μ l) | 0.08–0.34 | 0.15–0.90 | 0.14–0.32 |
| MONO (%) | 3.90–7.80 | 4.5–40.7 | 3.1–7.9 |
| EOS (K/ μ l) | 0.03–0.05 | 0.03–0.08 | 0.04–0.05 |
| EOS (%) | 0.8–2.0 | 1.4–1.6 | 0.9–1.5 |
| BASO (K/ μ l) | 0 | 0 | 0 |
| BASO (%) | 0 | 0 | 0 |
| RBC (M/ μ l) | 9.12–9.9 | 6.5–9.0 | 8.15–9.46 |
| HGB (g/dl) | 12.9–14.6 | 10.0–13.6 | 12.2–13.4 |
| HCT (%) | 40.9–43.5 | 33.0–40.3 | 38.2–42.0 |
| MCV (fl) | 43.2–44.8 | 43.7–50.7 | 42.5–48.3 |
| MCH (Pg) | 14.1–14.8 | 14.2–15.4 | 14.2–15.2 |
| MCHC (g/dl) | 32.7–33.6 | 30.4–33.7 | 31.5–33.3 |
| RDW-CV (%) | 22.2–23.8 | 22.2–23.3 | 24.5–27.0 |
| RDW-SD (fl) | 29.7–32.3 | 31.0–36.8 | 37.8–39.50 |
| PLT (K/ μ l) | 1751–2368 | 733–1954 | 1738–2148 |
| MPV (fl) | 6.7–6.9 | 6.3–8.2 | 4.6–7.7 |
| PCT | 1.2–1.6 | 0.52–1.40 | 1.3–1.4 |
| P-LCR | 5.0–6.0 | 4.0–12.1 | 4.6–7.7 |
| PDW | 7.7–8.4 | 7.5–9.2 | 7.7–8.5 |
| RET (%) | 4.7–5.5 | 4.3–7.4 | 9.1–13.5 |
| RET (M/ μ l) | 0.42–0.51 | 0.40–0.48 | 0.9–1.1 |
| IRF (%) | 56.3–58.0 | 53.0–59.6 | 58.6–59.4 |
| LFR (%) | 41.4–43.7 | 40.4–47.1 | 40.6–41.3 |
| MFR (%) | 16.3–17.0 | 16.1–18.6 | 14.7–16.9 |
| HFR (%) | 39.6–42.3 | 36.9–41.0 | 42.5–43.9 |

*Three mice were used to obtain hematology panels for each group. Six months after AAV8-TBG-PON1-IF11 administration, the mice were euthanized, and blood was collected and processed for hematology panels.

Anti-PON1-IF11 antibody development in mouse blood

PON1-IF11 is a variant of wild-type human PON1 with sequences from rabbit, human, and mouse PON1s (29). If PON1-IF11 is highly immunogenic in the mouse, it will have a serious consequence on

the protein's bioavailability and half-life in vivo. This possibility is addressed by screening the plasma samples collected from the AAV8-TBG-PON1-IF11- and control vector-injected animals (8 and 10 weeks after vector injection) for antibodies against PON1-IF11 by enzyme-linked immunosorbent assay (ELISA) using bacterial PON1-VIID11 variant as an antigen. PON1-IF11 differs from PON1-VIID11 by only two amino acids, at positions 55 and 291 (29). This study revealed a 2.5-fold increase in the immunoreactivity of the plasma samples diluted less than 800 times; however, this increase is negligible with 1:1600 diluted plasma (Fig. 4A). These results suggest the production of anti-PON1-IF11 antibodies in mouse blood, but at low levels.

Next, we investigated whether these antibodies are capable of inhibiting the activity of PON1-IF11 in hydrolyzing paraoxon in vitro. In this assay, control plasma and plasma samples from mice injected with AAV8-TBG-PON1-IF11 vector on day 3 and at weeks 3, 8, and 10 were incubated with or without bacterial PON1-IF11 (30 ng), and paraoxon hydrolysis assay was performed. PON1-IF11 added to these reactions was also assayed separately (lane marked Enz). As shown in Fig. 4B, the bacterial PON1-IF11 activity was fully recovered when PON1-IF11 (Enz) was added to control plasma (lane marked Enz + CP) and third day plasma (lane marked 3rd day + Enz). In contrast, the bacterial PON1-IF11 activity was partially recovered when it was incubated with 3rd week plasma (lane marked 3rd week + Enz) and not at all recovered from 8th week plasma samples (lane marked 8th week + Enz) and 10th week samples (lane marked 10th week + Enz). These results suggest that the 3rd, 8th, and 10th week plasma samples from AAV8-TBG-PON1-IF11 vector-injected mice contain PON1-IF11 inhibitory antibodies, whereas control mouse plasma and plasma from mice injected with AAV8-TBG-PON1-IF11 on day 3 do not contain such antibodies (Fig. 4B). Together, these results suggest that mice are making anti-PON1-IF11 antibodies, but they are not produced in concentrations sufficient to inhibit the entire recombinant PON1-IF11 in mouse blood.

DISCUSSION

In this proof-of-principle study, we have demonstrated AAV8-TBG-PON1-IF11 gene therapy as a viable option for the abundant expression of recombinant PON1-IF11, a promising catalytic bioscavenger that hydrolyzes G-type CWNAs in the mouse bloodstream and provides asymptomatic protection for weeks to months to the host. On the basis of results obtained in the present mouse study, a one-time injection of AAV8-PON1-IF11 vectors carrying a liver-specific TBG promoter has resulted in recombinant PON1-IF11 protein expression in milligram concentrations for at least 5 months in mouse blood circulation. These mice tolerated multiple lethal doses of G-type CWNAs including GD, GF, GB, and GA and remained asymptomatic throughout the study. Mice expressing recombinant PON1-IF11 protein abundantly in their bloodstream did not show any signs of clinical toxicity, suggesting that PON1-IF11 prophylactic is nontoxic in mouse. Together, our study provides experimental evidence and forms a basis for the development of an AAV8-TBG-PON1-IF11 vector-based prophylactic with potential to protect soldiers and medical personnel against G-type CWNA threats in medical and military operations as well as agricultural workers from certain OP pesticide toxicity.

Table 3. Effect of the long-term expression of PON1-IF11 on mouse serum chemistry parameters.*

| Parameter | Control | PON1-IF11 | PON1-IF11-CWNAs | Normal range |
|-----------|---------|-----------|-----------------|--------------------|
| ALB | 2.6 | 2.5 | 2.6 | 2.5–4.6 (g/liter) |
| ALKP | 182 | 118 | 150 | 35–222 (U/liter) |
| ALT | 71 | 99 | 85 | 17–77 (U/liter) |
| AST | 76 | 151 | 70 | 52–298 (U/liter) |
| BUN | 22 | 26 | 26 | 9–33 (mg/dl) |
| Calcium | 10.5 | 10.7 | 10.8 | 6–13 (mg/dl) |
| CK | 391 | 2327 | 159 | 115–1300 (U/liter) |
| Chloride | 111 | 109 | 107 | 81–115 (mM) |
| CREA | 0.2 | 0.3 | 0.3 | 0.5–2.2 (mg/dl) |
| ECO2 | 22 | 24 | 24 | 15–23 (mM) |
| GGT | 10 | 10 | 10 | 17–61 (U/liter) |
| GLU | 237 | 203 | 224 | 140–263 (mg/dl) |
| K | 6.1 | 6.1 | 5.7 | 4–10.5 (mM) |
| LDH | 1436 | 2505 | 910 | 50–600 (U/liter) |
| Na | 149 | 146 | 146 | 110–195 (mM) |
| TBIL | 0.5 | 0.3 | 0.2 | 0–1.0 (mg/dl) |
| TP | 4.8 | 4.6 | 5 | 3.9–6.4 (g/dl) |

*Three mice were used to obtain serum chemistry panels for each group. Six months after AAV8-TBG-PON1-IF11 administration, the mice were euthanized, and blood was collected and processed for chemistry panels. Same amount of serum was used from each animal to make one pooled sample for obtaining serum chemistry panels.

Methods and technologies to develop stoichiometric and catalytic bioscavengers and their sustained expression in the human bloodstream for providing prophylactic protection against a broad spectrum of CWNAs are the need of the hour due to the inherent limitations and shortcomings of the current chemical regimen (2, 8). Many strategies have been developed to introduce therapeutic scavengers in the bloodstream of experimental animals to rapidly hydrolyze CWNAs and to prevent them from reaching their primary target, AChE at the neuromuscular junctions, and other targets in the brain (30, 31). Among the strategies, direct injection of native, recombinant, and/or chemically modified recombinant stoichiometric/catalytic bioscavengers into blood circulation has failed to provide long-term prophylactic protection against CWNAs because the bioscavengers have had poor circulatory stability/rapid clearance (18–20, 24, 32). Adenovirus-mediated gene therapy is somewhat successful by delivering human and mouse BChE, wild-type PON1, and its variants PON1-VIID11 and PON1-IF11 genes into mice but for only 6 to 8 days (23, 25, 33). In contrast, the AAV8 vector with TBG promoter used in the present study has not only displayed long-term expression (at least 5 months) of PON1-IF11 catalytic bioscavenger but also produced the bioscavenger in the amounts required to afford asymptomatic protection against 2 to 5 × LD₅₀ dosages of G-type CWNAs. Also, we tested PON1-IF11 expression under CMV and CASI promoters in mouse blood circulation but found very little expression with these two promoters. Investigating the reasons for substantially low amount expression of PON1-IF11 under CMV and CASI promoters is beyond the scope of the present study. Previously, using AAV8 vectors carrying CASI promoter, lifelong expression of mouse cocaine hydrolase, a mutant BChE,

was reported by Geng *et al.* (34). Although the lifetime expression of mouse cocaine hydrolase showed no toxicity in mice, the enzyme activity reported in that study was in milliunits per milliliter of mouse blood. Therefore, direct comparison to the amount of PON1-IF11 protein expressed in our study to that of the activity of cocaine hydrolase observed in mouse blood by Geng *et al.* (34) could not be made. In addition, Swiss Webster mice were used in our study and BALB/c mice were used in their study (34). Nevertheless, both studies have highlighted the successful application of AAV8 vectors to introduce therapeutic concentrations of scavenger enzymes such as cocaine hydrolase and PON1-IF11 for several months in the mouse bloodstream. More recently, circulation of nanoparticle-based OPH-YT in the rodent bloodstream for 6 to 8 days, offering protection against a dosage of 2 × LD₅₀ paraoxon and GB, was reported (24). In addition, a repeat injection of the nanoparticle-based OPH-YT 2 weeks after the first injection displayed a circulatory stability profile that is identical to the first injection, suggesting that this technology may be promising for developing the enzyme-based therapeutics against CWNA. However, the question remains whether rodents develop inhibitory antidrug antibodies against nanoparticle-based OPH-YT at later time periods, i.e., months and years, which may inhibit or decrease the therapeutic efficacy of repeat injections of nanoparticle-based OPH-YT.

PB is the only prophylactic available against CWNA to date, but a single dose of this chemical drug cannot offer protection for more than 8 hours (16, 35). Therefore, a nontoxic and easily injectable prophylactic that can offer protection against CWNA for several weeks and months is highly desirable. In the present study, we showed that AAV8-TBG-PON1-IF11 vector-mediated gene therapy

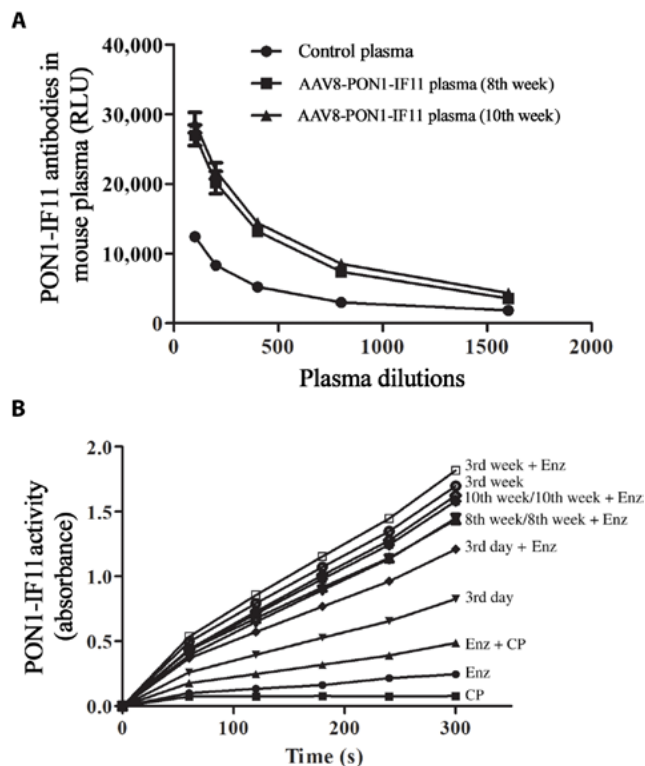


Fig. 4. Development of anti-PON1-IF11 antibodies and their ability to inhibit PON1-IF11 enzyme activity. (A) ELISA to test the presence of anti-PON1-IF11 antibodies in mouse plasma. The presence of antibodies against PON1-IF11 is represented as relative luminescence units (RLUs). (B) Circulating anti-PON1-IF11 antibodies and inhibition of PON1-IF11 enzyme activity in vitro. Purified bacterial PON1-IF11 protein was mixed and incubated at 37°C for 20 min, and enzyme assays were performed using paraoxon as a substrate. Absorbance was measured at 405 nm for 5 min.

meets these criteria in mice. The AAV8 vector-produced PON1-IF11 stays intact and remains active for at least 5 months. AAV8-TBG-PON1-IF11 vectors are easily administered via intramuscular route for the expression of PON1-IF11 at the desired therapeutic concentrations in the mouse bloodstream. The mice carrying milligrams of recombinant PON1-IF11 protein in their systemic circulations for 5 months or longer did not show any clinical signs of overt toxicity, and their serum chemistry and hematology panels and necropsy were not different from those of age-matched controls. Recombinant PON1-IF11 has the added advantage of it being an enzyme that rapidly detoxifies G-type CWNA in a catalytic fashion. Thus, PON1-IF11 in blood circulation will not be consumed during repeated G-type CWNA exposures and is required in much lower concentrations than a stoichiometric enzyme, such as BChE (16). Thus, mice containing as little as 0.7 mg of PON1-IF11 protein per milliliter of blood survived nine times against a dosage of $5 \times LD_{50}$ GD, GF, GB, and GA over a period of 42 days. If exposed every day, these experimental animals with such low concentrations of recombinant PON1-IF11 in their bloodstreams could have survived G-type CWNA toxicity throughout the 5-month experimental period.

In the present study, we have attempted to estimate the approximate amount of PON1-IF11 protein that should be circulating in the mouse bloodstream to afford protection against $2 \times LD_{50}$ dosages of GD, GF, GB, and GA. These studies revealed that the requirement of PON1-IF11 in the circulation is about 1.2 mg/kg body weight to

provide protection against GD versus 2.0 mg/kg body weight for GF, 4.0 mg/kg body weight for GB, and ~9.0 mg/kg body weight for GA. At present, we are not able to translate these data for human use. Humans and nonhuman primates differ from mice in their sensitivity to G-type CWNA; LD_{50} dosages of G-type agents for humans and nonhuman primates are lower than those for mice based on per-kilogram basis. This is because carboxylesterase, an enzyme that detoxifies CWNA, is present in large amounts in mouse blood but lacking in human and nonhuman primate's blood. It has been estimated that a dose of ~3 mg/kg of human BChE is required to afford protection against a $2 \times LD_{50}$ of GD in humans. In comparison, a much lower concentration of PON1-IF11 (1.2 mg/kg body weight) affords protection against $2 \times LD_{50}$ of GD in the mouse. Moreover, the LD_{50} of GD in the mouse is 124 μ g/kg body weight versus 7 and 3.8 μ g/kg body weight for rhesus and cynomolgus macaques, respectively (36). Thus, LD_{50} dosage of GD in the mouse is 18- to 35-fold higher than that for nonhuman primates. Together, our results suggest that PON1-IF11 at a much lower concentration than BChE can afford the same level of protection against G-type CWNA in humans and nonhuman primates. Recently, we showed that PON1-IF11 protein expressed in the mouse bloodstream is in association with high-density lipoprotein (HDL) similar to the endogenous wild-type PON1 (23). It has been shown that the HDL-associated PON1 prevents the oxidation of low-density lipoprotein and plays a beneficial role in preventing diabetes mellitus, atherosclerosis, and cardiovascular diseases (37). It appears that the recombinant PON1-IF11 is a nontoxic "friendly" enzyme to the host by offering protection against G-type CWNA as well as by playing perhaps a beneficial role in preventing cardiovascular diseases.

During the past decade, gene therapy has gained importance in treating hemophilia B, cystic fibrosis, Leber's congenital amaurosis/blind disease involving RPE65 protein deficiency, adenosine deaminase, ornithine transcarbamylase, and lipoprotein lipase deficiency disorders, and cancer (38). AAV is currently among the most frequently used viral vectors for gene therapy because of its potential in delivering therapeutic genes for long-term expression in both dividing and nondividing target cells without causing any known side effects. Also, the advent of recombinant systems, tissue-specific serotypes, organ-specific promoters, and better understanding of immune response have led to their usage in many ongoing clinical trials to treat muscle, eye, dental, neuronal, hematological, metabolic, cardiac, and cancer diseases. The first AAV clinical trial was conducted two decades ago to treat cystic fibrosis, and now, more than 200 AAV-mediated clinical trials are being conducted worldwide. Alipogene tiparvovec or Glybera, an AAV1-based drug, has been approved and used in Europe to treat a lipoprotein lipase deficiency, a rare monogenic genetic disorder that leads to accumulation of triglycerides in human plasma due to lipoprotein lipase gene mutations. Recently, the U.S. Food and Drug Administration has approved an AAV2-based voretigene neparvovec (Luxturna) to treat progressive blindness involving RPE65 protein deficiency (39).

As discussed above, AAV vectors are being used in humans for treating diseases associated with a single gene deficiency and/or terminal disorders where there is no cure available and/or the treatment is very expensive. Our goal is to deliver a prophylactic enzyme to healthy soldiers and medical personnel who may be exposed to CWNA in military warfare and agricultural workers handling OP pesticides. Therefore, both the prophylactic itself and the gene-delivering AAV8 vectors are expected to be absolutely nontoxic to

recipients. Although the past decade of research in nonhuman primates and humans with hemophilia B has shown an excellent safety record for AAV vectors, their long-term safety in healthy humans is still a matter of concern (40, 41). This is due, in part, to the fact that a healthy human being has never been infused with a large dosage of AAV8 vectors and monitored for toxic signs/abnormalities. Until such data are available, we consider our study as a proof of principle that showed promising results in mice: (i) PON1-IF11 catalytic bioscavenger is expressed for at least months in the mouse bloodstream using AAV8-vectored gene therapy, (ii) PON1-IF11 catalytic bioscavenger is efficacious against lethal dosages of G-type CWNAs, (iii) PON1-IF11 catalytic bioscavenger is injectable intramuscularly, and (iv) mice expressing milligrams of recombinant PON1-IF11 show no clinical signs of toxicity to the host. The longest clinical study using AAV vectors is currently ongoing in the United Kingdom, and it is with 15 patients with severe hemophilia B (4 to 7 years) (42). This group published a report in 2014 about the long-term safety and efficacy of factor IX gene therapy using AAV8 in hemophilia B. This study (42) concluded, "a single infusion of AAV8 vector resulted in durable factor IX expression and long-lasting amelioration of bleeding episodes in patients with severe hemophilia B." The findings with respect to the safety of this approach are encouraging, with the main vector-related adverse event being an elevated serum alanine aminotransferase (ALT) amount, an effect that appears to be readily attenuated by a short, tapering course of prednisolone. Therefore, we are cautiously optimistic that AAV8 vectors could be applicable in the future for delivering prophylactics such as PON1-IF11 catalytic bioscavenger in agricultural workers, healthy soldiers, medical personnel, and working dogs to provide protection in CWNA exposure scenarios.

Together, AAV8 vectors carrying the gene for PON1-IF11 under the influence of TBG promoter have the potential to transduce the expression of a fully functional recombinant PON1-IF11 for several months at therapeutic amounts and without evidence of severe side effects in the mouse model. Mice containing recombinant PON1-IF11 in their blood survived multiple exposures to 2 to $5 \times \text{LD}_{50}$ doses of G-type CWNAs to include GD, GF, GB, and GA over a 7-week period. However, few issues must be resolved before this approach can be adopted to soldiers, medical personnel, and agricultural workers. Long-term safety associated with a large-dose infusion of AAV8 vectors in healthy humans is not known. Moreover, each recipient may respond differently to AAV8 and produce differing amounts recombinant PON1-IF11 in their blood. Whether recombinant PON1-IF11 expression is for the life term of the animal and, if a second injection is required, would maintain similar therapeutic concentrations of PON1-IF11 in the animal remains to be investigated. These studies need to be repeated in large animal models, preferably nonhuman primates and dogs, and the results from these large animal models would be helpful to evaluate the application of AAV8-TBG-PON1-IF11 vectored gene therapy approach for soldiers, medical personnel, agricultural workers, and working dogs in combat zones.

MATERIALS AND METHODS

Study design

The main objective of the present study was to test a gene therapy approach as a viable one-time prophylactic treatment option for an effective, long-term protection of humans and animals against

CWNAs, a class of weapons of mass destruction. We used a non-pathogenic, relatively safe, and liver-specific AAV8 to deliver a candidate catalytic bioscavenger, namely, PON1-IF11, to the mouse bloodstream. The abundant expression and G-type CWNA hydrolysis potential of circulating PON1-IF11 was evaluated by substrate hydrolysis assays, Western blotting, and G-type CWNA hydrolysis assays in vitro. The study was then followed up evaluating the therapeutic potential of PON1-IF11 in vivo. This was done by exposing mice containing different concentrations of PON1-IF11 in their blood to lethal dosages of G-type CWNAs to include GD, GF, GB, and GA repeatedly over an 8-week period. Last, animal health and physiology were also assessed by studying hematology profiles, serum chemistry parameters, and histological evaluations. The experimental protocol was approved by the Animal Care and Use Committee of the U.S. Army Medical Research Institute of Chemical Defense (USAMRICD), Aberdeen Proving Ground, MD, and all procedures were conducted in accordance with the principles stated in the *Guide for the Care and Use of Laboratory Animals* (National Research Council) and the Animal Welfare Act of 1966 (P.L. 89-544), as amended. Oak Ridge Institute for Science and Education (ORISE) participant L.S. was supported by an appointment to the Internship/Research participation program for the USAMRICD, administered by the ORISE through an agreement between the U.S. Department of Energy and the U.S. Army Medical Research and Materiel Command.

AAV8 vector construction and preparation

PON1-IF11 was codon-harmonized for mammalian cell expression and cloned into pENT-CMV adenoviral transfer vector (43). PON1-IF11 gene from pENT-CMV adenoviral vector was then cloned into AAV8 shuttle plasmid containing three different types of promoters: TBG (AAV8-TBG-PON1-IF11), synthetic CASI promoter (AAV8-CASI-PON1-IF11) (27), and CMV (AAV8-CMV-PON1-IF11). The AAV8 vector used with the CMV promoter was a self-complementary type (44). Production, amplification, and purification of AAV8-CASI-PON1-IF11 and AAV8-CMV-PON1-IF11 vectors were performed by Welgen Inc. (Worcester, MA). Production, amplification, and purification of AAV8-TBG-PON1-IF11 vectors were done by Vector Core Inc. (University of Pennsylvania Gene Therapy Center, Philadelphia, PA). Routine quality control tests included determination of titer and yield by quantitative polymerase chain reaction and endotoxin concentrations in the vector preparations.

Animal experiments

The experimental protocol was approved by the Animal Care and Use Committee of the USAMRICD, Aberdeen Proving Ground, MD, and all procedures were conducted in accordance with the principles stated in the *Guide for the Care and Use of Laboratory Animals* (National Research Council) and the Animal Welfare Act of 1966 (P.L. 89-544), as amended. Adult male mice (25 to 30 g body weight/Swiss Webster/Charles River Laboratories) were housed at 20° to 26°C and provided food and water ad libitum. Mice were given 100 to 200 μl of phosphate-buffered saline (PBS) containing 5×10^{13} to 9.7×10^{13} GC/ml of either AAV8-PON1-IF11 or control AAV8 (lacking the PON1-IF11 gene) through tail vein injections. Blood (25 to 50 μl) was drawn at various time points after virus injection, collected into heparin-coated tubes, and centrifuged at 3000 rpm for 10 min at 4°C. The plasma was removed and diluted 10-fold with PBS. This diluted plasma sample was used in the

enzyme activity assays; SDS-PAGE gel electrophoresis; Western blotting; *in vitro* GA, GB, GD, and GF hydrolysis assays; and ELISA to measure antibody concentrations against PON1-IF11. Plasma samples obtained from mice injected with control vector (AAV8 vector) were prepared similarly. In some experiments, the AAV8-PON1-IF11 and control vector particles were administered intramuscularly. Mice were given 50 μ l of PBS containing 5×10^{12} GC of AAV8 vector particles through intramuscular injections at the caudal thigh muscle. Blood (25 to 50 μ l) was drawn 27 days after virus injection, collected into heparin-coated tubes, and centrifuged at 3000 rpm for 10 min at 4°C. The plasma was removed and diluted 10-fold with PBS, and an aliquot was assayed for PON1 activity.

PON1 enzyme assay

PON1 enzyme activity was determined in a 96-well format on a SpectraMax M5 (Molecular Devices) series spectrophotometer as described by Mata *et al.* (23). Briefly, PON1 activity was measured in a total of 200 μ l of assay buffer [50 mM tris-HCl (pH 7.4) and 10 mM CaCl₂] carrying 1 μ l of plasma sample and 2.5 μ M methyl paraoxon (catalog no. N-12816, Chem Service Inc., West Chester, PA). The formation of yellow-colored *p*-nitrophenol was followed at A₄₀₅ ($\epsilon = 17,000 \text{ M cm}^{-1}$) for 30 min at room temperature (43). Known concentrations of paraoxon were tested simultaneously to prepare a standard curve, which was used to calculate the concentration of PON1-IF11 in mouse plasma samples.

SDS-PAGE and Western blotting

SDS-PAGE of plasma samples was performed on precast 4 to 20% tris-glycine gels (Thermo Fisher Scientific), and proteins were transferred to nitrocellulose membrane using IBlot gel transfer apparatus (Invitrogen, CA). The membrane was blocked in a blocking buffer (LI-COR Inc.) for 2 hours at 24°C, rinsed once with wash buffer [20 mM tris-HCl (pH 7.4), 137 mM NaCl, 2.7 mM KCl, and 0.01% Tween 20], and incubated overnight in blocking buffer containing anti-PON1 antibody (catalog no. P0123, Sigma-Aldrich) (1:20,000 dilution). The membrane was then washed five times with intermittent shaking for 5 min and incubated with secondary antibody conjugated with infrared dye 680 (LI-COR Inc.; 1:10,000 dilution) made in blocking buffer for 1 hour, and protein bands were detected using Infrared Imager (LI-COR Inc.). A duplicate gel blot was similarly processed using anti-mouse serum albumin antibody (catalog no. ab19194, Abcam).

Hydrolysis of G-type CWNAs *in vitro*

The ability of AAV8-TBG-PON1-IF11 vector-produced recombinant PON1-IF11 protein in mouse blood to hydrolyze GA, GB, GD, and GF was determined by performing an indirect colorimetric micro-Ellman assay (28). Day 21 plasma samples from mice injected with AAV8-TBG-PON1-IF11 and control vectors were used to measure GA, GB, GF, and GD hydrolysis rates. The hydrolysis of each nerve agent (0.5 μ M) was performed in a 200- μ l assay buffer [100 mM Mops (pH 8.0) and 10 mM CaCl₂] using 8 ml of plasma (diluted 1:10). After incubating for 30 min at room temperature, 20 μ l of the reaction mixture was directly added to 280 μ l of AChE assay buffer [50 mM phosphate buffer (pH 7.4), 150 mM NaCl, 2 mM DTNB (catalog no. D8130, Sigma-Aldrich), and 2 mM ATC (catalog no. A5751, Sigma-Aldrich)] consisting of 10 μ l of the recombinant human AChE (final concentration, 0.3 U/ μ l). The formation of the yellow-colored product 5-thio-nitrobenzoic acid was followed

for 30 min by monitoring the absorbance at 412 nm using a plate reader. To interpret the results of this assay, the assay was also performed with AChE alone, and control plasma samples were spiked with 0.1, 0.2, 0.5, 1.0, and 2.0 μ g of purified bacterial PON1-IF11.

Enzyme-linked immunosorbent assay

The presence of circulating antibodies in mouse blood against PON1-IF11 was determined by performing ELISA in a 96-well plate. Each well was incubated with 100 μ l of 0.1 M sodium carbonate buffer (pH 9.6) carrying purified bacterial PON1-IF11 (5 μ g/ml) overnight at 4°C, and the unbound antigen was removed by washing wells with 200 μ l of TBST [15 mM tris-HCl buffer (pH 8.0), 0.15 M NaCl, 0.05% Tween 20] for three times. The remaining antibody-binding sites of the wells were blocked by incubating with 200 μ l of blocking buffer (TBST carrying 3% bovine serum albumin) for 2 hours at 24°C. After a quick rinse with TBST, 200 μ l of antibody-binding buffer (plasma samples diluted to 100- to 3200-fold in TBST containing 1% bovine serum albumin) was added to each well and incubated overnight at 4°C. Antibody-binding buffer was discarded, and wells were washed five times, each time for 3 min, with 200 μ l of TBST. The wells were then incubated with 100 μ l of TBST containing horseradish peroxidase-conjugated anti-mouse immunoglobulin G (Sigma-Aldrich) and incubated for 90 min at room temperature. The solution was discarded, and the wells were washed with TBST for five times. The wells were then incubated with SuperSignal ELISA Pico Chemiluminescent Substrate (catalog no. 37069, Thermo Fisher Scientific), and the absorbance was measured at 425 nm in an endpoint mode.

Animal exposure experiments to GD (soman), GF (cyclosarin), GB (sarin), and GA (tabun)

Mice were transduced with AAV8-TBG-PON1-IF11 vector particles ($n = 17$; 8×10^{12} to 9×10^{12} GC per mouse) as described under animal experiments. The expression of PON1-IF11 was studied in mouse circulation by performing a paraoxon hydrolysis assay *in vitro*. On day 21, the animals were challenged with a dosage of $5 \times \text{LD}_{50}$ GD (1 $\text{LD}_{50} = 124 \mu\text{g/kg}$ body weight) and observed continuously for 1 hour for cholinergic signs (tremors). G-type agents were injected subcutaneously as a 50- μ l inoculum between the shoulders or over the neck of the animal. Any moribund mice were euthanized immediately. Animals that survived the dosage of $5 \times \text{LD}_{50}$ GD were challenged 1 day later with a dosage of $5 \times \text{LD}_{50}$ GF (240 $\mu\text{g/kg}$ body weight). All animals that survived GF challenge were challenged 3 days later with a dosage of $5 \times \text{LD}_{50}$ GB (170 $\mu\text{g/kg}$ body weight), and the animals were observed similarly for tremors and survival rates. Animals that survived GB challenge few days later were challenged with dosage of $5 \times \text{LD}_{50}$ GA (270 $\mu\text{g/kg}$ body weight), and the animals were observed for cholinergic signs as described above. These challenge experiments were repeated in the same order with a dosage of $5 \times \text{LD}_{50}$ of all four G-type nerve agents. Last, all the surviving animals were exposed to a total dosage of $6 \times \text{LD}_{50}$ of a mixture of all four G-type nerve agents (a dosage of $1.5 \times \text{LD}_{50}$ each), and animals were observed for tremors and 24-hour survival rates. Thus, over a 42-day period, the same animals were exposed eight times to a dosage of $5 \times \text{LD}_{50}$ of each G-type nerve agent and once to a dosage of $6 \times \text{LD}_{50}$ mixture of all four G-type agents. Before each challenge experiment, the toxic potency of the G-type nerve agents was confirmed by testing on one or two naive mice.

In some experiments, the animals were transduced with a low dose (1×10^9 to 1×10^{12} GC per mouse) of the AAV8-TBG-PON1-IF11 vector via the tail vein injections ($n = 20$). The day before challenging the animals to a G-type nerve agent, plasma was collected and assayed for PON1-IF11 concentration. The animals were exposed to a dosage of 2 to $5 \times LD_{50}$ all four G-type nerve agents and observed for cholinergic signs as described above. Moribund mice were euthanized immediately. Mice that survived nerve agent challenge were exposed to a higher dose of the same or different G-type nerve agents after 24 hours. Thus, mice were exposed to a dosage of 2, 3, 4, and $5 \times LD_{50}$ of each of the four G-type nerve agents to obtain a therapeutic concentration of PON1-IF11 in the circulation.

Mouse serum chemistry, hematology, and necropsy

Mice containing recombinant PON1-IF11 in their bloodstreams for over 150 days ($n = 3$; enzyme concentration range, 1 to 1.5 mg/ml through 5-month duration), animals that have been exposed repeatedly to $5 \times LD_{50}$ dosages of all four G-type nerve agents, and age-matched controls were euthanized, their blood samples were collected, and serum chemistry profiles (Ortho Clinical Diagnostics, VITROS 4600 Chemistry System) and hematology parameters (Sysmex XT-2000i Automated Hematology Analyzer) were determined.

A complete necropsy was performed using a full set of tissues including brain, liver, heart, diaphragm, kidney, pancreas, lung, urinary bladder, prostate gland, epididymis, and skeletal muscle for any gross or histological changes. The slides were processed by trained technicians and read by board-certified veterinary pathologists.

Statistical analysis

Statistical analysis was performed using one-way analysis of variance (ANOVA) using GraphPad Prism (v.7), and data were reported as means \pm SEM with significance defined as $P < 0.05$.

SUPPLEMENTARY MATERIALS

stm.sciencemag.org/cgi/content/full/12/527/eaay0356/DC1

Fig. S1. Circular maps of AAV8 plasmid expression vectors carrying PON1-IF11 under tissue-specific promoters.

Fig. S2. SDS-PAGE analysis of the purified AAV8-PON1-IF11 viral particles.

Table S1. Concentration of PON1-IF11 in mouse blood on days 17 and 42 after AAV8-TBG-PON1-F11 injection.

Table S2. PON1-IF11 concentration in mouse plasma required to afford protection against GD and GF.

Table S3. PON1-IF11 concentration in mouse plasma required to afford protection against GB and GA.

[View/request a protocol for this paper from Bio-protocol.](#)

REFERENCES AND NOTES

- S. Costanzi, J.-H. Machado, M. Mitchell, Nerve agents: What they are, how they work, how to counter them. *ACS Chem. Neurosci.* **9**, 873–885 (2018).
- R. Stone, Weapons in waiting. *Science* **359**, 24 (2018).
- P. Gee, Chemical weapons are intentionally deployed against the most vulnerable groups of people. *BMJ* **361**, k1672 (2018).
- L. Shang, M. Crowley, M. Dando, Act now to close chemical-weapons loophole. *Nature* **562**, 344 (2018).
- C. M. Timperley, M. Abdollahi, A. S. Al-Amri, A. Baulig, D. Benachour, V. Borrett, F. A. Cariño, M. Geist, D. Gonzalez, W. Kane, Z. Kovarik, R. Martínez-Álvarez, N. M. Fusaro Mourão, S. Neffe, S. K. Raza, V. Rubaylo, A. Graciela Suárez, K. Takeuchi, C. Tang, F. Trifirò, F. M. van Straten, P. S. Vanninen, S. Vučinić, V. Zaitsev, M. Zafar-Uz-Zaman, M. S. Zina, S. Holen, J. E. Forman, W. S. Alwan, V. Suri, Advice on assistance and protection from the Scientific Advisory Board of the Organisation for the Prohibition of Chemical Weapons: Part 2. On preventing and treating health effects from acute, prolonged, and repeated nerve agent exposure, and the identification of medical countermeasures able to reduce or eliminate the longer term health effects of nerve agents. *Toxicology* **413**, 13–23 (2019).
- M. Schwenk, Chemical warfare agents. Classes and targets. *Toxicol. Lett.* **293**, 253–263 (2018).
- M. Williams, D. C. Sizemore, in *StatPearls* (StatPearls Publishing StatPearls Publishing LLC, 2018).
- M. Crowley, L. Shang, M. Dando, Preventing chemical weapons as sciences converge. *Science* **362**, 753–755 (2018).
- R. Stone, Chemical martyrs. *Science* **359**, 20–25 (2018).
- M. Eddleston, N. A. Buckley, P. Eyer, A. H. Dawson, Management of acute organophosphorus pesticide poisoning. *Lancet* **371**, 597–607 (2008).
- M. Moshiri, E. Darchini-Maragheh, M. Balali-Mood, Advances in toxicology and medical treatment of chemical warfare nerve agents. *Daru* **20**, 81 (2012).
- K. Candioti, A primer on nerve agents: What the emergency responder, anesthesiologist, and intensivist needs to know. *Can. J. Anaesth.* **64**, 1059–1070 (2017).
- M. Jokanović, Medical treatment of acute poisoning with organophosphorus and carbamate pesticides. *Toxicol. Lett.* **190**, 107–115 (2009).
- L. Gorecki, J. Korabecny, K. Musilek, E. Nepovimova, D. Malinak, T. Kucera, R. Dolezal, D. Jun, O. Soukup, K. Kuca, Progress in acetylcholinesterase reactivators and in the treatment of organophosphorus intoxication: A patent review (2006–2016). *Expert Opin. Ther. Pat.* **27**, 971–985 (2017).
- R. F. White, L. Steele, J. P. O'Callaghan, K. Sullivan, J. H. Binns, B. A. Golomb, F. E. Bloom, J. A. Bunker, F. Crawford, J. C. Graves, A. Hardie, N. Klimas, M. Knox, W. J. Meggs, J. Melling, M. A. Philibert, R. Grashow, Recent research on Gulf War illness and other health problems in veterans of the 1991 Gulf War: Effects of toxicant exposures during deployment. *Cortex* **74**, 449–475 (2016).
- A. R. Iyengar, A. H. Pande, Organophosphate-hydrolyzing enzymes as first-line of defence against nerve agent-poisoning: Perspectives and the road ahead. *Protein J.* **35**, 424–439 (2016).
- Y. Ashani, H. Leader, N. Aggarwal, I. Silman, F. Worek, J. L. Sussman, M. Goldsmith, In vitro evaluation of the catalytic activity of paraoxonases and phosphotriesterases predicts the enzyme circulatory levels required for in vivo protection against organophosphate intoxications. *Chem. Biol. Interact.* **259**, 252–256 (2016).
- X. Brazzolotto, A. Iger, V. Guillon, G. Santoni, F. Nachon, Bacterial expression of human butyrylcholinesterase as a tool for nerve agent bioscavengers development. *Molecules* **22**, E1828 (2017).
- B. A. Reed, C. L. Sabourin, D. E. Lenz, Human butyrylcholinesterase efficacy against nerve agent exposure. *J. Biochem. Mol. Toxicol.* **31**, e21886 (2017).
- S. V. Lushchekina, L. M. Schopfer, B. L. Grigorenko, A. V. Nemukhin, S. D. Varfolomeev, O. Lockridge, P. Masson, Optimization of cholinesterase-based catalytic bioscavengers against organophosphorus agents. *Front. Pharmacol.* **9**, 211 (2018).
- P. Zhang, F. Sun, S. Liu, S. Jiang, Anti-PEG antibodies in the clinic: Current issues and beyond PEGylation. *J. Control. Release* **244**, 184–193 (2016).
- I. V. Smirnov, I. I. Vorobiev, A. A. Belogurov, D. D. Genkin, S. M. Deyev, A. G. Gabibov, Chemical polysialylation of recombinant human proteins. *Methods Mol. Biol.* **1321**, 389–404 (2015).
- D. G. Mata, P. Sabnekar, C. A. Watson, P. E. Rezk, N. Chilukuri, Assessing the stoichiometric efficacy of mammalian expressed paraoxonase-1 variant I-F11 to afford protection against G-type nerve agents. *Chem. Biol. Interact.* **259**, 233–241 (2016).
- P. Zhang, E. J. Liu, C. Tsao, S. A. Kasten, M. V. Boeri, T. L. Dao, S. J. DeBus, C. L. Cadieux, C. A. Baker, T. C. Otto, D. M. Cerasoli, Y. Chen, P. Jain, F. Sun, W. Li, H.-C. Hung, Z. Yuan, J. Ma, A. N. Bignley, F. M. Rauschel, S. Jiang, Nanoscavenger provides long-term prophylactic protection against nerve agents in rodents. *Sci. Transl. Med.* **11**, eaay7091 (2019).
- E. G. Duysen, K. Parikh, V. Aleti, V. Manne, O. Lockridge, N. Chilukuri, Adenovirus-mediated human paraoxonase1 gene transfer to provide protection against the toxicity of the organophosphorus pesticide toxicant diazoxon. *Gene Ther.* **18**, 250–257 (2011).
- G. Gao, Y. Lu, R. Calcedo, R. L. Grant, P. Bell, L. Wang, J. Figueredo, M. Lock, J. M. Wilson, Biology of AAV serotype vectors in liver-directed gene transfer to nonhuman primates. *Mol. Ther.* **13**, 77–87 (2006).
- A. B. Balazs, J. Chen, C. M. Hong, D. S. Rao, L. Yang, D. Baltimore, Antibody-based protection against HIV infection by vectored immunoprophylaxis. *Nature* **481**, 81–84 (2011).
- G. L. Ellman, K. D. Courtney, V. Andres Jr., R. M. Featherstone, A new and rapid colorimetric determination of acetylcholinesterase activity. *Biochem. Pharmacol.* **7**, 88–95 (1961).
- M. Goldsmith, Y. Ashani, Y. Simo, M. Ben-David, H. Leader, I. Silman, J. L. Sussman, D. S. Tawfik, Evolved stereoselective hydrolases for broad-spectrum G-type nerve agent detoxification. *Chem. Biol.* **19**, 456–466 (2012).
- D. A. Jett, S. M. Spriggs, Translational research on chemical nerve agents. *Neurobiol. Dis.* **133**, 104335 (2020).
- D. A. Jett, The NIH countermeasures against chemical threats program: Overview and special challenges. *Ann. N. Y. Acad. Sci.* **1374**, 5–9 (2016).

32. N. Chilukuri, K. Parikh, W. Sun, R. Naik, P. Tipparaju, B. P. Doctor, A. Saxena, Polyethylene glycosylation prolongs the circulatory stability of recombinant human butyrylcholinesterase. *Chem. Biol. Interact.* **157-158**, 115–121 (2005).
33. K. Parikh, E. G. Duysen, B. Snow, N. S. Jensen, V. Manne, O. Lockridge, N. Chilukuri, Gene-delivered butyrylcholinesterase is prophylactic against the toxicity of chemical warfare nerve agents and organophosphorus compounds. *J. Pharmacol. Exp. Ther.* **337**, 92–101 (2011).
34. L. Geng, Y. Gao, X. Chen, S. Hou, C.-G. Zhan, Z. Radic, R. J. Parks, S. J. Russell, L. Pham, S. Brimjoin, Gene transfer of mutant mouse cholinesterase provides high lifetime expression and reduced cocaine responses with no evident toxicity. *PLOS ONE* **8**, e67446 (2013).
35. A. R. Mawson, A. M. Croft, Gulf war illness: Unifying hypothesis for a continuing health problem. *Int. J. Environ. Res. Public Health* **16**, E111 (2019).
36. A. D. Wolfe, D. W. Blick, M. R. Murphy, S. A. Miller, M. K. Gentry, S. L. Hartgraves, B. P. Doctor, Use of cholinesterases as pretreatment drugs for the protection of rhesus monkeys against soman toxicity. *Toxicol. Appl. Pharmacol.* **117**, 189–193 (1992).
37. M. I. Mackness, B. Mackness, P. N. Durrington, A. M. Fogelman, J. Berliner, A. J. Lusis, M. Navab, D. Shih, G. C. Fonarow, Paraoxonase and coronary heart disease. *Curr. Opin. Lipidol.* **9**, 319–324 (1998).
38. C. E. Dunbar, K. A. High, J. K. Joung, D. B. Kohn, K. Ozawa, M. Sadelain, Gene therapy comes of age. *Science* **359**, eaan4672 (2018).
39. H. Ameri, Prospect of retinal gene therapy following commercialization of voretigene neparvovec-rzyl for retinal dystrophy mediated by RPE65 mutation. *J. Curr. Ophthalmol.* **30**, 1–2 (2018).
40. X. Pei, T. He, N. E. Hall, D. Gerber, R. JudeSamulski, C. Li, AAV8 virions hijack serum proteins to increase hepatocyte binding for transduction enhancement. *Virology* **518**, 95–102 (2018).
41. B. T. Assaf, L. O. Whiteley, Considerations for preclinical safety assessment of adeno-associated virus gene therapy products. *Toxicol. Pathol.* **46**, 1020–1027 (2018).
42. A. C. Nathwani, A. M. Davidoff, E. G. D. Tuddenham, Gene therapy for hemophilia. *Hematol. Oncol. Clin. North Am.* **31**, 853–868 (2017).
43. D. G. Mata, P. E. Rezk, P. Sabnekar, D. M. Cerasoli, N. Chilukuri, Investigation of evolved paraoxonase-1 variants for prevention of organophosphorous pesticide compound intoxication. *J. Pharmacol. Exp. Ther.* **349**, 549–558 (2014).
44. A. C. Nathwani, E. G. D. Tuddenham, S. Rangarajan, C. Rosales, J. McIntosh, D. C. Linch, P. Chowdary, A. Riddell, A. J. Pie, C. Harrington, J. O'Beirne, K. Smith, J. Pasi, B. Glader, P. Rustagi, C. Y. C. Ng, M. A. Kay, J. Zhou, Y. Spence, C. L. Morton, J. Allay, J. Coleman, S. Sleep, J. M. Cunningham, D. Srivastava, E. Basner-Tschakarjan, F. Mingozzi, K. A. High, J. T. Gray, U. M. Reiss, A. W. Nienhuis, A. M. Davidoff, Adenovirus-associated virus vector-mediated gene transfer in hemophilia B. *N. Engl. J. Med.* **365**, 2357–2365 (2011).
- Acknowledgments:** We thank the veterinary staff for their support in maintaining animals in good health, members of the graphics group for creating artwork figures, and A. McGuire, Deputy Director of Research, USAMRICD, for suggestions over the manuscript. The views expressed in this article are those of the author(s) and do not reflect the official policy of the Department of Army, Department of Defense, or the U.S. Government. ORISE participant L.S. was supported by an appointment to the Internship/Research participation program for the USAMRICD, administered by ORISE through an agreement between the U.S. Department of Energy and the U.S. Army Medical Research and Materiel Command. **Funding:** This research work was supported by the Defense Threat Reduction Agency (DTRA) (CB3945), Joint Science and Technology Office, Medical S&T Division, Department of the Army. **Author contributions:** V.B. designed and performed experiments, collected and analyzed data, and wrote the manuscript. R.G. performed ELISA. L.S. assisted in injecting viral particles, collecting blood samples, and exposing animals to nerve agents. D.M.D. ordered reagents and assisted in nerve agent exposure studies. N.C. initiated the gene therapy concept, designed experiments, assisted in collecting blood samples and exposing animals to nerve agents, and wrote and edited the manuscript. **Competing interests:** V.B. and N.C. have a patent application for use of the present method to offer prophylactic protection against nerve gases (U.S. patent no. PCT/US2018/023746, titled "A method developing and employing recombinant adeno-associated virus-F11 particles for prophylactic protection against G-type chemical warfare nerve agents"). The other authors declare that they have no competing interests. **Data and materials availability:** All the data are present in the main text or in the Supplementary Materials.

Submitted 16 May 2019
 Resubmitted 19 August 2019
 Accepted 13 November 2019
 Published 22 January 2020
 10.1126/scitranslmed.aay0356

Citation: V. Betapudi, R. Goswami, L. Silayeva, D. M. Doctor, N. Chilukuri, Gene therapy delivering a paraoxonase 1 variant offers long-term prophylactic protection against nerve agents in mice. *Sci. Transl. Med.* **12**, eaay0356 (2020).